

Cassini/MIMI Instrument Data User Guide

Jon Vandegriff¹

Robert DiFabio³, Doug Hamilton³, Martha Kusterer¹,
Jerry Manweiler⁴, Donald Mitchell¹, Chris Paranicas¹,
Elias Roussos², David LaVallee¹

¹*Johns Hopkins University Applied Physics Lab*

²*Max Planck Institute for Solar System Research* ³*University of Maryland*

⁴*Fundamental Technologies, Inc.*

September 26, 2018

Contents

1	Background and General Info	9
1.1	Instrument Overview	9
1.2	Science Objectives	10
1.3	Terminology	10
1.4	Data Product Overview	11
1.5	Calibration Documentation	18
1.6	File Formats	19
1.7	Data Time Stamps	21
1.8	Data Collection Strategies	22
1.9	Generic instrument and data issues	22
2	Calibration Overview	24
2.1	MIMI calibration files	24
2.2	Format of the primary MIMI calibration file	24
2.3	Example usage of the primary MIMI calibration file	29
2.4	INCA flat fielding calibration files	30
2.5	Use of SPICE for trajectory and orientation	30
3	LEMMS	31
3.1	The LEMMS Telescopes	31
3.1.1	LEMMS LET	31
3.1.2	LEMMS HET	33
3.1.3	LEMMS Turntable and Orientation	33
3.2	LEMMS Data Products	35
3.2.1	Normal Accumulator Rates	35
3.2.2	Fine Accumulator Rates	36
3.2.3	PHA Data	39
3.3	Calibrating LEMMS Normal Accumulator Rates	41
3.4	Calibrating LEMMS Fine Accumulator Rates	43
3.5	Calibrating LEMMS PHA Data	44
3.6	Sample Plots and Interpretation for Commonly Used LEMMS Channels	47
4	CHEMS	68
4.1	Principles of Operation	68
4.2	CHEMS Data Products	70
4.2.1	CHEMS Accumulator Rates	72
4.2.2	CHEMS PHA Data	72

4.2.3	CHEMS Science Rates	74
4.3	Calibrating CHEMS Accumulator Rates	75
4.4	Calibrating CHEMS Science Rates	75
4.4.1	Counts per Second	75
4.4.2	Differential Intensity	75
4.5	Calibrating the PHA data	78
4.6	Understanding the PHA Species Boxes	86
4.7	CHEMS PHA Species Box Background Issues	96
5	INCA	105
5.1	Overview	105
5.2	INCA Images	107
5.3	INCA Accumulator Rates	108
5.4	INCA PHA Events	108
5.5	End-to-End Examples for INCA ACC and PHA Data	111
5.6	INCA Image Data Files	117
5.7	End-to-End Example for INCA Images	117
5.8	Features in INCA Data	142
6	Obtaining Calibrated Data	166
6.1	Data Download Tool	166
6.2	INCA IDL Routines	168
6.3	MIMI Analysis Tools - MIDL	168
6.3.1	Line Plots	169
6.3.2	Spectrograms	172
6.3.3	Pitch Angle Plots	173
A	SPICE Usage on MIMI	180
B	MIMI Data Gaps	181
C	Auxiliary Data Files: MIMI Stare/Spin Time Ranges	182
D	CHEMS Data Used to Define the PHA Species Boxes	183
D.1	Magnetospheric Data	183
D.2	Interplanetary Data	214
E	CHEMS PHA Species Box Definitions	225
F	CHEMS Efficiencies	243
G	INCA MCP Efficiencies	259

List of Figures

1.1	Data Directories at the PDS	12
1.2	Directory Structure for MIMI PDS Products	13
1.3	Standard File Header and Data Line Prefix	21
3.1	LEMMS Schematic	32
3.2	LEMMS Photograph and Engineering Diagram	32
3.3	LEMMS Orientation and Rotation	34
3.4	LEMMS Fixed Orientation	35
3.5	Magnetospheric regions in LEMMS rate channel data	48
3.6	Average LEMMS rate channel data (electrons)	49
3.7	Average LEMMS rate channel data (ions)	50
3.8	Magnetospheric regions in LEMMS PHA-channel data	51
3.9	Energetic electron microsignatures in PHA-channel data	52
3.10	Energetic electron microsignatures and Cassini rotations	53
3.11	Energetic proton macrosignatures and transient belts	54
3.12	LEMMS rotation	55
3.13	LEMMS priority	56
3.14	LEMMS priority PAD	57
3.15	LEMMS ion spectra belts	58
3.16	LEMMS electron spectra ring current	59
3.17	LEMMS ion spectra ring current	60
3.18	LEMMS electron spectra belts	61
3.19	LEMMS gring	62
3.20	LEMMS SW	63
3.21	LEMMS Conics	64
3.22	LEMMS Periodicities	65
3.23	LEMMS light	66
3.24	LEMMS light	67
4.1	CHEMS Look Directions	69
4.2	CHEMS Schematic	69
4.3	Basic and Species Rates Ranges in mass vs mass/charge.	74
4.4	CHEMS Doubles 1-D histogram Example	87
4.5	CHEMS Triples 2-D histogram Example	88
4.6	CHEMS H_2^+ Background Problems	92
4.7	CHEMS H_2^+ M=2 to M=1 Counts Ratios	92
4.8	CHEMS M/Q = 2 amu/e histograms of He^{++} and H_2^+	93
4.9	CHEMS M/Q = 2 amu/e histograms of He^{++} and H_2^+	94

4.10	CHEMS Bogus TOF Channels	98
4.11	CHEMS Bogus TOF Channels	99
4.12	CHEMS PHA Species Trail Contamination for DPPS 30 and 31	102
4.13	CHEMS Wide TOF Causes Double Peak	103
5.1	INCA Photograph	105
5.2	INCA Field of View	106
5.3	INCA Image File Layout	119
5.4	INCA Image Read Example Plot	127
5.5	The INCA motion compensation process.	141
5.6	INCA Plasmoids in Saturn’s Magnetotail.	142
5.7	Hot Plasma Ions	143
5.8	MIMI INCA and UVIS Auroral Images	144
5.9	Saturn ENA Emission Shows Rotation of Peak Emission	145
5.10	ENA Emission Covering Full Saturn Rotation	146
5.11	Ring Current Image	147
5.12	Another Ring Current Image	148
5.13	Intense Hydrogen Emission	149
5.14	ENA Image of Titan’s Exosphere	150
5.15	Titan Energetic Hydrogen Images	151
5.16	Titan ENA Hydrogen Flux	152
5.17	ENA Emission at Titan	153
5.18	Field-aligned Ion Beam	154
5.19	Long Duration Field-aligned Ion Beams	155
5.20	Antiplanetward field-aligned Ion Conic and Bidirectional Electron Beam	156
5.21	Ion Beams with Pitch Angle Contours	157
5.22	Saturated Count Rates	158
5.23	High Edge Pixel Image	159
5.24	High Edge Pixel Image 2	160
5.25	Oxygen Contamination of Hydrogen Image	161
5.26	Electron Background in Ion Image	162
5.27	SSR Bit Errors 1	163
5.28	SSR Bit Errors 2	164
5.29	Sun Contamination	165
6.1	Data Download Tool	167
6.2	MIDL Screen Shot	168
6.3	MIDL Particle Line Plot Tool	170
6.4	Line Plot Settings Panels	170
6.5	MIDL Energy Spectrogram Plotter	172
6.6	MIDL Interactive Pitch Angle Plotter	173
6.7	MIDL Pitch Angle Spectrogram Plotter	174
6.8	Typical Post-Stuck MIDL Pitch Angle Spectrogram Plot	174
D.1	CHEMS Magnetospheric TOF histogram for DPPS step 0	184
D.2	CHEMS Magnetospheric TOF histogram for DPPS step 1	184
D.3	CHEMS Magnetospheric TOF histogram for DPPS step 2	185
D.4	CHEMS Magnetospheric TOF histogram for DPPS step 3	185

D.5	CHEMS Magnetospheric TOF histogram for DPPS step 4	186
D.6	CHEMS Magnetospheric TOF histogram for DPPS step 5	186
D.7	CHEMS Magnetospheric TOF histogram for DPPS step 6	187
D.8	CHEMS Magnetospheric TOF histogram for DPPS step 7	187
D.9	CHEMS Magnetospheric TOF histogram for DPPS step 8	188
D.10	CHEMS Magnetospheric TOF histogram for DPPS step 9	188
D.11	CHEMS Magnetospheric TOF histogram for DPPS step 10	189
D.12	CHEMS Magnetospheric TOF histogram for DPPS step 11	189
D.13	CHEMS Magnetospheric TOF histogram for DPPS step 12	190
D.14	CHEMS Magnetospheric TOF histogram for DPPS step 13	190
D.15	CHEMS Magnetospheric TOF histogram for DPPS step 14	191
D.16	CHEMS Magnetospheric TOF histogram for DPPS step 15	191
D.17	CHEMS Magnetospheric TOF histogram for DPPS step 16	192
D.18	CHEMS Magnetospheric TOF histogram for DPPS step 17	192
D.19	CHEMS Magnetospheric TOF histogram for DPPS step 18	193
D.20	CHEMS Magnetospheric TOF histogram for DPPS step 19	193
D.21	CHEMS Magnetospheric E versus TOF histogram for DPPS step 12	194
D.22	CHEMS Magnetospheric E versus TOF histogram for DPPS step 13	195
D.23	CHEMS Magnetospheric E versus TOF histogram for DPPS step 14	196
D.24	CHEMS Magnetospheric E versus TOF histogram for DPPS step 15	197
D.25	CHEMS Magnetospheric E versus TOF histogram for DPPS step 16	198
D.26	CHEMS Magnetospheric E versus TOF histogram for DPPS step 17	199
D.27	CHEMS Magnetospheric E versus TOF histogram for DPPS step 18	200
D.28	CHEMS Magnetospheric E versus TOF histogram for DPPS step 19	201
D.29	CHEMS Magnetospheric E versus TOF histogram for DPPS step 20	202
D.30	CHEMS Magnetospheric E versus TOF histogram for DPPS step 21	203
D.31	CHEMS Magnetospheric E versus TOF histogram for DPPS step 22	204
D.32	CHEMS Magnetospheric E versus TOF histogram for DPPS step 23	205
D.33	CHEMS Magnetospheric E versus TOF histogram for DPPS step 24	206
D.34	CHEMS Magnetospheric E versus TOF histogram for DPPS step 25	207
D.35	CHEMS Magnetospheric E versus TOF histogram for DPPS step 26	208
D.36	CHEMS Magnetospheric E versus TOF histogram for DPPS step 27	209
D.37	CHEMS Magnetospheric E versus TOF histogram for DPPS step 28	210
D.38	CHEMS Magnetospheric E versus TOF histogram for DPPS step 29	211
D.39	CHEMS Magnetospheric E versus TOF histogram for DPPS step 30	212
D.40	CHEMS Magnetospheric E versus TOF histogram for DPPS step 31	213
D.41	CHEMS Interplanetary TOF histogram for DPPS step 0	215
D.42	CHEMS Interplanetary TOF histogram for DPPS step 1	215
D.43	CHEMS Interplanetary TOF histogram for DPPS step 2	216
D.44	CHEMS Interplanetary TOF histogram for DPPS step 3	216
D.45	CHEMS Interplanetary TOF histogram for DPPS step 4	217
D.46	CHEMS Interplanetary TOF histogram for DPPS step 5	217
D.47	CHEMS Interplanetary TOF histogram for DPPS step 6	218
D.48	CHEMS Interplanetary TOF histogram for DPPS step 7	218
D.49	CHEMS Interplanetary TOF histogram for DPPS step 8	219
D.50	CHEMS Interplanetary TOF histogram for DPPS step 9	219
D.51	CHEMS Interplanetary TOF histogram for DPPS step 10	220
D.52	CHEMS Interplanetary TOF histogram for DPPS step 11	220

D.53	CHEMS Interplanetary TOF histogram for DPPS step 12	221
D.54	CHEMS Interplanetary TOF histogram for DPPS step 13	221
D.55	CHEMS Interplanetary TOF histogram for DPPS step 14	222
D.56	CHEMS Interplanetary TOF histogram for DPPS step 15	222
D.57	CHEMS Interplanetary TOF histogram for DPPS step 16	223
D.58	CHEMS Interplanetary TOF histogram for DPPS step 17	223
D.59	CHEMS Interplanetary TOF histogram for DPPS step 18	224
D.60	CHEMS Interplanetary TOF histogram for DPPS step 19	224
F.1	CHEMS PHA Species Efficiencies for H^+	249
F.2	CHEMS PHA Species Efficiencies for H_2^+	250
F.3	CHEMS PHA Species Efficiencies for He^{++}	251
F.4	CHEMS PHA Species Efficiencies for H_3^+	252
F.5	CHEMS PHA Species Efficiencies for He^+	253
F.6	CHEMS PHA Species Efficiencies for O^{++}	254
F.7	CHEMS PHA Species Efficiencies for W^+	255
F.8	CHEMS PHA Species Efficiencies for O^{+++}	256
F.9	CHEMS PHA Species Efficiencies for C^+	257
F.10	CHEMS PHA Species Efficiencies for O_2^+	258

List of Tables

1.1	MIMI data sets in the PDS	11
1.2	MIMI Higher Order data product locations in the PDS	14
1.3	MIMI Higher Order data products in the PDS	17
1.4	File formats for MIMI Higher Order data products in the PDS	18
1.5	MIMI PDS File Standard Header	19
1.6	MIMI PDS File Standard Data Row Prefix	20
2.1	MIMI Calibration File Column Definitions	25
2.2	PDS Data Products Referenced in the Calibration File	26
2.3	Purpose Code Values and Definitions for Calibration Values	27
2.4	Species Label Definitions in the MIMI Conglomerate Cal. File	28
3.1	LEMMS Priority Channels Over Time	33
3.2	LEMMS Normal Rate Channels	37
3.3	Columns in LACC1 LEMMS Data Files	38
3.4	Columns in LACC2 LEMMS Data Files	38
3.5	Columns in LACC4 LEMMS Data Files	38
3.6	Columns in LFRT1 LEMMS Data Files	40
3.7	Columns in LFRT2 LEMMS Data Files	40
3.8	Columns in LFRT4 LEMMS Data Files	40
3.9	LEMMS PHA Typical Channels for Science Analysis	41
3.10	Columns in LEMMS PHA Data Files	41
3.11	Normalizing rate channels for LEMMS PHA spectra	45
3.12	Accumulation times for LEMMS PHA data	45
4.1	E/Q Values for CHEMS DPPS Steps	71
4.2	Quantities in CHEMS PHA Events	72
4.3a	CHEMS Range ID definitions	73
4.3b	CHEMS Pre-defined Species Boxes	73
4.4	Column Names for CHEMS Accumulator Rate Data	76
4.5	CHEMS Science Rate Data Columns	77
4.6	CHEMS Science Rate Efficiencies	79
4.7	Sample Calibration File Data Rows for CHEMS	79
4.8	CHEMS PHA Species with Flux Box Definitions	82
4.9	Magnetospheric time periods used to define CHEMS species boxes	89
4.10	Interplanetary time periods used to define CHEMS species boxes	90
4.11	CHEMS Bogus TOF Channels by Telescope	97
4.12	CHEMS DPPS steps affected by Bogus TOF Counts	103

5.1	INCA Image Types and Sizes	107
5.2	INCA Accumulator Rate Column Names	109
5.3	INCA PHA Event Column Names	110
5.4	PDS_READ_MIMI - an IDL Reader for INCA Accumulator Rate Data	113
5.5	Example Code that Reads INCA ACC Data	114
5.6	UTC2ET - an IDL Function for Converting UTC into ET	115
5.7	ET2UTC - an IDL Function for Converting ET into UTC	115
5.8	INCA Image Column Names	118
5.9	PDS_READ_MIMIIMG - Inputs to INCA Image Data Reader	120
5.10	PDS_READ_MIMIIMG - Outputs from INCA Image Data Reader	121
5.11	Code to Read INCA IMG Data	123
5.12	Code to Select A Single INCA IMG	124
5.13	Code to Plot An INCA IMG	125
5.14	Output From INCA IMG Data	126
5.15	PDS_READ_IMAGECAL - an IDL Reader for INCA Calibration Parameters	128
5.16	Code to Use INCA IMG Calibration Reader	129
5.17	INCA Image Calibration Matrix Structures	131
5.18	MIMI Calibration File Column Definitions	132
5.19	INCA Image Energy Widths, Ranges and Background Value Structures	134
5.20	PDS_CALIBRATE_IMAGES - Routine to calibrate INCA images	137
E.1	Ranges in TOF(ch) and Essd(ch) that define the PHA species boxes for H ⁺	226
E.2	Ranges in TOF(ch) and Essd(ch) that define the PHA species boxes for He ⁺⁺	227
E.3	Ranges in TOF(ch) and Essd(ch) that define the PHA species boxes for H ₂ ⁺	228
E.4	Ranges in TOF(ch) and Essd(ch) that define the PHA species boxes for He ⁺	229
E.5	Ranges in TOF(ch) and Essd(ch) that define the PHA species boxes for W ⁺	230
E.6	Ranges in TOF(ch) and Essd(ch) that define the PHA species boxes for O ⁺⁺	231
E.7	Ranges in TOF(ch) and Essd(ch) that define the PHA species boxes for H ₃ ⁺	232
E.8	Ranges in TOF(ch) and Essd(ch) that define the PHA species boxes for C ⁺	233
E.9	Ranges in TOF(ch) and Essd(ch) that define the PHA species boxes for N ⁺	234
E.10	Ranges in TOF(ch) and Essd(ch) that define the PHA species boxes for O ⁺⁺⁺	235
E.11	Ranges in TOF(ch) and Essd(ch) that define the PHA species boxes for O ₂ ⁺	236
E.12	CHEMS DPPS steps affected by Bogus TOF Counts	237
E.13	Narrow PHA species box definitions for H ⁺	238
E.14	Narrow PHA species box definitions for H ₂ ⁺	239
E.15	Narrow PHA species box definitions for He ⁺⁺	240
E.16	Narrow PHA species box definitions for He ⁺	241
E.17	Narrow PHA species box definitions for O ⁺⁺	242
F.1	Time periods used for CHEMS in-flight determination of TCR/DCR.	248

Section 1

Background and General Info

1.1 Instrument Overview

The Magnetospheric Imaging Investigation (MIMI) functions both as an in situ instrument that detects charged particles in the local environment of the Cassini spacecraft as well as a remote-sensing imager of energetic neutral atoms that may be emitted over extended regions of space. A complete description of MIMI has been presented in the instrument paper (Krimigis et al. 2004). This user guide assumes a basic familiarity with the instrument, and users are encouraged to read the instrument paper before attempting to analyze the data. This short instrument overview summarizes the sensors and augments the science discussion in the original article.

Briefly, MIMI has three main sensors: a charge-energy-mass spectrometer (CHEMS), the low energy magnetospheric measurements system (LEMMS), and the ion and neutral camera (INCA). The CHEMS sensor detects energetic ions in the energy range 2 to 220 keV/e. It has the capacity to measure ions with triple coincidence, meaning that it can often discriminate among ion species in the few to hundreds of keV energy range, even in somewhat harsh radiation environments. Because it can discriminate among ion species, CHEMS is very useful for understanding particle sources. For instance, it can detect the relative amount of solar wind Helium, useful for determining the influence of the heliosphere on different magnetospheric regions.

The LEMMS sensor uses two oppositely directed telescopes to measure ions and electrons in the energy range 0.03 to 18 MeV for ions and 0.015 to 0.884 MeV for electrons. Because it extends well into the MeV, it is the main sensor used for studying the radiation belts of Saturn. LEMMS is the only MIMI sensor that measures electrons. It does so in two ways: the first method of detection uses magnets to bend low-energy electrons into detectors and the second uses a stack of detectors capable of separating electrons by energy discrimination. Since the telescopes are bi-directional, LEMMS can, for example, determine when the spacecraft is on open/closed planetary field lines.

Finally, INCA is a type of pin-hole camera that can detect both ions and neutral particles. In very intense radiation environments, INCA is typically configured to measure the ambient ions in the medium. INCA ion counts are categorized as either protons or oxygen and are captured into 8 logarithmically spaced energy channels from 5 to 360 keV for protons and 36 to 1000 keV for O⁺ ions. When the spacecraft is in low flux environments, such as the magnetospheric lobes, deflection plates can often sweep out enough of the ambient ions that INCA can make accurate remote sensing

measurements of the energetic neutral atoms (ENAs) emitted elsewhere. The species classification and energy ranges for the neutrals are very similar to that of the ions. Since it is an imager, INCA is very useful for monitoring the whole inner magnetosphere of Saturn for activity, for monitoring the magnetospheric impact on Titan’s atmosphere, or for studying emissions from the heliospheric boundaries.

1.2 Science Objectives

While not an exhaustive list, MIMI science has included the following accomplishments. INCA conducted the first ENA imaging of Jupiter’s magnetosphere and the Europa neutral torus. INCA has also imaged the global dynamics of the Saturnian system, following large-scale particle injections from the tail to the dipolar regions. It has imaged the polar regions of the planet, the connections between injections and aurora and the effects of the magnetosphere on Titan’s surroundings. The planetary radiation belts, their asymmetries and dynamics, have been catalogued, as has their interactions with planetary satellites and rings. Flux levels of the proton belt have been correlated with solar cycle. Other structural features of the magnetosphere such as the ring current and its role in force balance have been articulated. Surveys of particle flux in the magnetosphere have been performed, and they illuminated the importance of charge exchange on flux levels and revealed features of periodic distributions. Local transport has been extensively studied including the relative roles of injections and diffusion, the connection between injections and flux-tube interchange and the relevance of local time to these processes. The interactions of the planetary rings and satellites with the magnetosphere have been used to identify ring arcs and small moons, and to understand surface and atmospheric weathering and surface charging. Signatures of moon-magnetosphere interactions have informed studies of local and global magnetospheric dynamics and the footprint of Enceladus on the aurora. Magnetospheric composition has been surveyed and its long-term behavior monitored. Periodicities in various quantities such as charged particle flux and neutral atoms have been documented and connections have been made to injections and the periodic shedding of magnetospheric plasma. Science of the heliosphere done by MIMI has involved the local heliosphere, including solar wind flow speeds and shocks, and the distant heliospheric boundaries using ENA imaging. In summary, MIMI has been actively contributing to heliospheric science as well as to our understanding of the structure and dynamics of Saturn’s magnetosphere, and its interaction with the planet, rings and satellites.

1.3 Terminology

Throughout this guide, we refer to MIMI in its totality as an “instrument,” while the three components of MIMI (LEMMS, CHEMS, and INCA) are referred to as “sensors.”

For each sensor, there are three data products available at the PDS. Each product is essentially a table of time series data – columns of counts for a set of ion/electron/neutral particle channels, with each row in the table containing timing information followed by multiple data values. Note that the INCA images (which are relatively low resolution compared to optical images) are also archived as tables that must be properly interpreted in order to reconstruct ENA images.

A particle channel refers to a unique combination of sensor, detector within the sensor (CHEMS has three solid state detectors, for example), species, and energy range. Each channel has its own label consisting of one or more letters followed by an index. Consider LEMMS, which has two oppositely directed telescopes. Protons can be detected from either telescope, but separate channels are used to label protons detected from each telescope. The LEMMS channels A0, A1, A2, . . . , A8 each contain counts for protons from the low energy telescope in contiguous energy ranges from 27 keV to 35 keV, 35 to 56 keV, 56 to 106 keV, etc. up to 1615 to 4000 keV for A8. Note that while these channels are contiguous in energy, this is not the case for all MIMI channels, especially for CHEMS. All channel energy ranges are discussed in detail when describing data for each instrument.

1.4 Data Product Overview

MIMI PDS Data Products			
Sensor	Data Type	Directory Name	Filename Mnemonic
LEMMS	Accumulation Rates	LEMMS_ACCUMULATION_RATES	ACC
	Fine Accumulation Rates	LEMMS_FINE_ACCUMULATION_RATI	FRT
	Pulse Height Analysis Data	LEMMS_PULSE_HEIGHT_ANALYSIS	PHA
CHEMS	Science Accumulation Rates	CHEMS_SCIENCE_RATES	SCI
	Accumulation Rates	CHEMS_ACUMULATION_RATES	ACC
	Pulse Height Analysis Data	CHEMS_PULSE_HEIGHT_ANALYSIS	PHA
INCA	Accumulation Rates	INCA_ACCUMULATION_RATES	ACC
	Pulse Height Analysis Data	INCA_PULSE_HEIGHT_ANALYSIS	PHA
	Images	INCA_IMAGES	IMG

Table 1.1: MIMI data sets in the PDS, the data type for each, as well as the exact labels for the directories and filenames for each data type. Each of the nine data products is either accumulation rates, pulse height analysis data, or images (INCA only).

MIMI data products available at the PDS are shown in Table 1.1. The directory names shown are all subdirectories below this URL at the PDS web site:

https://pds-ppi.igpp.ucla.edu/archive1/COMIMI_OSAT/DATA

Figure 1.1 shows how the data directories appears in a web browser that is pointed at the above URL. Descending into any of the data directories will lead to a set of yearly directories, and within these yearly directories are daily files. Figure 1.2 shows the layout of subdirectories below the data product directories.

The naming convention for daily MIMI data files captures the sensor, data type, the date (year and day of year), and the version of the file, as shown in filenames in Figure 1.2. The first character indicates the sensor (C = CHEMS, I = INCA, L = LEMMS). The next three characters are the data type filename mnemonic, whose possible values are listed in Table 1.1 (see the last column). If the operating mode of the instrument changes, then the contents or format for one or more data types may change, and therefore the data type mnemonic has a version number. For example, the

Filename	Size	Last Modified
CHEMS_ACCUMULATION_RATES/		Thu, 06 Jan 2011 17:13:33 GMT
CHEMS_PULSE_HEIGHT_ANALYSIS/		Thu, 06 Jan 2011 17:19:22 GMT
CHEMS_SCIENCE_RATES/		Thu, 06 Jan 2011 17:20:31 GMT
CSV.LOG	84.8 kb	Tue, 02 Mar 2010 00:23:19 GMT
DATAINFO.TXT	3.9 kb	Thu, 30 Jun 2005 16:06:27 GMT
INCA_ACCUMULATION_RATES/		Thu, 06 Jan 2011 17:20:42 GMT
INCA_IMAGES/		Thu, 06 Jan 2011 17:22:24 GMT
INCA_PULSE_HEIGHT_ANALYSIS/		Thu, 06 Jan 2011 17:22:33 GMT
LEMMS_ACCUMULATION_RATES/		Thu, 06 Jan 2011 17:22:43 GMT
LEMMS_FINE_ACCUMULATION_RATES/		Thu, 06 Jan 2011 17:22:52 GMT
LEMMS_PULSE_HEIGHT_ANALYSIS/		Thu, 06 Jan 2011 17:23:00 GMT

Figure 1.1: A listing of all MIMI data directories at the PDS can be accessed directly from the URL https://pds-ppi.igpp.ucla.edu/archive1/COMIMI_OSAT/DATA. There are nine types of data, each in their own subdirectory.

specific LEMMS channels chosen for inclusion in the higher time resolution “Fine Accumulation Rates” change over time, and so each time period (within which the choice of LEMMS FRT channels is fixed) has a different index for the version number on the data type mnemonic. LEMMS data files labeled with FRT0 contain the first selection of high time resolution channels, and when this was changed, the mnemonic label was also changed to FRT1. Finally, the revision number of the file itself is the final four-digit integer in the filename. If the data are reprocessed, then this version number is incremented.

An example filename for INCA data is IPHA0_2007191_0003.CSV, where

- I → INCA
- PHA → Pulse Height Analysis Data
- 0 → the version indicator for the contents/format of the INCA PHA data file
- 2007191 → the four digit year and three digit day of year for the data
- 0003 → the revision number for the file, indicating reprocessing had been done to fix errors
- CSV → extension indicating ASCII data with comma separated values

Currently, the highest revision number for MIMI data at the PDS is revision 3, as shown above (see the revision string 0003). However, not all of the data has been brought up to revision 3 yet. Data for years 2004 through 2006 is still at revision 0, and these files have some format differences (fewer columns) that will be discussed below. It is expected that within a few months, all the older data will be reprocessed and all years will have files with revision number 3.

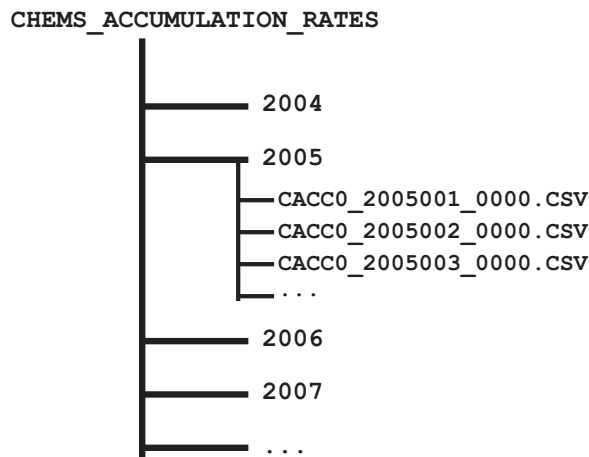


Figure 1.2: Within each data directory are yearly sub-directories filled with daily files, as shown in this example for one CHEMS data product. The naming convention for the daily files (described fully in the text) includes a sensor prefix (C), a data type (ACCO), a date stamp (2005001), and a version number (0000).

LEMMS

For LEMMS, there are three types of data: two kinds of accumulator rates plus Pulse Height Analysis (PHA) data. The normal Accumulator Rates and Fine Rates (also called priority rates) are both tables of counts for various particle channels. The fine rate data are comprised of a small subset of the channels measured at a finer time cadence, typically eight times more frequently than the normal accumulator rates. The LEMMS PHA data is different than the PHA data from other sensors. Usually, PHA events capture a list of instrument response parameters for a subset of particle. For LEMMS, the PHA data is a set of 64 closely spaced energy channels covering 12 to 833 keV for protons, 39 to 2295 keV for F detector electrons and 6.7 to 451 keV for E channel electrons. However, like regular PHA data, these LEMMS PHA channels do need to be properly normalized (see Section 3.2.3).

CHEMS

CHEMS is similar to LEMMS in that there are two kinds of rate channel data along with PHA data. The Science Accumulator Rates contain counts for all of the science channels, and the Accumulation Rates are more diagnostic in nature, i.e., all valid triggers, or all time of flight (TOF) stop events. CHEMS PHA data is more typical than LEMMS PHA in that it provides a list of individually detected particles, with specific detection parameters for each event, including TOF, energy deposited in the SSD, and telescope number. Telemetry data volume constraints do not allow all particle events detected by CHEMS to be sent in the MIMI data stream, so the PHA data need to be carefully normalized, and the procedures for doing this are described in the section on CHEMS. Note that the parameters stored in PHA events correspond to the parameters used within the CHEMS instrument flight software to categorize an incident particle into the correct rate channel counter.

INCA

For INCA, there are also three types of data: images, rate data, and PHA data. INCA images are relatively low resolution (up to 64 by 64 pixels), large field of view (90° by 120°) pictures of neutrals, similar to any remote sensing imager. Note however, that INCA has an ion mode in which neutral counts are drowned by incident ions. These ion images offer very good pitch angle distributions of in-situ particle distributions. There is also INCA rate channel data consisting of diagnostic counters for assessing instrument performance and health. Finally, INCA PHA data is similar in concept to the CHEMS PHA data, providing event characteristics for a subset of incident particles, either ions or neutrals.

Higher Order Data Product Overview

Sensor	PDS Web Site
CHEMS	https://pds-ppi.igpp.ucla.edu/archive1/COMIMI_C001/ DATA = Data Files BROWSE = PNG, PDF
LEMMS	https://pds-ppi.igpp.ucla.edu/archive1/COMIMI_L001/ DATA = Data Files BROWSE = PNG, PDF
INCA	https://pds-ppi.igpp.ucla.edu/archive1/COMIMI_I001/ DATA = Data Files BROWSE = PNG, PDF, MP4

Table 1.2: MIMI higher order data product locations at the PDS. The directory names are all sub-directories below these URLs at the PDS web site.

Table 1.3 lists the MIMI higher order data products available at the PDS. The time ranges of the different products vary so will be described during the description of the individual product. All data types contain yearly sub-directories. The Higher Order MIMI PDS products file formats are described in Table 1.4.

For CHEMS higher order products, there are two types of data, 20-day energy per charge spectrograms for six ion species (H⁺, He⁺, H₂⁺, He⁺⁺, O⁺⁺, W⁺) and 20-day plots of ion mass per charge versus time of detection (UT) for multiple E/Q steps. Both types of plots have one-hour resolution and are based on CHEMS PHA data. The numeric data from both plots is also available.

For INCA higher order products, there are four types of data. The Angle image averages are an effort to make an INCA data product directly comparable to data products from the LEMMS and CHEMS telescopes. The images are collapsed in angle to form an image-integrated intensity. These averages are calculated for a combination of species and time-of-flight (TOF) for the high mass TOF, high spatial and high time resolution images. The Angle Image Average Hydrogen plots show the high mass TOF image data. These data types are available at all the times INCA is collecting images.

The INCA differential intensity image data files contain the image pixel values in differential intensity for a combination of resolution, species and energy values. Similar format files were made containing the pitch angle and pixel value uncertainties. The pitch angle is the angle between the direction of the magnetic field and the look direction of the pixel. These data types are available at all the times INCA is collecting images.

The INCA Energetic Neutral Atom (ENA) Hydrogen and Oxygen skymap browse products display three rows by N columns of spin averaged high spatial ENA image skymaps (each one accumulated over four sectors), displayed for one species and TOF combination. The browse products are available when the INCA sensor was in neutral mode, so they are not available every day.

The INCA ENA skymap movies are MP4 movies displaying averaged ENA image skymaps (averaged over a variable, listed number of original on-board images), for high spatial resolution Hydrogen and Oxygen images for one TOF. There are a few ENA image skymap movies available for the high time resolution images.

Sensor	Data Type	Directory Name	Filename Mnemonic
CHEMS	Mass Per Charge Spectrograms	CMSPGM0_<ECR>_<CE> Energy/charge range (ECR) [0007,0815,1623,2431,0031] Coincidence Events (CE) [DT,T]	CMSPGM0_0007_DT CMSPGM0_0007_T CMSPGM0_0815_DT CMSPGM0_0815_T CMSPGM0_1623_DT CMSPGM0_1623_T CMSPGM0_2431_DT CMSPGM0_2431_T CMSPGM0_0031_DT CMSPGM0_0031_T
CHEMS	Mass Per Charge Numerical Data	CMAVGO_<ECR>_<CE> Energy/charge range (ECR) [0007,0815,1623,2431,0031] Coincidence Events (CE) [DT,T]	CMAVGO_0007_DT CMAVGO_0007_T CMAVGO_0815_DT CMAVGO_0815_T CMAVGO_1623_DT CMAVGO_1623_T CMAVGO_2431_DT CMAVGO_2431_T CMAVGO_0031_DT CMAVGO_0031_T
CHEMS	Energy Per Charge Spectrograms	CSPGM0_<ion species> Ion Species [H2P,HEP,HEPP,HP,OPP,WP]	CSPGM0_H2P CSPGM0_HEP CSPGM0_HEPP CSPGM0_HP CSPGM0_OPP CSPGM0_WP
CHEMS	Energy Per Charge Numerical Data	CPAVEGO_<ion species> Ion Species [H2P,HEP,HEPP,HP,OPP,WP]	CPAVEGO_H2P CPAVEGO_HEP CPAVEGO_HEPP CPAVEGO_HP CPAVEGO_OPP CPAVEGO_WP
INCA	Angle Image Averages	IANGAVEO_<image type> Image Type [M, S, T] M=High mass TOF resolution S=High spatial resolution T=High time resolution	IANGAVEO_M IANGAVEO_S IANGAVEO_T
INCA	Angle Image Average Hydrogen Plots	IAVEPLTO_H Species = H	IAVEPLTO_H

Sensor	Data Type	Directory Name	Filename Mnemonic
INCA	Differential intensity image ASCII data files	ICIMG0_<data type> Data Type = [I,P,U] I = Image Data P = Pitch Angle U = Uncertainty	ICIMG0_I ICIMG0_P ICIMG0_U
INCA	ENA Hydrogen and Oxygen Skymap Browse Products	IENAIMGO_HO	IENAIMGO_HO
INCA	ENA Skymap Movies	IENAMV0_<ResSpeTOF> Image Type ResolutionSpeciesTOF Resolution S = High Spatial T = High Time Species H = Hydrogen O = Oxygen A = All TOF 0 = High TOF 7 = Low TOF	IENAMV0_SH0 IENAMV0_SH7 IENAMV0_SO0 IENAMV0_SO7 IENAMV0_TA0 IENAMV0_TA7

Table 1.3: MIMI higher order data products available at the PDS.

Sensor	Data Type	File Format
CHEMS	Mass Per Charge Spectrograms	PNG File
CHEMS	Mass Per Charge Numerical Data	CSV file that follows the format detailed in Section 1.6 File Formats.
CHEMS	Energy Per Charge Spectrograms	PNG File
CHEMS	Energy Per Charge Numerical Data	CSV file that does not follow the format in Section 1.6 File Formats
INCA	Angle Image Averages	CSV file that follows the format detailed in Section 1.6 File Formats.
INCA	Angle Image Average Hydrogen Plots	PNG File
INCA	Differential intensity image ASCII data files	CSV file that follows the format detailed in Section 1.6 File Formats.
INCA	ENA Hydrogen and Oxygen Skymap Browse Products	PNG File
INCA	ENA Skymap Movies	MP4 File

Table 1.4: File formats for MIMI higher order data products available at the PDS.

1.5 Calibration Documentation

This guide covers uncalibrated MIMI data products in the PDS. The guide describes how to extract raw values from the existing data files and how to apply the correct calibration procedures to convert raw values into physical units.

Note that while the PDS contains uncalibrated MIMI data for the entire mission, this user guide covers only the Saturn data. Different instrument modes were utilized when collecting data during earlier mission phases, and thus the data products from these phases have different arrangements and calibration procedures. Also, instrument and telemetry issues that existed before arrival at Saturn make interpretation of this data more difficult.

Standard PDS documentation for the MIMI datasets can also be found in the Cassini MIMI Software Interface Specification (SIS) entitled “MIMI Standard Data Products and Archive Volume Software Interface Specification” located in the documents section of PDS archive for MIMI. The PDS has this document here:

<https://pds-ppi.igpp.ucla.edu/archive1/>

COMIMI_0000/DOCUMENT/MIMI_VOLUME_DESCRIPTION/MIMI_VOLUME_DESCRIPTION.PDF

(Note: the line break is artificial and that the version number may get incremented over time.)

Calibrated data for MIMI are also present in the PDS. They were created using the principles described in this document, and a detailed description of their contents is outside the scope of this guide. The calibrated products have documentation describing their contents.

1.6 File Formats

File Header

All PDS data for MIMI are ASCII files with comma-separated values (CSV). Each data file (for all data types) begins with a short, seven-line header, each line of which is described in Table 1.5. The first row of the header is a list of quoted strings, each string being a column name. The remaining header rows contain summary information about each column: the valid minimum and maximum values for each data column, the actual minimum, maximum, mean and standard deviation of the data within each file. Note that all rows except the first header row begin with a purpose string.

MIMI PDS File Standard Header	
Row Index	Description
0	names of the data elements (columns) in this file as quoted strings separated by commas
1	"valid_min" followed by the smallest possible valid value for items in each column
2	"valid_max" followed by the largest possible valid value for items in each column
3	"min" followed by the actual minimum value for items in each column
4	"max" followed by the actual maximum value for items in each column
5	"mean" followed by the average value for items in each column
6	"stddev" followed by the standard deviation for items in each column

Table 1.5: All MIMI PDS files start with these seven header lines. Note that the quote marks are actually present in the file. While the first row contains just the quoted column names of the data, all other header rows begin with a quoted purpose string.

MIMI PDS File Standard Data Row Prefix		
Column Index	Column Name	Description
0	PURPOSE	string value; all data rows begin with "sci", header rows begin with one of "valid_min", "valid_max", "min", "max", "mean", "stddev"
1	UTC	string value (in ISO 8601 format) giving the start time of data for this row obtained by converting START_EPHEMERIS_S to UTC using SPICE
2	SCLOCK	string representing spacecraft clock value at the start of this data record (expressed in SPICE format)
3	START_EPHEMERIS_S	ephemeris time (ET) for start time of data in this row; ET is seconds past the J2000 epoch on a clock at the solar system barycenter (this is a SPICE convention)
4	END_EPHEMERIS_S	stop time in ET for data in this row
5	SPIN_COUNTER	integer count of spacecraft spin; since its max is 16383, it will turn over, usually one or two times per year
6	SECTOR	integer sector number, 0 to 15
7	START_SECTOR_SCLOCK_MAJOR	major field of spacecraft clock counter at start of sector
8	SUBSECTOR	integer subsector number, 0 to 15
9	MICROSECTORS_COVERED	width of the measurement in microsectors
10	SPIN_PERIOD_S	floating point value in seconds for the current spin period
11	STARING	integer flag: 0 = no (not starring) and 1=yes (staring)
12	SENSOR_BITRATE	integer enumeration indicating telemetry allocation with 1 = very low, 2 = low, 3 = medium, 4 = high, 5 = very high; MIMI sensors may operate in different modes depending on bit rate and so some data structures change when the bit rate changes

Table 1.6: Names and descriptions for the ten prefix columns found on every MIMI data row for revision 3 data files. (Revision 0 data files are still present for years 2004 through 2006, but these will be updated soon. Revision 0 files are missing the UTC, SCLOCK, and SENCOR_BITRATE columns.) Data rows follow the 7 line header described in Table 1.5.

Label Files

Each PDS data file also has an associated label file with the extension LBL. These files provide metadata for the data file and the fields present within the file. When describing ASCII data in the PDS, there are several choices for PDS label file formats. The SPREADSHEET option was chosen because this captures the intended use of the comma delimited data.

Data Rows and the Data Row Prefix

Following the header are data rows. Every data row in all data types begins with a common prefix having the thirteen items listed in Table 1.6. Every data row has the same PURPOSE value, namely

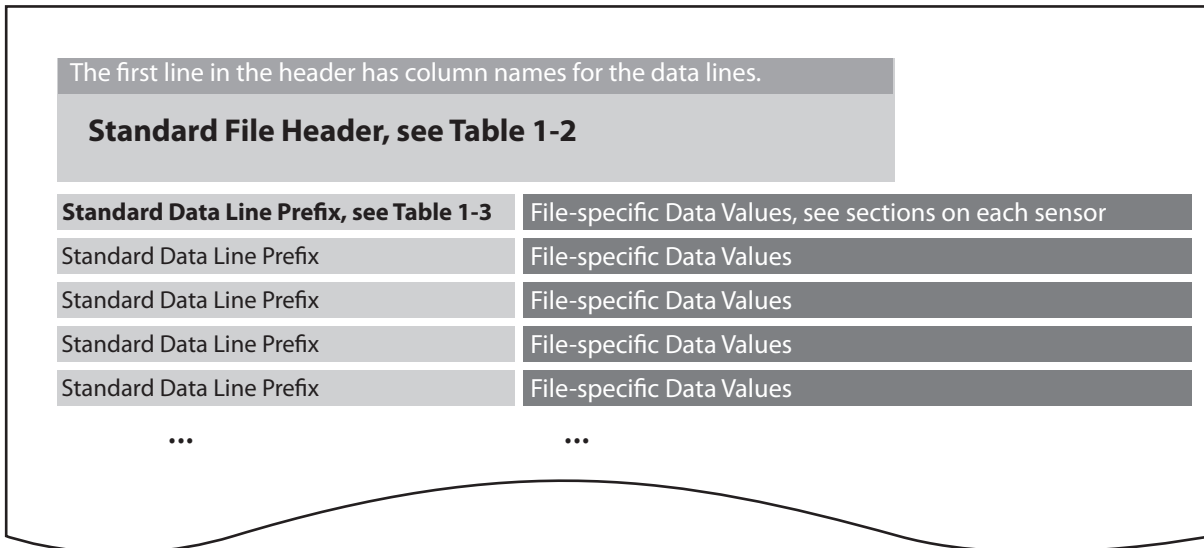


Figure 1.3: Every MIMI data file in the PDS has a standard header with seven lines. Each data line is prefixed with ten standard values that include timing information for that row. After the prefix are the file-specific data values. All header rows and data rows are ASCII values separated by commas.

the string "sci". The values for `START_EPHEMERIS_S` and `END_EPHEMERIS_S` give the start and stop times of the measurement on a given row. These time values are in dynamical barycentric time (TDB, also known in SPICE parlance as ephemeris time, ET). A TDB time value is the number of seconds past noon on January 1, 2000 for a clock ticking at the barycenter of the Solar system. The `SPIN_COUNTER` is a fourteen-bit integer counter (maximum value of $2^{14} - 1 = 16383$) indicating the current spin index. Some flight software transitions happen only on spin boundaries, so it can be useful to know the spin index to which a measurement belongs. This counter turns over one or two times per year or when the instrument is reset. The `SECTOR` index indicates from which subsection of a spin a measurement was made. Note that because the spacecraft is not always spinning, both spins and subsectors are primarily timing mechanisms for segmenting the data.

The `MICROSECTORS_COVERED` is a way of indicating the duration of the measurement in microsectors. The `SPIN_PERIOD_S` is the duration of one spin in seconds. The `STARING` flag indicates if the instrument is in spin mode or not, where `STARING=0` corresponds to spin mode. The next section explains the use of the spin period for the timing of MIMI data.

The overall layout of a MIMI PDS data file is shown in Figure 1.3, which shows how the standard header of 7 lines is followed by data lines, each starting with the 13 element data line prefix.

1.7 Data Time Stamps

Although the spacecraft is three axis stabilized, there are times when the spacecraft does spin. In these cases, the spin axis is usually the +Z axis of the spacecraft. Each rotation is divided up into 16 spatial sectors, and each sector into 16 subsectors, and finally there are 16 microsectors in a subsector. Different MIMI data elements are collected in multiples of these divisions. For example, some INCA images have an exposure time of 4 sectors, LEMMS normal rate channels are obtained every subsector, and priority LEMMS channels are read out every other microsector.

When the spacecraft is not spinning (or spinning about any axis other than the +Z axis), the data is still divided into sectors, subsectors, and microsectors, where the time durations are based on a fictional spin period value chosen by the MIMI flight software. This allows a consistent scheme for organizing the data into sectors, subsectors, etc., whether or not these divisions correspond to spacecraft motion. The value used for the spin period is always reported in the data as `SPIN_PERIOD_S`, and whether or not the spin period is real can be determined from the `STARING` flag.

Since Cassini is usually not spinning, the best way to think about the sectors and subsectors is in terms of timing divisions only. Look directions for each measurement can be obtained by using the data time stamps along with spacecraft orientation data (usually in the form of SPICE attitude files or kernels).

1.8 Data Collection Strategies

MIMI instruments are designed to operate and collect data continuously. INCA can be switched from neutral mode (all ions up to about 180 keV/e swept out of the way by an electric field) to ion mode (electric field turned off). The neutral mode observations for INCA are generally scheduled when the images will include all of Saturn in the FOV. Ion mode is used when Cassini is projected to be in the charged particle trapping region within Saturn's magnetosphere. Note that even when INCA is in ion mode, it is still sensitive to neutrals, so if the ion intensity is very low (as sometimes happens when Cassini is over the polar regions, for example), acceptable neutral images can still be obtained in ion mode.

INCA images are taken at sector boundaries. LEMMS and CHEMS data are taken every subsector. A few LEMMS channels are measured every other microsector, and these are referred to as fine rate data. When MIMI must reduce its data volume to its lowest setting, the time resolution of the LEMMS normal channels is reduced from every subsector to every other subsector. The LEMMS fine rate data is unchanged. CHEMS is also unchanged.

The LEMMS telescope is mounted on a spinning platform, which rotated once per sector until becoming permanently stuck in early 2005. The turntable degradations began on 2005 day 32, and the table became stuck on day 109 of 2005. When it was spinning, the subsector data from LEMMS represents 16 measurements per turntable rotation. When combined with a spinning spacecraft, LEMMS turntable motion allowed measurement of ions from a large fraction of the sky.

When in ion mode, INCA often obtains good coverage of the sky owing to its large FOV.

1.9 Generic instrument and data issues

Instrumental and data-related issues are discussed within the sensor-specific sections of this user guide, but two overarching concerns are worth mentioning. First, rapid changes in counts can be caused by changes in spacecraft attitude. Understanding the spacecraft orientation is very important in understanding variability in the data. SPICE kernels for the Cassini project contain the definitive attitude determination for the spacecraft. Also summary plots with attitude information are available at the MIMI web site.

Secondly, MIMI data products occasionally have gaps. Appendix B describes the known gap list, where a gap is defined as any interval during which there is no data from any MIMI sensor. Only large gaps affecting all data products are described in this file.

Section 2

Calibration Overview

2.1 MIMI calibration files

A large, conglomerate calibration file contains many of the calibration parameters for MIMI. All LEMMS calibration parameters are contained in this conglomerate file, including the channel definitions (energy ranges, efficiencies, and geometric factors) as well as background levels for each channel. The file also contains channel definitions for CHEMS and INCA, although additional calibration files for these sensors are needed for handling sensor specific calibration issues, such as PHA box definitions and efficiencies for CHEMS and flat-fielding matrices for INCA images.

In this section, we describe the main conglomerate calibration file. A similar discussion of this file can be found in the MIMI PDS documentation [Manweiler et al., 2005].

2.2 Format of the primary MIMI calibration file

The primary MIMI calibration file is an ASCII file with comma-separated values (CSV), and is named `MIMI_CALIBRATION_XXXX.CSV`, where `XXXX` is the version number. The highest available version should always be used, and currently this is version 9 (shown as 0009 in the filename). The CSV (comma-separated value) nature of the calibration file allows it to be conveniently viewed in a spreadsheet application. There are two places to get this file:

1. the PDS: https://pds-ppi.igpp.ucla.edu/archive1/COMIMI_0000/CALIBRATION
2. the MIMI team site devoted to PDS data:
http://sd-www.jhuapl.edu/CASSINI/data_auxiliary.html

The MIMI team location will usually have a more up to date version of the calibration file, owing to the phasing of periodically delivering this file to the PDS. Although few calibration changes are being introduced at this point, new background levels for recent time periods are still being appended every six months or so.

Each value in the conglomerate calibration file is contained on one row of the file, and all rows are described by a consistent record structure of seventeen fields (i.e., columns). The definitions of all columns are given in Table 2.1. The first several columns are identifiers indicating the sensor

MIMI Conglomerate Calibration File Column Definitions

Column

No.	Field Name	Description
1	Purpose	the intended use for the calibration value on this row; see Table 2.3 for purpose codes and definitions.
2	Data_Type	PDS Data Product; one of PHA, SCI, ACC, IMG, or FRT; Table 2.2 lists the products for each sensor
3	Sensor	MIMI sensor name (CHEMS, INCA, or LEMMS)
4	Channel	the channel name (for CHEMS, a value of DPPS indicates a row with a voltage step value)
5	Channel_Index	channel index or DPPS step number
6	Particle	nominal particle species associated with this measurement if known; (<i>note: often this is not definitive</i>)
7	Start_Year	start year of valid time range for the value on this row (to be combined with day of year value in next column)
8	Start_DDOY	day of year for start date of valid time range for this row
9	End_Year	end year of valid time range for this row (to be combined with day of year value in next column)
10	End_DDOY	day of year for end date of valid time range for this row
11	Units	units for the numeric calibration value in this row
12	Low	if the calibration value is a range, this is the low value in the range
13	Hi	if the calibration value is a range, this is the upper end of the range
14	Delta	if the calibration value is a range, this is the width of the range; for background level values, it is the uncertainty in the background value
15	Midpoint	the calibration value for this row; if the calibration value is a range, this field is the midpoint between the Hi and Low values; see Table 2.3 for a full explanation of midpoints for each purpose type (<i>note that some midpoints are geometric means</i>)
16	Source	the institution responsible for generating this calibration value; UMD = Univ. of Maryland, APL = Applied Physics Laboratory, KS = Fundamental Technologies in Kansas, or Team = the entire MIMI team; the Team values are always the most up to date
17	Comment	any relevant comments regarding this record; on calibration lines dealing with CHEMS efficiencies, the comment contains space separated rate channel names of the channels to be summed before applying the efficiency

Table 2.1: Names and definitions of the columns in the MIMI conglomerate calibration file. Calibration values (the actual numbers) are in columns 12 through 15 (**Low**, **Hi**, **Delta**, **Midpoint**). The value in the **Purpose** column dictates how to interpret the calibration value columns in the same row. The allowed **Purpose** values are explained in Table 2.3. Note that in some cases the **Midpoint** is the calibration value, and in some other cases the **Low** and **Hi** columns contain the crucial information (as with channel energy ranges).

PDS Data Products Referenced in the Calibration File

Sensor (column 3)	Allowed values for the Data_Type column (column 2)
CHEMS	SCI, PHA
INCA	ACC, PHA, and IMG
LEMMS	ACC, PHA, and FRT

Table 2.2: A list for each sensor of the allowed values for the `Data_Type` column in the calibration file. Note that there is also an `ACC` data type for CHEMS, but it is not referenced in the table above nor in the calibration file because there are no calibration values needed to use it. (The CHEMS `ACC` data in raw form is counts, and can be converted to counts/sec, but this requires no calibration values).

(LEMMS, CHEMS and INCA) and the intended use of the calibration value on any given row. The actual calibration value occurs in a later column. Because each sensor has multiple data products in the PDS (see Table 1.1), it is necessary to indicate the data product type to which a calibration value applies, and this is done in column 2, labeled `Data_Type`. Sample `Data_Type` values include `PHA`, `IMG`, and `ACC` for PHA data, image data, and accumulator data, respectively.

For any specific `Data_Type`, there are usually multiple kinds of calibration values, such as energy ranges for particle channels, as well as geometry factors, field of view sizes, efficiencies, etc. The first column, the `Purpose` column, indicates which type of calibration value is stored on that row. The numerical calibration quantities themselves are stored in columns 12 through 15, labeled with `Lo`, `Hi`, `Delta`, and `Midpoint_Value` respectively. Which of these value columns contains the actual calibration number depends on the `Purpose` for that row. For example, a row storing an energy range for a channel (i.e., `Purpose = ENERGY`) will have the relevant numbers in `Lo` and `Hi` columns, and the other columns (`Delta` and `Midpoint_Value`) are computed from these two and provided as a convenience. In a row with the geometry factor for a channel (`Purpose = GEOM_FACTOR`), the `Midpoint_Value` column will have the actual geometry factor. The `Units` column gives a string indicating the units for the calibration value.

In Table 2.3, the different calibration `Purpose` values are explained, along with the proper interpretation of the value columns for each purpose.

A calibration value may change with time. Background levels, for example, are time-varying. Columns 7 through 10 capture the valid date range for the calibration value in that row. Many calibration values are constant over the life of the mission, and thus have only a single, all-encompassing date range, but some calibration quantities do have multiple entries that are valid over different but contiguous time ranges. Note that in the date range specification, the day of year values often have non-integer days, indicating that the calibration change occurred a certain fraction into the given day.

The careful observer will notice that there are multiple energy range specifications for some channels. This is because some channels may detect more than one type of particle species, and the energy range definitions for particle channels are dependent on the mass of the detected particle. Thus the calibration file provides species-specific energy ranges for some channels. Table 2.4 defines the particle species labels found in the calibration file. In practice, most MIMI analysis generally assumes a single species for any given channel. For example, LEMMS A1 counts are almost always assumed to be protons, but this is the nominal case only – there can be contamination by other species. The first species listed in the calibration file is the primary species for a given channel, and most MIMI tools assume that this species is the one responsible for the counts in that channel.

Purpose Code Values and Definitions for Calibration Values

Purpose	Description	Value Column Interpretation
ENERGY	the energy range for a channel; usually upper and lower bounds; if a channel has no upper bound, then the value for the upper end of the range will be an effective value that can be used under most conditions	Lo and Hi give channel energy bounds; Delta and Mid are computed from Lo and Hi and are provided for convenience only; $\Delta = (Hi - Lo)$ and $Mid = \sqrt{Lo \cdot Hi}$
ENERGY/CHARGE	defines the energy/charge range for a CHEMS channel; recall that CHEMS filters incoming particles first on E/Q and only measures E directly if the particle has enough energy to trigger the SSD	same as for Energy: Lo and Hi are the bounds; other values (Delta and Mid) are provided for convenience only; Delta is the difference and Mid is the geometric mean
GEOM_FACTOR	the geometric factor for a given channel	Midpoint contains the value; others blank
EFFICIENCY	the efficiency of a given channel	Midpoint contains the value; others blank
BACKGROUND	background level to be subtracted from a given channel	Midpoint contains the value and Delta contains the uncertainty; others blank
FOV	the size of the field of view for a given sensor element	Midpoint contains the value; others blank
MASS	<i>for CHEMS only</i> ; rectangular regions in mass versus mass/charge space define rate channels (both the generic basic rate channels and smaller species rate channels); this row in the calibration table gives the low and high values for the mass range of a basic rate or a species rate; combine this with the mass/charge range to get the full box definition	Lo and Hi contain the mass range for the rate box being defined; Delta and Mid are provided as a convenience; $\Delta = (Hi - Lo)$ and $Mid = \sqrt{Lo \cdot Hi}$
MASS/CHARGE	the mass/charge range for a CHEMS basic rate channel or species rate channel; the mass range for this region is defined on another row (with the same CHEMS channel name but with purpose = MASS)	same as for the MASS rows where Lo and Hi contain the mass/charge range, $\Delta = (Hi - Lo)$ and $Mid = \sqrt{Lo \cdot Hi}$

Table 2.3: An explanation of how to get calibration values for the rows of a given Purpose code in the calibration file. Purpose codes other than those listed here are not used for storing calibration values and should be ignored.

Species Label Definitions in the MIMI Conglomerate Cal. File

Particle	
Label	Definition
ALL	the calibration value on this row applies to any particle
CNO >4+	particles with species of C, N, or O and charge > 4; specific to CHEMS
e	electrons
H	hydrogen atoms; specific to INCA
H+	singly ionized hydrogen atoms; specific to CHEMS and INCA
H2	singly ionized hydrogen molecule (H-H); specific to LEMMS
H3	singly ionized hydrogen molecule (H-H-H); specific to LEMMS
He	any helium ion; specific to LEMMS
He+	singly ionized helium atom; specific to CHEMS
He++	doubly ionized helium atom; specific to CHEMS
Ions	any positively ionized species; specific to INCA and LEMMS
MperQ=2	any ionized species with mass per charge of 2; specific to CHEMS
NA	this record does not need a particle specification
Neutrals	any un-ionized species; specific to INCA
O	any ionized oxygen atom; specific to all LEMMS records and the INCA geometrical factor
O+	any singly ionized oxygen atom; specific to CHEMS
O++	any doubly ionized oxygen atom; specific to CHEMS
Ox	any ionized oxygen atom; specific to INCA
P	any proton; specific to INCA and LEMMS
W+	water group ions; specific to CHEMS
Xray	calibration record for an X-Ray event; specific to LEMMS

Table 2.4: Descriptions of the particle species labels used in the conglomerate MIMI calibration file. Note that the species names are not completely consistent across the sensors. For example, LEMMS calibration lines use **He** to refer to any charge state of helium because LEMMS cannot determine charge state. For CHEMS, there are two helium species, **He+** and **He++**, depending on the charge state, which CHEMS can measure. A similar situation exists for the names of oxygen ions.

Practical tip: When manually finding values in the MIMI conglomerate calibration file, use a spreadsheet application that can filter the massive table down to just the rows of interest. Select the entire table, and then use the Filter feature (sometimes called Filter or possibly AutoFilter but usually under the “Data” menu) that allows you to then select specific values to view for each column. This works in both Microsoft Excel and the OpenOffice Calc application.

2.3 Example usage of the primary MIMI calibration file

The following example illustrates how to extract calibration parameters from the MIMI calibration file. The example task involves finding the calibration values needed in order to compute a LEMMS proton spectrum: the energy ranges, geometry factors, and efficiencies for proton channels A0 through A7.

Suppose that the time range of interest is around Saturn Orbit insertion (SOI), which occurred on day 183 of 2004. The energy ranges of the LEMMS A channels are valid over all times (meaning you don’t have to care about the date range columns when looking for energy ranges of LEMMS A channels), and so you select the rows which have:

```
Sensor = LEMMS
Data_Type = ACC
Purpose = ENERGY
Channel = A
Particle = P
```

The rows with these settings are the energy ranges for channels A0 through A7. The Lo and Hi columns for each of these rows have the energy bounds of the various A channels in units of keV, and you should get the following energy ranges (also in keV):

```
A0: 27 to 35
A1: 35 to 56
A2: 56 to 106
A3: 106 to 255
A4: 255 to 506
A5: 506 to 805
A6: 805 to 1600
A7: 1615 to 4000
```

There is another LEMMS channel, A8, but this channel does not respond significantly to protons, and so energy ranges for A8 are only provided for He and heavier ions.

The geometry factors are also constant over time, and they are the same for all particle species (notice the Particle = ALL below), so find the rows with:

```
Sensor = LEMMS
Data_Type = ACC
Purpose = GEOM_FACTOR
Channel = A
Channel_Index = 0, 1, 2, 3, 4, 5, 6, 7, 8
Particle = ALL
```

For geometric factors, you should get (in units of $\text{cm}^2 \cdot \text{steradians}$):

A0: 0.00464
A1: 0.0049
A2: 0.00532
A3: 0.00586
A4: 0.006
A5: 0.006
A6: 0.006
A7: 0.006
A8: 0.006

These geometry factors have the (energy dependent) efficiencies included, so although the efficiencies are recorded separately in the calibration table and can be obtained in the same way (choosing the `Purpose = EFFICIENCY` rows for LEMMS accumulator A channels), the efficiency values are all 1.0 for LEMMS A channels.

Other calibration values are extracted using the same approach of selecting only the rows relevant to the sensor and purpose of interest. The use of all relevant calibration values in converting LEMMS counts to intensity is described in Section 3.3.

2.4 INCA flat fielding calibration files

The INCA flat fielding calibration files are matrices of geometric factors and the efficiencies for each INCA pixel. Because INCA produces several image sizes (8x8 up to 64x64, each with varying pixel sizes), there is a separate calibration file for each of these image sizes. Furthermore, there are different sets of files to use for different time periods. These calibration values were different enough from the content of the conglomerate file described above that they have been maintained independently. The layout and usage of these files is described in detail in the example of how to use INCA image data (Section 5.7).

2.5 Use of SPICE for trajectory and orientation

The MIMI team uses the SPICE system for ephemeris and pointing information. However, none of the routines in this user guide require the use of SPICE. Nevertheless, if you already know how to use SPICE and you want to use it to assist with MIMI data analysis, then Appendix A describes how to obtain and use the set of SPICE kernels used by the MIMI team.

Section 3

LEMMS

The LEMMS sensor consists of two oppositely directed telescopes, the Low Energy Telescope (LET) and the High Energy Telescope (HET), each containing a stack of solid-state detectors (SSDs). Figures 3.1 and 3.2 provide conceptual and engineering views of LEMMS, as well as a photograph. A thorough discussion of LEMMS is available in the MIMI instrument paper [Krimigis et al., 2004a].

3.1 The LEMMS Telescopes

3.1.1 LEMMS LET

The low energy end of LEMMS has a 15° aperture and is designed to measure ions with $E \geq 30$ keV and electrons in the range 15 keV – 1 MeV. Electrons are swept to side-facing detectors by permanent magnets. Electron detectors are divided into E and F detectors, where the E detector consists of a unique E1 detector component and a shared E2/F2 component, and the F detector consists of F1 and the shared E2/F2. Incident ions are not significantly deflected by the magnet and proceed to the rear of the LET where they strike detectors A and B. Note that electrons higher than 884 keV can also reach detectors A and B, in which case they get counted as ions. Particles penetrating B are prevented from continuing into the back of the HET by a gold absorber (1000 μm , 75 mm^2).

LEMMS data from detectors A, E1, and F1 are also processed through a pulse height analyzer that produces 64-channel energy spectra. The way in which a count is assigned to one of the 64 channels causes some events to be missed. However, the missing or dropped events are equally distributed throughout the 64 channels. Therefore a counter with the total number of events (dropped plus included) must be used to normalize the incomplete counts in the 64 channels. In the MIMI PDS data, this normalization has not been applied, but the normalization procedures are described in Section 3.5.

Some rate channels from the LET are collected at a faster cadence – the LEMMS priority channels. These priority channels are captured every other microsector (i.e., 8 times per subsector). Recall that normal rate channels are collected once per subsector. Different channels have been selected as priority channels during different time periods. The MIMI conglomerate calibration file lists

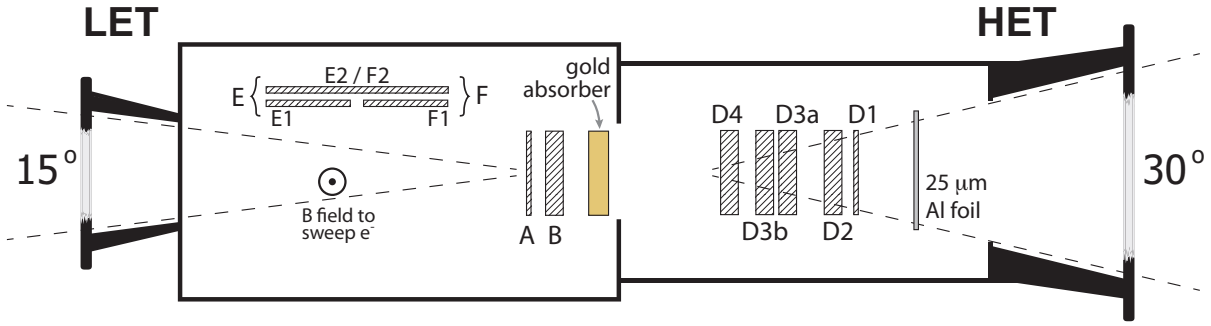


Figure 3.1: A conceptual diagram of LEMMS, showing the low and high energy ends of the detector and the solid-state detectors employed in each. In the LET, a magnetic field sweeps electrons aside onto the E and F detectors.

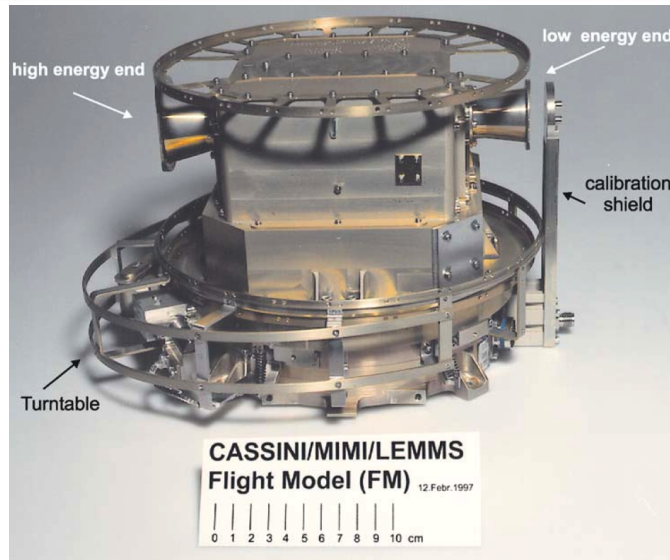
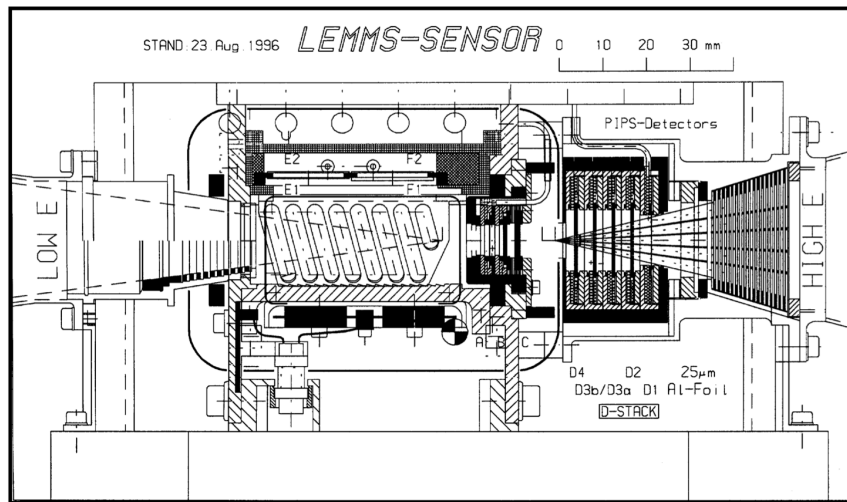


Figure 3.2: An engineering diagram of LEMMS shown with the same orientation as the conceptual presentation in Figure 3.1. In the photograph, the LET is pointed to the right.

Start Date	End Date	Priority Channel Names
1998:001	1999:230	A0 A1 E0 E1
1999:230	2003:256	A0 A1 C0 C1
2003:256	2004:295	A1 A5 C1 C5 E4 P2
2004:295	2009:052	A1 A0 C1 C5 E4 P2
2009:052	2011:365	A1 C3 C1 C5 E4 E0

Table 3.1: LEMMS channels can be put into a special list of priority channels that are sampled at a higher time resolution. This table lists the priority channel designations from 1998 to the end of 2011.

the priority channels and the time ranges during which a given channel has been designated as a priority channel. A summary of these designations is provided in Table 3.1.

3.1.2 LEMMS HET

The HET consists of a stack of five detectors D1, D2, D3a, D3b, and D4 to measure high-energy ions (1.5 – 160 MeV/N) and electrons (0.1 – 5 MeV). In front of detector D1, a 25 μm aluminum foil is inserted to suppress incoming light and reduce the flux of low-energy ions. The opening angle of the HET collimator is 30°.

3.1.3 LEMMS Turntable and Orientation

The LEMMS detector assembly is mounted onto a turntable capable of continuous rotation. When the spacecraft itself is also rotating, the platform allows LEMMS to detect particles covering essentially the entire unit sphere. The turntable rotates smoothly (as opposed to moving and pausing). When looking at the turntable with the spacecraft -Y axis pointed at you, the turntable rotation can be in either a clockwise or counter clockwise direction. In practice the rotation is almost always clockwise. After arrival at Saturn (the time period covered by this guide), it was always clockwise.

Figure 3.3 shows the orientation of LEMMS on the Cassini spacecraft. The -Y axis of the spacecraft frame (also referred to as $-Y_{\text{SC}}$) points out of the page, with the $-Z_{\text{SC}}$ axis pointing up (the HGA also points along $-Z_{\text{SC}}$). Thus a clockwise rotation of the LEMMS platform gives a right-handed rotation axis for LEMMS pointing into the page (parallel to $+Y_{\text{SC}}$).

One LEMMS turntable rotation is divided into 16 divisions called subsectors. Subsectors are divided into 16 microsectors, but the priority data are taken every other microsector, so in practice, there are a maximum of 8 priority data values taken within a subsector, as shown in Figure 3.3. Note that even though the rotation is divided into subsectors or microsectors, the actual rotation was continuous.

The orientation of the LEMMS turntable was not well characterized before 2000:154, before which no platform rotation angle data is available. From 2000:154 to 2005:032, the turntable operated normally, and the rotation angle is known. After 2005:032, the turntable began operating erratically and soon became stuck. Figure 3.4 shows the stuck position of LEMMS in the Cassini spacecraft frame, where the LET boresight is 77° off -Z towards -X.

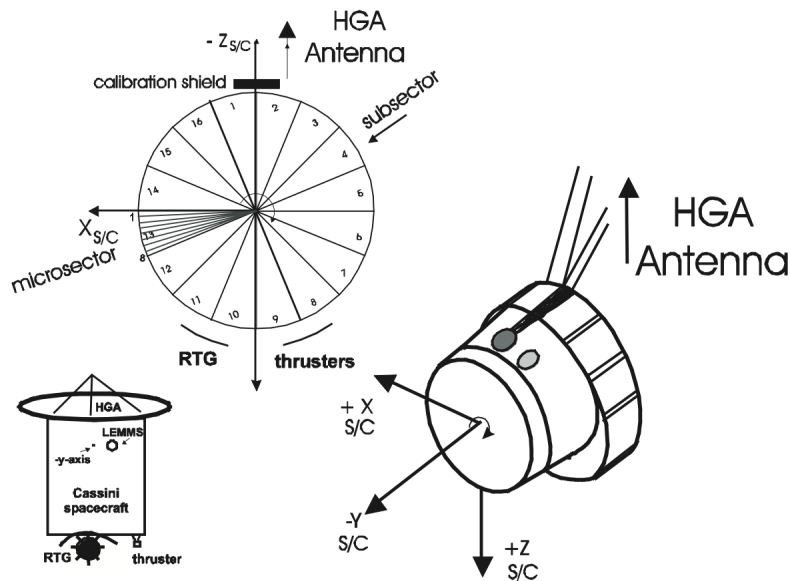


Figure 3.3: LEMMS orientation on the Cassini spacecraft, indicating how the rotation axis for the platform is the spacecraft $-Y$ axis. Also shown are the HGA and RTG, which partially obscure the FOV of LEMMS for some subsectors. The direction of increasing subsector numbers corresponds to a clockwise rotation of the LEMMS platform. This clockwise direction is also indicated with a small arrow around the $-Y$ spacecraft axis in the bottom right diagram.

For times when LEMMS was rotating, the angle of the LET is defined in a right-handed sense about the spacecraft $+Y$ axis, with zero corresponding to a look direction along the $-Z$ spacecraft axis. This angle is $+77^\circ$ in Figure 3.4. In MIMI PDS data files for LEMMS, the column titled `CENTER_LOOK_ANGLE_DEGREES` refers to this angle. When this angle is zero, LEMMS is in its “home” position with the LET pointed along $-Z$. LEMMS completes one rotation every sector, and the LEMMS controller software modifies the the rotation rate slightly so that the LET starts each sector lined up with $-Z$.

Note that when using these directions to compute pitch angles, the particle flow direction is opposite to the LEMMS boresight directions. The following formulas compute the Cartesian direction components of the flow direction vector using the `CENTER_LOOK_ANGLE_DEGREES`.

$$\begin{aligned} x &= \sin(\text{CENTER_LOOK_ANGLE_DEGREES}) \\ y &= 0 \\ z &= \cos(\text{CENTER_LOOK_ANGLE_DEGREES}) \end{aligned}$$

All the orientation data for LEMMS after 2000:154 (including the stuck period) has been captured in SPICE c-kernels, which are archived in the PDS at NAIF. For times when LEMMS was spinning, high-resolution angular information is available in monthly c-kernel files (although a few months had to be split in half to fit within SPICE’s size limits). After LEMMS stopped rotating, a single c-kernel defines the orientation from then on.

- Launch (1997) to 2000:154 → rotating, but orientation not well characterized
- 2000:154 to 2005:032 → rotating and orientation known (as monthly c-kernels)
- 2005:032 to 2005:109 → rotation sporadic with intermittent sticking
- 2005:109 and beyond → stuck (position available in single c-kernel)

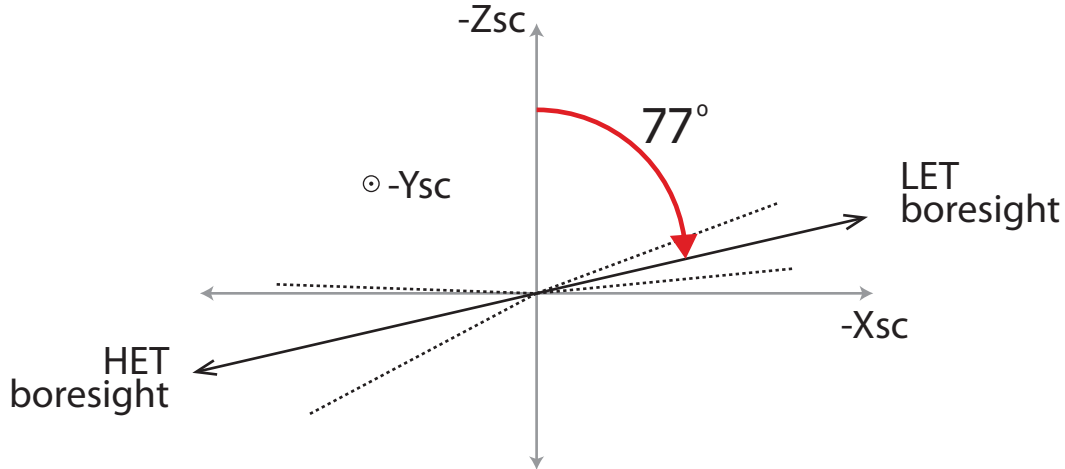


Figure 3.4: The orientation of LEMMS after it stopped rotating. The LET boresight is 77° away from $-Z$ towards $-X$, and the HET boresight is oppositely directed. The dashed lines indicate the width of the conical field of view for each detector, 15° for the LET and 30° for the HET. The red arrow indicates the direction of what is called a clockwise rotation of the LEMMS platform.

The preferred way to compute pitch angles is to use the LEMMS c-kernel to find the look direction of the LET in the spacecraft frame. Note that particles entering the LET have a direction opposite to the boresight vector, and this particle flow direction can be combined with the magnetic field data (also in the spacecraft frame) to determine the pitch angle.

3.2 LEMMS Data Products

In the following content descriptions for LEMMS data types, the header and prefix lines are not described since they are the same in all MIMI PDS data and were discussed in Section 1.6 and in Tables 1.5 and 1.6.

Unfortunately, the LEMMS data products “Normal Accumulator Rates” and “Fine Accumulator Rates” were named in a confusing way. A rate refers to counts per second, but the data in these products are just counts accumulated during the interval `START_EPHEMERIS_S` to `END_EPHEMERIS_S`. The misnomer arose because the channels in these products are often referred to as rate channels in order to distinguish them from PHA channels. Sections 3.3 and 3.4 describe the processes for computing actual rates as well as intensity from the raw counts in the data files.

As was pointed out in Section 1.6, uncalibrated MIMI PDS data in years 2004 through 2006 are still at revision 0, and therefore lack three prefix columns. In LEMMS data files, revision 3 also added three additional columns at the end that include angle information. Soon all data will be at revision 3 and these differences will disappear.

3.2.1 Normal Accumulator Rates

LEMMS normal rate data are found within yearly subdirectories `LEMMS_ACCUMULATION_RATES` below the top-level MIMI PDS data directory, as was discussed in Section 1.4, which also discusses file naming conventions. An example URL for a LEMMS accumulator rates data file is:

[https://pds-ppi.igpp.ucla.edu/archive1/COMIMI_OSAT/DATA/
LEMMS_ACCUMULATION_RATES/2012/LACC1_2012001_0003.CSV](https://pds-ppi.igpp.ucla.edu/archive1/COMIMI_OSAT/DATA/LEMMS_ACCUMULATION_RATES/2012/LACC1_2012001_0003.CSV)

These are daily data files with the year and day of year embedded in the filename. Here are a few more examples of LEMMS data files without any directory prefixes:

LACC1_2004013_0000.CSV first day of ACC1 data; note that it is still revision 0
LACC2_2004295_0000.CSV ACC2 starts on this date; some of this data is still revision 0
LACC2_2007001_0003.CSV starting in 2007, ACC2 is revision 3
LACC4_2009052_0003.CSV ACC4 data starts on this date; all is present as revision 3

Note that some files start with LACC1, LACC2 or LACC4. Each variant implies a slightly different set of columns. There is no ACC3. The only difference however, is in the last few columns that contain the summed priority channel data. (Note: This will be completely true when all the data is converted to revision 3. Currently all ACC1 and some ACC2 data are still at revision 0. Revision 0 lacks a few prefix columns and three angle columns. There are no revision 1 or revision 2 data.) Priority channel data are collected at a higher cadence than normal channel data, but a subsector summation of priority rates is included in the normal rates file for convenience. Thus when there is a change to the LEMMS channels that are designated as priority counters, the names of the last few columns in the accumulator data file will change, and the PDS requires a distinct file prefix for files with different columns. The column names in a data file also described in detail within the PDS label file. (As with all PDS products, each data file is accompanied by a description file called a label file.)

In PDS files of LEMMS accumulator rate data, the normal rate channels start at column index 13 (where the first column is index 0) and go through index 69. The channel names and energy ranges for each channel are presented in Table 3.2. These are the same energy ranges present in the calibration file, and they have remained constant for the duration of the mission so far (up to the start of 2013). Note that the energy range given is for one specific species, and that species is listed in the final column of the table.

Tables 3.3 through 3.5 list the column names and descriptions for columns after the normal rate channels for each variant of the LEMMS accumulator data (LACC1 through LACC4). Different fine rate channels (summed and presented at the cadence of the normal rate channels) are present in each variant. After the fine rate channels, there are angular orientation values that describe the pointing of the LEMMS sensor. Recall that in revision 0 data (years 2004 through 2006), there are no angular orientation columns.

3.2.2 Fine Accumulator Rates

The subdirectory LEMMS_FINE_ACCUMULATION_RATES contains the fine accumulator rate data for LEMMS. Yearly subdirectories below this contain daily files. See Section 1.4 for the top-level directory and a more full description of the file naming convention. An example URL for a LEMMS fine accumulator rate data file is (note that the line break is artificial):

[https://pds-ppi.igpp.ucla.edu/archive1/COMIMI_OSAT/DATA/
LEMMS_FINE_ACCUMULATION_RATES/2012/LFRT1_2012001_0003.CSV](https://pds-ppi.igpp.ucla.edu/archive1/COMIMI_OSAT/DATA/LEMMS_FINE_ACCUMULATION_RATES/2012/LFRT1_2012001_0003.CSV)

As was pointed out in Section 1.6, uncalibrated MIMI PDS data in years 2004 through 2006 are still at revision 0, and therefore lack some prefix columns. In all LEMMS data files, revision 3 also

Telescope	Column Index	Column Name	E Low (keV)	E High (keV)	Species
LET	13	Channel_A0	27	35	p
	14	Channel_A1	35	56	p
	15	Channel_A2	56	106	p
	16	Channel_A3	106	255	p
	17	Channel_A4	255	506	p
	18	Channel_A5	506	805	p
	19	Channel_A6	805	1600	p
	20	Channel_A7	1615	4000	p
	21	Channel_A8	1270	3930	He
	22	Channel_B0	4000	7500	p
	23	Channel_B1	7500	18600	p
	24	Channel_B2	3920	5470	He
	25	Channel_B3	5470	9900	He
	26	Channel_BE	1000	2900	e
	27	Channel_C0	18	40	e
	28	Channel_C1	27	48	e
	29	Channel_C2	41	60	e
	30	Channel_C3	56	100	e
	31	Channel_C4	92	183	e
	32	Channel_C5	175	300	e
	33	Channel_C6	265	550	e
	34	Channel_C7	510	832	e
	35	Channel_AS	27	-1	p
	36	Channel_BS	4000	-1	p
	37	Channel_ES	20	-1	e
	38	Channel_E2_F2S	1000	-1	e
	39	Channel_FS	100	-1	e
HET	40	Channel_E0	110	365	e
	41	Channel_E1	220	485	e
	42	Channel_E2	340	1350	e
	43	Channel_E3	600	4950	e
	44	Channel_E4	790	4750	e
	45	Channel_E5	800	-1	e
	46	Channel_E6	1600	21000	e
	47	Channel_E7	7000	20000	e
	48	Channel_G1	50	400	X-ray
	49	Channel_P1	1424	2278	p
	50	Channel_P2	2280	4492	p
	51	Channel_P3	4491	5744	p
	52	Channel_P4	13200	25400	p
	53	Channel_P5	8311	11449	p
	54	Channel_P6	11474	13433	p
	55	Channel_P7	12101	58902	p
	56	Channel_P8	25185	59000	p
	57	Channel_P9	58650	158700	p
	58	Channel_H1	2100	4400	He
	59	Channel_H2	4400	10300	He
	60	Channel_H3	11200	25400	He
	61	Channel_H4	25400	43300	He
	62	Channel_H5	20000	25000	p
	63	Channel_Z1	3430	9370	O
	64	Channel_Z2	9370	24700	O
	65	Channel_Z3	24700	193000	O
	66	Channel_D1	1400	-1	p
67	Channel_D2	4400	-1	p	
68	Channel_D3	11200	-1	p	
69	Channel_D41	19000	-1	p	

Table 3.2: Descriptions of the rate channel columns in all LEMMS accumulator files. Each channel belongs to only one telescope. The energy range for each channel is applicable only to the species shown in the table. A value of -1 for the upper energy indicates no upper energy limit.

Column Index	Column Name	Description
70	Priority_Counter_0_A1_Sum	sum of 8 double microsector counts for A1
71	Priority_Counter_1_A5_Sum	sum of 8 double microsector counts for A5
72	Priority_Counter_2_C1_Sum	sum of 8 double microsector counts for C1
73	Priority_Counter_3_C5_Sum	sum of 8 double microsector counts for C5
74	Priority_Counter_4_E4_Sum	sum of 8 double microsector counts for E4
75	Priority_Counter_5_P2_Sum	sum of 8 double microsector counts for P2
76	Center_Look_Angle	angle in deg. between LET boresight and SC -Z
77	Lemms_Sun_Angle	angle in deg. between LET boresight and the SC-to-Sun vector
78	Lemms_Sun_Angle_Phi	angle in deg. between LET boresight and projection of SC-Sun line into SC XZ plane
79	Lemms_Sun_Angle_Theta	angle in deg. Between the SC-to-Sun vector and the SC X-Z plane

Table 3.3: Final columns for LEMMS accumulator files of type LACC1, which are used for files from 2004 day 13 through 2004 day 294.

Column Index	Column Name	Description
70	Priority_Counter_0_A0_Sum	sum of 8 double microsector counts for A0
71	Priority_Counter_1_A1_Sum	sum of 8 double microsector counts for A1
72	Priority_Counter_2_C1_Sum	sum of 8 double microsector counts for C1
73	Priority_Counter_3_C5_Sum	sum of 8 double microsector counts for C5
74	Priority_Counter_4_E4_Sum	sum of 8 double microsector counts for E4
75	Priority_Counter_5_P2_Sum	sum of 8 double microsector counts for P2
76	Center_Look_Angle	angle in deg. between LET boresight and SC -Z
77	Lemms_Sun_Angle	angle in deg. between LET boresight and the SC-to-Sun vector
78	Lemms_Sun_Angle_Phi	angle in deg. between LET boresight and projection of SC-Sun line into SC XZ plane
79	Lemms_Sun_Angle_Theta	angle in deg. Between the SC-to-Sun vector and the SC X-Z plane

Table 3.4: Final columns for LEMMS accumulator files of type LACC2, which are used for files from 2004 day 295 through 2009 day 51.

Column Index	Column Name	Description
70	Priority_Counter_0_A1_Sum	sum of 8 double microsector counts for A1
71	Priority_Counter_1_C3_Sum	sum of 8 double microsector counts for C3
72	Priority_Counter_2_C1_Sum	sum of 8 double microsector counts for C1
73	Priority_Counter_3_C5_Sum	sum of 8 double microsector counts for C5
74	Priority_Counter_4_E4_Sum	sum of 8 double microsector counts for E4
75	Priority_Counter_5_E0_Sum	sum of 8 double microsector counts for E0
76	Center_Look_Angle	angle in deg. between LET boresight and SC -Z
77	Lemms_Sun_Angle	angle in deg. between LET boresight and the SC-to-Sun vector
78	Lemms_Sun_Angle_Phi	angle in deg. between LET boresight and projection of SC-Sun line into SC XZ plane
79	Lemms_Sun_Angle_Theta	angle in deg. Between the SC-to-Sun vector and the SC X-Z plane

Table 3.5: Final columns for LEMMS accumulator files of type LACC4, which are used for files from 2009 day 52 through the present (PDS currently has up to 2010 day 365).

added three additional columns at the end that include angle information. Soon all data will be at revision 3 and these confusing differences will disappear.

Here are a few more examples of LEMMS data files without any directory prefixes:

```
LFRT1_2004013_0000.CSV  first day of FRT1 data; note that it is still revision 0
LFRT2_2004295_0000.CSV  FRT2 starts on this date; some of this data is still revision 0
LFRT2_2007001_0003.CSV  starting in 2007, FRT2 is revision 3
LFRT4_2009052_0003.CSV  FRT4 data starts on this date; all is present as revision 3
```

Note that some files start with LFRT1, LFRT2 or LFRT4. There are no LFRT3 data. Each variant contains a different set of channels representing the priority channels active at the time. Tables 3.6 through Tables 3.8 describe the column names (beyond the standard prefix columns) for each type of LEMMS priority rate data. (Note: Years 2004 through 2006 are still the older revision 0 data that has not been converted to revision 3, which added a few more prefix columns, and for the LEMMS FRT data, three more angle columns at the end.)

The energy ranges for the priority channels are the same as for the corresponding normal rate channel. All priority channel data are collected at a cadence of every other microsector. This cadence is maintained for all data rates, even the very lowest, so that the time cadence of the priority rates is consistent across the mission.

3.2.3 PHA Data

The subdirectory LEMMS_PULSE_HEIGHT_ANALYSIS contains LEMMS PHA data. Yearly subdirectories below this contain daily files. See Section 1.4 for the top-level directory and a more full description of the file naming convention. An example URL for a LEMMS fine accumulator rate data file is (note that the line break is artificial):

```
https://pds-ppi.igpp.ucla.edu/archive1/COMIMI_OSAT/DATA/
  LEMMS_PULSE_HEIGHT_ANALYSIS/2012/LPHAO_2012001_0003.CSV
```

Here are a few more examples of LEMMS PHA data files without any directory prefixes:

```
LPHAO_2010199_0003.CSV
LPHAO_2010200_0003.CSV
LPHAO_2010201_0003.CSV
LPHAO_2010301_0003.CSV
```

Each PHA data file contains the standard header lines, and each line after this begins with the standard prefix columns. Following the prefix columns are three sets of high resolution energy channels listed in Table 3.10. The A channels are for 13 to 807 keV protons, and the E and F channels are for electrons ranging from 7 to 437 keV and 42 to 2220 keV respectively. The exact energy ranges for each LEMMS PHA channel are provided in the MIMI calibration file and can be found by selecting rows with PURPOSE=ENERGY, DATA_TYPE = PHA, and SENSOR=LEMMS.

It is important to note that a subset of the PHA channels are typically used for science analysis. For all sensor elements (A, E, and F1), the highest energy channel (index 63, with 0 being the first channel) contains all the counts that did not fit into any other channel, and so it is often very noisy. Some of the lowest energy channels are also not used because the detection efficiency drops off rapidly as energy decreases, and also the efficiency is less well characterized at those lower energies. Thus the counts in these low energy channels are very uncertain. The commonly used

Column Index	Column Name	Description
10	MICROSECTOR	microsector counter at start of measurement
11	A1	counts in A1 in two microsectors
12	A5	counts in A5 in two microsectors
13	C1	counts in C1 in two microsectors
14	C5	counts in C5 in two microsectors
15	E4	counts in E4 in two microsectors
16	P2	counts in P2 in two microsectors
17	CENTER_LOOK_ANGLE_DEGREES	angle in deg. between LET boresight and SC -Z

Table 3.6: Column names and descriptions for LEMMS fine accumulator rate data files of type LFRT1. These channels were used as fine rate channels from 2004 day 13 through 2004 day 294.

Column Index	Column Name	Description
10	MICROSECTOR	microsector counter at start of measurement
11	A0	counts in A0 in two microsectors
12	A1	counts in A1 in two microsectors
13	C1	counts in C1 in two microsectors
14	C5	counts in C5 in two microsectors
15	E4	counts in E4 in two microsectors
16	P2	counts in P2 in two microsectors
17	CENTER_LOOK_ANGLE_DEGREES	angle in deg. between LET boresight and SC -Z

Table 3.7: Column names and descriptions for LEMMS fine accumulator rate data files of type LFRT2. These channels were used as fine rate channels from 2004 day 295 through 2009 day 51.

Column Index	Column Name	Description
13	MICROSECTOR	microsector counter at start of measurement
14	A1	counts in A1 in two microsectors
15	C3	counts in C3 in two microsectors
16	C1	counts in C1 in two microsectors
17	C5	counts in C5 in two microsectors
18	E4	counts in E4 in two microsectors
19	E0	counts in E0 in two microsectors
20	CENTER_LOOK_ANGLE_DEGREES	angle in deg. between LET boresight and SC -Z
21	LEMMS_SUN_ANGLE	
22	LEMMS_SUN_ANGLE_PHI	
23	LEMMS_SUN_ANGLE_THETA	

Table 3.8: Column names and descriptions for LEMMS fine accumulator rate data files of type LFRT4. These channels were used as fine rate channels from 2009 day 52 through the present (PDS currently has up to 2010 day 365).

LEMMS PHA Detector Element	Indices of Typically Used for Channels	Energy Range of these Channels
A	8 to 62	26 to 758 keV
E	15 to 62	20 to 410 keV
F1	26 to 59	206 to 1717 keV

Table 3.9: Channel index ranges for the LEMMS PHA channels that are commonly used in science analysis. The resulting energy range for each index range is also given.

Column Index	Column Name	Species	E_{low}	E_{high}
13	Detector_A_Bin_0	protons	13.6	15.2
14	Detector_A_Bin_1	protons	15.2	16.8
15	Detector_A_Bin_2	protons	16.8	18.5
...				
75	Detector_A_Bin_62	protons	736	781
76	Detector_A_Bin_63	protons	781	833
77	Detector_E_Bin_0	electrons	6.73	7.6
78	Detector_E_Bin_1	electrons	7.6	8.48
...				
140	Detector_E_Bin_63	electrons	423	451
141	Detector_F1_Bin_0	electrons	39.8	44.2
142	Detector_F1_Bin_1	electrons	44.2	48.7
...				
204	Detector_F1_Bin_63	electrons	2150	2300
205	Center_Look_Angle			
206	Lemms_Sun_Angle			
207	Lemms_Sun_Angle_Phi			
208	Lemms_Sun_Angle_Theta			

Table 3.10: Column names for the three high energy resolution spectra present in LEMMS PHA data. For brevity, not all column names are shown.

channels are listed in Table 3.9. For ions (the A channels), these indices are 8 through 62 (26 to 758 keV). For PHA electrons, high energy E channels overlap in energy with low energy F1 channels. Efficiencies in the transition energies between E and F1 are difficult to characterize, since they depend on spectral shape and incident angle. Thus the constant values used for these efficiencies (in the energy overlap region) are only an approximation. The choice of typical channels for E and F1 was made to provide some overlap in energy but still provide good agreement in intensities in most situations. For E, indices 15 to 62 are used (20 to 410 keV), and for F1, indices 26 through 59 (206 to 1717 keV) are used. All indices are zero-based.

3.3 Calibrating LEMMS Normal Accumulator Rates

LEMMS accumulator rates can be calibrated to counts/second, integral intensity, or differential intensity. Here “intensity” is the same as “flux.”

Counts per Second

Counts for each channel listed in Table 3.2 are available in LEMMS accumulator rate files. Note that the units are really counts, even though it is common practice to refer to these files as accumulator rate files. To compute a rate r in counts per second, simply divide the counts C by the accumulation time, Δt .

$$r = \frac{C}{\Delta t} \quad (3.1)$$

Computing Δt , requires knowledge of the spin period and bit rate, because although the readout time for these counters is normally one subsector, for the lowest bit rate (the so called “very low bit rate”), the readout interval changes two subsectors. The spin period and bit rate flag are both present on each data line as part of the standard data line prefix (see Table 1.6 on page 20). Because 16 subsectors make a sector, and 16 sectors make a spin, the accumulation time is thus

$$\Delta t = (\tau_{\text{spin}}/256) n_{\text{subsectors}} \quad (3.2)$$

where $n_{\text{subsectors}}$ is 1 for all bit rate values except very low bit rate, when it is 2. There is no dead time between readouts.

For many LEMMS channels, it is possible to do a background subtraction. Background levels are variable over time, and the MIMI conglomerate calibration file contains background levels for many LEMMS channels obtained at numerous points throughout the mission. The background points in the calibration file are arranged in time order for each channel. A reasonable background at any particular time can be obtained by interpolating between the nearest two background points that bracket the time of interest. All background values are provided in units of counts per second. The method shown here for computing backgrounds will not be repeated in subsequent descriptions of LEMMS calibration procedures.

The background should be removed from the counts before dividing by the integration time. LEMMS backgrounds are provided in counts per second, and so the corrected counts C' is then

$$C' = C - B(t)\Delta t \quad (3.3)$$

The background value as a function of time, $B(t)$, can be constructed for each channel by interpolating between the background points provided in the calibration file. If the background measured at two points t_0 and t_1 , is $B(t_0)$ and $B(t_1)$, then the background at a time t between t_0 and t_1 is

$$B(t) = (1 - f)B(t_0) + fB(t_1) \quad (3.4)$$

where f is the normalized location of t in the interval from t_0 to t_1 .

$$f = \frac{t - t_0}{t_1 - t_0} \quad (3.5)$$

Using C' instead of C for the counts results in the equation for the background-subtracted count rate, r' :

$$r' = \frac{C'}{\Delta t} \quad (3.6)$$

Uncertainties are calculated as follows. Poisson uncertainties are assumed for the counts so that $\sigma_C = \sqrt{C}$. Uncertainty values are also provided for the background rates, and these must be taken into account as well. When interpolating between two background values, the uncertainty associated with the interpolated point can be computed from the uncertainties of the surrounding points. If the uncertainties in the background measured at two points t_0 and t_1 are $U(t_0)$ and $U(t_1)$ respectively, then the uncertainty $U(t)$ at a time t between t_0 and t_1 is

$$U(t) = \sqrt{(1-f)^2 U(t_0)^2 + f^2 U(t_1)^2} \quad (3.7)$$

where f has the same meaning as in equation 3.5. This uncertainty is in units of counts per second, so the overall uncertainty in the background-subtracted count rate $\sigma_{r'}$ is then

$$\sigma_{r'} = \frac{\sqrt{\sigma_C^2 + (U(t) \Delta t)^2}}{\Delta t} \quad (3.8)$$

Differential and Integral Intensity

To compute differential intensity, j , the count rate must also be divided by the efficiency ϵ , the geometry factor g , and channel energy width ΔE .

$$j = \frac{C}{\Delta t g \epsilon \Delta E} \quad (3.9)$$

Using background subtracted counts C' (equation 3.3) instead of counts C will provide a background subtracted value for the intensity.

The MIMI conglomerate calibration file (Section 2.2) provides the efficiencies and energy widths for all LEMMS channels. Note that the efficiencies for LEMMS also include the geometry factor, so that g is unnecessary (i.e., can be set to 1) in the above equation. The accumulation time Δt is computed in the same way as outlined above in the discussion about calculating counts per second.

Procedures for navigating the calibration file to extract the correct efficiency and energy width are described in Sections 2.2 and 2.3.

To compute integral intensity, I , simply leave the energy width out of the denominator:

$$I = \frac{C}{\Delta t g \epsilon} \quad (3.10)$$

3.4 Calibrating LEMMS Fine Accumulator Rates

Calibration for these channels is very similar to the normal accumulator rates. The only difference is that the accumulation time does not depend on the bit rate and is always two microsectors. Equations 3.1, 3.9, and 3.10 for count rate, differential intensity, and integral intensity can be used if the definition of Δt is changed to

$$\Delta t = \tau_{\text{spin}} / (256 \times 8) \quad (3.11)$$

where the extra factor of 8 in the denominator comes from the fact that there are 16 microsectors per subsector, and each measurement is two microsectors in duration.

One correction that is sometimes applied to the fine accumulator rates involves averaging the final measurement in one sector with the first measurement of the next sector. When the subsector counter is 15 (i.e., the final subsector of a sector), and the microsector counter is 14 (i.e., the last 2-microsector measurement in a subsector), something happens within the LEMMS instrument that gives unequal accumulation times to the next two measurements. This can be corrected by averaging the measurements. The following pseudo-code algorithm loops over the rows in a fine accumulator data table, finds the two problematic microsector measurements, averages them, and replaces both values with the average.

```

for i=0 to N-1
  if (subsector[i] is 0 AND microsector[i] is 0)
    if (i is 0)
      (with no previous measurement, the average cannot
       be done, and so this value should be reported as fill)
      counts[i] = FILL
    else
      (check if the previous measurement was actually from
       the last microsector measurement of the previous spin
       and if it was, average the previous measurement
       with this measurements counts and use the average
       to replace both this and the previous measurement)
      if (subsector[i-1] is 15 AND microsector[i-1] is 14 AND
          spin[i-1] is the previous spin)
        (compute an average counts)
        avg = (counts[i] + counts[i-1]) / 2.0
        counts[i-1] = avg
        counts[i] = avg
      endif
    endif
  endif
endif
endfor

```

It is also necessary to check if the counts at the last index $i=N-1$ correspond to subsector 15 and microsector 14, in which case there is no subsequent data to average, indicating that the counts at $i=N-1$ should be replaced with FILL.

3.5 Calibrating LEMMS PHA Data

Each LEMMS PHA data file contains three spectra, one for protons (A channels) and two for electrons (E and F channels). Although the data are in units of counts, these counts must be normalized, because not all of the counts are recorded for each channel. The normalization is done on a per spectrum basis. For each spectrum, a separate counter captures the total number of events that should have been recorded in all channels of the spectrum. The actual number of events in the spectrum is always less (because the processing was not fast enough to categorize all incident events). The normalization factor is then the ratio of the total event counter to the sum of all the

PHA Spectrum	Normalizing Rate Channel
A channel protons	Channel_AS
E channel electrons	Channel_ES
F channel electrons	Channel_FS

Table 3.11: The counts in each of the three PHA spectra must be normalized using a specific rate counter from LEMMS normal accumulator rate. For each PHA spectrum listed in the first column, the normalizing rate counter is given in the second column.

Bit Rate	PHA Accum. Time		Subsctrs. Present in PHA data	Subsctrs. Present in Normal Accum. Rate Data
	in Subsectors	Ratio of PHA:rates		
1 - very high	$n_{\text{subsectors}} = 1$	1:1	all (0, 1, ...15)	all (0, 1, ...15)
2 - high	1	1:1	all (0, 1, ...15)	all (0, 1, ...15)
3 - medium	2	1:2	0-1, 2-3, ... 14-15	all (0, 1, ...15)
4 - low	4	1:4	0-3, 4-7, 8-11, 12-15	all (0, 1, ...15)
5 - very low	8	1:4	0-7, 8-15	0-1, 2-3, ... 14-15

Table 3.12: Accumulation times for LEMMS PHA data and a comparison with the duration of measurements for LEMMS normal accumulator rates. This comparison is needed when using the channels in Table 3.11 to normalize the PHA data, because, depending on bit rate, multiple normal accumulator rate measurements will need to be combined to get the correct normalizing factor for the PHA data.

counts actually recorded at each energy step of the spectrum. Let x represent one of the three spectrum types (A, E, or F), and $C_{x,i}$ is then number of raw (un-normalized) counts in channel i of spectrum x , where i ranges from 0 to 63. The normalizing factor n_x is then

$$n_x = \frac{S_x}{\sum_{i=0}^{63} C_{x,i}} \quad (3.12)$$

where S_x is the counter recording the actual total number of counts that should have been present in the spectrum, i.e., one of the channels `Channel_AS`, `Channel_ES`, or `Channel_FS`. These counters do not live in PHA data files, but must be obtained from the normal rate counter data files. Table 3.11 lists the names of the rate channels for normalizing PHA data.

One complication in obtaining S_x for each spectrum is that there can be a difference in cadence between the PHA data and the normalizing rate channels. Thus, when computing S_x , the total actual counts that should be present in a PHA spectrum, multiple measurements from the corresponding rate data may need to be summed. Recall that normal accumulator rate data is obtained every subsector, except in very low bit rate, when it is collected every other subsector. LEMMS PHA data are taken every subsector only when the bit rate is “very hi” or “hi.” In “medium” bit rate, PHA data accumulation happens over two subsectors, in “low” four subsectors, and for “very low,” PHA data bins are eight subsectors in duration. These accumulation intervals are described in Table 3.12.

In the case of “very high” or “hi” bit rate data, the normalizing counts S_x will be a single value that can be looked up by finding the counts from the normal accumulator rate data with the same spin counter and sector counter and subsector counter. In the case of “medium” bit rate, the PHA data will be summed over 2 subsectors, and so two values from the normal accumulator rate data will

need to be summed. For example, consider a PHA measurement in “medium” bit rate that covers subsectors 0 and 1. The normalizing counts come from looking up two values: one from subsector 0 and one from subsector 1 of the same spin and sector. For a “very low” bit rate example, consider the PHA data that includes measurements from subsector 0 through 7. In this case, four normal accumulator rate data count values will need to be summed to get S_x , where the first is the 0 to 1 subsector sum, the second is the 2 to 3 subsector sum, the third is the 4 to 5 subsector sum, and the fourth is the 6 to 7 subsector sum from the same spin and sector,

Counts Per Second

Once normalized, PHA data are converted to other units in the same way as the rate channels. With $C_{x,i}$ as the un-normalized counts, n_x as the normalizing factor for spectrum x , and Δt as the accumulation time, the count rate $r_{x,i}$ for channel i of spectrum x

$$r_{x,i} = \frac{C_{x,i} n_x}{\Delta t} \quad (3.13)$$

The accumulation time Δt is computed using equation 3.2, where the number of subsectors $n_{\text{subsectors}}$ is obtained from Table 3.12 using the bit rate for the given measurement.

A background subtracted rate for an LEMMS PHA channel can also be computed:

$$r'_{x,i} = \frac{C'_{x,i} n_x}{\Delta t} \quad (3.14)$$

$$\text{with } C'_{x,i} = C_{x,i} - B_{x,i}(t) \Delta t \quad (3.15)$$

The function $B_{x,i}(t)$ is constructed by linearly interpolating between the background rates provided at multiple times for each PHA channel as was discussed above in Section 3.3 on Calibrating the LEMMS Normal Accumulator Rates.

Differential and Integral Intensity

Differential and integral intensity for LEMMS PHA channels are computed in the same way as for the LEMMS rate channels. The following equation shows the differential intensity calculation using background subtracted counts.

$$j_{x,i} = \frac{C'_{x,i}}{\Delta t g \epsilon \Delta E} \quad (3.16)$$

Efficiencies and energy ranges for all PHA channels are recorded in the MIMI conglomerate calibration file.

Obtaining Calibrated Data

The LEMMS calibration formulas described here are implemented in two software applications that can be used to access the PDS MIMI data. These tools are described in Sections 6.1 and 6.3.

3.6 Sample Plots and Interpretation for Commonly Used LEMMS Channels

The channels most commonly used in publications containing LEMMS data are the rate channels (C0-C7, E0-E7, A0-A7, P2-P8) and the PHA channels (from the PHA-E, PHA-F1 and PHA-A detectors). This section contains Figures 3.5 through 3.24 that illustrate the use of these channels.

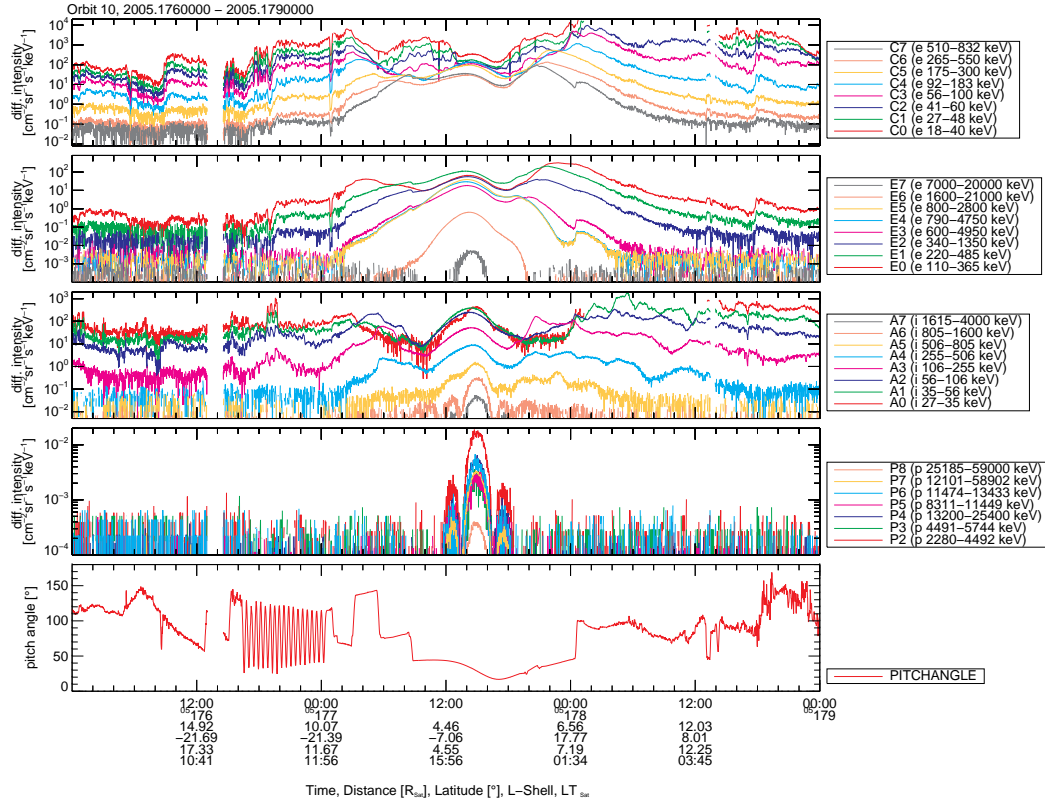


Figure 3.5: Overview of LEMMS rate channel data from the 10th orbit around Saturn. The plot contains many of the common features observed with LEMMS, the statistical significance of which is discussed in [Kollmann et al., 2011]. Plotted as a function of time are differential intensities ($\text{cm}^{-2}\text{sr}^{-1}\text{s}^{-1}\text{keV}^{-1}$) of energetic electrons and ions. Starting from the top, panels show data from the C-channels (LET electrons), E-channels (HET electrons), A-channels (LET protons) and P-channels (HET protons). The bottom panel shows the particle pitch angle observed from LET. Position information is given below the time tags of the x-axis. Periapsis was around 13:30 (DOY 177/2005). Far from Saturn (start and end of the plot) LEMMS fluxes and profiles change considerably from orbit to orbit in all channels that measure foreground. In the middle magnetosphere (L-shells between about 8 and 13), fluxes are still variable, but show consistently a broad peak, associated with the ring current [Krimigis et al., 2007a, Kollmann et al., 2011]. Within that distance, fluxes in many C- and A-channels start to drop, due to losses in the neutral cloud [Paranicas et al., 2008, Kollmann et al., 2011]. Narrow flux enhancements within that broad dropout region are usually attributed to injections [Mauk et al., 2005, Müller et al., 2010, Paranicas et al., 2010]. Sharper, short-duration dropouts in the C-channels (seen between 02:00-23:00 - DOY 177/2005) are moon absorption signatures, or “microsignatures” [Paranicas et al., 2005, Roussos et al., 2005, 2007, 2008a]. Around periapsis, all channels record fluxes above the instrumental background (radiation belts), but many of the lowest energy C- and A-channels (the fluxes of which recover) may be getting significant contributions in the signal from penetrating radiation [Kollmann et al., 2011]. The highest energy proton channels go above background typically inside a dipole-L of 4.9 (L-shell of Tethys) and show deep and extended dropouts that map to the orbits of several Saturnian moons [Paranicas et al., 2008, Roussos et al., 2008b, Armstrong et al., 2009, Roussos et al., 2011]. These dropouts are called macrosignatures and the ones visible here are from Enceladus. Data gaps in several channels are from regions that LEMMS was light contaminated. The particle pitch angle in the bottom panel is a useful index that can help understand if abrupt changes in fluxes are due to temporal/spatial variability in the particle distributions or due to rapid changes in the pitch angle pointing. For instance, an intense change in the fluxes of channels E4-E6 around 00:00 of DOY 178/2005 coincides with a sharp change in pitch angle (and spacecraft) pointing.

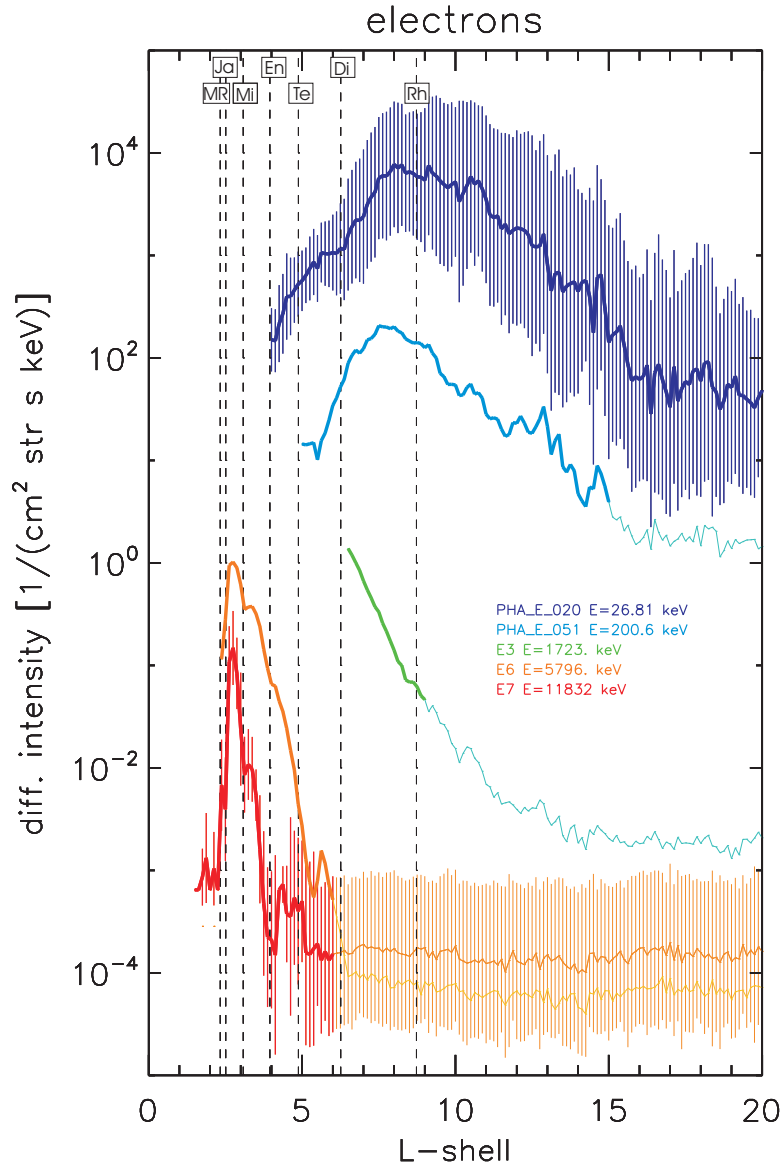


Figure 3.6: Average flux profiles for various LEMMS electron channels, from [Kollmann et al., 2011]. In several cases, error bars are shown, which are primarily related to the variability in the magnetosphere (note that these error bars show a kind of systematic, variability-based uncertainty and are not the uncertainties derived from simple counting statistics as presented above in calibration calculations.) Thinner lines on each profile indicate where each LEMMS channel is close to the instrumental background levels. Profiles are not shown for the inner regions, if there is uncertainty on whether their signal is dominated by radiation belt noise, or not. The locations of various moon L-shells and the main rings (“MR”) are also indicated.

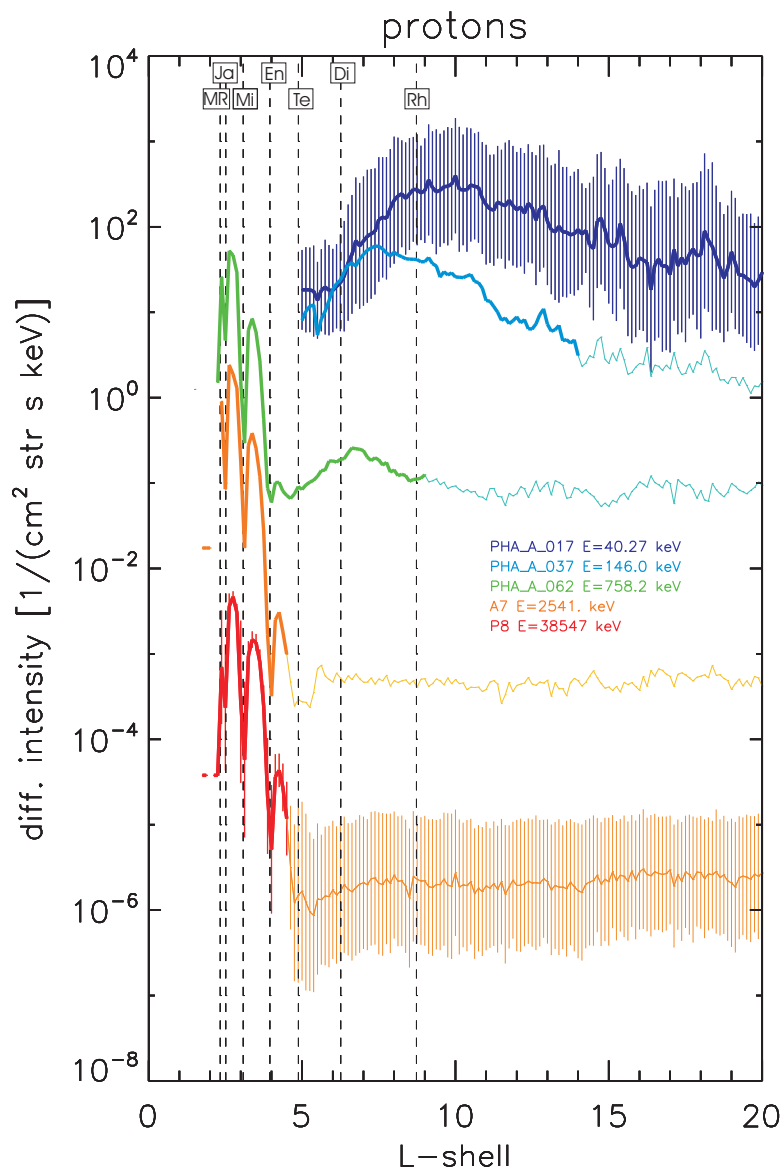


Figure 3.7: Same as in Figure 3.7, but for protons.

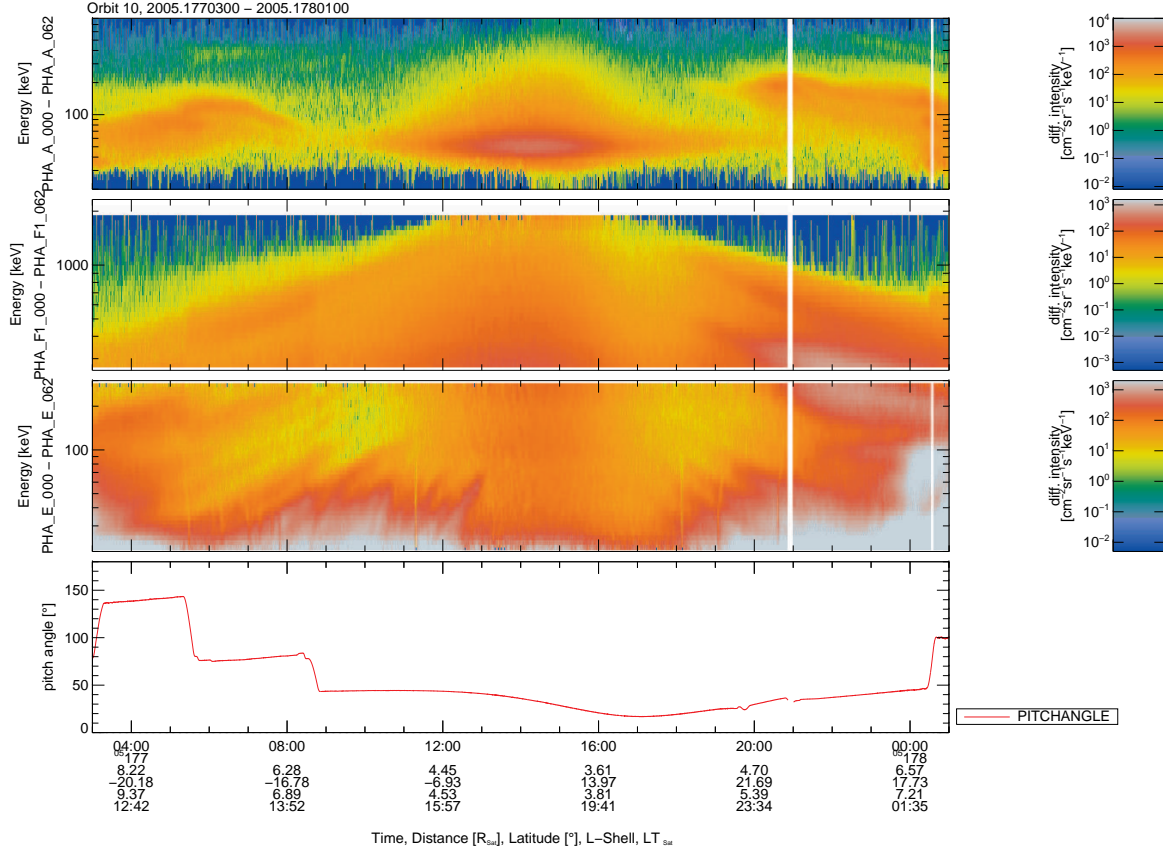


Figure 3.8: Overview of LEMMS PHA channel data, for a similar period as in Figure 3.5, zoomed in the interval around periapsis. Plotted as a function of time are energy-flux spectrograms, where the differential intensities (or fluxes) are color coded. The top panel shows data from the PHA-A proton channels, the second and third panels are from the top show fluxes from the PHA-F1 (high energy electrons) and PHA-E (low energy electron) detector channels. The bottom panel shows the particle pitch angle observed from LET. Some of the features described in Figure 3.5 are better resolved here. One example are the injections [Mauk et al., 2005, Müller et al., 2010, Paranicas et al., 2010], the signature of which is typically a time and energy-dispersed flux enhancement (here examples are best visible in the PHA-E spectrogram). Energetic ion injections are less resolved because they survive less in Saturn’s neutral torus [Paranicas et al., 2008]. Another commonly observed structure is the evolution of the peak electron energy below which foreground is measured, as a function of L-shell. This is resolved in data from the PHA-F1 detector and its origin is discussed in [Paranicas et al., 2010]. Data gaps correspond to light contaminated intervals. The low fluxes for the PHA-A channels with energies lower than 30 keV (at all times) are due to a decrease in the corresponding geometry factors. As was discussed in Section 3.2.3, these channels should not be used. Energetic electron microsignatures from several moons are also well-resolved in PHA-E channel data.

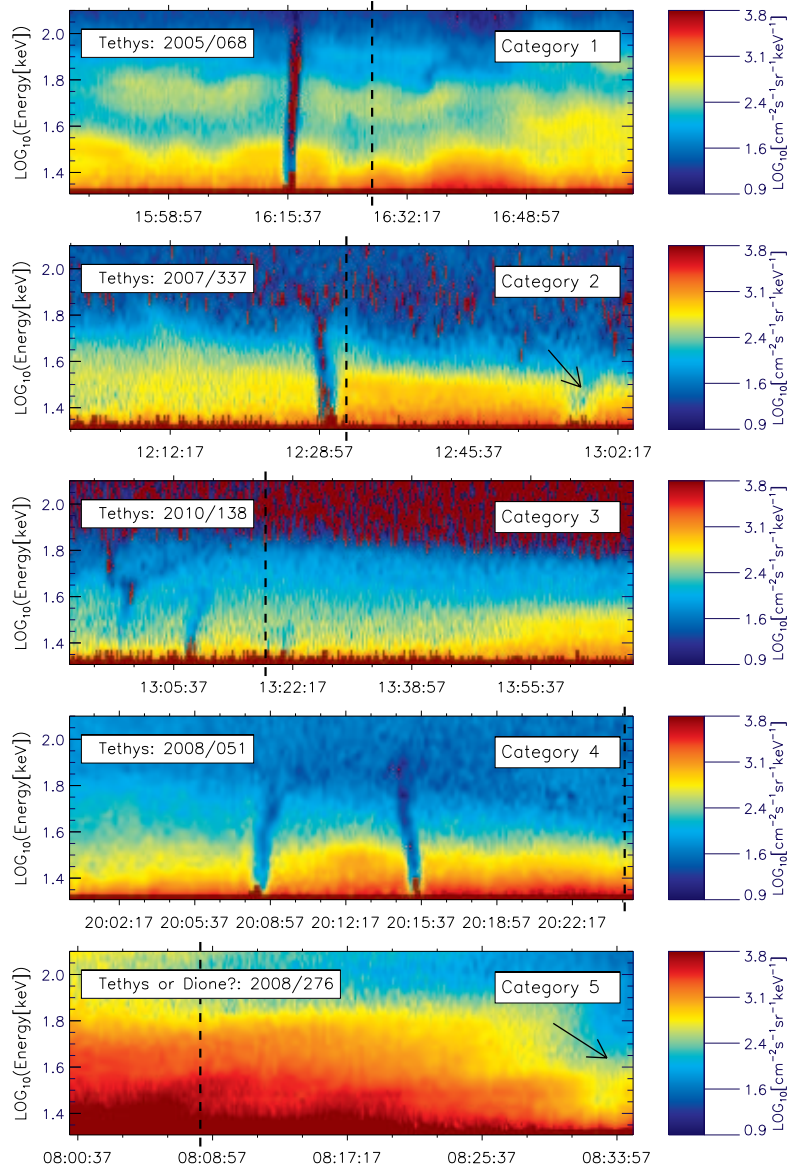


Figure 3.9: Typical examples of electron time-energy spectrograms of Tethys microsignature events in LEMMS’s PHA dataset. [Andriopoulou et al., 2011] (and also see a full write up to be published in 2012) organized these events in different categories, according to structuring of the energy dependent microsignature location. Panel (a) depicts a Tethys microsignature with an organized energy dispersion (category one). In panel (b) we can see two events, one of the first and one of the second category (microsignature) from the same moon but with significantly reduced flux dropout levels). Panel (c) shows a microsignature with a complex structure (category three) caused again from the moon Tethys. In panel (d) we can see two microsignature events with similar depth (category four). Panel (e) depicts a depletion-like event that is uncertain if it was caused from Tethys or from Dione. The dashed line indicates the L-shell of Tethys (expected position of microsignature observation). Offsets from these positions are common for microsignatures. See also [Roussos et al., 2010].

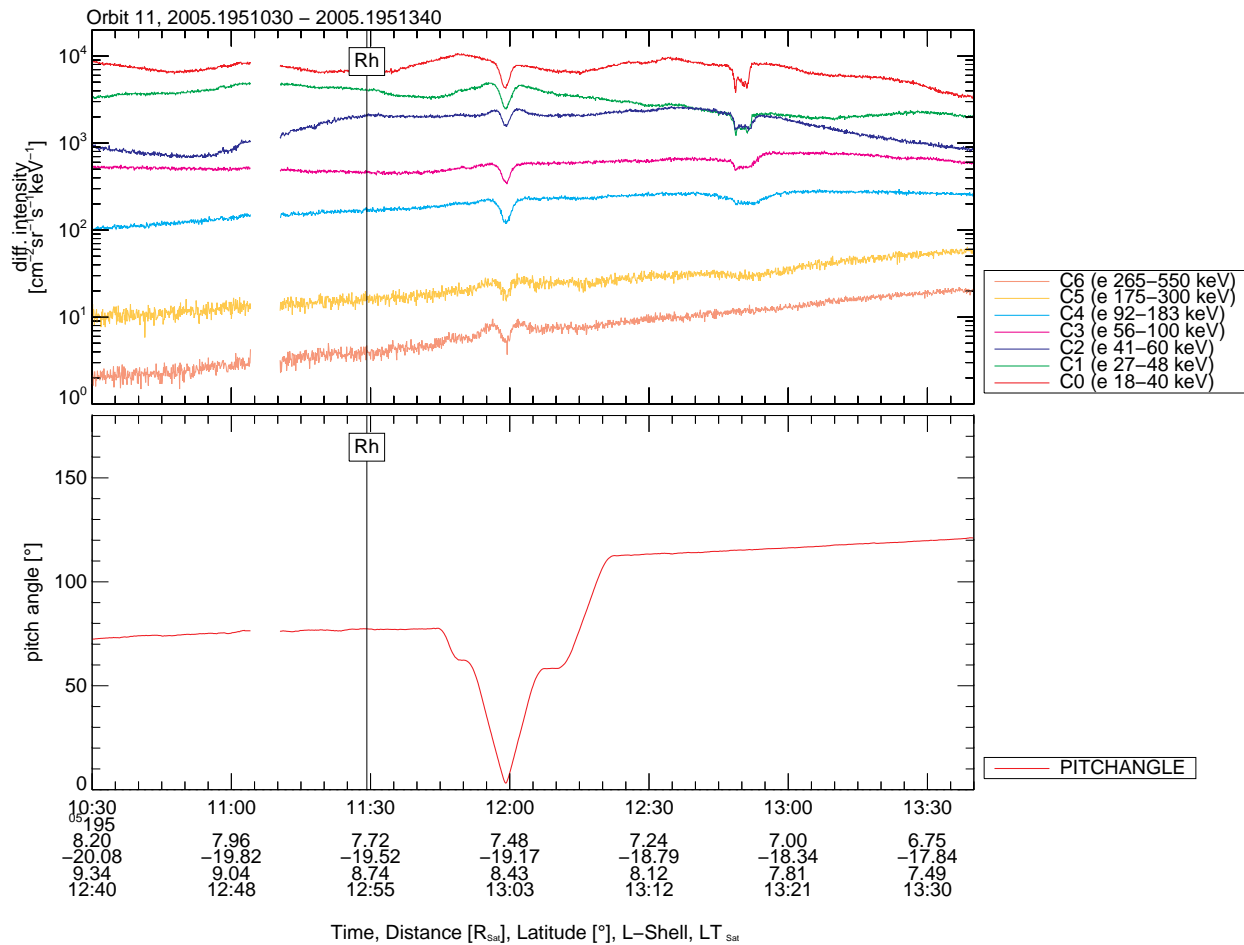


Figure 3.10: Line plots of C-channel electron fluxes as a function of time, during the inbound segment of Cassini’s 11th orbit around Saturn (DOY 195/2005). Cassini crossed the L-shell of Rhea around 11:30, only 5 degrees downstream of the moon. A microsignature from Rhea was expected around that time. Two candidate features are visible: one around 12:00, which, however, results from a spacecraft rotation (as inspection of the pitch angle pointing in the bottom panel shows), and one around 12:50, which is the actual absorption by Rhea. When a microsignature is resolved in several energy channels, higher energy channels are typically the ones with the shallower, more diffuse profiles. The large offset of this specific microsignature from the expected location is due to the dipole magnetic field model used to make this prediction. The current sheet perturbation of Saturn’s magnetic field is important at Rhea and will always result in a systematic outward shift in the predicted microsignature location, if this prediction is based on a simple dipole. The higher the latitude of Cassini, the greater this shift will be. In this case, Cassini’s latitude is about -19° .

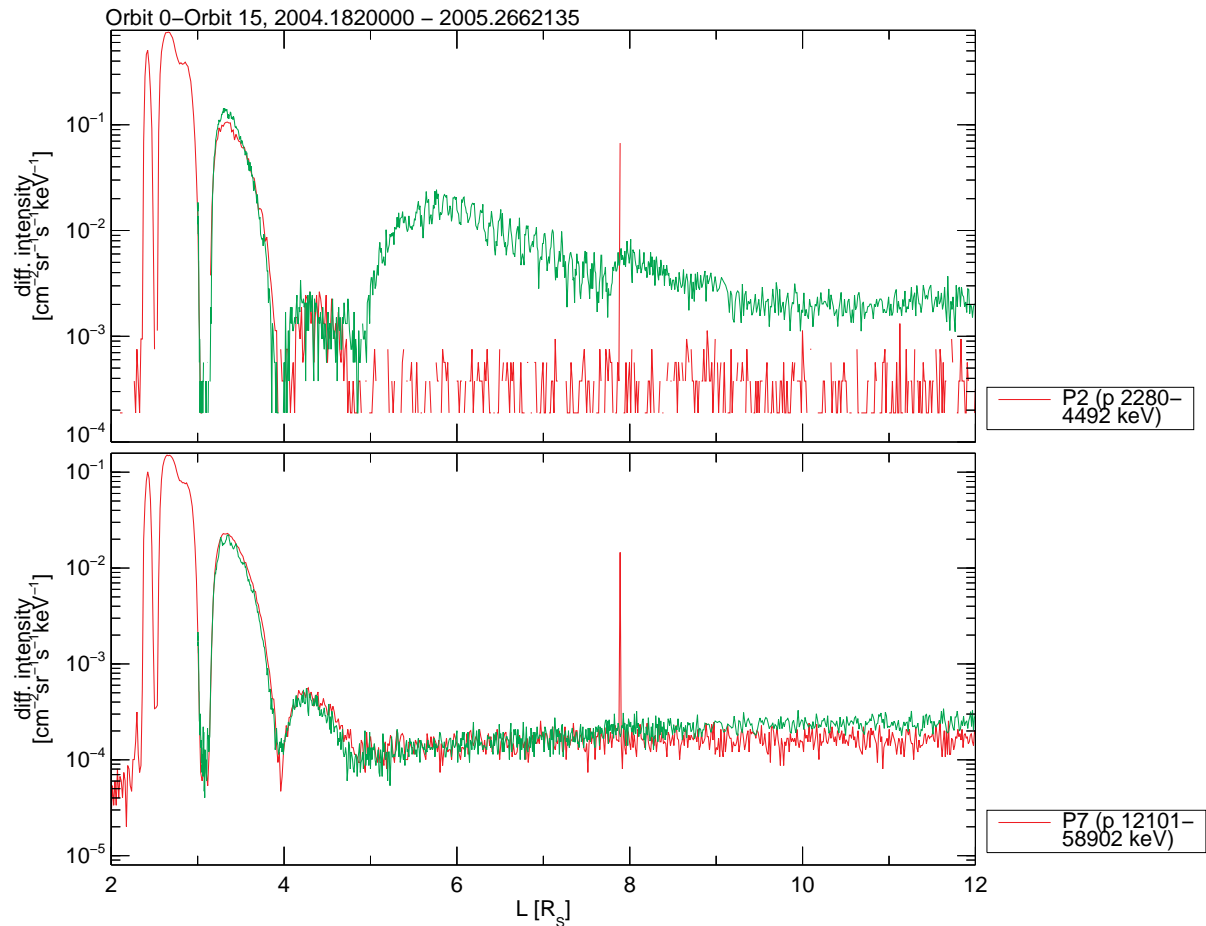


Figure 3.11: Energetic proton fluxes as a function of dipole L-shell. Data are shown for two periods: the first (red line) is from the inbound segment of SOI (DOY 182-183 of 2004) and the second (green line) is from Cassini’s 10th orbit around Saturn, on day 265-266 of 2005. Top panel is for protons of few MeV (channel P2), the bottom panel is for protons with energies of more than 10 MeV (channel P7). SOI occurred during quiet solar wind conditions. In that case, MeV proton belts extend up to an L-shell of about 4.9, which is the L-shell of Tethys. Inside that distance, MeV ion fluxes drop to background levels at the L-shells of Enceladus ($L \sim 3.95$), Mimas (3.1), the Janus/Epimetheus pair (2.5) and the main rings ($L < 2.3$). Data from the second period (green line) are after an intense solar energetic particle event impacted Saturn’s magnetosphere, resulting in the appearance of a transient radiation belt outside Tethys’s orbit [Roussos et al., 2008b]. Periodic modulations in this transient belt are caused by the sampling of different pitch angles during a series of LEMMS rotations. The transient radiation belt, which, however, did not appear in data of the P7 channel, gradually decayed, before it disappeared by the end of 2005. The inner belts remained unaffected throughout this period. A dropout in the background of P7, between L-shells of 5 and 9, in both time periods, is also visible. This dropout occurs because the instrumental background of P7 is dominated by penetrating galactic cosmic rays (GCRs). Close to Saturn, where the magnetic field of the planet is stronger, the GCRs are excluded, resulting in this apparent noise reduction. To illustrate this, fluxes in this plot are shown without the instrumental background subtracted.

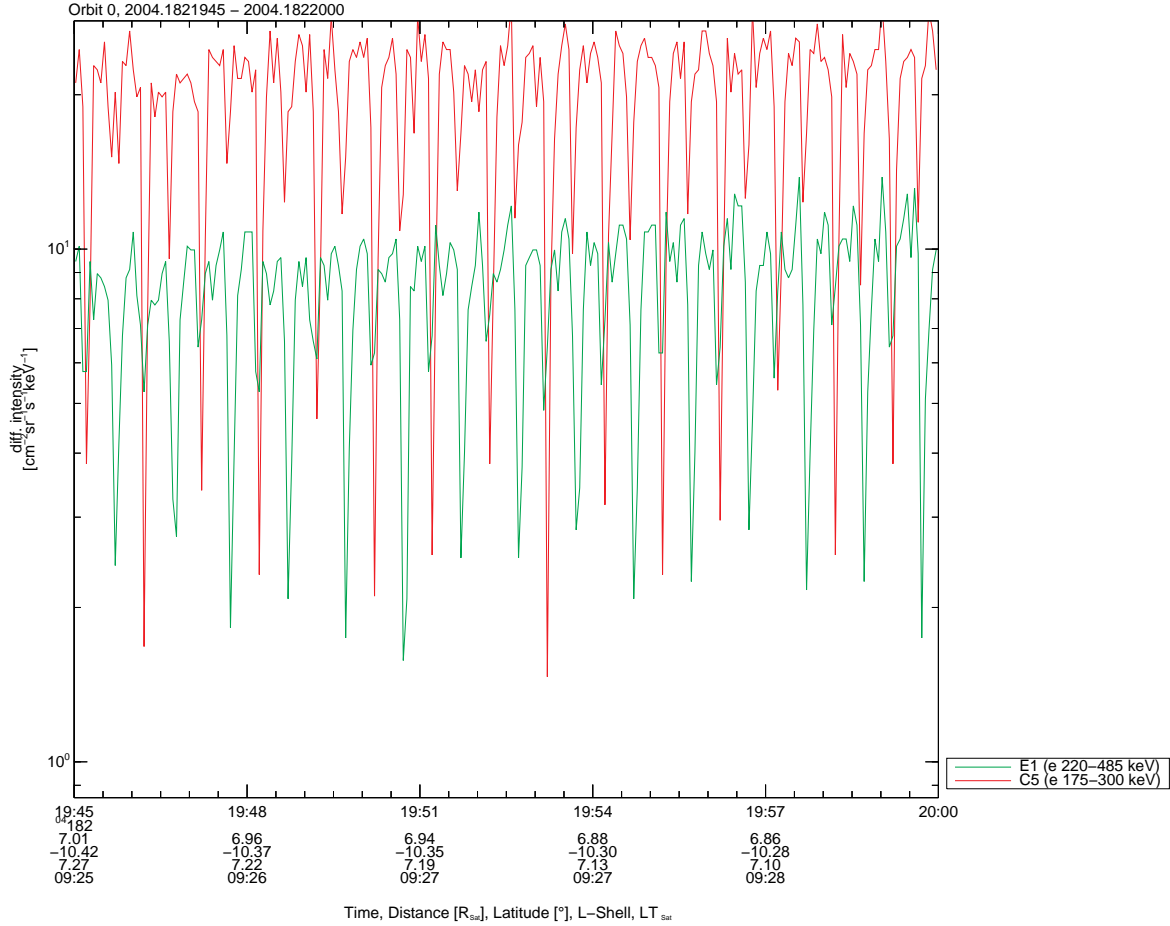


Figure 3.12: Energetic electron fluxes from channels C5 and E1 during the inbound segment of SOI. The periodic changes in the fluxes are due to the sampling of different pitch angles as LEMMS is spinning. The two most prominent flux dropouts for each LEMMS spin are caused by obscuration from spacecraft structures. The deepest feature occurs at a position where LEMMS points towards Cassini’s parabolic antenna (subsector 0 for LET, 8 for HET). Contribution to the dropout may also come from the time that LEMMS spends behind the calibration shield (between subsectors 15 and 0). The second dropout is for a pointing towards Cassini’s RTG shielding (subsector 8 for LET, 0 for HET). The LEMMS motor stopped working on day 32/2005, since then LEMMS observes different pitch angles only during Cassini rotations. The position where LEMMS is currently parked is not obscured by any spacecraft structure. Different channels respond to obscuration in a different way. The effect of obscuration may also be used to identify whether a channel is dominated by penetrating radiation or not [Armstrong et al., 2009, Roussos et al., 2010].

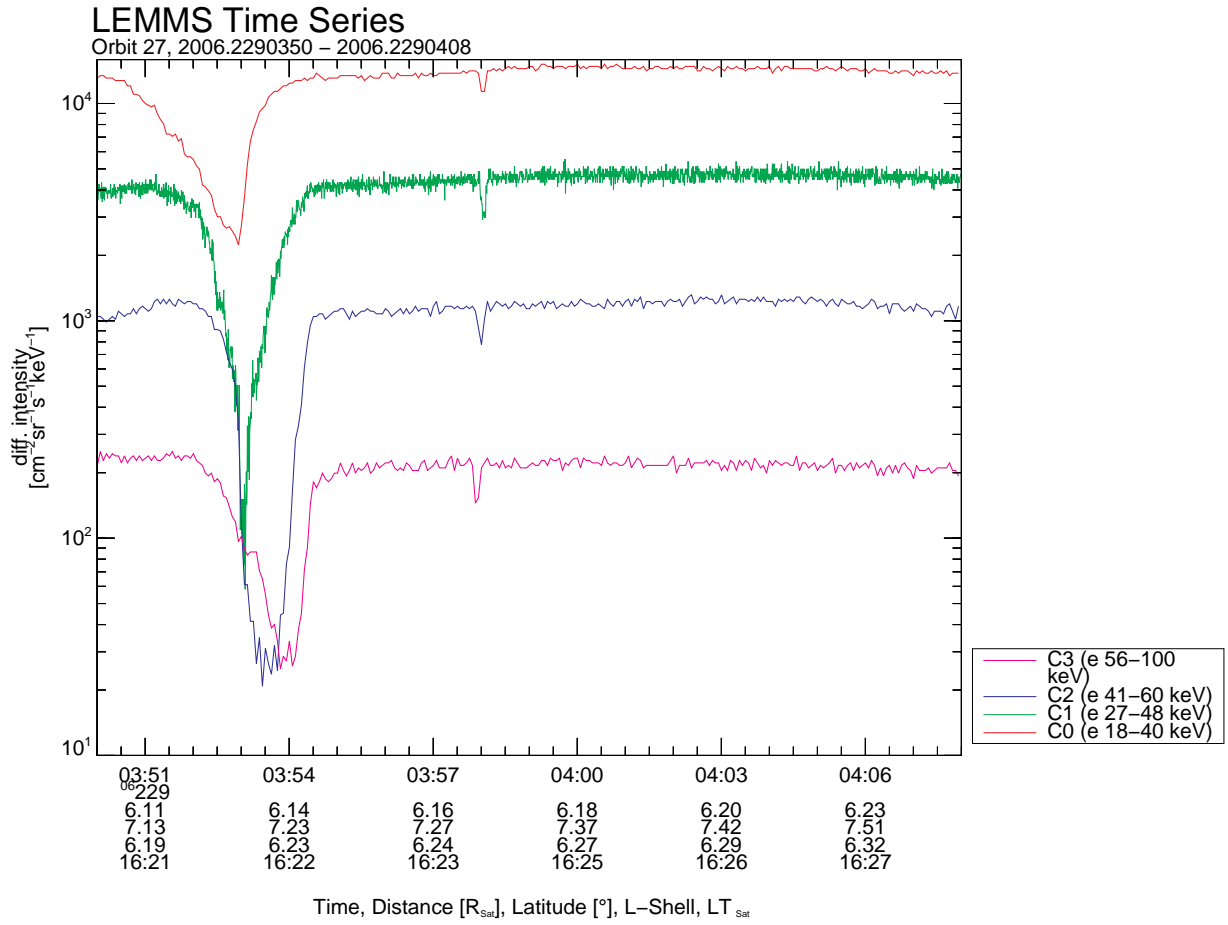


Figure 3.13: A microsignature from Dione and from a small, asteroid-sized coorbital moon of Dione, named Helene. Due to Helene’s small size (few tens of km across), its microsignature (around 03:58 UT) lasts only several seconds. It is therefore better resolved with the high time resolution (priority) channels of LEMMS, as shown in this plot [Roussos et al., 2008a].

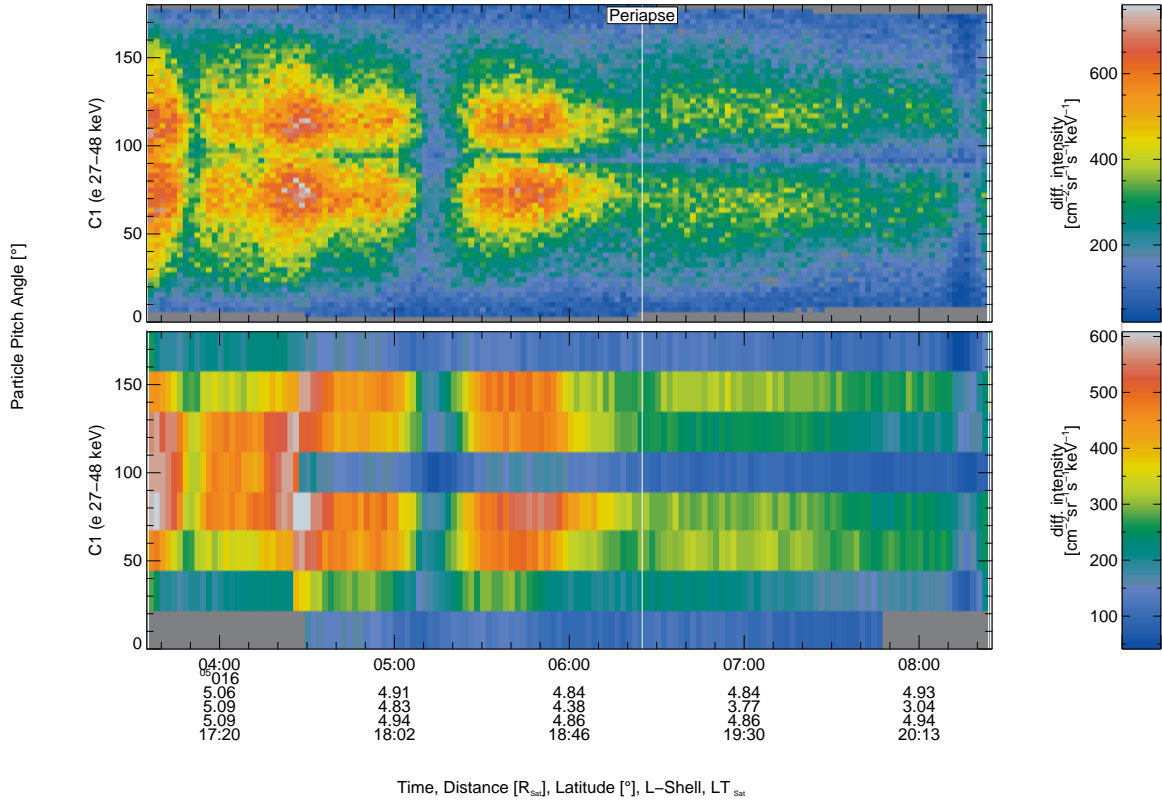


Figure 3.14: When LEMMS is spinning, the priority channels are mainly used to render pitch angle distributions (PAD) with high angular resolution. The two panels illustrate this: pitch angle anisotropy plots are shown, where the differential intensities (or fluxes) are color coded. The top panel shows the PAD structures visible when the C1 priority channel data are used (which samples data in 128 directions/microsectors) and when the normal, C1 rate channel data are used (bottom), that have 16 times worse time (angular resolution). In order to construct this plot, obscured subsectors 0,1,2,8,9,10 and 15 were excluded. Note that this pitch angle distribution is not centered on 90°. The magnetic deflection system used in LEMMS to capture electrons affects how pitch angles are reported and can introduce a shift like the one in this plot.

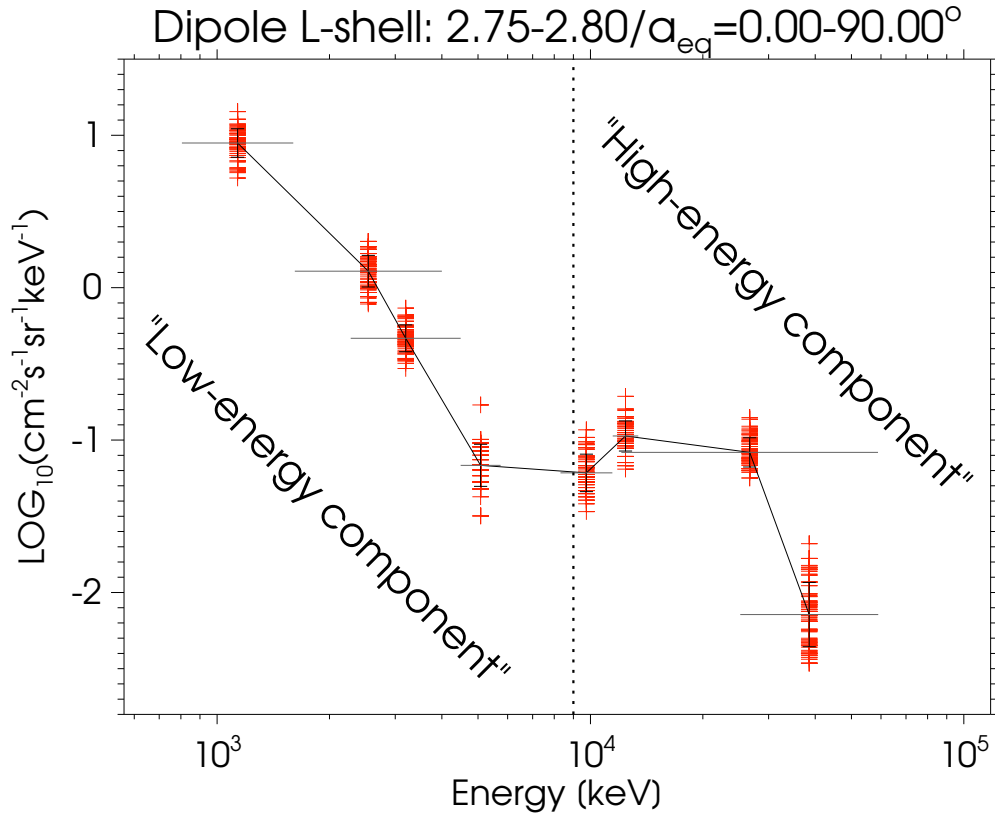


Figure 3.15: Energetic ion spectrum at a dipole L-shell range of 2.7-2.75 and all pitch angles, using data from LEMMS channels A6-A7 and P2-P8 but not P4. The low and the high energy components are indicated. The high energy component features a peak which is probably associated with the Cosmic Ray Albedo Neutron Decay process (CRAND). The origin of the power-law shape of the low energy component is undetermined. According to the latest LEMMS calibration [Armstrong et al., 2009], P4 is centred around 18 MeV, in the middle of the high energy component. The original calibration had P4 around 6.5 MeV [Krimigis et al., 2004b]. Pitch angle distributions from P4, however, are not representative of those of the high energy component and because of this controversy we do not use data from this channel here. A-channels measuring protons of lower energy are also not used here because their contamination levels from energetic ions or protons within the radiation belts, is uncertain [Roussos et al., 2010].

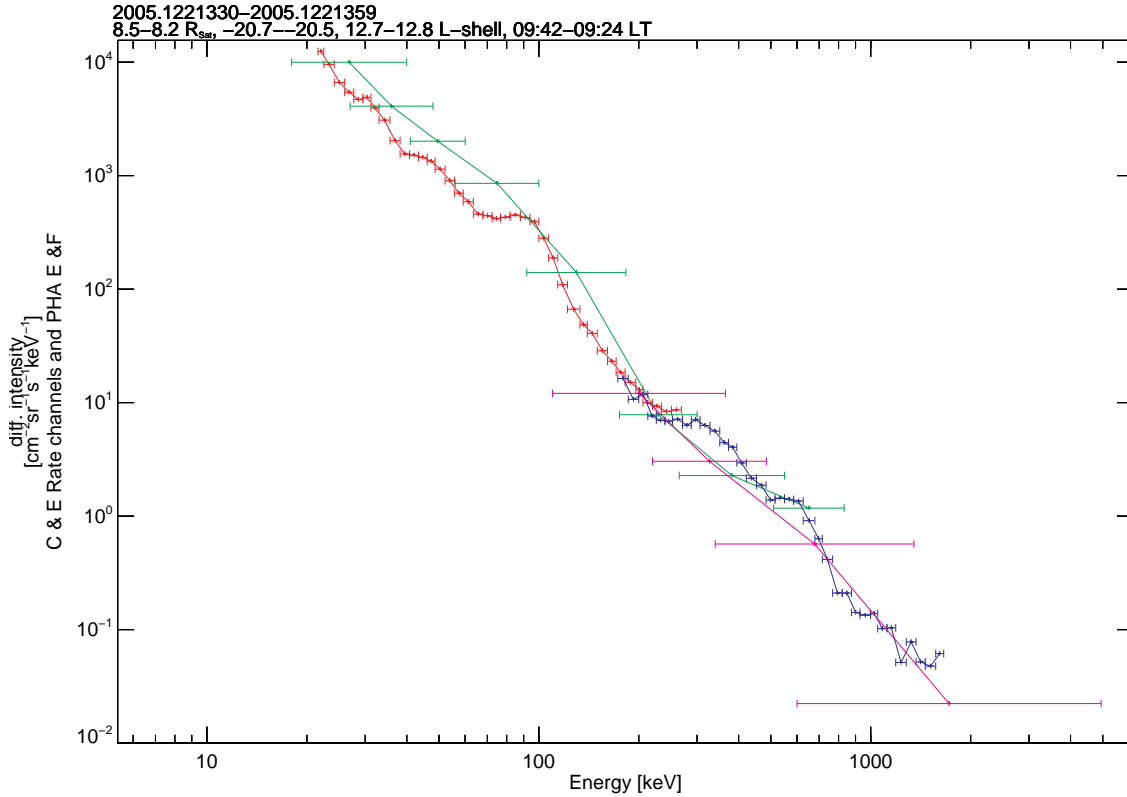


Figure 3.16: Energetic electron spectrum at a dipole L-shell range of about 13 (ring current region), using data from LEMMS channels PHA-E (red), PHA-F1 (blue), C (green) and E (magenta), averaged over an interval of about 30 minutes. Fluxes for the PHA-E and PHA-F1 channels have been calculated using a normalization to the singles rates of the ES and FS channels. Fluxes from different channels agree well on the various overlapping energy ranges, a common observation for the middle and outer magnetosphere.

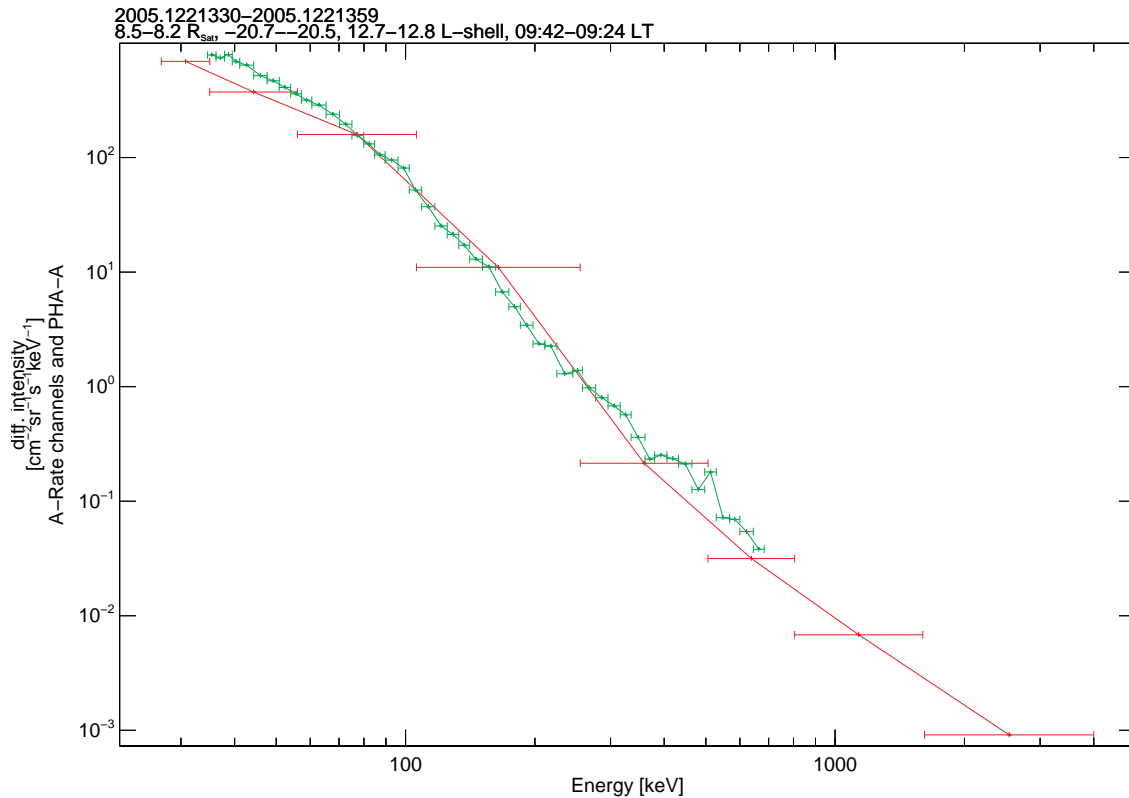


Figure 3.17: Energetic proton spectrum at a dipole L-shell range of about 13 (ring current region), using data from LEMMS A channels (red) and PHA-A (green), averaged over an interval of about 30 minutes. Fluxes for the PHA-A channels have been calculated using a normalization to the singles rates of the AS channel. Fluxes from different channels agree well on the various overlapping energy ranges, a common observation for the middle and outer magnetosphere.

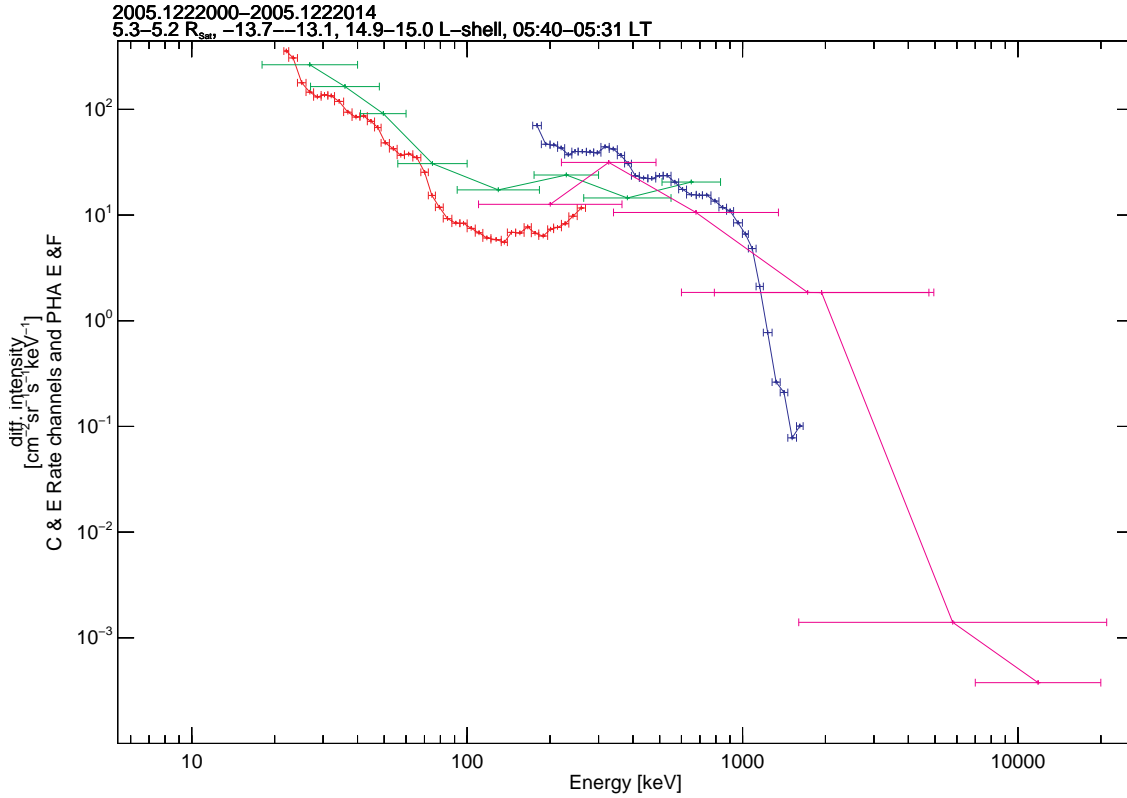


Figure 3.18: Energetic electron spectrum at a dipole L-shell range of about 6 (outer edge of radiation belts), using data from LEMMS channels PHA-E (red), PHA-F1 (blue), C (green) and E (magenta), averaged over an interval of about 15 minutes. Fluxes for the PHA-E and PHA-F1 channels have been calculated using a normalization to the singles rates of the ES and FS channels. PHA-F1 fluxes are higher than the PHA-E fluxes at the overlapping energy range, a problem resulting from the different response of the two detectors to radiation belt penetrating particles and the small geometric factor of the lowest energy PHA-F1 channels. Rate channel spectra show a similar trend as the PHA spectra. The flat spectrum between 100 and ~ 800 keV is probably real, but its exact characteristics are uncertain, due to the different responses of the different channels in this overlapping energy range. For higher energies, both PHA and rate channels indicate a steep power law flux dropout with energy. Problems in this spectrum from penetrating radiation belt particles become even more pronounced for spectra sampled at lower L-shells.

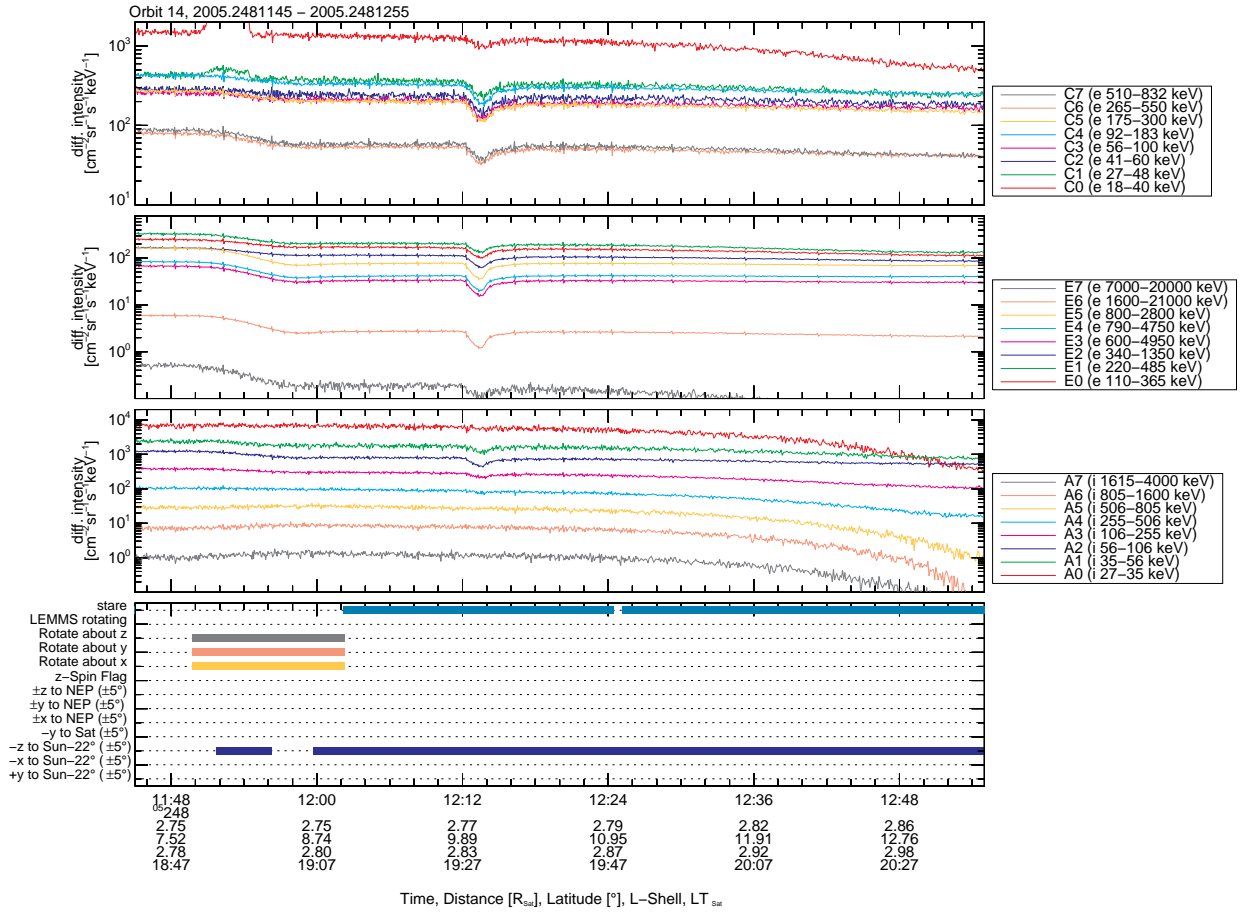


Figure 3.19: Energetic particle microsignature during a close flyby of the G-ring arc, at about $L=2.75$ [Hedman et al., 2007]. The microsignature is seen in almost all A, C, and E channels of LEMMS. P-channels are not shown here, as they contain no relevant feature. The bottom panel contains information about Cassini's attitude. Since it very unlikely that microsignatures appear simultaneously in channels spanning such a wide energy range (tens of keV to tens of MeV), we can conclude that several LEMMS channels are contaminated by penetrating radiation belt particles. Electrons and ions measured by the C and A-channels cannot contaminate channels such as E4, E5, E6 and E7, meaning that the actual energy of the microsignature is greater than few hundreds of keV. Identification of this energy (or energy range) requires a good understanding of the microsignature formation geometry and the exact responses of LEMMS in the radiation belts. The microsignature in the low energy channels appears because the flux of the contaminating high-energy electrons is reduced within the actual microsignature location. Observations in this G-ring flyby indicate that the signal of proton channels A0 and A5-A7, at $L=2.7$ has little or no contribution from high energy electrons. Similar cases are discussed in several published studies [Paranicas et al., 2005, Roussos et al., 2007]. Note also some enhancements in the C0 and C1 channels from light contamination.

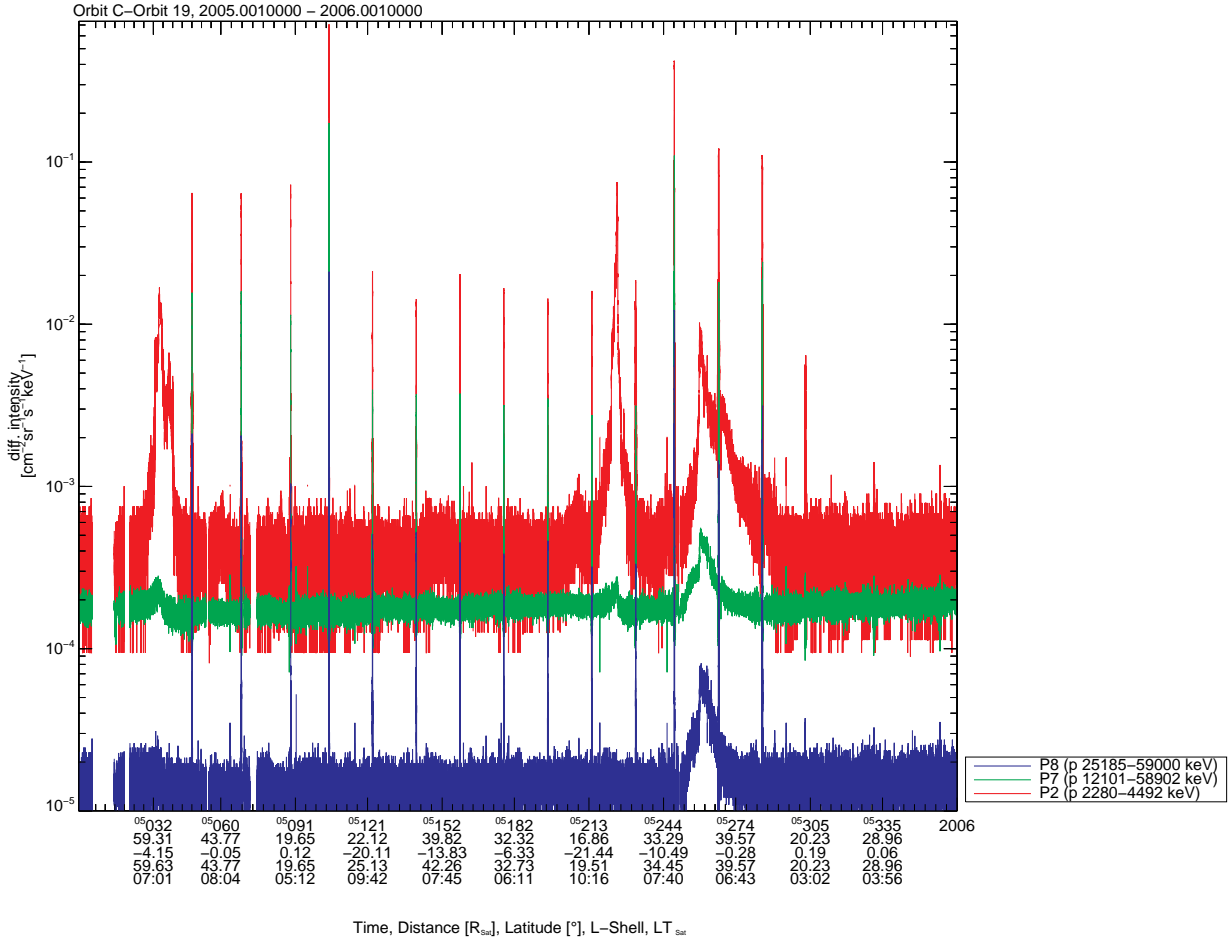


Figure 3.20: Energetic particle measurements of LEMMS in the solar wind, for the period 2005-2006. Most LEMMS channels are typically at instrumental background levels outside Saturn’s magnetosphere, with only few exceptions. One of this exception occurs during solar wind energetic particle events. These are shown here as large flux enhancements, in the MeV proton channels P2, P7 and P8. These events may last from few week up to months and may also lead to the formation of transient radiation belts within Saturn’s magnetosphere [Roussos et al., 2008b]. They rarely produce significant foreground for channels P7 and P8 or trigger electron channels above E4. Instead, the highest energy LEMMS channels may see a reduction of their instrumental background, the origin of which is discussed in [Roussos et al., 2010]. The various spikes in the plotted interval are from fast periapsis crossings of Cassini through the planet’s radiation belts.

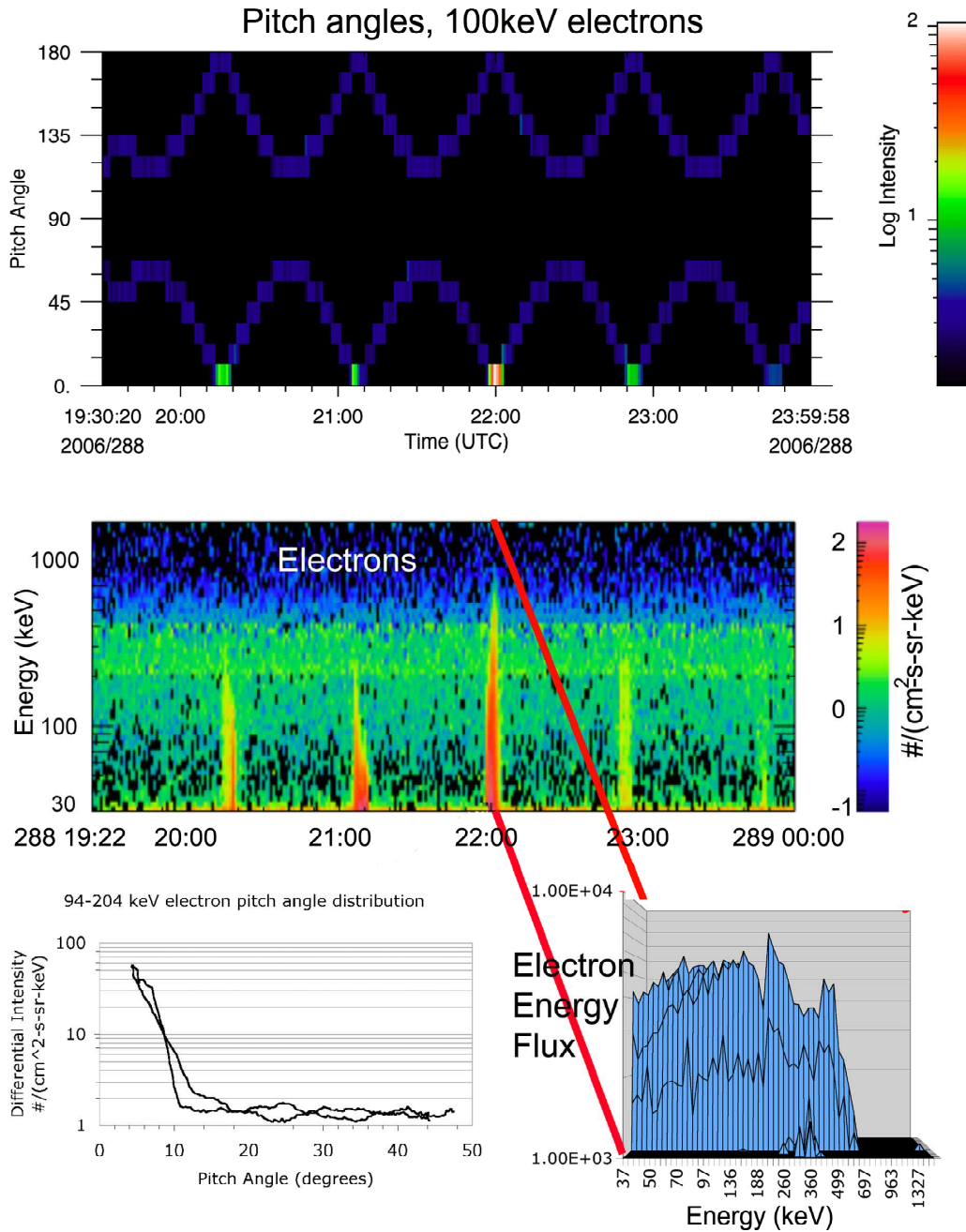


Figure 3.21: Energetic electron beam characteristics, from [Mitchell et al., 2009b] (top) The time history of 100 keV electrons measured in opposite facing telescopes on the LEMMS sensor as the spacecraft spin sweeps the sensor through various angles with respect to the magnetic field. The sensors are counting near background except when they sample near 0° pitch angle. (middle) Electron intensity as a function of time and energy. Spikes appear when the sensor samples 0° pitch angle. (bottom left) A quantitative plot of the electron pitch angles. Since the detector cone has a 7.5° half angle, the data are consistent with electrons confined to $<3^\circ$ from the magnetic field. (bottom right) The electron energy flux in the highest spike shows significant energy up to 700 keV. Similar features are discussed in [Krupp et al., 2009] and [Saur et al., 2006].

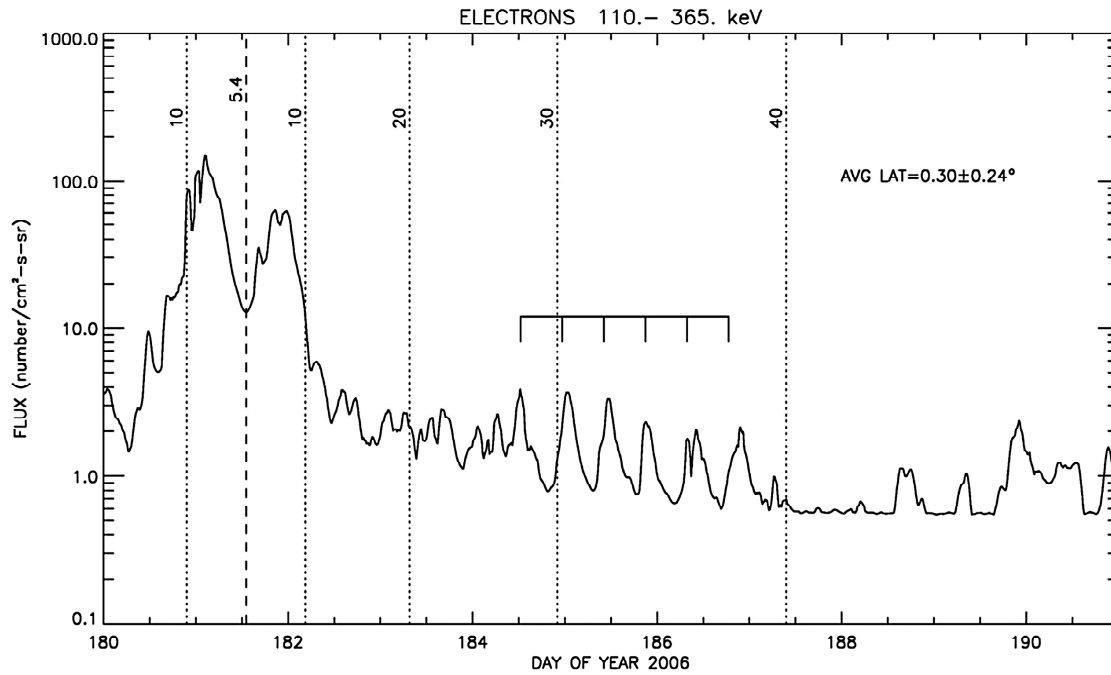


Figure 3.22: Energetic electron data from LEMMS exhibit numerous periodic features [Carbary et al., 2009]. Here shown are energetic electron fluxes for a period of 11 days in 2006. The 15-minute averages were smoothed to emphasize the periodic behavior of the fluxes. Vertical dotted lines indicate radial distances in $10 R_s$ increments, where $1 R_s$ is a Saturn radius. The dashed line shows closest approach at $5.4 R_s$. A fiducial scale indicates a 10.8-hour periodicity manifest for days 184 to 187. During this time the spacecraft was very near the equator. See also [Carbary et al., 2007, 2011].

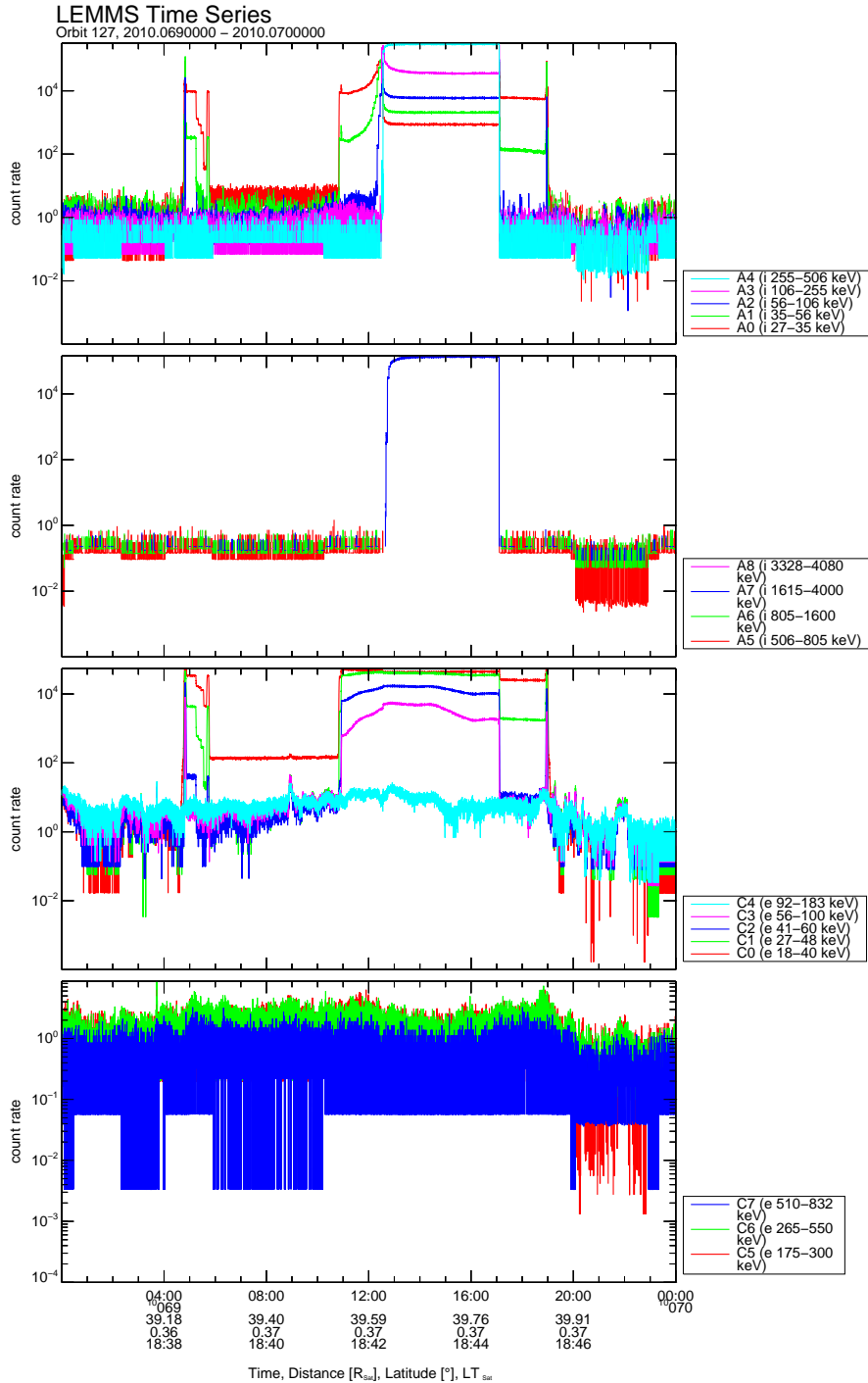


Figure 3.23: Example of light contamination in the LEMMS data of day 69 of 2010. The erroneous intervals are easily identified from the very high count rates and/or the unrealistic time profile of the signal of some channels, usually the lowest energy channels. We can also see that the response from the different channels is not the same. Such extremely light contaminated intervals can be easily identified by visual inspection of the data, but for statistical studies an automatic exclusion algorithm is necessary. This is done by using data on LEMMS’s pointing relative to the Sun (see next Figure).

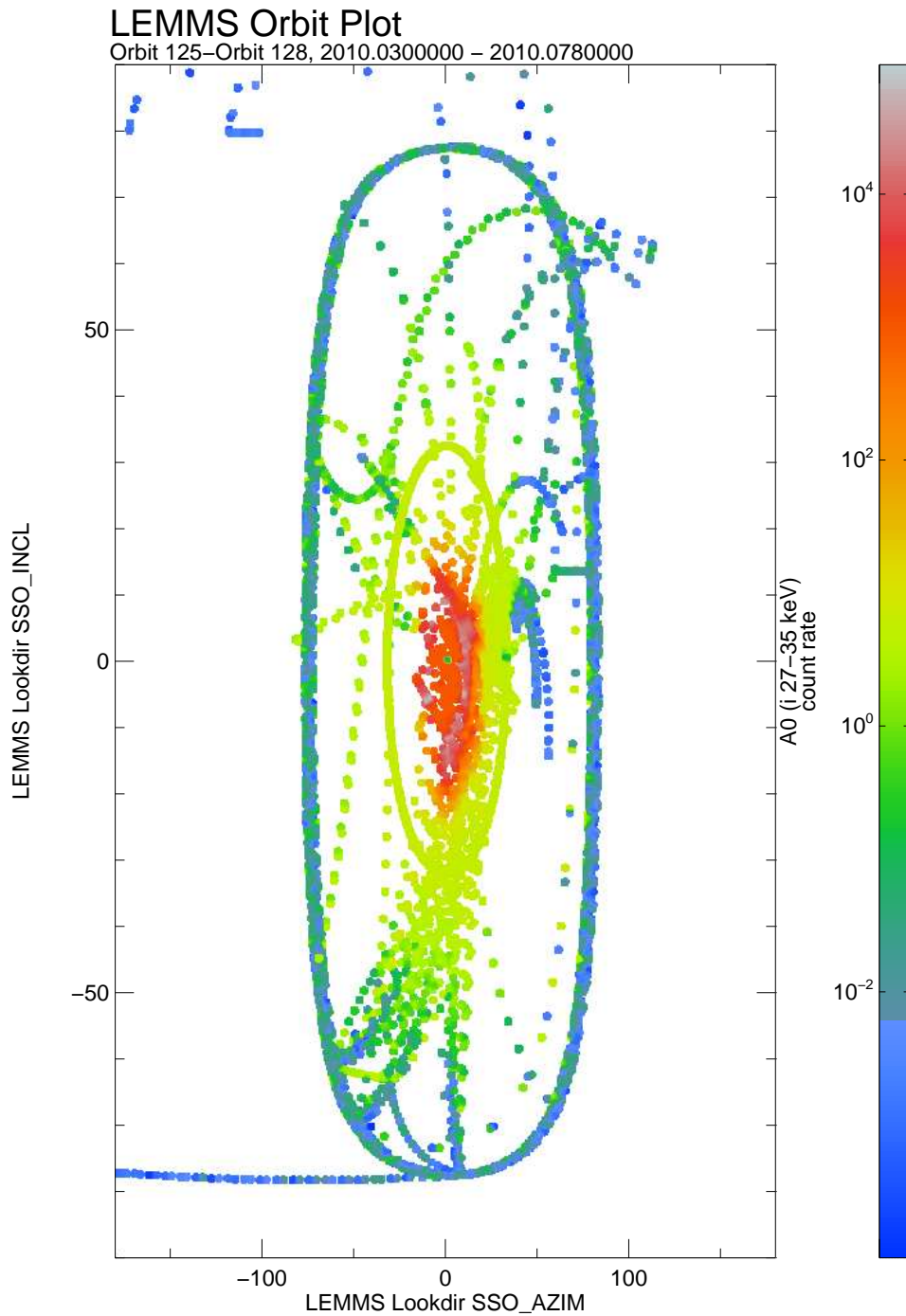


Figure 3.24: LEMMS count rates as a function of azimuth and inclination from the Sun. The case for A0 channel is shown here. Plotted data are from three different intervals starting on day 30/2010 until day 78/2010. Ring current and radiation belt crossings from that period were excluded, since in the latter regions fluxes can be very high and therefore misleading. A0 is very sensitive and enhanced count rates are seen even 30° – 40° away from the Sun. The most sensitive electron channel is C0. Both A0 and C0 record very high count rates for viewing geometries centered around the Sun direction. This supports the idea that the source of these extreme signals is directly associated with sunlight.

Section 4

CHEMS

4.1 Principles of Operation

CHEMS detects ions with energy per charge (E/Q) ranging from 3 – 220 keV/e and can determine plasma composition by combining an E/Q measurement with a time of flight (TOF) determination and, for high enough energy particles, a total E measurement. CHEMS contains a deflection system and an overall field of view of $159^\circ \times 4^\circ$ that is comprised of three distinct energetic particle telescopes each having a field of view of $53^\circ \times 4^\circ$ (Figure 4.1). All telescopes share the same deflection mechanism, but each has its own start and stop microchannel plate (MCP) and its own solid-state detector (SSD). Much of the data returned by CHEMS is separated by telescope. When the Cassini spacecraft is rolling (always about the +Z axis), CHEMS can obtain 3-D ion distributions. The instrument is able to determine the ionic charge, mass, and energy of incoming ions.

A diagram showing the principle of operation of CHEMS is shown in Figure 4.2. First, the incoming ions encounter an electrostatic deflection analyzer system consisting of two concentric spherical plates with a positive voltage applied to the outer plate and a negative voltage applied to the inner plate. The deflection plate power supply (DPPS) has 32 different voltages (also called steps) that can be applied across the deflection plates. For any single DPPS step, the electrostatic analyzer only transmits incoming ions within a narrow range of energy per charge (a 3% pass band). The E/Q values are logarithmically spaced and are listed in Table 4.1.

When Cassini is rolling, a complete spectrum is obtained by commanding the DPPS to sweep through the 16 odd steps during each 1/16th of a roll. At the beginning of a cycle, the DPPS step is 31 and it then sweeps through the odd steps (29, 27, 25, . . . , 1). Given a nominal roll period of 23 minutes, CHEMS spends about 5.39 seconds at each E/Q . When Cassini is not rolling, the stepping sequence is based on a commanded time interval (called the pseudo-spin period even though the spacecraft is not actually spinning) and CHEMS spends an amount of time at each step. The stepping sequence for non-rolling periods can be adjusted. Typically, the DPPS steps through the odd steps (31, 29, 27, . . . , 1) and then through the even steps (30, 28, 26, . . . , 0) during the following 1/16th of a roll so that all steps are covered every 2 spins (really pseudo spin periods).

After an incoming ion passes through the electrostatic analyzer, it penetrates a thin carbon foil causing the emission of secondary electrons (see Figure 2-1). The emitted electrons are deflected by electric fields to the start MCP, generating the start signal for the TOF system. The ion then strikes one of the solid-state detectors (SSD) producing secondary electrons that are guided to the

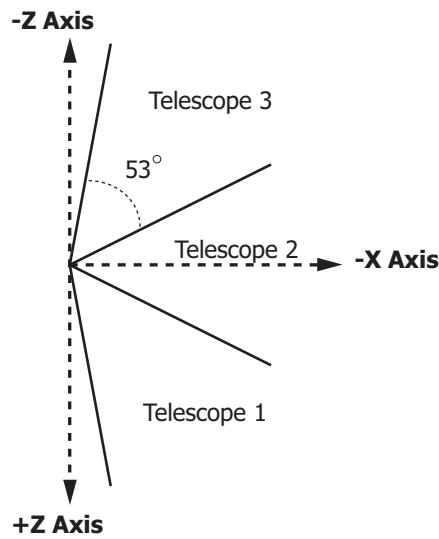


Figure 4.1: CHEMS telescope view directions relative to the indicated spacecraft axes.

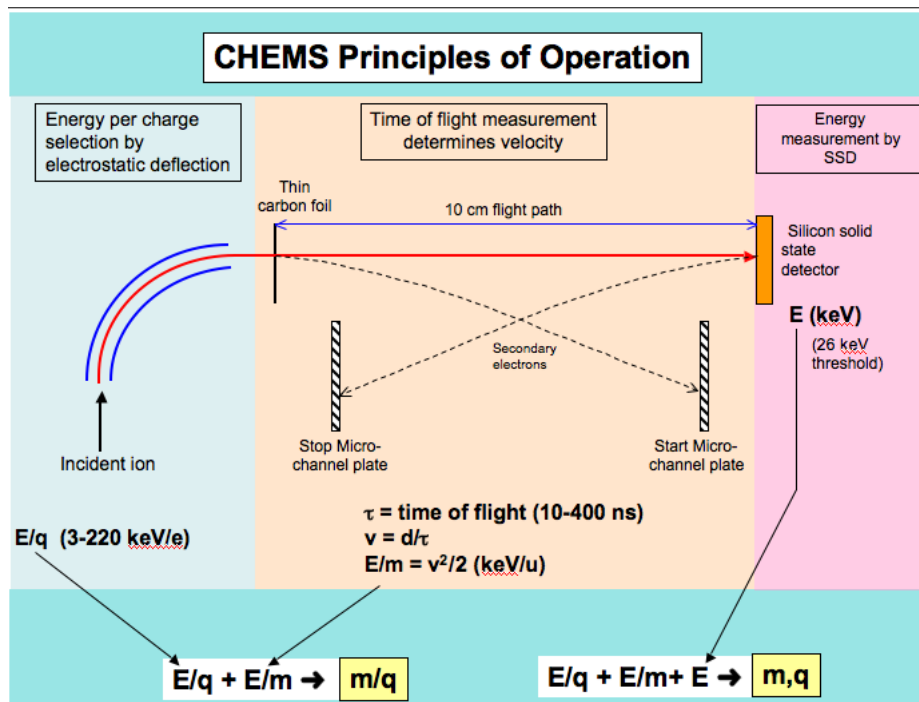


Figure 4.2: The basic operation of CHEMS utilizes electrostatic deflection to filter particles within a narrow range of E/Q . Following this, a time of flight determination is made, and for high enough energy particles, a total energy measurement is also made in a solid state detector.

stop MCP providing the stop signal. The SSD also measures the kinetic energy of the ion, but only if the ion deposits enough energy in the SSD to overcome its electronic threshold of 26 keV.

Particles without enough energy to trigger the SSD are called double coincident, because only the energy per charge (E/Q) and TOF (τ) are measured. Without an energy measurement, it is impossible to measure the mass of an incident ion. However, the mass per charge M/Q can be obtained. Solving the formula for kinetic energy, $E/Q = \frac{1}{2}(\frac{M}{Q})v^2$ for M/Q yields

$$\frac{M}{Q} = \frac{2}{v^2} \left(\frac{E'}{Q} \right) \quad (4.1)$$

where $v = d/\tau$ is the velocity obtained by dividing d (the 10.0 cm flight path through the TOF section of the instrument) by τ (the TOF measurement). Note that E'/Q is slightly less than the E/Q measured by the electrostatic analyzer because of the small energy loss in the thin (2.5 $\mu\text{g}/\text{cm}^2$) carbon foil.

Particles that do trigger the SSD are considered triple coincident, because in addition to the E/Q and TOF measurements, the SSD yields an energy measurement. With a value for this measured energy E_{meas} , it is possible to determine the mass, charge, and initial energy of the incoming ion. To calculate the mass M and charge Q , use:

$$M = 2 \left(\frac{\tau}{d} \right)^2 \left(\frac{E_{\text{meas}}}{\alpha} \right) \quad (4.2)$$

$$Q = \frac{\left(\frac{E_{\text{meas}}}{\alpha} \right)}{\left(\frac{E'}{Q} \right)} \quad (4.3)$$

In the above equation, α gives the ratio of the energy measured in the SSD to the energy incident at the detector. Because of nuclear defect, α is always less than one. Nuclear defect is caused by the collisions between the incoming ions and Si nuclei of the SSD (that do not create electron hole pairs) and becomes more significant for particles at lower energies and higher atomic masses. For example, protons trigger the SSD at a 50% rate at an incident energy of 30 keV, while oxygen ions do so at 55 keV.

4.2 CHEMS Data Products

There are three PDS data products for CHEMS: accumulator(engineering) rates, PHA data, and science rates (see Table 1.1). Note that PDS data files for the accumulator rates and science rates actually contain counts, even though the name of the product refers to them as rates.

At the present time (early 2013), the highest revision of uncalibrated MIMI PDS data is revision 3, and all the descriptions below apply to this revision. However, data in years 2004 through 2006 has not yet been converted to this revision and is only available as revision 0 (there is no revision 1 or 2 data). For CHEMS, the only difference is that revision 0 data lacks three of the standard prefix columns that were added to revision 3 (UTC, SCLOCK, and SENCOR_BITRATE).

Actual Channel Widths			Expanded Channel Widths		
DPPS Step	Midpoint E/Q in keV/e	Passband ($\Delta E/Q = 3\%$)	Lower E/Q (keV/e)	Upper E/Q (keV/e)	Delta E/Q
0	2.81	0.0843	2.61	3.04	0.43
1	3.29	0.0987	3.04	3.53	0.49
2	3.78	0.1134	3.53	4.08	0.55
3	4.40	0.132	4.08	4.71	0.63
4	5.05	0.1515	4.71	5.44	0.73
5	5.86	0.1758	5.44	6.29	0.85
6	6.75	0.2025	6.29	7.26	0.97
7	7.81	0.2343	7.26	8.35	1.09
8	8.92	0.2676	8.35	9.59	1.24
9	10.3	0.309	9.59	11.02	1.43
10	11.8	0.354	11.02	12.67	1.65
11	13.6	0.408	12.67	14.61	1.94
12	15.7	0.471	14.61	16.86	2.25
13	18.1	0.543	16.86	19.40	2.54
14	20.8	0.624	19.40	22.30	2.90
15	23.9	0.717	22.30	25.59	3.29
16	27.4	0.822	25.59	29.38	3.79
17	31.5	0.945	29.38	33.77	4.39
18	36.2	1.086	33.77	38.81	5.04
19	41.6	1.248	38.81	44.59	5.78
20	47.8	1.434	44.59	51.23	6.64
21	54.9	1.647	51.23	58.90	7.67
22	63.2	1.896	58.90	67.74	8.84
23	72.6	2.178	67.74	77.81	10.07
24	83.4	2.502	77.81	89.43	11.62
25	95.9	2.877	89.43	102.75	13.32
26	110.1	3.303	102.75	118.06	15.31
27	126.6	3.798	118.06	135.63	17.57
28	145.3	4.359	135.63	155.73	20.10
29	166.9	5.007	155.73	178.82	23.09
30	191.6	5.748	178.82	205.40	26.58
31	220.2	6.606	205.40	236.05	30.65

Table 4.1: Energy per charge values in keV/e for each DPPS step and the $\Delta E/Q$ passband (3% of the midpoint E/Q) for that step. The actual CHEMS channels only capture particles within a narrow 3% passband centered around the midpoint E/Q, but when computing number density, the narrow energy band measurements are assumed valid for the entire region in energy space between the channels. Number density calculations are described in [DiFabio et al., 2011] and so are not covered here.

Name in PDS File	Description	Number of Bits
DPPS_Level	DPPS step number	5
Energy	Energy channel number	10
Time_of_Flight	TOF channel number	10
Solid_State_Detector	SSD ID	2
Start_Micro_Channel_Plate	Start MCP ID	2
Range	Range ID	3

Table 4.2: Quantities present in CHEMS PHA data and the number of bits allocated to each quantity.

4.2.1 CHEMS Accumulator Rates

Accumulator rate data contains counters for individual detector elements or coincidence detections. For each telescope, there are counters for the start and stop MCPs, the SSDs, the double coincidence rate (DCR), and the triple coincident counting rate (TCR). These are essentially engineering quantities, used to monitor the health of the instrument and determine the number of expected accidental coincidences. But they are also used to normalize PHA fluxes during high rate periods.

4.2.2 CHEMS PHA Data

PHA data contains event characteristics for individually detected ions. Understanding how CHEMS captures and categorizes PHA events is essential to understanding both the PHA data and the science rates.

Quantities available in each PHA event are shown in Table 4.2, which lists the column name of each quantity within PDS data files, and also the number of bits allocated to each quantity. The SSD ID and Start MCP ID both give an indication of which telescope an ion entered, but because the SSD is not always triggered, the Start MCP ID is used to separate events by telescope. Start MCP ID 1, 2, and 3 correspond to Telescope 1, 2, and 3 respectively.

The Range ID is a derived quantity based on the calculated mass and M/Q. On the spacecraft, the MIMI Data Processing Unit (DPU) assigns to each PHA event two integers, NM and NQ, that are logarithmically related to the mass and M/Q respectively. Rectangular regions in NM versus NQ space define distinct categories called ranges, and each range has a specific ID from 0 to 6. Table 4.3a lists the bounding values for each Range ID, and these are graphically depicted in Figure 4.3. For each incident ion, the DPU quickly determines NM and NQ, and then determines the Range ID. Counters record the total number of events (per integration period) falling within each Range ID, and these are the basic rate counters described below in the section on science rates.

During times with high count rates, full PHA characteristics for every event cannot be recorded because of telemetry restrictions. Therefore the DPU uses a priority scheme based on the Range ID to decide which events should be saved as full PHA events. The net result is that roughly equal numbers of events from each Range ID are captured, saved, and included in telemetry as PHA events. The total number of events that fell within each Range ID can be used to normalize the subset of PHA events that are recorded.

	Coincidence				
Range	Required	NM	NQ	Mass range	M/Q range
0	Double	0-0	1-22	0-0	0.7-1.60
1	Double	0-0	23-73	0-0	1.60-10.9
2	Double	0-0	74-126	0-0	10.9-80.0
3	Triple	1-62	1-22	0.5-95.0	0.7-1.6
4	Triple	1-32	23-73	0.5-7.5	1.60-10.9
5	Triple	1-62	74-126	0.5-95.0	10.9-80.0
6	Triple	33-62	23-73	7.5-95.0	1.60-10.9

Table 4.3a: Range ID definitions for the CHEMS Basic Rates.

Species	Coincidence Required	NM	NQ	Mass range	M/Q range
He ⁺	Double	0-0	44-52	0-0	3.53-4.95
He ⁺	Triple	14-32	44-52	1.50-7.50	3.53-4.95
He ²⁺	Double	0-0	22-33	0-0	1.60-4.42
He ²⁺	Triple	14-32	22-33	1.50-7.50	1.60-2.42
N ⁺ & O ⁺	Double	0-0	77-91	0-0	12.2-21.4
N ⁺ & O ⁺	Triple	28-51	77-91	4.91-37.4	12.2-21.4
N ²⁺ & O ²⁺	Double	0-0	62-70	0-0	6.94-9.74
N ²⁺ & O ²⁺	Triple	33-51	62-70	7.50-37.4	6.94-9.74
CNO > 4 ⁺	Triple	36-45	23-45	9.67-22.5	1.60-3.80

Table 4.3b: Species rates definitions as regions within NM vs. NQ space. Each species range is a subset of a single Range ID. Although particle intensities can be derived from species rates within these boxes, it is best to use custom boxes and PHA data to derive particle intensities.

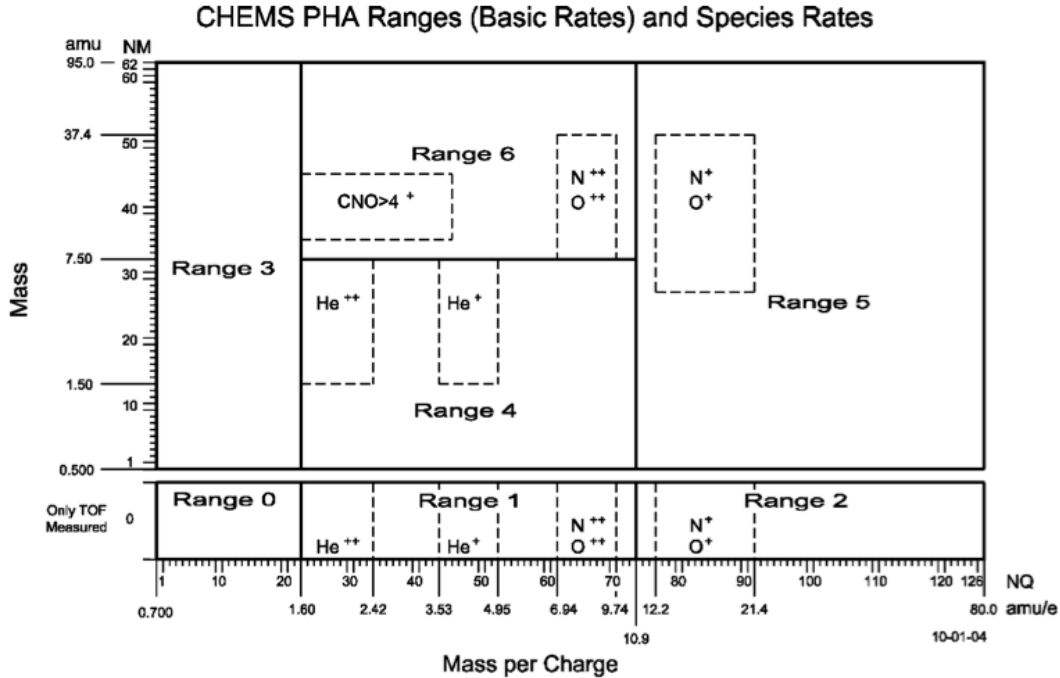


Figure 4.3: Definitions of the Range IDs for CHEMS basic rates and species rates as boxes in NM versus NQ space. The DPU computes the values NM and NQ for each CHEMS particle detected, and then these boxes allow the DPU to categorize the event. This plot is taken from Figure 32 of the instrument paper [Krimigis et al., 2004a].

If a particle passes the E/Q filter, triggers the Start and Stop MCPs, and triggers the SSD, it is considered a triple coincident detection, often referred to just as a triples count. As shown in Figure 4.3, Range IDs 3, 4, 5, and 6 are triples counters. A particle that does not trigger the SSD is considered double coincident, because only E/Q and TOF are measured. For doubles counts, NM cannot be determined and is set to zero. Range IDs 0, 1, and 2 are for double coincidence events, and these Range IDs are also shown in Figure 4.3. The transmitted PHA events are often simply referred to as 'Doubles PHAs' or 'Triples PHAs.'

4.2.3 CHEMS Science Rates

Within the PDS files for CHEMS Science Rates, there are two flavors of rates: CHEMS basic rates (counters for each Range ID as discussed above) and CHEMS species rates. Species rates are very similar to the basic rates in that they are defined by rectangular regions in NM versus NQ space. But for species rates, the rectangular regions are smaller and are designed so that only one particle species falls within the rectangle. Table 4.3b lists the species rate box definitions, which are also depicted in Figure 4.3. In practice, these species rate boxes have contamination issues, because the box definitions are basically constant over the life of the mission, and it is difficult to define regions that detect a single species in all circumstances and for long periods of time. The best way to determine species fluxes is to use custom species boxes for categorizing PHA events, and this is discussed in detail below in Section 4.5.

4.3 Calibrating CHEMS Accumulator (Engineering) Rates

CHEMS accumulator rates provide counts per accumulation interval for numerous engineering and diagnostic counters. Column names and descriptions for all accumulator rate counters are listed in Table 4.4.

The only calibration applicable to the accumulator rates is a conversion to counts per second. Section 4.4.1 below describes how to compute counts per second for CHEMS science rate counters, and the same procedure can be applied to the accumulator rates.

4.4 Calibrating CHEMS Science Rates

4.4.1 Counts per Second

The accumulation interval for basic and species rate counters is one DPPS step, which lasts for one subsector, where 16 subsectors make a sector, and 16 sectors make one spin (or pseudo-spin - see Section 1.7 for an explanation of the spin period). Note that for CHEMS, there is a 150 millisecond dead time per DPPS step, and this must be subtracted from the subsector duration. Thus the count rate R is:

$$R = \frac{C}{\tau_{\text{spin}}/256 - t_{\text{dead}}} \quad (4.4)$$

The counts, C , for various rate counters and the spin period in seconds, τ_{spin} , are obtained directly from the PDS files of CHEMS science rates. Column names and definitions for science rate counters are listed in Tables 4.5. Each PDS data file also includes the standard prefix columns (including, for example, the spin period) that were described earlier in Table 1.6 (on page 20 in Section 1.6).

While the rates R for various Range IDs and species boxes are intrinsically useful, they are also essential when converting PHA events into intensities as described later in Section (4.5).

4.4.2 Differential Intensity

Converting a species count rate in units of counts/sec into a differential intensity in units of counts/(sec·ster·cm²·keV) requires knowledge of the geometry factor of the instrument, the energy width of the channel, the detection efficiency for ions of that species, and the energy width of the channel expressed as an energy per charge. The differential intensity, j is given by:

$$j = \frac{C}{\Delta t g \epsilon \Delta E} \quad (4.5)$$

where C is the counts in a given integration period, Δt is the integration period in seconds, g is the geometry factor, ϵ is the efficiency and ΔE is the energy width of the channel in keV/Q.

Each CHEMS telescope has an identical geometry factor of 0.007 cm² · ster. ΔE is 3% of the current E/Q based on the DPPS step. See Table 4.1 for energies and energy widths for each DPPS step. The time width, Δt is one subsector, or 1/256th of a spin period minus the 150 millisecond settling time, $\Delta t = \tau_{\text{spin}}/256 - 0.150$.

Column Index	Column Name	Description	Coinc. Type
13	DPPS_LEVEL	E/Q setting for data on this row	n/a
14	START_HEAD_1	telescope 1 start MCP	single
15	START_HEAD_2	telescope 2 start MCP	single
16	START_HEAD_3	telescope 3 start MCP	single
17	START_SUM	total counts on any of the start MCPs	single
18	STOP_HEAD_1	telescope 1 stop MCP	single
19	STOP_HEAD_2	telescope 2 stop MCP	single
20	STOP_HEAD_3	telescope 3 stop MCP	single
21	STOP_SUM	total counts on any of the stop MCPs	single
22	ENERGY_HEAD_1	telescope 1 SSD	single
23	ENERGY_HEAD_2	telescope 2 SSD	single
24	ENERGY_HEAD_3	telescope 3 SSD	single
25	ENERGY_SUM	total counts for all three SSDs	single
26	DCR_HEAD_1	telescope 1 start and stop MCPs	double
27	DCR_HEAD_2	telescope 2 start and stop MCPs	double
28	DCR_HEAD_3	telescope 3 start and stop MCPs	double
29	DCR_SUM	start and stop MCP coinc. from any tel.	double
30	TCR_HEAD_1	tel. 1 start MCP, stop MCP, and SSD	triple
31	TCR_HEAD_2	tel. 2 start MCP, stop MCP, and SSD	triple
32	TCR_HEAD_3	tel. 3 start MCP, stop MCP, and SSD	triple
33	TCR_SUM	start MCP, stop MCP, and SSD coincidences from any telescope	triple
34	UFSR	a separate way to detect a start MCP signal from of any telescope (uses a different discriminator that initiates Valid Event logic); should be nearly identical to START_Sum; note that UFSR = Universal Front SEDA Rate where SEDA = Secondary Electron Detector Assembly	single
35	URSR	a separate way to detect a stop MCP signal from any telescope; should be nearly identical to STOP_Sum. URSR = Universal Rear SEDA Rate	single

Table 4.4: Column names and descriptions for the accumulator rates. These columns follow the standard prefix columns, which are given in Table 1.6. Note that in the older revision 0 data (2004 through 2006), three prefix columns will be missing, and so the indices here would be smaller by 3. All revision 0 data will soon be replaced with revision 3 data.

Column Index	Column Name	Description	Coinc. Type
13	DPPS_LEVEL	E/Q setting for data on this row	n/a
14	Range_0_Tele_1	telescope 1, Range 0 counts	double
15	Range_0_Tele_2	telescope 2, Range 0	double
16	Range_0_Tele_3	telescope 2, Range 0	double
17	Range_0_Sum	any telescope, Range 0 counts	double
18	Range_1_Tele_1	telescope 1, Range 1 counts	double
19	Range_1_Tele_2	telescope 2, Range 1 counts	double
20	Range_1_Tele_3	telescope 3, Range 1 counts	double
21	Range_1_Sum	any telescope, Range 1 counts	double
22	Range_2_Tele_1	telescope 1, Range 2 counts	double
23	Range_2_Tele_2	telescope 2, Range 2 counts	double
24	Range_2_Tele_3	telescope 3, Range 2 counts	double
25	Range_2_Sum	any telescope, Range 2 counts	double
26	Range_3_Tele_1	telescope 1, Range 3 counts	triple
27	Range_3_Tele_2	telescope 2, Range 3 counts	triple
28	Range_3_Tele_3	telescope 3, Range 3 counts	triple
29	Range_3_Sum	any telescope, Range 3 counts	triple
30	Range_4_Tele_1	telescope 1, Range 4 counts	triple
31	Range_4_Tele_2	telescope 2, Range 4 counts	triple
32	Range_4_Tele_3	telescope 3, Range 4 counts	triple
33	Range_4_Sum	any telescope, Range 4 counts	triple
34	Range_5_Tele_1	telescope 1, Range 5 counts	triple
35	Range_5_Tele_2	telescope 2, Range 5 counts	triple
36	Range_5_Tele_3	telescope 2, Range 5 counts	triple
37	Range_5_Sum	any telescope, Range 5 counts	triple
38	Range_6_Tele_1	telescope 1, Range 6 counts	triple
39	Range_6_Tele_2	telescope 2, Range 6 counts	triple
40	Range_6_Tele_3	telescope 3, Range 6 counts	triple
41	Range_6_Sum	any telescope, Range 6 counts	triple
42	He_Plus_Doubles	any telescope, pre-defined He ⁺ doubles box	double
43	He_Plus_Triples	any telescope, pre-defined He ⁺ triples box	triple
44	He_Plus_2_Doubles	any telescope, pre-defined He ⁺⁺ doubles box	double
45	He_Plus_2_Triples	any telescope, pre-defined He ⁺⁺ triples box	triple
46	O_Plus_Doubles_Tele_1	telescope 1, pre-defined W ⁺ doubles box	double
47	O_Plus_Doubles_Tele_2	telescope 2, pre-defined W ⁺ doubles box	double
48	O_Plus_Doubles_Tele_3	telescope 3, pre-defined W ⁺ doubles box	double
49	O_Plus_Triples_Tele_1	telescope 1, pre-defined W ⁺ triples box	triple
50	O_Plus_Triples_Tele_2	telescope 2, pre-defined W ⁺ triples box	triple
51	O_Plus_Triples_Tele_3	telescope 3, pre-defined W ⁺ triples box	triple
52	O_Plus_2_Doubles	any telescope, pre-defined O ⁺⁺ doubles box	double
53	O_Plus_2_Triples	any telescope, pre-defined O ⁺⁺ triples box	triple
54	CNO_over_4_and_T	any telescope, pre-defined triples box for C, N or O with charge above +4	triples
55	Energy_Underflow	any telescope, energy underflow counts	single
56	Energy_Overflow	any telescope, energy overflow counts	single
57	TOF_Underflow	any telescope, TOF underflow counts	single
58	TOF_Overflow	any telescope, TOF overflow counts	single
59	Mass_Overflow	any telescope, mass overflow counts	single
60	M_Over_Q_Underflow	any telescope, mass over charge underflow	single
61	M_Over_Q_Overflow	any telescope, mass over charge overflow	single
62	O_Plus_Doubles_Sum	any telescope, pre-defined W ⁺ doubles box	double
63	O_Plus_Triples_Sum	any telescope, pre-defined W ⁺ triples box	triple

Table 4.5: Column names and descriptions for CHEMS science rates. These columns follow the standard prefix columns, which are given in Table 1.6. Note that in the older revision 0 data (2004 through 2006), three prefix columns will be missing, and so the indices here would be smaller by 3. All revision 0 data will soon be replaced with revision 3 data.

Efficiencies are known only for a few science rate species, and these are listed in Table 4.6. Triples-only counters have less background, but these can only be used above a certain (species-dependent) DPPS step. At lower DPPS steps, the efficiency for triples detections is very small, and the counts C must be computed using a double coincidence measurement. Table 4.6 lists the doubles column and the triples column that need to be added to compute counts for the given species. Also in the table is the DPPS level for each species above which the triples-only counts can be used.

The actual efficiencies depend on the DPPS level, and so the conglomerate MIMI calibration file (Section 2.2) contains one efficiency per DPPS level for each species in Table 4.6. At each DPPS step, the efficiency value should be applied to counts that, for low DPPS levels, are a summation of a doubles and a triples counter. But starting at the transition step, the efficiency is applied to counts from just a triples counter. This transition point is also indicated in the conglomerate calibration file in the comments column, which lists either one (triples only) or two (triples+doubles) rate channels for which the efficiency is relevant.

As an example, consider H^+ , the first entry in Table 4.6. Up to DPPS step 15, the counts in RANGE_0_TELE_1 and RANGE_3_TELE_1 must be added to get the total H^+ counts for this telescope (Telescope 1 in this example, but other telescopes are done in the same way). From DPPS step 16 and above, only RANGE_3_TELE_1 should be included in the counts C for this species. A segment of the calibration file is shown in Table 4.7, where only the rows around the transition from double+triples to just triples are listed. (Also, some columns have been eliminated for brevity). The intensity for H^+ , Telescope 1, DPPS step 15 is then:

$$j_{H^+} = \frac{C}{\Delta t g \epsilon \Delta E} = \frac{\text{RANGE_0_TELE_1} + \text{RANGE_3_TELE_1}}{(\tau_{\text{spin}}/256 - 0.15) (0.007\text{cm}^2 \cdot \text{ster})(0.289)(0.717\text{keV})} \quad (4.6)$$

The energy width of 0.717 is obtained from Table 4.1 and the efficiency of 0.289 is obtained from Table 4.7. Both of these values are available in the conglomerate MIMI calibration file.

For H^+ , DPPS steps 16 and above, the numerator only needs to include the triples counts from RANGE_3_TELE_1. The H^+ intensity for Telescope 1 at DPPS step 17 is thus:

$$j_{H^+} = \frac{\text{RANGE_3_TELE_1}}{(\tau_{\text{spin}}/256 - 0.15) (0.007\text{cm}^2 \cdot \text{ster})(0.185)(0.945\text{keV})} \quad (4.7)$$

4.5 Calibrating the PHA data

Note to reader: The remainder of Section 4 (i.e., Sections 4.5, 4.6, and 4.7) go into considerable detail on the proper interpretation of the CHEMS PHA data. This detail is necessary for those who need to derive physically meaningful, calibrated results from the CHEMS PHA data. However, if the reader's interest is not specifically in this data product, we suggest skipping these sections.

The most accurate way to extract ion intensities from CHEMS requires combining the basic rates and the PHA data. This approach has several advantages over just using the species rates. The species rate boxes have the same boundaries for all DPPS steps, whereas the PHA species boxes are defined separately for each step. Using DPPS-specific boxes limits the amount of contamination in each box, and this contamination does overwhelm some species rate boxes at some steps. Because the species rates are predefined, they are limited to the ions with species rate boxes: H^+ , He^+ , He^{++} , O^+ , O^{++} , and $CNO>4^+$, and efficiencies are only known for some of these species. Using

Species			First DPPS Step
Label	Doubles Column Name	Triples Column Name	for Triples Only
H ⁺	RANGE_0_TELE_X	RANGE_3_TELE_X	16
He ⁺	HE_PLUS_DOUBLES	HE_PLUS_TRIPLES	99
He ⁺⁺	HE_PLUS_2_DOUBLES	HE_PLUS_2_TRIPLES	99
W ⁺	O_PLUS_DOUBLES_TELE_X	O_PLUS_TRIPLES_TELE_X	99

Note on He⁺⁺: this is really M/Q = 2, since both H₂⁺ and He⁺⁺ show up in this species box
Note on W⁺: water group ions such as H₂O⁺, OH⁺, and even O⁺

Table 4.6: The limited set of CHEMS science rate species for which efficiencies are known. These efficiencies allow conversion of science rate counters into differential intensity. The column names refer to the field names within the records inside PDS data files. Note that for H⁺ and W⁺, there are columns for each telescope, indicated here with a postfix **X**, where **X** can be 1, 2, or 3. Up to a certain DPPS step, the counts are obtained as a summation of two counters, a doubles counter and a triples counter. At and above the transition step, just the triples counter should be used. Actual efficiency values are listed in the MIMI conglomerate calibration file and are dependent on the DPPS step. The same efficiencies are used for each telescope.

Purpose	Data_Type	Sensor	Channel _Index	Particle	Midpoint _Value	Comment
...
EFFICIENCY	SCI	CHEMS	10	H+	1.21E-01	BR0 BR3
EFFICIENCY	SCI	CHEMS	11	H+	1.55E-01	BR0 BR3
EFFICIENCY	SCI	CHEMS	12	H+	1.89E-01	BR0 BR3
EFFICIENCY	SCI	CHEMS	13	H+	2.23E-01	BR0 BR3
EFFICIENCY	SCI	CHEMS	14	H+	2.56E-01	BR0 BR3
EFFICIENCY	SCI	CHEMS	15	H+	2.89E-01	BR0 BR3
EFFICIENCY	SCI	CHEMS	16	H+	9.57E-02	BR3
EFFICIENCY	SCI	CHEMS	17	H+	1.85E-01	BR3
EFFICIENCY	SCI	CHEMS	18	H+	2.88E-01	BR3
EFFICIENCY	SCI	CHEMS	19	H+	3.49E-01	BR3
EFFICIENCY	SCI	CHEMS	20	H+	3.71E-01	BR3
EFFICIENCY	SCI	CHEMS	21	H+	3.91E-01	BR3
EFFICIENCY	SCI	CHEMS	22	H+	4.07E-01	BR3
EFFICIENCY	SCI	CHEMS	23	H+	4.14E-01	BR3
...

Table 4.7: Sample from calibration file for H⁺ ions species rate efficiencies. Only the rows surrounding the transition from doubles+triples to triples-only are shown. Also, some columns are omitted for brevity. The efficiencies listed (in the Midpoint_Value column) apply to either a sum of the basic rate counters for Range ID 0 and Range ID 3 (DPPS steps 0 to 15), or to just the counts in the basic rate for Range ID 3 (DPPS steps 16 to 31).

the PHA data allows custom regions in NM and NQ to be defined to capture additional ions, such as H_2^+ , H_3^+ , O_2^+ , etc. Another advantage is that some intensity measurements can be separated by telescope. The species rate boxes for He^+ and He^{++} data are summed for all telescopes by the instrument flight software, but the PHA data retains the telescope identification. Finally, it is easy to adjust the box limits of the PHA data, avoiding background issues which affect the fixed species rate boxes. These background issues are dependent on the particle environment and on the operating performance, which can only be determined post-launch.

Converting PHA Quantities into Scientific Units

The raw TOF channel number and raw Energy channel number in a PHA event (recall Table 4.2 showing all PHA event quantities) can be converted to nanoseconds and keV respectively. The PHA species box definitions originally were defined in terms of calibrated TOF and calibrated energy, but now the box definitions are based on raw TOF and energy values. Therefore, the conversions in this section are useful for creating histograms out of collections of PHA events, but having the PHA quantities in scientific units is not needed when computing fluxes from PHA events.

In the formulas that follow, the TOF channel number (`Time_of_Flight` in PDS data files as described in Table 4.2) will be referred to as $TOF(ch)$ and $TOF(ns)$ is the value converted to nanoseconds. The Energy channel number (just called `Energy` in the PDS data files as described in Table 4.2) will be referred to as $Essd(ch)$ and its value converted to keV is labeled $Essd(keV)$.

$$\begin{aligned} TOF(ch) &\implies TOF(ns) \\ Essd(ch) &\implies Essd(keV) \end{aligned}$$

Computing the time of flight is then

$$TOF(ns) = \begin{cases} 0.60891 \cdot TOF(ch) - 9.86 & \text{when } TOF(ch) \leq 108 \\ 0.50597 \cdot TOF(ch) + 1.29 & \text{when } TOF(ch) > 108 \end{cases} \quad (4.8)$$

The conversion of Energy channel number to energy in keV is different for each telescope.

$$\text{Telescope 1: } Essd(keV) = \begin{cases} 2.4418 \times Essd(ch) - 14.73 & \text{when } Essd(ch) \leq 205 \\ 2.5026 \times Essd(ch) - 27.21 & \text{when } Essd(ch) > 205 \end{cases} \quad (4.9)$$

$$\text{Telescope 2: } Essd(keV) = \begin{cases} 2.41270 \times Essd(ch) - 14.22 & \text{when } Essd(ch) \leq 218 \\ 2.4670 \times Essd(ch) - 26.08 & \text{when } Essd(ch) > 218 \end{cases} \quad (4.10)$$

$$\text{Telescope 3: } Essd(keV) = \begin{cases} 2.42650 \times Essd(ch) - 15.25 & \text{when } Essd(ch) \leq 212 \\ 2.48520 \times Essd(ch) - 27.74 & \text{when } Essd(ch) > 212 \end{cases} \quad (4.11)$$

Given $TOF(ns)$ and $Essd(keV)$, the next step is to use the E/Q value (determined using the DPPS step) to compute the Mass and M/Q for the PHA event. Because the DPU uses an approximation to compute E/Q :

$$\frac{E}{Q} \text{ (keV/e)} \approx 3 \times (1.1487)^{DPPS} \quad (4.12)$$

(where the DPPS in the exponent is the DPPS step number ranging from 0 to 31) we will also use this approximation in order to ensure that PHA events analyzed on the ground will be categorized in the same way that the DPU categorized them on the spacecraft. Only in this limited case (i.e., during the computation of E/Q) is this shortcut used – the exact values of E/Q for each DPPS step listed in Table 4.1 are used everywhere else.

The M/Q calculation is done in two steps, where the second step is only calculated if the result from the first step exceeds 11.0:

$$\text{Step 1: } \frac{M}{Q} \text{ in amu/e} = 1.92 \times 10^{-5} \cdot [\text{TOF(ns)}]^2 \cdot \left(\frac{E}{Q} - 0.8 \right) \quad (4.13)$$

If $M/Q > 11.0$ from Step 1, then redo:

$$\text{Step 2: } \frac{M}{Q} \text{ in amu/e} = 1.92 \times 10^{-5} \cdot [\text{TOF(ns)}]^2 \cdot \left(\frac{E}{Q} - 4.0 \right) \quad (4.14)$$

Finally, with $\ln E$ representing $\ln(E(\text{keV}))$ and $\ln TOF$ representing $\ln(\text{TOF(ns)})$, the calculation of the mass is:

$$\text{Mass (amu)} = \exp \left\{ a_0 + a_1 \ln E + a_2 \ln TOF + a_3 (\ln E) (\ln TOF) + a_4 (\ln E)^2 + a_5 (\ln TOF)^3 \right\} \quad (4.15)$$

where a_0 through a_5 are defined as:

a_0	2.69575
a_1	-0.843766
a_2	-2.38009
a_3	0.385641
a_4	0.0513127
a_5	0.0690096

Computing Ion Species Intensity from PHA Events

By categorizing PHA events and normalizing them with the appropriate counters, it is possible to obtain differential intensities for the ion species listed in Table 4.8. Each ion is characterized by a rectangular PHA species box expressed as limits in Essd(ch) and TOF(ch) . In PDS data files containing PHA events, these parameters are called **Energy** and **Time_of_Flight** respectively (see Table 4.2). The box definitions depend on the DPPS step, so that for any species, there are actually up to 32 box definitions.

Determining box boundaries is straightforward for some species, but for others, there are significant challenges, and in some cases, valid box definitions are only available over a limited range of DPPS steps. Earlier in the mission, PHA species boxes had been defined as ranges in Mass versus M/Q , but now Essd(ch) versus TOF(ch) boxes are used since this allows smaller regions to be defined, which in turn allows better background exclusion. The box definition process for all species is described in section 4.6.

Tables E.1 through E.11 provide the box definitions at each DPPS step for all of the species listed in Table 4.8. These tables are also available numerically as ASCII files at the PDS (alongside this user guide) and via the MIMI web page dedicated to this user guide [Kusterer and Vandegriff, 2011]. Each table is for a single species at all 32 DPPS steps and contains box definitions for each telescope. Across telescopes, the Essd(ch) ranges are the same (for one species at a particular DPPS step), but the TOF(ch) ranges are potentially unique for each telescope. Because there are so many species boxes, it is not practical to show box boundaries graphically, but conceptually, they resemble the species rate boxes in Figure 4.3. For some species, box definitions are available only for a limited range of DPPS steps. Note that because the species boxes are a subset of the Essd(ch) versus TOF(ch) space, not every PHA event will fall into one of the PHA species boxes.

PHA Species with Flux Box Definitions				
Species	Doubles Range ID	Triples Range ID	PHA Species Box Definitions	Efficiencies
<i>straightforward species</i>				
H ⁺	0	3	Table E.1	Figure F.1
He ⁺⁺	1	4	Table E.2	Figure F.3
H ₂ ⁺	1	4	Table E.3	Figure F.2
He ⁺	1	4	Table E.4	Figure F.5
W ⁺	2	5	Table E.5	Figure F.7
O ⁺⁺	1	4 and 6	Table E.6	Figure F.6
<i>more difficult species</i>				
H ₃ ⁺	1	4	Table E.7	Figure F.4
C ⁺	2	5	Table E.8	Figure F.9
N ⁺	2	5	Table E.9	Figure F.9
O ⁺⁺⁺	1	4	Table E.10	Figure F.8
O ₂ ⁺	2	5	Table E.11	Figure F.10

Table 4.8: The ion species for which differential intensity measurements can be obtained using CHEMS PHA data. Note that W⁺ encompasses the following ions: O⁺, OH⁺, H₂O⁺, H₃O⁺. The PHA species boxes for the first six PHA species are relatively straightforward to define, although there are still significant caveats to understand when calculating fluxes for these species. The final five species present some significant challenges when computing flux, and PHA species box definitions for these species do not cover the full CHEMS energy range. The Range ID for the doubles and triples ranges are also listed here, as are the Table references for the species box definitions and efficiencies.

The easiest categorization of PHA events is by Range ID. The intensity calculation below will require a count of all PHA events for each Range ID within the time interval of interest. Unlike the PHA species boxes, all PHA events will fall into one of the Range ID categories, since every PHA event contains a Range ID. Note that the count of all PHA events in a specific Range ID is different from the counts in the CHEMS Science Rate counter for that Range ID. Not all of the events that triggered a count in the science rate counter will always be selected for inclusion in the PHA event stream. Indeed below we show how to use the science rate counter to normalize the PHA events.

It is important to distinguish PHA species counts as doubles counts or triples counts. Each event falls into just one of these categories. All doubles counts come from PHA events where $\text{Essd}(\text{ch})$ is zero (no energy measurement). The Range ID for doubles events will be 0, 1, or 2, but the primary way to detect a doubles event is with $\text{Essd}(\text{ch}) = 0$. A doubles count means that a particle has been detected by the TOF system, but not by the SSD. Triples counts include a non-zero value for $\text{Essd}(\text{ch})$ and will have a Range ID of 3, 4, 5, or 6. In most cases, each ion species has one doubles counter and one triples counter. O^{++} is unique in that it has two triples counters (in Range IDs 4 and 6), and so a different approach (described below) is necessary for computing O^{++} intensity.

One important concept to understand is that triples events are also, in a sense, doubles events. The sense in which this is important arises when answering the question “How many particles within specified $\text{TOF}(\text{ch})$ limits were detected by the TOF system?” The answer will require a sum of doubles plus triples, because each triples event also passed the $\text{TOF}(\text{ch})$ filter. Including triples counts in this sum essentially ignores their “triple-ness” and treats them as additional doubles counts.

To determine if an event falls within any PHA species box, start with the DPPS level, and use that to find the relevant rows in the tables of $\text{Essd}(\text{ch})$ and $\text{TOF}(\text{ch})$ box definitions (Tables E.1 through E.11). Each table has a distinct set of $\text{Essd}(\text{ch})$ and $\text{TOF}(\text{ch})$ ranges, and if the values for the event fall within the ranges specified by a particular table, then the event corresponds to an ion of the type specified by the table.

As an example, consider the following two PHA events:

Quantity	Event A	Event B
DPPS_Level	12	25
E(ch)	0	45
TOF(ch)	240	130
SSD ID	0	0
Start MCP ID	1	2
Range ID	1	4

For event A, the Start MCP of 1 indicates Telescope 1. The search for a matching PHA species box involves searching through Tables E.1 to E.11, looking only at the Telescope 1 columns and the rows with $\text{DPPS} = 12$. The He^+ table (E.4) has a row for $\text{DPPS} = 12$ and Telescope 1 with a range of 222 to 255 for $\text{TOF}(\text{ch})$. The $\text{Essd}(\text{ch})$ of 0 for this row also matches Event A, which is therefore categorized as He^+ doubles. Note that the event also increments the PHA counter for Range ID 1 events. Also notice that if the $\text{TOF}(\text{ch})$ had been 200, this would have meant that the event did not fall into any PHA species box and would only be counted as a PHA count for the appropriate Range ID (which was Range ID 1 in this case).

For Event B, the same procedure is followed: search through the columns of the given telescope number in Tables E.1 to E.11, and look only at rows for the right DPPS level to see if any species table has TOF(ch) and Essd(ch) bounds that include the given event parameters. Event B corresponds to O⁺⁺ triples.

Differential intensity for a PHA species is calculated by first determining a count rate for that PHA species. Then the count rate can be converted to intensity using a standard approach (like that used in Section 4.4.2 for CHEMS Science Rate data). When determining the PHA species count rate, it is important to recognize that while the Range ID counters (the CHEMS Science Rate counters) do categorize and count every incident ion, not all of these events can always be captured as PHA events. Therefore, it is assumed that out of the events that were recorded by Range ID counters, the subset of these that were selected as PHA events is representative of all events.

Using the count of all incident ion events (maintained in the rate counters for each Range ID), the count rate for a PHA species can be computed by multiplying:

- a) the ratio of PHA species events to total PHA events in the enclosing Range ID, *by*
- b) the count rate for that Range ID.

Said another way, the count rate for a particular PHA species is a fraction of the basic rate for that Range ID, where the fraction is the ratio of PHA species events (counts inside the Range ID that also fell within the species box) to total PHA events within the entire Range ID.

Each Range ID is either a doubles range or a triples range. Thus, if R_i is the basic rate for the Range ID i , then the species rate for a PHA species box inside that Range ID will be either

$$\text{PHA doubles species rate} = \frac{D_{\text{species}}}{D_i} R_i \quad (4.16)$$

$$\text{or PHA triples species rate} = \frac{T_{\text{species}}}{T_i} R_i \quad (4.17)$$

where D_i is the total number of PHA doubles events tagged as having Range ID i , and D_{species} is the number of events in Range ID i that fall within the PHA species doubles box. For a PHA species box in a triples Range ID, the notation in equation 4.17 is used, where T_{species} is the number of events within the PHA species triples box, and T_i is the number of PHA triples counts tagged as having Range ID i . The species PHA counts, D_{species} (or T_{species} for triples) are always less than or equal to the number of PHA events in the larger Range ID, D_i (or T_i for triples).

Equations 4.16 and 4.17 define what is meant by “using the basic rates to normalize the PHA species counts,” and thus it becomes apparent why PHA triples events and doubles events need to be tallied separately – doubles PHA events are normalized with a doubles basic rate, and likewise for triples PHA events.

Intensities for each DPPS step are computed separately, and it would be ideal to use only the triples events at each step, simply because backgrounds are lower when requiring a triple coincidence. But at the very lowest values for E/Q (i.e., small DPPS steps), the detection efficiency for triples can be vanishingly small, since low energy particles do not deposit enough energy in the SSD to produce an energy signal (i.e., Essd(ch) is 0). Thus at low energies (small DPPS steps), a species count rate will be computed using a sum of doubles and triples PHA species rates. *Note that triples events are included in this sum even though the efficiencies are low because they do start to contribute as the DPPS step increases* (they may contribute nothing at step 0 but 10-20% at the step just below the switch to triples only). These triples counts are effectively being treated like doubles counts – they represent particles that passed the TOF(ch) filter for the given species.

At high enough energies, the species rate can reliably be determined using a cleaner triples only PHA species counter. The DPPS step at which to transition from a doubles+triples count rate to a triples-only count rate varies by species. Also note that for some species, there simply are no doubles PHA boxes that can isolate the species, and so these species can only be detected over a limited range of higher energy DPPS steps.

Consider first a triples-only intensity J_T :

$$J_T = \frac{1}{g \Delta E \epsilon_T} \left(\frac{T_{\text{species}}}{T_i} \right) R_i \quad (4.18)$$

This is similar to Equation 4.5, where the count rate is now a normalized PHA count rate. Note also that the efficiency ϵ_T refers to the triples-only efficiency. Efficiencies are tabulated and discussed in detail in Appendix F. The geometry factor g is the same for all telescopes, $g = 0.007 \text{ cm}^2 \cdot \text{sr}$, and ΔE is the passband of the DPPS step (recall that ΔE is 3% of the E/Q midpoint - see Table 4.1).

When combining doubles and triples, the intensity J_{T+D} is:

$$J_{D+T} = \frac{1}{g \Delta E \epsilon_{\text{tof}}} \left[\left(\frac{D_{\text{species}}}{D_i} \right) R_i + \left(\frac{T_{\text{species}}}{T_j} \right) R_j \right] \quad (4.19)$$

where the subscript i indicates the doubles Range ID and j is a triples Range ID. The basic rate to use must be for the Range ID that contains the PHA species box.

Note that equations 4.18 and 4.19 each use a different efficiency, ϵ_T for triples only, and ϵ_{tof} for doubles and triples combined. The TOF efficiency refers to any particle that makes it through the TOF system, and this is why doubles and triples must be added to get the correct counts in this situation. For each PHA species there is a table with efficiencies for each DPPS step, namely Tables F.1 to F.10 in Appendix F. The tables include efficiencies for triples (meaning triples only) and TOF (meaning doubles+triples). The triples-only efficiencies are different for each telescope. Each table has values for ϵ_{tof} and ϵ_T for all DPPS steps, but the triples-only efficiencies should only be used above a species specific threshold. The point at which to switch from using doubles+triples to triples-only is described along with the efficiency data (i.e., in the captions of Tables F.1 through F.10 in Appendix F).

The PHA triples species box for O^{++} is unique in that it overlaps not just one but two Range IDs, namely 4 and 6. Thus the triples-only intensity for O^{++} contains a sum of normalized rates derived from two basic rates:

$$O^{++} J_T = \frac{1}{g \Delta E \epsilon_T} \left[\left(\frac{T_{O^{++}(4)}}{T_4} \right) R_4 + \left(\frac{T_{O^{++}(6)}}{T_6} \right) R_6 \right] \quad (4.20)$$

where $T_{O^{++}(4)}$ is the number of counts in the portion of the O^{++} box within Range ID 4, T_4 is the count of all PHA events tagged as Range ID 4, and R_4 is the basic rate for Range ID 4. Analogous quantities are shown in the second term of the sum for Range ID 6.

The equation for $O^{++} J_{D+T}$ has one additional term to include the normalized PHA doubles rate for O^{++} , which comes from Range ID 1.

$$O^{++} J_{D+T} = \frac{1}{g \Delta E \epsilon_{\text{tof}}} \left[\left(\frac{T_{O^{++}(4)}}{T_4} \right) R_4 + \left(\frac{T_{O^{++}(6)}}{T_6} \right) R_6 + \left(\frac{D_{O^{++}(1)}}{D_1} \right) R_1 \right] \quad (4.21)$$

4.6 Understanding the PHA Species Boxes

If you intend to study a particular species using CHEMS PHA data, you must read this section. It contains details about the species box definitions, including the spatial regions where various box definitions are valid and what backgrounds may be relevant for particular species.

This section describes the process by which CHEMS flight data was used to determine the optimal ranges of Essd(ch) and TOF(ch) for capturing the 11 PHA species listed in Table 4.8. Species box definitions are provided in Tables E.1 through E.11 in Appendix E.

Important caveats exist in terms of interpreting the contents of the species boxes. For example, He^{++} doubles cannot be distinguished from H_2^+ doubles because, on a histogram of counts versus M/Q, both appear in the same peak at M/Q = 2. Within Saturn's magnetosphere we assume that the counts at M/Q = 2 at low energies in the doubles events are due to H_2^+ . We base this on the low He^{++} abundance at energies above 27 keV/e, where the species *can* be distinguished in the *triples* data ($\text{He}^{++}/\text{H}_2^+ \approx 0.03$). Also since H_2^+ is not significantly present in the solar wind, periods when Cassini is outside the magnetosphere are used when defining the He^{++} doubles box. But this low energy He^{++} doubles box would not be used inside the magnetosphere, since it will mostly be counting H_2^+ .

Source Data for PHA Species Box Definitions

Interplanetary space and Saturn's magnetosphere provide two distinct composition environments that are useful for isolating particular species. A set of time periods from each region was used to create two large collections of PHA events. Magnetospheric time periods consist of equatorial ring current passes (L = 7-16, latitude = -10 ° to 10 °) from 2004 to 2010. Interplanetary PHA events were obtained during times of high interplanetary activity (CHEMS counts significantly above background) using a set non-contiguous time intervals from 2001 to Saturn orbit insertion. Tables 4.10 and 4.9 list the time ranges used for interplanetary and magnetospheric time periods, respectively.

Doubles species ranges in TOF(ch) are determined by plotting doubles events on a 1-D histogram. Figure 4.4 provides a histogram containing all the doubles events at DPPS step 0 from all magnetospheric periods mentioned above. If there are significant counts of an ion species, a peak will form in the TOF(ch) histogram. To determine which species each peak corresponds to, the TOF(ch) at the center of each peak is converted to M/Q. With the exception of the M/Q = 2 peak, the M/Q value can be used to uniquely identify the ion species. For example, the lowest two peaks in each telescope are centered on M/Q=1 and M/Q=4, and represent H^+ and He^+ respectively. The distribution around M/Q = 2 contains both He^{++} and H_2^+ , so an Essd(ch) measurement is needed to separate these species. This procedure is then repeated for each DPPS step. Plots similar to Figure 4.4 for all relevant DPPS steps are provided in Appendix D.

At higher incident particle energies, PHA events will contain a non-zero value for Essd(ch) because the SSD becomes more efficient at higher energies. These events are triple coincident detections, PHA events for such particles are plotted on a 2-D histogram of Essd(ch) versus TOF(ch), and each species is visible as an island of counts. A sample plot illustrating a few triples box definitions is provided in Figure 4.5, which shows a collection of magnetospheric events at DPPS step 12. The top three panels show 2-D histograms of the counts for each telescope, and each bottom panel shows a corresponding 1-D histogram of counts versus TOF(ch). Species boxes are shown for H^+

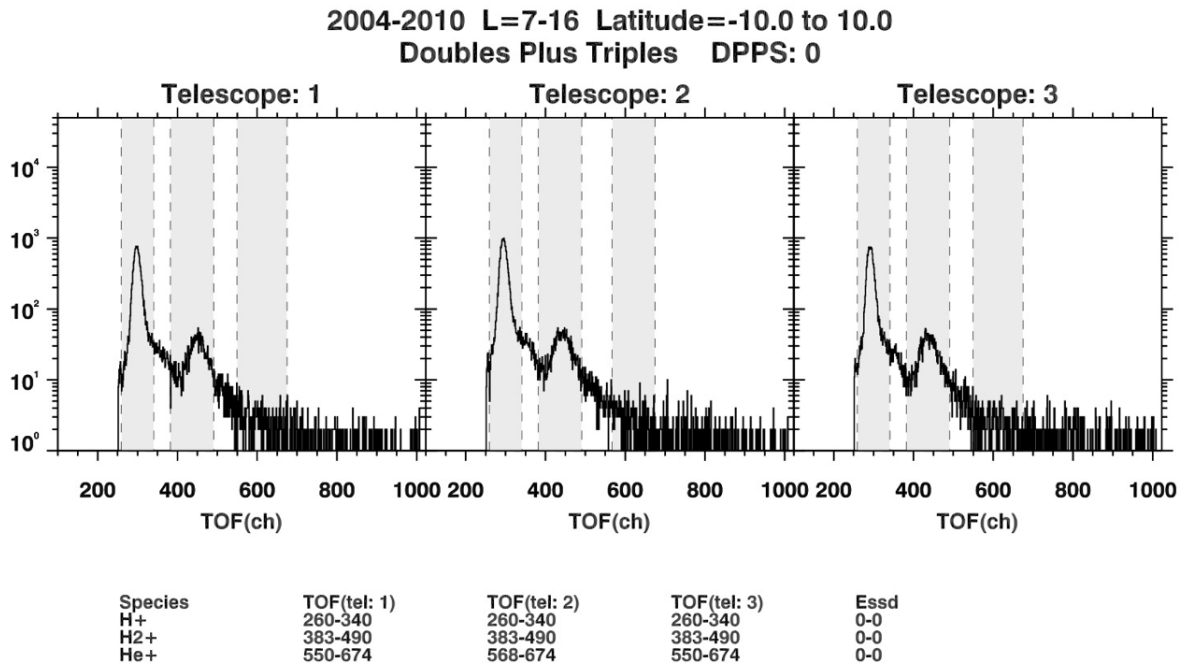
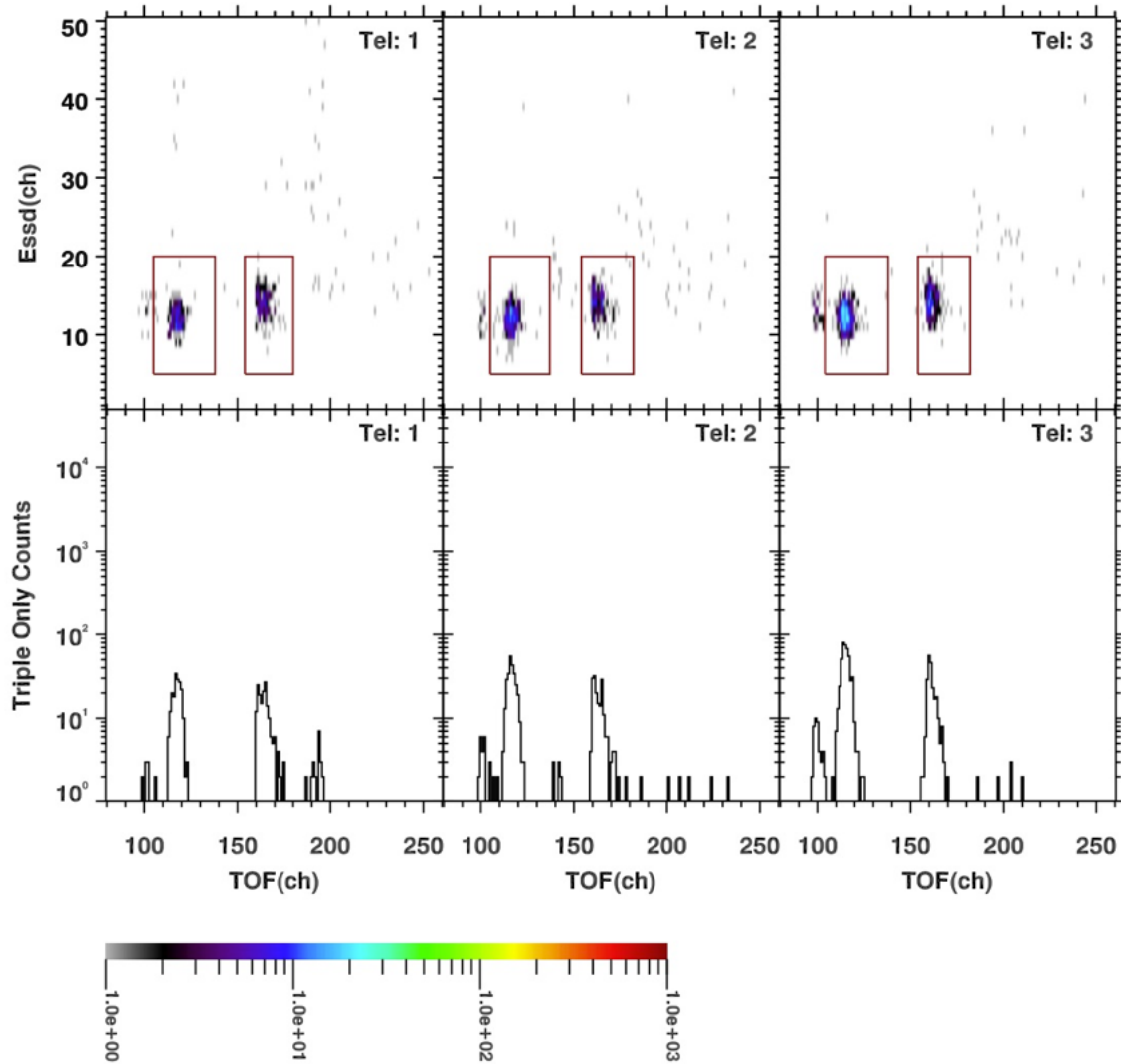


Figure 4.4: An example of a 1-D histogram used for examining CHEMS PHA doubles events. Data for this plot was taken from multiple magnetospheric passes from 2004 to 2010. Recall that doubles events also include the triples events. Abundant species show up as peaks with centroids at specific TOF(ch) values. Highlighted here are peaks for H⁺, H₂⁺, and He⁺, and notice that these peaks have slightly different locations in each telescope. This plot is for only for particles at DPPS step 0. The TOF(ch) ranges change at different values of E/Q, and PHA doubles box limits must be determined separately for each DPPS step. Appendix D provides versions of this plot for all relevant DPPS step.

2004-2010 L=7-16 Latitude=-10.0 to 10.0
DPPS: 12



Species	TOF(tel: 1)	TOF(tel: 2)	TOF(tel: 3)	Esdd
H ⁺	105-138	105-137	104-138	5-20
H ₂ ⁺	154-190	154-191	154-191	0-0
He ⁺⁺	154-180	154-182	154-182	5-20

Figure 4.5: An example of a 2-D histogram used for examining CHEMS PHA triples events. Data for this plot was taken from multiple magnetospheric passes from 2004 to 2010. Abundant species show up as islands of counts with centroids at at specific TOF(ch) values and Esdd(ch) values. Highlighted here are peaks for He⁺⁺ (distinguishable from H₂⁺ in triples events only) and H⁺, and notice that while the Esdd(ch) limits are the same for each telescope, unique TOF(ch) limits must be defined for each telescope. This plot is only for particles at DPPS step 12. Because the TOF(ch) and Esdd(ch) ranges change as the DPPS level changes, the triples box limits for each species must be determined separately for each DPPS steps. Appendix D provides versions of this plot for all relevant DPPS steps.

Start Time	End Time	Duration (minutes)	Start Time	End Time	Duration (minutes)
2004-348T23:20	2004-349T21:30	1330	2009-285T23:30	2009-286T20:10	1240
2004-350T14:20	2004-351T12:00	1300	2009-287T14:10	2009-288T10:50	1240
2005-046T19:00	2005-047T15:50	1250	2009-304T23:00	2009-305T19:40	1240
2005-048T10:00	2005-049T06:50	1250	2009-306T13:40	2009-307T10:10	1230
2005-067T05:50	2005-068T02:40	1250	2009-323T23:40	2009-324T20:10	1230
2005-068T20:40	2005-069T17:30	1250	2009-325T14:20	2009-326T10:50	1230
2005-089T08:40	2005-090T05:30	1250	2009-343T00:30	2009-343T21:00	1230
2005-105T08:00	2005-106T04:20	1220	2009-344T15:10	2009-345T11:40	1230
2005-265T16:10	2005-266T12:40	1230	2009-359T00:50	2009-359T21:00	1210
2005-267T06:40	2005-268T03:00	1220	2009-360T14:30	2009-361T10:40	1210
2005-285T10:30	2005-286T07:00	1230	2010-025T23:20	2010-026T19:20	1200
2005-301T16:20	2005-302T14:20	1320	2010-027T13:00	2010-028T09:10	1210
2005-303T07:30	2005-304T05:30	1320	2010-043T11:40	2010-044T08:00	1220
2005-330T04:40	2005-331T02:40	1320	2010-062T15:00	2010-063T11:20	1220
2005-331T20:00	2005-332T18:00	1320	2010-078T16:00	2010-079T12:20	1220
2005-357T14:40	2005-358T12:40	1320	2010-080T06:20	2010-081T02:40	1220
2005-359T06:00	2005-360T04:00	1320	2010-096T07:00	2010-097T03:50	1250
2006-016T00:00	2006-016T23:40	1420	2010-097T22:00	2010-098T18:50	1250
2006-017T14:20	2006-018T13:50	1410	2010-116T15:40	2010-117T12:40	1260
2006-056T18:20	2006-057T17:50	1410	2010-118T06:50	2010-119T03:40	1250
2006-078T13:20	2006-079T12:30	1390	2010-137T02:40	2010-137T23:30	1250
2006-080T03:40	2006-081T02:50	1390	2010-138T17:40	2010-139T14:30	1250
2006-117T17:10	2006-118T16:30	1400	2010-154T16:30	2010-155T13:10	1240
2006-141T02:10	2006-142T01:30	1400	2010-169T02:00	2010-169T22:10	1210
2006-142T16:30	2006-143T15:50	1400	2010-170T16:00	2010-171T12:10	1210
2006-180T06:20	2006-181T05:30	1390	2010-204T21:40	2010-205T18:10	1230
2006-181T20:40	2006-182T19:50	1390	2010-206T12:10	2010-207T09:10	1260
2007-177T20:10	2007-178T16:10	1200	2010-224T19:30	2010-225T16:00	1230
2007-179T09:40	2007-180T05:40	1200	2010-226T10:00	2010-227T07:00	1260
2007-200T13:50	2007-201T12:50	1380	2010-244T20:00	2010-245T16:40	1240
2007-202T04:10	2007-203T03:10	1380	2010-246T10:40	2010-247T07:30	1250
2007-240T06:30	2007-241T05:20	1370	2010-264T18:20	2010-265T15:00	1240
2007-241T20:50	2007-242T19:40	1370	2010-266T09:00	2010-267T05:50	1250
2007-272T05:30	2007-273T03:00	1290	2010-288T11:40	2010-289T09:00	1280
2007-296T02:20	2007-296T23:00	1240	2010-290T02:50	2010-291T00:20	1290
2007-297T16:50	2007-298T13:50	1260	2010-333T03:30	2010-334T00:30	1260
2007-320T02:20	2007-320T23:00	1240	2010-334T18:40	2010-335T15:30	1250
2007-321T16:50	2007-322T13:40	1250	2010-353T16:50	2010-354T13:40	1250
2007-337T16:10	2007-338T12:30	1220	2010-355T07:50	2010-356T04:50	1260

Table 4.9: Time periods when Cassini is inside the magnetosphere of Saturn. The PHA events within all of these time periods were collected and used to create species box definitions for ions found within the magnetosphere, including H^+ , H_2^+ , W^+ , O^{++} , O_2^+ , H_3^+ , C^+ , and N^+ . Times were chosen when Cassini was within $7 < L < 16$ and $-10^\circ < \text{latitude} < +10^\circ$. Furthermore, time ranges were selected only if the data was continuous (i.e., no data gaps) over the wider range $6 < L < 21$ and if the spacecraft remained in the magnetosphere out to $L = 21$.

Start Time	End Time	Duration (minutes)
2004-001T00:00	2004-002T00:00	1440
2004-002T16:00	2004-004T08:00	2400
2004-004T20:00	2004-009T08:00	6480
2004-010T04:00	2004-011T00:00	1200
2004-011T12:00	2004-013T00:00	2160
2004-013T16:00	2004-015T20:00	3120
2004-016T08:00	2004-017T20:00	2160
2004-018T20:00	2004-020T00:00	1680
2004-020T12:00	2004-022T16:00	3120
2004-024T16:00	2004-027T04:00	3600
2004-027T16:00	2004-029T20:00	3120
2004-030T04:00	2004-032T00:00	2640
2004-032T12:00	2004-033T20:00	1920
2004-034T16:00	2004-036T04:00	2160
2004-037T00:00	2004-040T00:00	4320
2004-040T00:00	2004-160T00:00	172800
2004-165T00:00	2004-179T00:00	20160

Table 4.10: Time periods when Cassini is in interplanetary space. PHA events from these time periods were collected and used to define species box definitions for He^{++} , He^+ , O^{+++} , each of which is more abundant in the solar wind than inside Saturn’s magnetosphere. Each time period was examined to ensure that no solar wind oxygen was present.

and He^{++} . Note that the TOF(ch) limits are telescope dependent, and that the box ranges are different for every DPSS step. Appendix D contains versions of Figure 4.4 for all relevant DPSS steps.

H^+ , W^+ , and O^{++} boxes

The boxes for H^+ , W^+ , and O^{++} are the easiest to identify. Only the Saturn magnetospheric PHA events are used to determine the boxes for these species. The peaks in the TOF(ch) 1-D histogram and in the Essd(ch) versus TOF(ch) 2-D histograms are easy to distinguish from other species and there are good counting statistics for all three species. Since the signal for O^{++} and W^+ is weak for $E/Q < 8$ keV/e, boxes cannot be defined for these two species at the lowest 8 DPSS steps ($E/Q = 2.8\text{-}7.8$ keV/e). The boxes for H^+ , W^+ , and O^{++} are shown in Tables E.1, E.5, and E.6 respectively.

H_2^+ boxes

The boxes for H_2^+ are shown in Table E.3. Because H_2^+ is rare in interplanetary space and abundant in Saturn’s magnetosphere, data from Saturn magnetospheric periods are used to define the H_2^+ box. To calculate the differential intensity for H_2^+ at low energies ($E/Q < 27$ keV/e), doubles data must be used. Since the doubles data only gives M/Q , H_2^+ cannot be separated from He^{++} at these low energies. However, since H_2^+ dominates He^{++} in Saturn’s magnetosphere ($\text{He}^{++}/\text{H}_2^+ \sim 0.03$),

it is generally safe to assume that during magnetospheric periods, the doubles data in the $M/Q = 2$ box is H_2^+ .

Above 27 keV/e, triples data correctly isolates the H_2^+ counts. At energies greater than 54 keV/e, H_2^+ dissociates into two components when it passes through the carbon foil. When only one component triggers the SSD, the PHA event is assigned a mass value near $M=1$ amu. When both components trigger the SSD, the PHA event gets a mass value near $M=2$ amu. An accumulation of many one-component and two-component H_2^+ events shows up as two peaks in the $Essd(ch)$ versus $TOF(ch)$ plots. Both of these peaks are included in the PHA species box for H_2^+ .

But for $E/Q > 145$ keV/e (step 28), there are two separate background problems with the $M=1$ H_2^+ peak, and so the H_2^+ species box for the highest four DPPS steps (i.e., 28 through 31) includes only the $M=2$ peak. Copied from Table 4.1 for convenience, the E/Q midpoints for these steps are:

28	145.3 keV/e
29	166.9 keV/e
30	191.6 keV/e
31	220.2 keV/e

One background problem involves ion trails from the H^+ peak for steps 30 and 31, and the other problem is bogus TOF counts. Explanations for these background issues are given later in Section 4.7, but Figure 4.6 shows clearly how the background signal affects the $M=1$ peak but not the $M=2$ peak. A correction factor is applied to the counts obtained from just the $M=2$ peak to make up for the counts that would have been registered had the counts around $M=1$ peak been included. This correction factor is shown in Figure 4.7, which indicates that the percentage of counts in the $M=2$ box approaches 80% of the total counts in H_2^+ box at the highest three energy steps. At step 28, 78% of the total H_2^+ counts are in the $M=2$ peak, while at steps 29-31 80% of the total H_2^+ counts are in the $M=2$ peak. To compensate for only using the $M=2$ box at these four DPPS steps, the triples only efficiency for H_2^+ is multiplied by 78% for step 28 and 80% for steps 29-31. The efficiencies for H_2^+ (described in Appendix F and listed in Figure F.2 as well as in the calibration file) include these factors.

He⁺⁺ Boxes

Because helium is a minor ion in Saturn's magnetosphere, the interplanetary time periods are used to determine the boxes for the helium ions. Using the interplanetary data also prevents the accidental inclusion of H_2^+ data when creating the box boundaries. He^{++} and H_2^+ both have $M/Q = 2$ amu/e, and will therefore show up in the same region on a 1-D histogram of $TOF(ch)$. And while H_2^+ is very common in Saturn's magnetosphere, it is essentially absent from the solar wind. Thus it is safe to assume that TOF peaks corresponding to $M/Q = 2$ amu/e during the interplanetary period are all due to He^{++} .

The boxes for He^{++} are shown in Table E.2.

Once the He^{++} boxes are defined using just the interplanetary data, it would be possible to use them for any time period. But when Cassini is inside Saturn's magnetosphere, all the He^{++} doubles boxes (those with an $Essd(ch)$ range of 0 - 0, i.e., no energy measurement) will be swamped with magnetospheric H_2^+ , and therefore should not be used as He^{++} boxes. The triples boxes for He^{++} , which starts at $E/Q > 15.7$ keV/e (step 12 and greater) can distinguish He^{++} from H_2^+ , but there are complications for steps 12-15, where the $Essd(ch)$ resolution is not high enough to separate

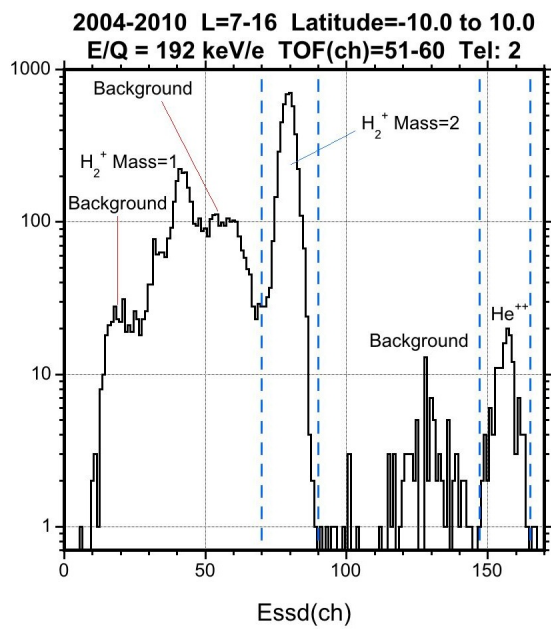


Figure 4.6: An Esd(ch) histogram for step 30 of the $M/Q = 2$ region. There is a large amount of background counts that interferes with the Mass=1 peak. To avoid this problem, only the Mass=2 peak is used to define the H_2^+ PHA species box at higher energies.

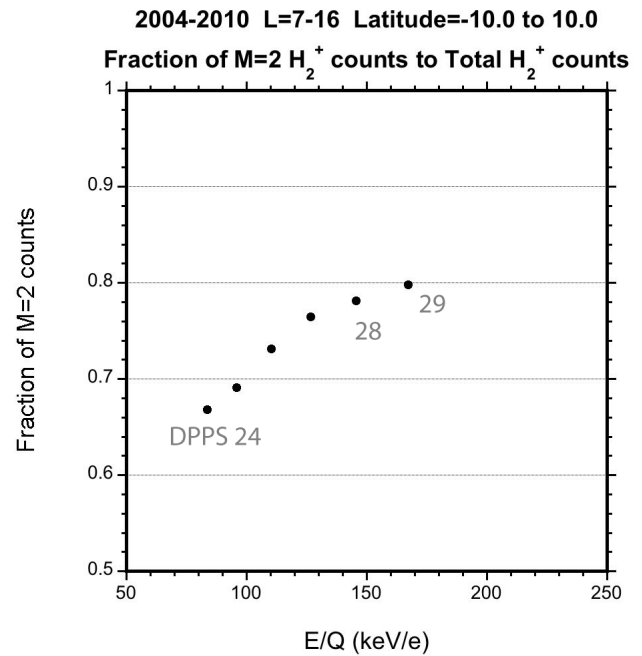


Figure 4.7: Ratio of H_2^+ M=2 counts to M=1 counts as a function of energy per charge for DPPS steps 24 through 29. The ratio approaches 0.80 at high energies.

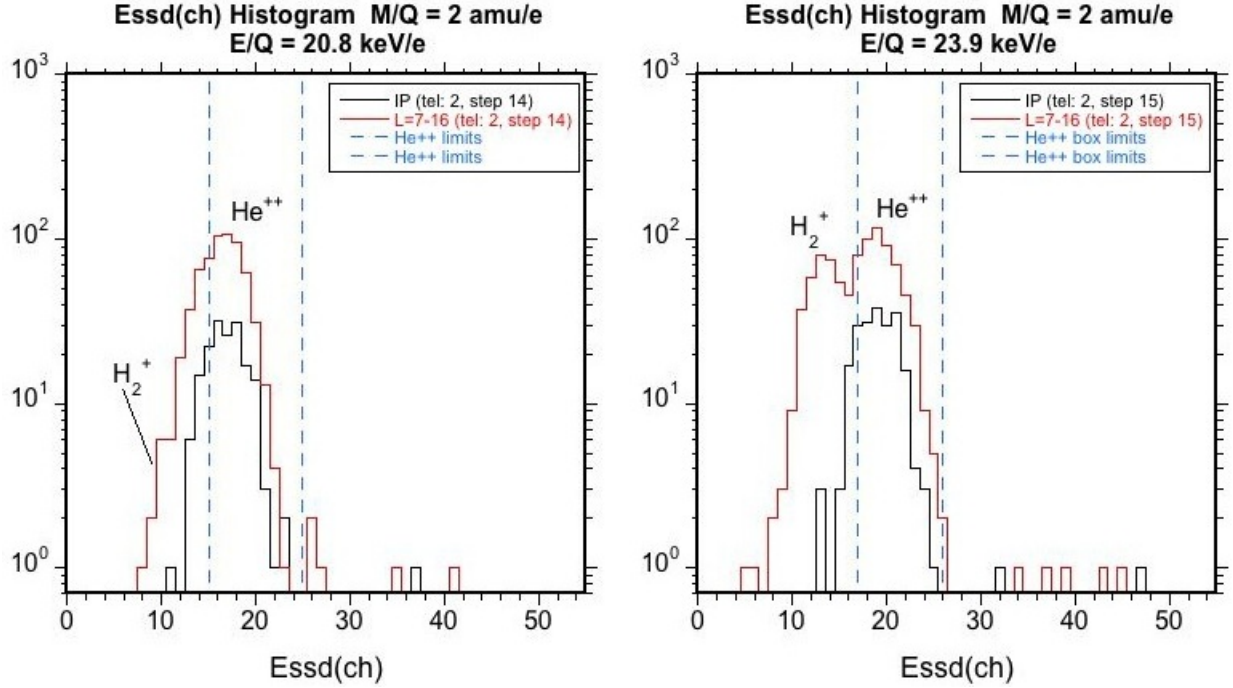


Figure 4.8: Ecss(ch) histogram of the $M/Q = 2$ region. The plot on the left is data from step 14 ($E/Q = 20.8$ keV/e) and the plot on the right is from step 15 ($E/Q = 23.9$ keV/e). We only show data from telescope 2, but the distributions are similar for the other telescopes. The black curves represent interplanetary periods, while the red curves represent magnetospheric periods. Since the magnetospheric period contains both H_2^+ and He^{++} counts, the left side of the distribution from the magnetosphere is wider. To avoid including H_2^+ counts in our He^{++} box, we had to use narrow Ecss(ch) bounds. To compensate for the He^{++} counts lost due to these narrow boxes, we lowered the triples only efficiency.

He^{++} from H_2^+ . Fortunately, at steps 12 and 13, the triples efficiency for H_2^+ is so low, that you can still assume that all the counts are from He^{++} . But at DPSS steps 14 and 15, the H_2^+ efficiency is high, and the peak locations overlap, as shown in Figure 4.8. Each panel (left is for DPSS step 14 and the right panel is for step 15) shows two histograms, a black one from interplanetary data only, where there is a clear, single peak of He^{++} , and a larger red line showing data from magnetospheric periods where the He^{++} and H_2^+ peaks overlap. In order to ensure that the box counts only He^{++} , the box limits are defined closely around the He^{++} peak. This excludes H_2^+ counts, but also removes some He^{++} signal as well. Therefore the efficiencies for the step 14 and 15 He^{++} boxes were reduced to account for this.

The following list of ratios indicates by how much the triples efficiencies were lowered to account for the smaller He^{++} box sizes at step 14 and 15. These ratios were calculated using data from the interplanetary period, and each represents the number of triples counts in the narrowed He^{++} box to the total number of He^{++} counts in the full sized He^{++} box. We then multiply the TCR/DCR for He^{++} by this ratio to correct for the narrow box. The ratios are

Telescopes 1 and 2, step 14:	0.871
Telescopes 1 and 2, step 15:	0.918
Telescope 3, step 14:	0.95
Telescope 3, step 15:	0.95.9

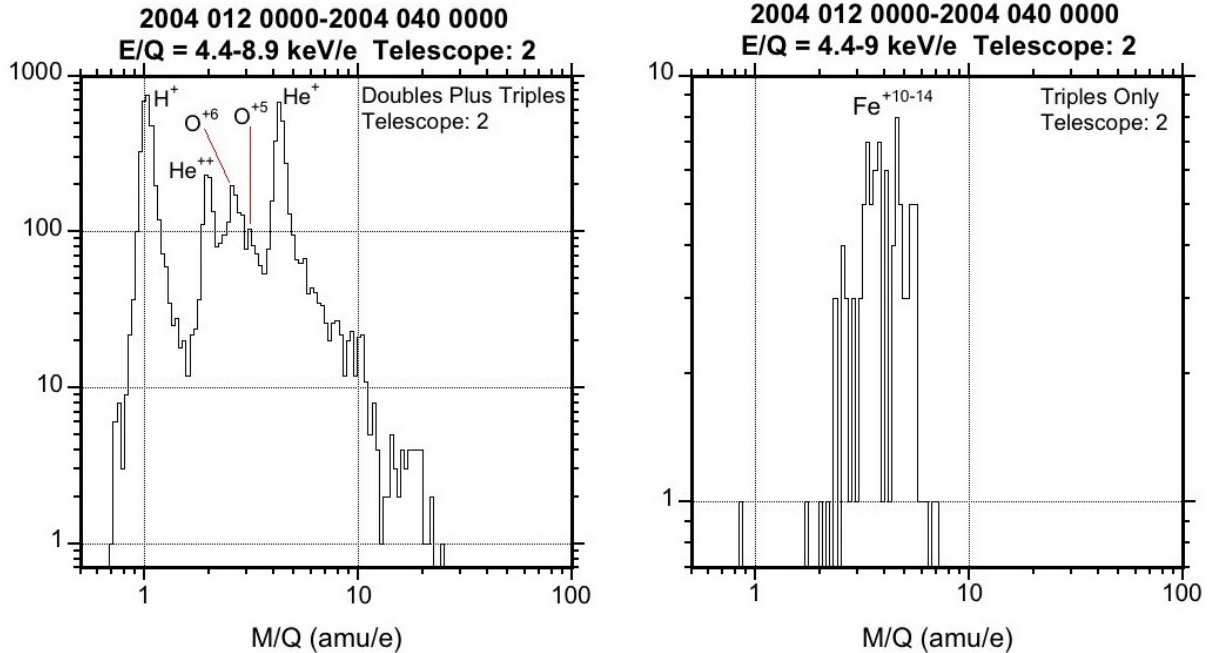


Figure 4.9: M/Q histogram for an interplanetary period (2004-012T00:00 to 2004-040T00:00). Note that solar wind oxygen ions interfere with the He^{++} peak. The peak in the triples data cannot be due to He^+ since it does not have enough energy to overcome the threshold of the solid state detector. The calculation of the mass reveals these ions to be Fe with $Q=10-14$. Sometimes these heavy solar wind ions interfere with our helium data and can make it impossible to measure the helium flux at low energies.

(Note: users will not need these ratios since they have already been factored into the reported efficiencies, but they help explain the He^{++} box sizes and efficiencies.) Since interplanetary data for telescope 1 contains too few counts to calculate these ratios, the ratios for telescope 1 are assumed to be the same as that of telescope 2. Since the SSD on telescopes 1 and 2 have the same threshold, it is reasonable to expect the triples only efficiency for these telescopes to be approximately the same.

There is an additional problem with the He^{++} differential intensity calculation at step 15. For some time periods, there is a basic rate spike in range ID 4. As a result, the He^{++} spectra (which are normalized using this basic rate) sometimes contain a small spike at step 15. We are unable to remove this basic rates spike, so it will still show up in the data, and therefore some caution should be used when using the He^{++} at step 15.

He^+ PHA Species Boxes

The He^+ doubles counts are far easier to identify in interplanetary space, so the interplanetary periods were used to define the He^+ boxes. The boxes for He^+ are shown in Table E.4.

Similar to the He^{++} boxes, care must be taken when using the He^+ boxes inside Saturn's magnetosphere. During magnetospheric periods, the doubles data from the H_2^+ box interferes with the He^+ doubles peak. Thus for $E/Q < 10$ keV/e, it is impossible to see the He^+ peak in the doubles data. A peak begins to emerge for $E/Q > 10$ keV/e, but it still contains a significant amount of background. It is possible to subtract the doubles background in the He^+ data when a peak is

visible, but it requires a detailed, case-by-case analysis that we do not discuss here.

During interplanetary periods, a doubles He^+ box can be defined for the entire CHEMS energy range. However, He^+ is not detected that efficiently for the first few E/Q steps, so a long sum is required to get an accurate estimate of the He^+ TOF range at the two lowest energy steps. We can use triples data for $E/Q > 27.4$ keV/e. The triples He^+ peak is easy to identify and contains very little background.

There are some periods in interplanetary space when heavy ion species in the solar wind interfere with the doubles helium data. Solar wind oxygen (O^{+6} , O^{+7}) sometimes interferes with the He^{++} data, while Fe^{+10-14} can interfere with the He^+ data. The interference of heavy solar wind ions typically occurs at the lowest DPPS steps ($E/Q = 3-8$ keV/e). Figure 4.9 shows an example of a solar wind period where heavy solar wind ions interfere with the helium data. Usually the heavy solar wind ions only occur in the telescope that is facing the direction of the solar wind. When heavy solar wind ions interfere with the helium boxes, it is impossible to get an accurate differential intensity calculation for He^+ and He^{++} in interplanetary space.

This concludes the species box definitions which are the easiest to identify. The remaining species require using triples boxes only, and therefore are only valid over a limited range of DPPS steps. Some species present significant identification challenges.

O^{+++} PHA Species Boxes

O^{+++} is a very rare species in Saturn's magnetosphere, so it requires a long sum to identify. But for a long enough accumulation time, O^{+++} shows up as a clear peak in a 2-D histogram of $\text{Essd}(\text{ch})$ versus $\text{TOF}(\text{ch})$ at and above DPPS step 18 ($E/Q > 36$ keV/e). Thus, for the triples data, O^{+++} boxes were not difficult to define, but it is not possible to distinguish O^{+++} from just doubles data.

The box definitions for O^{+++} are shown in Table E.10.

O_2^+ PHA Species Boxes

The boxes for O_2^+ are shown in Table E.11.

Identifying an O_2^+ box was possible for only DPPS steps 24-29 ($E/Q = 83-167$ keV/e). Doubles data for O_2^+ is unusable because the doubles counts from the wide W^+ distribution interfere with the O_2^+ peak. Below step 24 ($E/Q = 83$ keV/e) the O_2^+ triples signal is too weak to create a box, so it is not possible to use O_2^+ data below 83 keV/e. Like H_2^+ , the O_2^+ ions dissociate in the carbon foil resulting in two peaks in the $\text{Essd}(\text{ch})$ versus $\text{TOF}(\text{ch})$. One peak occurs for $\text{Mass} \sim 16$, while the other occurs for $\text{Mass} \sim 32$. The majority of the counts are in the $\text{Mass} \sim 16$ peak. For the two highest energy steps ($E/Q=192-220$ keV/e), the trail from the W^+ interferes with the $\text{Mass} = 16$ O_2^+ peak, making it impossible to estimate the box counts at these energies. A discussion of these ion trails can be found in Section 4.7 that covers background issues for CHEMS PHA data.

H_3^+ PHA Species Boxes

The boxes for H_3^+ are shown in Table E.7.

Because the H_3^+ box appears between two far more abundant species, H_2^+ and He^+ , in most cases it is impossible to use doubles counts for this species. Triples data can be used for steps 18-29 ($E/Q = 36-167$ keV/e). On steps 30 and 31, trails from the H^+ and H_2^+ data interfere with H_3^+ box. A discussion of these ion trails can be found in Section 4.7 on the background issues for CHEMS PHA data.

C⁺ and N⁺ PHA Species Boxes

The boxes for C⁺ and N⁺ are shown in Tables E.8 and E.9, respectively.

Both C⁺ and N⁺ are minor species and far less abundant than W⁺ in Saturn's magnetosphere. Separating these species from the W⁺ is very difficult and only possible for a few DPPS steps. Not only do the C⁺ and N⁺ peaks overlap with W⁺, they also overlap with each other. To accurately estimate differential intensity for C⁺ and N⁺ separately, only the triples data can be used. Including the doubles data results in wider and more overlapping C⁺ and N⁺ distributions, making it impossible to separate the species. We can create pure N⁺ boxes for steps 25-31 ($E/Q = 96-220$ keV/e) and pure C⁺ boxes for steps 24-31 ($E/Q = 83-220$ keV/e). In some cases separating C⁺ from N⁺ on step 24 ($E/Q = 83$ keV/e) can be difficult, so caution should be used when calculating the C⁺ differential intensity at this step. For steps 25-31 ($E/Q = 96-220$ keV/e), it is usually possible to get an accurate estimate of the C⁺ differential intensity.

Calculating the N⁺ differential intensity is more difficult. We include boxes for steps 25 and 26, but there are some cases where background problems make it impossible to calculate the differential intensity. Step 27 ($E/Q = 127$ keV/e) is the best step and all three telescopes produce a good N⁺ peak. For $E/Q > 145$ keV/e, however, only the telescope 3 data contains an N⁺ peak that consistently distinguishes itself from the combined C⁺ and N⁺ peak. The telescope 1 data on step 29 ($E/Q = 167$ keV/e) produces a very poor N⁺ signal, while the telescope 2 data on steps 30-31 contains an N⁺ peak that is not well separated from W⁺.

The C⁺, N⁺, and W⁺ distributions overlap. There is always one TOF bin between the upper TOF limit of the C⁺ box and the lower TOF limit of the N⁺ box. Similarly, there is always one TOF bin between the upper TOF limit of the N⁺ box and the lower TOF limit of the W⁺ box. As a result, our box limits for C⁺ and N⁺ are narrow and do not include all the counts. More careful analysis is required to obtain a more accurate estimate of the C⁺ and N⁺ counts. One way to compensate for these narrow boxes is to assume the TOF bin between the C⁺ and N⁺ boxes contains half C⁺ and half N⁺. We can make a similar assumption about the TOF bin between the N⁺ and W⁺ box (i.e. assume it contains half N⁺ and half W⁺). Curve fitting the C⁺ and N⁺ peaks is another way to better estimate the C⁺ and N⁺ counts.

4.7 CHEMS PHA Species Box Background Issues

There are a few background problems with CHEMS PHA data, mostly during quiet periods and with minor ion species.

CHEMS Telescope	Bogus TOF Channels
1	51-57, 175-179
2	47-58
3	48-60, 94-99, 192-198, 239-254, 292-304

Table 4.11: For each telescope, the ranges in TOF(ch) that are peppered with bogus TOF events.

Bogus TOF counts

Bogus TOF counts are PHA events that occur in the same TOF channels for all DPPS steps. It is not clear what causes these events, but they do not represent ions – they are an artifact of instrumental/spacecraft noise. When detecting a real ion population (with an arbitrary energy distribution), the counts for a given species shift to higher TOF channels at lower DPPS steps. Therefore, the easiest way to identify the channels containing bogus TOF events is to collect, for a long time interval, a 2-D histogram of counts accumulated in bins of DPPS step versus TOF(ch), as is done in Figure 4.10, which contains data from a collection of quiet interplanetary periods. The top row of histograms are for doubles data (telescopes 1, 2, and 3, left to right), and each bottom panel provides triples data for the same telescope as the corresponding top panel. Counts from real ion species show up as curved tracks that start at the top left (with low TOF(ch) and high DPPS), and end up on the bottom right (at high TOF(ch) and low DPPS). But also visible are solid vertical lines from counts that appear at the same TOF(ch) regardless of DPPS step. The counts in vertical bars cannot be due to real ions, hence their designation as bogus TOF events. These events must be excluded from PHA species boxes.

The problematic TOF channels for each telescope are listed in Table 4.11. Comparing these channel ranges with the PHA species box definitions in Tables E.1 to E.11 reveals that most of the bad TOF channels fall within values of TOF(ch) ranges corresponding to doubles species boxes, but there are cases where the triples data gets affected. The important point is that the rate of bogus TOF events is small enough so that during active periods, such as a ring current pass, bogus TOF counts are negligible. Recall that many time periods were accumulated to illustrate the bogus TOF channels in Figure 4.10. However, during quiet times such as interplanetary periods or Saturn’s outer magnetosphere, the bogus counts can dominate the counts in some PHA species boxes.

All telescopes have a major bogus TOF region between channels 50 and 60, and telescopes 1 and 3 have other problem ranges. Telescope 1 gets bogus TOF counts between channels 170-200. Even the triples only data in this TOF range contains a significant amount of counts. There are several other bogus TOF problems in telescope 1 (channels ~ 115 , ~ 140 , ~ 155), but they tend to be minor and only affect extremely quiet periods. Telescope 3 contains several regions with intense bogus TOF events (including channels 48-60, 94-99, 192-198, 239-254, and 292-304), and two regions with less intense bogus TOF counts around channels ~ 125 and ~ 155 . While telescope 3 contains more bogus TOF channels, none of the channels are as large as channels 170-200 in telescope 1. Using triples only data for the high-energy steps will eliminate almost all the bogus TOF problems for telescope 3. Telescope 2 is the cleanest telescope. The only bogus TOF channel is the one that occurs between channels 50 and 60. Fortunately, this bogus TOF channel only interferes with our box counts at high E/Q. Therefore, we can use triples only data to eliminate most of the bogus counts from this channel.

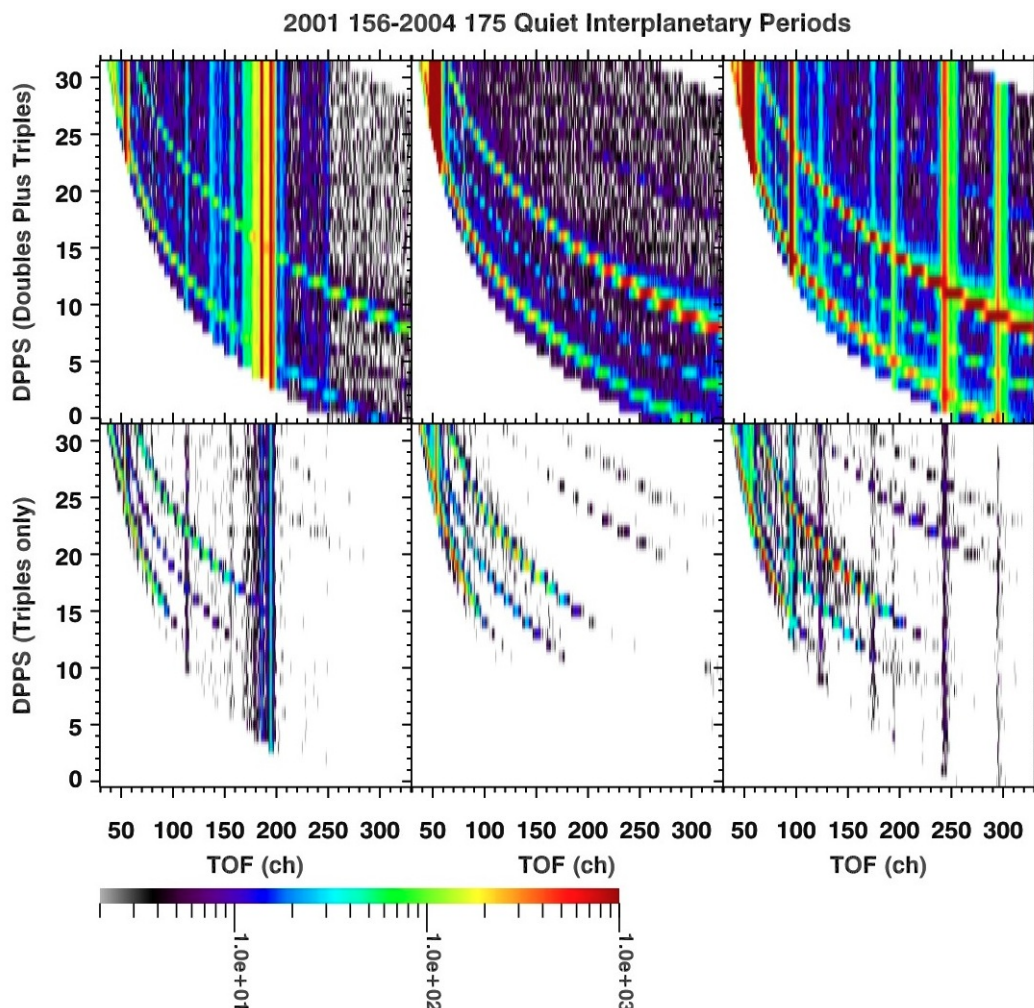


Figure 4.10: Vertical bars indicating counts accumulating within bogus TOF channels for all three telescopes. These DPPS versus TOF(ch) plots are for a collection of quiet interplanetary periods. The leftmost vertical pair of panels is for telescope 1, with the doubles panel on top (i.e., doubles plus triples) and the triples-only panel below. The middle pair of panels is for telescope 2, and the rightmost panels are for telescope 3. The color represents the number of PHA counts at each combination of DPPS and TOF(ch). All bogus counts occur on the same TOF(ch) channel regardless of DPPS step and are easily visible as vertical lines, in contrast with the curved lines (from high DPPS and low TOF(ch) to low DPPS/high TOF(ch)) that are typical of real species detections. Telescope 2 is by far the cleanest telescope. Telescopes 1 and 3 both have several channels with bogus TOF counts. Notice how most of the bogus counts are eliminated when using triples only data. Table 4.11 lists the affected ranges in TOF(ch) for each telescope.

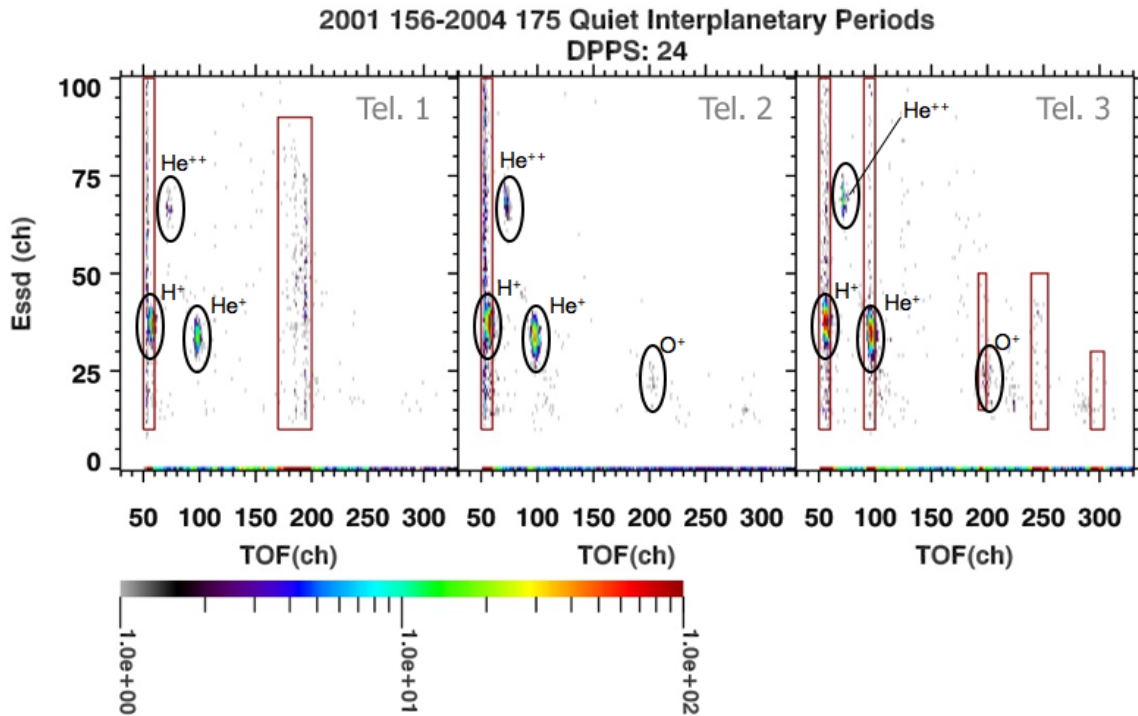


Figure 4.11: Triples data showing how restrictions in Essd(ch) limit the effect of bogus TOF counts. This is a 2-D histogram of counts in Essd(ch) versus TOF(ch) bins at DPPS step 24 ($E/Q=83.4$ keV/e) for a quiet interplanetary period. The bogus TOF counts are located within the red rectangles, while the real species peaks are located within the black circles. Although the triples data contains bogus TOF counts, the ability to restrict a PHA species box to a specific range in Essd(ch) means that during high rate periods, it is possible to ignore the few extra bogus TOF counts that make it into the triples species boxes. Bogus TOF counts remain a problem in rare species and during times of low count rates.

Figure 4.11 illustrates how the use of triples data reduces the effects of bogus PHA events. Each panel in the figure shows PHA events on a 2-D histogram of $\text{Essd}(\text{ch})$ versus $\text{TOF}(\text{ch})$ for quiet interplanetary periods from 2001 to SOI, the same time periods used in the previous plot, Figure 4.10. All the events shown are for DPPS step 24, ensuring that there are plenty of triples counts, i.e., events with enough energy to trigger a signal in the SSD. The triples bogus TOF counts typically extend over a wide range of $\text{Essd}(\text{ch})$, and notice how one vertical band of bogus counts overlaps with the H^+ events. Also notice that in defining the H^+ triples box to have a limited range in $\text{Essd}(\text{ch})$ from 30 to 45, many (but not all) of the bogus TOF events are excluded from interfering with the H^+ counts.

At different DPPS steps, the vertical bands of bogus TOF counts show up at the same $\text{TOF}(\text{ch})$ bins, but the species peaks will change (the peaks shift to lower $\text{TOF}(\text{ch})$ at higher DPPS steps). Thus the bogus TOF counts are only a problem for triples data at the DPPS steps when the triples peak lands inside a vertical bogus TOF band.

The PHA species boxes used for H_2^+ (not shown in Figure 4.11) can now be explained more fully. Recall that H_2 breaks up and creates two peaks, one at $M=1$ (if only one of the dissociated products is captured) and one at $M=2$ (if both products are captured). At the highest three DPPS steps, the $M=1$ peak overlaps a bogus TOF region. But the $M=2$ peak remains outside any bogus TOF regions at these steps. Therefore, the bogus TOF events are avoided in this case by only relying on the counts in the clean $M=2$ peak and adjusting the efficiency to account for the events in the $M=1$ peak.

When counting PHA doubles events, it is impossible to filter out the bogus TOF events by energy (since there is no energy signal). If the species count rate is high enough, as is the case with H^+ , H_2^+ , and W^+ during active ring current passes, the doubles data are not significantly affected and can still be used. But during periods with low count rates, or for any rare species (such as O^{++} that always has a low count rate even in the magnetosphere), the doubles data contains a substantial number of bogus TOF events. Note that although bogus TOF events also occur at a low rate in the triple events, they occur at a much higher rate in the doubles events. Therefore we cannot use the occurrence rate with a high $\text{Essd}(\text{ch})$ value to estimate the rate in the doubles data.

Besides ignoring doubles boxes with bogus TOF events, there is another way to exclude bogus events that works during quiet periods. The width of the species peaks during periods of low count rate (i.e. outer magnetosphere, interplanetary space) is smaller, and so it is possible to define boxes with more narrow $\text{TOF}(\text{ch})$ bounds that will exclude more bogus TOF events and still contain nearly all of the real species counts. This technique only works for five species, namely H^+ , He^{++} , H_2^+ , He^+ , and O^{++} . The DPPS steps for which narrow PHA boxes can remove background for these species are listed in Table 4.12. The revised (more narrow) PHA species box limits for these species are listed in Tables E.13 to E.17 in Appendix E. The restriction in $\text{TOF}(\text{ch})$ bounds only works for some of the contaminated DPPS steps. For those DPPS steps where even narrow $\text{TOF}(\text{ch})$ bounds cannot remove the bogus count, the bounds in Tables E.13 to E.17. are given as 0 – 0. It is important to emphasize that the use of the narrow PHA boxes is only applicable to low rate periods. During active times, these narrow boxes will exclude real PHA species counts.

To reiterate, if you use doubles data in a period of low counts, you must be sure to exclude all regions with bogus TOF problems. The DPPS steps for each species where bogus TOF doubles counts are a problem are listed in Table 4.12. Note that the problematic steps also depend on telescope. Telescope 2 is absent from the table because its single region of bad $\text{TOF}(\text{ch})$ channels does not affect any doubles PHA species boxes. The DPPS steps which cannot be corrected via a

narrow TOF(ch) region are listed in the “no box” column, and the DPPS steps for which a more narrow TOF(ch) region is applicable are labeled as “narrow box.” While the “no box” designation applies to all time periods, the use of the narrow boxes are only for low rate periods.

CHEMS Bogus TOF Example

An example will illustrate how to exclude bogus TOF events. Consider the process of computing the PHA species counts and the PHA range counts needed to determine the H^+ flux for DPPS step 3. Essentially, this involves finding D_{species} and D_i as well as T_{species} and T_j from equation 4.19, where the species is H^+ and the Range IDs i for doubles and j for triples are 0 and 1 respectively (see Table 4.8 for the Range IDs associated with each PHA species). The basic rate R_i for Range ID 0 and R_j for range ID 1 are also needed, but computing basic rates is already described in Section 4.4.1. A quick check in Table 4.12 indicates that at this step, telescope 3 has a narrow species box definition and according to Table E.13, the TOF(ch) ranges are 208 – 239. Assuming the period of interest is a low rate period, this range should be used for identifying H^+ at DPPS step 3. For telescopes 1 and 2, there are no bogus TOF channels, so the normal (non-narrow) ranges should be used to define the species boxes for these telescopes. From Table E.1, TOF(ch) values between 205 – 285 define the H^+ species box at DPPS step 3 for both telescope 1 and 2. To find the species boxes for the triples counters, a similar procedure is followed except there is no need to check for narrow TOF(ch) bounds.

Computing D_{species} then involves counting all PHA events within the time period of interest that fall inside the given species boxes for each telescope. Computing D_i involves counting all PHA events falling within the larger Range ID (0 in this case). *Note that if an event is excluded because it falls inside a bogus TOF channel, it should still get counted as belonging to the appropriate Range ID.* These bogus counts are included by the DPU as part of the basic rate counter, so they must be included in the PHA Range ID counts as well.

With values for D_{species} and D_i (and similar triples equivalents for T_{species} and T_j), along with the appropriate basic rates for the doubles and triples Range IDs, equation 4.19 can be computed for each telescope. Recall that the efficiencies for H^+ detection in each telescope are different and are recorded in Table F.1. Fluxes from each telescope can be combined with simple averaging if desired.

PHA Trails on Steps 30 and 31

Another background problem occurs on steps 30 and 31. This problem can be identified by creating a 2-D histogram of counts in $\text{Essd}(\text{ch})$ versus TOF(ch) bins for steps 30 and 31 (see Figure 4.12). For steps 30 and 31, each species peak contains a trail that extends to lower $\text{Essd}(\text{ch})$ and higher TOF(ch). The intensity of this trail depends on the intensity of the species peak. Thus, these trails tend to be largest for H^+ and W^+ . The H^+ trail interferes with the mass equals 1 peak of the H_2^+ box, while the W^+ trail interferes with the mass equals 16 peak of the O_2^+ peak. The workaround for H_2^+ was already discussed above (only use the M=2 peak). But for O_2^+ , there is no workaround, so it is not possible to get an accurate O_2^+ flux calculation for steps 30 and 31.

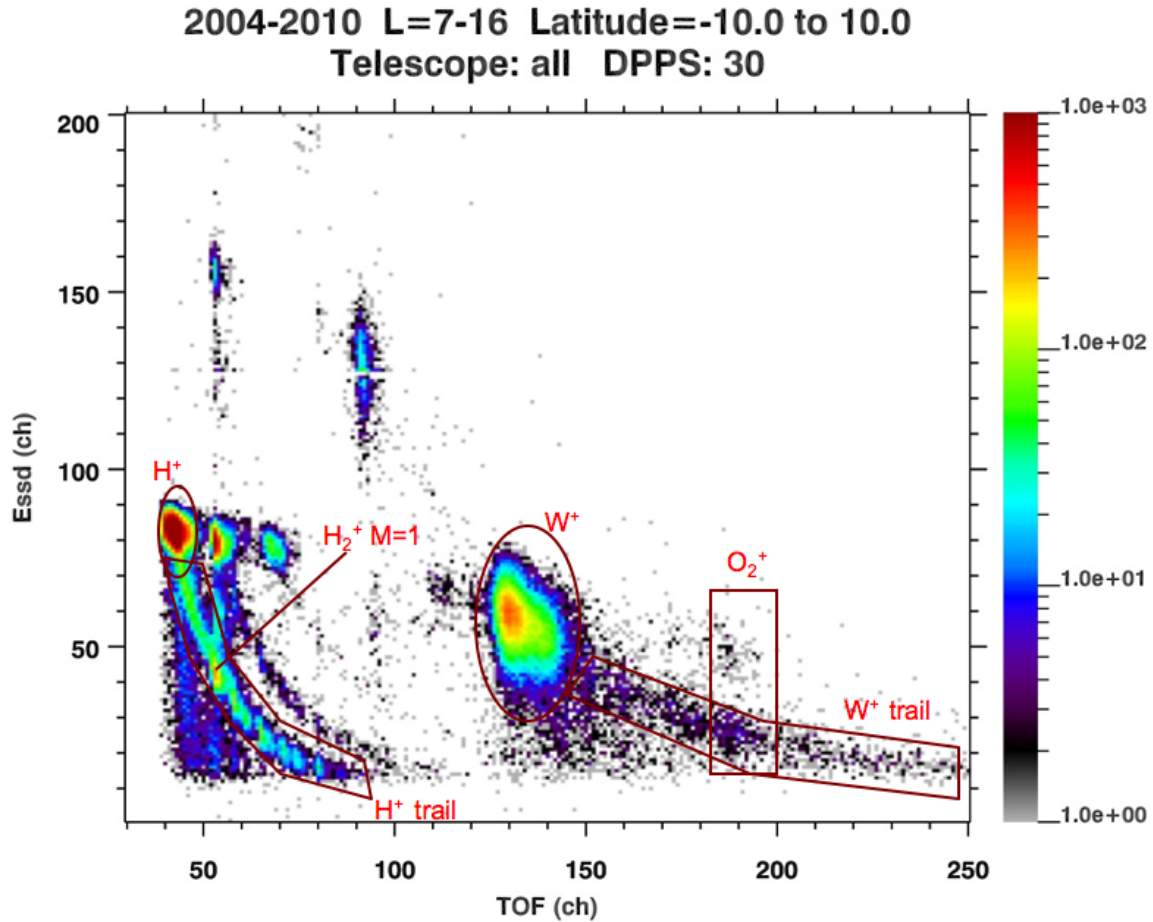


Figure 4.12: Erroneous species trails in CHEMS PHA data on DPPS step 30 ($E/Q = 192$ keV/e). This 2-D histogram of counts in bins of Essd(ch) versus TOF(ch) illustrates a problem that occurs on steps 30 and 31. Data are from a collection of ring current periods ($L = 7 - 16$ at Saturn). Notice how the peaks of the major ion species have trails that extend down and to the right. The trails for W^+ and H^+ are labeled. In the trails, counts from one species contaminate other regions of the histogram, ruining any PHA species boxes in the contaminated regions, because there is no way to distinguish events in the trails from real events at a particular location. Notice how the H_2^+ peak is completely swamped by the H^+ trail, and the O_2^+ peak is likewise overwhelmed by the W^+ trail. The cause of these trails is not well understood.

Species	Telescope 1		Telescope 3	
	“no box”	“narrow box”	“no box”	“narrow box”
H ⁺	5,6,7	4	0,2,5,14	1,3,4,13
H ₂ ⁺	9,10,11	12	4,5,6,7,9,10	8, 11
He ⁺	15	14	8,9,11,12,14,15	
He ⁺⁺	9,10,11		4,6,7,8,9	5,8,11
O ⁺⁺			14	13

Table 4.12: The steps where bogus TOF counts interfere with the box counts for each ion species and telescope. Since the TOF(ch) ranges in telescope 2 do not overlap any doubles channels, only telescopes 1 and 3 are shown. The column labeled “no box” means that the bogus TOF counts occur in the middle of the species peak and cannot be avoided, even with a narrow box. The column labeled “narrow box” means that the standard boxes contain bogus counts, but these bogus counts can be avoided using narrow TOF(ch) bounds. Tables E.13 to E.17 in Appendix E (on page 225) list narrow PHA species box definitions. Recall that the narrow boxes are only relevant for low rate periods.

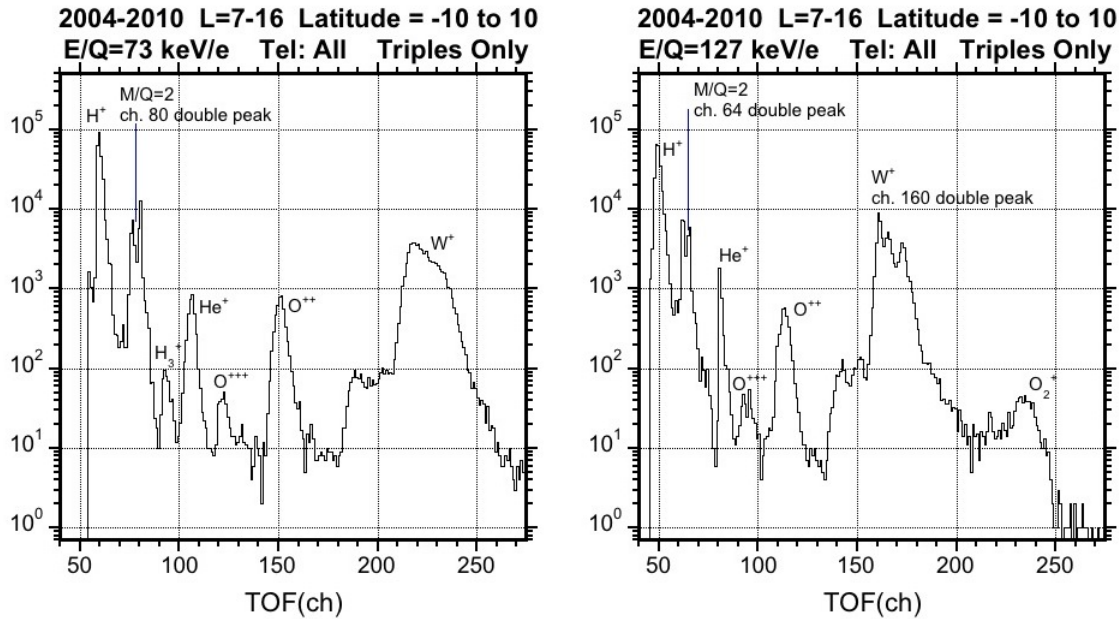


Figure 4.13: The effect of wide TOF channels on the 1-D TOF(ch) histograms. The plot on the left shows how $M/Q = 2$ counts are affected by the width of channel 80. Because it is too wide, channel 80 accumulates extra counts that show up as a second peak. The plot on the right shows data from step 27, where both channel 64 and 160 cause double peaks. Also in the plot on the right, notice how the left edge of the He⁺ near channel 80 is very narrow, presumably because the wide channel 80 at the He⁺ peak is absorbing counts that should appear on the left shoulder of the peak. These odd channels are not being affected by background, because their intensities are proportional to real species counts. However, the double peaks create problems when trying to perform fits on the data. The W⁺ for step 27 cannot be separated into O⁺, OH⁺, and H₂O⁺ because of the double peak problem with channel 160.

Wide TOF Channels

There are certain TOF channels that contain a large amount of counts compared to the surrounding channels. This results in either a very narrow TOF peak or what appears to be a double peak. So far, channels 64, 80, and 160 exhibit this behavior. The counts are not likely to be background, since they do not result in a spike in the differential intensity spectra. Unlike bogus TOF counts, the extra counts are only observed when a real species peak occurs near these channels. Although the counts are real, they can create problems when trying to perform fits on the data. Figure 4.13 shows the effect of these wide TOF channels. On step 27, the O^+ peak is near channel 160 and as a result, has a double peak. Because of the double peak, it is impossible to separate O^+ from the rest of the water group.

Range 7 counts

The expected value for the Range ID is between 0 and 6, inclusive, but some PHA events show up with a Range ID of 7. The reason for this incorrect range designation has not been determined. All events with a Range ID of 7 also have a telescope number of 0.

At Saturn, the majority of these events occur within $4 R_S$, but there are a few out to $\sim 15 R_S$. Currently, the best approach is just to ignore these events when calculating the PHA flux. Because there are so few counts inside of $6 R_S$, we rarely use the data within this radial distance. Outside of $6 R_S$, the Range 7 events make up a very small percentage of the PHA events and can be ignored.

Section 5

INCA

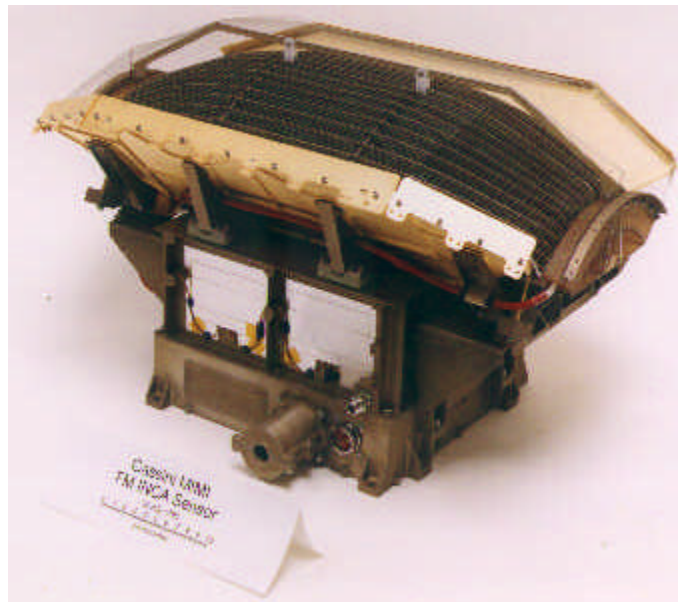


Figure 5.1: A picture of the INCA sensor. The long dimension of the sensor is oriented along the Z axis of the Cassini spacecraft. The fan-like collimator plates are charged to high voltages to sweep out incoming ions and electrons.

5.1 Overview

The Ion and Neutral Camera (INCA) obtains remote images of the global distribution of energetic ions for energies from 7 keV/nucleon to 8 MeV/nucleon, discriminated according to energy and mass species (oxygen and hydrogen). To obtain these images, INCA measures the arrival directions, energy, and mass species of Energetic Neutral Atoms (ENA's) using the relatively new technique of ENA imaging [Roelof, 1987] and [Roelof and Skinner, 2000]. For a brief overview of ENA imaging, see <http://sd-www.jhuapl.edu/CASSINI/enabase.html>. INCA also can be commanded to obtain very high sensitivity ion measurements, providing the angular, energy, and species distributions of in-situ O and H ions.

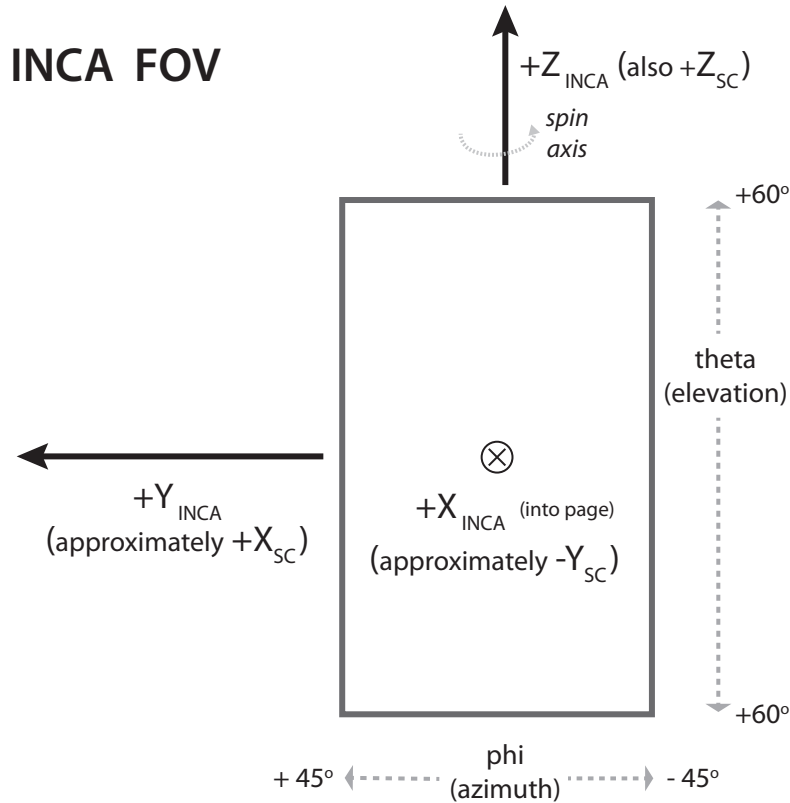


Figure 5.2: The orientation and shape of the INCA field of view. The 120° dimension is along the INCA Z axis, which is coincident with the spacecraft Z axis. The INCA boresight is in the XY spacecraft plane along a line rotated 9.5° away from the spacecraft $-Y$ axis toward the spacecraft $+X$ axis.

In neutral mode, which is used to obtain ENA images, alternate collimator plates are charged to a high positive and negative voltage, and these plates sweep up ions and electrons entering the sensor. Neutral atoms pass by the plates through a slit. Alternately, in ion mode, the plates are not charged and the ions and electrons pass into the detector.

The INCA detector has a field of view (FOV) of $90^\circ \times 120^\circ$ as illustrated in Figure 5.2. The 120° dimension (elevation) is a polar angle measured relative to the instrument Z axis, with zero lying in the instrument (and spacecraft) X-Y plane, while the 90° dimension (azimuth) measures rotation away from the boresite about Z. By analogy to a globe, angles in the 120° dimension are directly equivalent to latitude, while those in the 90° dimension are equivalent to longitude. The INCA boresight lies along *the instrument* (not spacecraft) $+X$ axis, which points into the page in Figure 5.2. The long dimension of the collimator fan plates is parallel to the INCA Z axis (using the globe analogy, the collimator plates lie in meridional planes). In terms of the spacecraft axes, the INCA boresight vector (the INCA $+X$ axis) is approximately parallel to the spacecraft $-Y$ axis, but offset by 9.5° in the direction of the spacecraft $+X$ axis. The INCA $+Z$ axis is coincident with the spacecraft $+Z$ axis, often referred to as the spin axis, because spacecraft spins usually revolve around (approximately) this axis. The INCA $+Y$ axis is approximately along the spacecraft $+X$ axis (again, shifted by 9.5° toward spacecraft $+Y$). If the boresight vector were rotated 279.5° clockwise (as viewed from above the XY plane) around the spacecraft Z axis, it would be parallel to the spacecraft $+X$ axis.

Note that Figure 5.2 labels the elevation angle as theta and the azimuth angle as phi. These

Image Type	Comments	Size	Num. Sctrs.	Num. Chnls.	Description
High Spatial	Low TOF (ch. 0)	64x64	4	2	only 2 energies and low time res. but good spatial res.
	High TOF (ch. 7)	32x32			
High Time	also chnl. 0 & 7	32x32	1	2	only 2 energy channels, but decent spatial resolution at frequent cadence
High Mass-TOF	neutral mode	16x16	4	8	8 energy channels, but low spatial and time resolution
	ion mode	8x8			

Table 5.1: The various INCA image types and their sizes. High spatial resolution images have the highest number of pixels (64x64 for channel 0 and 32x32 for channel 7), but only 2 energy channels and they are taken 4 times per spin (every 4 sectors). High time resolution images are taken 16 times per spin (every sector), but only for two energy channels (0 and 7) and at a resolution of 32x32. High Mass-TOF images are taken for channels 0 through 7, but at slower cadence (4 times per spin, or every 4 sectors) and at a lower spatial resolution of either 16x16 or 8x8.

designations are relevant when considering phi and theta offsets which show up in INCA image data. In some situations (such as raster or mosaic scans done by other Cassini imagers), the INCA flight software compensates for spacecraft motion by binning data into a large grid on the sky (larger than the INCA FOV - usually 180° by 180°). INCA pixels are accumulated into this larger binning area, and when the integration period is over, a selection of pixels (equal in shape and size to the current image resolution) is extracted from the binning region as the image to be captured for that integration period. The offset of this sub-image within the full binning region is present in the data as the phi and theta offsets. The implications and use of these offsets when interpreting INCA images is more fully described in Section 5.7 on page 138.

Recall that there are three kinds of INCA data in the PDS: accumulator rates, images and PHA data. INCA accumulator rates are periodic readouts of various hardware accumulators and are used mostly for diagnostic purposes. Accumulator data is provided as counts, and is generally converted to counts per second to allow comparison of times with different spin periods (recall that the spin period is used to define timing sectors and subsectors, see Section 1.7). Other than this conversion to counts per second, no further calibration procedures are relevant for INCA accumulator data.

5.2 INCA Images

INCA image data are available in three different flavors, each flavor being simultaneously generated. High spatial resolution images have a larger number of pixels than other INCA images (up to 64 by 64), but are available for fewer numbers of energies (usually just 2 energy channels) and are taken at lower time resolution (one image every 4 sectors). High time resolution images are acquired each sector, but have lower spatial resolution (usually 16 by 16 pixels) but have fewer energy channels. High time-of-flight and mass resolution images are taken for 9 energy ranges, but only every 4 sectors and with lower spatial resolution. Table 5.1 describes the different image types. There is only one kind of file for INCA images, and this ASCII file contains all the image types. Each image is a block of ASCII data records, and the prefix columns for each record include the image type, which then can be used to properly interpret the rest of the data record.

As was pointed out in Section 1.6, uncalibrated MIMI PDS data in years 2004 through 2006 are still at revision 0, and therefore lack three prefix columns. The discussion of data products below refer exclusively to revision 3. Soon all data will be at revision 3.

5.3 INCA Accumulator Rates

Accumulator rate data is a collection of counters sampled every subsector. The file naming convention, directory structure, and file content layout follow the conventions outlined in Sections 1.4 and 1.6. Therefore each data file has a name similar to

```
IACCO_2007001_003.CSV
```

and contains a 7 line header, the first of which is a list of the data column names. Following the header are data lines, and each data line begins with a standard 13 element prefix.

On each data line, INCA accumulator values start after the standard prefix columns. Table 5.2 lists the column labels used and provides a description of each accumulator rate value. The value for each counter came from a `long int` value (32 bit integer).

5.4 INCA PHA Events

INCA PHA data contains event information for a subset of the particle events detected by INCA. For each selected event, the TOF, pulse-height of the signal output from the front and rear MCPs, MCP identification (coincidence, start/stop), calculated azimuth and elevation, and mass range are recorded. Here, time of flight (TOF) represents the time for a particle to travel from the front MCP to the rear MCP, and is used to determine energy. No calibration is available for the INCA PHA Events.

The file naming convention, directory structure, and file content layout follow the conventions outlined in Sections 1.4 and 1.6. Therefore each data file has a name similar to

```
IPHA0_2006001_000.CSV
```

and contains a 7 line header, the first of which is a list of the data column names. Following the header are data lines, and each data line begins with a standard 13 element prefix.

Table 5.3 lists the names and descriptions of INCA PHA columns, which start after the standard prefix columns.

Column Name	Description
START_FAST	the number of counts generated as particles penetrate the Start foil, produce secondary electrons that impact the Start MCP and result in a timing pulse from the Start anode; this string of actions are referred to as a Start “event;” so START_FAST represents those events triggering the Start MCP Fast discriminator (used to start the TOF clock)
START_PULSE	number of events triggering the Start MCP Pulse discriminator (used in calculating Start Position)
START_COINCIDENCE	number of start events with START_FAST and COINCIDENCE signals within a ~ 200 ns window
STOP_FAST	number of events triggering the Stop MCP Fast discriminator (used to stop the TOF clock)
STOP_PULSE	number of events triggering the Stop MCP Pulse discriminator (used in calculating Stop Position)
FULL	events triggering START_FAST, STOP_FAST, and COINCIDENCE discriminators within the maximum timing windows
COINCIDENCE	number of events triggering the Coincidence MCP discriminator (designed as a clean-up signal against accidental Start-Stop coincidences; used in practice as a sunlight monitor for automatic Start and Stop MCP high voltage sun-safing)
TIME	number of events with valid START_FAST and STOP_FAST pairs (Start and Stop timing signals that fall within the maximum TOF timing window of ~ 150 ns)
STOP_COINCIDENCE	number of events with COINCIDENCE and STOP_FAST signals within a 40 ns window
EVENTS_RECEIVED	number of events judged valid by the front-end fast logic (typically in flight, those events with valid TOFs) and passed on to the DPU for binning into images; this number may differ from the number of valid TOFs if the valid TOF event rate exceeds the rate at which the DPU can accept events; only present in data on 2000 day 154 and after
EVENTS_PROCESSED	number of the EVENTS_RECEIVED that are in fact processed by the DPU for binning into images. This number may differ from EVENTS_RECEIVED because the DPU filters the incoming events, rejecting classes of events it recognizes as invalid (for criteria not checked by the front-end valid event logic); only present in data on 2000 day 154 and after

Table 5.2: Names and descriptions for the columns in INCA accumulator rate data files beyond the standard prefix columns. The standard prefix columns (see Table 1.6) and file header (see Table 1.5 and Figure 1.3) are not repeated here. Note that all INCA accumulator rate values are `long int` values (32 bit).

Column Name	Description
INDEX_IN_FOUR_SUBSECTORS	An id number that represents the zero based index of this record within a certain sclock value. This along with sclock is unique.
COINCIDENCE	This field identifies whether the PHA event includes a coincidence signal (1), or not (0).
START_STOP	This field identifies whether the PHA event included both start and stop (1) or only one of the two (0).
PULSE_HEIGHT_FRONT	This field contains the encoded pulse height data for the front (Start) microplate. It was added on day 154 of 2000 and is only present at and beyond that date.
PULSE_HEIGHT_REAR	This field contains the encoded pulse height data for the rear (Stop) microplate. It is present on 2000 day 154 and beyond.
TIME_OF_FLIGHT	This field contains the PHA event 10 most significant bits of the on-board-corrected particle time of flight (in Data Number – needs conversion to seconds).
AZIMUTH	This field contains the encoded value of the calculated azimuth for the PHA event. Azimuth ranges from 0 to 63 (-90° to +90°)
ELEVATION	This field contains the encoded value of the calculated elevation for the PHA event. Elevation ranges from 0 to 47 (-60° to +60°)
MASS_RANGE	This field contains the encoded value of the calculated mass.

Table 5.3: Names and descriptions for the columns in INCA PHA data. These are the columns beyond the standard prefix columns. The standard prefix columns (see Table 1.6) and file header (see Table 1.5 and Figure 1.3) are not repeated here.

5.5 End-to-End Examples for INCA ACC and PHA Data

The format and usage of the accumulator rate data and the PHA data are very similar, and a single procedure can be used to illustrate the use of these data.

Step 1: Obtain data

Download the desired files from the PDS. You can do this manually, traversing the directory structure described in Section 1.4, or using a data downloading program provided by the MIMI team and described in Section 6.1.

Step 2: Obtain MIMI IDL Code and Auxiliary File Set

Users should be able to create data reading software for INCA Accumulator Rates and PHA event data based on the file formats discussed in the preceding sections. Alternatively, a set of IDL read-routines and auxiliary files has been provided by the MIMI team, and these are available in a single gzipped tar file from the following URL:

```
http://sd-www.jhuapl.edu/CASSINI/data_auxiliary.html
```

The routines are standalone IDL code – they do not require other libraries to run (i.e., no SPICE libraries or kernels are needed) and all necessary calibration files are included in the download.

After obtaining the gzipped code and auxiliary file set, the user should unzip and untar it.

```
gunzip MIMI_code_calibration.tar.gz
tar -xvf MIMI_code_calibration.tar
```

This creates a directory `MIMI_code_calibration` in the current directory. All code and calibration files live in a directory structure below this directory. The IDL routines assume by default that `MIMI_code_calibration` lives in your home directory, but you can put it somewhere else - you will just need to edit one variable in the `setup.pro` file as described below.

Step 3: Edit IDL setup program

If the `MIMI_code_calibration` directory is placed anywhere except your home directory, then you will need to edit the `rootdir` variable in the `setup.pro` routine. All IDL routines are found in the IDL directory, which is below the `MIMI_code_calibration` directory.

Within `setup.pro`, the default value for the `rootdir` variable is

```
rootdir = GETENV('HOME')+p+'MIMI_code_calibration'
      (where p is the path separator, usually '/')
```

But if you install the tarball into `/project/cassini`, then `rootdir` should be

```
rootdir = '/project/cassini/MIMI_code_calibration'
```

In that same section of `setup.pro`, there are some commands to setup up a true color display, and you can edit those as appropriate for your monitor.

Occasionally, other edits may be necessary. If a new MIMI calibration file is issued, you can download just the new file from http://sd-www.jhuapl.edu/CASSINI/data_auxiliary.html and put it in this directory:

```
MIMI_code_calibration/MIMI_cal
```

Then in `setup.pro`, update this line to indicate the name of the new calibration file:

```
SETENV, 'MIMICAL_NAME='+rootdir+p+'MIMI_cal'+p+'MIMI_CALIBRATION_0009.csv'
      (update to change to version 10 or whatever version you downloaded)
```


Similarly, the leap second kernel may change, and the user can obtain it from the same URL and place it in the `MIMI_code_calibration/spice_kernel` directory and edit the leap second file variable in the `setup.pro` routine. (This SPICE kernel is used by our own IDL code to do time conversions and our IDL code does not require the SPICE library, as was previously mentioned.)

Note also that when a new calibration or leap second kernel is issued, a new tarball of all routines and files will be made available so that you could also just download the new code and re-install that (after uninstalling the old version).

Step 4: Read Data

A single routine, `PDS_READ_MIMI` (which is found in the file `pds_read_mimi.pro` in the IDL sub-directory), is capable of reading and interpreting both accumulator rate data and PHA data. The reader code makes columns from the data file available in IDL as a two dimensional array. A description of the routine is provided in Table 5.4.

The routine `TEST_READ_MIMI` (within `test_read_mimi.pro` in the IDL directory) provides an example of how to call `PDS_READ_MIMI` and how to use the return values. Table 5.5 shows portions of the `TEST_READ_MIMI` routine and illustrates how to read INCA accumulator rate data and select a specific data column out of the returned values. Note how the code uses the `PDS_READ_MIMI` routine to read from two previously downloaded INCA accumulator rate files for days 182 and 183 of year 2010. The routine loads data for all columns from 12:30 on day 182 to 04:30 on day 183, but then the data printed out is only the UTC time column and the `START_PULSE` column from 19:00 to 19:02 on day 182. Table 5.5 also includes the output obtained by running the example code.

Note that within the sample routine, `TEST_READ_MIMI`, the indices of prefix header columns are obtained as a set of IDL variables via the included file `pds_data_hdr_h.pro`. This file can be included in your own IDL programs with this line:

```
@pds_data_hdr_h
```

Thus in the main data array returned by `PDS_READ_MIMI`, the index of the column containing ephemeris time is defined by the variable `DATA_SCLK_SECS_C`, such that `data[N, DATA_SCLK_SECS_C]` gives the N^{th} ephemeris time value.

The example also illustrates time conversion from UTC to ephemeris time (ET) using an additional time conversion routine provided alongside the read routines. Table 5.6 describes the `UTC2ET` function and Table 5.7 describes its inverse function, `ET2UTC`.

For reading INCA PHA data, the example would be very similar. The data files would of course need to be PHA data files, and the column name to extract would need to be a PHA event column.

FUNCTION	PDS_READ_MIMI		(startyear, startdoy, starthours, startmins, startsecs, \$ stopyear, stopdoy, stophours, stopmins, stopsecs, files,\$ labels, data, datautc, auxdata, auxlabels)
	Parameter	Type	Description
<i>Inputs</i>	startyear	long	4 digit year for start date
	startdoy	long	day of year (1 to 365 or 366) for start date
	starthours	long	hour of day (0 to 24) for start date
	startmins	long	minute of hour (0 to 59) for start date
	startsecs	long	second of minute (0 to 59 or 60 for leap second)
	<i>note: corresponding stop date elements have the same definitions</i>		
	files	array	string array with names of files covering the data of interest
<i>Outputs</i>	data	double	data[number rows, number columns]. The rows are the samples in time. The columns are the parameters. The data array does not include the first PURPOSE column (since is always just the same string 'sci'), but starts with the first column after the PURPOSE column.
	labels	string	labels[number columns]. Labels are the column titles.
	datautc	string	UTC character string giving the start of the accumulation time for data in that row
	auxdata	double	auxdata[6, number columns]. Contains content from the 6 standard file header lines at the top of the file. Each of the 6 lines has a different purpose (mean, max, etc.) and contains one column entry for each data column in the file.
	auxlabels	string	auxlabels[6]. A label indicating the purpose of each row of auxdata.
<i>Returns</i>		integer	status of read, 0=ok, -1=error opening file

Table 5.4: Signature and parameter definitions for PDS_READ_MIMI, a function that reads INCA accumulator rate files into IDL.

```

@pds_data_hdr_h ; include this file to get column definition constants

files = ['<userdirectory>/IACCO_2010182_0002.CSV', $
        '<userdirectory>/IACCO_2010183_0002.CSV']

status1 = PDS_READ_MIMI( 2010,182,12,30,0,$
                        2010,183,4,30,0, files,$
                        labels, data, datautc, auxdata, auxlabels)

; find two time values in ET to use as the start and stop times
; (this can be a subset but not a superset of the time range
; above, since only certain files were loaded)
s = UTC2ET(['2010-182T19:00', '2010-182T19:02'], et)

; find where column index of START_PULSE in the data array
; (the label array can give you the right index into the data array)
icol = WHERE(STRLOWCASE(labels) EQ STRLOWCASE('START_PULSE'))

; find the indices bracketed by the start and stop times
at = WHERE(data[* , DATA_ET_SECS_C] GE et[0] AND $
          data[* , DATA_ET_SECS_C] LE et[1])

; for any data values found within the desired time range, print them
; along with the UTC string for the start time of this counter
IF at[0] NE -1 THEN BEGIN
    FOR n=0,N_ELEMENTS(at)-1 DO PRINT, datautc[at[n]], ' ', $
        data[at[n], icol]
ENDIF

```

Output:

"2010-182T19:00:00.870"	33792.000
"2010-182T19:00:05.553"	32256.000
"2010-182T19:00:10.241"	31744.000
"2010-182T19:00:14.928"	32768.000
"2010-182T19:00:19.616"	32768.000
"2010-182T19:00:24.303"	33792.000
"2010-182T19:00:28.991"	35840.000
"2010-182T19:00:33.678"	35840.000
"2010-182T19:00:38.365"	34816.000
"2010-182T19:00:43.053"	36864.000
"2010-182T19:00:47.740"	37888.000
"2010-182T19:00:52.428"	37888.000
"2010-182T19:00:57.115"	38912.000

Table 5.5: A working example showing how to read INCA ACC or PHA data, which have very similar layouts.

FUNCTION UTC2ET(utc, et)			
	Parameter	Type	Description
<i>Input</i>	utc	string	UTC time string or string array in ISO 8601 format, such as 'yyyy-doyThh:mm:ss.msc', where the field definitions are: yyyy = 4 digit year doy = day of year, must be 3 digits, for example '001' T = you must include the letter T hh = hours, must be 2 digits, for example '09', range 00-23 mm = minutes, must be 2 digits, for example '06', range 00-59 ss = seconds, must be 2 digits, for example '06', range 00-59 msc = milliseconds, must be 3 digits, for example, '060', range 000-999
<i>Output</i>	et	double	single value or array of Ephemeris Time, ET
<i>Return</i>		int	Always returns 0. This is left in to make it easier for the user to switch to using SPICE.UTC2ET if they install the JPL NAIF SPICE software

Table 5.6: Signature and parameter definitions for UTC2ET, a function that converts UTC strings into ET doubles (without using SPICE).

FUNCTION ET2UTC(et, utc)			
	Parameter	Type	Description
<i>Input</i>	et	double	single value or array of Ephemeris Time, ET
<i>Output</i>	utc	string	UTC time string or string array in ISO 8601 format such as 'yyyy-doyThh:mm:ss.msc' where the field definitions are the same as those above in Table 5.6.
<i>Return</i>			Always returns 0. This is left in to make it easier for the user to switch to using SPICE.UTC2ET if they install the JPL NAIF SPICE software.

Table 5.7: Signature and parameter definitions for ET2UTC, a function that converts ET double values into UTC strings (without using SPICE).

Step 5: Read Calibration Files

There are no calibration values relevant for the INCA accumulator rates or PHA data.

Step 6: Calibrate the Data

There are no calibrations to apply to PHA event data. The only applicable modification to the accumulator counters is to convert them to count rates by dividing by the subsector duration. The spin period is provided within the prefix elements of each data line (column name = SPIN_PERIOD_S) and there are 256 subsectors per spin. Therefore

$$\text{rate} = \frac{\text{counter}}{\tau_{\text{spin}} * 256}$$

Subsector duration would be calculated using the MIMI spin period field included in the data array, `data[N, SPIN_PERIOD_C_C]`. The following IDL code shows the formula to calculate the subsector duration.

```
@pds_data_hdr_h ; SPIN_PERIOD_C_C (and other column indices) defined in here

; use column index definitions to find things in the data,
; such as the spin period shown here:
spin_period_in_seconds = DOUBLE(data[n,SPIN_PERIOD_C_C])/256.d0
```

Step 7: Filter Out Bad Data

Any data, which was missing during downlink had the values set to fill, which for the PDS data is the empty string “”. Also, any data that has values greater than the allowed maximum (listed for each column as part of the standard header) has also been set to fill “”. The read routine searches for cells with the empty string and sets those to 0 value when it reads in the data.

Step 8: Deal with Data Gaps

If data is absent for a significant period, it may be during a known data gap. A list of data gaps has been provided online at the URL http://sd-www.jhuapl.edu/CASSINI/data_auxiliary.html and is included as auxiliary data in the code set in subdirectory `gaps_times` beneath the `MIMI_code_calibration` directory.

The gaps are listed in yearly files have names like `MIMI_Gap_SummaryYYYY.txt` where YYYY is the 4 digit year. The files contain comma delimited values for the gap start time, gap stop time (both in UTC) followed by the total gap time in hh:mm:ss. The following is an excerpt from the file:

```
Gap Start in UTC,   Gap Stop in UTC,   Total Gap Time
2011-024T08:50:30, 2011-024T23:59:59, 15:09:00
2011-025T00:00:00, 2011-025T14:22:36, 14:22:00
```

5.6 INCA Image Data Files

All the various types of INCA images for a given day are available in a single ASCII file for that day. The file naming convention, directory structure, and file content layout are the same as all the other timeseries-like data products for MIMI and likewise follow the conventions outlined in Sections 1.4 and 1.6. Therefore each data file has a name similar to

IIMG0_2006001_000.CSV.

Each file contains the standard 7 line header followed by data lines, and each data line has a standard 13 element prefix.

Table 5.8 provides names and definitions of the INCA image data columns. There are 13 image header columns on every row. Note that this is in addition to the 13 standard prefix columns at the start of every row. These image prefix values are needed to properly interpret the image data. After the prefix columns and the image header columns, each line in the file contains one row of pixels from an image. For the largest images, there will be 64 such columns. Thus a single image spans multiple lines in the file. Prefix and header columns are repeated (duplicated) for every row of an image. The overall file structure is illustrated in Figure 5.3, which shows how the counts from one row of an image follow the two sets of prefix columns.

Because INCA images can have different sizes, the number of data columns (i.e., the columns after the prefix and image header columns) is also different from image to image. The maximum image size is 64x64 pixels and the minimum size available from the PDS is 16x16 pixels. Table 5.1 (on page 107) describes the sizes of each image type. The image header contains a field, `NUM_COLS`, that indicates the number of columns. The `NUM_ROWS` field indicates the number of rows for the image, and the `ROW_ID` field indicates the current row index within the image, starting at zero for the first row.

5.7 End-to-End Example for INCA Images

The first three steps for analyzing INCA images are the same as for INCA accumulator rates and PHA data. Section 5.5 on page 111 has the details for these steps:

Step 1: Obtain data

Step 2: Obtain MIMI IDL Code and Auxiliary File Set

Step 3: Edit IDL setup program

Step 4: Read Data

The read routine, `PDS_READ_MIMIIMG`, (which is found in the file `pds_read_mimiimg.pro` in the IDL subdirectory) properly interprets INCA image files. Input and output parameters for this routine are described in Tables 5.9 and 5.10 respectively. The primary values of interest returned by `PDS_READ_MIMIIMG` are:

the 2-D array `data[N,24]` and

the 3-D array `images[N,64,64]`, where `N` is the number of images read.

The `data[N,24]` array captures all the prefix and image header elements for each image, using just the values from the first row (recall that prefix columns are repeated for every image row). There are only 24 prefix columns because the `PURPOSE` column is not included. Thus, for the i^{th} image,

Column Name	Description
TYPE_ID	4 byte word describing the type of image collected Byte 0 - Type: 0 = High Spatial, 1 = High Time, 2 = High m-TOF Byte 1 - Charge: 0 = Neutral, 1 = Ion Byte 2 - Species: 0 = H, 1 = He, 2 = CNO, 3 = Heavy, 4 = Other, 5 = All Byte 3 - TOF: 0 = Low, 1-6 = Medium, 7 = High
ROW_ID	Row number of the image. Row 0 corresponds to a theta (elevation) of -60° and the last row corresponds to a theta of 60°. Each image has 120° in the direction perpendicular to the spin plane (elevation), centered on the spin plane.
NUM_ROWS	Number of rows in the image. Each row of the image is on a separate line of the file.
NUM_COLS	Number of columns in the image. The columns of the image go from left to right in the file. The image has an FOV of 90° in the azimuthal direction. Column 0 corresponds to a phi (azimuth) of -45° and the last column corresponds to a phi of 45°, where angles are in the INCA coordinate system.
COMPRESSION_BITS	Number of compression bits used for the image.
COMPRESSION_METHOD	Compression algorithm used for the image. Options are None, Fast, or Rice.
LOG_COMPRESSION	Identifies whether the field is log compressed (1) or not (0).
THETA_OFFSET	Offset in number of pixels of the transmitted image with respect to the DPU image memory. Image theta (elevation) is relative to the spacecraft -Z axis.
PHI_OFFSET	Offset in number of pixels of the transmitted image with respect to the DPU image memory. Image phi (azimuth) is in the spacecraft X-Y plane, relative to the spacecraft X axis.
HIGH_RESOLUTION	This field identifies the Image Type [High Spatial (0), High Time (1), or high m-TOF (2)].
CHARGED	This field identifies whether the image was taken of neutrals (0) or charged particles and neutrals (1).
SPECIES	(string) This field identifies the type of particle imaged as H - hydrogen, He - Helium, CNO - Carbon, Nitrogen, Oxygen, Heavy - others, All - all particles.
TOF	This field contains the encoded TOF range.
COL_0	The particle count for this row and column 0 of the image. It corresponds to a phi (azimuth) of -45°.
...	
COL_63	The particle count for this row and column 63 of the image. It corresponds to a phi (azimuth) of 45°.

Table 5.8: Names and descriptions for the columns in INCA image data files beyond the standard prefix columns. The standard prefix columns (see Table 1.6) and file header (see Table 1.5 and Figure 1.3) are not repeated here. All values shown here are `long int` values (32 bit).

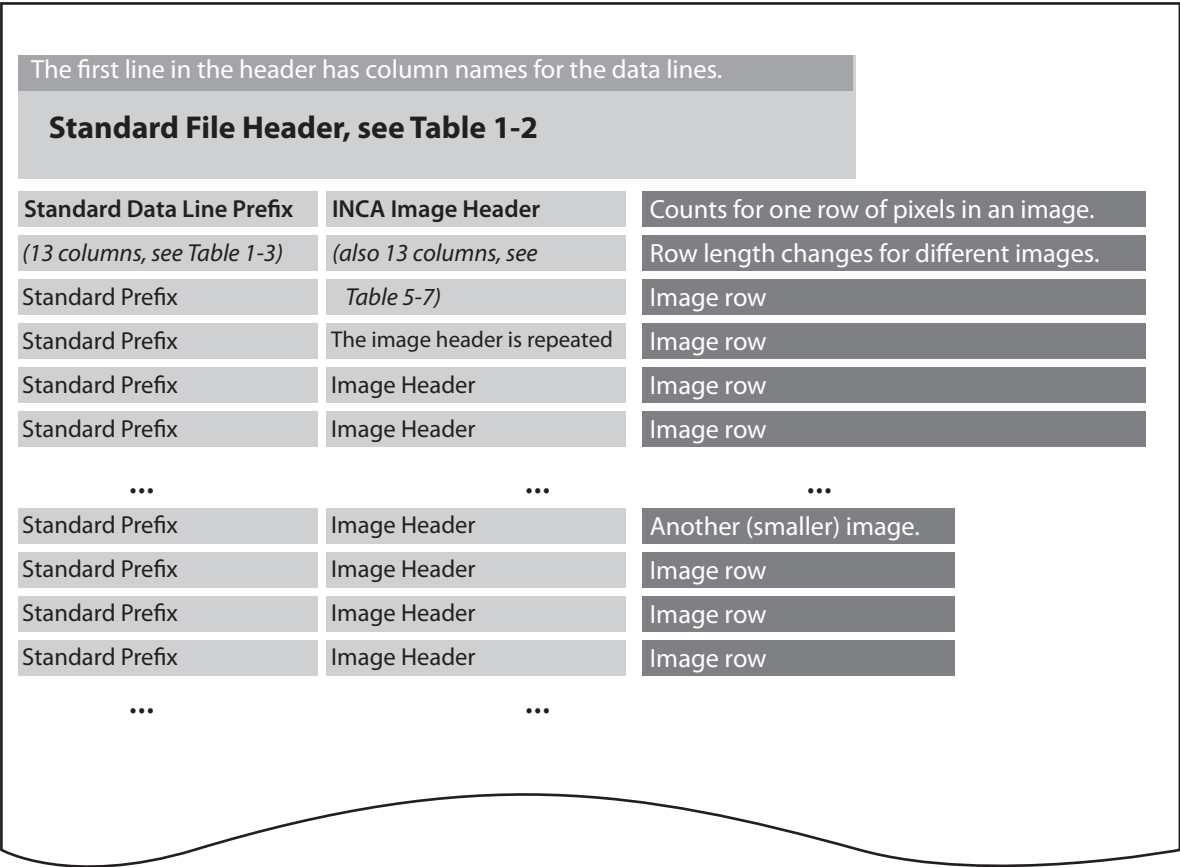


Figure 5.3: The layout of an INCA image file. Each file contains images for an entire day. The standard header is present, and each line begins with a standard set of prefix columns. Each data line has counts from one row of pixels in an image, with all the prefix columns repeated for each row. Images are of different size, so the file is set up to handle rows of the maximum size (64 pixels of counts).

FUNCTION PDS_READ_MIMIIMG		(startyear, startdoy, starthours, startmins, startsecs, \$ stopyear, stopdoy, stophours, stopmins, stopsecs, \$ files, arfiles, imagetype, units, \$ labels, data, images, datautc, stopdatautc, \$ auxdata, auxlabels)
Input		
Parameter	Type	Description
startyear	long	4 digit year for start date
startdoy	long	day of year (1 to 365 or 366) for start date
starthours	long	hour of day (0 to 24) for start date
startmins	long	minute of hour (0 to 59) for start date
startsecs	long	second of minute (0 to 59 or 60 for leap second)
<i>note: corresponding stop date elements have the same definitions</i>		
files	string	array of INCA image data files with paths (full path or relative to current location)
arfiles	string	array of INCA accumulator data files corresponding to each image file. The image calibration process requires the accumulator data.
<i>The INCA image calibration process is described in Step 4 of the End-to-End example.</i>		
imagetype	string	image type requested, where 'Spatial' = high spatial image type; 'Time' = high time image type; 'm-TOF' = high mass TOF image type
units	string	desired calibration level for the image data to be returned, where 'Counts' = counts 'Counts/s' = counts per second 'Counts/(cm*s*sr)' = Integral intensity 'Counts/(cm*s*sr*Kev)' = Differential Intensity

Table 5.9: Calling signature and input parameter definitions for PDS_READ_MIMIIMG, a function that reads INCA image files into IDL. Note that for each image file, the corresponding accumulator rates file is also needed.

`data[i,*]` contains the prefix plus header columns, and image pixels (counts, count/sec, flux, etc., depending on requested calibration level) are in `image[i,*,*]`.

FUNCTION PDS_READ_MIMIIMG		(startyear, startdoy, starthours, startmins, startsecs, \$ stopyear, stopdoy, stophours, stopmins, stopsecs, \$ files, arfiles, \$ imagetype, units, \$ labels, data, images, datautc, stopdatautc, \$ auxdata, auxlabels)
Output		
Parameter	Type	Description
labels	string	labels[number columns]. Labels are the column titles for the image header parameters (minus the PURPOSE label).
data	double	data[number images, number columns]. The columns are the image header parameters. The data array does not include the first purpose column, but rather starts with the START_EPHEMERIS column.
images	double	images[num. images, max. imagesize, max. imagesize], such that images[i, j, *] is the j th row of the i th image and images[i, *, k] is the k th column of the i th image. (Note: all indices are zero-based.) IMPORTANT: The size of an actual image may not fill up the allocated space within the images array. The high spatial images can be either 32x32 (the High TOF channel) or 64x64 (the low TOF channel), while the high time images are always 32x32 and the high mass-TOF images are always 16x16. Be sure to use the correct number of rows or columns fields when referring to the images, i.e., use images[n, 0:nrows-1, 0:ncols] to get the data where nrows and ncols are obtained from the image header parameters.
datautc	string	datautc[number images]. The accumulation start time for each image.
stopdatautc	string	stopdatautc[number images]. The time data accumulation stopped for each image.
auxdata	double	auxdata[6, number columns]. Contains content from the 6 standard file header lines at the top of the file. Each of the 6 lines has a different purpose (mean, max, etc.) and contains one column entry for each data column in the file.
auxlabels	string	auxlabels[6]. A label indicating the purpose of each row of auxdata.
bandwidths	double	bandwidths[number images]. The bandwidth in keV of each image.
energy_ranges	double	energy_ranges[2, number images]. The energy range in keV of each image.
Returns a status value, where 0=ok, -1 = error opening file		

Table 5.10: Calling signature and output parameter definitions for PDS_READ_MIMIIMG, a function that reads INCA image files into IDL. Note that interpreting the image data correctly requires paying attention to the size of each image, because the array holding the image data is uniformly sized (to hold the maximum number of image pixels), but some images are smaller.

Proper use of the `image` array requires knowing the actual size of the image. The number of rows always equals the number of columns, so it is enough to look up just the `NUM_COLS` from the image header. In the MIMI reader code, the indices of prefix and image header columns are available via a set of IDL variables in `pds_image_hdr_h.pro` and `pds_data_hdr_h.pro`, which can be included in other IDL programs with these two lines:

```
@pds_image_hdr_h
@pds_data_hdr_h
```

Thus for the i^{th} image, the image size is

```
ysize = data[i,NUMCOLS_C] ; get the number of cols. (same num. of rows)
```

and then the corresponding image would be:

```
img = image[ i, 0:ysize-1, 0:ysize-1] ;
```

Each image pixel has a particular look direction out of the INCA instrument specified in azimuth and elevation. The azimuth index is the first index and the elevation index is the second index:

```
image[ i, azimuth_index, elevation_index ]
```

The azimuth directions range from -45 to 45 degrees over the index range 0 to $N-1$, where N is the number of rows in the image. The elevation values for each pixel range from 60 to -60 degrees (note: this is backwards) over the index range 0 to $N-1$, where N is the number of columns in the image. The pixel sizes are different depending on the resolution of the image. Also note that the look direction angles for each pixel are relative to the center of the INCA image, which may be offset from its nominal center due to the way images are integrated on the spacecraft. The registration of an INCA image against the sky in a specific coordinate system involves proper interpretation of the offset of the image center from its nominal direction. This process is described below near the end of this section (on page 138) in the discussion about the **Phi and Theta Offset of the Images**.

When the image is plotted in an IDL window, the horizontal axis will display -45 to 45 degrees in azimuth (left to right respectively) and the vertical axis will display -60 to 60 degrees in elevation (bottom to top respectively). The default IDL image display command `TV` will put the 0^{th} index row at the bottom of the displayed image.

A complete example showing how to read INCA image data is shown in Tables 5.11, 5.12 and 5.13 with the resulting output listed in Table 5.14 and the plotted image shown in Figure 5.4. The example shows how to find images containing both Ions and Neutrals, species Hydrogen, and TOF channel 3 (55-90 keV). The data shown are for the time period 2010-267T18:32 to 2010-267T18:32 and the ENA image shows an interaction between Titan's exosphere and magnetospheric ions from Saturn.

```

@pds_image_hdr_h ; include these to get column definition constants
@pds_data_hdr_h

; first define the input files and directories
topdir = '/path/to/PDS/downloads/COMIMI_OSAT/DATA/'

inca_img_dir = topdir + '/INCA_IMAGES/2010'
files = [inca_img_dir+'/IIMG0_2010267_0002.CSV'] ; include more days if desired

inca_acc_dir = topdir + 'INCA_ACCUMULATION_RATES/2010'
arfiles = [inca_acc_dir + '/IACCO_2010267_0002.CSV']

; set up image type, the read routine only takes specific strings
; after the data is read, the mytype value will be used to locate high
; m-TOF resolution images in the image array
imagetypes = ['Spatial','Time','m-TOF']
mytype = 2

; set up units, the read routine only takes specific strings
unittypes = ['Counts','Counts/s', 'Counts/(cm*s*sr)', 'Counts/(cm*s*sr*Kev)']
myunit = 3

; set up species, after the data is read, the myspecies value
; will be used to locate H images in the image array
species = ['H','NotUsed','0','NotUsed','NotUsed','All']
myspecies = 0

; set up TOF, if using high m-tof images, the tof = 3
; selects the energy range is 55-90 keV ,
; after the data is read, the myspecies variable
; will be used to locate 55-90 keV images in the image array
; the bandwidths and energy_ranges arrays contain
; the bandwidth and energy range of the image in keV
mytof = 3

; set up titles for charge, after the data is read, the mycharge value
; will be used to locate Ion images in the image array
charge = ['Neutral','Ion']
mycharge = 1

;read in all m-TOF images in differential intensity,
;only the image type selected will be returned, but each image
; type contains multiple TOF, charge and species images!
status = PDS_READ_MIMIIMG(2010,267,18,0,0,$
    2010,267,19,0,0,$
    files, arfiles, $
    imagetypes[mytype], unittypes[myunit], $
    labels, data, images, datautc, stopdatautc, $
    auxdata, auxlabels, bandwidths, energy_ranges)

```

Table 5.11: A working example showing how to read INCA image data.

```

; find the start and stop times in ET (this can be a subset but not a superset
; of the time range above because only certain files were loaded)
status2 = UTC2ET(['2010-267T18:29','2010-267T18:32'], et)

;identify images within that time range, image type, species, charge and tof
;only images with type = high m-TOF will be returned but the test for type is left
;in for completeness.
etcol = DATA_ET_SECS_C ; gets this index from pds_image_hdr_h.pro
at = WHERE((data[*,etcol] GE et[0] AND data[*,etcol] LE et[1]) AND $
           (data[*,TYPE_C] EQ mytype AND $
            data[*,SPECIE_C] EQ myspecies AND $
            data[*,CHARGE_C] EQ mycharge AND $
            data[*,TOF_C] EQ mytof))

; for any images within the time range, print the UTC time
; followed by the image rows
IF at[0] NE -1 THEN BEGIN
    ;Loop through images, since only one image type, tof, species and charge were
    ;selected, the resultant images should be in ascending time order. However,
    ;if more than one tof or species are present in the array, then they will not
    ;be in ascending time order since all tof, and specie images for an image
    ;type are collected at the same time periods.
    FOR n=0, N_ELEMENTS(at)-1 DO BEGIN
        utc = datautc[at[n]]
        PRINT, utc

        ;save the following variables from the image for printing out
        size = data[at[n], NUMCOLS_C]
        er = energy_ranges[*,at[n]]
        bw = bandwidths[at[n]]
        crg = data[at[n],CHARGE_C

        ;when the image is plotted in the window
        ;the horizontal axis is -45 to 45 azimuth (left to right) and
        ;the vertical axis is -60 to 60 elevation (bottom to top)
        ;but when the image is printed out as follows to the command window,
        ;the horizontal axis is -45 to 45 azimuth (left to right)
        ;and the vertical axis is 60 to -60 elevation (first row to last row)
        myimage = REFORM(images[at[n],0:isize-1,0:isize-1])

        strisize = STRCOMPRESS(STRING(isize), /REMOVE_ALL)
        ;small format is used to fit data on page
        fmt_str = '('+strisize+'(D5.2,"")'
        FOR j=0, isize-1 DO BEGIN ; print each row
            PRINT, myimage[j, 0:isize-1], FORMAT=fmt_str
        ENDFOR
    ENDFOR
ENDIF

```

Table 5.12: A working example showing how to select one image from INCA image data. The pixel values are printed row by row in the j loop. The n indexes the images.

```

;open an IDL window and load colormap and setup colors and linestyles
WINDOW,/FREE,retain=2,xsize=900,ysize=800
WSET,!D.WINDOW
colormapsize = 256
PDS_LOAD_COLORMAP, 33, colormapsize
PDS_LOAD_COLOR_INDEXES, 10, colors, lstyles

;increase imagesize on window according to imagesize
IF isize EQ 16 THEN sizetoincrease = 27 $
ELSE IF isize EQ 32 THEN sizetoincrease = 15 $
ELSE sizetoincrease = 7

;size the image to maintain aspect ratio since there are
;90 pixels in azimuth (x axis), 120 pixels in elevation (y axis)
xsize = isize*sizetoincrease
ysize = isize*sizetoincrease*(1.2/.9)
myimage = CONGRID(myimage, xsize, ysize)

;set the image color scale min and max
;xmin = MIN(myimage, MAX=xmax,/NAN)
xmin = 0.1
xmax = 4.0

;display image using log scale
enamin = ALOG10(xmin > 1e-5)
enamax = ALOG10(xmax > 1e-5)
myimage = ALOG10(myimage+0.000001)

;bytescale image and display
temp = BYTSCAL(myimage,MIN =enamin, MAX=enamax, TOP=colormapsize)
TV,temp,0.1,0.1,/normal

;plot axis and titles. Convert location and size of image to normal
;coordinates so the axis can be plotted around it
temp = CONVERT_COORD(0.1,0.1,/NORM,/TO_DEVICE)
temp2 = CONVERT_COORD(temp[0]+xsize,temp[1]+ysize,/DEVICE,/TO_NORM)
pos = [0.1,0.1,temp2[0],temp2[1]]
PLOT,[-45.,45.],[-60.,60.],/nodata,XSTYLE=17,YSTYLE=17,$
XTICKS=9, YTICKS=12,XTITLE='Azimuth',YTITLE='Elevation',$
XRANGE=[-45.,45.],YRANGE=[-60.,60.],POSITION=pos,/NOERASE,/NORM

;plot colorbar on right side of plot and titles at the top of the page
position = [0.88, 0.1, 0.91, 0.8]
BARFORMAT = '(g10.4)'
COLORBAR, position, vertical = 1, min = enamin, $
max = enamax, f = barformat, title = ytitle, ncolors = colormapsize+1, $
ps = (!d.name eq 'PS'), color = !p.color, charsize = small_text_size, $
divisions = 2
XYOUTS,0.05,0.95,'Cassini/MIMI INCA High '+imagetypes[mytype]+' Resolution '+$
species[myspecies]+' Image '+utc,/normal,charsize=1.5
XYOUTS,0.05,0.9,STRJOIN(STRCOMPRESS(er,/REMOVE_ALL),' - ')+' keV '+$
charge[crgr]+' image '+unittypes[myunit],/normal,charsize=1.3

```

Table 5.13: A working example showing how to plot an image from INCA image data.

```

Sample Output:
2010-267T18:29:22.101
energy range      55.000000      90.000000
bandwidth        35.000000
Ion image
0.00,0.00,0.00,0.00,0.00,0.12,0.20,0.00,0.00,0.00,0.00,0.23,0.36,0.62,0.00,0.00,
0.00,1.15,0.19,0.00,0.17,0.27,0.23,0.30,0.06,0.31,0.10,0.14,0.42,0.31,0.00,0.00,
0.00,0.24,0.44,0.37,0.21,0.61,0.23,0.18,0.20,0.23,0.37,0.25,0.00,0.00,0.51,0.00,
0.64,0.85,0.73,0.33,0.61,0.57,0.48,0.20,0.35,0.51,0.73,0.52,0.00,0.00,0.47,0.00,
0.97,0.35,0.94,0.82,0.45,1.20,0.79,0.91,0.84,0.56,0.62,0.68,0.18,0.00,0.00,0.00,
0.89,0.62,0.71,0.65,1.36,1.71,0.95,1.07,0.91,0.52,0.76,0.60,0.37,0.00,0.00,3.09,
0.39,1.44,0.94,1.06,1.95,1.91,1.13,0.37,0.74,1.31,1.20,0.42,0.69,0.21,0.30,0.00,
0.00,0.79,0.72,1.86,2.17,0.89,0.17,0.31,0.36,1.44,0.94,0.29,0.70,0.20,0.66,1.49,
1.05,0.92,1.37,1.99,2.38,0.86,0.18,0.07,0.51,0.89,1.88,0.44,0.52,0.20,0.32,0.00,
0.00,0.64,0.88,2.62,3.08,0.54,0.20,0.07,0.16,1.12,2.06,0.75,0.77,0.00,0.35,0.00,
1.37,0.79,1.44,2.52,2.20,0.89,0.23,0.38,0.48,1.90,2.33,1.31,0.50,0.62,0.00,0.92,
1.18,0.28,1.30,1.96,2.69,0.94,0.42,0.23,0.55,2.11,1.97,0.72,0.33,0.00,0.33,0.00,
0.00,0.48,0.64,1.44,2.65,2.24,1.62,1.30,1.60,1.67,1.18,0.97,0.81,0.22,0.00,1.20,
0.00,0.81,0.59,1.26,1.94,3.29,2.20,2.11,1.51,1.01,0.86,0.58,0.16,0.47,0.00,0.00,
0.00,0.79,0.74,0.36,0.96,1.93,1.73,1.57,1.11,1.26,0.54,0.51,0.19,0.79,0.00,0.00,
0.00,0.00,0.68,0.41,0.87,0.97,0.78,0.92,0.63,0.20,0.26,0.54,0.55,0.00,0.00,0.00,

```

Table 5.14: Output from reading an INCA image. The output is for a 16 x 16 pixel image. Each row contains counts for pixels at a single elevation, whereas each column contains counts from one value of azimuth. The top row shown here is the bottom row of the image as displayed in the IDL example plotting code of Table 5.13.

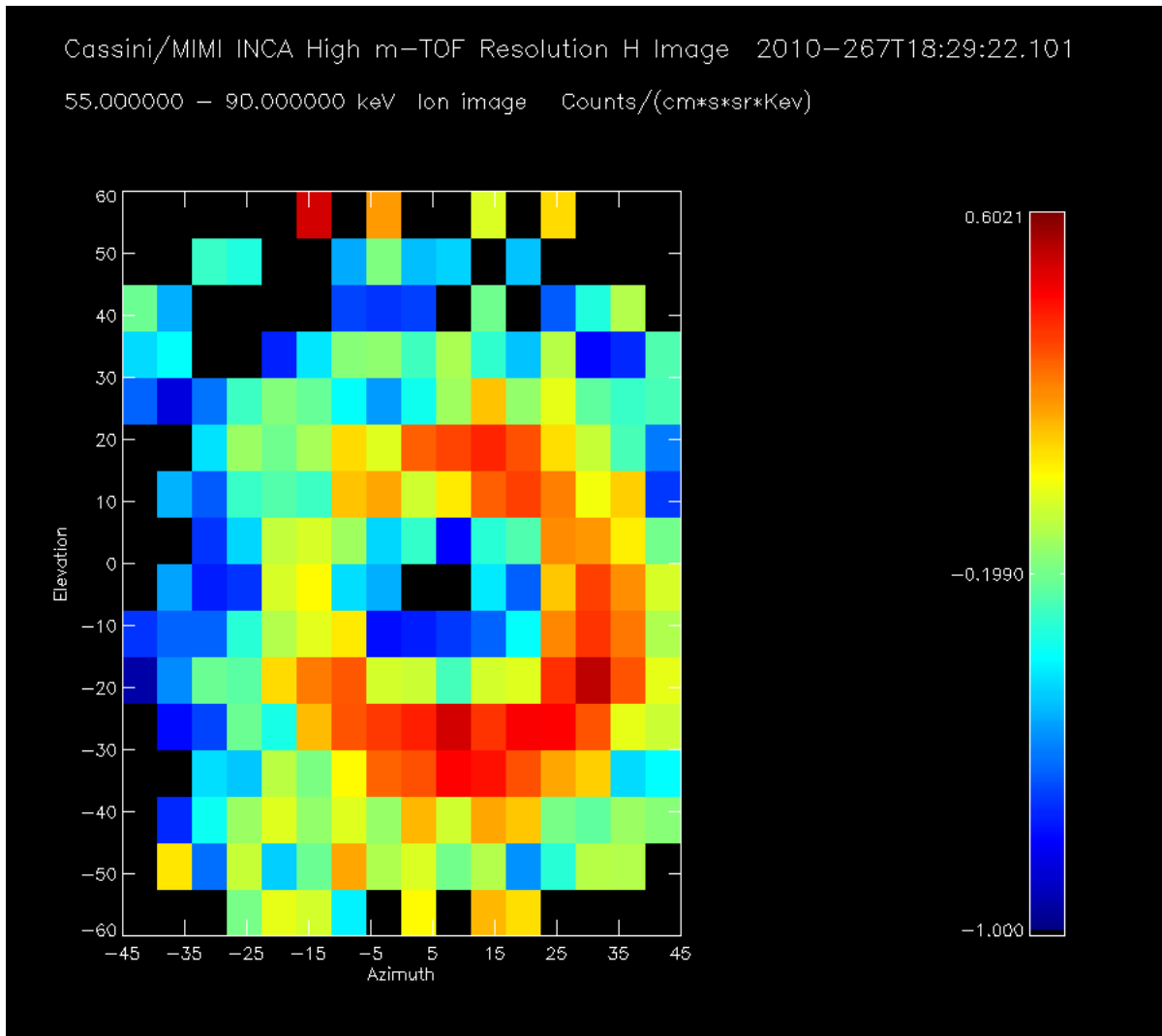


Figure 5.4: The `test_read_mimiimg` routine plots the last image read in to the window with a colorbar and the image field-of-view elevation and azimuth scale. This image illustrates an ENA image of Titan's exospheric interaction with magnetospheric ions. INCA images field-of-view is 120 degrees by 90 degrees. The high TOF resolution image has 16 by 16 pixels but is displayed to keep the proper pixel aspect ratio between elevation and azimuth. The color bar displays the differential intensity with a log scale.

Step 5: Read Calibration Files

The IDL routine `PDS_READ_MIMIIMG` calibrates INCA image data to the requested level. Here we describe the inner workings of this calibration process. Within `PDS_READ_MIMIIMG` are calls to two other significant routines. The `PDS_READ_IMAGECAL` function reads the flux factor matrixes, backgrounds, and energy ranges. This routine is described in Table 5.15, and an example showing how to read the calibration values is shown in Table 5.16. The program outputs are described in Table 5.17 and Table 5.19. The IDL function `PDS_CALIBRATE_IMAGES` performs the actual calibration and is described in the next step.

The INCA calibration process relies on three sources of calibration data: **a.** INCA-specific files with flux factor matrices, **b.** the regular conglomerate MIMI calibration file, and **c.** a few values from the accumulator rates. The flux factor matrices are described first.

FUNCTION PDS_READ_IMAGECAL (starttime, fill_data, imagetype, usecal,\$ energy_widths, energy_ranges, backgrounds, calib)			
	Parameter	Type	Description
<i>Inputs</i>	starttime	string	array, start utc and stop utc
	fill_data	double	any data points found to be fill will be given this value
	imagetype	string	image resolution type flag 'Spatial' = high spatial resolution 'Time' = high time resolution 'm-TOF' = high mass-TOF resolution
	usecal	long	calibration level of image data; 0 = 'Counts' 1 = 'Counts/s' 2 = 'Counts/(cm*s*sr)', Integral intensity 3 = 'Counts/(cm*s*sr*keV)', Differential Intensity
<i>Outputs</i>	energy_width	structure	contains arrays of energy widths for the high mass TOF image types and values for the high time and high spatial resolution images; this is used to convert the counts to integral and differential flux.
	energy_ranges	structure	contains arrays of energy ranges for all the image types
	backgrounds	structure	contains the background values for the various image types and the selected calibration level; background levels are subtracted after the image is calibrated to counts/second, integral intensity and differential intensity
	calib	structure	contains tags for all the image types, but only the requested image types will be filled out with the flux factor matrixes
<i>Returns</i>		integer	status of read, 0=ok, -1=error

Table 5.15: Signature and parameter definitions for PDS_READ_IMAGECAL, a function that reads INCA calibration data. All calibration files are available in the code and calibration set tarball downloadable from http://sd-www.jhuapl.edu/CASSINI/DataAuxiliaryInfo/MIMI_code_calibration.tar.gz.

```

imagetype = 'm-TOF'
strtime = ['2010-200T10:30', '2010-200T11:00']
usecal = 3 ;(0=counts,1=counts/s,2=counts/(cm*s*sr), 3= counts/(cm*s*sr*Kev)

status = PDS_READ_IMAGECAL(starttime, fill_data, imagetype, usecal, $
energy_widths, backgrounds, calib, energy_ranges)

print,energy_widths

Output:
Using geometricfactorXefficiency_matrix/postFlightv34
{
  35.000  31.000  35.000  31.000  35.000  31.000  60.000  80.0000
 133.000  78.000  59.000  35.000  20.000  11.000  10.500  8.3000
 411.000 257.000 101.000  62.000  40.000  39.300  21.300  22.4000
 133.000  78.000  59.000  35.000  20.000  11.000  10.5000  8.3000
 411.000 257.000 101.000  62.000  40.000  39.300  21.3000  22.4000
}

```

Table 5.16: Code showing how to read INCA image calibration values.

a. INCA Image Flux Factor Matrices

An INCA flux factor is an efficiency multiplied by a geometric factor. The matrices contain collections of these values for an image of a particular size, such that each value in the matrix should be multiplied by the value in an image pixel. Each matrix is in a separate file, and there are different matrices for each image size, each operating mode (spin versus stare mode), each species (hydrogen or oxygen), and for each energy channel (i.e., the 8 TOF channels, 0 through 7, with 0 being the highest energy channel and 7 the lowest). Additionally, the matrices have changed over time, and there are three distinct periods with a separate set of flux factor matrices for each. A directory structure with all the matrices is included with the code and calibration tarball download (find the tarball at http://sd-www.jhuapl.edu/CASSINI/data_auxiliary.html) in the `INCA_cal` directory and the calibration routine will use the environmental variables set in the `setup` routine to locate the calibration directories.

Some of the flux factor matrices should be ignored. Any flux factor matrix that is 8 by 8 refers to an essentially unused mode. The matrices are included for completeness only.

The three time periods for which there are different flux factor matrices are:

Mission Phase	Date Range
preJupiter	1997-244 to 2001-119T23:59
postJupiter	2001-120 to 2003-263T23:59
postFlightv34	2003-264 to the present

The set of matrices for each time range lives under its own directory. A table indicating which set of matrices to use for each time period is available in a separate file, `decom_incaflux_dates.txt`, that lives alongside the three time range directories. In each time range directory, there are subdirectories `spin` and `stare` with full sets of matrices for spin and stare modes. The naming scheme for the matrices is based on the number of pixels in the image, the time-of-flight, and the species:

`MxM_tofC_S.csv`

where `M` is the image size, `C` is the TOF channel and `S` is the species. Some examples are:

16x16_tof3_h.csv
64x64_tof3_o.csv
8x8_tof7_o.csv

Within the flux factor files, each matrix is laid out in the following order with respect to elevation and azimuth:

Row 0: covers -45° azimuth to $+45^\circ$ azimuth at a elevation of -60°

Row 1: covers -45° azimuth to $+45^\circ$ azimuth at a elevation of -58.2°

...

Row N: covers -45° azimuth to $+45^\circ$ azimuth at a elevation of $+60^\circ$

Choosing Matrices for High Time-of-Flight Resolution Images – Use the 16x16 matrices. (Ignore the 8x8 matrices as they are for an essentially unused mode). The species for these images (indicated in the image header) can be either Hydrogen or Oxygen, so use the matrixes with **h** or **o** respectively in the file names. These images can be for any of the 8 time-of-flight indexes, which are labeled 0 to 7, with 0 being the highest energy range (smallest TOF) and 7 the lowest energy range. How to find the energy ranges for each TOF index is discussed below.

Choosing Matrices for High Time Resolution Images – The high time resolution images are always 32x32 pixels and are not differentiated based on species, so for the flux factor matrixes, use files with the **h** species, although we consider the species to be all species. Two time-of-flight channels are available, low and high, which are designated with, indexes 3 and 45 respectively, where 45 means both 4 and 5. How to find the energy ranges of these channels are discussed in part **b** below.

Choosing Matrices for High Spatial Resolution Images – The high spatial resolution images have 32x32 pixels for the high time-of-flight images and 64x64 pixels for the low time-of-flight images. The two time-of-flight low and high, are designated with indexes 3 and 45 respectively. These images are available for Hydrogen or Oxygen, so use the matrix files with **h** or **o** respectively.

The matrices returned from `PDS_READ_IMAGECAL` (with values of efficiency times geometric factor) are stored in the IDL structure `calib` (see Table 5.17).

b. INCA Conglomerate Calibration File

The second source of INCA calibration information is the main MIMI conglomerate calibration file that was already described in Section 2.2. Described here are INCA-specific considerations for obtaining energy widths, ranges and backgrounds from this file. Recall that rows in the calibration file are valid over specific time ranges and you must choose the row that has calibration values covering the time range of your data.

As a practical tip, the easiest way to manually explore the calibration file is with a spreadsheet program that can filter the currently visible rows based on values present in the rows.

To find INCA channel energy ranges from the calibration file, select all the rows that have a `SENSOR` value of `INCA` and a `PURPOSE` value of `ENERGY`. For the background values, the `PURPOSE` would instead be `BACKGROUND`. The column with the desired calibration value will be different depending on the `PURPOSE`. For a channel energy range (`PURPOSE = ENERGY`), the `Low` and `Hi` columns contain the energy range. For `PURPOSE = BACKGROUND`, the `Midpoint` column has the background rate. Table 5.18 has details about which columns to use to get various INCA calibration values.

The calib structure contains the efficiency*geometric factor matrix for each image type, species, tof, and spin or stare.

```
calib = {hispat_loTOF_neu_H_caldata:DBLARR[64,64],$
        hispat_loTOF_neu_0_caldata:DBLARR[64,64],$
        hispat_hiTOF_neu_H_caldata:DBLARR[32,32],$
        hispat_hiTOF_neu_0_caldata:DBLARR[32,32],$
        hispat_loTOF_neu_H_caldata_spin:DBLARR[64,64],$
        hispat_loTOF_neu_0_caldata_spin:DBLARR[64,64],$
        hispat_hiTOF_neu_H_caldata_spin:DBLARR[32,32],$
        hispat_hiTOF_neu_0_caldata_spin:DBLARR[32,32],$
        hitime_loTOF_neu_caldata:DBLARR[32,32],$ 8
        hitime_hiTOF_neu_caldata:DBLARR[32,32],$
        hitime_loTOF_ion_caldata:DBLARR[32,32],$
        hitime_hiTOF_ion_caldata:DBLARR[32,32],$
        hitime_loTOF_neu_caldata_spin:DBLARR[32,32],$
        hitime_hiTOF_neu_caldata_spin:DBLARR[32,32],$
        hitime_loTOF_ion_caldata_spin:DBLARR[32,32],$
        hitime_hiTOF_ion_caldata_spin:DBLARR[32,32],$
        himTOF_neu_H_caldata:DBLARR[8,16,16],$
        himTOF_neu_0_caldata:DBLARR[8,16,16],$
        himTOF_ion_H_caldata:DBLARR[8,8,8],$
        himTOF_ion_0_caldata:DBLARR[8,8,8],$
        himTOF_neu_H_caldata_spin:DBLARR[8,16,16],$
        himTOF_neu_0_caldata_spin:DBLARR[8,16,16],$
        himTOF_ion_H_caldata_spin:DBLARR[8,8,8],$
        himTOF_ion_0_caldata_spin:DBLARR[8,8,8]}
```

Table 5.17: INCA image calibration structures (containing values of efficiency times geometric factor) are read using PDS_READ_IMAGECAL. These structures are loaded by reading the INCA image flux factor matrices.

MIMI Conglomerate Calibration File Column Definitions

Column

No.	Field Name	Description
1	Purpose	the intended use for the calibration value on this row; see Table 2.3 for purpose codes and definitions.
2	Data_Type	PDS Data Product; one of PHA, SCI, ACC, IMG, or FRT; Table 2.2 lists the products for each sensor
3	Sensor	MIMI sensor name (CHEMS, INCA, or LEMMS)
4	Channel	the channel name (for CHEMS, a value of DPPS indicates a row with a voltage step value)
5	Channel_Index	channel index or DPPS step number
6	Particle	nominal particle species associated with this measurement if known; (<i>note: often this is not definitive</i>)
7	Start_Year	start year of valid time range for the value on this row (to be combined with day of year value in next column)
8	Start_DDOY	day of year for start date of valid time range for this row
9	End_Year	end year of valid time range for this row (to be combined with day of year value in next column)
10	End_DDOY	day of year for end date of valid time range for this row
11	Units	units for the numeric calibration value in this row
12	Low	if the calibration value is a range, this is the low value in the range
13	Hi	if the calibration value is a range, this is the upper end of the range
14	Delta	if the calibration value is a range, this is the width of the range; for background level values, it is the uncertainty in the background value
15	Midpoint	the calibration value for this row; if the calibration value is a range, this field is the midpoint between the Hi and Low values; see Table 2.3 for a full explanation of midpoints for each purpose type (<i>note that some midpoints are geometric means</i>)
16	Source	the institution responsible for generating this calibration value; UMD = Univ. of Maryland, APL = Applied Physics Laboratory, KS = Fundamental Technologies in Kansas, or Team = the entire MIMI team
17	Comment	any relevant comments regarding this record; for CHEMS, efficiencies, also indicates the rate channels to be included

Table 5.18: Names and definitions of the columns in the MIMI conglomerate calibration file. Calibration values (the actual numbers) are in columns 12 through 15. The value in the **Purpose** column dictates how to interpret the value columns in the same row. The allowed **Purpose** values are explained in Table 2.3.

Obtaining Energy Range and Backgrounds for High Time-of-Flight Resolution Images – Use the rows that have a CHANNEL column of NEU – TOF. There are also rows with ION – TOF for the channel value, but these correspond to commanded ion mode and should be ignored as mentioned previously. There are 16 rows with energy values. The hydrogen images (SPECIES = H+) have 8 rows (the TOF channels 0 through 7), and likewise for the oxygen channels (SPECIES = 0x). As an example, a high time-of-flight image for hydrogen and for TOF channel 7 would have this row for its energy ranges ENERGY, IMG, INCA, NEU – TOF, 7, H+, 1997, 288.3990741, 2030, 1, keV, 5.2, 13.5, 8.3, 8.38,

and this row for its background values:
BACKGROUND, IMG, INCA, NEU – TOF, 7, H+, 1997, 288.39907410, 2030, 1.0,
counts/(cm*s*sr*keV), 0, 0, 0, 0, 0, 0, 0

(NOTE: The line break in the background value line is artificial.)

This gives an energy range of 5.2 to 13.5 keV, and a background flux value of 0.

Concerning species labels in the calibration file, 0x is used to emphasize that INCA does not measure the charge state of Oxygen. The H+ label for hydrogen, however, is somewhat of a misnomer, since this label gets used when describing neutrals.

Obtaining Energy Range and Backgrounds for High Time Resolution Images – First select calibration rows with SENSOR = INCA and PURPOSE = ENERGY, and then look at only the rows with CHANNEL = TIME – TOF. For commanded neutral mode, the PARTICLE column has the value Neutrals. Ignore the rows with PARTICLE = Ions because that corresponds to the rare commanded ion mode. The Channel_index (TOF index) is either 0 or 7. These images are not taken for separate species. So for a high time resolution image taken for time-of-flight channel 7, and species all, the proper energy range for the day 265 in year 2003 would be from 24 to 55 keV, according to this line:

ENERGY, IMG, INCA, TIME – TOF, 7, Neutrals, 1997, 288.3990741, 2030, 1, keV, 24, 55, 31, 36.33,

The matching background value for differential flux would be from the following line:

BACKGROUND, IMG, INCA, TIME – TOF, 7, Neutrals, 1997, 288.39907410, 2030, 1.0,
counts/(cm*s*sr*Kev), 0, 0, 0, 0, 0, 0, 0

(NOTE: The line break in the background value line is artificial.)

Obtaining Energy Range and Backgrounds for High Spatial Resolution Images – The CHANNEL column for high spatial images contains SPATIAL – TOF. The Channel_index (TOF index) can be 0 or 7, and the SPECIES can be either H+ or 0x. So for a high spatial resolution image, for time-of-flight index 7, and a species of oxygen, the proper energy width for the day 265 in 2003 would be 90 to 170 keV according to this line:

ENERGY, IMG, INCA, SPATIAL – TOF, 7, 0x, 2003, 264.0001273, 2030, 1, keV, 90, 170, 80, 123.69

The matching background value for differential flux would be 0, according to the following line:

BACKGROUND, IMG, INCA, SPATIAL – TOF, 7, H+, 1997, 288.39907410, 2030, 1.0,
counts/(cm*s*sr*keV), 0, 0, 0, 0, 0, 0, 0

The energy widths, ranges and backgrounds are returned from PDS_READ_IMAGECAL, are stored in the IDL structures energy_widths, energy_ranges and backgrounds (see Table 5.19).

c. Using INCA Accumulator Rates To Correct Image Calibration

To reduce saturation effects in the INCA data, all intensities should be multiplied by a factor derived from two INCA accumulator values. Table 5.2 on page 109 lists all the columns available in INCA accumulator data. Over the integration time of an image, sum up the total counts in the valid time-of-flight counter, which has a column label of TIME. Then sum the counts in the EVENTS_RECEIVED counter, and take the ratio of valid time of flights to total events received.

The `energy_widths` structure contains the energy bandwidths in keV for each type, species and TOF image. The structure field names are meant to be self defining.

```
energy_widths = {high_time_LowTOF_neu:0.,$
  high_time_HighTOF_neu:0.,$
  high_time_LowTOF_ion:0.,$
  high_time_HighTOF_ion:0.,$
  high_spat_LowTOF_H:0.,$
  high_spat_HighTOF_H:0.,$
  high_spat_LowTOF_O:0.,$
  high_spat_HighTOF_O:0.,$
  high_mTOF_H_neu:FLTARR(8),$
  high_mTOF_O_neu:FLTARR(8),$
  high_mTOF_H_ion:FLTARR(8),$
  high_mTOF_O_ion:FLTARR(8)}
```

The `energy_ranges` structure contains the energy ranges in keV for each type, species and TOF image.

```
energy_ranges = {high_time_LowTOF_neu:FLTARR(2),$
  high_time_HighTOF_neu:FLTARR(2),$
  high_time_LowTOF_ion:FLTARR(2),$
  high_time_HighTOF_ion:FLTARR(2),$
  high_spat_LowTOF_H:FLTARR(2),$
  high_spat_HighTOF_H:FLTARR(2),$
  high_spat_LowTOF_O:FLTARR(2),$
  high_spat_HighTOF_O:FLTARR(2),$
  high_mTOF_H_neu:FLTARR(2,8),$
  high_mTOF_O_neu:FLTARR(2,8),$
  high_mTOF_H_ion:FLTARR(2,8),$
  high_mTOF_O_ion:FLTARR(2,8) }
```

The `backgrounds` structure contains the background to subtract for each image type, species and tof for the selected units.

```
backgrounds = {high_time_LowTOF:FLTARR(2),$           ;[0] neutral, [1] ion
  high_time_HighTOF:FLTARR(2),$                       ;[0] neutral, [1] ion
  high_spat_LowTOF_H:0.0,$
  high_spat_HighTOF_H:0.0,$
  high_spat_LowTOF_O:0.0,$
  high_spat_HighTOF_O:0.0,$
  high_mTOF_H:FLTARR(2,8),$                           ;[0,*] neutral, [1] ion
  high_mTOF_O:FLTARR(2,8)}                           ;[0,*] neutral, [1] ion
```

Table 5.19: INCA image energy widths, ranges and background values structures read using `PDS_READ_IMAGECAL`. These structures are loaded by reading the MIMI team calibration file.

This ratio is calculated and automatically applied to INCA data (within the PDS_CALIBRATE_IMAGES program) if the user inputs the correct accumulator rate files using the arfiles argument to the PDS_READ_MIMIIMG function. The following IDL code calculates the ratio.

```

; This code computes the ratio of valid time of flights
;   to total events received.
; This ratio is applied to INCA data to account for possible
;   saturation effects.

@pds_data_hdr_h      ; include data header column indexes
@pds_image_hdr_h     ; include inca image header column indexes

;find if image is a quad image
quad = 1d
IF data[n,TYPE_C] EQ IMAGETYPE_HIGHSPATIAL OR $
    data[n,TYPE_C] EQ IMAGETYPE_HIGHMTOF THEN BEGIN
    quad = 4d
ENDIF

; find matching accumulator rates data and calculate ratio
; data is the array of header data matching the images
; ar_data is the INCA accumulator rates data as read in by PDS_READ_MIMI
; Note that n is the image index into the data array, which must
; already have been created by other code

IF (quad EQ 4d) THEN BEGIN
    at = WHERE(ar_data[* ,SPIN_COUNTER_C] EQ data[n,SPIN_COUNTER_C] AND $
        (ar_data[* ,SECTOR_NUMBER_C] GE data[n,SECTOR_NUMBER_C] AND $
        ar_data[* ,SECTOR_NUMBER_C] LT data[n,SECTOR_NUMBER_C]+4),count)
ENDIF ELSE BEGIN
    at = WHERE(ar_data[* ,SPIN_COUNTER_C] EQ data[n,SPIN_COUNTER_C] AND $
        ar_data[* ,SECTOR_NUMBER_C] EQ data[n,SECTOR_NUMBER_C],count)
ENDELSE
ratio = (at[0] NE -1) ? $
    (TOTAL(ar_data[at,timeat])/count)/$
    (TOTAL(ar_data[at,eventrec])/count) : 1.0

```

Step 6: Calibrate the Data

Calibration of INCA images requires the use of the geometric*efficiency matrixes, energy widths, INCA accumulator rates data and image accumulation time. The previous section described how to read in the matrixes, energy widths and INCA accumulator rates data. The routine PDS_CALIBRATE_IMAGES calibrates INCA images and is called from PDS_READ_MIMIIMG. The inputs and outputs of PDS_CALIBRATE_IMAGES are shown in Table 5.20. The following formula is used to calibrate the INCA images.

Counts per second	counts/s	= image/accum - back
Integral Intensity	counts /(cm ² sr s)	= image*geoeff*ratio/accum - back

Differential Intensity counts /(cm2 sr s keV) = image*geoeff*ratio/accum/ew - back

where the inputs are:

geoeff = geometric and efficiency matrix
ew = energy width for image time-of-flight and species
accum = image accumulation time
ratio = ratio of Valid Time-of-Flight Measurement/ Events Received
back = background value to subtract, specific for units

a. Accumulation Time

Accumulation time is calculated using the MIMI spin period field included in the data array, `data[N, SPIN_PERIOD_C_C]`. The image accumulation time also depends on whether the image is a quadrant image or sector image. The MIMI flight software divides the spin of the spacecraft into 16 sectors and labels each image with spin and sector of the start of the accumulation. The quadrant images are accumulated over 4 sectors so there will be four images per spin where non-quadrant images are accumulated over 1 sector so there would be 16 images per spin. Of the INCA images sent to the PDS, only the high time resolution images are collected over one sector, all high mTOF and high spatial resolution images are quadrant images. The following IDL code shows the formula to calculate the accumulation time for an image.

```
@pds_data_hdr_h          ;include data header column indexes
@pds_image_hdr_h        ;include inca image header column indexes

;find accumulation time in seconds from spin period
;pds_data_hdr_h contains SPIN_PERIOD_C_C
factor = 1./16.
timeofone = DOUBLE(data[n,SPIN_PERIOD_C_C]) * factor

;find if image is a quad image
quad = 1d
IF data[n,TYPE_C] EQ IMAGETYPE_HIGHSPATIAL OR $
    data[n,TYPE_C] EQ IMAGETYPE_HIGHMTOF THEN BEGIN
    quad = 4d
ENDIF
accum_secs = quad*timeofone
```

b. Filter Out Either Ion or Neutral Mode Data The images are usually grouped by whether they consist of just neutral particles or if they contain both ion and neutral particles. The charge field in the image header data is set to 0 for neutral particles and 1 for ion and neutral particle images. Files containing the time ranges when the images contain either neutral or ion and neutral particles are available at the following URL http://sd-www.jhuapl.edu/CASSINI/data_auxiliary.html. The file name is `MIMI_INCA_NeutralIonyyyy.txt` with yyyy being the 4 digit year. The format of the data in the file is start UTC, stop UTC, mode with mode = 0 for neutral and 1 for neutral and ion particles. The following is an excerpt from the file:

```
Start in UTC,      Stop in UTC,  Mode (0=Neutral,1=Ion)
2011-001T00:00:35, 2011-001T20:58:42,    1
2011-001T21:45:35, 2011-001T21:46:42,    1
```

The following IDL code shows an example of how to find the indexes of the neutral particle images

PRO PDS_CALIBRATE_IMAGES ,starttime, stoptime, imagetype, arfiles, units, data,\$ images, bandwidth, energyrange		
Input		
Parameter	Type	Description
starttime	string	array, start utc and stop utc
stoptime	string	array, start utc and stop utc
imagetype	string	image resolution type flag 'Spatial' = high spatial resolution 'Time' = high time resolution 'm-TOF' = high mass-TOF resolution
arfiles	string	array of INCA accumulator data files corresponding to each image file. The image calibration process requires the accumulator data.
units	long	calibration level of image data; 0 = 'Counts' 1 = 'Counts/s' 2 = 'Counts/(cm*s*sr)', Integral intensity 3 = 'Counts/(cm*s*sr*keV)', Differential Intensity
data	double	data[number rows, number columns]. The rows are the samples in time. The columns are the parameters.
Output		
Parameter	Type	Description
images	double	images[num. images, max. imagesize, max. imagesize], such that images[i, j, *] is the j th row of the i th image and images[i, *, k] is the k th column of the i th image. The input image array is calibrated and returned. (Note: all indices are zero-based.) IMPORTANT: The size of an actual image may not fill up the allocated space within the images array. The high spatial images can be either 32x32 (the High TOF channel) or 64x64 (the low TOF channel), while the high time images are always 32x32 and the high mass-TOF images are always 16x16. Be sure to use the correct number of rows or columns fields when referring to the images, i.e., use images[n, 0:nrows-1, 0:ncols] to get the data where nrows and ncols are obtained from the image header parameters.
bandwidth	structure	The energy width structure is described in Table 5.19
energyrange	structure	The energy range structure is described in Table 5.19

Table 5.20: Calling signature and output parameter definitions for PDS_CALIBRATE_IMAGES, a function that calibrates INCA images called by PDS_READ_MIMIIMG.

in the images array.

```
@pds_image_hdr_h
```

```
at = WHERE(data[* , CHARGE_C] EQ 0)  
IF at[0] NE -1 THEN neutralimages = images[at, *, *]
```

c. Phi and Theta Offset of the Images

After the image is calibrated, positioning it in a display with respect to a planetary body may require the use of the phi and theta offsets from the INCA image file ancillary data found to the left of the image pixel values.

At the start of image integration, the INCA flight software defines a block on the sky with an angular size of $180^\circ \times 180^\circ$. This region, known as the image buffer, contains angular bins into which counts will be accumulated. The center of the image buffer is the INCA boresight at the start of the integration period. INCA's actual field of view is smaller than the image buffer, and so any spacecraft motion will move the FOV around within the image buffer (translations and rotations are both possible). Every subsector, the flight software gets an attitude measurement and uses this to determine where the FOV is currently positioned within the image buffer so the counts from each INCA pixel can be mapped into the correct bins within the image buffer. At the end of the integration period, the flight software determines the average position of the boresight and selects a region of pixels around this location. This selected region is always the same size as the instantaneous INCA FOV, i.e., $90^\circ \times 120^\circ$. (If the average boresight is near the edge of the image buffer, the flight software forces the selected region to be fully within the image buffer.) The location of this selected region image within the image buffer is given as phi and theta offsets. A phi, theta offset of 0,0 would indicate that the selected region is at the bottom, left corner of the image buffer. The flight software uses the current pixel size as units for the offsets. For example, in a 16×16 image, a phi offset of 3 would be $3 \times (1/16) \times 90^\circ = 16.875^\circ$, and a theta offset of 4 would be $4 \times (1/16) \times 120^\circ = 30^\circ$. In many cases, the spacecraft attitude is constant, and so the image buffer only accumulates counts within the single FOV-sized region. In this case, the phi and theta offsets are not zero, but instead a nominal value (dependent on the current image size) that places the image in the middle of the image buffer.

Figure 5.5 provides an example illustrating the motion compensation process. The final $90^\circ \times 120^\circ$ region used to create the image that gets sent down in telemetry is shown with a bold, red outline, whereas the thinner or dashed outlines indicate the location of the instantaneous FOV at various times during the integration period. The phi and theta offsets of the final image are also indicated.

The phi and theta offsets are only applicable when MIMI is in stare mode, or for high time resolution images in spin mode. Note that stare mode includes slow moving targeted observations, such as mosaics.

During spin mode (except for high time resolution images), a different motion compensation algorithm is used. The flight software accumulates data such that the resulting image covers the region of the sky swept out during the accumulation time. This is not a full explanation, but the point is that for this data the resulting image can be registered without using the offsets.

The following IDL code figures out if the phi and theta offsets need to be applied. Note that this code calls the IDL routine `PDS_GET_PHITHETA_DEG` to convert the offsets from pixels to degrees which is included in the MIMI IDL code set.

```

@pds_data_hdr_h          ;include data header column indexes
@pds_image_hdr_h         ;include inca image header column indexes

;call routine to convert INCA image phi and theta offset from pixels to degrees
PDS_GET_PHITHEA_DEG, data[n, NUMROWS_C], $
    data[n, PHIOFFSET_C], data[n, THETAOFFSET_C], az_shift, el_shift

spinvalue = 1
IF (data[n, SPINSTAR_MODE_C] NE spinvalue) OR $
    ((data[n, SPINSTAR_MODE_C] EQ spinvalue) AND $
    (data[n, TYPE_C] NE IMAGETYPE_HIGHTIME)) THEN BEGIN

    ;add offsets converted to degrees to boresight vector of INCA image

ENDIF

```

Step 7: Filter Out Bad Data

Any data that has values greater than the allowed maximum (listed for each column in the 5th row) has been set to "". The read routine searches for cells with " " and sets those to 0 value when it reads in the data.

There are periods of time when the INCA start and stop voltages are not in the proper calibration range. One example of a planned out of calibration period would be while the voltages are being ramped up or down. A unplanned out of calibration period would occur when the instrument flight software automatically detects the INCA start or stop rate has exceeded a threshold and turns down the voltages until the rate is back within the normal range. Any data periods for which INCA start or stop voltages are out of the proper calibration range has been stored in a set of files included in the INCA_outofcal_times directory in the code and calibration download at http://sd-www.jhuapl.edu/CASSINI/DataAuxiliaryInfo/MIMI_code_calibration.tar.gz. If the SETUP routine is set up properly then the PDS_READ_MIMIIMG routine will know the path to the files, the routine will notify the user that the requested time range contains image taken during a time period when the voltages were out of calibration level. The user is responsible for changing the requested time period to exclude any out of calibration images if he so chooses.

The out of calibration files have a file name, `incahv_outofcal_yyyy.txt`. The yyyy is the 4 digit year. The contents of the file are start UTC, start ET, stop UTC, stop ET, out of calibration flag. The out of calibration flag = 1 indicates that the out of calibration state was an expected state due to commanding, and flag = 2 indicates that the out of calibration state was unexpected and may have multiple causes. Images collected during either state are considered to be out of calibration. The following is an excerpt from the file:

Start_UTC,	Start_ET,	Stop_UTC,	Stop_ET,	OutofCal_Flag
2011-008T09:33:51.4,	347751298.,	2011-009T00:18:06.1,	347804352.,	1.
2011-009T09:18:54.9,	347836801.,	2011-009T23:21:34.6,	347887361.,	1.

The user is should update these files periodically by downloading the tar set http://sd-www.jhuapl.edu/CASSINI/DataAuxiliaryInfo/MIMI_code_calibration.tar.gz to get the most up to date out of calibration files or obtaining them from the URL http://sd-www.jhuapl.edu/CASSINI/data_auxiliary.html.

Step 8: Deal with Data Gaps Any portions of images, which were missing during downlink had the values set to "". If data is absent for a significant period, it may be during a known data gap. A list of data gaps has been provided online at the following

URL: http://sd-www.jhuapl.edu/CASSINI/data_auxiliary.html.

and is included as auxiliary data in the code set in subdirectory gaps_times at the following URL: http://sd-www.jhuapl.edu/CASSINI/DataAuxiliaryInfo/MIMI_code_calibration.tar.gz.

The gaps are listed in yearly files have names like MIMI_Gap_SummaryYYYY.txt and YYYY is the 4 digit year. The files are comma delimited and contain lines with the gap start time, gap stop time in UTC followed by the total gap time in hh:mm:ss. The following is an excerpt from the file:

Gap Start in UTC,	Gap Stop in UTC,	Total Gap Time
2011-024T08:50:30,	2011-024T23:59:59,	15:09:00
2011-025T00:00:00,	2011-025T14:22:36,	14:22:00

The user should also update the data gap files periodically by downloading the tar set or obtaining them from the URL: http://sd-www.jhuapl.edu/CASSINI/data_auxiliary.html.

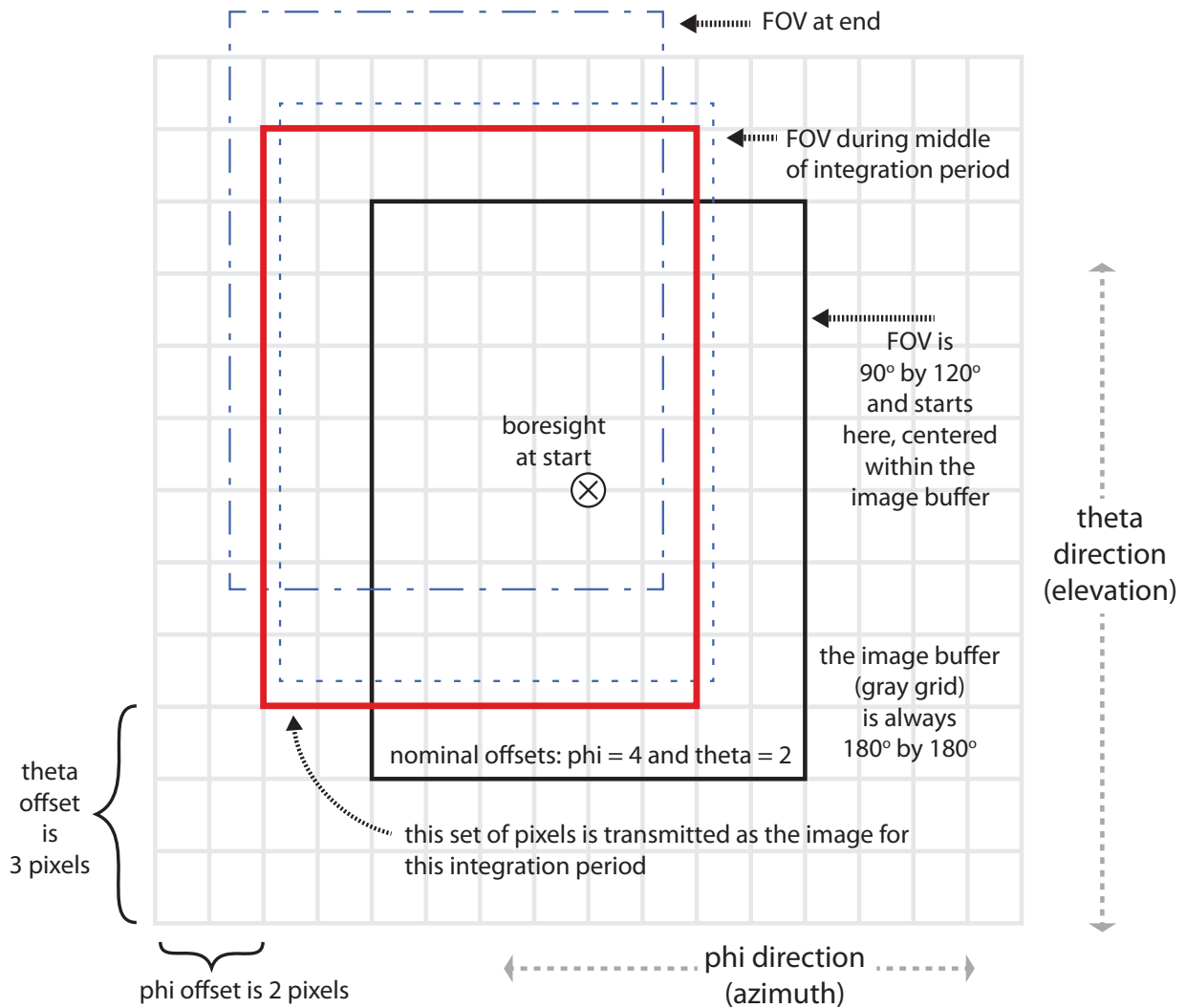


Figure 5.5: The INCA motion compensation process. In stare mode (or for high time resolution images in spin mode), the flight software begins each integration period by defining a 180° x 180° image buffer (large, gray grid) centered on the boresight (circled 'x' pointing into the page) at start time of the integration period (solid black outline box in center). Subsequent spacecraft motion is detected and used to place counts from the instantaneous FOV into the appropriate bins within the larger image buffer. The fine dashed and coarse dashed outlines show other locations of the FOV. The final image is selected at the end of the integration period and always has a size of 90° x 120° (thickest, solid red outline). In the data, the location of the final telemetered image within the image buffer is indicated with a phi offset and a theta offset, each in units of pixels. This example show a final phi offset of 2 and a final theta offset of 3. The image size shown is 8x8, so the pixels are $90/8 = 11.25^\circ$ in the phi direction and $120/8 = 15^\circ$ in the theta direction. For the case shown, the nominal phi and theta offsets (for no spacecraft motion) are 2 and 4 respectively. Note that PDS data contains no 8x8 images, but this size was used here for clarity.

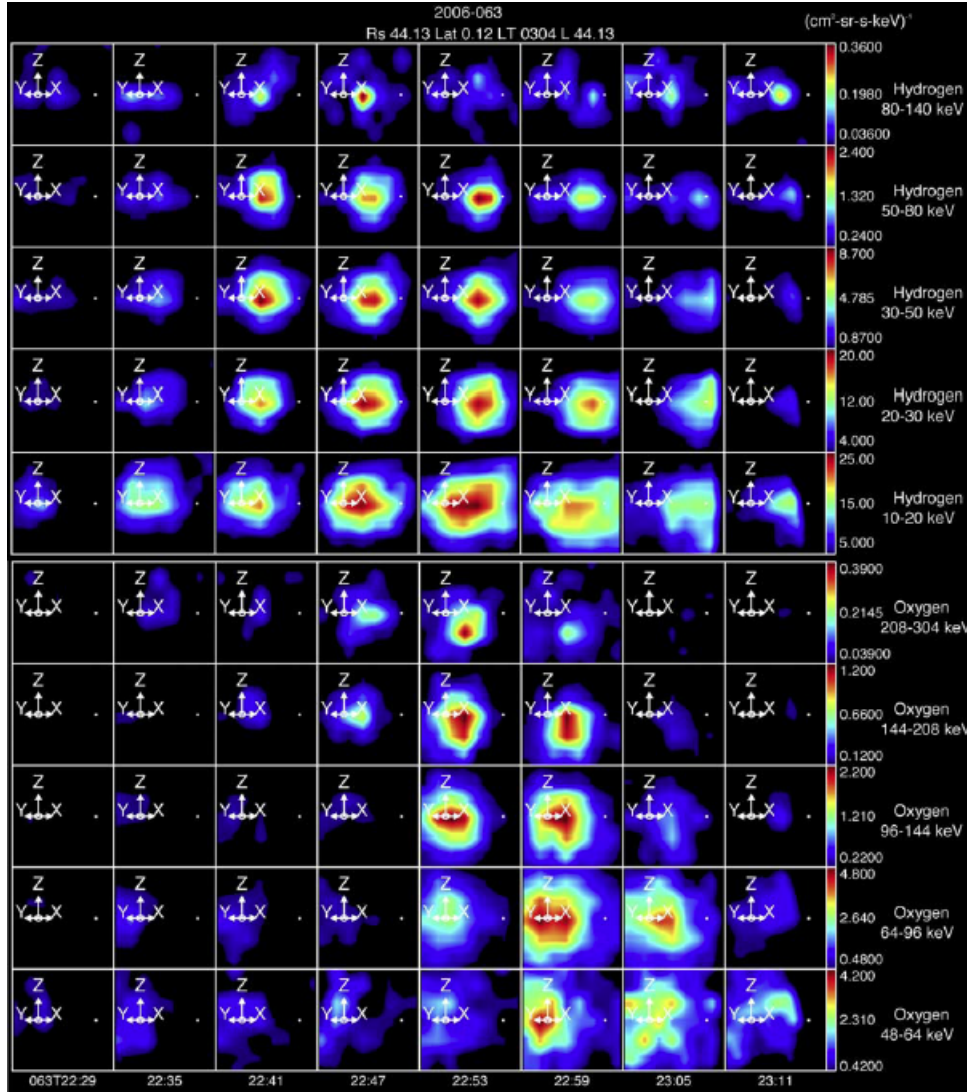


Figure 5.6: Plasmoids: The blobs in these images are plasmoids appearing in Saturn’s magnetotail. The ENA images are hydrogen (top five rows) and oxygen (bottom five rows) for times ranging from 22:29 (left column) to 23:11 (right column) on 4 March 2006. Hydrogen energies range from 80-140 keV (top row) down to 10-20 keV (row 5) and oxygen energies range from 208-304 keV (row 6) to 48-64 keV (row 10). The figure is from [Hill et al., 2008].

5.8 Features in INCA Data

This section illustrates the types of analyses possible with INCA and gives examples of the types of features, real and instrumental, that are likely to appear in the data. All descriptive text for each figure is fully contained in the associated caption.

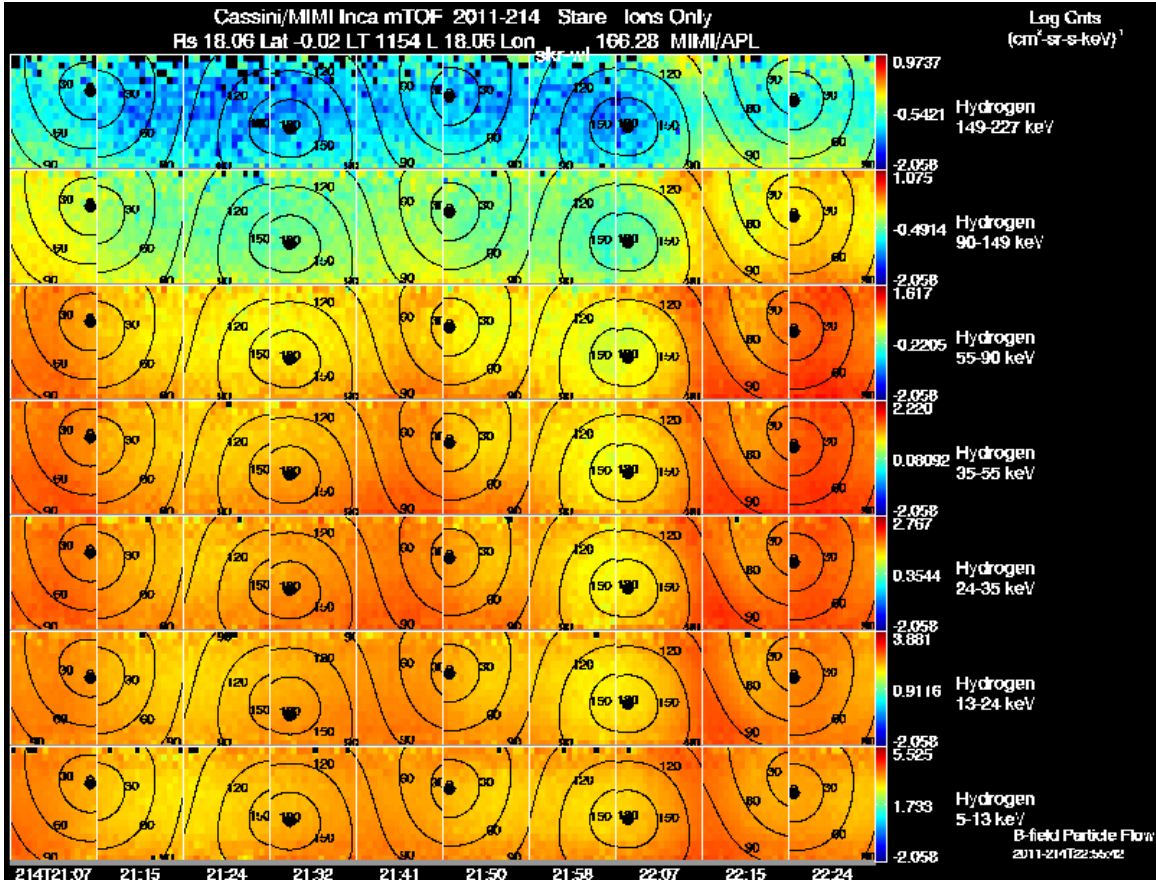


Figure 5.7: Hot Plasma Ions: This figure contains INCA images for hydrogen ions for times ranging from 21:07 (left column) to 22:24 (right column) on day 214, 2 August 2011. Hydrogen energies range from 149-227 keV (top row) down to 5-13 keV (row 7). Pitch angle is shown in each image for the range 30°, 60°, 90°, 120°, 150°.

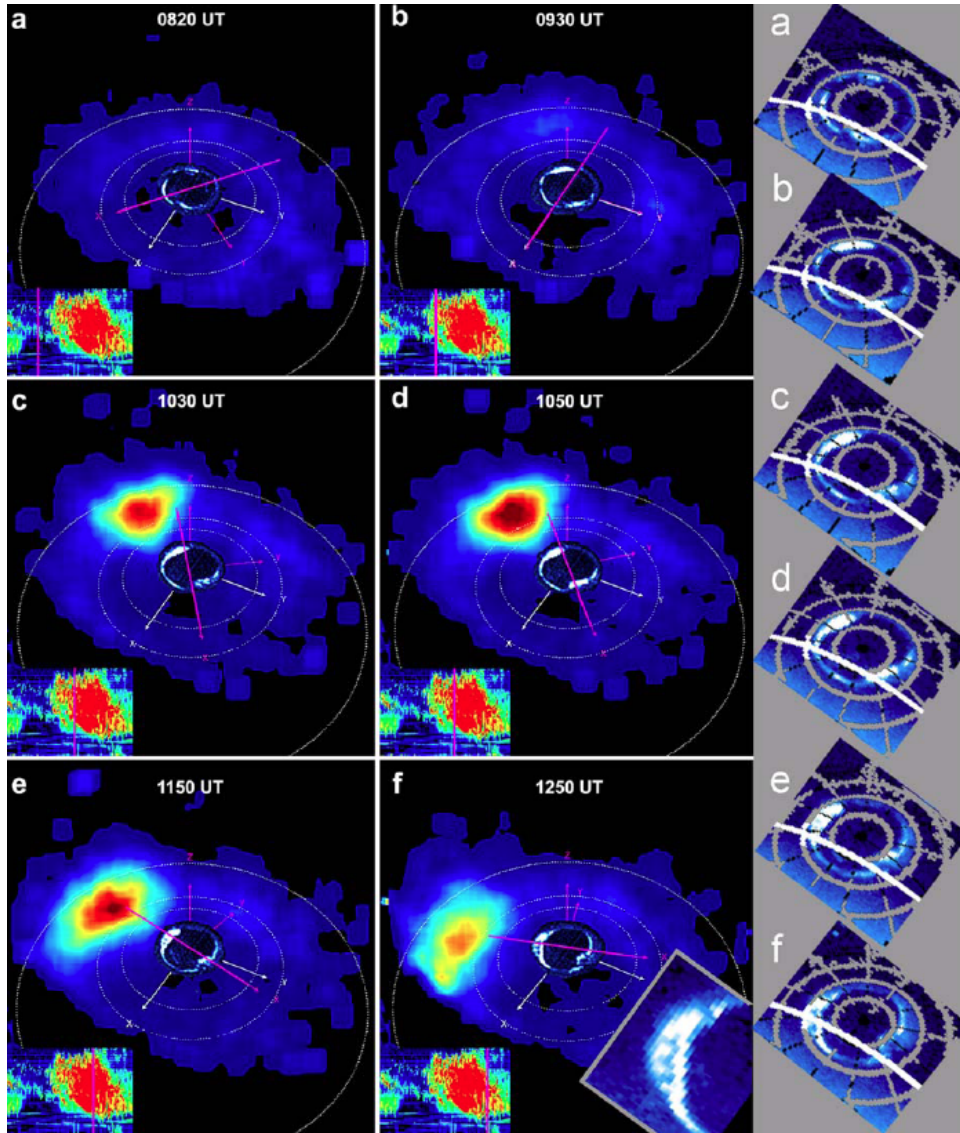


Figure 5.8: MIMI INCA ENA and UVIS Auroral Images on 8 May 2008. This figure shows six images from the day 129, 2008 sequence. UVIS auroral images scanned over approximately 15 minutes are superposed at a larger scale so they can be more easily seen. A pink line lies on top of the X axis of a coordinate system rotating about Saturn's spin axis, at the SLS3 (extrapolated) period. This is for reference, to follow the motion of the ENA enhancement and the bright auroral bulge over time. In the bottom left corner of each frame, the SKR data is reproduced, with a vertical pink line indicating the center time of the hour-long ENA accumulation (time given at top of each frame). To the right, each auroral image is reproduced with a latitude-longitude grid (every 10° of latitude). A white line indicates the terminator, and the 70° latitude line turns to white for a segment where it crosses the terminator. An inset in panel f shows a blow-up of the equatorward bulge at about that time. The figure is from [Mitchell et al., 2009a].

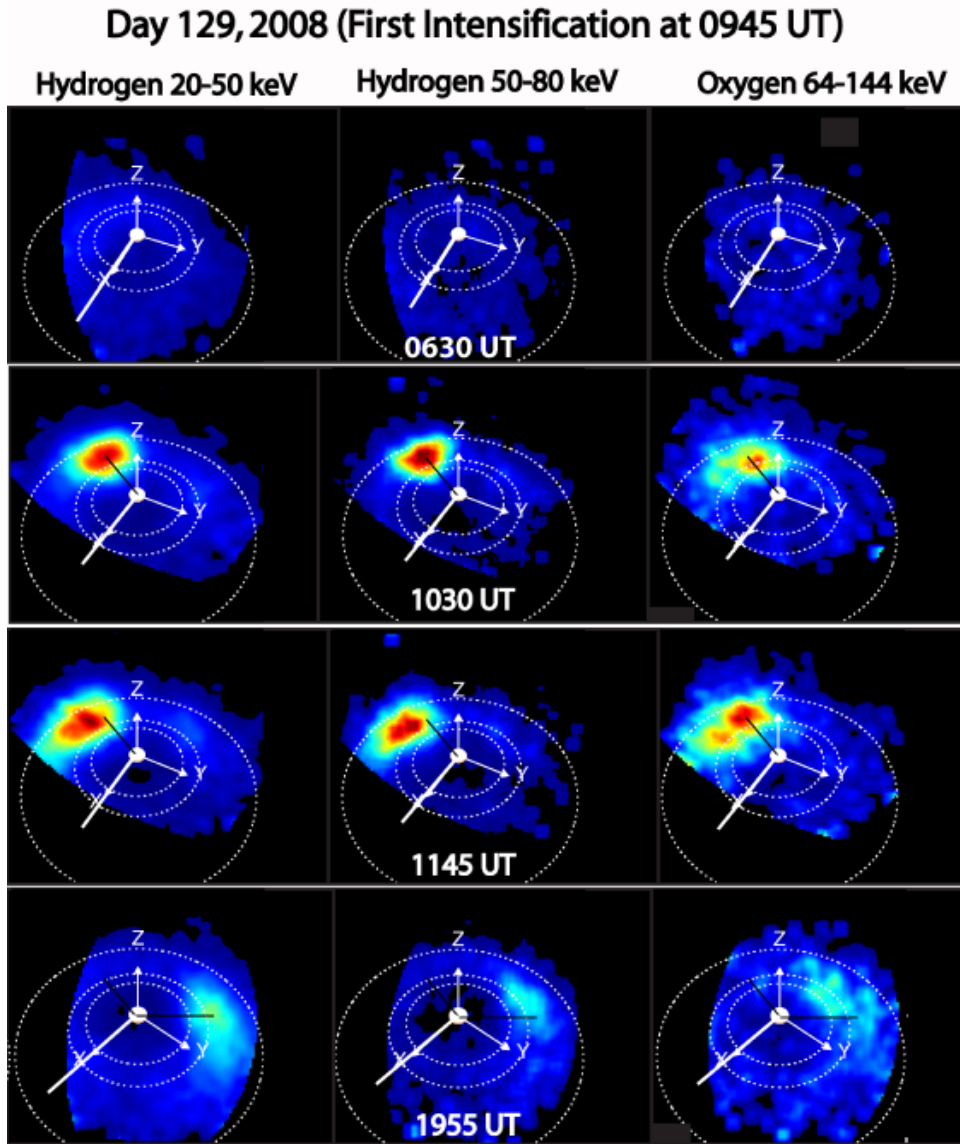


Figure 5.9: ENA Auroral Images: Saturn ENA Emission Shows Rotation of Peak Emission on 8 May 2008. This figure shows ENA emission from Saturn's magnetosphere on day 129, 2008. The heavy white line indicates the direction towards the sun in every image. The light white arrow points to dusk. Light white circles are orbits of Dione ($6.5 R_S$), Rhea ($8.5 R_S$) and Titan ($20 R_S$) for scale and perspective. Each column contains data for the species and energy indicated, and each row is from the time labeled in white in the center column. Each image shown is a 1 hour average comprised of 10 images (each with a 6 min. integration time) centered on the time shown. The black diagonal line in the images in the second row is drawn from the center of Saturn to the peak emission in the images. This line is repeated each column showing the initial enhancement in emission at the same location for each species and energy. The same line is drawn in the third row, to illustrate the rotation of the peak emission over the intervening 1.25 hours. In the bottom row, the line is repeated for reference, and a new line is drawn from the center of Saturn to the peak 20-50 keV H emission (left column). The same line is repeated in the center and right columns, illustrating the additional rotation experience by the higher energy source ions responsible for the ENA emission in those images. The figure is from [Mitchell et al., 2009a].

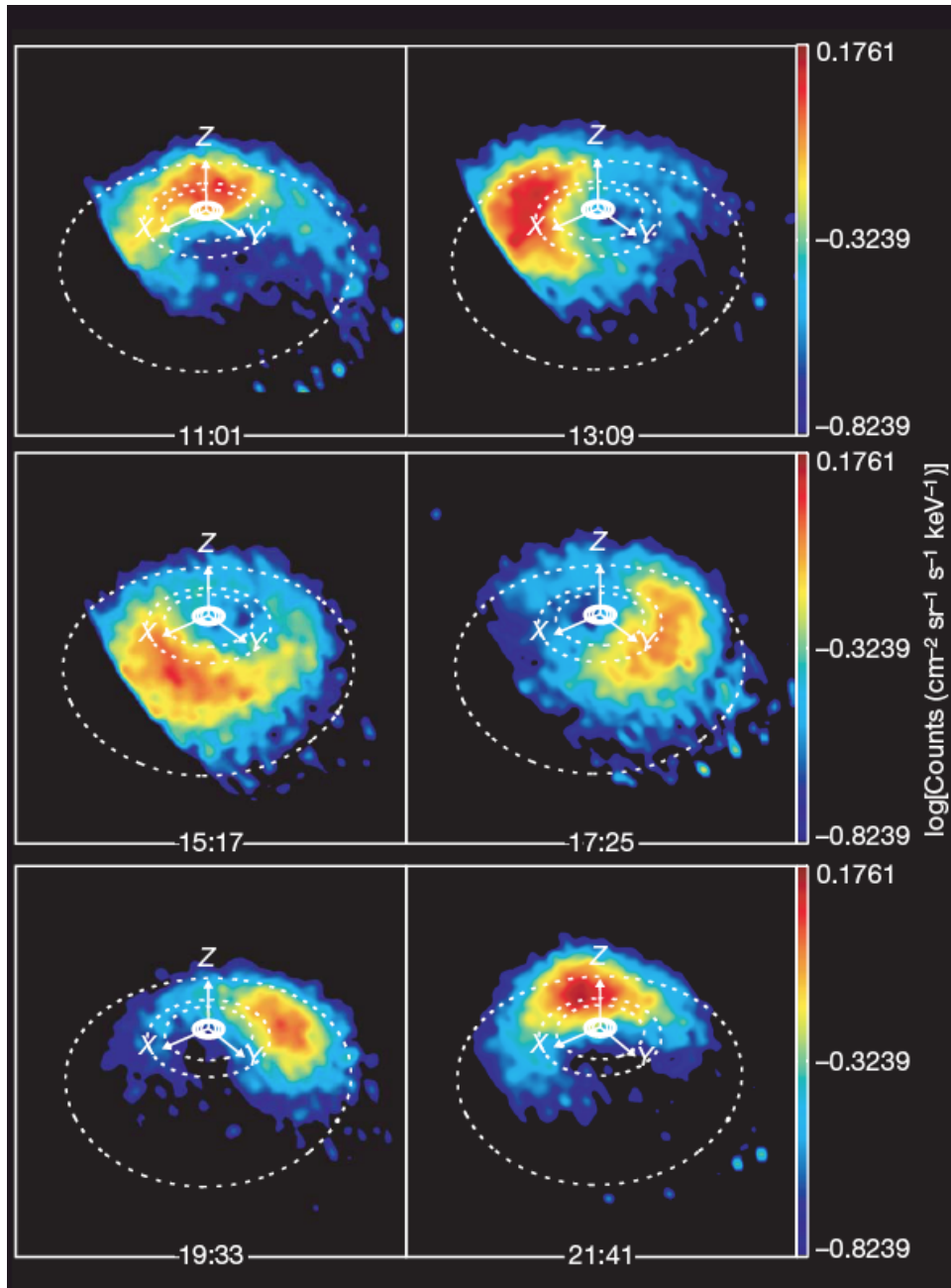


Figure 5.10: ENA Auroral Images: ENA Emission Covering Full Saturn Rotation on 24 February 2007. This figure shows a sequence of six ENA images in neutral hydrogen taken by INCA. This sequence of ENA images in the range 20-50 keV was obtained on 24 February 2007, and covered a full Saturn rotation. Cassini was located at $\sim 32^\circ$ latitude and $26 R_S$ from Saturn at local time $\sim 15:12$. Saturn is at the center, the X axis is pointing towards dusk, and Z is pointing along Saturn's spin vector. Dotted lines show the orbits of Dione ($6.2 R_S$), Rhea ($8.74 R_S$) and Titan ($20.2 R_S$) in proper perspective. Sharp edges on the left of the first three frames are attributable to the limit of INCA's field of view. The images are spaced at roughly 2-hour intervals. Figure reproduced with permission from [Krimigis et al., 2007b].

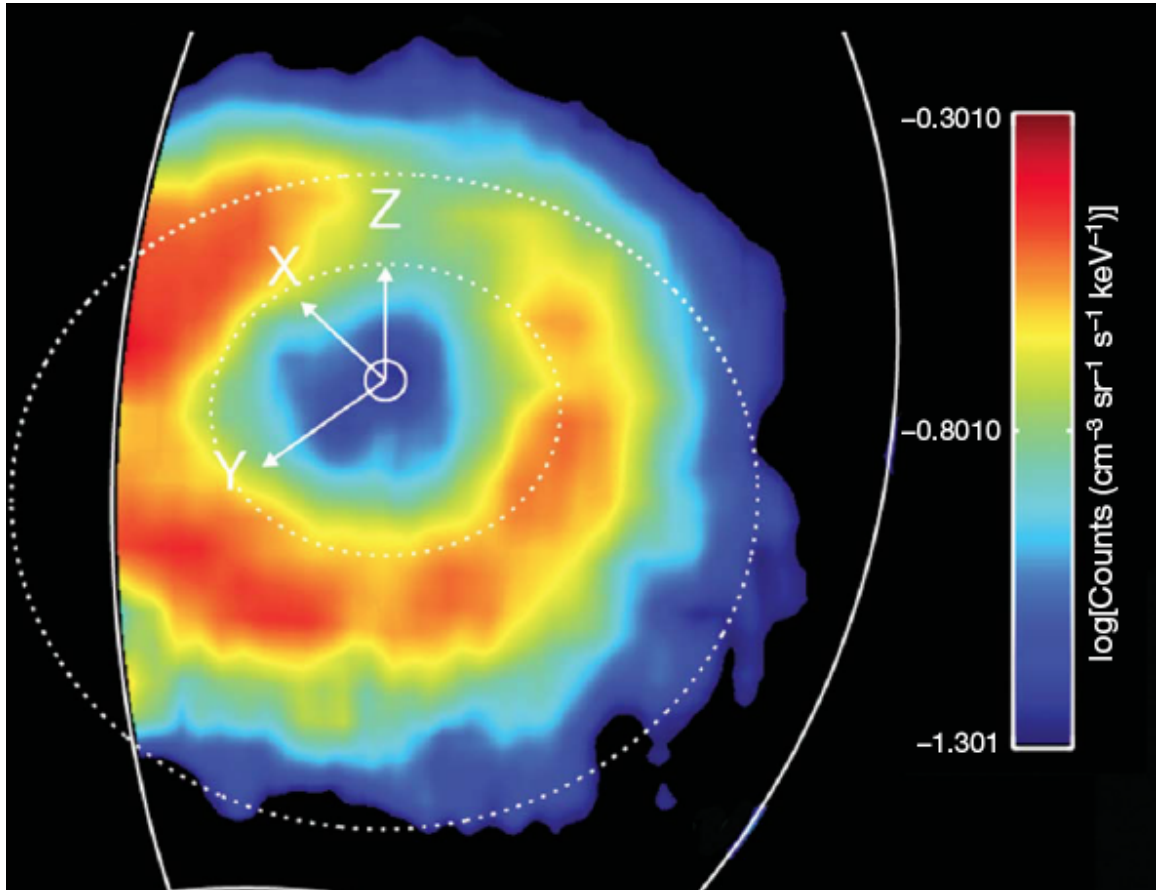


Figure 5.11: Ring Current on 19 March 2007. This figure shows an ENA image of the ring current as viewed from above the northern hemisphere. This image, in the range 20-50 keV, was obtained on 19 March 2007, with MIMI/INCA, at a latitude of $\sim 54.5^\circ$ and radial distance $\sim 24.5 R_S$. Saturn is at the center, and the dotted circles represent the orbits of Rhea ($8.74 R_S$) and Titan ($20.2 R_S$). The Z axis points parallel to Saturn's spin axis, the X axis points roughly sunward in the Sun-spin-axis plane, and the Y axis completes the system, pointing roughly towards dusk. The INCA field of view is marked by the white line and accounts for the cut-off of the image on the left. The image is a co-spatial average of several frames over the period 16:32-19:44 UTC (Universal Time). Figure is from [Krimigis et al., 2007b].

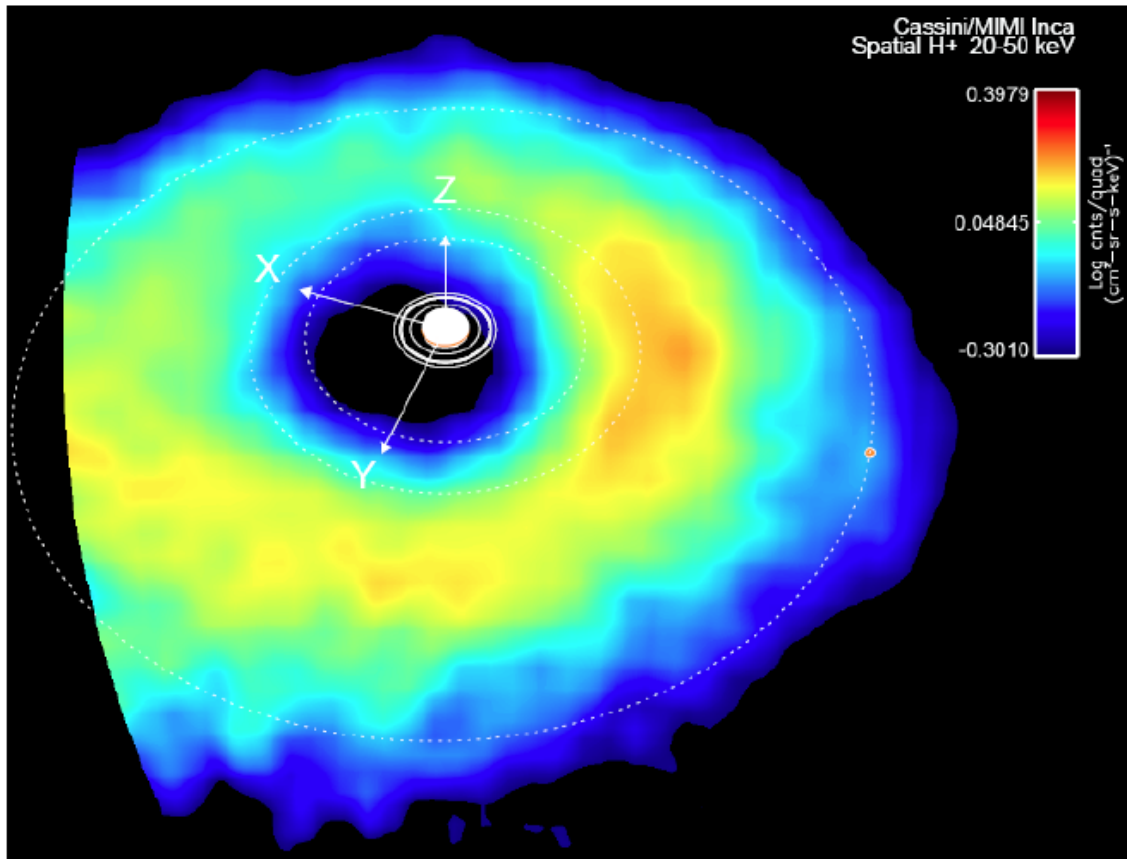


Figure 5.12: Ring Current on 28 February 2007. This figure shows an ENA image of the Saturnian ring current, as viewed from above the northern hemisphere. This image, in the range 20 to 50 keV, was obtained on 28 February 2007 with MIMI/INCA while Cassini was moving at latitude of 58° , at local time of 1902 and radial distance of $27.9 R_S$. Saturn is shown at the center, and the dotted circles represent the orbits of Dione ($6.29 R_S$), Rhea ($8.74 R_S$), and Titan ($20.2 R_S$). The z axis is parallel to Saturn's spin axis, the x axis points roughly sunward in the Sun-spin axis plane, and the y axis completes the system, pointing roughly toward the dusk. The INCA field of view is seen as the curved image cutoff on the left. The image is a cospatial average of several frames over the period between 13:42 and 00:22 UTC (following day). Figure from [Sergis et al., 2007].

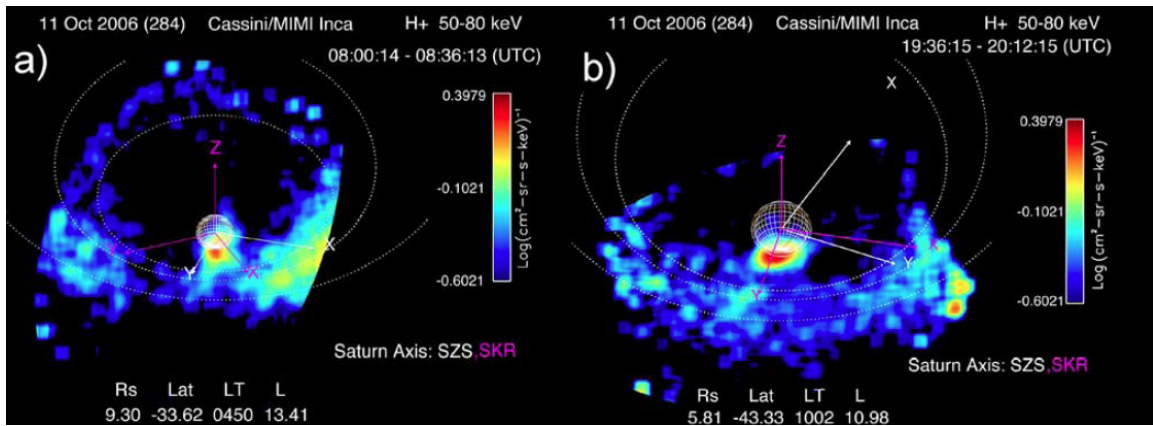


Figure 5.13: Intense Hydrogen Emission from Saturn’s South Polar Region on 11 October 2006. In this figure, panel **a**) is an ENA image of intense hydrogen emission from Saturn’s south polar region. Panel **b**) is an ENA image of south polar hydrogen emission. The orbits of Dione ($6.2 R_S$), Rhea ($8.74 R_S$) and Titan ($20.2 R_S$) are included as a reference. Axis corresponding to a fixed solar frame are shown in white (Z parallel to Saturn’s spin axis, X in the spin axis/Sun plane, pointed generally sunward, and Y completing the system). The violet axis also has Z aligned with the spin axis, but they rotate with the SLS3 coordinate system [Kurth et al., 2008]. The data is from day 284, 2006 and the hydrogen 50-80 keV channel. The figure is from [Mitchell et al., 2009a].

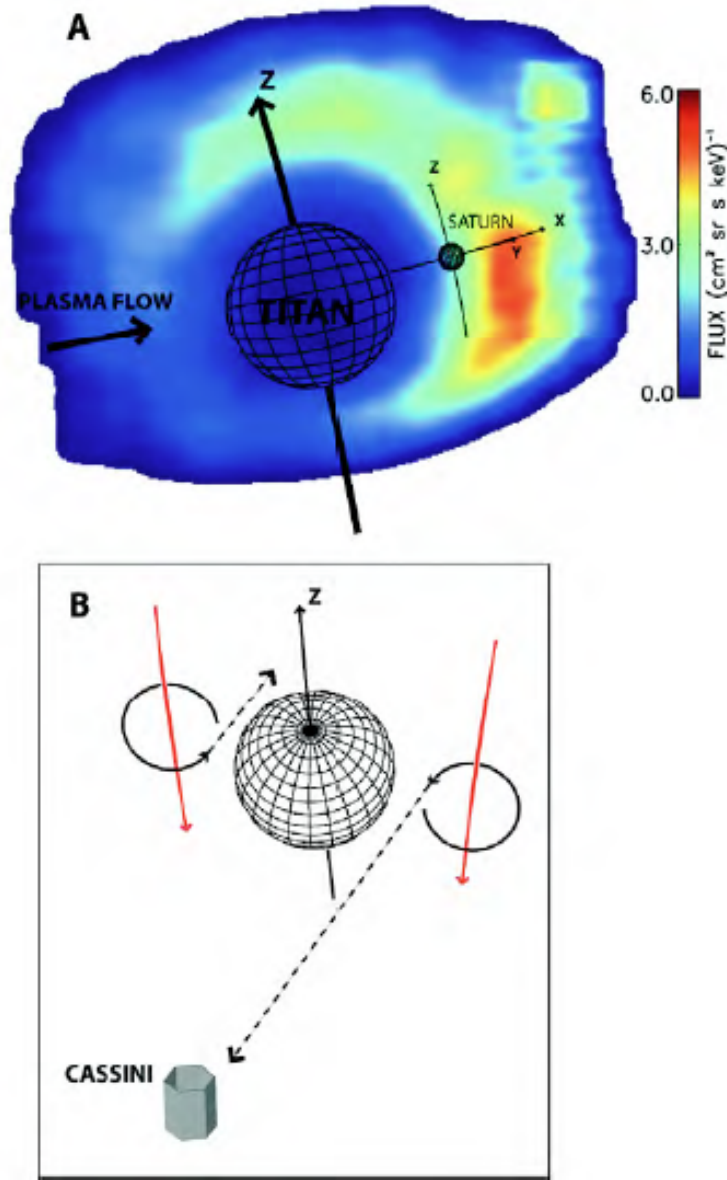


Figure 5.14: ENA Image of Titan's Exosphere on 26 October 2004. In this figure, image **A** is an ENA image in 20-50 keV H of magnetically trapped protons charge-exchanging in Titan's exosphere. Intensity is color coded on a linear scale from 0 to 10 ENA/($\text{cm}^2\text{-s-sr-keV}$). The limits of the emission are circumscribed by the INCA sensor $90^\circ \times 120^\circ$ FOV. The latitude-longitude grid locates Titan (north up) at 14:13:25 UT on 26 October 2004, the mid-point of the 8 minute image integration. Saturn is shown to the right of Titan. The ENA emission is dominated by the Titan interaction; general Saturnian magnetospheric emission is obscured by Titan's atmosphere. Schematic B shows proton gyration in a southward field at Titan. As the magnetic field guiding the proton to the left approached Titan, the right side of its circle of gyration encountered the dense atmosphere (absorbing the proton) before the left side, with the appropriate velocity vector to appear as an ENA at Cassini, reaches the altitude (exospheric density) of maximum likelihood for charge exchange. The figure is from [Mitchell et al., 2005].

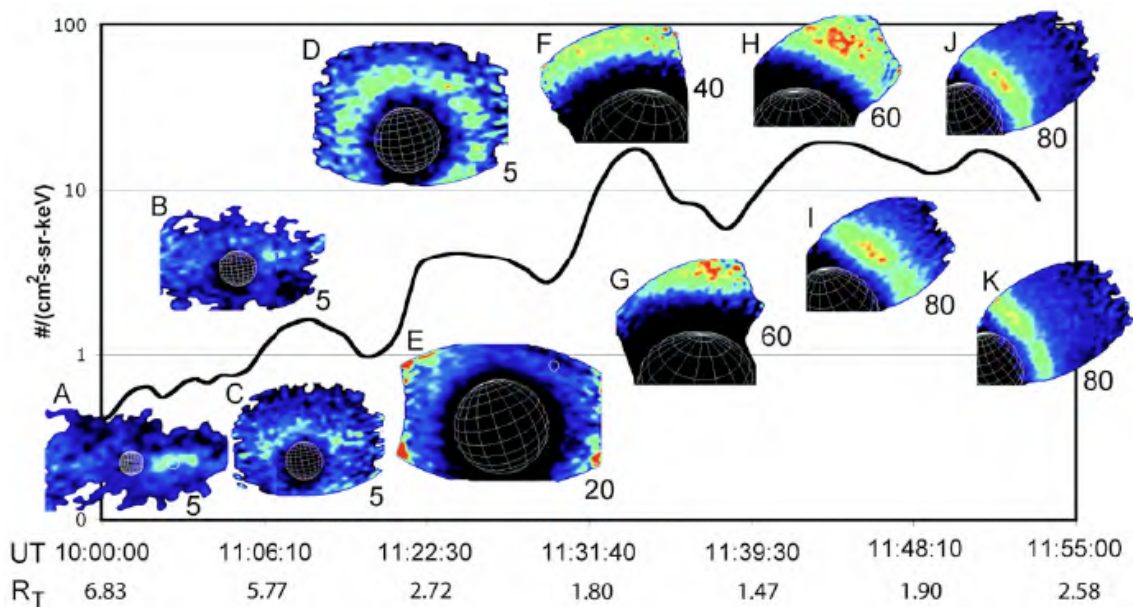


Figure 5.15: Titan Energetic Hydrogen Images on 13 December 2004. This figure shows energetic hydrogen images in the 20-50 keV passband during the 13 December, 2004 encounter. The black curve is the integrated ENA intensity in the same energy passband. The images are located according to their acquisition time. The timeline (horizontal axis) is not linear in time; rather, the time intervals along the axis have been scaled by the reciprocal of the spacecraft distance to Titan. This representation emphasizes the time around closest approach and provides a format through which the associated ENA images can be easily cross-referenced to both time and the variation in flux. Each image is scaled linearly in color (intensity) between 0 and the number immediately to the lower right, in ENA/(cm²-s-sr-keV). The figure is from [Mitchell et al., 2005].

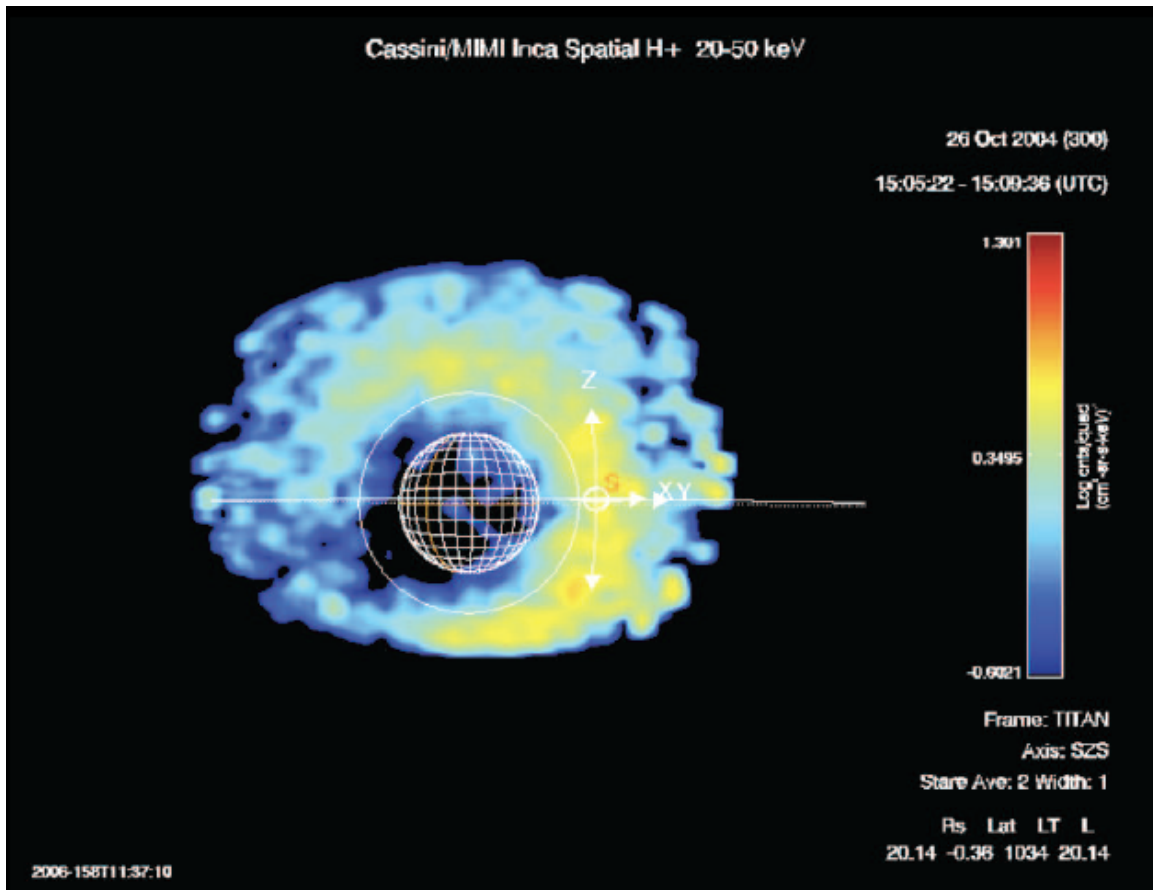


Figure 5.16: Titan ENA Hydrogen Flux on 26 October 2004. The figure shows ENA flux in the INCA hydrogen 20-50 keV range on 26 October 2004 during the Titan flyby of Rev A, also called TA. (Recall that Rev A refers to the first orbit of Cassini around Saturn and was renamed from Rev 1 after the first few orbits were re-planned to accommodate the Titan probe release issues.) A latitude-longitude grid is present for Titan, a small circle in white for Saturn. Axis corresponding to a fixed solar frame is shown in white (Z parallel to Saturn’s spin axis, X in the spin axis/Sun plane, pointed generally sunward, and Y completing the system). The figure is from [Wulms et al., 2010].

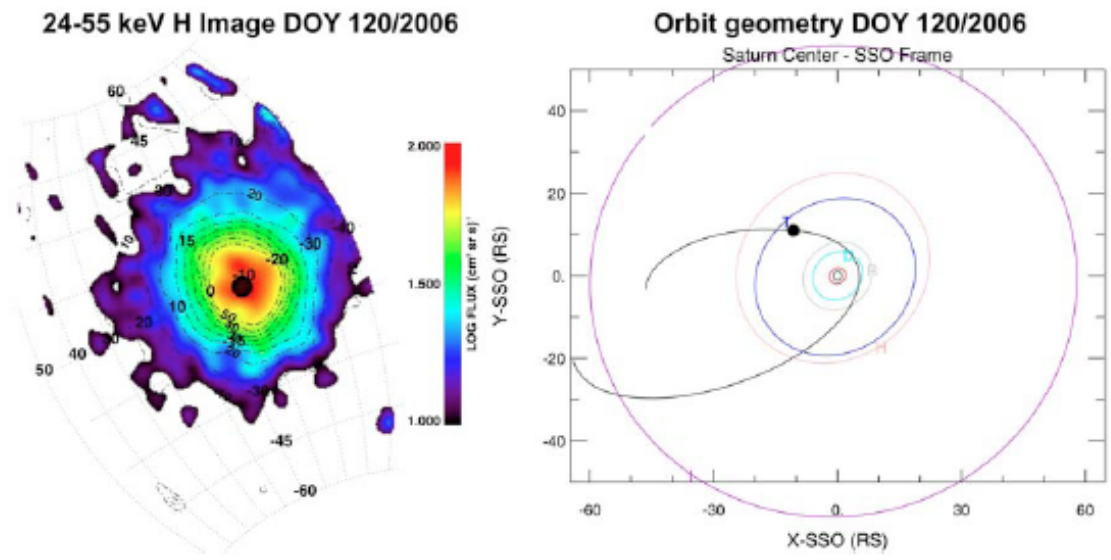


Figure 5.17: ENA Emission at Titan on 30 April 2006. The left panel in the figure shows color coded 24-55 keV Hydrogen integrated intensities obtained by the INCA imager on board Cassini during a close encounter at DOY 120, 2006. Labeled contours denote ENA intensities. Charge exchange process between Titan's neutral species and fast magnetospheric ions lead to the apparent intense ENA emissions around the moon. The right panel describes the orbit geometry during the Titan flyby on DOY 120, 2006, where the image on the left panel was obtained. Cassini is located at the post-dusk region at the equatorial plane, at an outbound orbit (black solid line) towards the magnetotail. Titan is located at $\sim 20.3 R_S$ at an orbit around Saturn (blue solid line), and the image data where obtained at a distance of $22.6 R_T$ from Titan. The figure is from [Brandt et al., 2009].

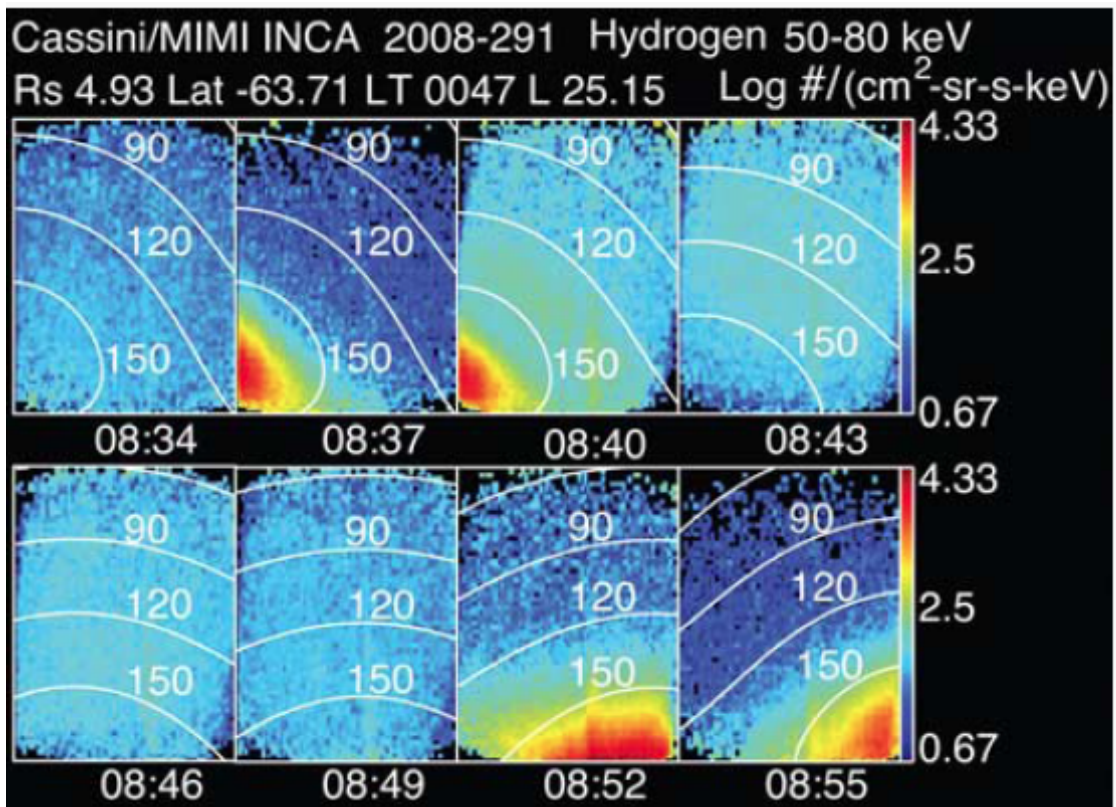


Figure 5.18: Field-aligned Ion Beam on 17 October 2008. The figure shows a very intense upward field-aligned ion beam, day 291, 2008. These are hydrogen 50-80 keV images from 08:34 (top left) to 08:55 (bottom left). Pitch angle is displayed from 30°, 90°, 120°, 150°. The figure is from [Mitchell et al., 2009c].

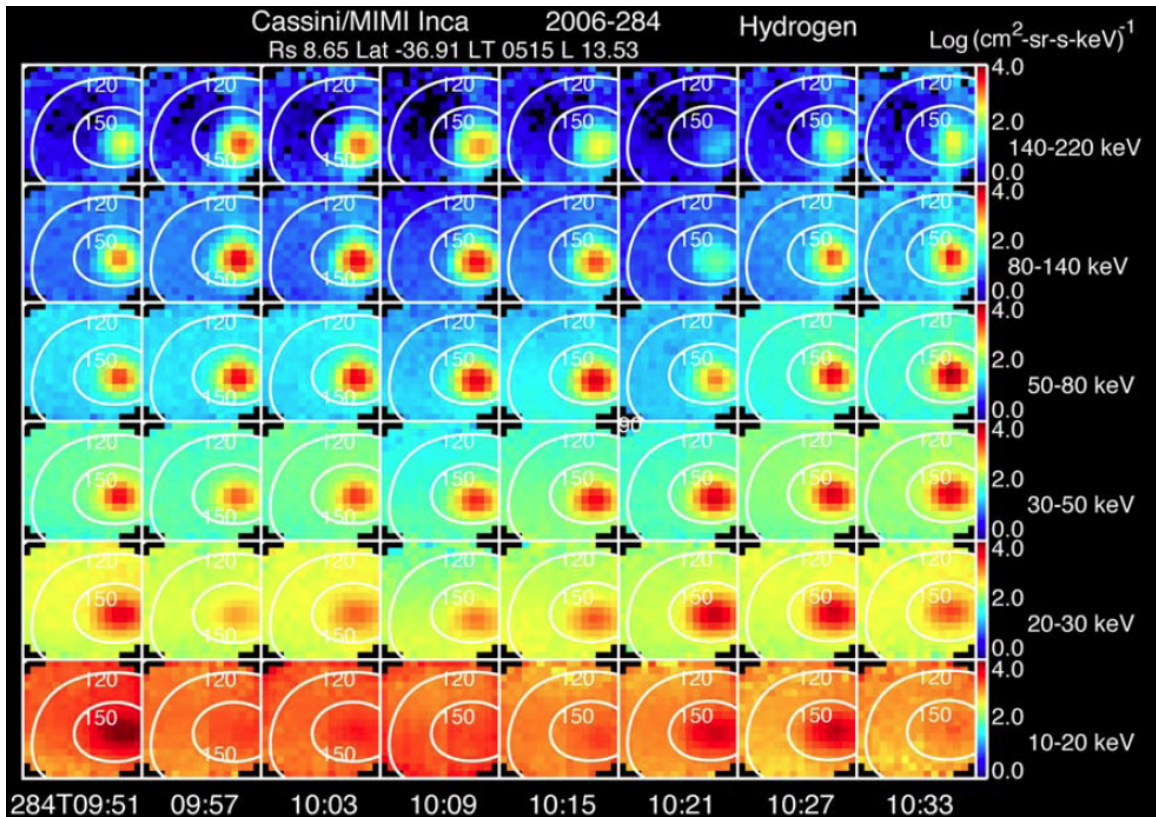


Figure 5.19: Long Duration Field-aligned Ion Beams on 11 October 2006. The figure shows a long-duration field-aligned ion event. Peak field-aligned intensity is mostly above 50 keV and often absent below 20 keV. This event continued, waxing and waning, for at least 9 hours as Cassini's inbound orbit remained within $13 < L < 14$. The data is from the hydrogen 140-220 keV (top row) to 10-20 keV (bottom row) on day 284, 2006. The figure from [Mitchell et al., 2009c].

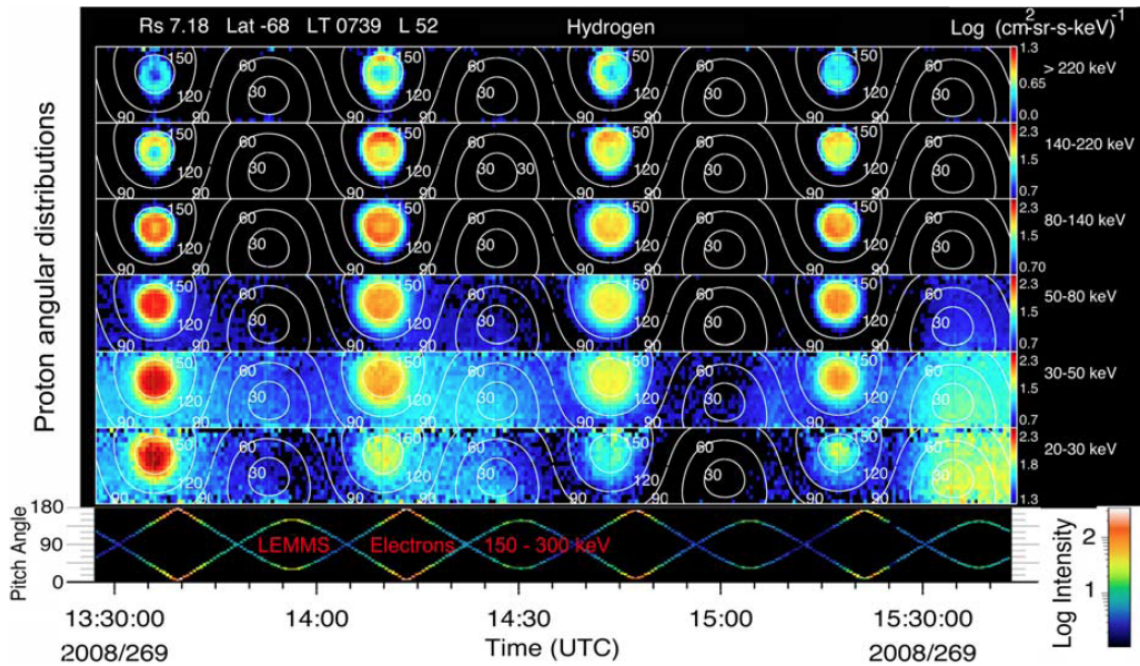


Figure 5.20: Anti-planetward field-aligned Ion Conic and Bidirectional Electron Beam on 25 September 2008. This figure shows anti-planetward field-aligned ion conic and bidirectional electron beam. Scale for the ion intensities is identical for all energies except for the first and sixth rows. Ion conics are clearly indicated at higher energies by the intensity depression about the field direction (180° pitch angle). Energetic electrons are clearly bidirectional field-aligned beams, with about a factor of 100 variation in intensity with pitch angle. The figure from [Mitchell et al., 2009c].

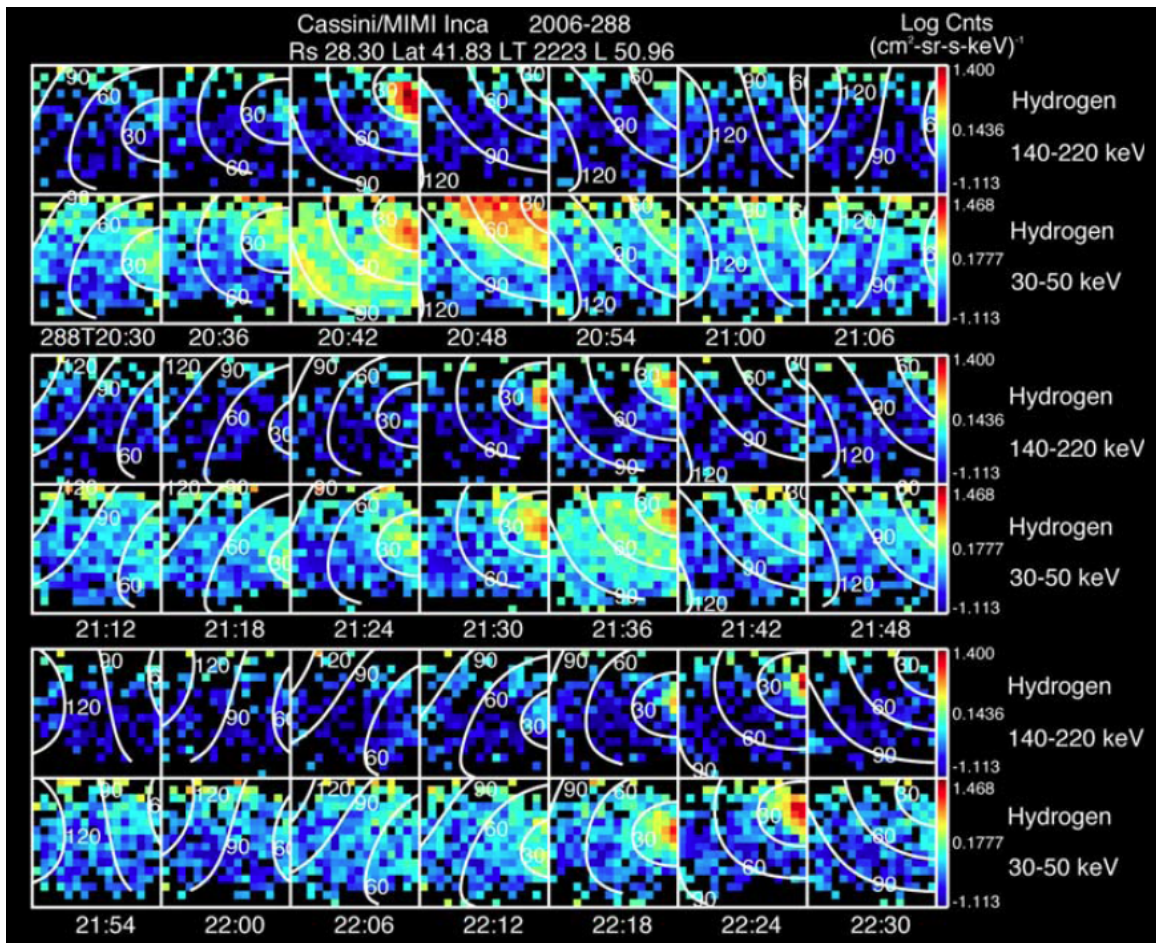


Figure 5.21: Ion Beams with Pitch Angle Contours 15 October 2006. In the figure, INCA sensor measures proton intensity in 16 x 16 pixel maps covering 90° x 120° field of view (known as angle-angle plots). Two of its eight energy channels are shown, with pitch angle contours overlain. Each time pitch angles close to zero degrees are covered, high-intensity field-aligned ions appear at energies between 30 and 200 keV. The figure from [Mitchell et al., 2009c].

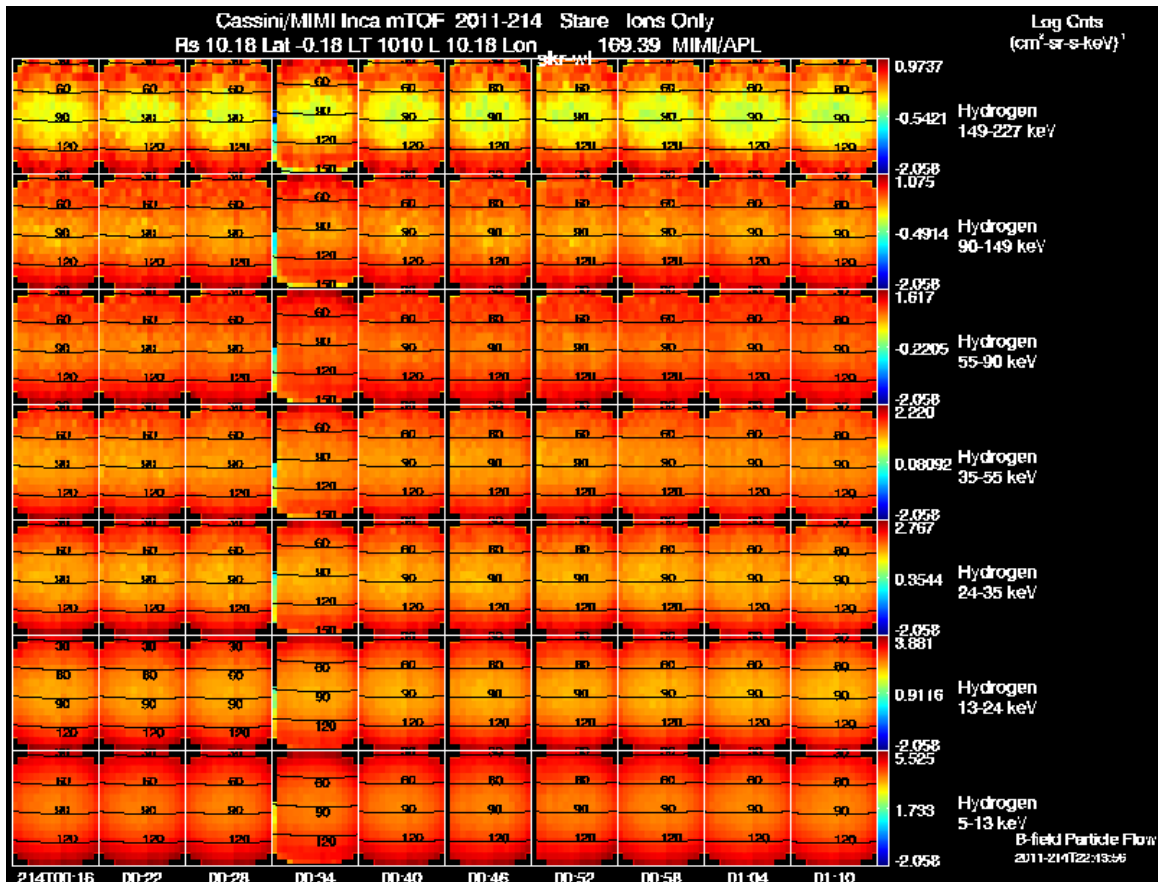


Figure 5.22: Undesirable Features: Hydrogen Pixel Maps Demonstrating Saturated Count Rates on 2 August 2011. The figure shows INCA hydrogen angle-angle plots of proton intensity that demonstrate saturated count rate. Seven of its eight energy channels, from 149-227 keV (top row) to 5-13 keV (bottom row) are shown, with pitch angles overlain. The pitch angles shown cover 30°, 60°, 90°, 120°, 150°. The time of the images ranges from 00:16 (left) to 01:10 (right).

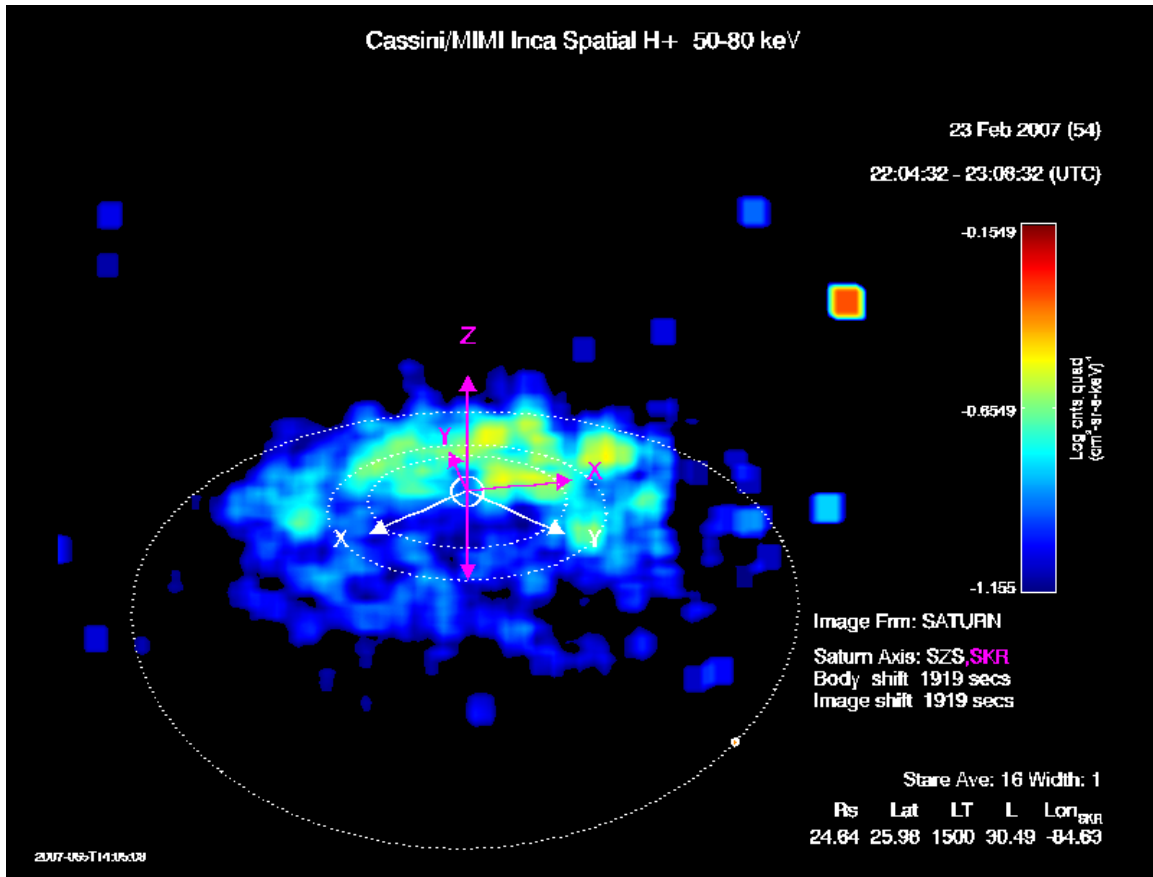


Figure 5.23: Undesirable Features: High Edge Pixel Image on 23 February 2007. The figure shows an ENA image of hydrogen emission, which demonstrates a high edge pixel on the upper right. The orbits of Dione ($6.2 R_S$), Rhea ($8.74 R_S$) and Titan ($20.2 R_S$) are included as a reference. Axis corresponding to a fixed solar frame are shown in white (Z parallel to Saturn's spin axis, X in the spin axis/Sun plane, pointed generally sunward, and Y completing the system). The violet axis also has Z aligned with the spin axis, but they rotate with the SLS3 coordinate system [Kurth et al., 2008]. The data is from day 23 February, 2007 and the hydrogen 50-80 keV channel.

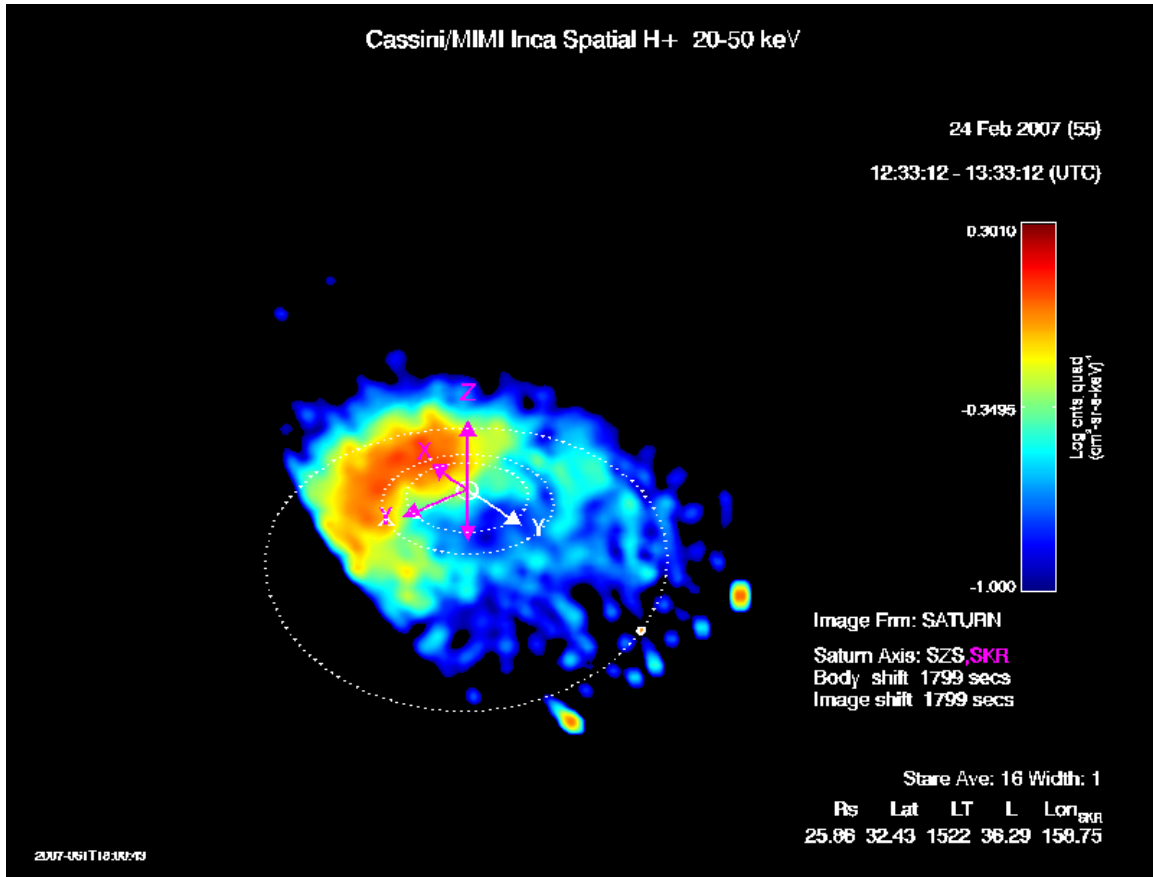


Figure 5.24: Undesirable Features: High Edge Pixel Image for Hydrogen 20-50 keV on 24 February 2007. The figure is another example of a high edge pixel on the middle right and center bottom. The orbits and axis are the same as in Figure 5.23. The data is from day 24 February 2007 and the hydrogen 20-50 keV channel.

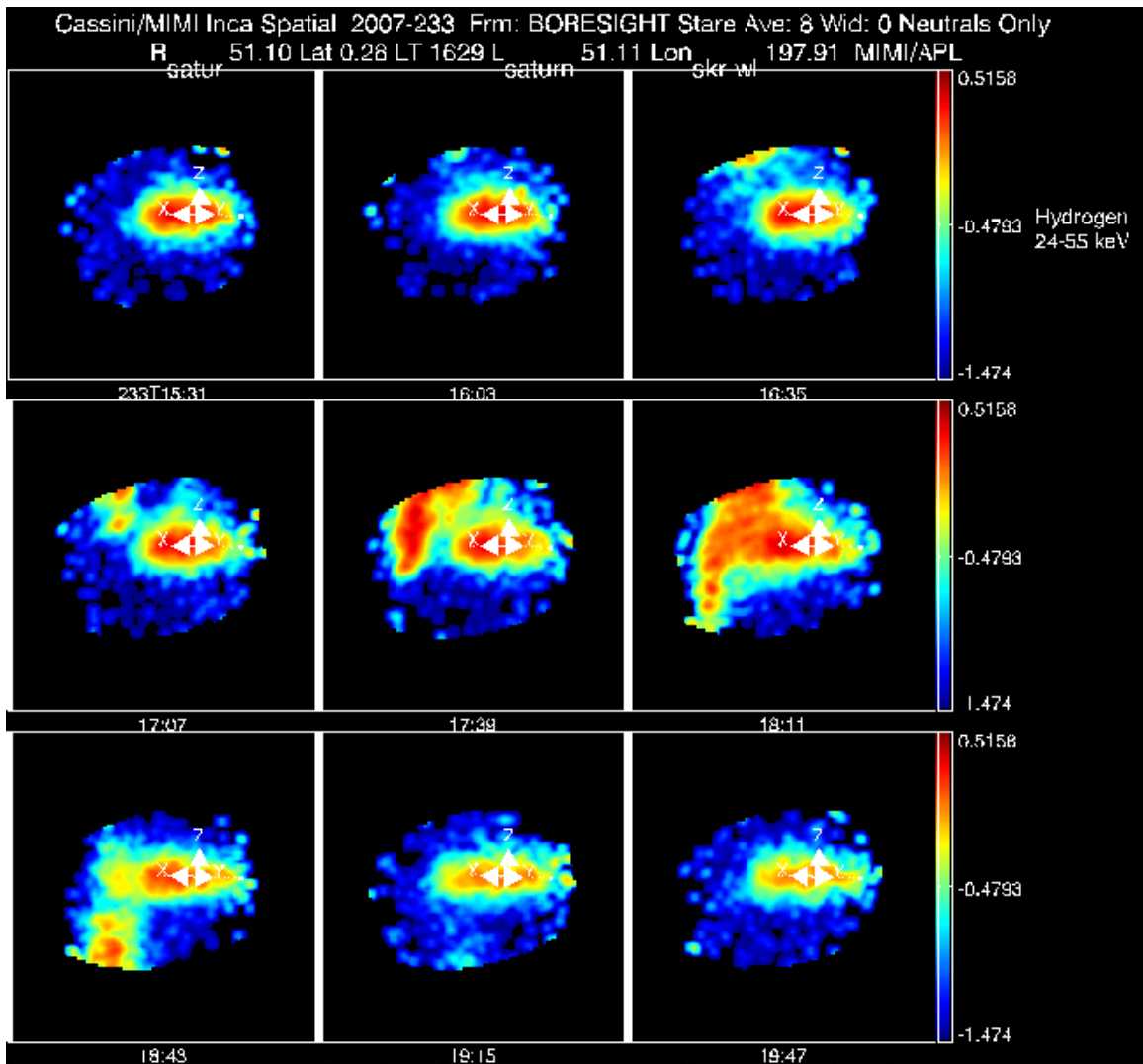


Figure 5.25: Undesirable Features: Oxygen Contamination of Hydrogen Image on 21 August 2007. The figure shows a sequence of nine ENA images in neutral hydrogen taken by INCA which demonstrate oxygen contamination. This sequence of ENA images in the range 24-55 keV was obtained on 21 August 2007. INCA boresight is the X axis, Z is pointing along Saturn's spin vector and the Y axis completes the right-handed frame. Sharp edges on the top and bottom are attributable to the limit of INCA's field of view. The images are spaced at roughly half hour intervals. The contamination is strongest in the frames at 17:39, 18:11, and 18:43, but is present in all of the frames shown except the first and last. The oxygen background contamination can be recognized because it typically contaminates the lower energy hydrogen images, but does not contaminate the low energy oxygen images, and has a minimal impact on the higher energy (55-90 keV) hydrogen images. Thus if a feature appears peculiar, and is seen almost exclusively in the lower energy hydrogen images, it is likely oxygen contamination. It can also be recognized by examining the INCA pulse height data from the same interval.

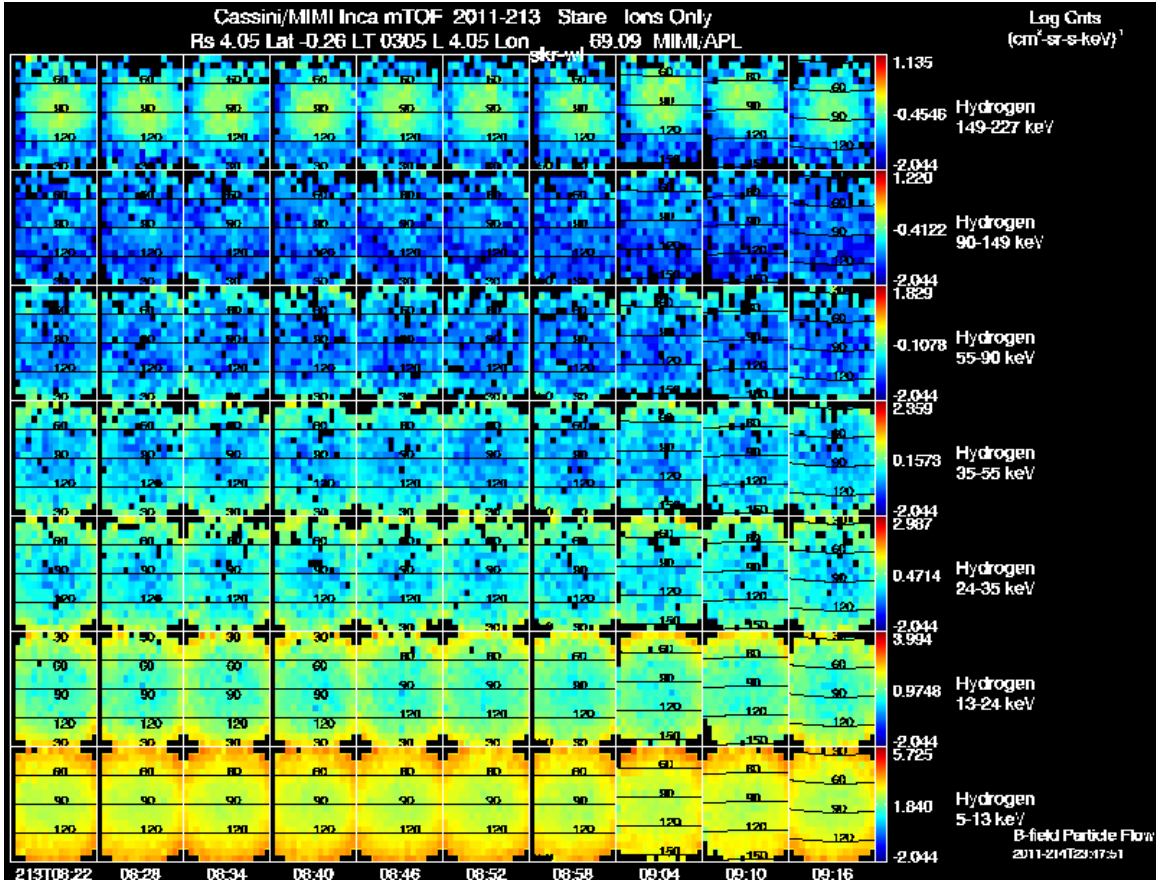


Figure 5.26: Undesirable Features: Electron Background in Ion Image on 1 August 2011. The figure shows INCA hydrogen angle-angle plots that demonstrate electron background. Seven of its eight energy channels, from 149-227 keV (top row) to 5-13 keV (bottom row) are shown, with pitch angles overlain. The pitch angles shown cover 30°, 60°, 90°, 120°, 150°. The time of the images ranges from 06:22 (left) to 09:16 (right). The electron background signature differs from one energy, or time-of-flight, channel to the next. It is most evident as an enhancement about the perimeter of the frame at the lowest energy for this example, but the central enhancement in the angular distributions for the highest energy is also a response to the electron background. This kind of background is only seen inside about L=6 Rs.

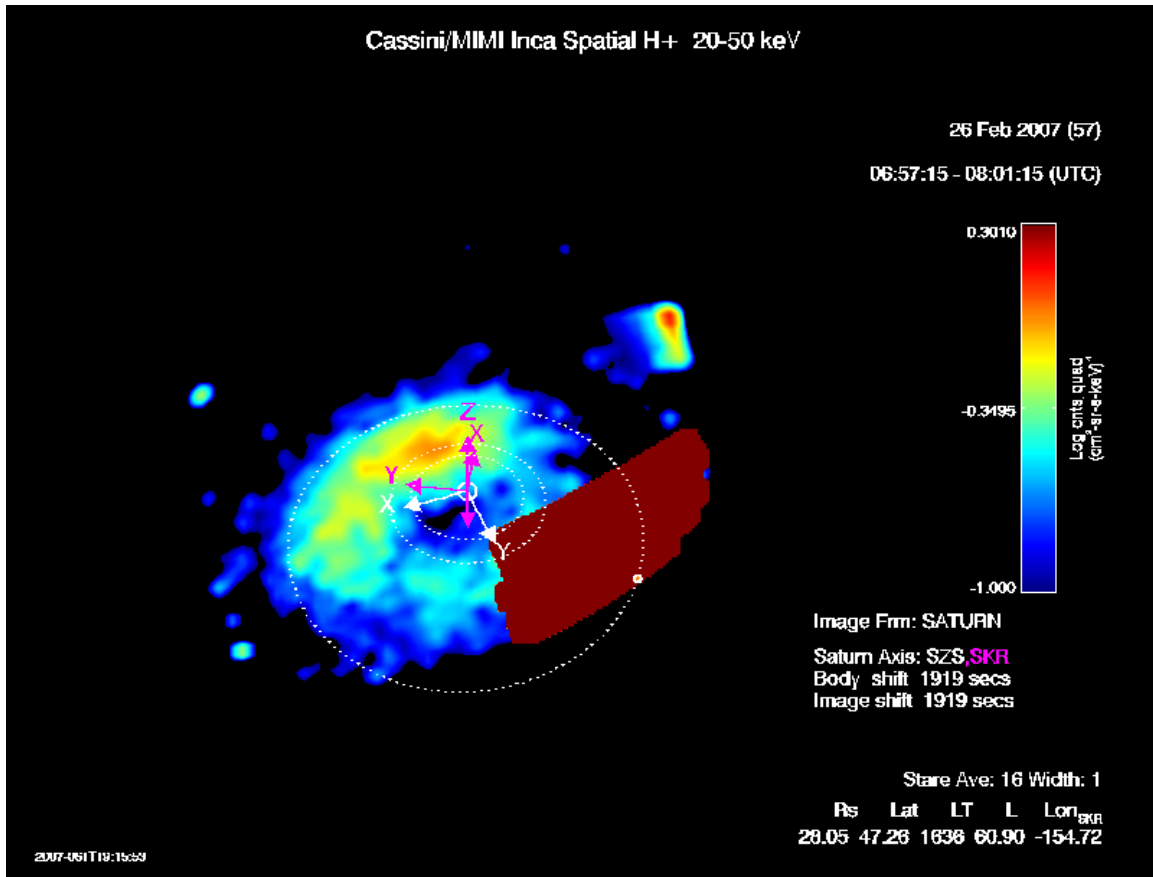


Figure 5.27: Undesirable Features: SSR Bit Errors on 26 February 2007. The figure is an ENA image of hydrogen emission, which demonstrates the effect of SSR bit errors on the right side of the image. The orbits of Dione ($6.2 R_S$), Rhea ($8.74 R_S$) and Titan ($20.2 R_S$) are included as a reference. Axis corresponding to a fixed solar frame are shown in white (Z parallel to Saturn's spin axis, X in the spin axis/Sun plane, pointed generally sunward, and Y completing the system). The violet axis also has Z aligned with the spin axis, but they rotate with the SLS3 coordinate system [Kurth et al., 2008]. The data is from day 26 February, 2007 and the hydrogen 20-50 keV channel.

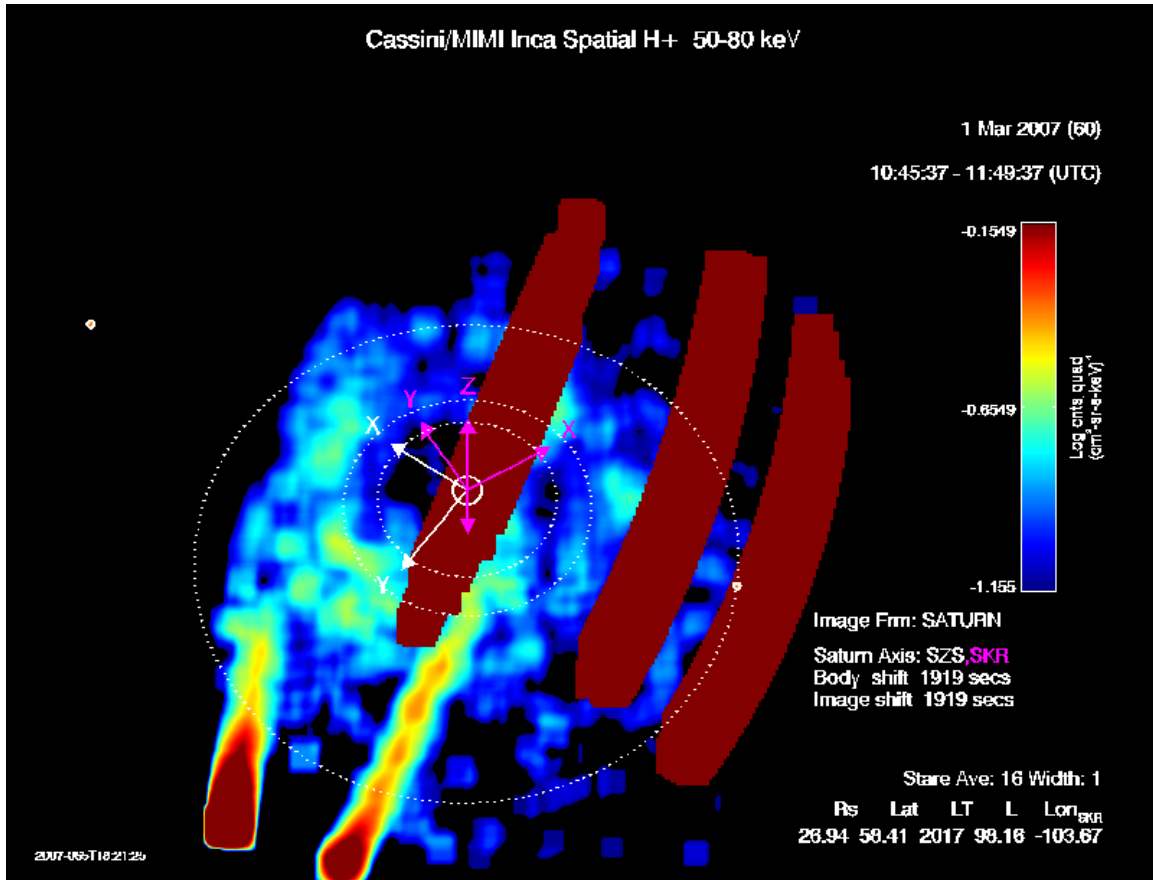


Figure 5.28: Undesirable Features: SSR Bit Errors on 1 May 2007. The figure is an ENA image of hydrogen emission that demonstrates the effect of SSR bit errors throughout the image. The orbits and axis are the same as in Figure 5.27. The data is the hydrogen 50-80 keV channel and was taken on 1 March, 2007.

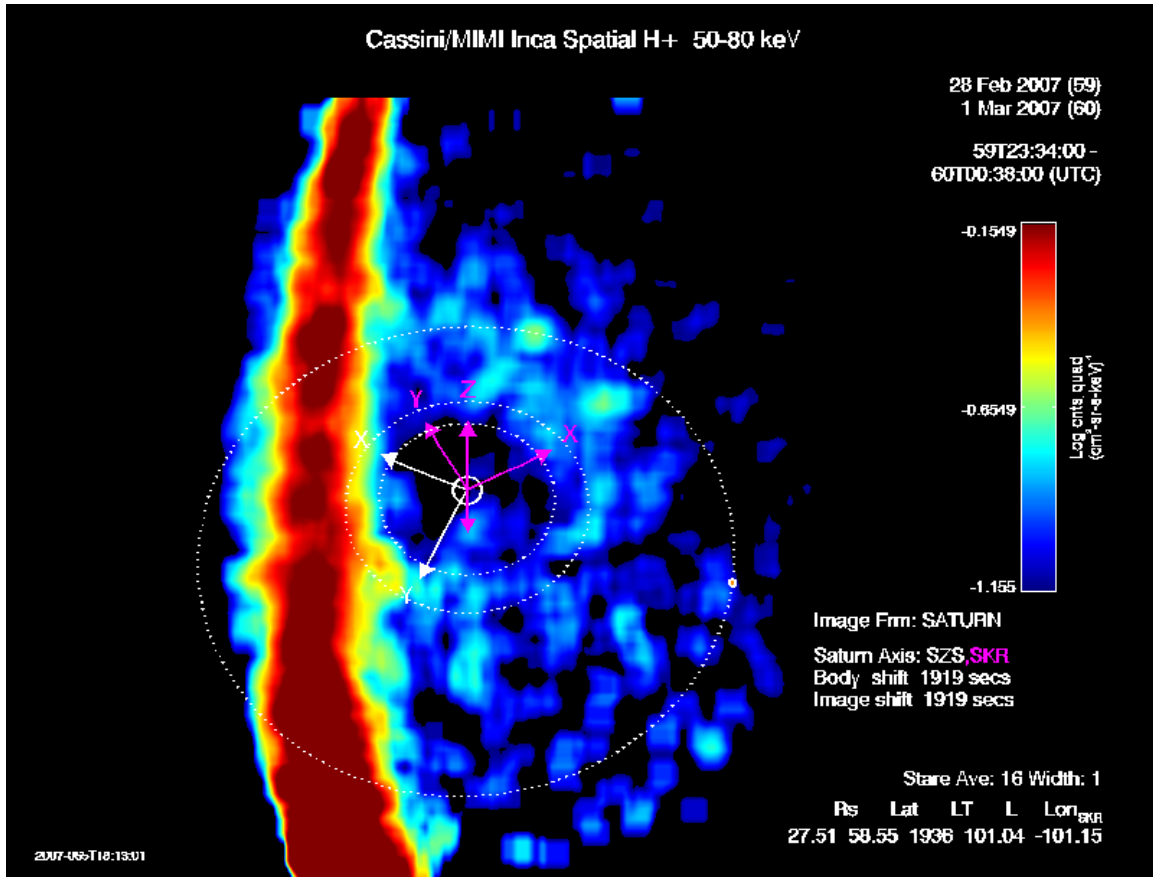


Figure 5.29: Undesirable Features: Sun Contamination on 28 February and 1 March 2007. The figure is an ENA image of hydrogen emission, which demonstrates the effect of sun contamination throughout the image. The orbits and axis are the same as in Figure 5.27. The data is from 28 February to 1 March, 2007 and the hydrogen 50-80 keV channel.

Section 6

Obtaining Calibrated Data

Several options exist for obtaining and calibrating MIMI PDS data. A simple download tool has been created that makes it easy to copy MIMI data files from the PDS archive to a local computer. This tool is also capable of applying the calibration procedures for LEMMS and CHEMS data. For INCA data, a set of IDL routines is available that will calibrate PDS files that have already been downloaded. Finally, a Java-based tool used by the MIMI team has been outfitted to work with the PDS data. This tool allows users to create exploratory plots and save the plot contents (i.e., calibrated PDS data) to local files. These three tools are described below.

6.1 Data Download Tool

Figure 6.1 shows the main screen of the download tool, available from the MIMI site devoted to the PDS data (http://sd-www.jhuapl.edu/CASSINI/data_auxiliary.html). This program is a Java program, and will run on all major platforms. It is deployed using Java WebStart, and so to run the program, just navigate to the URL mentioned above, and click on the link to the download tool. The program will be automatically installed and will start running.

Selecting data involves three steps. First, the user selects one or more of the nine available data types. Next, a list of time ranges is entered. Third, a local directory is provided where the PDS data will be copied. The resulting files on the user's computer will mirror the directory structure of the PDS data. Providing the same local directory each time the program is run enables the program to see what you have already downloaded. Any request for data that you already have will only cause new data to be downloaded in cases where the remote data has changed.

For LEMMS and CHEMS data types, it is also possible to apply the calibration to the downloaded files. The "Select Calibration" button next to each of these data types lets you choose settings relevant for the calibration of each data type. "The Get Data" button at the bottom will still cause the raw, uncalibrated files to be downloaded, but then for each raw data file, there will also be a corresponding calibrated data file. The calibrated data files are placed in a separate directory structure that parallels the PDS directories. The calibrated data are in the same format as the PDS data, but the numbers in the files have been converted to physical units.

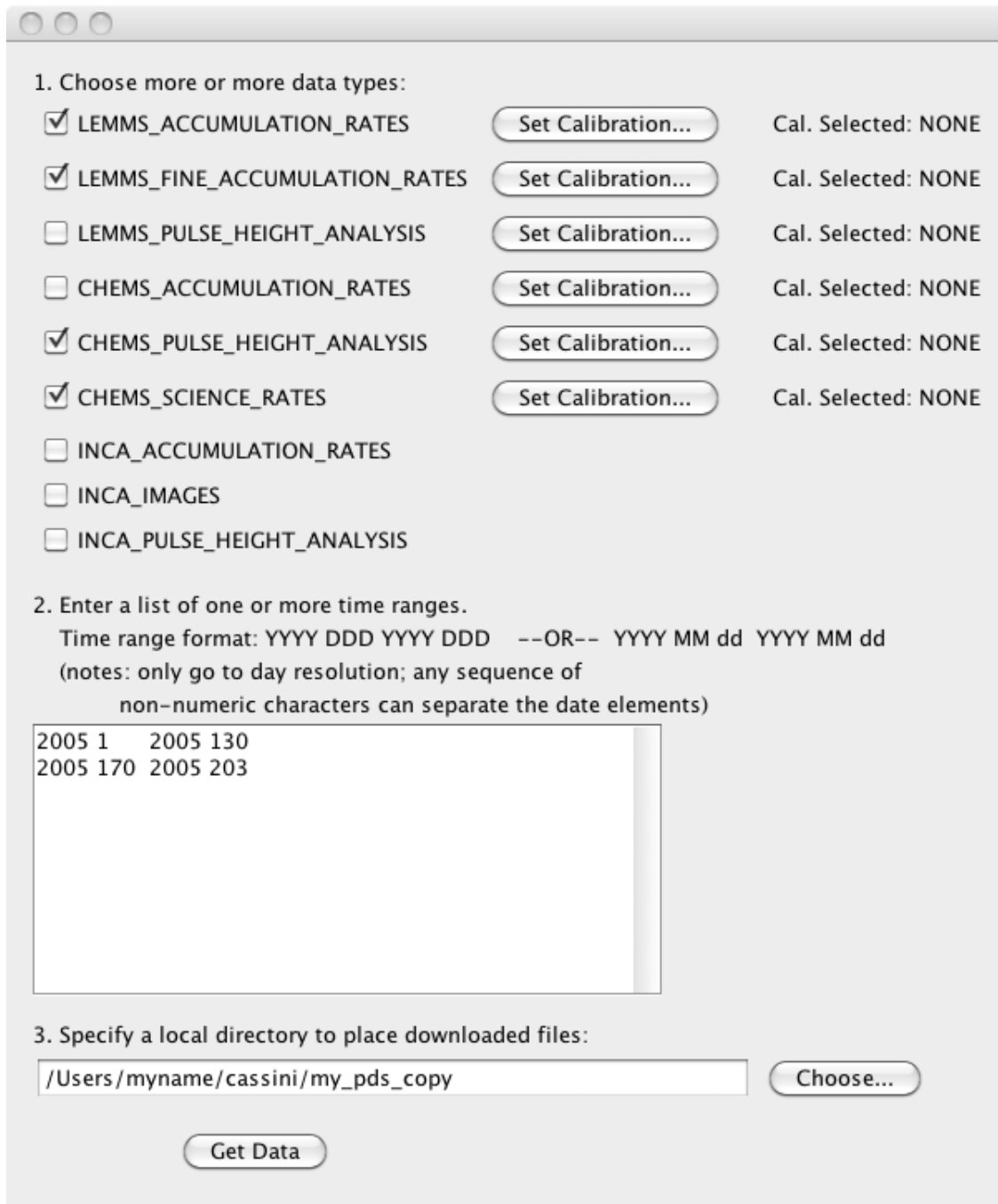


Figure 6.1: This tool creates a mirror of the directory structure and files at the PDS for any selected data types over the time ranges provided. The user also chooses the root directory for the downloaded files. The expected usage is to provide the same local directory each time so that any files already downloaded will not be downloaded again (unless their date stamp on the remote server has changed).



Figure 6.2: The main screen of MIDL. Pre-made summary plots are shown on the right as a quick way to explore the data. The left panel offers options for choosing data to view and the tool with which to view it. Key features are circled and labelled A through F. Feature A is the time range selector for the summary images. There are many different types of pre-made summary images, and the summary image selector (B), lets you choose the one to view in the right panel.

Users should beware that downloading large amounts of data may take a significant amount of time. In order to become accustomed to the file sizes and download times, it is suggested to first try downloading a small amount of data (i.e., a few days).

6.2 INCA IDL Routines

Chapter 5 describes how to download and use the IDL routines that use INCA data. The download tool in the previous section can be used to obtain the uncalibrated files, and then the IDL code can be pointed at the local mirror.

6.3 MIMI Analysis Tools - MIDL

The Mission Independent Data Layer (MIDL) tool reads raw MIMI data and applies appropriate calibration procedures on-the-fly. The tool is primarily meant for quick browsing and data exploration, and it also allows users to download digital versions of the fully calibrated data in any of

the plots it makes. Some of the datasets accessible through MIDL are team-specific and require a password to access, but all of the PDS datasets are openly available.

MIDL is launched from the MIMI page devoted to the PDS:

http://sd-www.jhuapl.edu/CASSINI/data_auxiliary.html

Like the download tool, MIDL uses Java WebStart, and so clicking on the MIDL link will install and run the program. Note that MIDL uses the PDS data directly, and you do not have to use the download tool first.

The main screen of MIDL is shown in Figure 6.2. The left side of the screen shows data selection options, and the right side shows a summary plot. Different features of the tool are circled and labelled with letters **A** through **F**. The time range chooser mechanism for the summary plots (feature **A**) is just above the summary plot itself. The “Previous” and “Next” buttons allow users to flip through summary plots and visually search for features. There are many different flavors of summary plots for MIMI data, and users can choose which type of summary plot to show in the summary plot panel. To use a different flavor of summary plot, select it from the list on the left panel titled “Summary Image Types for Cassini” (feature **B**).

While the summary plots provide pre-made views of the data, the main purpose of MIDL is to allow users to create more detailed plots of specific time ranges. The list of possible datasets to use for custom plots is on the left in the middle and is labelled “Datasets for Cassini” (feature **C** in Figure 6.2). The list of plot tools is feature **D**. To create a plot, select a data type (**C**) and a plot tool (**D**), and then choose a time range. The data time range selection panel (**E**) allows a specific time range to be entered manually, or you can select a time range graphically by moving the vertical red sliders which appear on top of the summary image. The pitch angle tool requires that you choose two datasets – one of energetic particles and one of magnetic field. In this case, however, if you forget to choose a magnetic field dataset, the tool will choose the first magnetic field in the list. For some datasets, you must also choose a coordinate frame (feature **F**). A message dialog will appear if the data does not exist in the chosen frame.

Having chosen a dataset (and possibly a coordinate frame), a plot tool, and a time range, click the “Launch Selected Tool” button under the list of plot tools (**D**). Each plot tool launches a new window with data loaded from the time range you selected.

For some datasets, there are options affecting how the data is presented. When you select (i.e., click on) a dataset, the “Instrument Settings” button below the list of datasets will become active, and clicking the instrument setting button will open a dialog window with options for calibrating that dataset. Typical choices include the desired calibration level (counts or counts/sec or differential intensity) and whether or not background subtraction is desired.

6.3.1 Line Plots

The line plot tool for MIDL is shown in Figure 6.3. The time range of the plot is controlled by the buttons and entry boxes within feature **A**. The “Next” and “Previous” buttons shift the time range to the next adjacent range. The particle channels to include in the plot are chosen using feature **B**, which allows selection of a single channel, all the channels in one or more spectra, or a custom list of channels. To apply averaging or other filtering options to the data in the plot, click the “Configure” button (feature **C**), and when a list of filters appears, users can choose filters that do time averaging, quartile filtering, pitch angle filtering, etc. The filters are applied in the

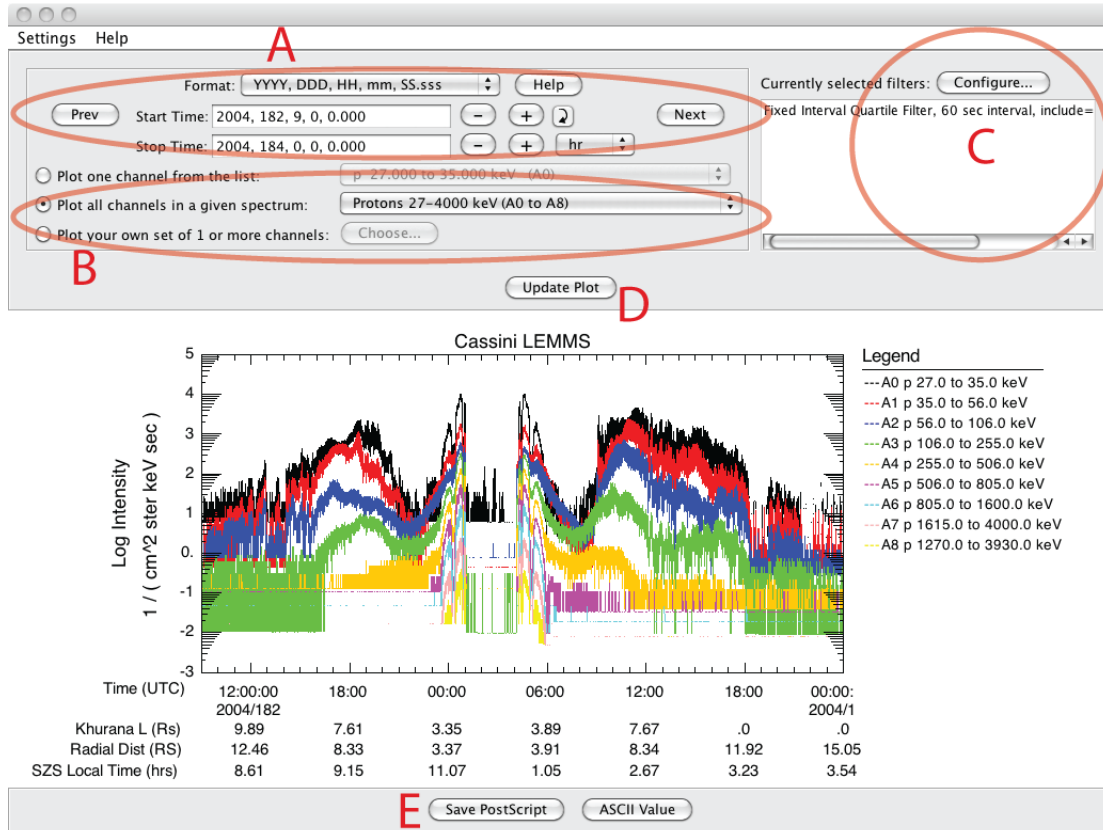


Figure 6.3: The tool for creating line plots of particle data. Feature **A** allows the time range to be changed. Particle channels to plot are selected using feature **B**. Filters (time averaging, pitch angle filtering, etc.) are chosen using **C**. The “Update Plot” (**D**) button applies any changes and regenerates the plot. The plot can be saved as ASCII data or as a Postscript file (**E**). The “Settings” menu near the top of the plot panel allows selection of x-axis labels and also offers other tweaks to the plot itself.

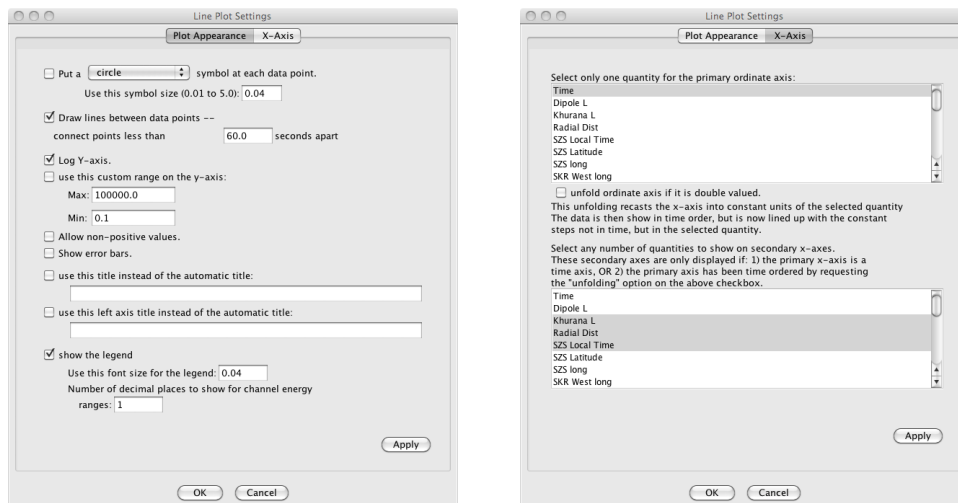


Figure 6.4: The two tabbed panels available through the “Settings” menu in the MIDL line plot tool. The first panel allows the plot symbol and y-axis features to be changed. The second panel configures the x-axis. Note that the x-axis does not need to represent time, but can be distance or L shell. Additionally, any number of secondary labels can be applied to the x-axis.

order selected, so any pitch angle filtering should be applied first, because time averaging does not preserve the directional information for the particles. To refresh the plot and apply any changes (to filters or desired particle channels, etc.) click the “Update Plot” button (**D**).

The details of the plot itself can be changed using the “Settings” menu at the top left of the line plot tool.

The line plot in Figure 6.3 shows several rows of labels on the x-axis. These are selected using the “Settings menu” at the top left of the panel. The axis settings panel is shown in Figure 6.4. Notice that it is possible to choose something other than time as the ordinate value for the x-axis. Often it is helpful to choose radial distance or L shell instead of time. Regardless of the primary ordinate, any number of secondary labels can be chosen for the x-axis, and these appear in the bottom panel of the axis settings dialog.

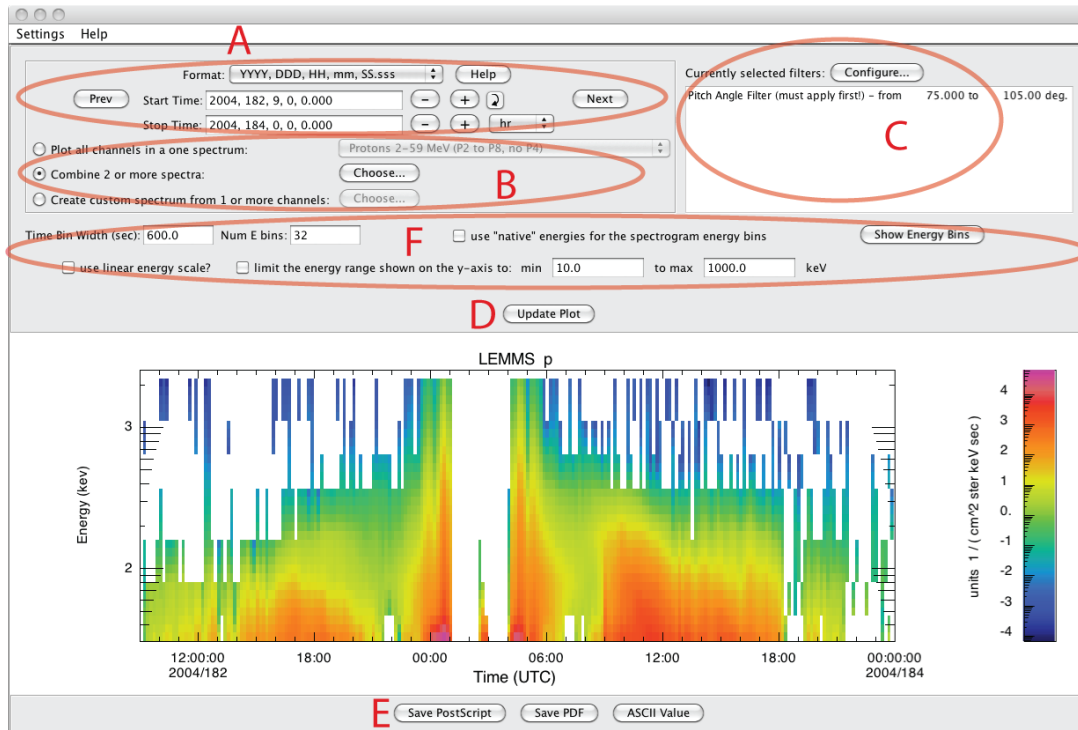


Figure 6.5: The tool for creating energy spectrograms of particle data. Similar to the line plot tool, feature **A** sets the time range, **B** determines the particle channels to plot, **C** allows configuration of filters. The “Update Plot” button refreshes the plot, and the plot or the data can be saved locally using the buttons near the bottom (**E**). This tool also offers ways to control the binning within the spectrogram via feature **F**.

6.3.2 Spectrograms

Figure 6.5 shows the Energy Spectrogram Tool in MIDL. This tool is very similar to the line plot tool in the way the time range (**A**), particle channels (**B**), and filters (**C**) are chosen and applied to the plot **D**. The plot or underlying data can be saved (**E**). There are also spectrogram-specific settings in feature **F**, where the time width of the spectrogram bins can be changed, as well as the number of displayed energy bins. Interpolation is used when the number of display bins is larger than the number of actual energy bins in the data. Notice that there is a checkbox option to force the plot to use the native energy bins of the data.

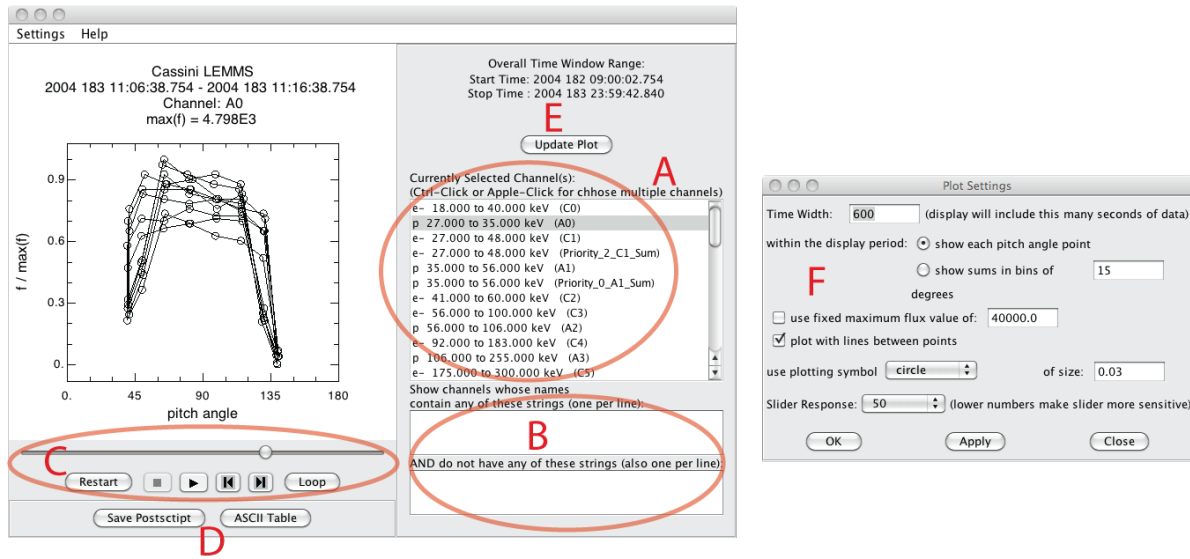


Figure 6.6: The tool for interactively viewing detailed pitch angle distributions. The overall time range was set when the tool was launched and cannot be changed. The channel or channels to display are selected in feature **A**. The two panels in feature **B** allow the potentially long list of channels to be reduced, making channel selection easier. An interactive slider **C** updates the narrow time range used for displaying pitch angle points.

6.3.3 Pitch Angle Plots

MIDL offers two types of pitch angle plots. One is interactive, where pitch angle points within a single window in time are displayed, and a slider is provided that interactively moves the time window forwards or backwards to see detailed changes in the pitch angle distribution. The other pitch angle plotter creates a pitch angle spectrogram.

The interactive pitch angle plotter is shown in Figure 6.6. Features **A** and **B** allow for the selection of one or more particle channels. In **B**, it is possible to reduce the number of channels in the selection list by entering one or more string values that either must be present (top entry box) or must not be present (bottom entry box) in the channel name in order for it to be listed. The overall time range of the data displayed in this tool is fixed when the tool is launched, and cannot be changed within the tool. The plot panel within the tool (on the left) shows a narrow time slice of points, and this time slice can be interactively dragged using the slider in feature **C**. To change the width of the narrow time slice, use the settings dialog (**F**), which is opened using the “Settings” menu at the top left of the tool window. The “Update Plot” button (**E**) applies any changes made to the channels or settings. Data or the plot can be saved using the buttons at the bottom (**D**).

Figure 6.7 shows the spectrogram pitch angle plotter. The time range of the data in this tool is determined when it is launched and cannot be changed within the tool. The time bin width and number of angle bins in the spectrogram are set within feature **A**, and feature **B** allows the user to change the channels shown. Any updates to the plot are activated when the “Update Plot” button is clicked, and the plot or the data in the plot can be saved using the save buttons below the actual plot (**D**). The grey background in this plot indicates that no pitch angle measurement was made, and the white background indicates a high value of the flux.

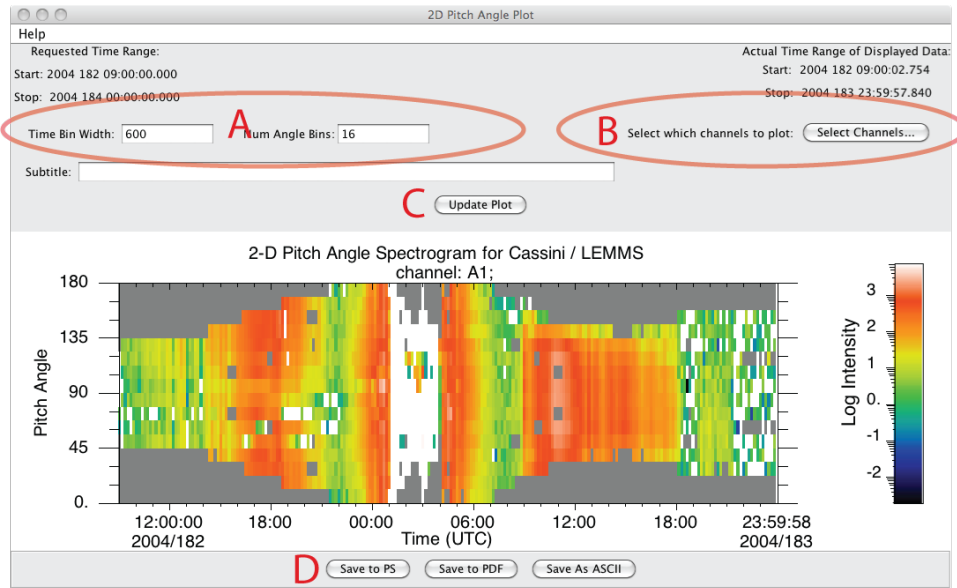


Figure 6.7: A tool for creating pitch angle spectrograms. The overall time range was set when the tool was launched and cannot be changed. Time and angle bin sizes are changed using feature **A**. The channel or channels to display are selected in feature **B**. The “Update Plot” button (**C**) applies changes made to the channels or bin sizes. The plot or the data can be saved locally using the buttons near the bottom (**D**).

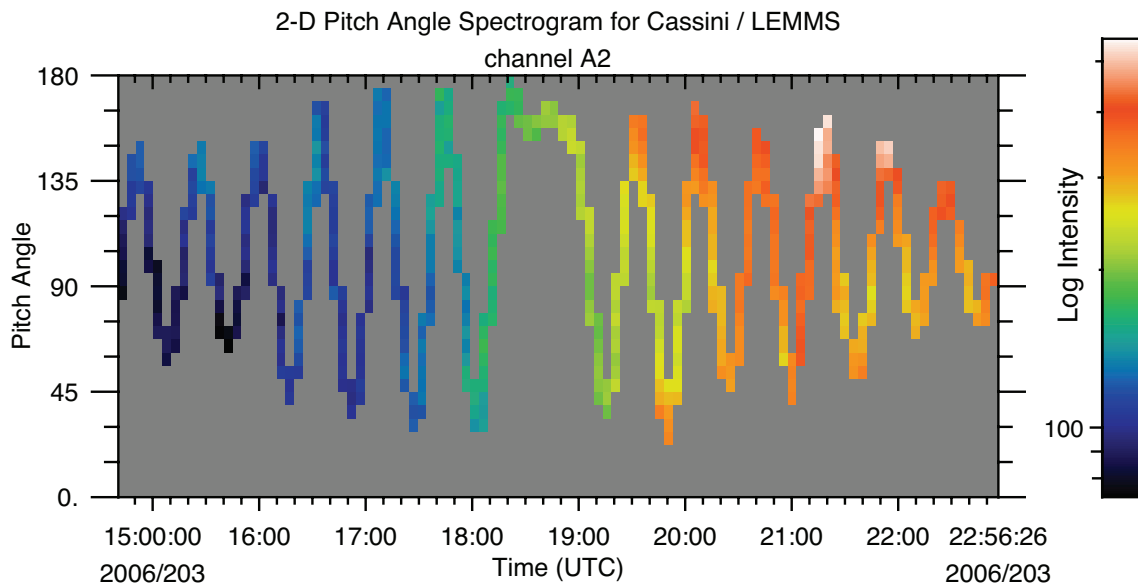


Figure 6.8: LEMMS A2 channel on day 2003 of 2006. This plot shows the type of pitch angle plot that can be obtained after the LEMMS platform stopped rotating. Note that the variations in pitch angle are due to spacecraft rotations.

Note that complete pitch angle coverage like that shown in Figure 6.7 is only possible for times when the LEMMS platform was rotating. After the LEMMS platform became stuck, pitch angle coverage is more limited, although if the spacecraft is spinning, it is still possible to obtain a smaller sampling of pitch angles, such as that shown in Figure 6.8. Also, Figure 3.21 on page 64 also shows another pitch angle spectrogram but includes data from two oppositely directed channels.

Bibliography

- C. Acton. Spice web page, November 2011. URL <http://naif.jpl.nasa.gov/naif/toolkit.html>.
- M. Andriopoulou, E. Roussos, N. Krupp, P. Kollmann, Z. Bebesi, C. Paranicas, and M. Thomsen. A statistical study of the energetic electron microsignatures from Tethys and Dione. In *EPSC-DPS Joint Meeting 2011*, page 211, Oct. 2011.
- T. P. Armstrong, S. Taherion, J. Manweiler, S. Krimigis, C. Paranicas, D. Mitchell, and N. Krupp. Energetic ions trapped in Saturn's inner magnetosphere. *Planetary and Space Science*, 57:1723–1731, Dec. 2009. doi: 10.1016/j.pss.2009.03.008.
- P. C. Brandt, K. Dialynas, I. Dandouras, D. G. Mitchell, P. Garnier, and S. M. Krimigis. Titan's extended atmosphere: INCA results. *EGU General Assembly 2009, held 19-24 April, 2009 in Vienna, Austria*, <http://meetings.copernicus.org/egu2009>, 111:11521, Apr. 2009.
- J. F. Carbary, D. G. Mitchell, S. M. Krimigis, and N. Krupp. Electron periodicities in Saturn's outer magnetosphere. *Journal of Geophysical Research (Space Physics)*, 112(A11):A03206, Mar. 2007. doi: 10.1029/2006JA012077.
- J. F. Carbary, D. G. Mitchell, S. M. Krimigis, and N. Krupp. Dual periodicities in energetic electrons at Saturn. *Geophys. Res. Lett.*, 36:L20103, Oct. 2009. doi: 10.1029/2009GL040517.
- J. F. Carbary, D. G. Mitchell, S. M. Krimigis, and N. Krupp. Post-equinox periodicities in Saturn's energetic electrons. *Geophys. Res. Lett.*, 38:L24104, Dec. 2011. doi: 10.1029/2011GL050259.
- R. D. DiFabio, D. C. Hamilton, S. M. Krimigis, and D. G. Mitchell. Long term time variations of the suprathermal ions in Saturn's magnetosphere. *Geophys. Res. Lett.*, 38:L18103, Sept. 2011. doi: 10.1029/2011GL048841.
- M. M. Hedman, J. A. Burns, M. S. Tiscareno, C. C. Porco, G. H. Jones, E. Roussos, N. Krupp, C. Paranicas, and S. Kempf. The Source of Saturn's G Ring. *Science*, 317:653–, Aug. 2007. doi: 10.1126/science.1143964.
- T. W. Hill, M. F. Thomsen, M. G. Henderson, R. L. Tokar, A. J. Coates, H. J. McAndrews, G. R. Lewis, D. G. Mitchell, C. M. Jackman, C. T. Russell, M. K. Dougherty, F. J. Crary, and D. T. Young. Plasmoids in Saturn's magnetotail. *Journal of Geophysical Research (Space Physics)*, 113(A12):A01214, Jan. 2008. doi: 10.1029/2007JA012626.
- P. Kollmann, E. Roussos, C. Paranicas, N. Krupp, C. M. Jackman, E. Kirsch, and K.-H. Glassmeier. Energetic particle phase space densities at Saturn: Cassini observations and interpretations. *Journal of Geophysical Research (Space Physics)*, 116(A15):A05222, May 2011. doi: 10.1029/2010JA016221.

- S. M. Krimigis, D. G. Mitchell, D. C. Hamilton, S. Livi, J. Dandouras, S. Jaskulek, T. P. Armstrong, J. D. Boldt, A. F. Cheng, G. Gloeckler, J. R. Hayes, K. C. Hsieh, W.-H. Ip, E. P. Keath, E. Kirsch, N. Krupp, L. J. Lanzerotti, R. Lundgren, B. H. Mauk, R. W. McEntire, E. C. Roelof, C. E. Schlemm, B. E. Tossman, B. Wilken, and D. J. Williams. Magnetosphere Imaging Instrument (MIMI) on the Cassini Mission to Saturn/Titan. *Space Sci. Rev.*, 114:233–329, Sept. 2004a. doi: 10.1007/s11214-004-1410-8.
- S. M. Krimigis, D. G. Mitchell, D. C. Hamilton, S. Livi, J. Dandouras, S. Jaskulek, T. P. Armstrong, J. D. Boldt, A. F. Cheng, G. Gloeckler, J. R. Hayes, K. C. Hsieh, W.-H. Ip, E. P. Keath, E. Kirsch, N. Krupp, L. J. Lanzerotti, R. Lundgren, B. H. Mauk, R. W. McEntire, E. C. Roelof, C. E. Schlemm, B. E. Tossman, B. Wilken, and D. J. Williams. Magnetosphere Imaging Instrument (MIMI) on the Cassini Mission to Saturn/Titan. *Space Science Reviews*, 114:233–329, Sept. 2004b. doi: 10.1007/s11214-004-1410-8.
- S. M. Krimigis, N. Sergis, D. G. Mitchell, D. C. Hamilton, and N. Krupp. A dynamic, rotating ring current around Saturn. *Nature*, 450:1050–1053, Dec. 2007a. doi: 10.1038/nature06425.
- S. M. Krimigis, N. Sergis, D. G. Mitchell, D. C. Hamilton, and N. Krupp. A dynamic, rotating ring current around Saturn. *Nature*, 450:1050–1053, Dec. 2007b. doi: 10.1038/nature06425.
- N. Krupp, E. Roussos, A. Lagg, J. Woch, A. L. Müller, S. M. Krimigis, D. G. Mitchell, E. C. Roelof, C. Paranicas, J. Carbary, G. H. Jones, D. C. Hamilton, S. Livi, T. P. Armstrong, M. K. Dougherty, and N. Sergis. Energetic particles in Saturn’s magnetosphere during the Cassini nominal mission (July 2004–July 2008). *Planetary and Space Science*, 57:1754–1768, Dec. 2009. doi: 10.1016/j.pss.2009.06.010.
- W. S. Kurth, T. F. Averkamp, D. A. Gurnett, J. B. Groene, and A. Lecacheux. An update to a Saturnian longitude system based on kilometric radio emissions. *Journal of Geophysical Research (Space Physics)*, 113(A12):A05222, May 2008. doi: 10.1029/2007JA012861.
- M. B. Kusterer and J. D. Vandegriff. Mimi pds data and calibration support web page, November 2011. URL http://sd-www.jhuapl.edu/CASSINI/data_auxiliary.html/.
- J. W. Manweiler, W. Rasmuss, and S. Joy. Mimi standard data products and archive volume software interface specification, May 2005. URL http://pds-ppi.igpp.ucla.edu/cache1/COMIMI_0000/DOCUMENT/MIMI_VOLUME_DESCRIPTION/.
- B. H. Mauk, J. Saur, D. G. Mitchell, E. C. Roelof, P. C. Brandt, T. P. Armstrong, D. C. Hamilton, S. M. Krimigis, N. Krupp, S. A. Livi, J. W. Manweiler, and C. P. Paranicas. Energetic particle injections in Saturn’s magnetosphere. *Geophys. Res. Lett.*, 32:14–+, June 2005. doi: 10.1029/2005GL022485.
- D. G. Mitchell, P. C. Brandt, E. C. Roelof, J. Dandouras, S. M. Krimigis, and B. H. Mauk. Energetic Neutral Atom Emissions from Titan Interaction with Saturn’s Magnetosphere. *Science*, 308:989–992, May 2005. doi: 10.1126/science.1109805.
- D. G. Mitchell, S. M. Krimigis, C. Paranicas, P. C. Brandt, J. F. Carbary, E. C. Roelof, W. S. Kurth, D. A. Gurnett, J. T. Clarke, J. D. Nichols, J.-C. Gérard, D. C. Grodent, M. K. Dougherty, and W. R. Pryor. Recurrent energization of plasma in the midnight-to-dawn quadrant of Saturn’s magnetosphere, and its relationship to auroral UV and radio emissions. *Planet. Space Sci.*, 57: 1732–1742, Dec. 2009a. doi: 10.1016/j.pss.2009.04.002.

- D. G. Mitchell, W. S. Kurth, G. B. Hospodarsky, N. Krupp, J. Saur, B. H. Mauk, J. F. Carbary, S. M. Krimigis, M. K. Dougherty, and D. C. Hamilton. Ion conics and electron beams associated with auroral processes on Saturn. *Journal of Geophysical Research (Space Physics)*, 114(A13): A02212, Feb. 2009b. doi: 10.1029/2008JA013621.
- D. G. Mitchell, W. S. Kurth, G. B. Hospodarsky, N. Krupp, J. Saur, B. H. Mauk, J. F. Carbary, S. M. Krimigis, M. K. Dougherty, and D. C. Hamilton. Ion conics and electron beams associated with auroral processes on Saturn. *Journal of Geophysical Research (Space Physics)*, 114(A13): A02212, Feb. 2009c. doi: 10.1029/2008JA013621.
- A. L. Müller, J. Saur, N. Krupp, E. Roussos, B. H. Mauk, A. M. Rymer, D. G. Mitchell, and S. M. Krimigis. Azimuthal plasma flow in the Kronian magnetosphere. *Journal of Geophysical Research (Space Physics)*, 115(A14):A08203, Aug. 2010. doi: 10.1029/2009JA015122.
- C. Paranicas, D. G. Mitchell, S. Livi, S. M. Krimigis, E. Roussos, N. Krupp, J. Woch, A. Lagg, J. Saur, and F. S. Turner. Evidence of Enceladus and Tethys microsignatures. *Geophys. Res. Lett.*, 32:20101, Oct. 2005. doi: 10.1029/2005GL024072.
- C. Paranicas, D. G. Mitchell, S. M. Krimigis, D. C. Hamilton, E. Roussos, N. Krupp, G. H. Jones, R. E. Johnson, J. F. Cooper, and T. P. Armstrong. Sources and losses of energetic protons in Saturn’s magnetosphere. *Icarus*, 197:519–525, Oct. 2008. doi: 10.1016/j.icarus.2008.05.011.
- C. Paranicas, D. G. Mitchell, E. Roussos, P. Kollmann, N. Krupp, A. L. Müller, S. M. Krimigis, F. S. Turner, P. C. Brandt, A. M. Rymer, and R. E. Johnson. Transport of energetic electrons into Saturn’s inner magnetosphere. *Journal of Geophysical Research (Space Physics)*, 115(A14): 9214, Sept. 2010. doi: 10.1029/2010JA015853.
- E. C. Roelof. Energetic neutral atom image of a storm-time ring current. *Geophys. Res. Lett.*, 14: 652 – 655, May 1987. doi: 10.1029/GL014i006p00652.
- E. Roussos, N. Krupp, J. Woch, A. Lagg, G. H. Jones, C. Paranicas, D. G. Mitchell, S. Livi, S. M. Krimigis, M. K. Dougherty, T. Armstrong, W.-H. Ip, and U. Motschmann. Low energy electron microsignatures at the orbit of Tethys: Cassini MIMI/LEMMS observations. *Geophys. Res. Lett.*, 32:24107, Dec. 2005. doi: 10.1029/2005GL024084.
- E. Roussos, G. H. Jones, N. Krupp, C. Paranicas, D. G. Mitchell, A. Lagg, J. Woch, U. Motschmann, S. M. Krimigis, and M. K. Dougherty. Electron microdiffusion in the Saturnian radiation belts: Cassini MIMI/LEMMS observations of energetic electron absorption by the icy moons. *Journal of Geophysical Research (Space Physics)*, 112(A11):6214, June 2007. doi: 10.1029/2006JA012027.
- E. Roussos, G. H. Jones, N. Krupp, C. Paranicas, D. G. Mitchell, S. M. Krimigis, J. Woch, A. Lagg, and K. Khurana. Energetic electron signatures of Saturn’s smaller moons: Evidence of an arc of material at Methone. *Icarus*, 193:455–464, Feb. 2008a. doi: 10.1016/j.icarus.2007.03.034.
- E. Roussos, N. Krupp, T. P. Armstrong, C. Paranicas, D. G. Mitchell, S. M. Krimigis, G. H. Jones, K. Dialynas, N. Sergis, and D. C. Hamilton. Discovery of a transient radiation belt at Saturn. *Geophys. Res. Lett.*, 35:22106, Nov. 2008b. doi: 10.1029/2008GL035767.
- E. Roussos, N. Krupp, C. P. Paranicas, D. G. Mitchell, A. L. Müller, P. Kollmann, Z. Bebesi, S. M. Krimigis, and A. J. Coates. Energetic electron microsignatures as tracers of radial flows and dynamics in Saturn’s innermost magnetosphere. *Journal of Geophysical Research (Space Physics)*, 115(A14):3202, Mar. 2010. doi: 10.1029/2009JA014808.

- E. Roussos, N. Krupp, C. P. Paranicas, P. Kollmann, D. G. Mitchell, S. M. Krimigis, T. P. Armstrong, D. R. Went, M. K. Dougherty, and G. H. Jones. Long- and short-term variability of Saturn's ionic radiation belts. *Journal of Geophysical Research (Space Physics)*, 116(A15):A02217, Feb. 2011. doi: 10.1029/2010JA015954.
- J. Saur, B. H. Mauk, D. G. Mitchell, N. Krupp, K. K. Khurana, S. Livi, S. M. Krimigis, P. T. Newell, D. J. Williams, P. C. Brandt, A. Lagg, E. Roussos, and M. K. Dougherty. Anti-planetward auroral electron beams at Saturn. *Nature*, 439:699–702, Feb. 2006. doi: 10.1038/nature04401.
- N. Sergis, S. M. Krimigis, D. G. Mitchell, D. C. Hamilton, N. Krupp, B. M. Mauk, E. C. Roelof, and M. Dougherty. Ring current at Saturn: Energetic particle pressure in Saturn's equatorial magnetosphere measured with Cassini/MIMI. *Geophys. Res. Lett.*, 340:L09102, May 2007. doi: 10.1029/2006GL029223.
- V. Wulms, J. Saur, D. F. Strobel, S. Simon, and D. G. Mitchell. Energetic neutral atoms from Titan: Particle simulations in draped magnetic and electric fields. *Journal of Geophysical Research (Space Physics)*, 115(A14):A06310, June 2010. doi: 10.1029/2009JA014893.

Appendix A

SPICE Usage on MIMI

The SPICE library is a set of routines for dealing with spacecraft and planetary trajectories and orientations ([Acton, 2011]). None of the code described in this user guide requires users to understand the SPICE system, but if users are familiar already with SPICE, they can take advantage of the same kernels used by the MIMI team to compute Cassini locations and attitude. The MIMI SPICE kernels also include instrument and frame kernels for MIMI-specific coordinate frames and instrument fields of view.

The MIMI team has created a collection of kernels relevant for MIMI analysis, including a meta-kernel that allows all necessary kernels to be loaded easily into SPICE. A single gzipped tar file (a tarball) containing the entire MIMI-related collection of kernels is available from the web page devoted to the MIMI User Guide: http://sd-www.jhuapl.edu/CASSINI/data_auxiliary.html.

Within the tarball of SPICE kernels, there are several meta-kernels:

```
mimi.tm  
mimick_p.tm  
mimick_r.tm  
lemms.tm
```

These meta-kernels live in the top directory of the SPICE kernel tree, and each of these files is actually a link to the most recent numbered version of that meta-kernel.

The primary meta-kernel is `mimi.tm`, and this references all trajectory info as well as relevant frame and instrument definitions. Separate from the main meta-kernel are two pointing meta-kernels, `mimick_p.tm` and `mimick_r.tm`, and these refer to predict and reconstructed attitude respectively. Load these two only if you need attitude information (because attitude kernels are very large and take a while to load) and load them in a specific order (predict first, then reconstructed, because SPICE gives a higher priority to the most recently loaded kernels). Finally, there is a meta-kernel `lemms.tm` that loads all the orientation data for the rotating LEMMS platform.

Appendix B

MIMI Data Gaps

Normally, MIMI instruments take data continuously, but occasionally there are data gaps. Many different issues can cause these gaps – spacecraft problems, instrument resets, calibration activities (during which normal science data is not taken), communication outages, etc. A list of large gaps more than two hours is provided at the MIMI web site devoted to this user guide: http://sd-www.jhuapl.edu/CASSINI/data_auxiliary.html.

Note that these gaps are for intervals during which there is no data for any MIMI instrument. Smaller gaps and gaps involving a single data products are not listed in this file.

The gaps are listed in yearly files with names like

`MIMI_Gap_SummaryYYYY.txt`

where YYYY is the 4 digit year. The files contain comma delimited values for the gap start time, gap stop time (both in UTC) followed by the total gap time in hh:mm:ss. The following is an excerpt from the file:

```
Gap Start in UTC,   Gap Stop in UTC,   Total Gap Time
2011-024T08:50:30, 2011-024T23:59:59, 15:09:00
2011-025T00:00:00, 2011-025T14:22:36, 14:22:00
```

The yearly files of gap lists are accessible individually on the previously mentioned web page, and they are included in the tarball download of calibration routines and data. Look in the subdirectory `gaps_times` beneath the `MIMI_code_calibration` directory.

Below the gaps files on the web page, are a set of files that list the individual sensor data gaps. The sensor data gaps are listed in yearly files with names like `MIMI_DetailedGap_SummaryYYYY.txt` where YYYY is the 4-digit year. The files contain comma delimited values for the sensor name (HSKP, LEMMS, CHEMS, INCA), gap start time, and gap stop time.

Appendix C

Auxiliary Data Files: MIMI Stare/Spin Time Ranges

MIMI Stare/Spin Time Ranges

When the MIMI instrument is commanded to spin mode, the spacecraft spins about the Z axis and the spin rate is above certain threshold, then spin mode is used for that spin. Otherwise the DPU ignores the spin rate data from the spacecraft and synthesizes a sector time and that spin is marked as stare mode. The spin versus stare mode affects how the INCA images are collected.

A list of MIMI stare versus spin mode data files are provided at the MIMI web site devoted to this user guide: http://sd-www.jhuapl.edu/CASSINI/data_auxiliary.html.

The MIMI stare/spin files are comma delimited files, containing start and stop times, spin mode, spin direction and spin direction validity values. The values for spin mode are (0=Stare, 1=Spin). The spin direction flag values are (0 = clockwise, 1 = counter clockwise and 2 = both). During some spacecraft maneuvers, the instrument interprets the motion as a spin about the spacecraft Z axis, and can erroneously detect both directions. These spins will be reported to have a spin direction as 2. The direction validity flag values are (0 = invalid (or for stare mode), 1 = valid). The spin direction validity flag is only included when the instrument detects a spin and is 0 otherwise. During spacecraft spin up and spin down periods, the spin direction can be difficult to detect

Appendix D

CHEMS Data Used to Define the PHA Species Boxes

This appendix contains plots of $\text{Essd}(\text{ch})$ versus $\text{TOF}(\text{ch})$ as well as $\text{TOF}(\text{ch})$ histograms that were used to define the PHA species boxes. Recall time intervals are categorized into two spatially distinct regions: magnetospheric or interplanetary. The collection of time intervals for each spatial region is more fully described in Section 4.6, which also contains lists of the actual time intervals used (see Tables 4.9 and 4.10). The basic definitions of each category are:

Saturn's magnetosphere: $7 < L < 16$ and $-10^\circ < \text{latitude} < +10^\circ$

Interplanetary: 2004 days 001-179 (times with no solar wind oxygen)

While Section 4.6 in the main text provided sample plots at one DPPS step to illustrate various issues related to choosing the species boxes, this appendix includes the plots for all relevant DPPS steps as a reference and to give users a perspective on the data. So this appendix provides plots for all DPPS steps what Figure 4.5 (page 88) provided just for DPPS step 12.

D.1 Magnetospheric Data

The first period shown is Saturn's magnetosphere. Since doubles data are not used above step 19, the plots of doubles plus triples $\text{TOF}(\text{ch})$ histograms are provided only up to DPPS step 19. These histograms illustrate how at each DPPS step, a different $\text{TOF}(\text{ch})$ range is needed to capture the counts from one species.

Triples data for He^{++} is only used starting at step 12, so the plots of $\text{Essd}(\text{ch})$ versus $\text{TOF}(\text{ch})$ cover DPPS steps 12 to 31. Each plot has three components. The top row has a row of the 2-D histograms (one for each telescope) showing islands of species counts. The next row are $\text{TOF}(\text{ch})$ triples-only 1-D histograms. The table below the figure lists the ranges used for each species box. A more readable format for these ranges is given in Appendix E, and the values here should agree with the Appendix E tables, but if there is a conflict, Appendix E is the definitive source. Also there are downloadable ASCII files with these box definitions.

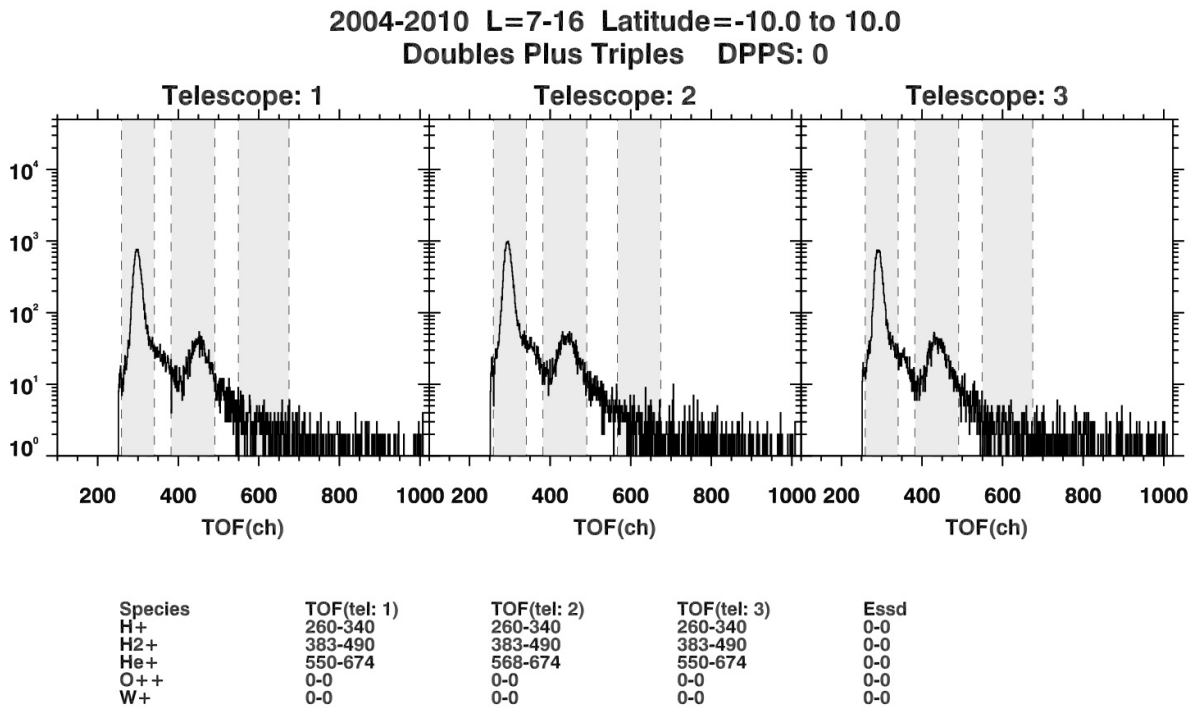


Figure D.1: Histogram of doubles plus triples counts in the magnetospheric period for DPPS step 0.

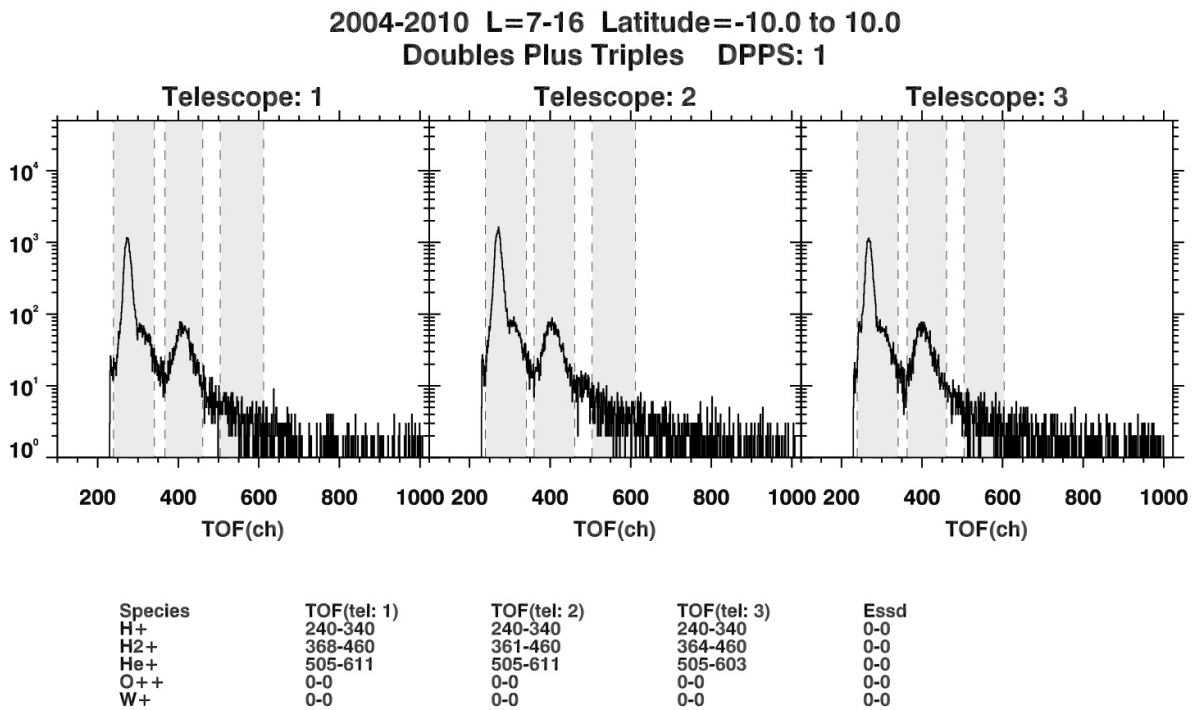


Figure D.2: Histogram of doubles plus triples counts in the magnetospheric period for DPPS step 1.

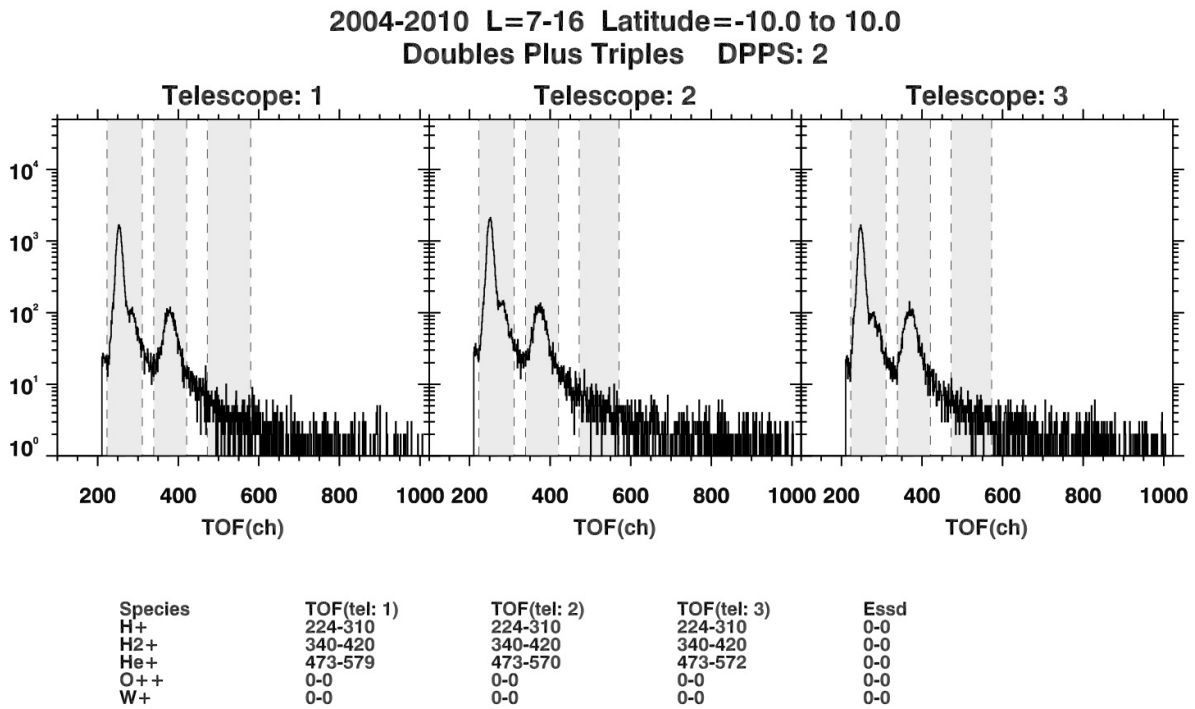


Figure D.3: Histogram of doubles plus triples counts in the magnetospheric period for DPPS step 2.

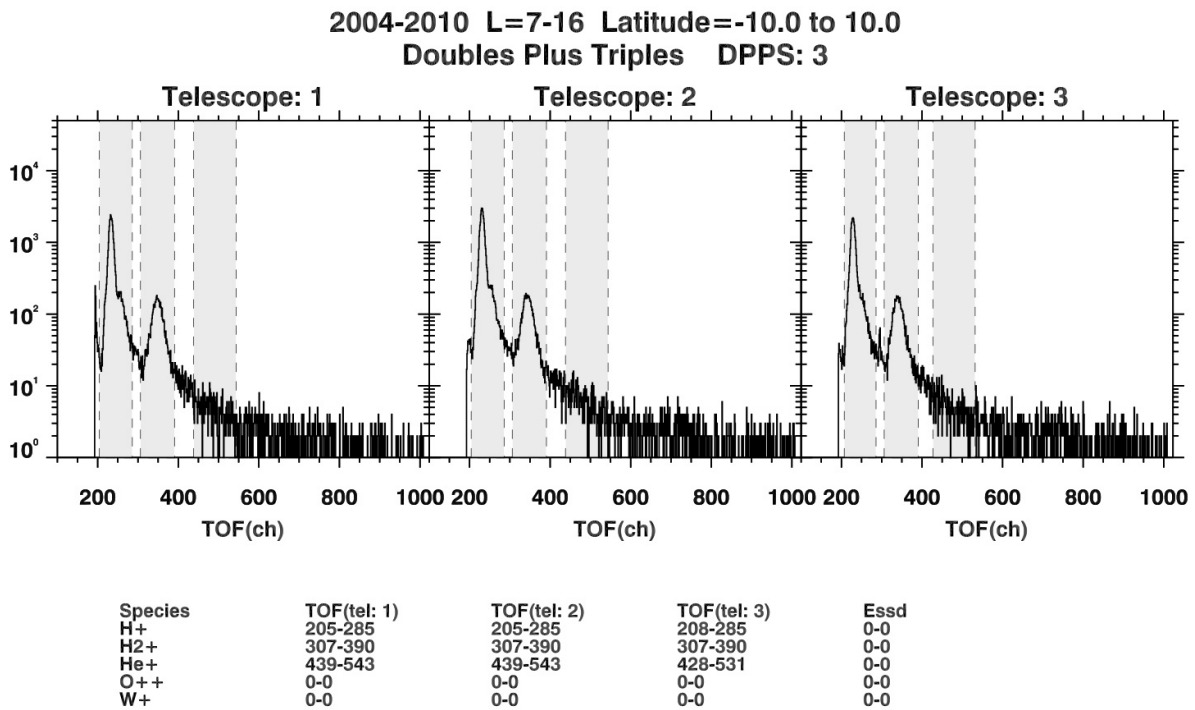


Figure D.4: Histogram of doubles plus triples counts in the magnetospheric period for DPPS step 3.

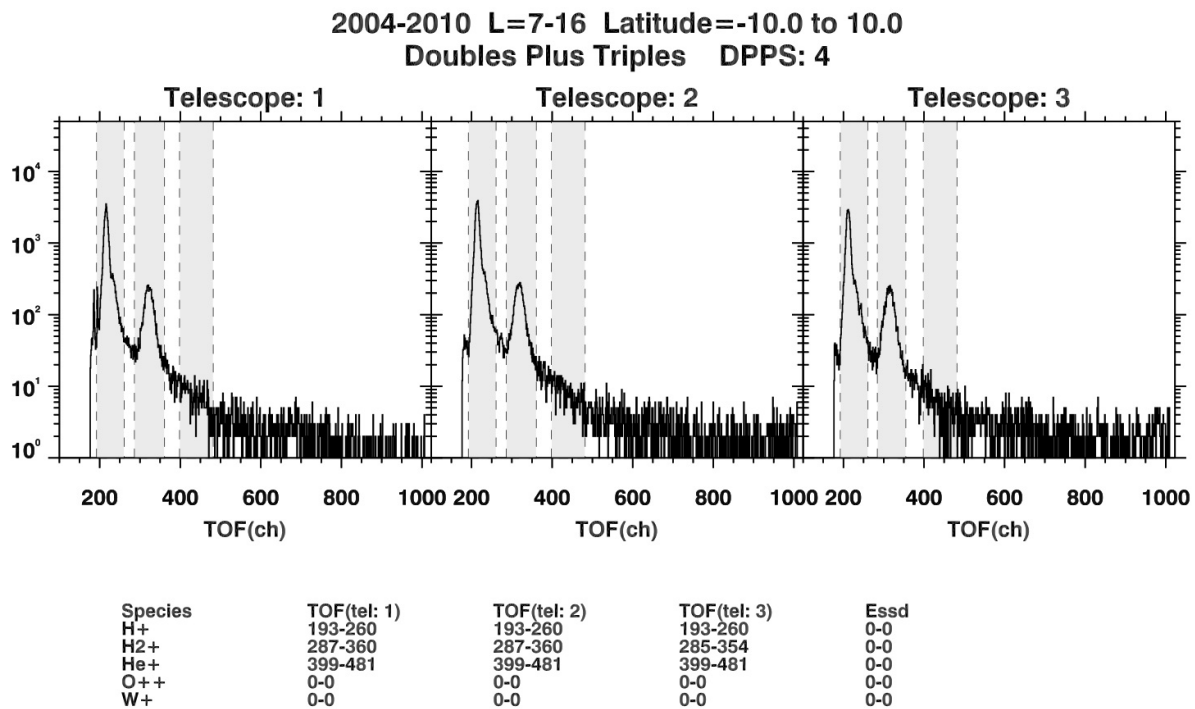


Figure D.5: Histogram of doubles plus triples counts in the magnetospheric period for DPPS step 4.

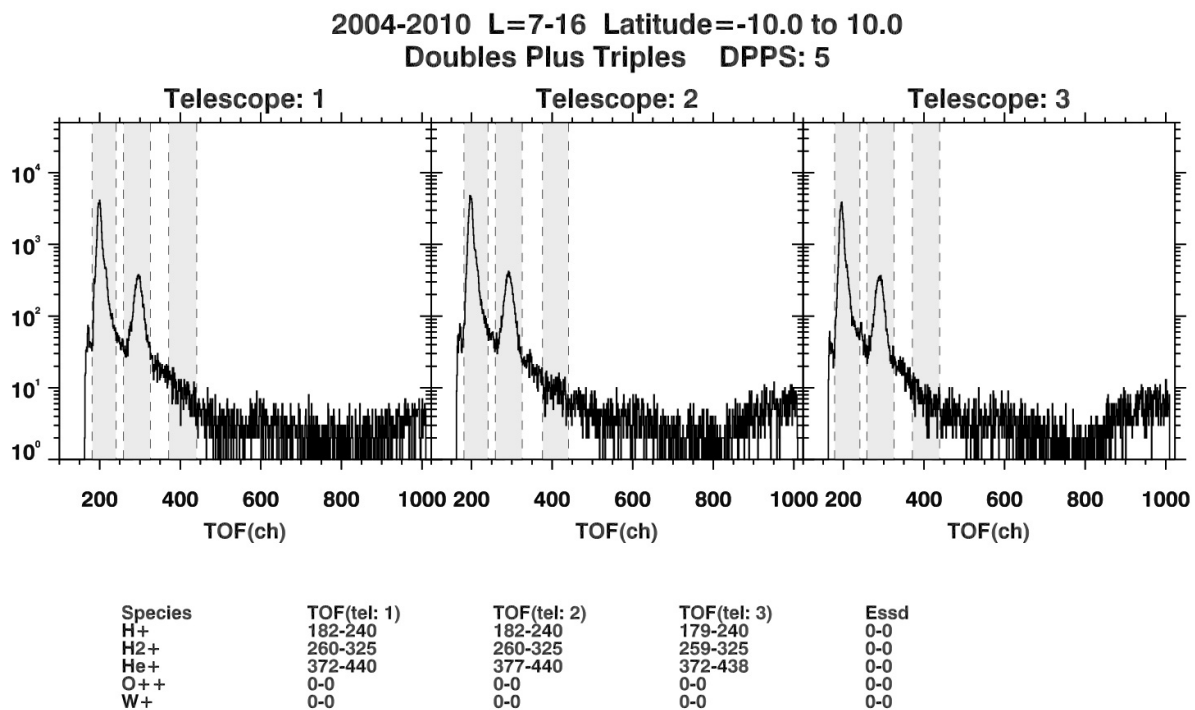


Figure D.6: Histogram of doubles plus triples counts in the magnetospheric period for DPPS step 5.

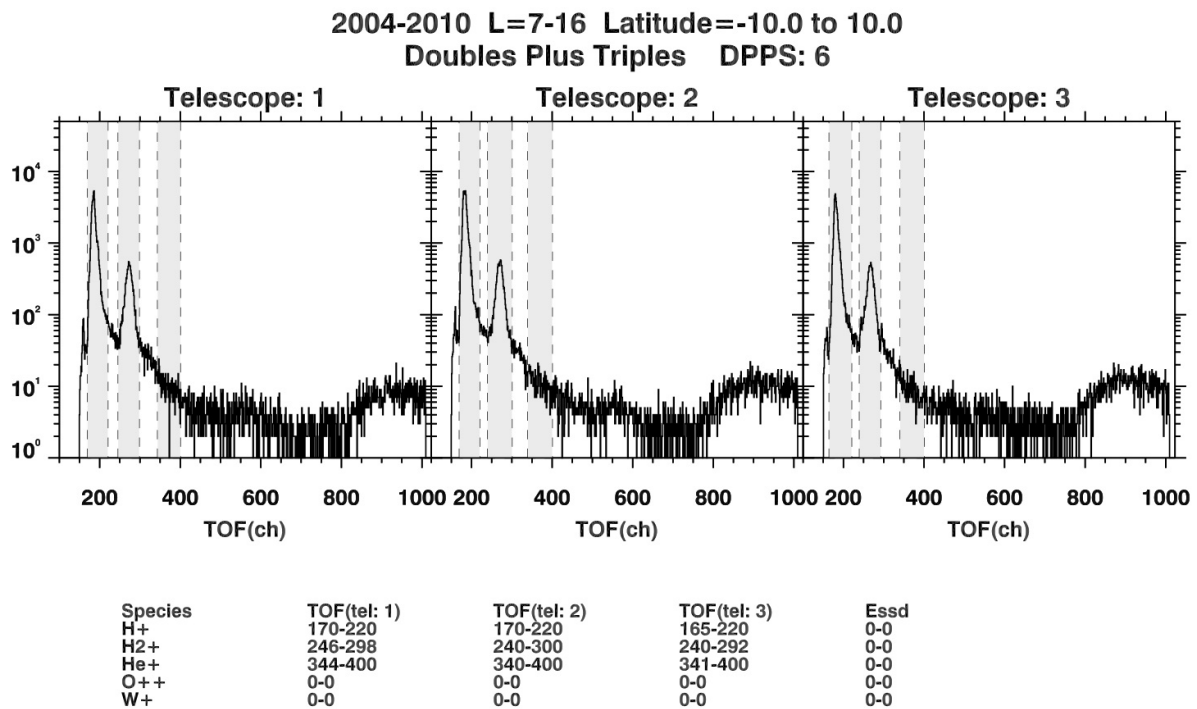


Figure D.7: Histogram of doubles plus triples counts in the magnetospheric period for DPPS step 6.

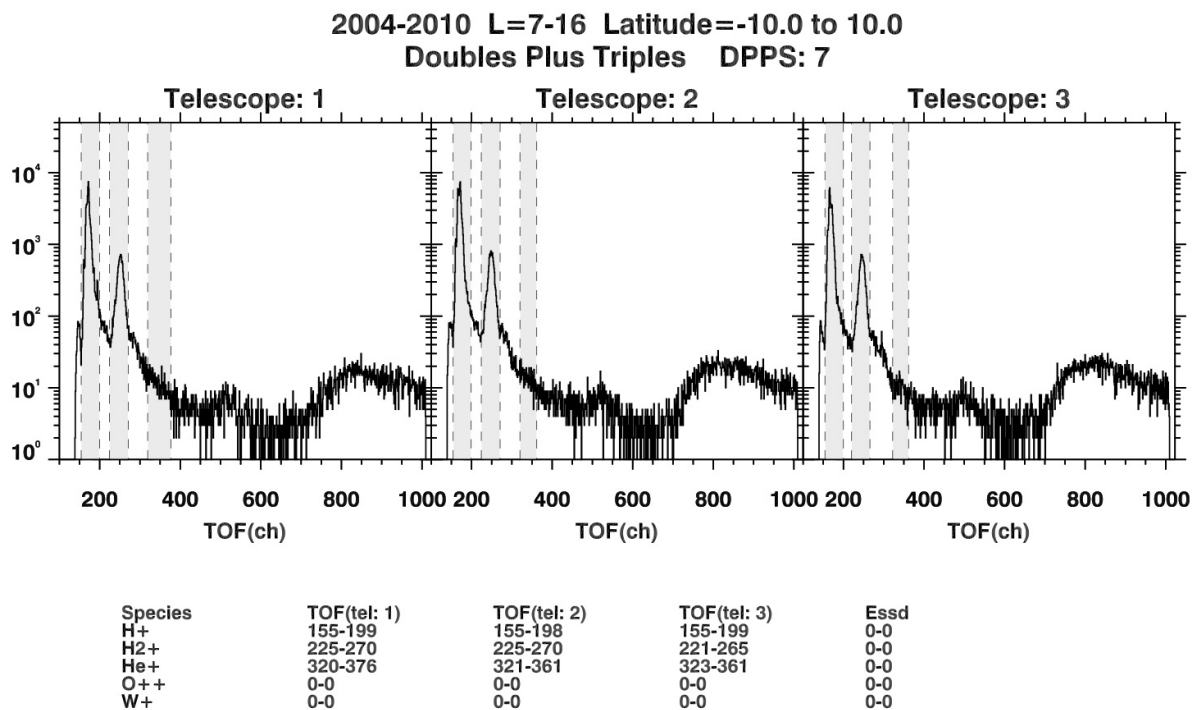


Figure D.8: Histogram of doubles plus triples counts in the magnetospheric period for DPPS step 7.

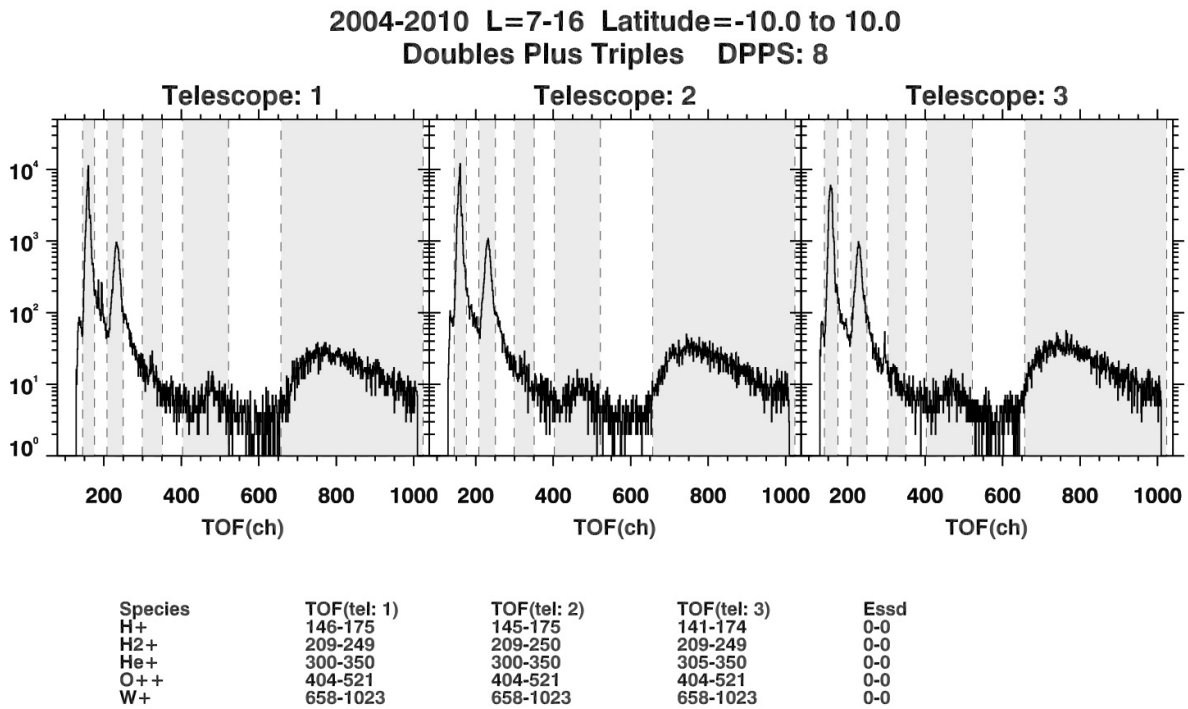


Figure D.9: Histogram of doubles plus triples counts in the magnetospheric period for DPPS step 8.

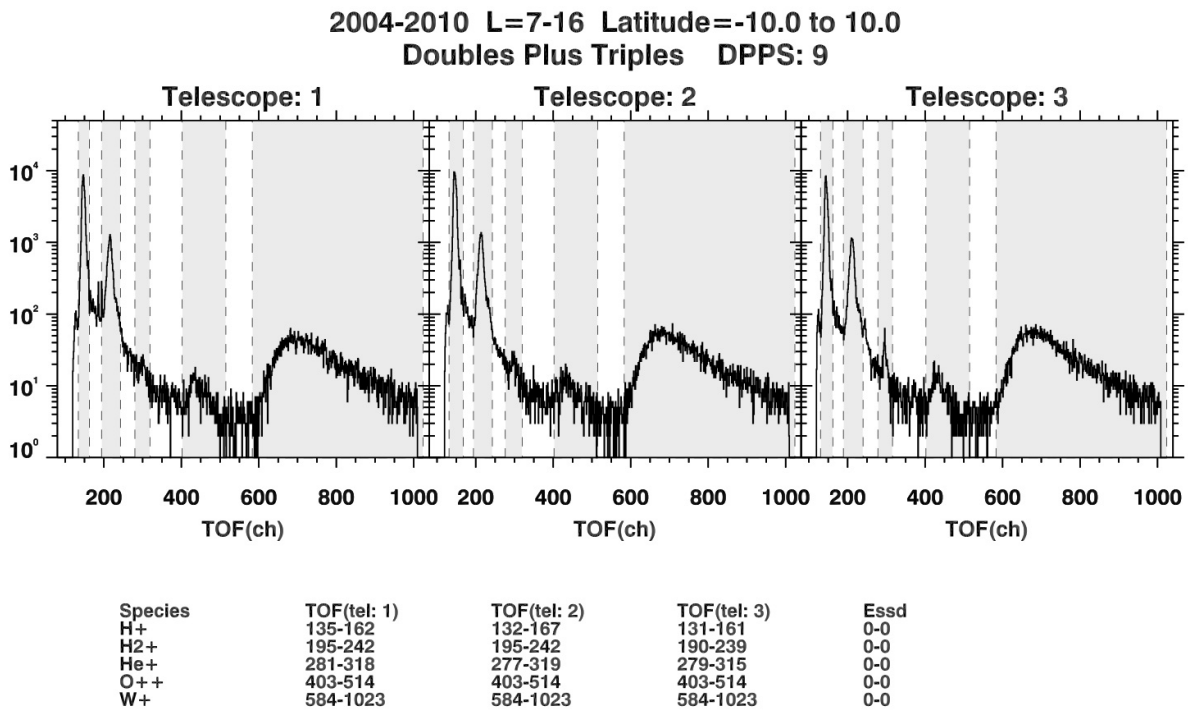


Figure D.10: Histogram of doubles plus triples counts in the magnetospheric period for DPPS step 9.

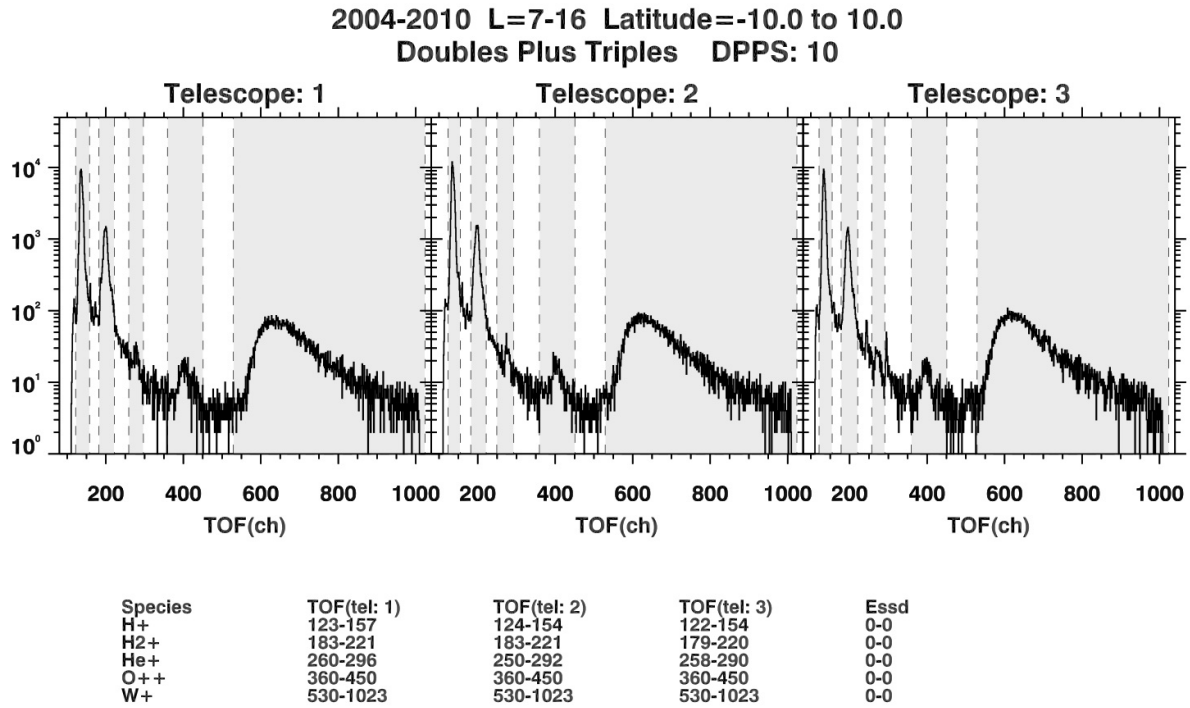


Figure D.11: Histogram of doubles plus triples counts in the magnetospheric period for DPPS step 10.

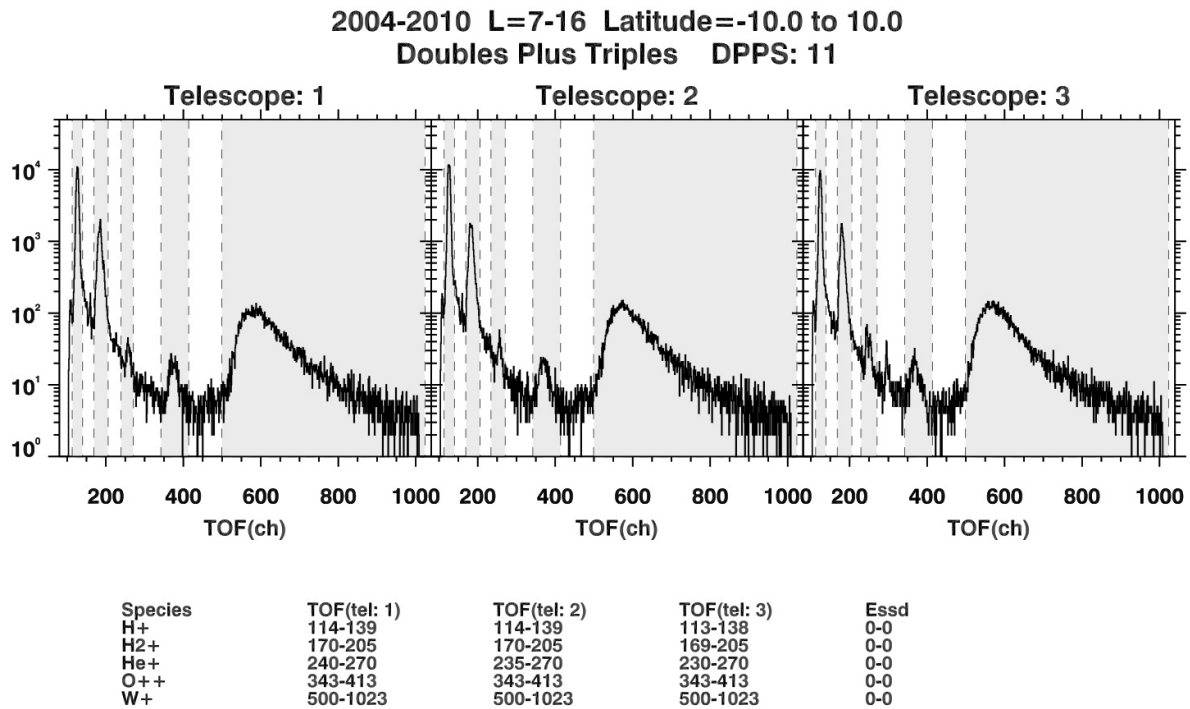


Figure D.12: Histogram of doubles plus triples counts in the magnetospheric period for DPPS step 11.

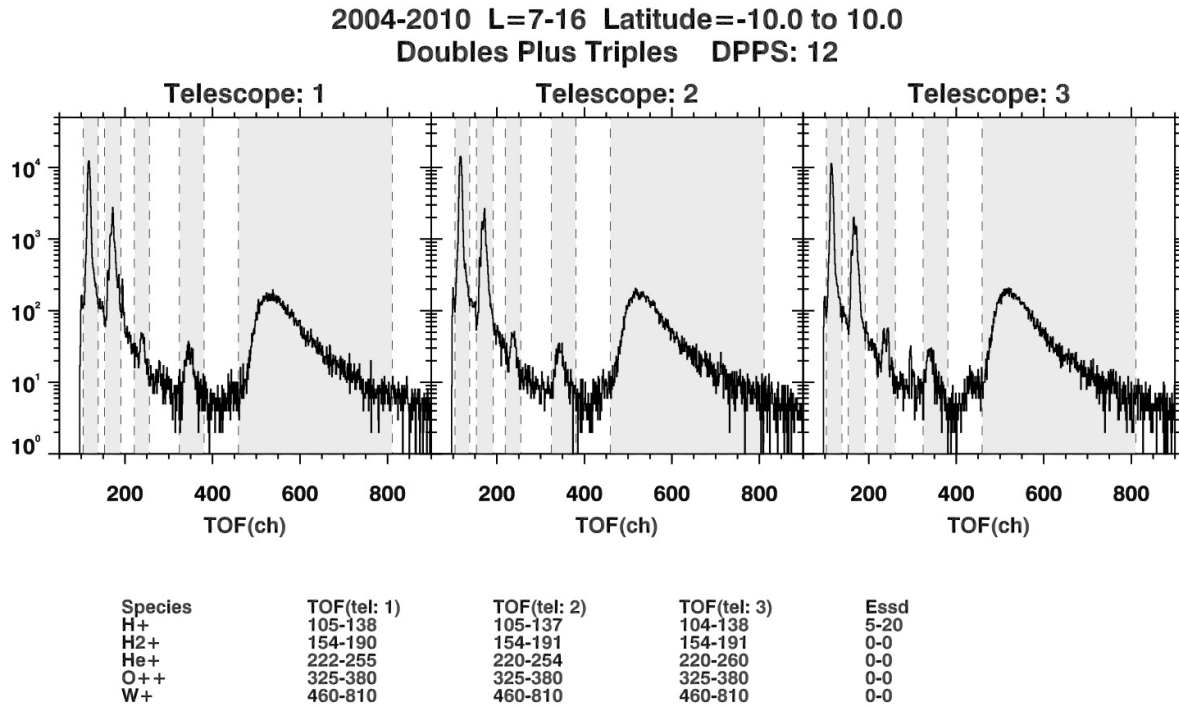


Figure D.13: Histogram of doubles plus triples counts in the magnetospheric period for DPPS step 12.

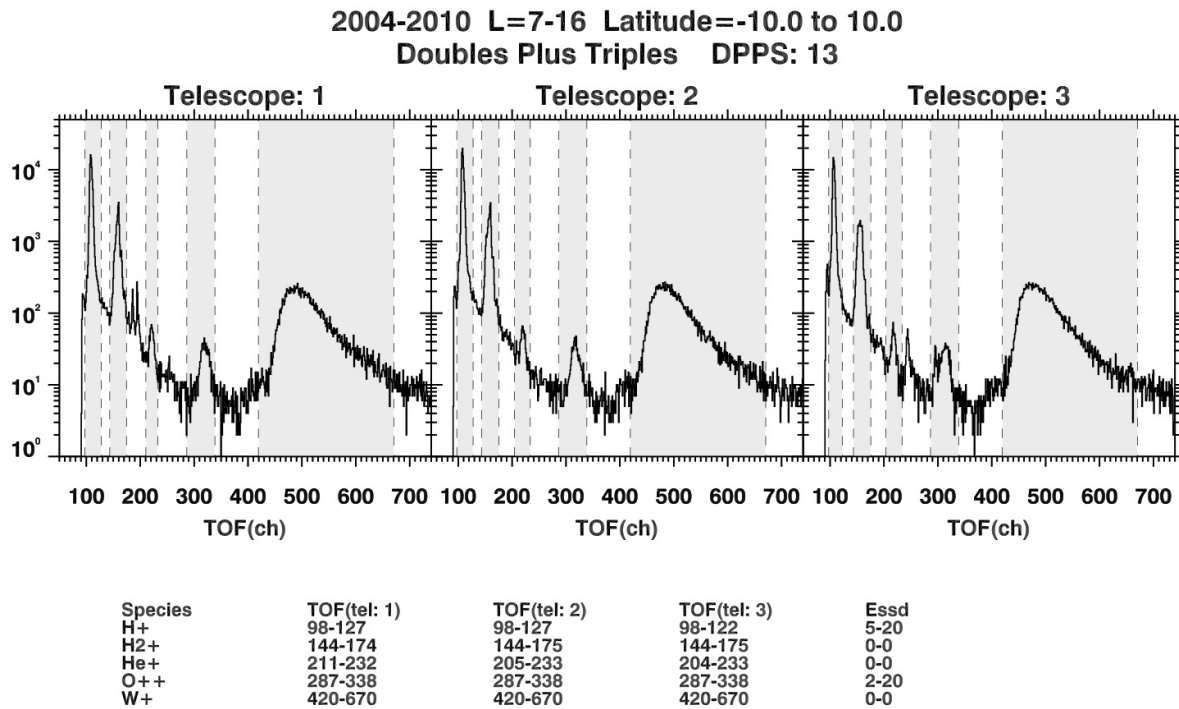


Figure D.14: Histogram of doubles plus triples counts in the magnetospheric period for DPPS step 13.

2004-2010 L=7-16 Latitude=-10.0 to 10.0
 Doubles Plus Triples DPPS: 14

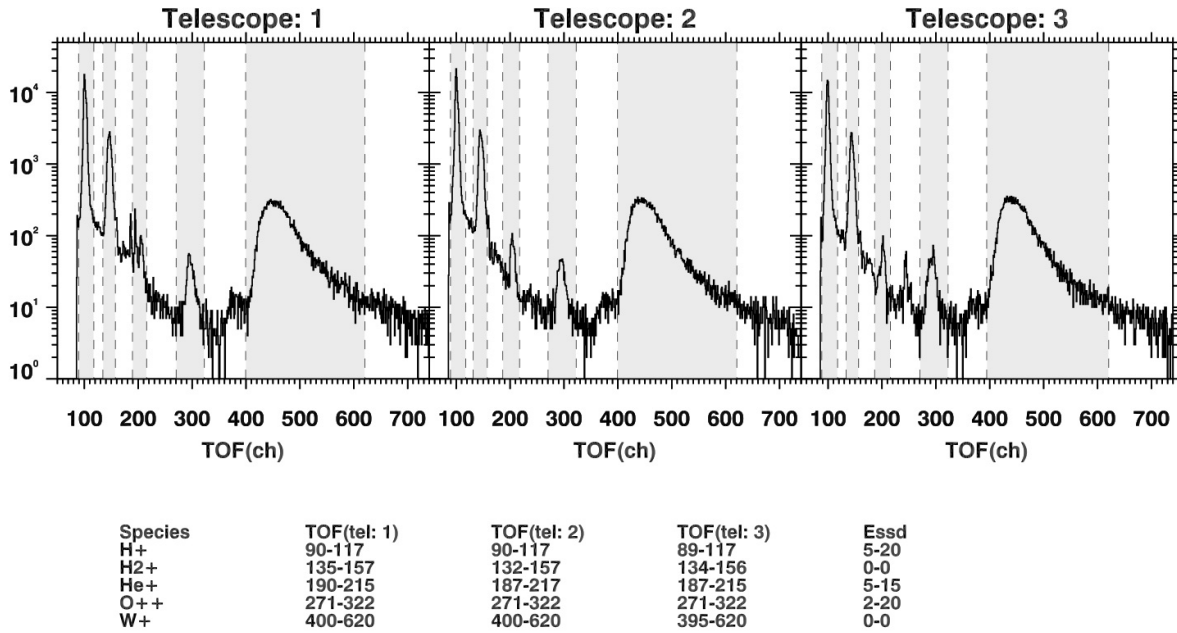


Figure D.15: Histogram of doubles plus triples counts in the magnetospheric period for DPPS step 14.

2004-2010 L=7-16 Latitude=-10.0 to 10.0
 Doubles Plus Triples DPPS: 15

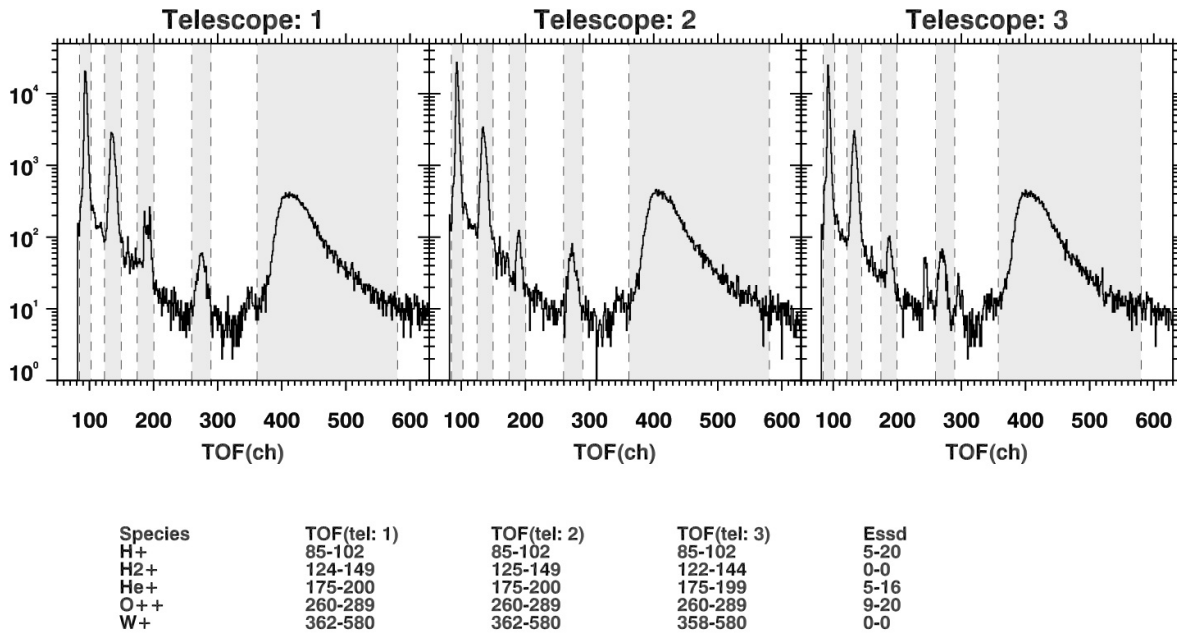


Figure D.16: Histogram of doubles plus triples counts in the magnetospheric period for DPPS step 15.

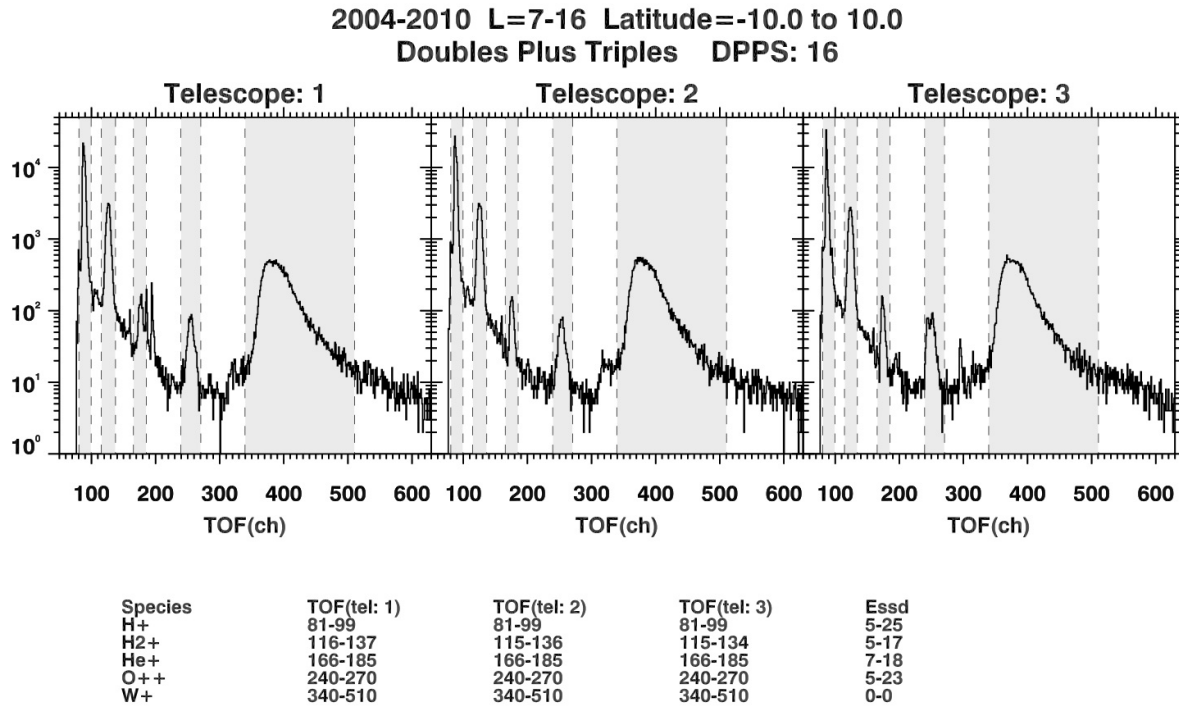


Figure D.17: Histogram of doubles plus triples counts in the magnetospheric period for DPPS step 16.

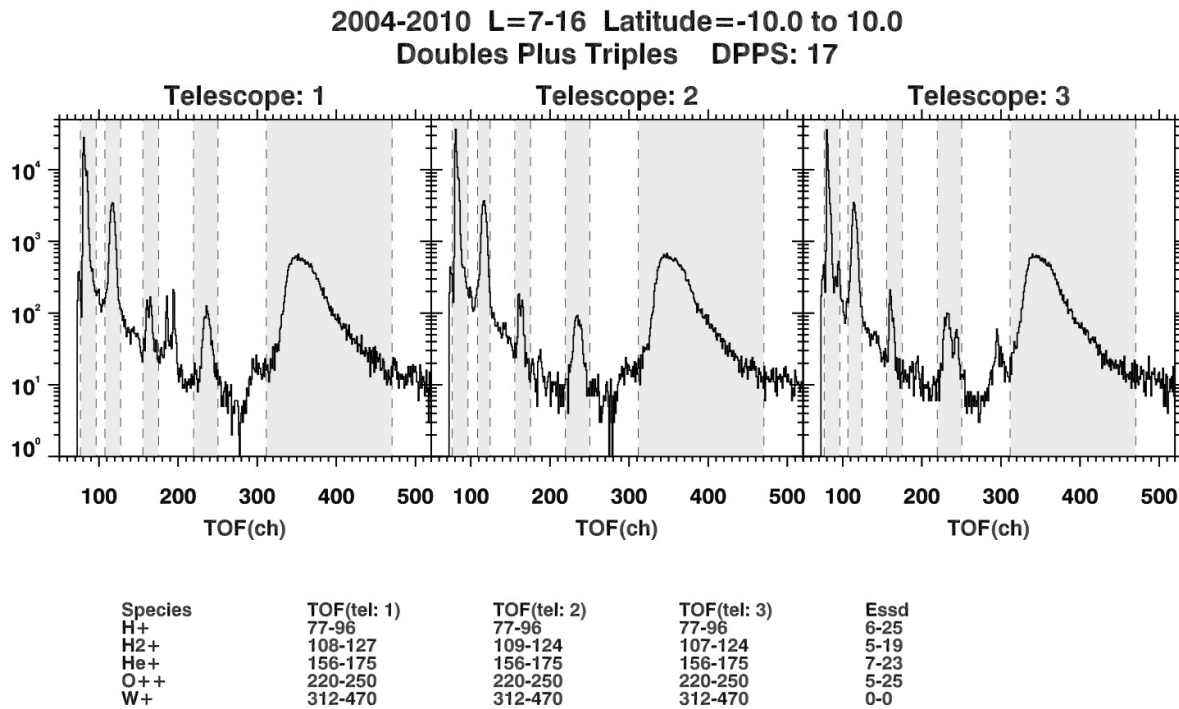


Figure D.18: Histogram of doubles plus triples counts in the magnetospheric period for DPPS step 17.

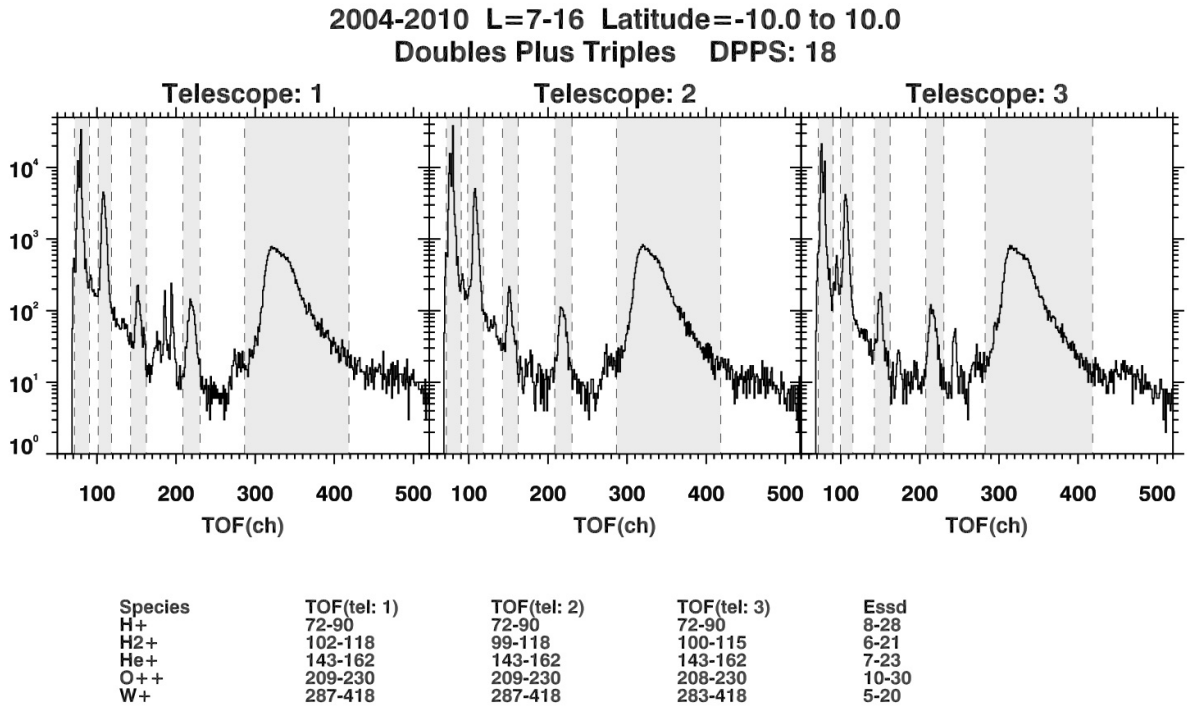


Figure D.19: Histogram of doubles plus triples counts in the magnetospheric period for DPPS step 18.

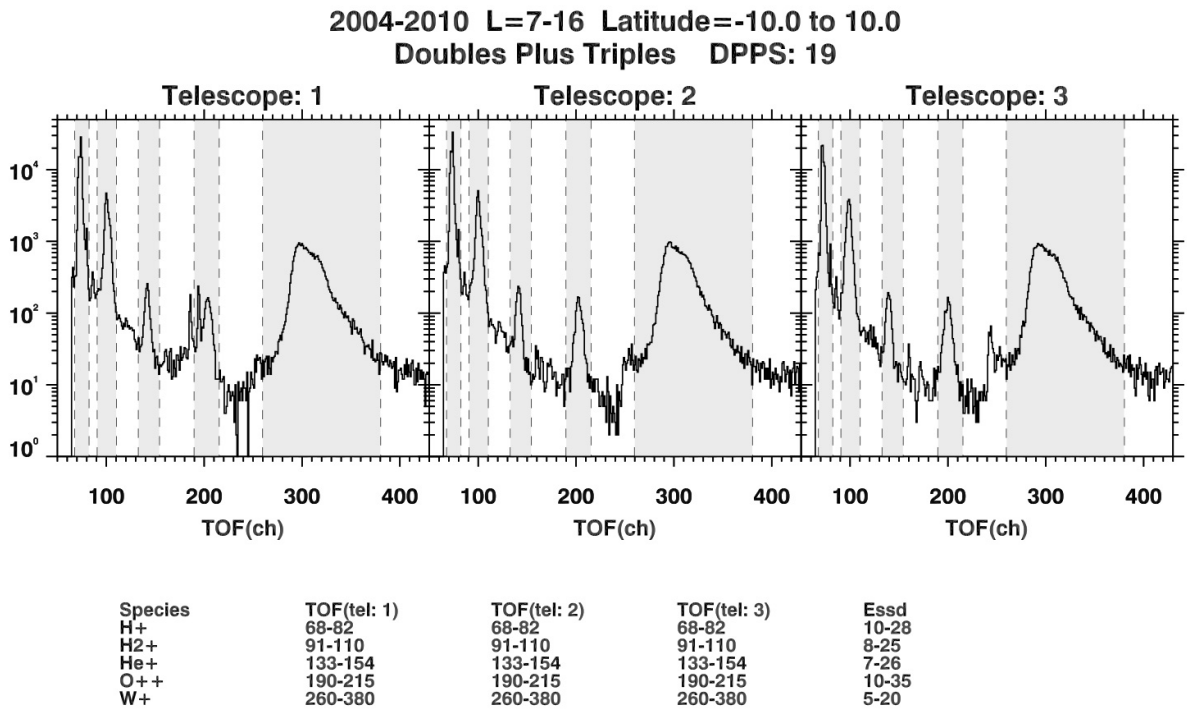
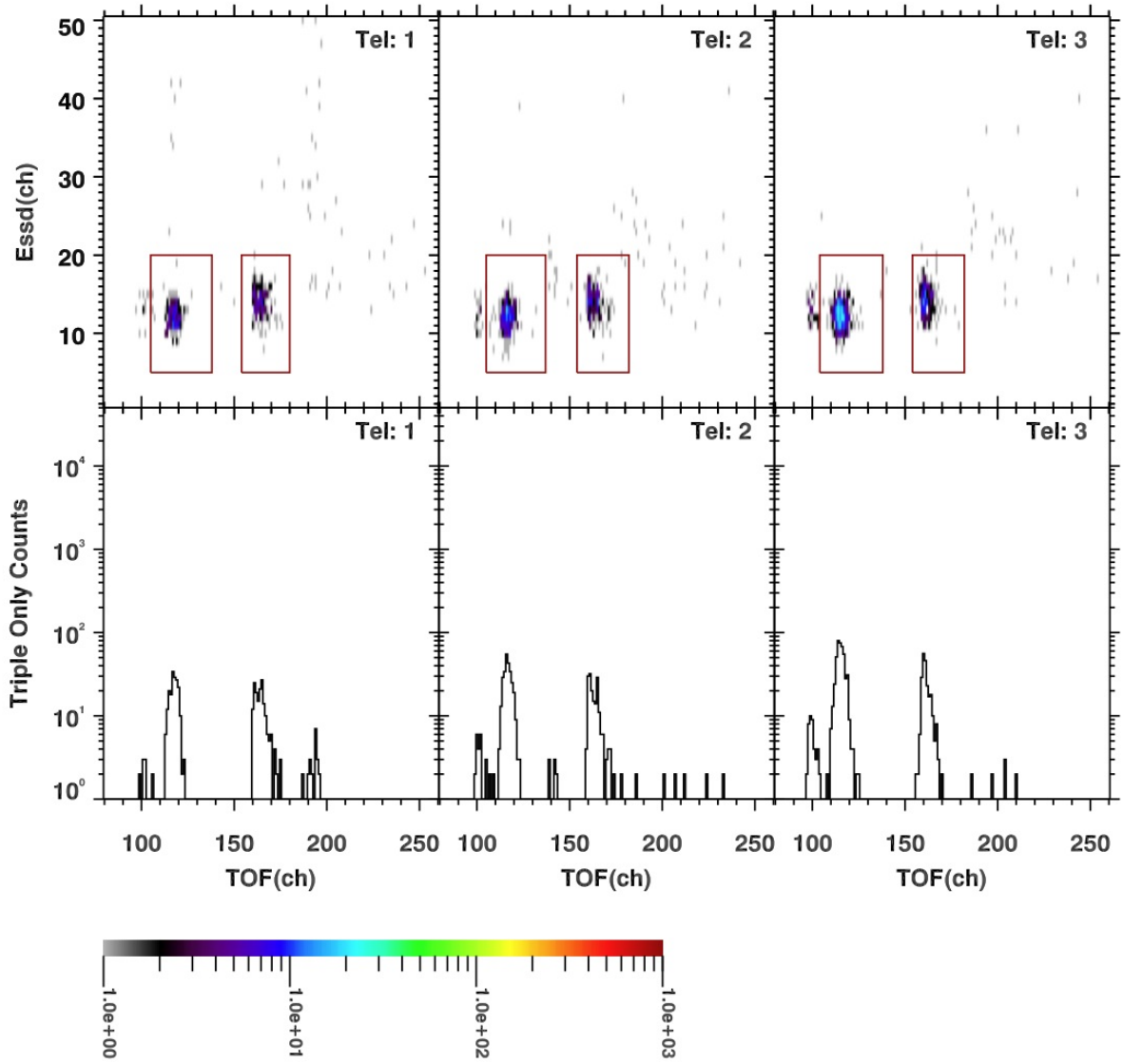


Figure D.20: Histogram of doubles plus triples counts in the magnetospheric period for DPPS step 19.

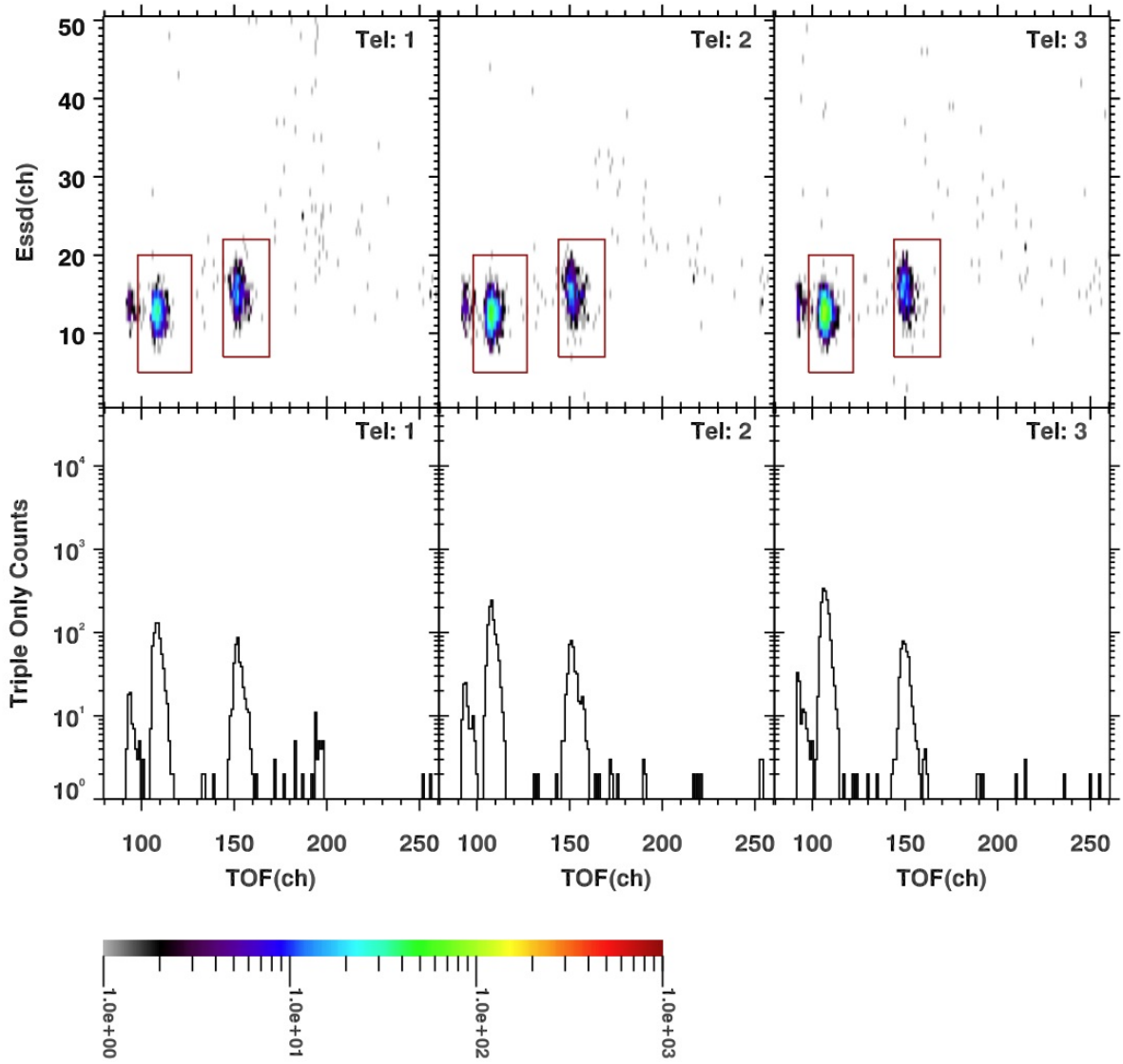
2004-2010 L=7-16 Latitude=-10.0 to 10.0
DPPS: 12



Species	TOF(tel: 1)	TOF(tel: 2)	TOF(tel: 3)	Essd
H+	105-138	105-137	104-138	5-20
H2+	154-190	154-191	154-191	0-0
He++	154-180	154-182	154-182	5-20
H3+	0-0	0-0	0-0	0-0
He+	222-255	220-254	220-260	0-0
O++	325-380	325-380	325-380	0-0
W+	460-810	460-810	460-810	0-0
O+++	0-0	0-0	0-0	0-0
C+	0-0	0-0	0-0	0-0
N+	0-0	0-0	0-0	0-0
O2+	0-0	0-0	0-0	0-0

Figure D.21: Histogram of all counts in the magnetospheric period for DPPS step 12.

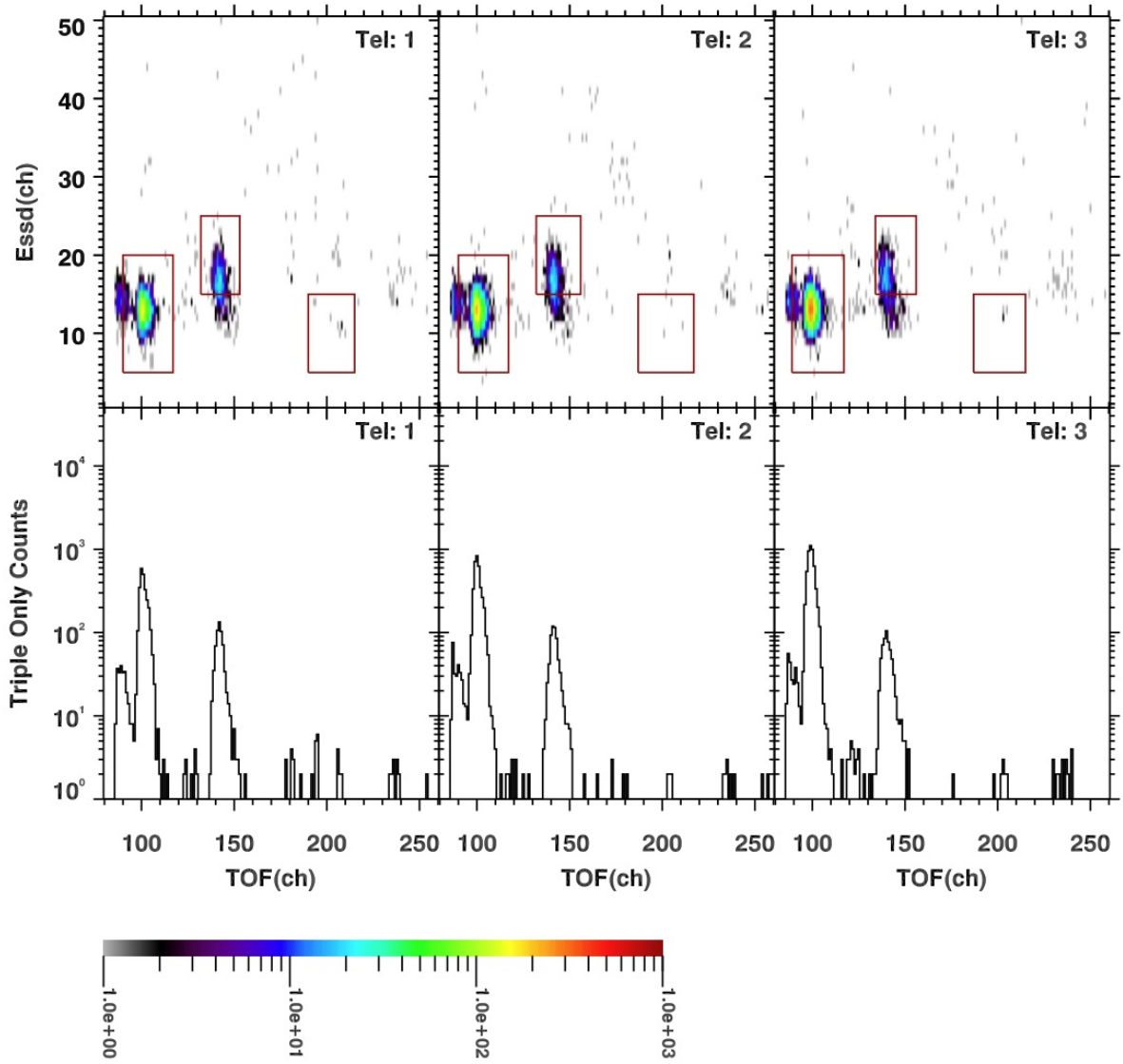
2004-2010 L=7-16 Latitude=-10.0 to 10.0
DPPS: 13



Species	TOF(tel: 1)	TOF(tel: 2)	TOF(tel: 3)	Esd
H+	98-127	98-127	98-122	5-20
H2+	144-174	144-175	144-175	0-0
He++	144-169	144-169	144-169	7-22
H3+	0-0	0-0	0-0	0-0
He+	211-232	205-233	204-233	0-0
O++	287-338	287-338	287-338	2-20
W+	420-670	420-670	420-670	0-0
O+++	0-0	0-0	0-0	0-0
C+	0-0	0-0	0-0	0-0
N+	0-0	0-0	0-0	0-0
O2+	0-0	0-0	0-0	0-0

Figure D.22: Histogram of all counts in the magnetospheric period for DPPS step 13.

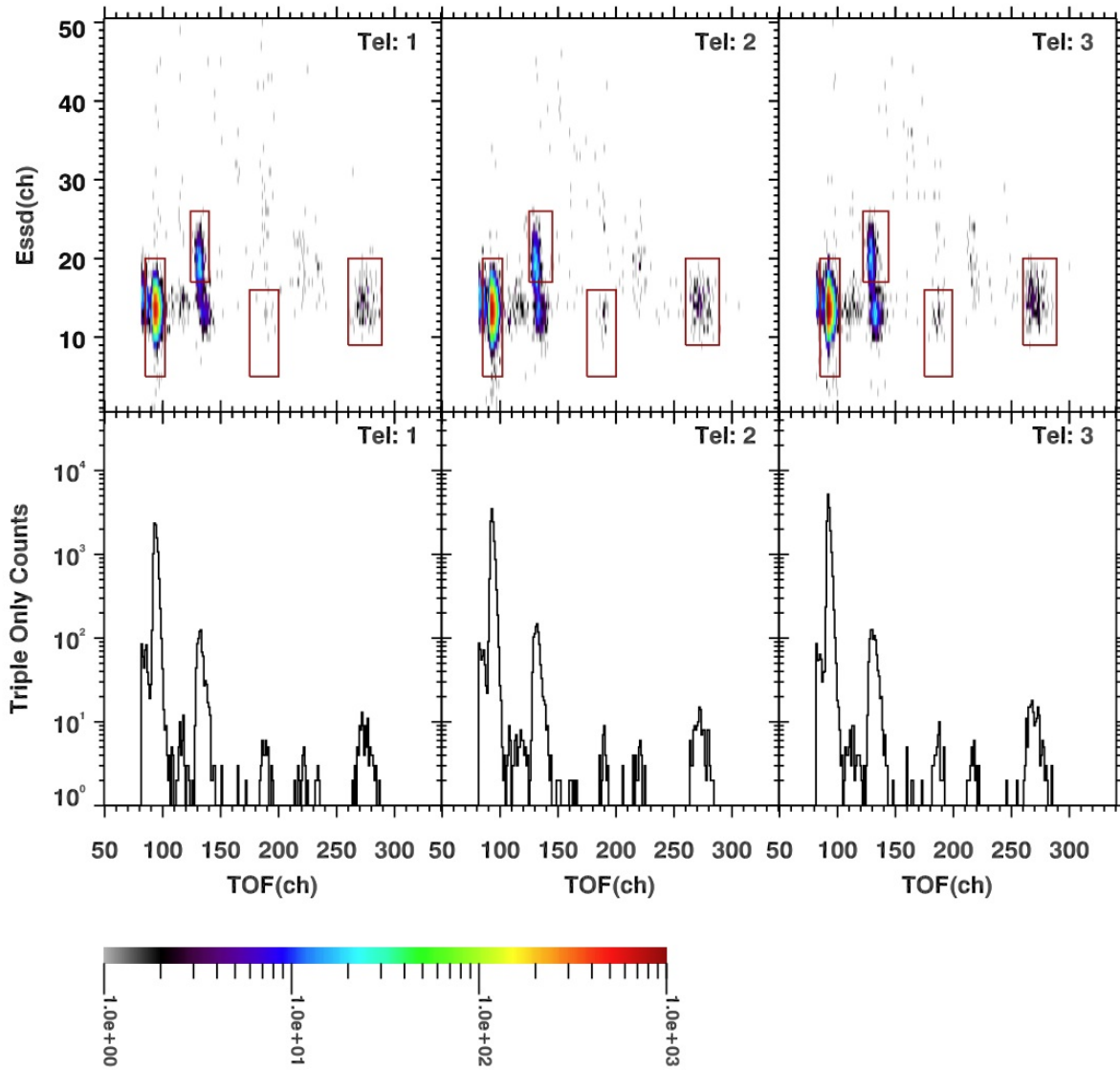
2004-2010 L=7-16 Latitude=-10.0 to 10.0
DPPS: 14



Species	TOF(tel: 1)	TOF(tel: 2)	TOF(tel: 3)	Essd
H+	90-117	90-117	89-117	5-20
H2+	135-157	132-157	134-156	0-0
He++	132-153	132-156	134-156	15-25
H3+	0-0	0-0	0-0	0-0
He+	190-215	187-217	187-215	5-15
O++	271-322	271-322	271-322	2-20
W+	400-620	400-620	395-620	0-0
O+++	0-0	0-0	0-0	0-0
C+	0-0	0-0	0-0	0-0
N+	0-0	0-0	0-0	0-0
O2+	0-0	0-0	0-0	0-0

Figure D.23: Histogram of all counts in the magnetospheric period for DPPS step 14.

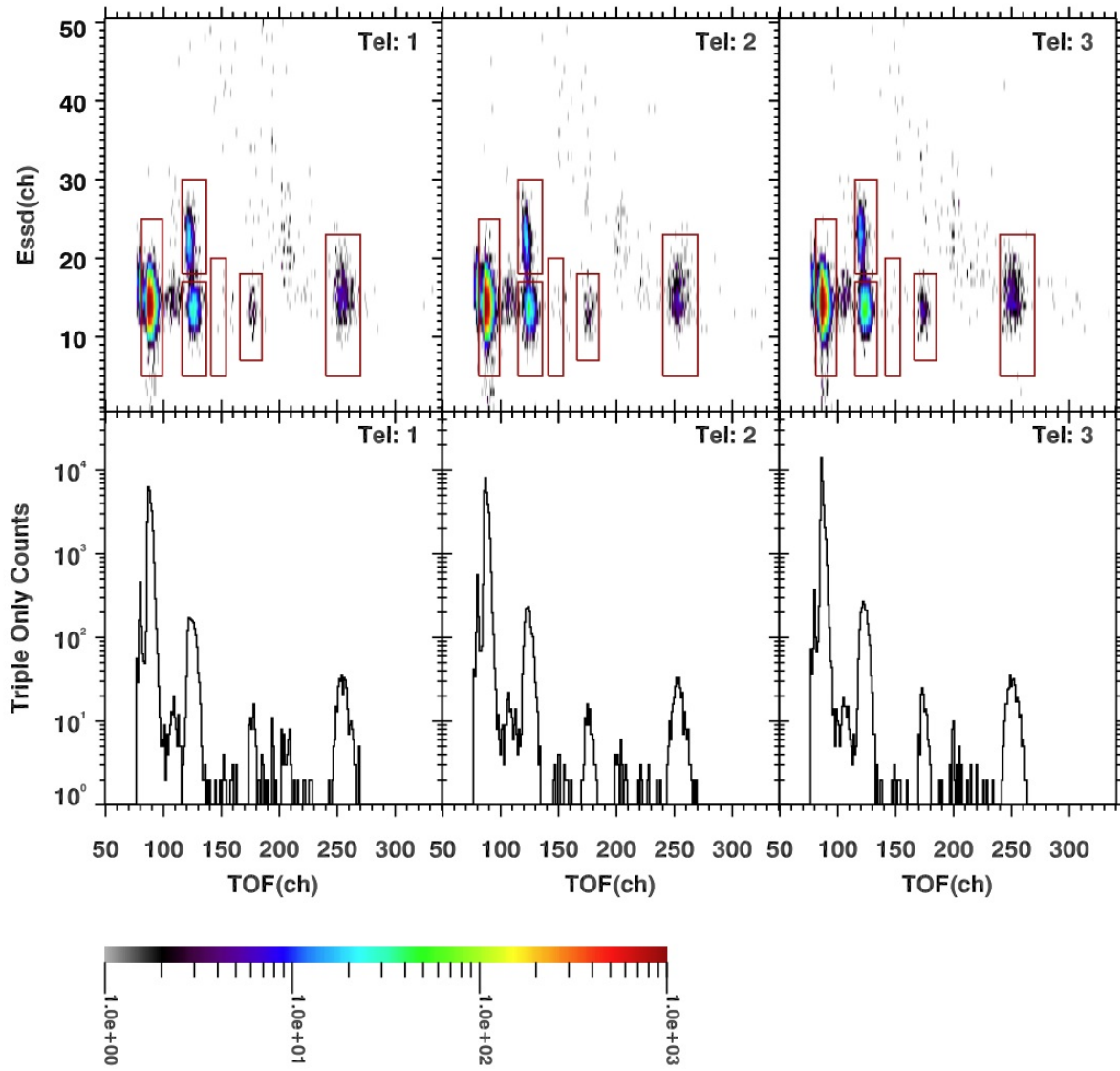
2004-2010 L=7-16 Latitude=-10.0 to 10.0
DPPS: 15



Species	TOF(tel: 1)	TOF(tel: 2)	TOF(tel: 3)	Esd
H+	85-102	85-102	85-102	5-20
H2+	124-149	125-149	122-144	0-0
He++	124-140	125-145	122-144	17-26
H3+	0-0	0-0	0-0	0-0
He+	175-200	175-200	175-199	5-16
O++	260-289	260-289	260-289	9-20
W+	362-580	362-580	358-580	0-0
O+++	0-0	0-0	0-0	0-0
C+	0-0	0-0	0-0	0-0
N+	0-0	0-0	0-0	0-0
O2+	0-0	0-0	0-0	0-0

Figure D.24: Histogram of all counts in the magnetospheric period for DPPS step 15.

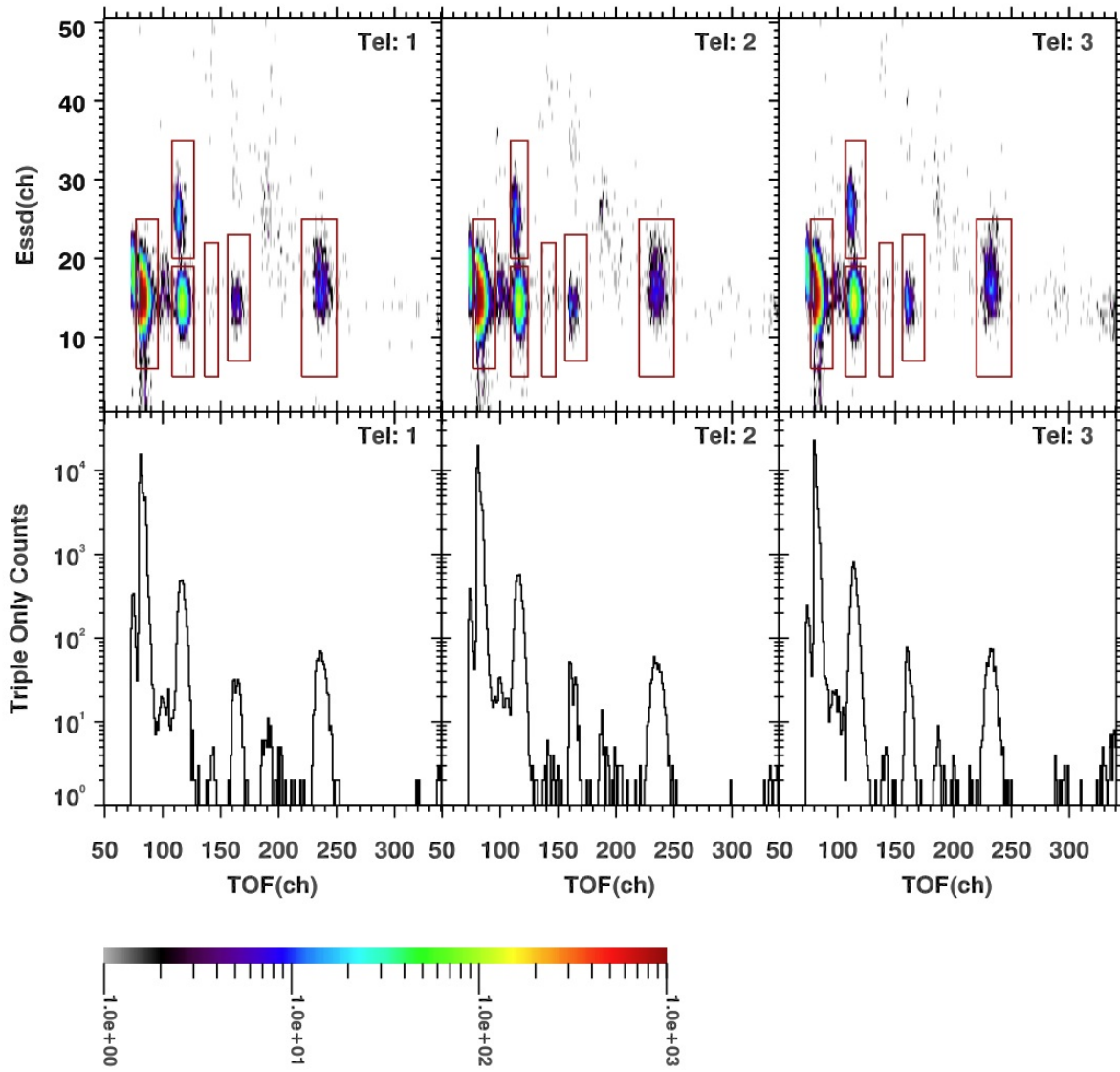
2004-2010 L=7-16 Latitude=-10.0 to 10.0
DPPS: 16



Species	TOF(tel: 1)	TOF(tel: 2)	TOF(tel: 3)	Essd
H+	81-99	81-99	81-99	5-25
H2+	116-137	115-136	115-134	5-17
He++	116-137	115-136	115-134	18-30
H3+	141-154	141-154	141-154	5-20
He+	166-185	166-185	166-185	7-18
O++	240-270	240-270	240-270	5-23
W+	340-510	340-510	340-510	0-0
O+++	0-0	0-0	0-0	0-0
C+	0-0	0-0	0-0	0-0
N+	0-0	0-0	0-0	0-0
O2+	0-0	0-0	0-0	0-0

Figure D.25: Histogram of all counts in the magnetospheric period for DPPS step 16.

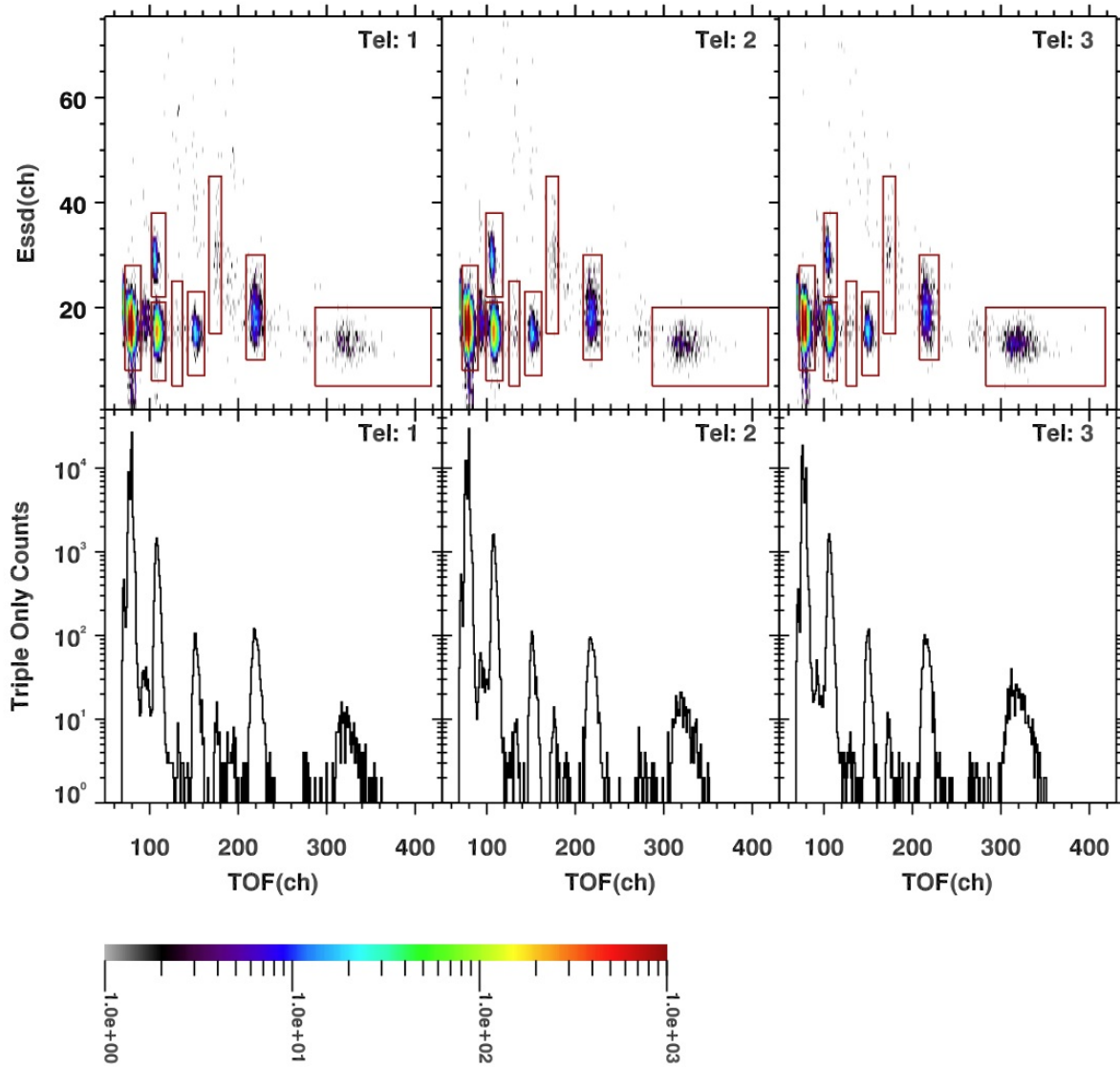
2004-2010 L=7-16 Latitude=-10.0 to 10.0
DPPS: 17



Species	TOF(tel: 1)	TOF(tel: 2)	TOF(tel: 3)	EsSD
H+	77-96	77-96	77-96	6-25
H2+	108-127	109-124	107-124	5-19
He++	108-127	109-124	107-124	20-35
H3+	136-148	136-148	136-148	5-22
He+	156-175	156-175	156-175	7-23
O++	220-250	220-250	220-250	5-25
W+	312-470	312-470	312-470	0-0
O+++	0-0	0-0	0-0	0-0
C+	0-0	0-0	0-0	0-0
N+	0-0	0-0	0-0	0-0
O2+	0-0	0-0	0-0	0-0

Figure D.26: Histogram of all counts in the magnetospheric period for DPPS step 17.

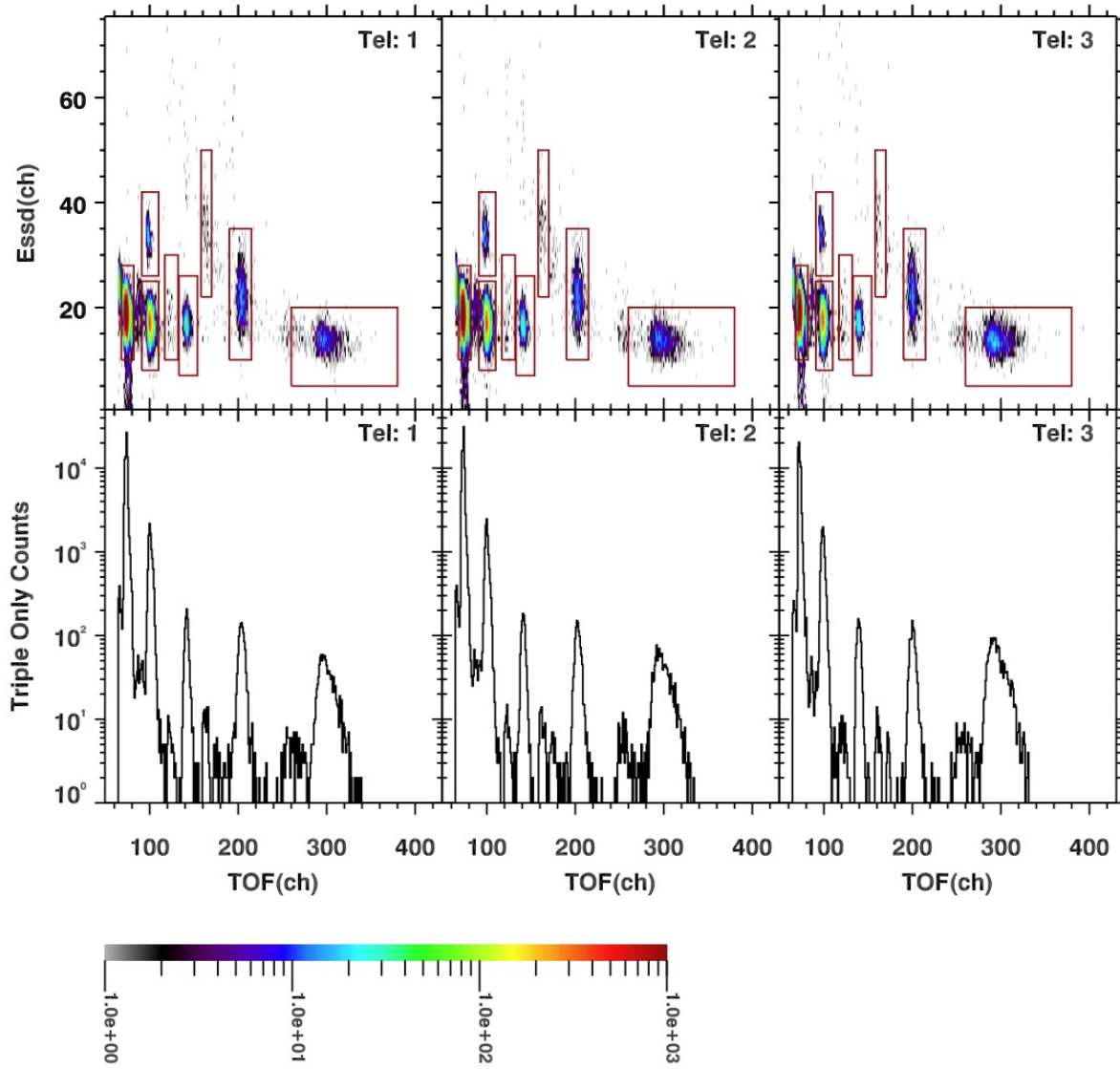
2004-2010 L=7-16 Latitude=-10.0 to 10.0
DPPS: 18



Species	TOF(tel: 1)	TOF(tel: 2)	TOF(tel: 3)	Essd
H+	72-90	72-90	72-90	8-28
H2+	102-118	99-118	100-115	6-21
He++	102-118	99-118	100-115	22-38
H3+	125-137	125-137	125-137	5-25
He+	143-162	143-162	143-162	7-23
O++	209-230	209-230	208-230	10-30
W+	287-418	287-418	283-418	5-20
O+++	167-181	167-181	167-181	15-45
C+	0-0	0-0	0-0	0-0
N+	0-0	0-0	0-0	0-0
O2+	0-0	0-0	0-0	0-0

Figure D.27: Histogram of all counts in the magnetospheric period for DPPS step 18.

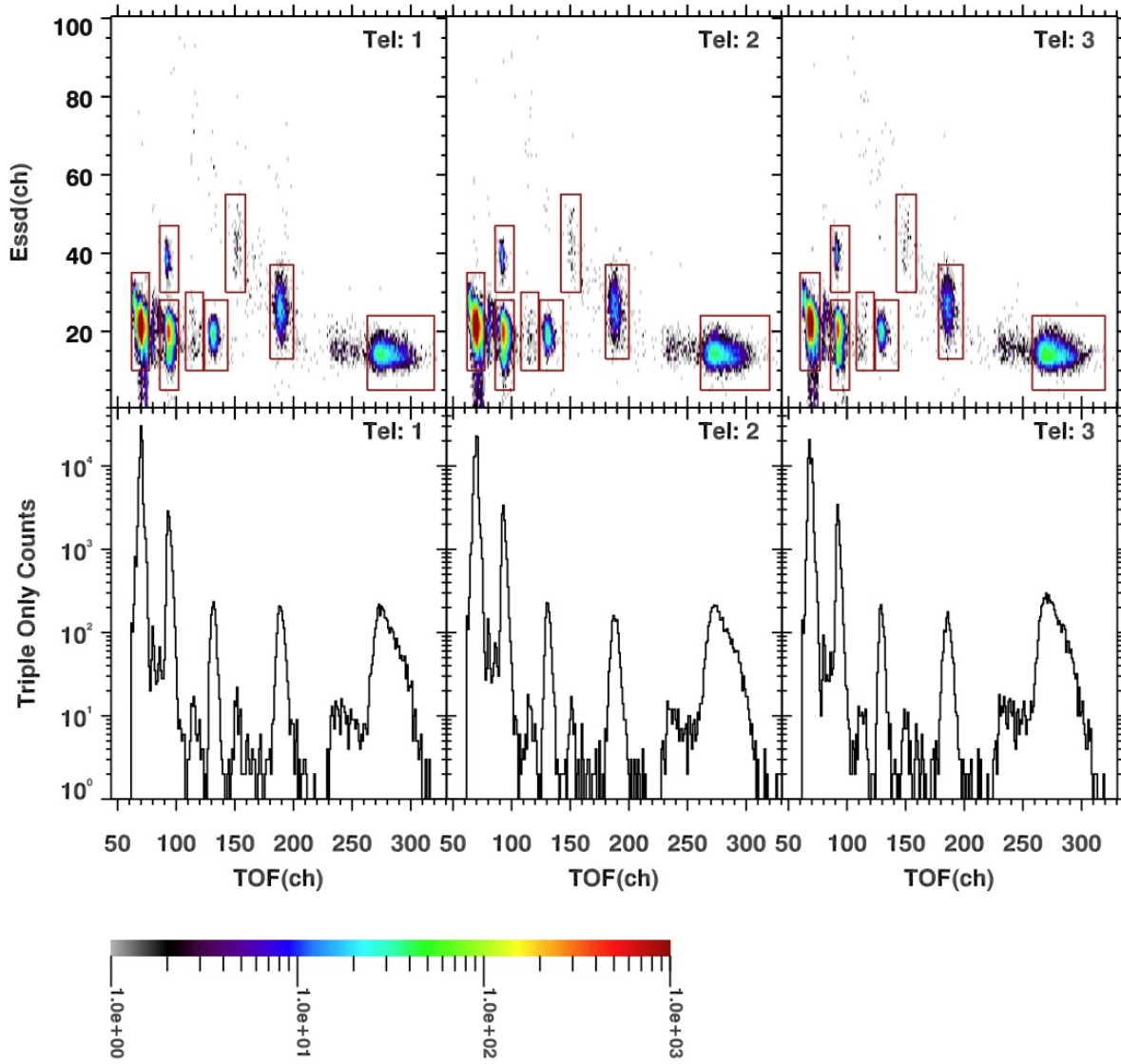
2004-2010 L=7-16 Latitude=-10.0 to 10.0
DPPS: 19



Species	TOF(tel: 1)	TOF(tel: 2)	TOF(tel: 3)	Essd
H+	68-82	68-82	68-82	10-28
H2+	91-110	91-110	91-110	8-25
He++	91-110	91-110	91-110	26-42
H3+	117-132	117-132	117-132	10-30
He+	133-154	133-154	133-154	7-26
O++	190-215	190-215	190-215	10-35
W+	260-380	260-380	260-380	5-20
O+++	158-170	158-170	158-170	22-50
C+	0-0	0-0	0-0	0-0
N+	0-0	0-0	0-0	0-0
O2+	0-0	0-0	0-0	0-0

Figure D.28: Histogram of all counts in the magnetospheric period for DPPS step 19.

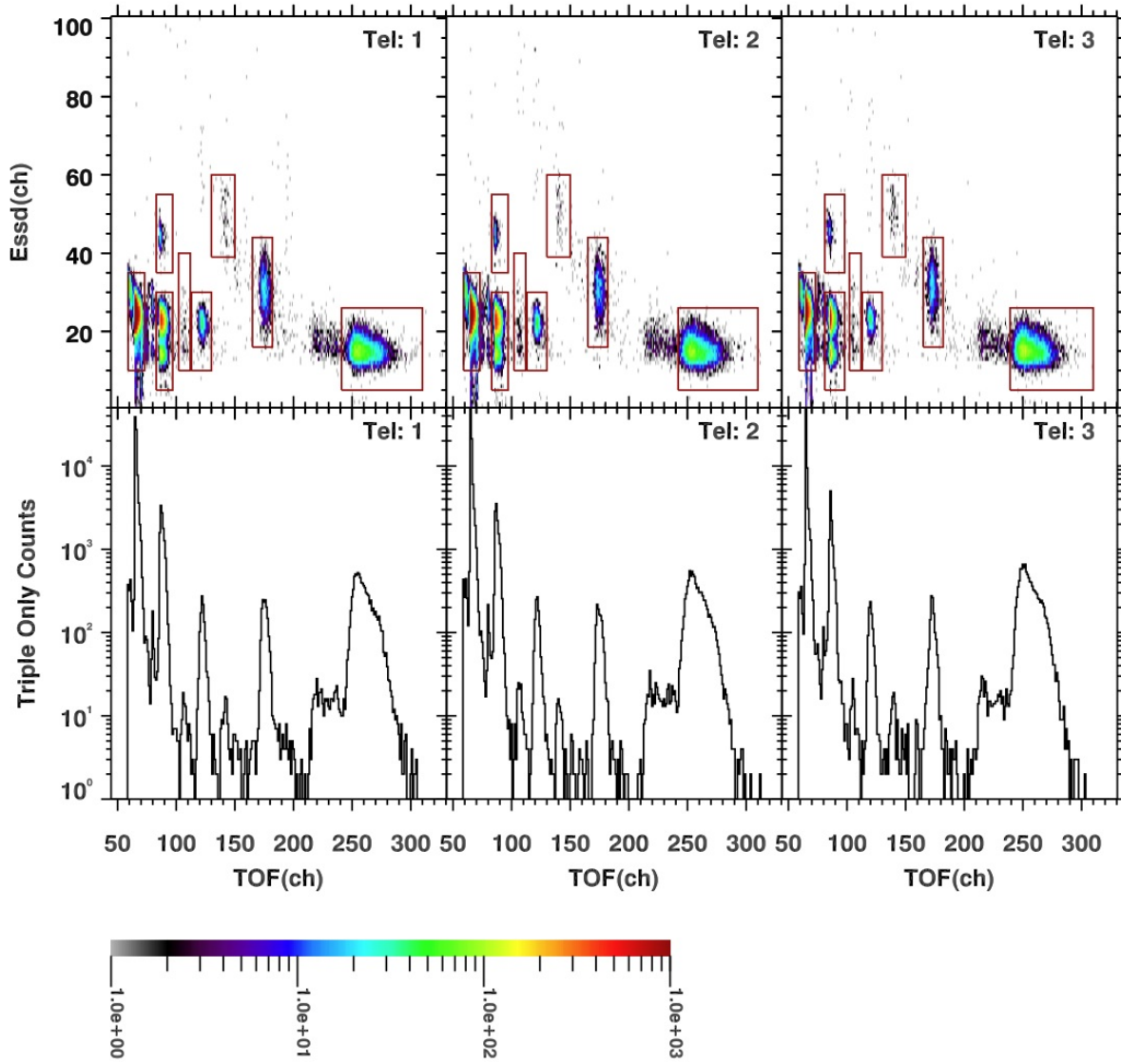
2004-2010 L=7-16 Latitude=-10.0 to 10.0
DPPS: 20



Species	TOF(tel: 1)	TOF(tel: 2)	TOF(tel: 3)	Essd
H+	62-77	62-77	60-77	10-35
H2+	86-102	86-102	86-102	5-28
He++	86-102	86-102	86-102	30-47
H3+	108-123	108-123	108-123	10-30
He+	124-144	124-144	124-144	10-28
O++	180-200	180-200	178-199	13-37
W+	263-320	261-320	258-320	5-24
O+++	142-159	142-159	142-159	30-55
C+	0-0	0-0	0-0	0-0
N+	0-0	0-0	0-0	0-0
O2+	0-0	0-0	0-0	0-0

Figure D.29: Histogram of all counts in the magnetospheric period for DPPS step 20.

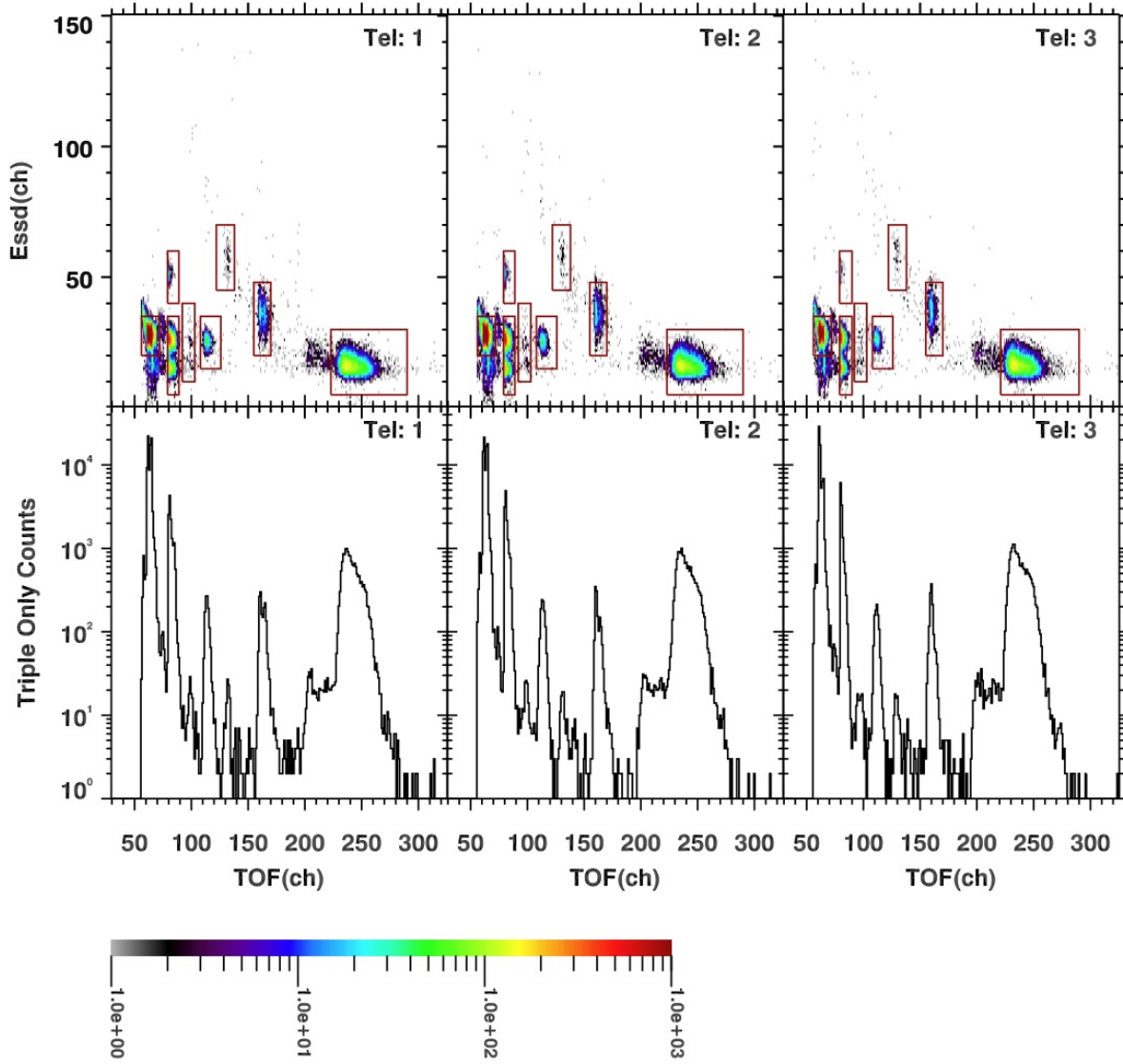
2004-2010 L=7-16 Latitude=-10.0 to 10.0
DPPS: 21



Species	TOF(tel: 1)	TOF(tel: 2)	TOF(tel: 3)	Es sd
H+	59-73	59-73	59-73	10-35
H2+	83-97	83-97	81-98	5-30
He++	83-97	83-97	81-98	35-55
H3+	102-112	102-112	102-112	10-40
He+	113-130	113-130	113-130	10-30
O++	165-182	165-182	165-182	16-44
W+	241-310	242-310	239-310	5-26
O+++	130-150	130-150	130-150	39-60
C+	0-0	0-0	0-0	0-0
N+	0-0	0-0	0-0	0-0
O2+	0-0	0-0	0-0	0-0

Figure D.30: Histogram of all counts in the magnetospheric period for DPPS step 21.

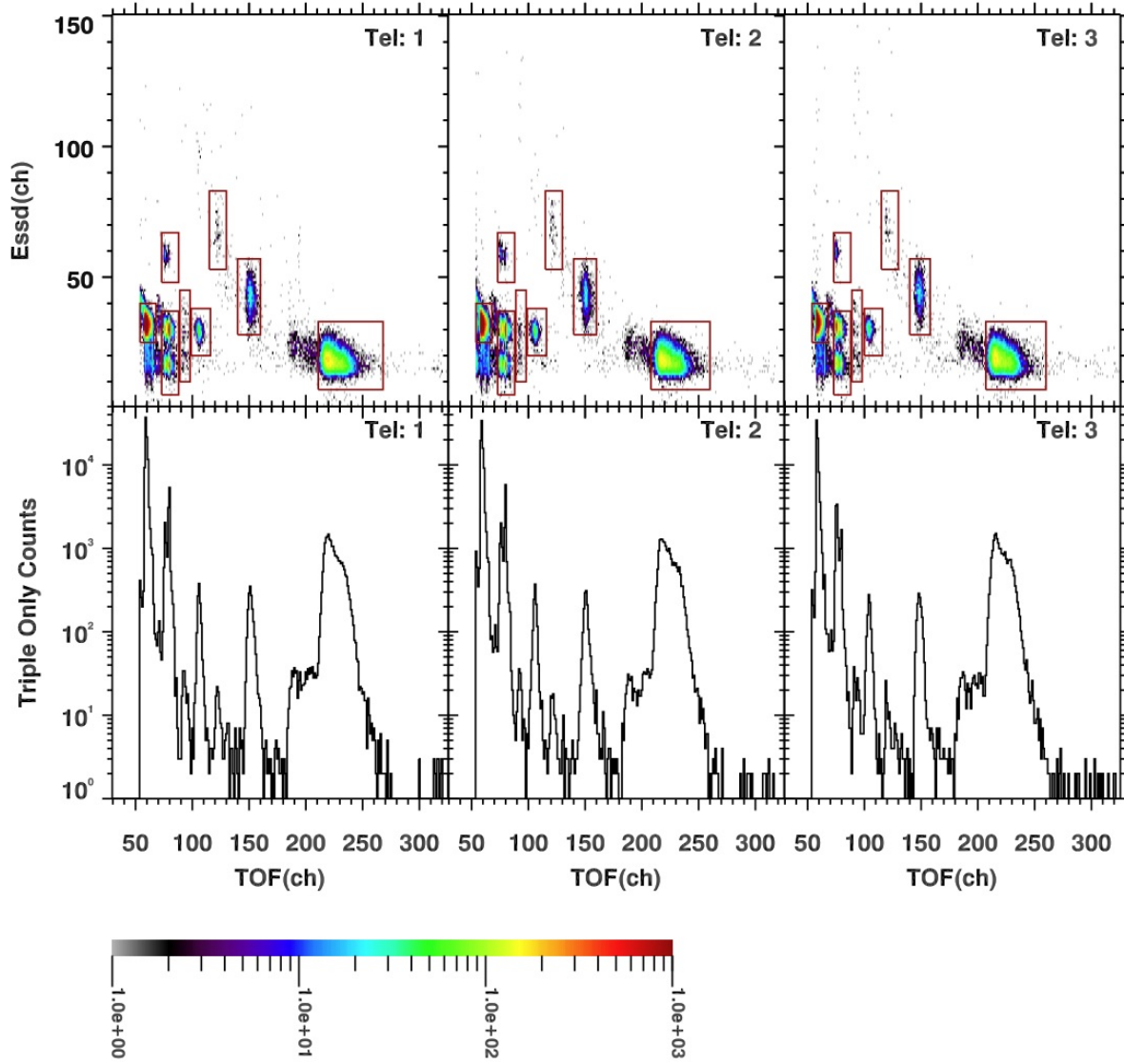
2004-2010 L=7-16 Latitude=-10.0 to 10.0
DPPS: 22



Species	TOF(tel: 1)	TOF(tel: 2)	TOF(tel: 3)	Esd
H+	56-72	56-72	56-72	20-35
H2+	79-89	79-89	79-90	5-35
He++	79-89	79-89	79-90	40-60
H3+	92-103	92-103	92-103	10-40
He+	108-126	108-126	108-126	15-35
O++	155-170	155-170	155-170	20-48
W+	223-290	223-290	221-290	5-30
O+++	122-138	122-138	122-138	45-70
C+	0-0	0-0	0-0	0-0
N+	0-0	0-0	0-0	0-0
O2+	0-0	0-0	0-0	0-0

Figure D.31: Histogram of all counts in the magnetospheric period for DPPS step 22.

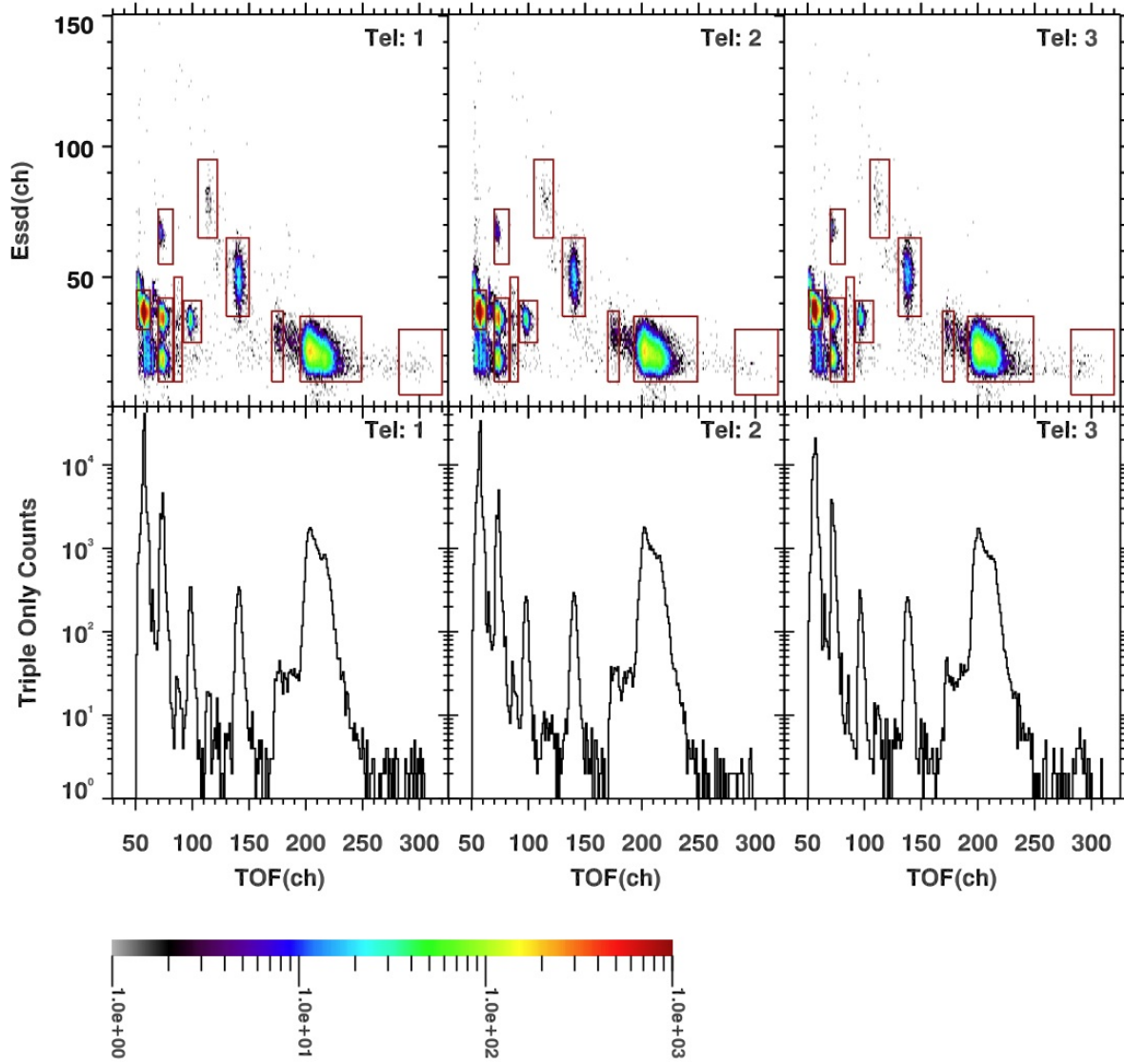
2004-2010 L=7-16 Latitude=-10.0 to 10.0
DPPS: 23



Species	TOF(tel: 1)	TOF(tel: 2)	TOF(tel: 3)	Esd
H+	54-68	54-68	54-68	25-40
H2+	73-88	73-88	73-88	5-37
He++	73-88	73-88	73-88	48-67
H3+	89-98	89-98	89-98	10-45
He+	99-116	99-116	100-116	20-38
O++	140-160	140-160	140-158	28-57
W+	211-268	208-260	207-260	7-33
O+++	115-130	115-130	115-130	53-83
C+	0-0	0-0	0-0	0-0
N+	0-0	0-0	0-0	0-0
O2+	0-0	0-0	0-0	0-0

Figure D.32: Histogram of all counts in the magnetospheric period for DPPS step 23.

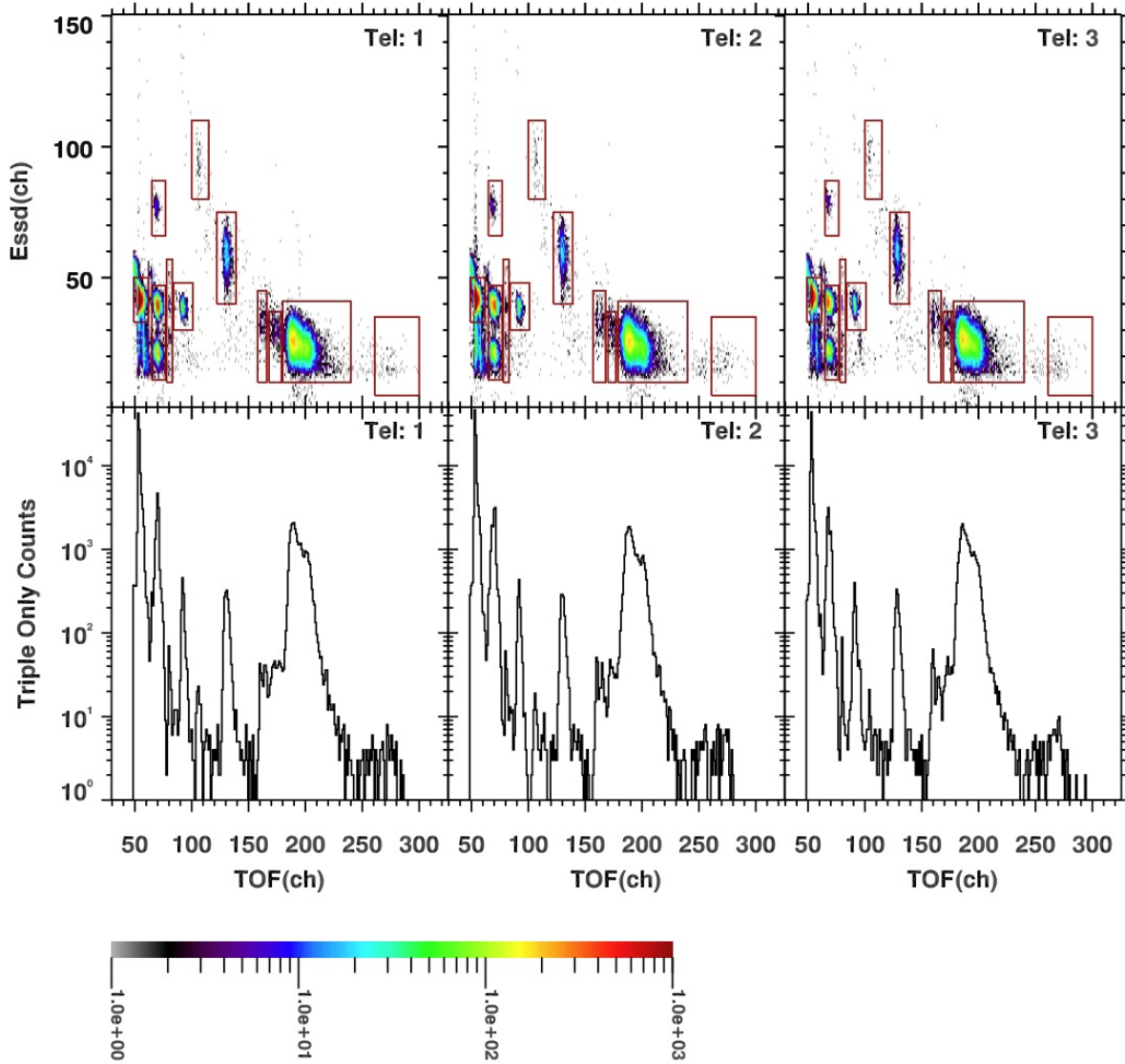
2004-2010 L=7-16 Latitude=-10.0 to 10.0
DPPS: 24



Species	TOF(tel: 1)	TOF(tel: 2)	TOF(tel: 3)	Esd
H+	51-63	51-63	51-63	30-45
H2+	70-83	70-83	70-83	10-42
He++	70-83	70-83	70-83	55-76
H3+	84-91	84-91	84-91	10-50
He+	92-108	92-108	92-108	25-41
O++	130-150	130-150	130-150	35-65
W+	195-249	193-249	191-249	10-35
O+++	105-122	105-122	105-122	65-95
C+	170-180	170-180	169-179	10-37
N+	0-0	0-0	0-0	0-0
O2+	282-320	282-320	282-320	5-30

Figure D.33: Histogram of all counts in the magnetospheric period for DPPS step 24.

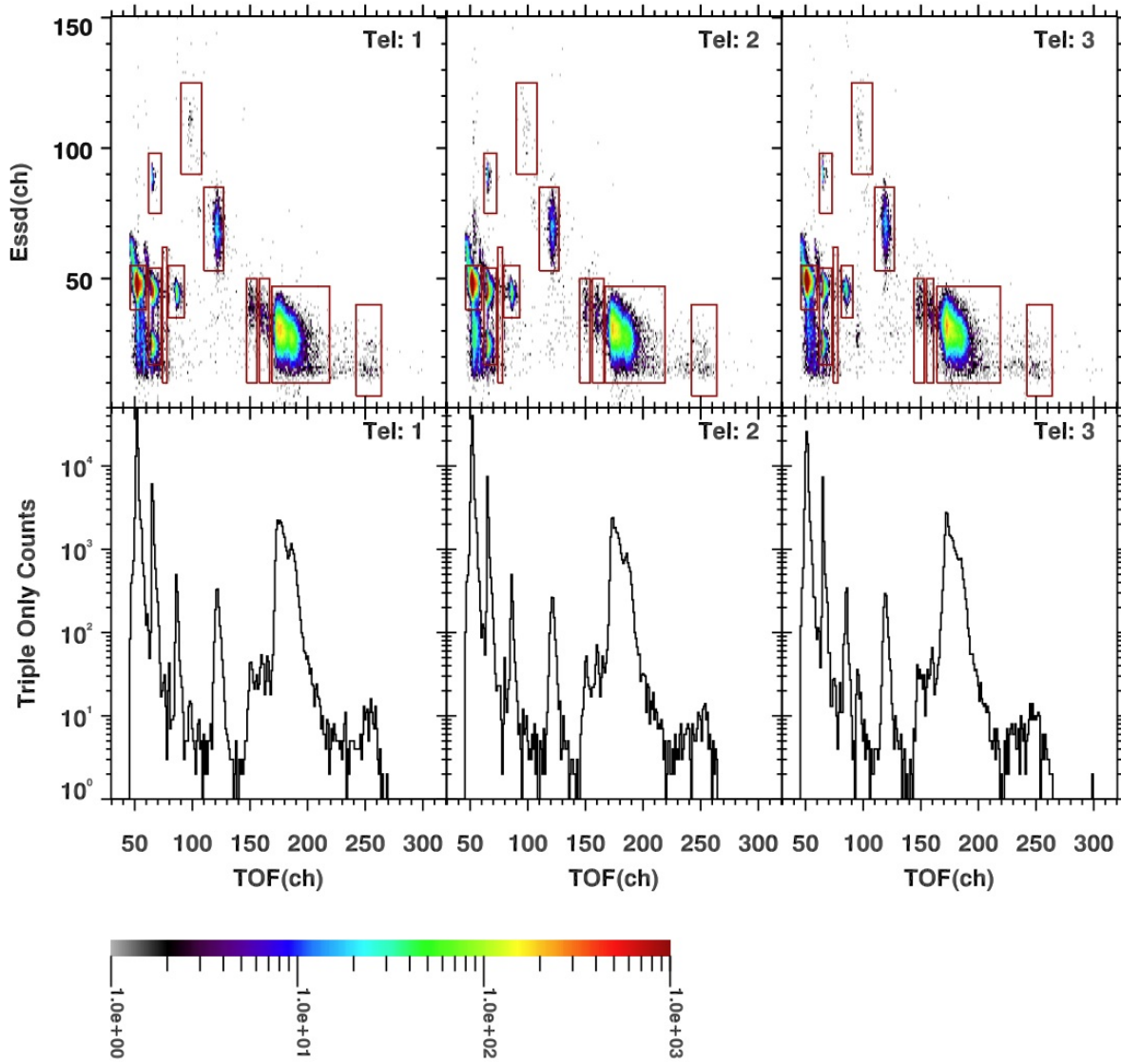
2004-2010 L=7-16 Latitude=-10.0 to 10.0
DPPS: 25



Species	TOF(tel: 1)	TOF(tel: 2)	TOF(tel: 3)	Essd
H+	49-62	49-62	49-62	33-50
H2+	65-77	65-77	65-77	11-47
He++	65-77	65-77	65-77	66-87
H3+	78-83	78-83	78-83	10-57
He+	84-101	84-101	84-101	30-48
O++	122-139	122-139	122-139	40-75
W+	180-240	179-240	178-240	10-41
O+++	100-115	100-115	100-115	80-110
C+	158-166	157-168	156-167	10-45
N+	168-179	170-177	169-176	10-37
O2+	261-300	261-300	261-300	5-35

Figure D.34: Histogram of all counts in the magnetospheric period for DPPS step 25.

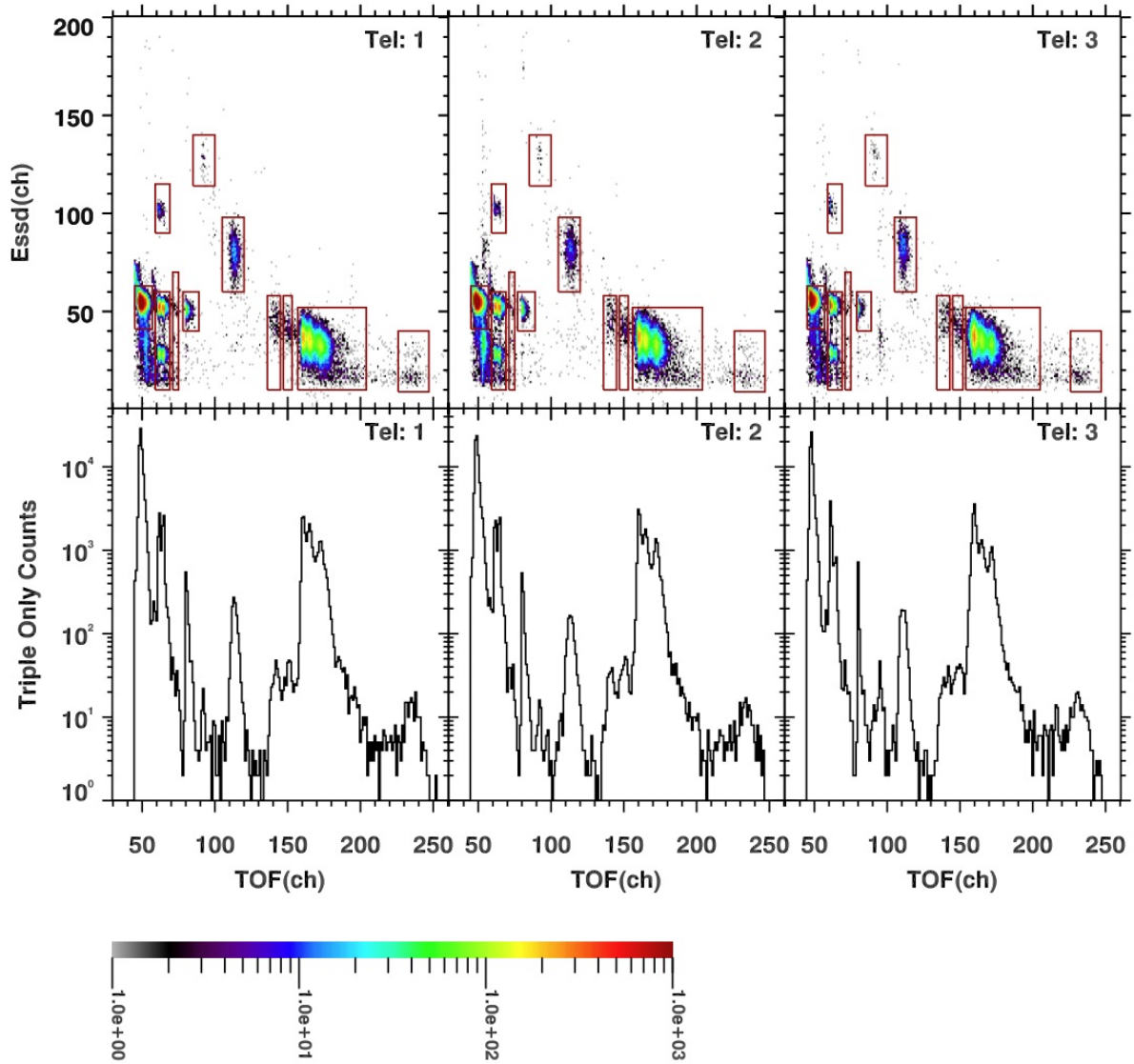
2004-2010 L=7-16 Latitude=-10.0 to 10.0
DPPS: 26



Species	TOF(tel: 1)	TOF(tel: 2)	TOF(tel: 3)	Esd
H+	46-60	46-60	46-60	38-55
H2+	62-73	62-73	62-73	17-54
He++	62-73	62-73	62-73	75-98
H3+	74-78	74-78	74-78	10-62
He+	79-93	79-93	81-91	35-55
O++	110-127	110-127	110-127	53-85
W+	169-219	167-219	164-219	10-47
O+++	90-108	90-108	90-108	90-125
C+	147-156	145-154	144-153	10-50
N+	158-167	156-166	155-161	10-50
O2+	242-264	242-264	242-264	5-40

Figure D.35: Histogram of all counts in the magnetospheric period for DPPS step 26.

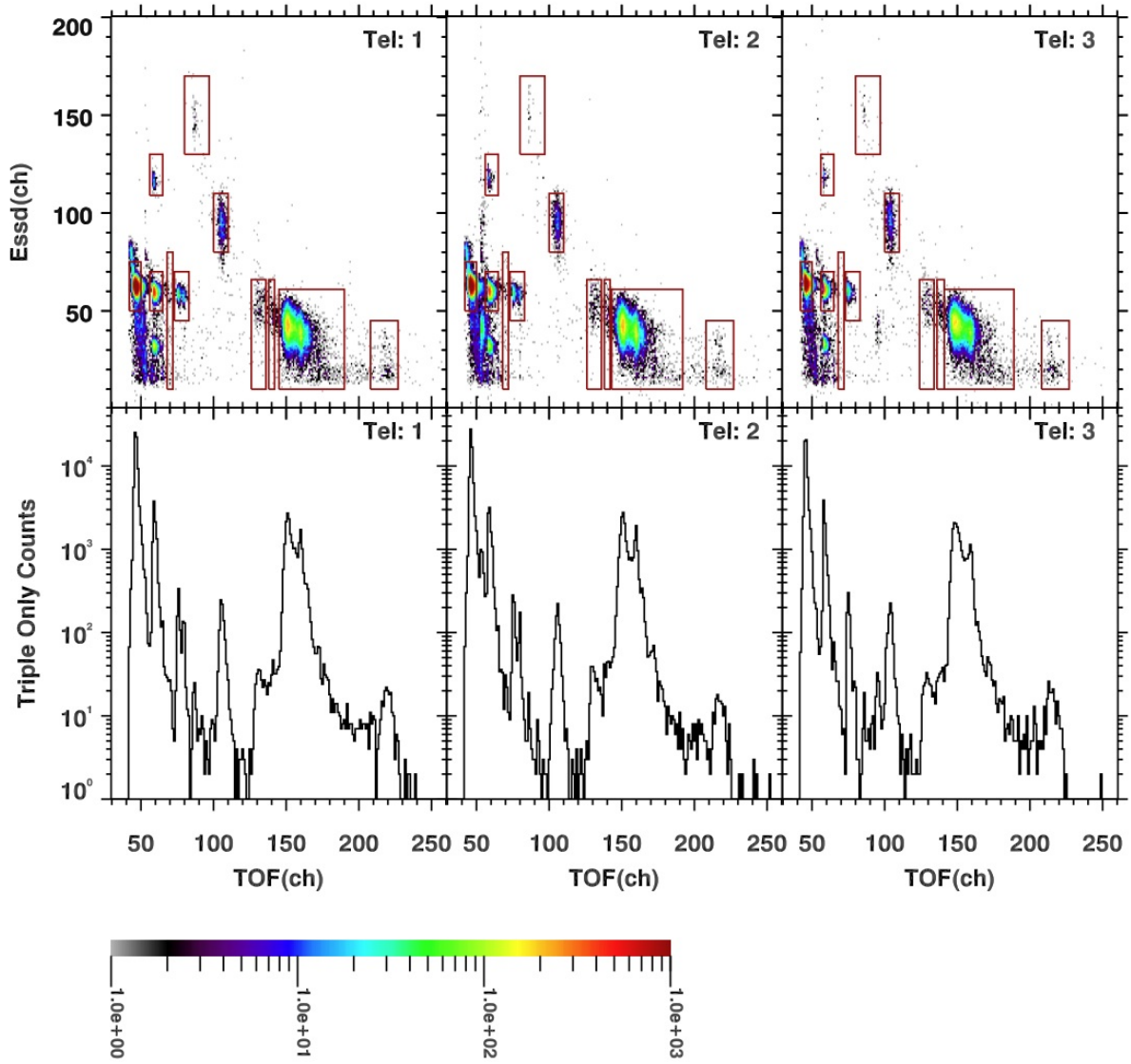
2004-2010 L=7-16 Latitude=-10.0 to 10.0
DPPS: 27



Species	TOF(tel: 1)	TOF(tel: 2)	TOF(tel: 3)	Essd
H+	45-57	45-57	45-57	41-63
H2+	59-69	59-69	59-69	10-60
He++	59-69	59-69	59-69	90-115
H3+	71-75	71-75	71-75	10-70
He+	78-89	77-89	79-89	40-60
O++	105-120	105-120	105-120	60-98
W+	157-204	156-204	154-205	10-52
O+++	85-100	85-100	85-100	114-140
C+	136-145	136-145	134-143	10-58
N+	147-153	147-153	145-152	10-58
O2+	226-247	226-247	226-247	9-40

Figure D.36: Histogram of all counts in the magnetospheric period for DPPS step 27.

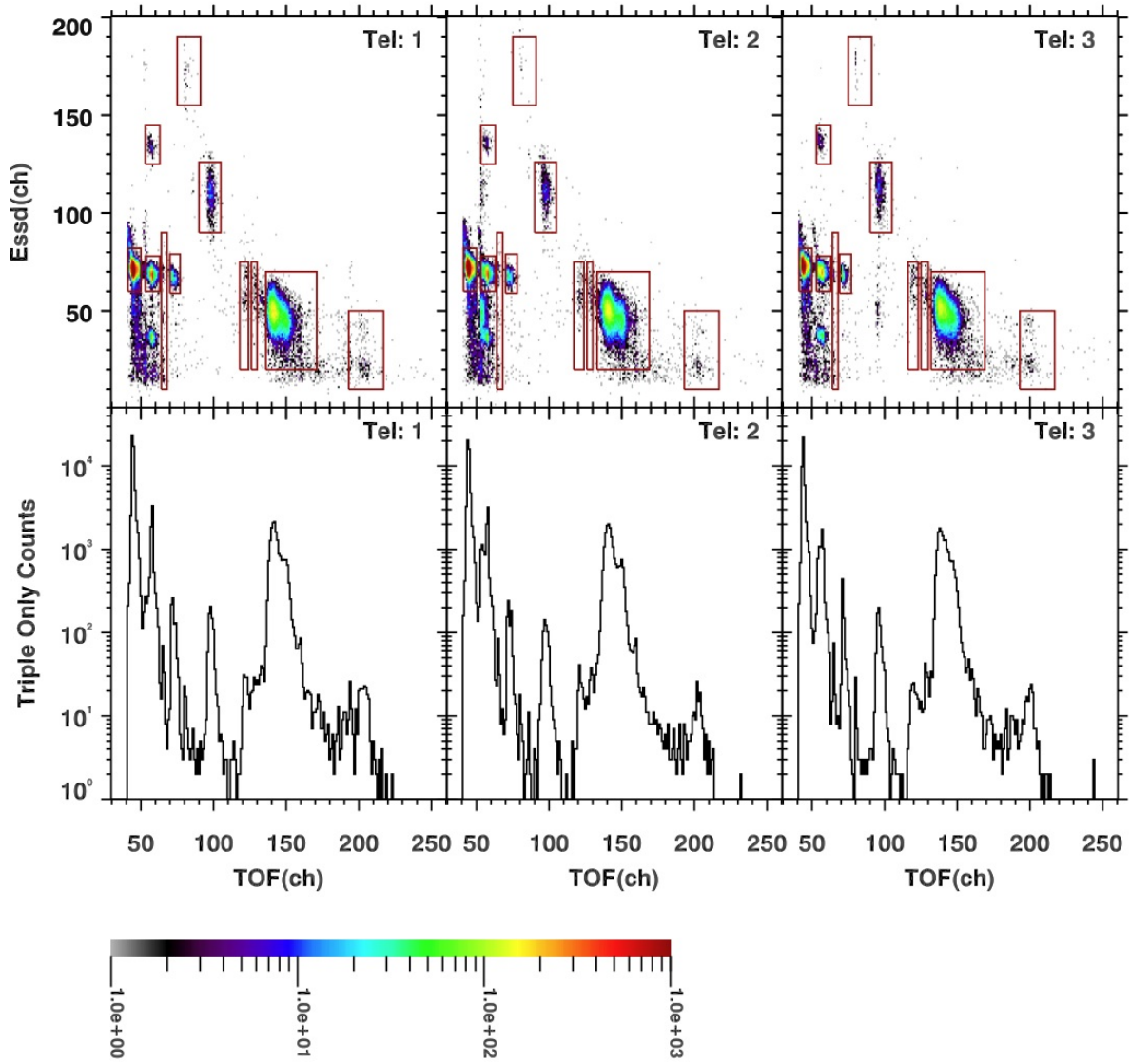
2004-2010 L=7-16 Latitude=-10.0 to 10.0
DPPS: 28



Species	TOF(tel: 1)	TOF(tel: 2)	TOF(tel: 3)	Essd
H+	42-50	42-50	42-50	50-75
H2+	56-65	56-65	56-65	50-70
He++	56-65	56-65	56-65	109-130
H3+	68-72	68-72	68-72	10-80
He+	73-83	73-83	73-83	45-70
O++	100-110	100-110	100-110	80-110
W+	145-190	143-192	141-189	10-61
O+++	80-97	80-97	80-97	130-170
C+	126-136	126-136	124-134	10-66
N+	138-142	138-142	136-141	10-66
O2+	208-227	208-227	208-227	10-45

Figure D.37: Histogram of all counts in the magnetospheric period for DPPS step 28.

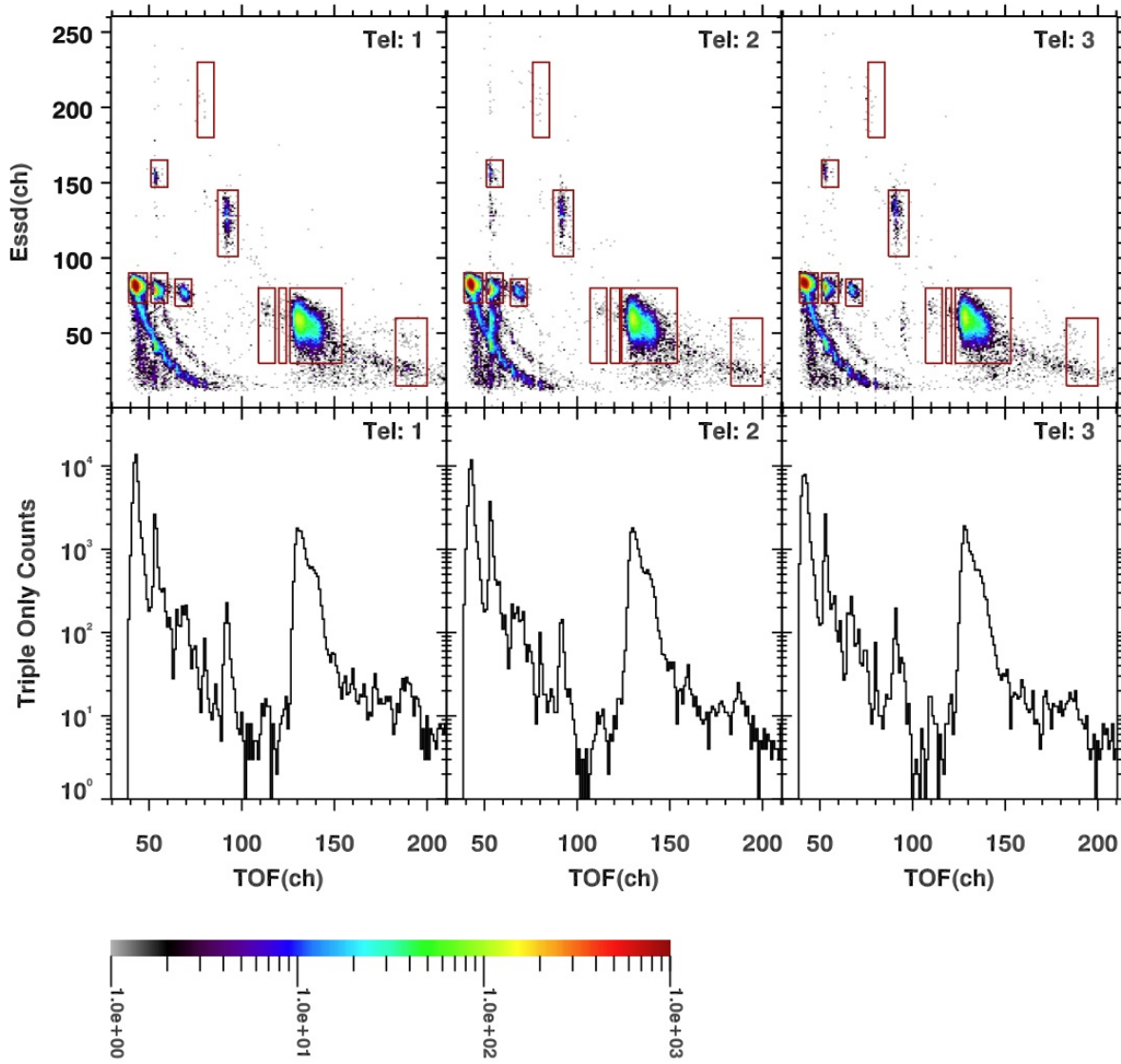
2004-2010 L=7-16 Latitude=-10.0 to 10.0
DPPS: 29



Species	TOF(tel: 1)	TOF(tel: 2)	TOF(tel: 3)	Essd
H+	41-50	41-50	41-50	60-82
H2+	53-63	53-63	53-63	60-78
He++	53-63	53-63	53-63	125-145
H3+	64-68	64-68	64-68	10-90
He+	70-77	70-78	69-77	59-79
O++	90-105	90-105	90-105	90-126
W+	136-171	133-169	132-169	20-70
O+++	75-91	75-91	75-91	155-190
C+	118-124	117-124	116-123	20-75
N+	126-130	126-130	125-130	20-75
O2+	193-217	193-217	193-217	10-50

Figure D.38: Histogram of all counts in the magnetospheric period for DPPS step 29.

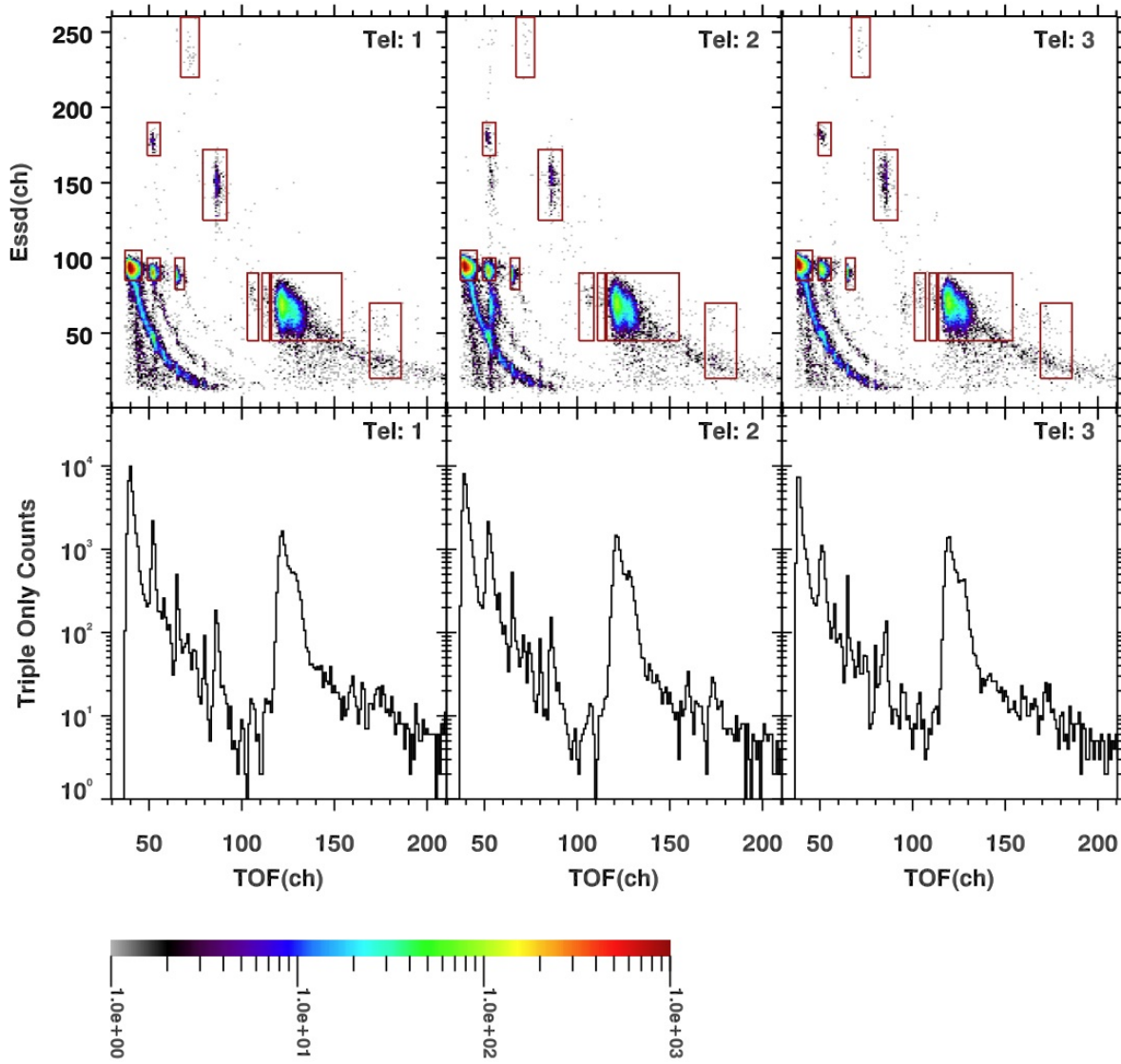
2004-2010 L=7-16 Latitude=-10.0 to 10.0
DPPS: 30



Species	TOF(tel: 1)	TOF(tel: 2)	TOF(tel: 3)	Esd
H+	39-49	39-49	39-49	70-90
H2+	51-60	51-60	51-60	70-90
He++	51-60	51-60	51-60	147-165
H3+	0-0	0-0	0-0	0-0
He+	64-73	64-73	64-73	68-86
O++	87-98	87-98	87-98	101-145
W+	126-154	124-154	123-153	30-80
O+++	76-85	76-85	76-85	180-230
C+	109-118	107-116	107-116	30-80
N+	120-124	118-123	118-121	30-80
O2+	183-200	183-200	183-200	15-60

Figure D.39: Histogram of all counts in the magnetospheric period for DPPS step 30.

2004-2010 L=7-16 Latitude=-10.0 to 10.0
DPPS: 31



Species	TOF(tel: 1)	TOF(tel: 2)	TOF(tel: 3)	Esd
H+	37-46	37-46	37-46	85-105
H2+	49-56	49-56	49-56	85-100
He++	49-56	49-56	49-56	168-190
H3+	0-0	0-0	0-0	0-0
He+	64-69	64-69	64-69	79-100
O++	79-92	79-92	79-92	125-172
W+	116-154	116-155	114-154	45-90
O+++	67-77	67-77	67-77	220-260
C+	103-109	101-109	101-107	45-90
N+	111-115	111-115	109-113	45-90
O2+	169-186	169-186	169-186	20-70

Figure D.40: Histogram of all counts in the magnetospheric period for DPPS step 31.

D.2 Interplanetary Data

The following TOF(ch) histograms are from the interplanetary periods used to determine CHEMS PHA species boxes. Interplanetary data are useful for distinguishing the helium peaks at low energies, therefore a separate section with TOF(ch) histograms for these data is provided. Actually it is impossible to see the helium peaks at low energies in Saturn's magnetosphere. The quieter interplanetary period makes it easier to identify the helium peaks. We do not include Essd(ch) versus TOF(ch) plots for the interplanetary period, because the helium triples data distinguishes itself from the other species. Keep in mind that the interplanetary period is quiet, so there are some bogus TOF peaks in the TOF(ch) histograms. See Section 4.7 on the PHA species box backgrounds for a discussion of bogus TOF.

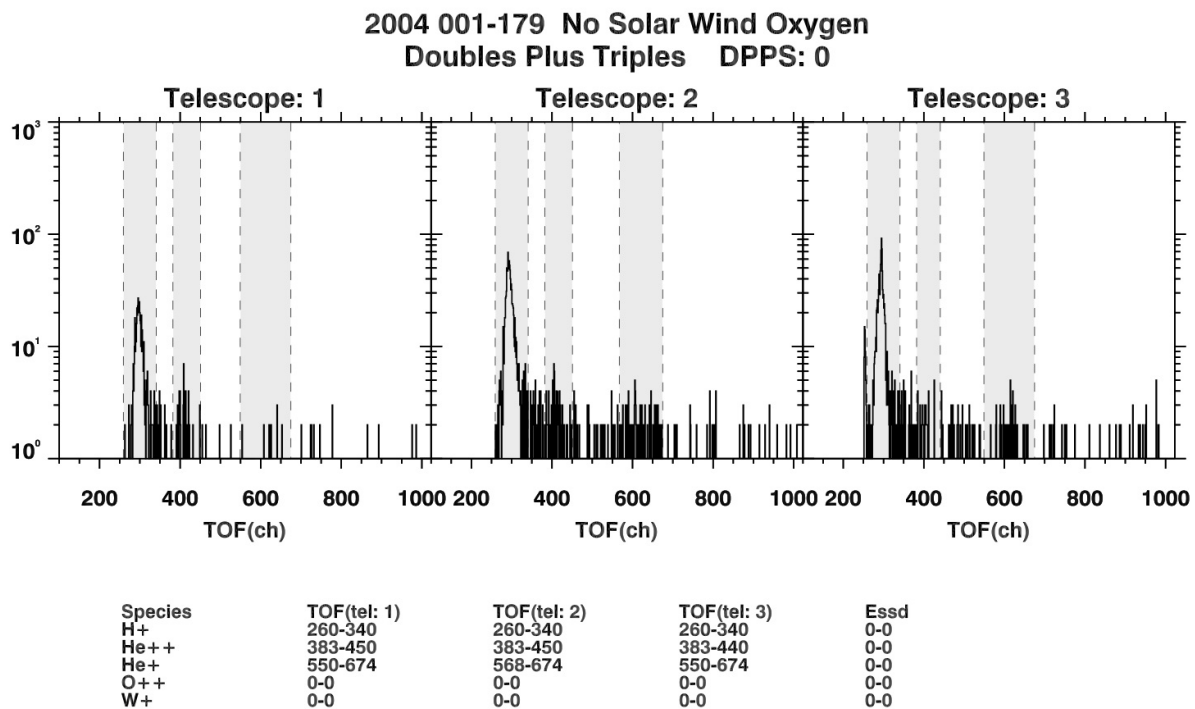


Figure D.41: Histogram of doubles plus triples counts in the interplanetary regime for DPPS step 0.

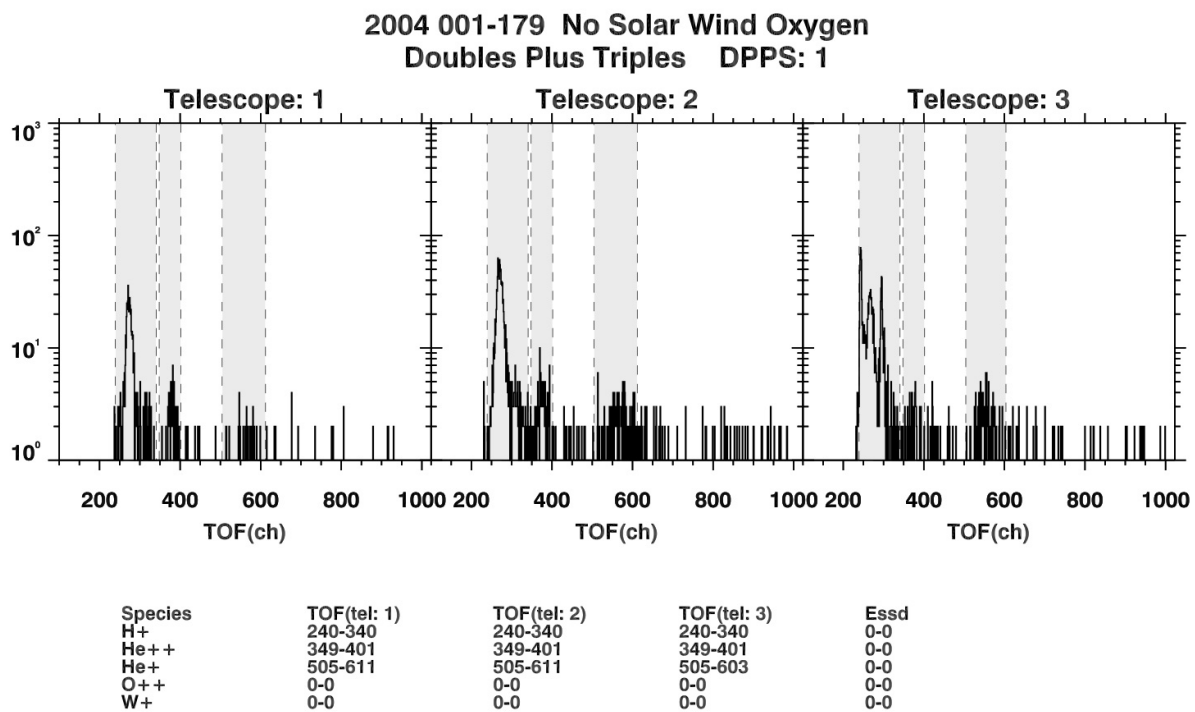


Figure D.42: Histogram of doubles plus triples counts in the interplanetary regime for DPPS step 1.

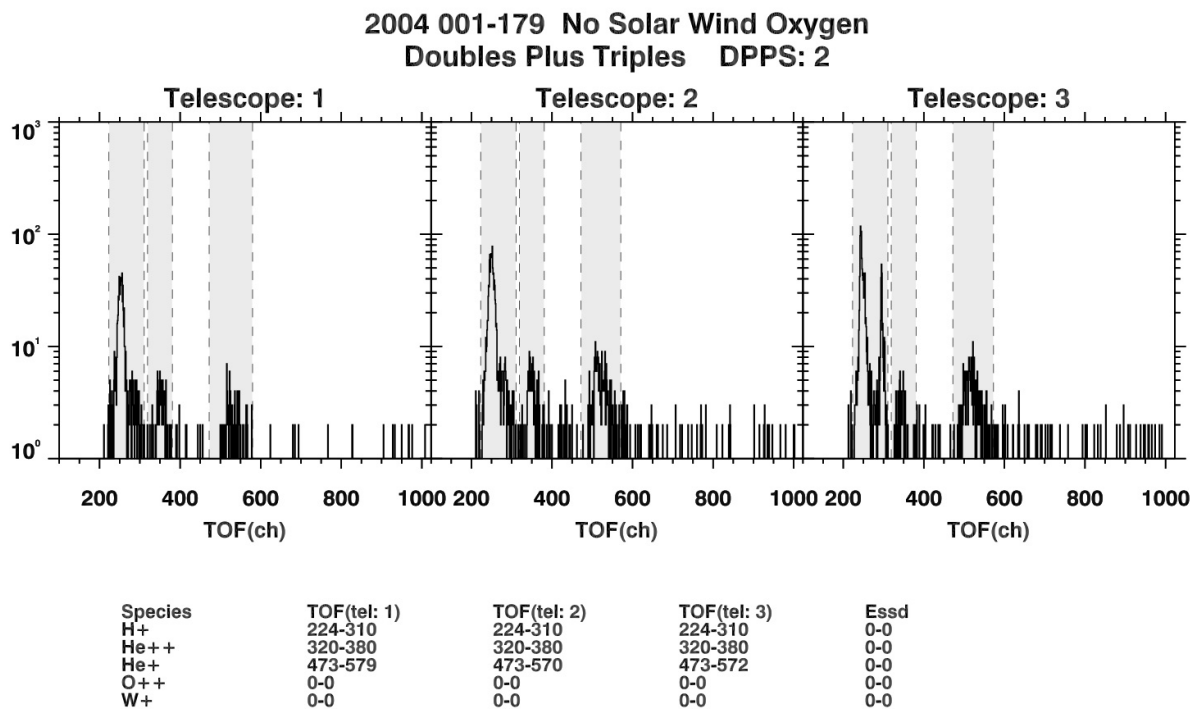


Figure D.43: Histogram of doubles plus triples counts in the interplanetary regime for DPPS step 2.

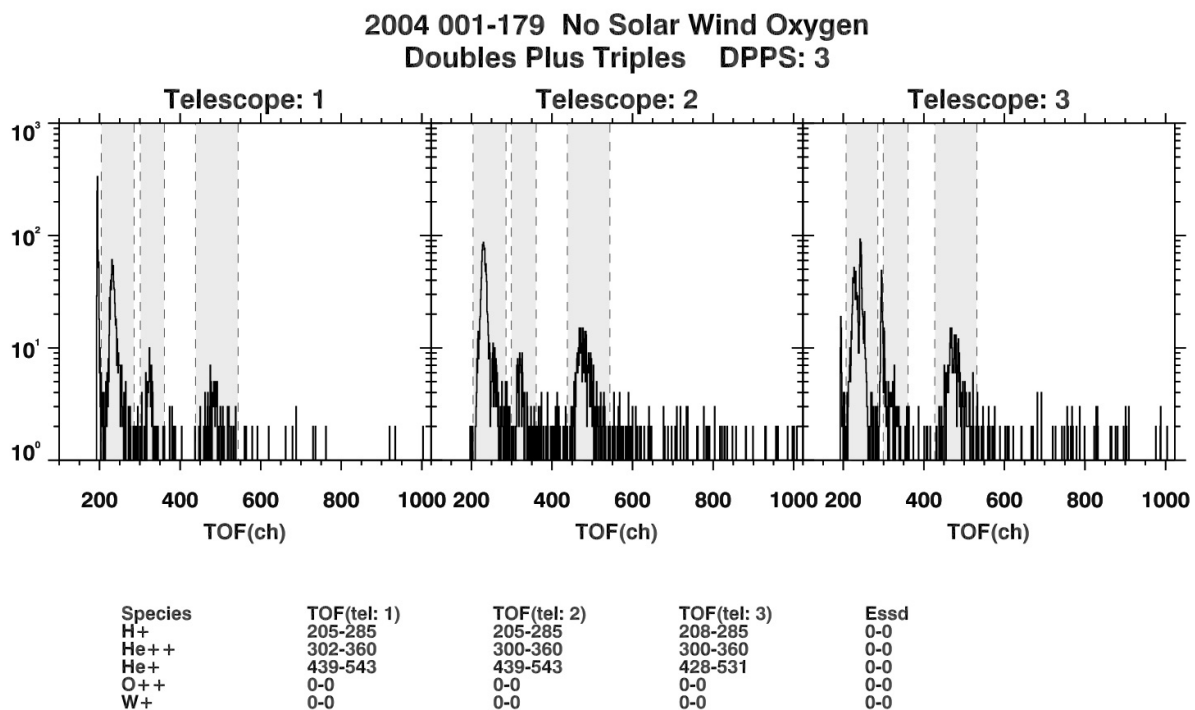


Figure D.44: Histogram of doubles plus triples counts in the interplanetary regime for DPPS step 3.

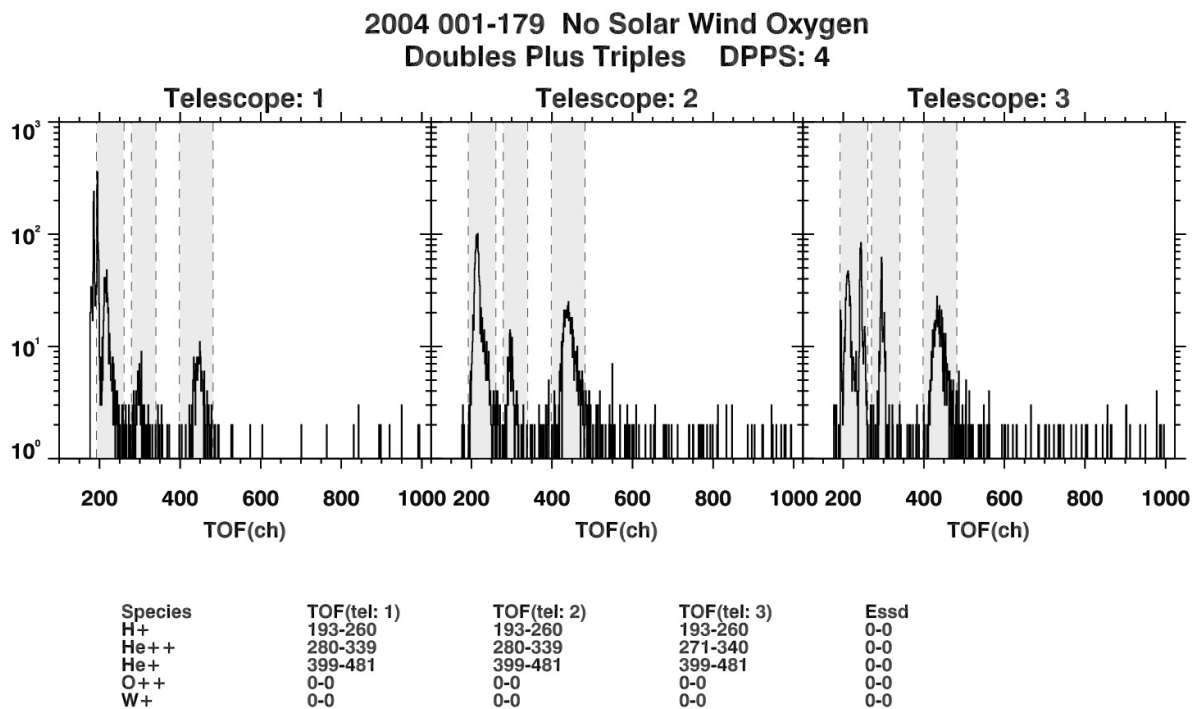


Figure D.45: Histogram of doubles plus triples counts in the interplanetary regime for DPPS step 4.

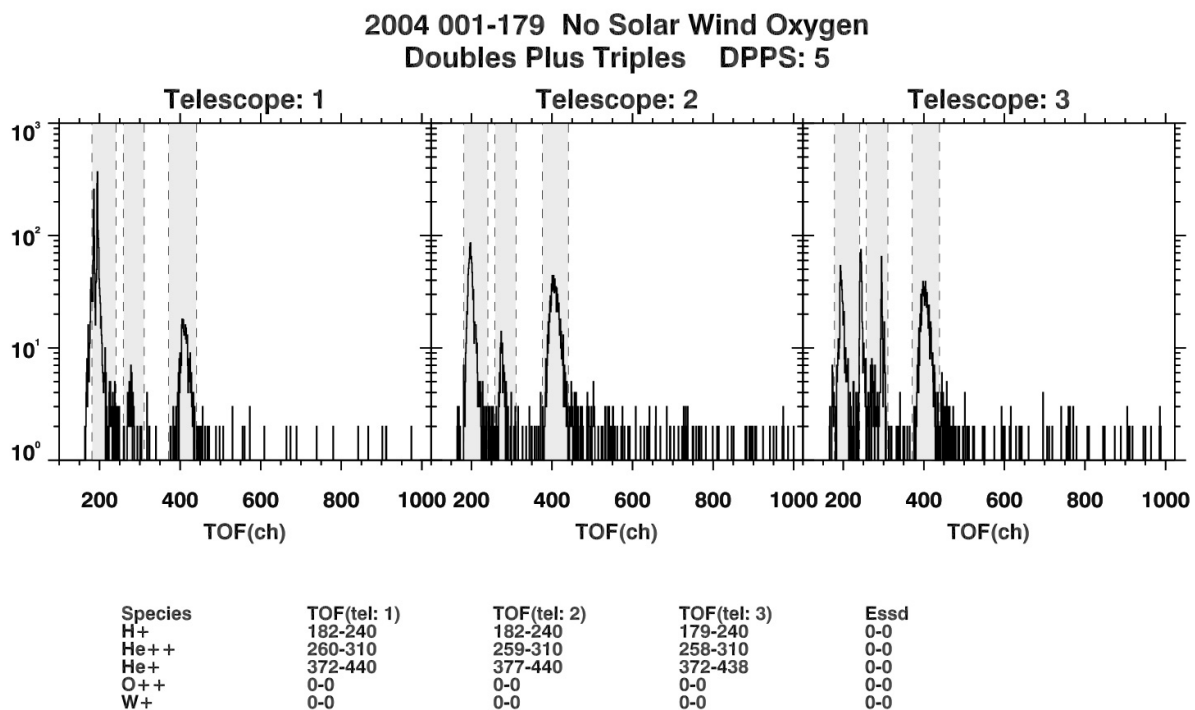


Figure D.46: Histogram of doubles plus triples counts in the interplanetary regime for DPPS step 5.

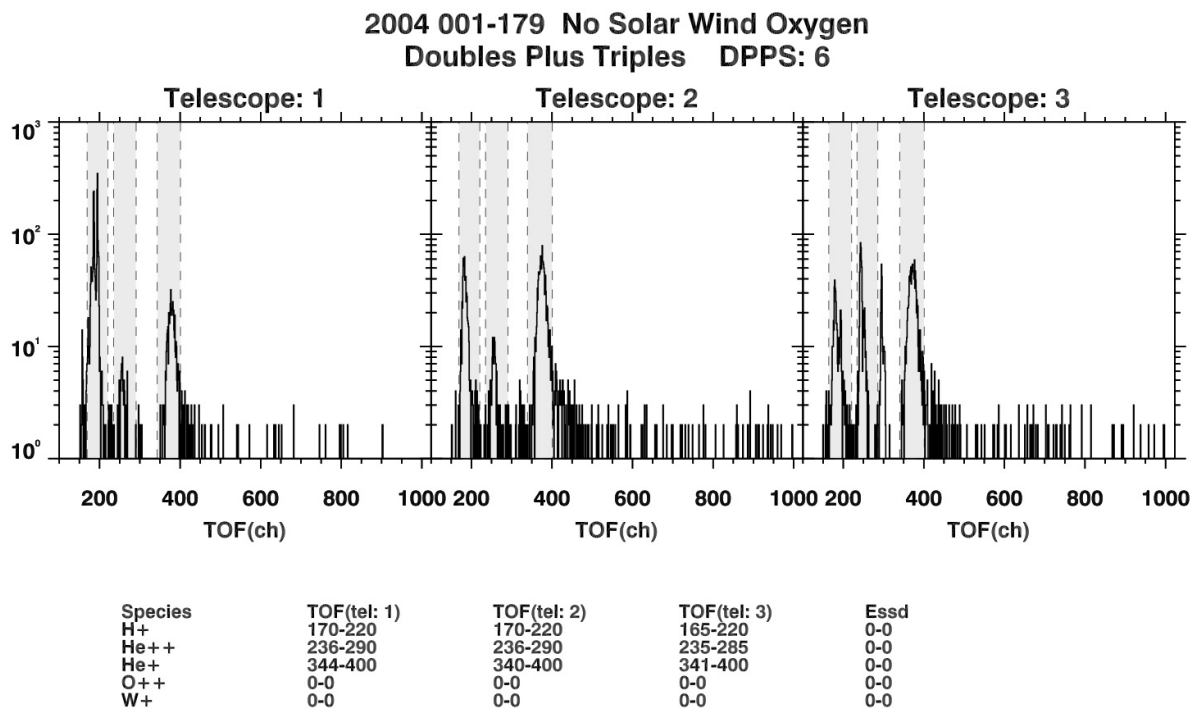


Figure D.47: Histogram of doubles plus triples counts in the interplanetary regime for DPPS step 6.

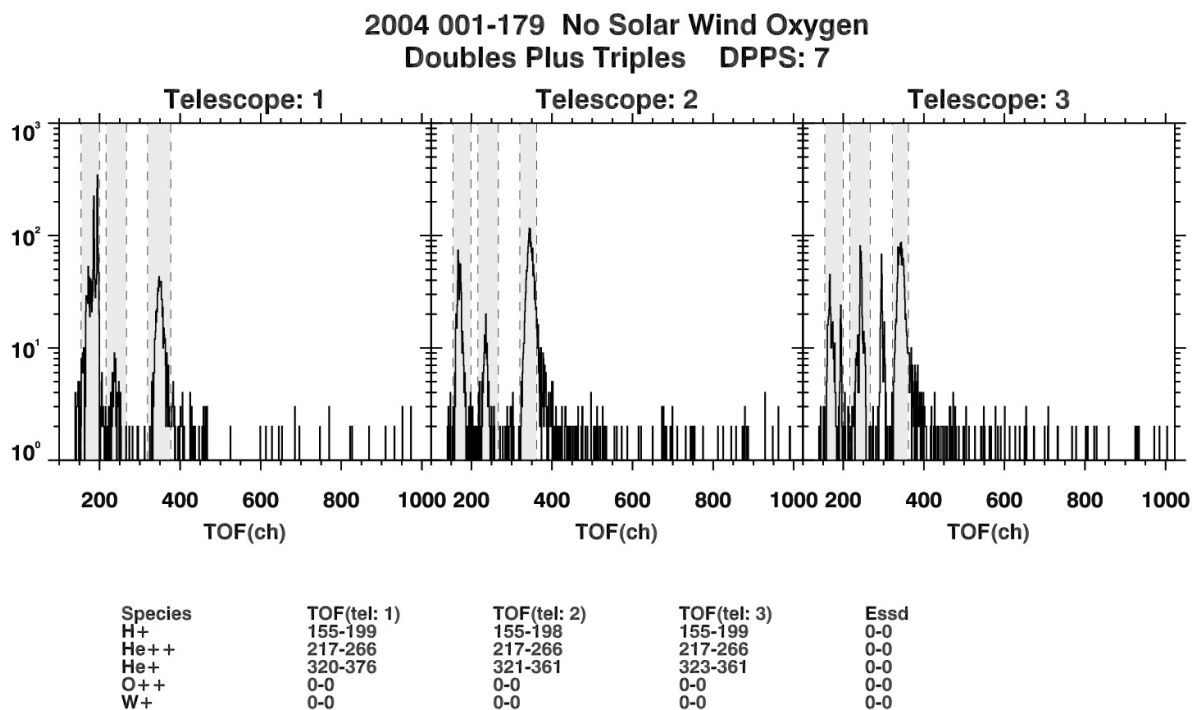


Figure D.48: Histogram of doubles plus triples counts in the interplanetary regime for DPPS step 7.

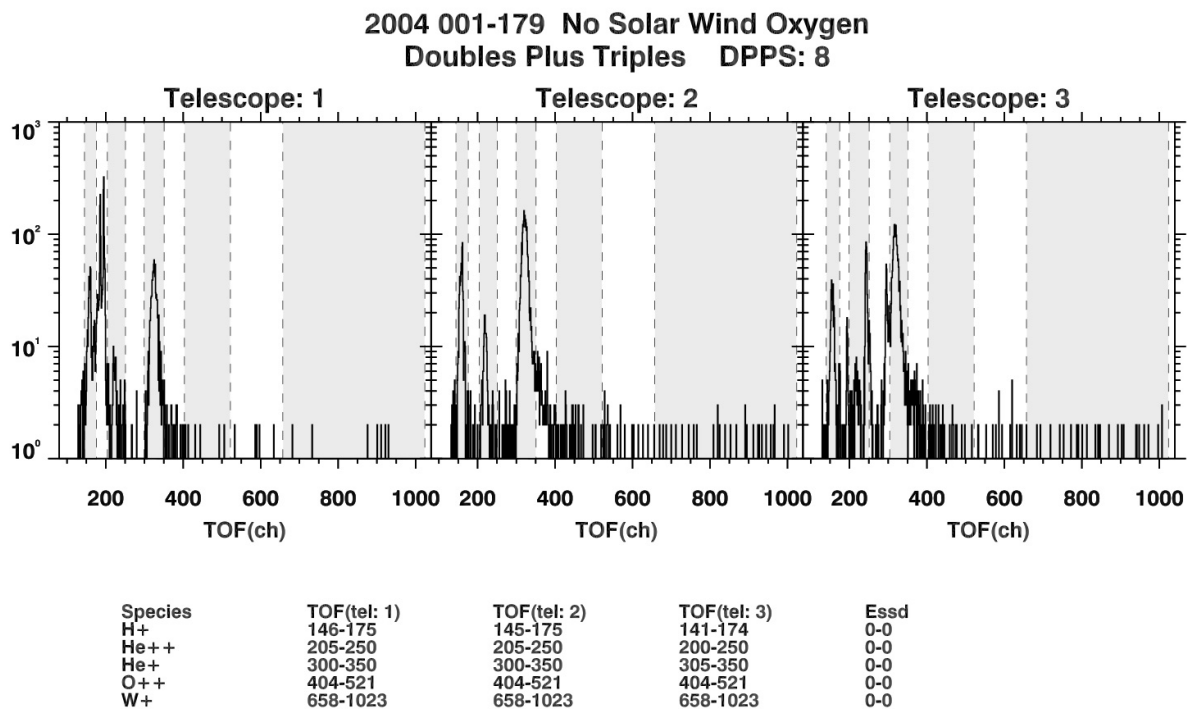


Figure D.49: Histogram of doubles plus triples counts in the interplanetary regime for DPPS step 8.

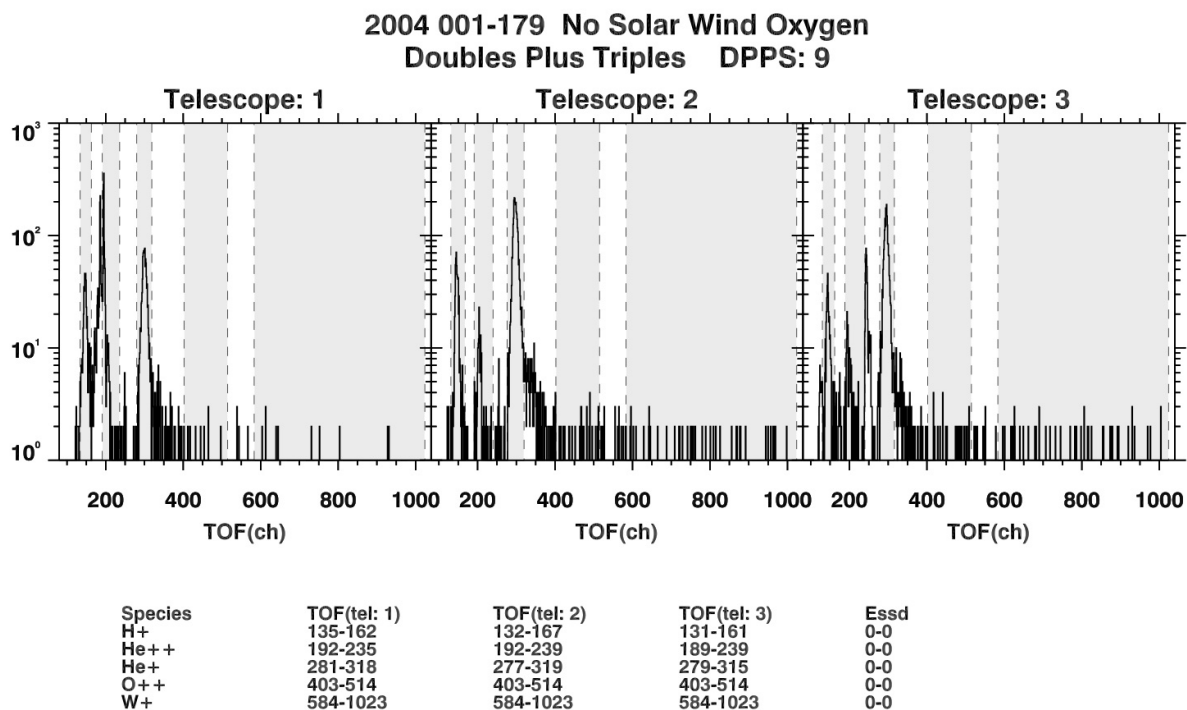


Figure D.50: Histogram of doubles plus triples counts in the interplanetary regime for DPPS step 9.

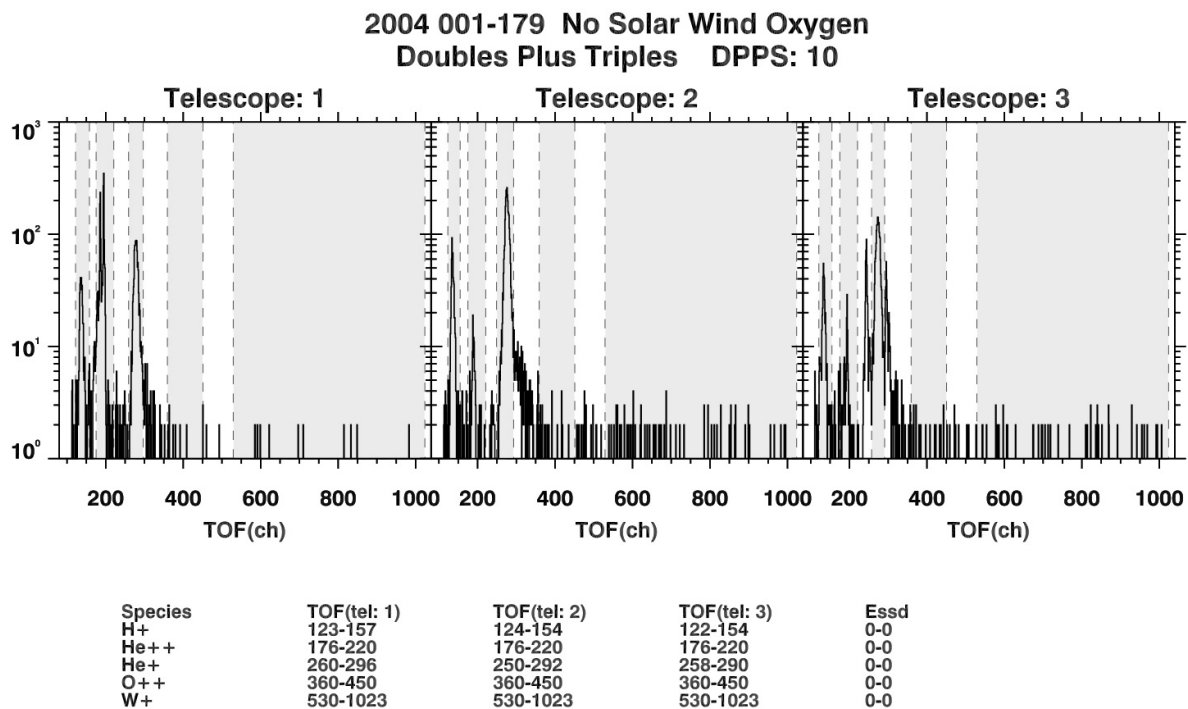


Figure D.51: Histogram of doubles plus triples counts in the interplanetary regime for DPPS step 10.

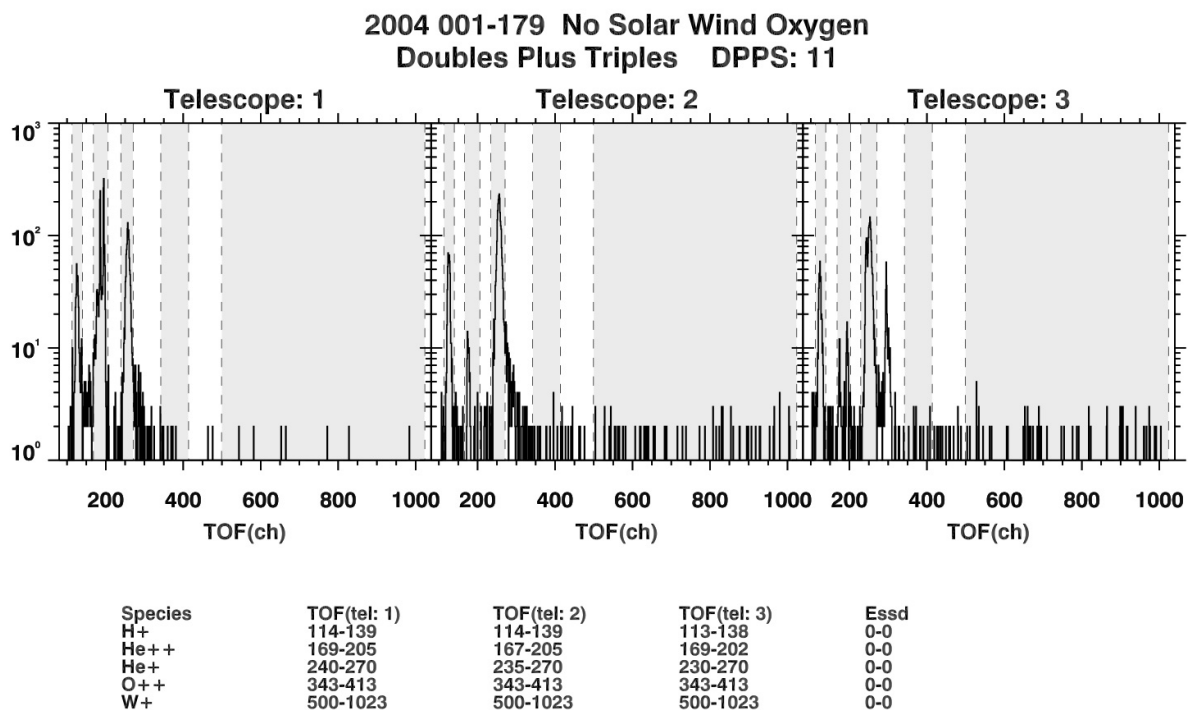


Figure D.52: Histogram of doubles plus triples counts in the interplanetary regime for DPPS step 11.

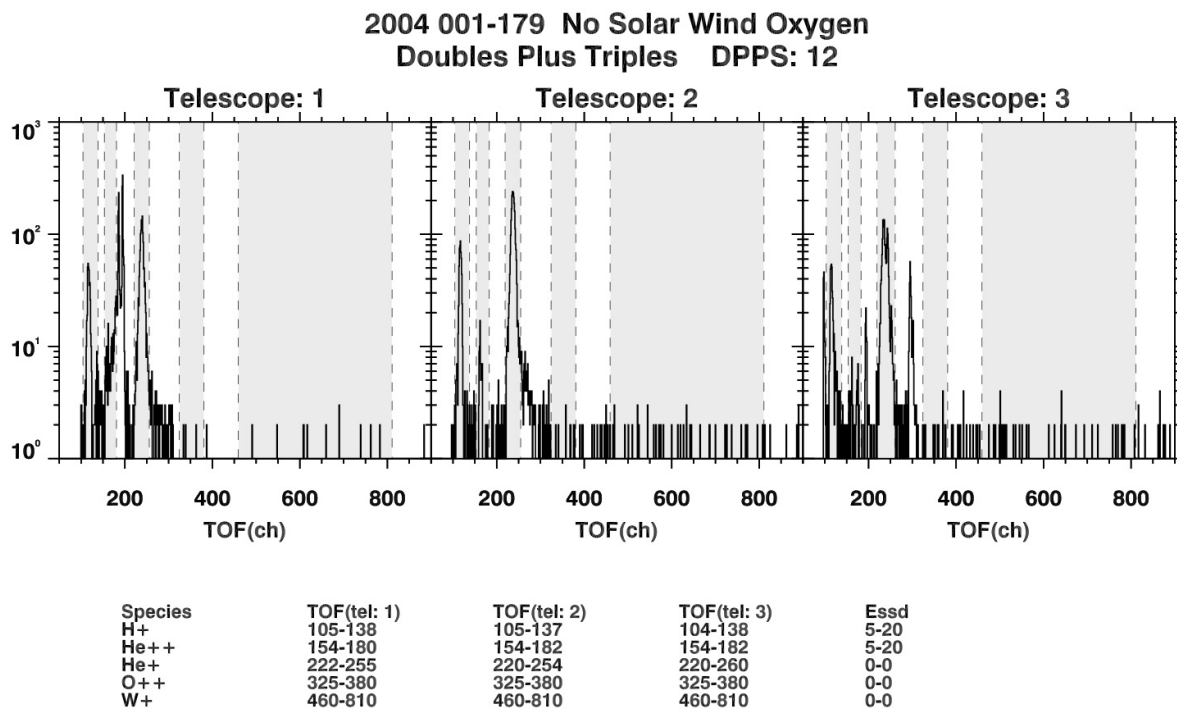


Figure D.53: Histogram of doubles plus triples counts in the interplanetary regime for DPPS step 12.

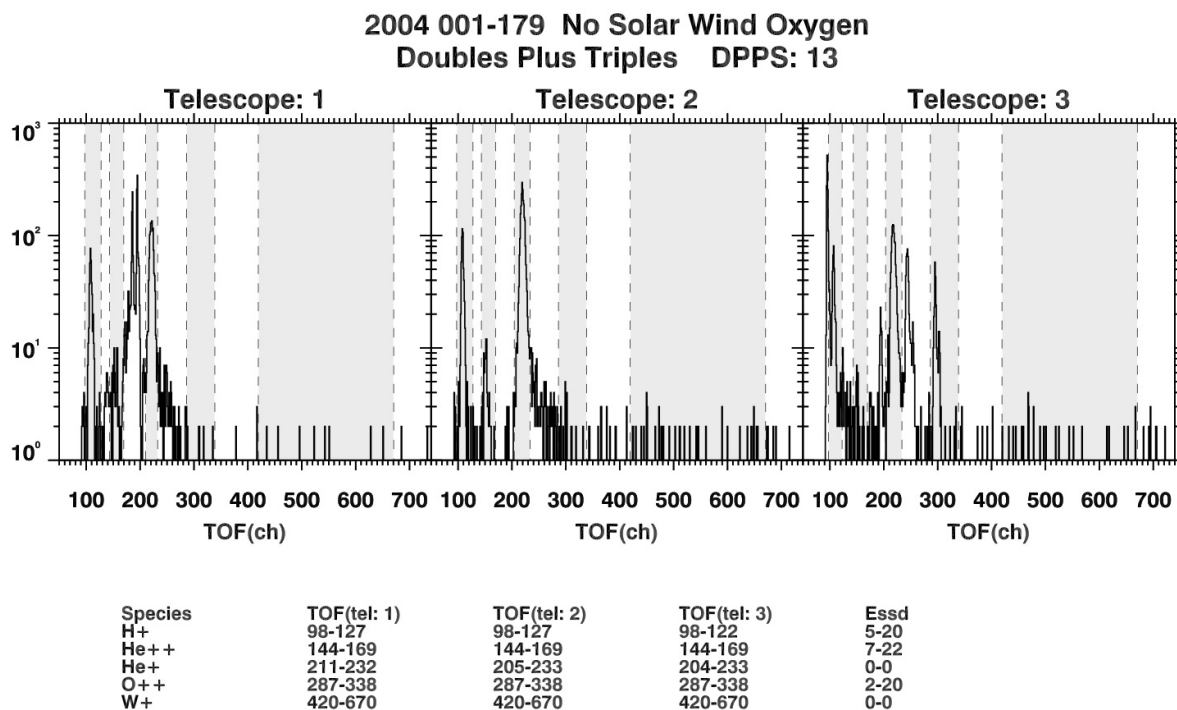


Figure D.54: Histogram of doubles plus triples counts in the interplanetary regime for DPPS step 13.

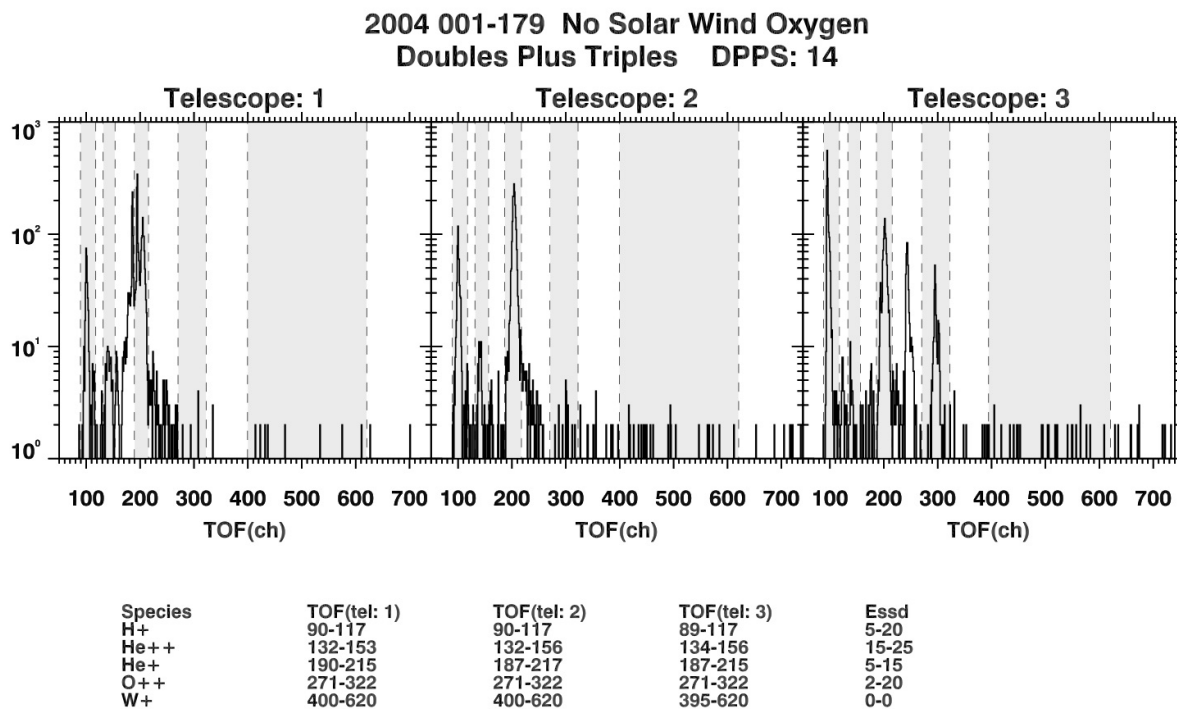


Figure D.55: Histogram of doubles plus triples counts in the interplanetary regime for DPPS step 14.

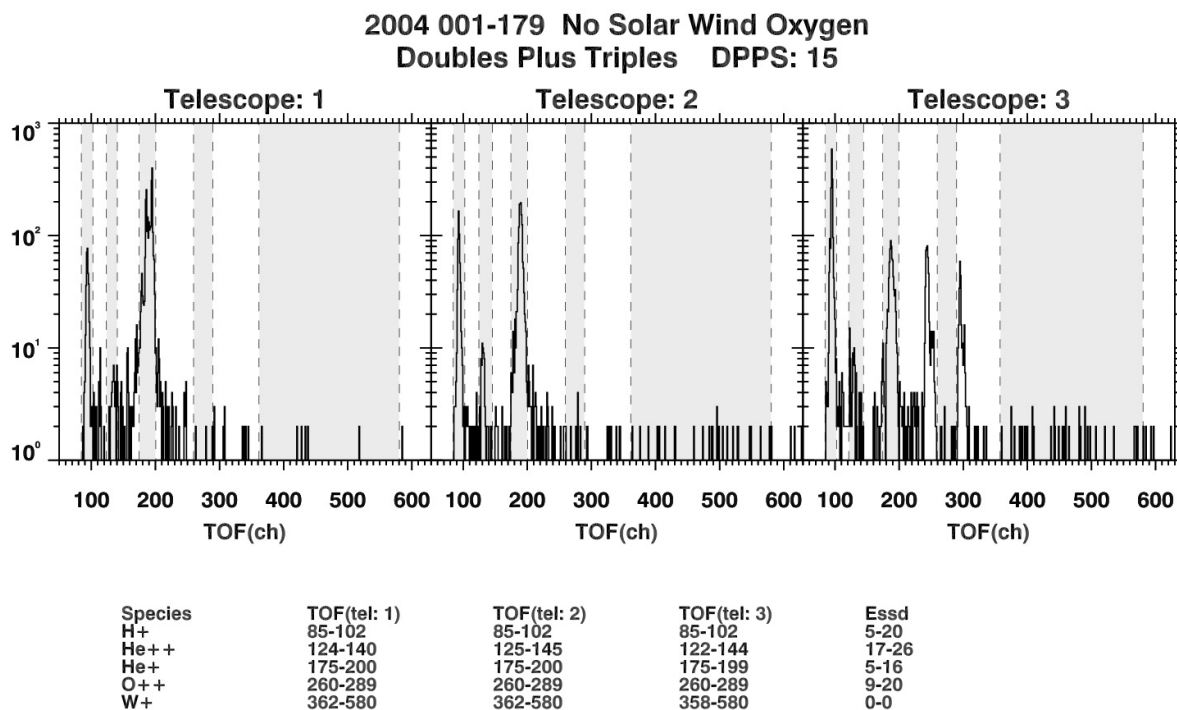


Figure D.56: Histogram of doubles plus triples counts in the interplanetary regime for DPPS step 15.

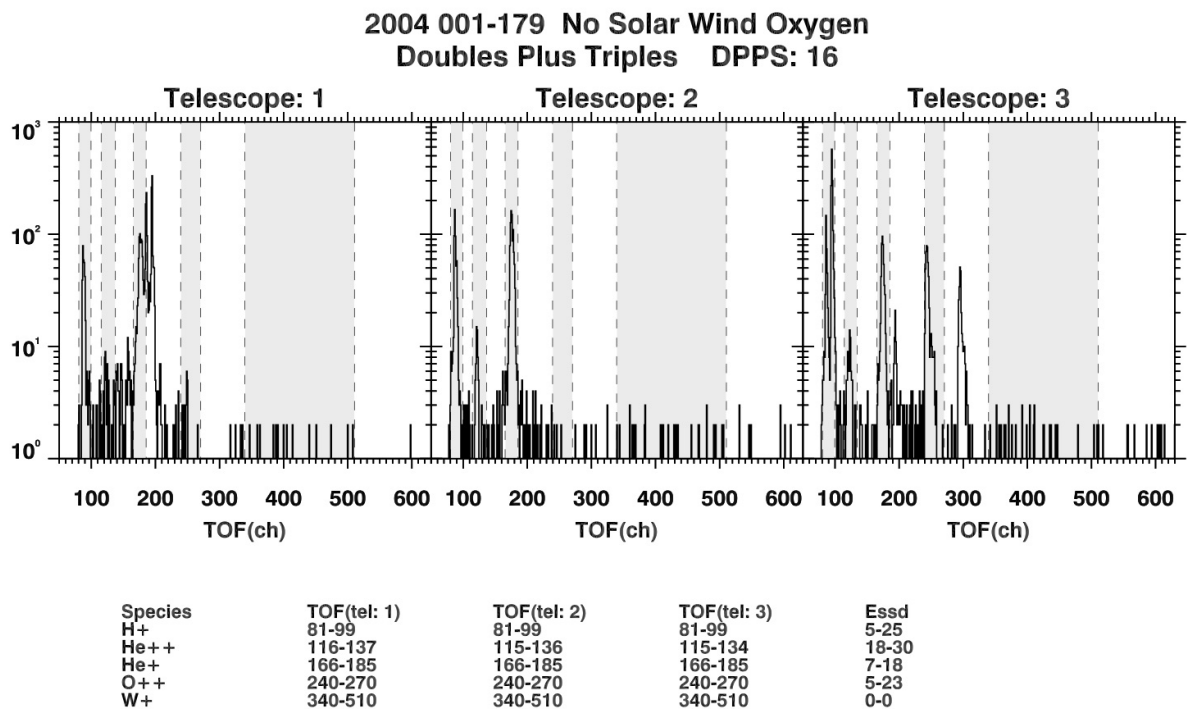


Figure D.57: Histogram of doubles plus triples counts in the interplanetary regime for DPPS step 16.

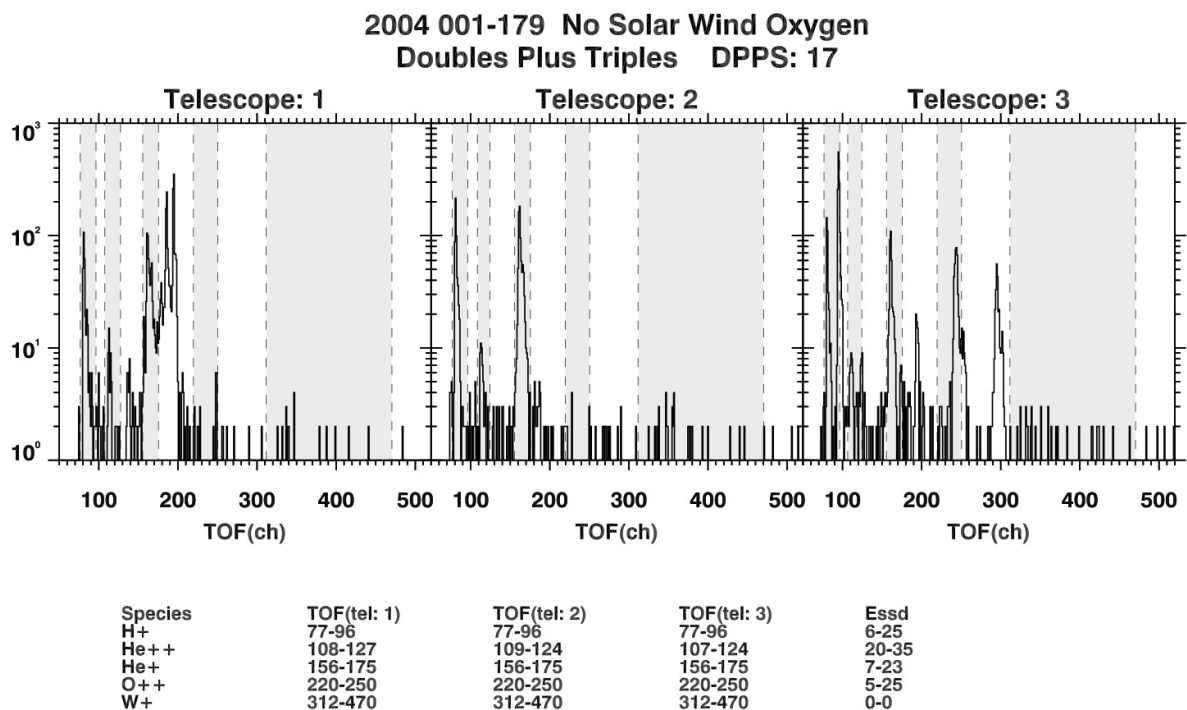


Figure D.58: Histogram of doubles plus triples counts in the interplanetary regime for DPPS step 17.

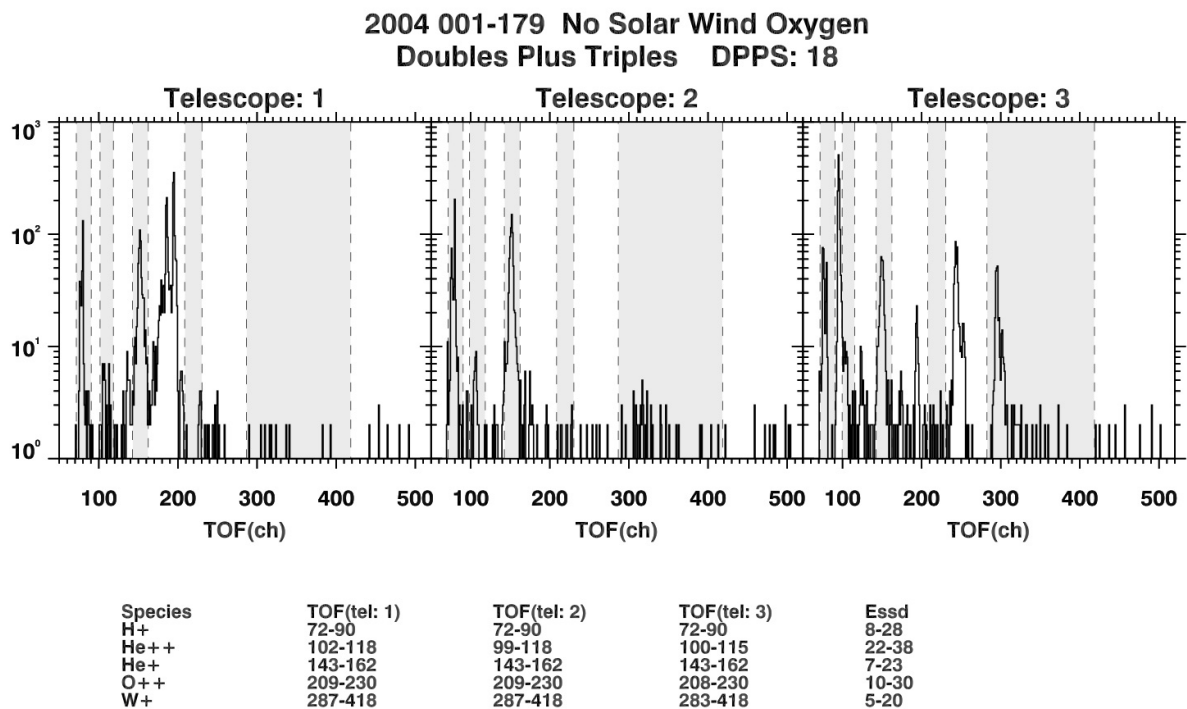


Figure D.59: Histogram of doubles plus triples counts in the interplanetary regime for DPPS step 18.

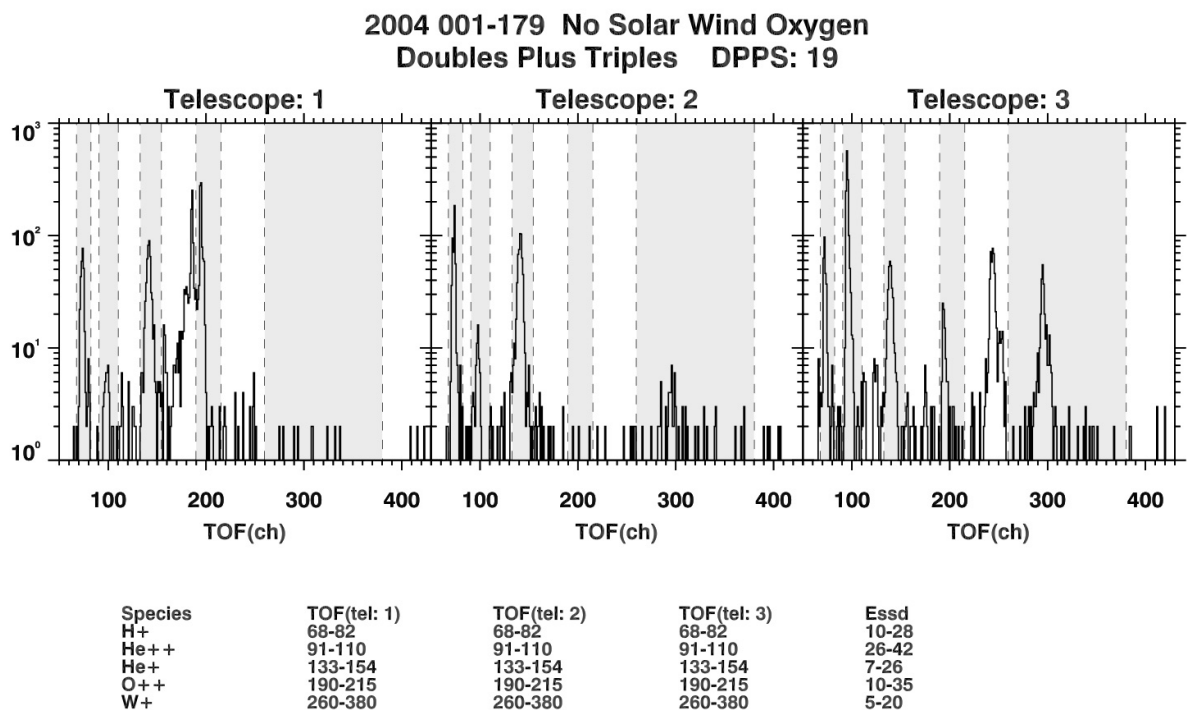


Figure D.60: Histogram of doubles plus triples counts in the interplanetary regime for DPPS step 19.

Appendix E

CHEMS PHA Species Box Definitions

Included here are tabulations of PHA species box definitions for the CHEMS PHA species listed in Table 4.8. The use of these boxes for computing species intensities is described in Sections 4.6 and 4.7.

Digital versions of these tables are available alongside this user guide and also at the MIMI team web page for this user guide [Kusterer and Vandegriff, 2011].

Tables of CHEMS PHA Species Box Definitions

PHA Box Limits for H ⁺				
DPPS Step	TOF(ch) Ranges			Essd(ch) Ranges
	Tel. 1	Tel. 2	Tel. 3	
0	260 - 340	260 - 340	260 - 340	0 - 0
1	240 - 340	240 - 340	240 - 340	0 - 0
2	224 - 310	224 - 310	224 - 310	0 - 0
3	205 - 285	205 - 285	208 - 285	0 - 0
4	193 - 260	193 - 260	193 - 260	0 - 0
5	182 - 240	182 - 240	179 - 240	0 - 0
6	170 - 220	170 - 220	165 - 220	0 - 0
7	155 - 199	155 - 198	155 - 199	0 - 0
8	146 - 175	145 - 175	141 - 174	0 - 0
9	135 - 162	132 - 167	131 - 161	0 - 0
10	123 - 157	124 - 154	122 - 154	0 - 0
11	114 - 139	114 - 139	113 - 138	0 - 0
12	105 - 138	105 - 137	104 - 138	5 - 20
13	98 - 127	98 - 127	98 - 122	5 - 20
14	90 - 117	90 - 117	89 - 117	5 - 20
15	85 - 102	85 - 102	85 - 102	5 - 20
16	81 - 99	81 - 99	81 - 99	5 - 25
17	77 - 96	77 - 96	77 - 96	6 - 25
18	72 - 90	72 - 90	72 - 90	8 - 28
19	68 - 82	68 - 82	68 - 82	10 - 28
20	62 - 77	62 - 77	60 - 77	10 - 35
21	59 - 73	59 - 73	59 - 73	10 - 35
22	56 - 72	56 - 72	56 - 72	20 - 35
23	54 - 68	54 - 68	54 - 68	25 - 40
24	51 - 63	51 - 63	51 - 63	30 - 45
25	49 - 62	49 - 62	49 - 62	33 - 50
26	46 - 60	46 - 60	46 - 60	38 - 55
27	45 - 57	45 - 57	45 - 57	41 - 63
28	42 - 50	42 - 50	42 - 50	50 - 75
29	41 - 50	41 - 50	41 - 50	60 - 82
30	39 - 49	39 - 49	39 - 49	70 - 90
31	37 - 46	37 - 46	37 - 46	85 - 105

Table E.1: Ranges in TOF(ch) and Essd(ch) that define the PHA species boxes for H⁺.

PHA Box Limits for He ⁺⁺				
DPPS Step	TOF(ch) Ranges			Essd(ch) Ranges
	Tel. 1	Tel. 2	Tel. 3	
0	383 - 450	383 - 450	383 - 440	0 - 0
1	349 - 401	349 - 401	349 - 401	0 - 0
2	320 - 380	320 - 380	320 - 380	0 - 0
3	302 - 360	300 - 360	300 - 360	0 - 0
4	280 - 339	280 - 339	271 - 340	0 - 0
5	260 - 310	259 - 310	258 - 310	0 - 0
6	236 - 290	236 - 290	235 - 285	0 - 0
7	217 - 266	217 - 266	217 - 266	0 - 0
8	205 - 250	205 - 250	200 - 250	0 - 0
9	192 - 235	192 - 239	189 - 239	0 - 0
10	176 - 220	176 - 220	176 - 220	0 - 0
11	169 - 205	167 - 205	169 - 202	0 - 0
12	154 - 180	154 - 182	154 - 182	5 - 20
13	144 - 169	144 - 169	144 - 169	7 - 22
14	132 - 153	132 - 156	134 - 156	15 - 25
15	124 - 140	125 - 145	122 - 144	17 - 26
16	116 - 137	115 - 136	115 - 134	18 - 30
17	108 - 127	109 - 124	107 - 124	20 - 35
18	102 - 118	99 - 118	100 - 115	22 - 38
19	91 - 110	91 - 110	91 - 110	26 - 42
20	86 - 102	86 - 102	86 - 102	30 - 47
21	83 - 97	83 - 97	81 - 98	35 - 55
22	79 - 89	79 - 89	79 - 90	40 - 60
23	73 - 88	73 - 88	73 - 88	48 - 67
24	70 - 83	70 - 83	70 - 83	55 - 76
25	65 - 77	65 - 77	65 - 77	66 - 87
26	62 - 73	62 - 73	62 - 73	75 - 98
27	59 - 69	59 - 69	59 - 69	90 - 115
28	56 - 65	56 - 65	56 - 65	109 - 130
29	53 - 63	53 - 63	53 - 63	125 - 145
30	51 - 60	51 - 60	51 - 60	147 - 165
31	49 - 56	49 - 56	49 - 56	168 - 190

Table E.2: Ranges in TOF(ch) and Essd(ch) that define the PHA species boxes for He⁺⁺.

PHA Box Limits for H ₂ ⁺				
DPPS Step	TOF(ch) Ranges			Essd(ch) Ranges
	Tel. 1	Tel. 2	Tel. 3	
0	383 - 490	383 - 490	383 - 490	0 - 0
1	368 - 460	361 - 460	364 - 460	0 - 0
2	340 - 420	340 - 420	340 - 420	0 - 0
3	307 - 390	307 - 390	307 - 390	0 - 0
4	287 - 360	287 - 360	285 - 354	0 - 0
5	260 - 325	260 - 325	259 - 325	0 - 0
6	246 - 298	240 - 300	240 - 292	0 - 0
7	225 - 270	225 - 270	221 - 265	0 - 0
8	209 - 249	209 - 250	209 - 249	0 - 0
9	195 - 242	195 - 242	190 - 239	0 - 0
10	183 - 221	183 - 221	179 - 220	0 - 0
11	170 - 205	170 - 205	169 - 205	0 - 0
12	154 - 190	154 - 191	154 - 191	0 - 0
13	144 - 174	144 - 175	144 - 175	0 - 0
14	135 - 157	132 - 157	134 - 156	0 - 0
15	124 - 149	125 - 149	122 - 144	0 - 0
16	116 - 137	115 - 136	115 - 134	5 - 17
17	108 - 127	109 - 124	107 - 124	5 - 19
18	102 - 118	99 - 118	100 - 115	6 - 21
19	91 - 110	91 - 110	91 - 110	8 - 25
20	86 - 102	86 - 102	86 - 102	5 - 28
21	83 - 97	83 - 97	81 - 98	5 - 30
22	79 - 89	79 - 89	79 - 90	5 - 35
23	73 - 88	73 - 88	73 - 88	5 - 37
24	70 - 83	70 - 83	70 - 83	10 - 42
25	65 - 77	65 - 77	65 - 77	11 - 47
26	62 - 73	62 - 73	62 - 73	17 - 54
27	59 - 69	59 - 69	59 - 69	10 - 60
28	56 - 65	56 - 65	56 - 65	50 - 70
29	53 - 63	53 - 63	53 - 63	60 - 78
30	51 - 60	51 - 60	51 - 60	70 - 90
31	49 - 56	49 - 56	49 - 56	85 - 100

Table E.3: Ranges in TOF(ch) and Essd(ch) that define the PHA species boxes for H₂⁺.

PHA Box Limits for He⁺				
DPPS Step	TOF(ch) Ranges			Essd(ch) Ranges
	Tel. 1	Tel. 2	Tel. 3	
0	550 - 674	568 - 674	550 - 674	0 - 0
1	505 - 611	505 - 611	505 - 603	0 - 0
2	473 - 579	473 - 570	473 - 572	0 - 0
3	439 - 543	439 - 543	428 - 531	0 - 0
4	399 - 481	399 - 481	399 - 481	0 - 0
5	372 - 440	377 - 440	372 - 438	0 - 0
6	344 - 400	340 - 400	341 - 400	0 - 0
7	320 - 376	321 - 361	323 - 361	0 - 0
8	300 - 350	300 - 350	305 - 350	0 - 0
9	281 - 318	277 - 319	279 - 315	0 - 0
10	260 - 296	250 - 292	258 - 290	0 - 0
11	240 - 270	235 - 270	230 - 270	0 - 0
12	222 - 255	220 - 254	220 - 260	0 - 0
13	211 - 232	205 - 233	204 - 233	0 - 0
14	190 - 215	187 - 217	187 - 215	5 - 15
15	175 - 200	175 - 200	175 - 199	5 - 16
16	166 - 185	166 - 185	166 - 185	7 - 18
17	156 - 175	156 - 175	156 - 175	7 - 23
18	143 - 162	143 - 162	143 - 162	7 - 23
19	133 - 154	133 - 154	133 - 154	7 - 26
20	124 - 144	124 - 144	124 - 144	10 - 28
21	113 - 130	113 - 130	113 - 130	10 - 30
22	108 - 126	108 - 126	108 - 126	15 - 35
23	99 - 116	99 - 116	100 - 116	20 - 38
24	92 - 108	92 - 108	92 - 108	25 - 41
25	84 - 101	84 - 101	84 - 101	30 - 48
26	79 - 93	79 - 93	81 - 91	35 - 55
27	78 - 89	77 - 89	79 - 89	40 - 60
28	73 - 83	73 - 83	73 - 83	45 - 70
29	70 - 77	70 - 78	69 - 77	59 - 79
30	64 - 73	64 - 73	64 - 73	68 - 86
31	64 - 69	64 - 69	64 - 69	79 - 100

Table E.4: Ranges in TOF(ch) and Essd(ch) that define the PHA species boxes for He⁺.

PHA Box Limits for W^+				
DPPS Step	TOF(ch) Ranges			Essd(ch) Ranges
	Tel. 1	Tel. 2	Tel. 3	
0	0 - 0	0 - 0	0 - 0	0 - 0
1	0 - 0	0 - 0	0 - 0	0 - 0
2	0 - 0	0 - 0	0 - 0	0 - 0
3	0 - 0	0 - 0	0 - 0	0 - 0
4	0 - 0	0 - 0	0 - 0	0 - 0
5	0 - 0	0 - 0	0 - 0	0 - 0
6	0 - 0	0 - 0	0 - 0	0 - 0
7	0 - 0	0 - 0	0 - 0	0 - 0
8	658 - 1023	658 - 1023	658 - 1023	0 - 0
9	584 - 1023	584 - 1023	584 - 1023	0 - 0
10	530 - 1023	530 - 1023	530 - 1023	0 - 0
11	500 - 1023	500 - 1023	500 - 1023	0 - 0
12	460 - 810	460 - 810	460 - 810	0 - 0
13	420 - 670	420 - 670	420 - 670	0 - 0
14	400 - 620	400 - 620	395 - 620	0 - 0
15	362 - 580	362 - 580	358 - 580	0 - 0
16	340 - 510	340 - 510	340 - 510	0 - 0
17	312 - 470	312 - 470	312 - 470	0 - 0
18	287 - 418	287 - 418	283 - 418	5 - 20
19	260 - 380	260 - 380	260 - 380	5 - 20
20	263 - 320	261 - 320	258 - 320	5 - 24
21	241 - 310	242 - 310	239 - 310	5 - 26
22	223 - 290	223 - 290	221 - 290	5 - 30
23	211 - 268	208 - 260	207 - 260	7 - 33
24	195 - 249	193 - 249	191 - 249	10 - 35
25	180 - 240	179 - 240	178 - 240	10 - 41
26	169 - 219	167 - 219	164 - 219	10 - 47
27	157 - 204	156 - 204	154 - 205	10 - 52
28	145 - 190	143 - 192	141 - 189	10 - 61
29	136 - 171	133 - 169	132 - 169	20 - 70
30	126 - 154	124 - 154	123 - 153	30 - 80
31	116 - 154	116 - 155	114 - 154	45 - 90

Table E.5: Ranges in TOF(ch) and Essd(ch) that define the PHA species boxes for W^+ .

PHA Box Limits for O ⁺⁺				
DPPS Step	TOF(ch) Ranges			Essd(ch) Ranges
	Tel. 1	Tel. 2	Tel. 3	
0	0 - 0	0 - 0	0 - 0	0 - 0
1	0 - 0	0 - 0	0 - 0	0 - 0
2	0 - 0	0 - 0	0 - 0	0 - 0
3	0 - 0	0 - 0	0 - 0	0 - 0
4	0 - 0	0 - 0	0 - 0	0 - 0
5	0 - 0	0 - 0	0 - 0	0 - 0
6	0 - 0	0 - 0	0 - 0	0 - 0
7	0 - 0	0 - 0	0 - 0	0 - 0
8	404 - 521	404 - 521	404 - 521	0 - 0
9	403 - 514	403 - 514	403 - 514	0 - 0
10	360 - 450	360 - 450	360 - 450	0 - 0
11	343 - 413	343 - 413	343 - 413	0 - 0
12	325 - 380	325 - 380	325 - 380	0 - 0
13	287 - 338	287 - 338	287 - 338	2 - 20
14	271 - 322	271 - 322	271 - 322	2 - 20
15	260 - 289	260 - 289	260 - 289	9 - 20
16	240 - 270	240 - 270	240 - 270	5 - 23
17	220 - 250	220 - 250	220 - 250	5 - 25
18	209 - 230	209 - 230	208 - 230	10 - 30
19	190 - 215	190 - 215	190 - 215	10 - 35
20	180 - 200	180 - 200	178 - 199	13 - 37
21	165 - 182	165 - 182	165 - 182	16 - 44
22	155 - 170	155 - 170	155 - 170	20 - 48
23	140 - 160	140 - 160	140 - 158	28 - 57
24	130 - 150	130 - 150	130 - 150	35 - 65
25	122 - 139	122 - 139	122 - 139	40 - 75
26	110 - 127	110 - 127	110 - 127	53 - 85
27	105 - 120	105 - 120	105 - 120	60 - 98
28	100 - 110	100 - 110	100 - 110	80 - 110
29	90 - 105	90 - 105	90 - 105	90 - 126
30	87 - 98	87 - 98	87 - 98	101 - 145
31	79 - 92	79 - 92	79 - 92	125 - 172

Table E.6: Ranges in TOF(ch) and Essd(ch) that define the PHA species boxes for O⁺⁺.

PHA Box Limits for H ₃ ⁺				
DPPS Step	TOF(ch) Ranges			Essd(ch) Ranges
	Tel. 1	Tel. 2	Tel. 3	
0	0 - 0	0 - 0	0 - 0	0 - 0
1	0 - 0	0 - 0	0 - 0	0 - 0
2	0 - 0	0 - 0	0 - 0	0 - 0
3	0 - 0	0 - 0	0 - 0	0 - 0
4	0 - 0	0 - 0	0 - 0	0 - 0
5	0 - 0	0 - 0	0 - 0	0 - 0
6	0 - 0	0 - 0	0 - 0	0 - 0
7	0 - 0	0 - 0	0 - 0	0 - 0
8	0 - 0	0 - 0	0 - 0	0 - 0
9	0 - 0	0 - 0	0 - 0	0 - 0
10	0 - 0	0 - 0	0 - 0	0 - 0
11	0 - 0	0 - 0	0 - 0	0 - 0
12	0 - 0	0 - 0	0 - 0	0 - 0
13	0 - 0	0 - 0	0 - 0	0 - 0
14	0 - 0	0 - 0	0 - 0	0 - 0
15	0 - 0	0 - 0	0 - 0	0 - 0
16	141 - 154	141 - 154	141 - 154	5 - 20
17	136 - 148	136 - 148	136 - 148	5 - 22
18	125 - 137	125 - 137	125 - 137	5 - 25
19	117 - 132	117 - 132	117 - 132	10 - 30
20	108 - 123	108 - 123	108 - 123	10 - 30
21	102 - 112	102 - 112	102 - 112	10 - 40
22	92 - 103	92 - 103	92 - 103	10 - 40
23	89 - 98	89 - 98	89 - 98	10 - 45
24	84 - 91	84 - 91	84 - 91	10 - 50
25	78 - 83	78 - 83	78 - 83	10 - 57
26	74 - 78	74 - 78	74 - 78	10 - 62
27	71 - 75	71 - 75	71 - 75	10 - 70
28	68 - 72	68 - 72	68 - 72	10 - 80
29	64 - 68	64 - 68	64 - 68	10 - 90
30	0 - 0	0 - 0	0 - 0	0 - 0
31	0 - 0	0 - 0	0 - 0	0 - 0

Table E.7: Ranges in TOF(ch) and Essd(ch) that define the PHA species boxes for H₃⁺.

PHA Box Limits for C ⁺				
DPPS Step	TOF(ch) Ranges			Essd(ch) Ranges
	Tel. 1	Tel. 2	Tel. 3	
0	0 - 0	0 - 0	0 - 0	0 - 0
1	0 - 0	0 - 0	0 - 0	0 - 0
2	0 - 0	0 - 0	0 - 0	0 - 0
3	0 - 0	0 - 0	0 - 0	0 - 0
4	0 - 0	0 - 0	0 - 0	0 - 0
5	0 - 0	0 - 0	0 - 0	0 - 0
6	0 - 0	0 - 0	0 - 0	0 - 0
7	0 - 0	0 - 0	0 - 0	0 - 0
8	0 - 0	0 - 0	0 - 0	0 - 0
9	0 - 0	0 - 0	0 - 0	0 - 0
10	0 - 0	0 - 0	0 - 0	0 - 0
11	0 - 0	0 - 0	0 - 0	0 - 0
12	0 - 0	0 - 0	0 - 0	0 - 0
13	0 - 0	0 - 0	0 - 0	0 - 0
14	0 - 0	0 - 0	0 - 0	0 - 0
15	0 - 0	0 - 0	0 - 0	0 - 0
16	0 - 0	0 - 0	0 - 0	0 - 0
17	0 - 0	0 - 0	0 - 0	0 - 0
18	0 - 0	0 - 0	0 - 0	0 - 0
19	0 - 0	0 - 0	0 - 0	0 - 0
20	0 - 0	0 - 0	0 - 0	0 - 0
21	0 - 0	0 - 0	0 - 0	0 - 0
22	0 - 0	0 - 0	0 - 0	0 - 0
23	0 - 0	0 - 0	0 - 0	0 - 0
24	170 - 180	170 - 180	169 - 179	10 - 37
25	158 - 166	157 - 168	156 - 167	10 - 45
26	147 - 156	145 - 154	144 - 153	10 - 50
27	136 - 145	136 - 145	134 - 143	10 - 58
28	126 - 136	126 - 136	124 - 134	10 - 66
29	118 - 124	117 - 124	116 - 123	20 - 75
30	109 - 118	107 - 116	107 - 116	30 - 80
31	103 - 109	101 - 109	101 - 107	45 - 90

Table E.8: Ranges in TOF(ch) and Essd(ch) that define the PHA species boxes for C⁺.

PHA Box Limits for N ⁺				
DPPS Step	TOF(ch) Ranges			Essd(ch) Ranges
	Tel. 1	Tel. 2	Tel. 3	
0	0 - 0	0 - 0	0 - 0	0 - 0
1	0 - 0	0 - 0	0 - 0	0 - 0
2	0 - 0	0 - 0	0 - 0	0 - 0
3	0 - 0	0 - 0	0 - 0	0 - 0
4	0 - 0	0 - 0	0 - 0	0 - 0
5	0 - 0	0 - 0	0 - 0	0 - 0
6	0 - 0	0 - 0	0 - 0	0 - 0
7	0 - 0	0 - 0	0 - 0	0 - 0
8	0 - 0	0 - 0	0 - 0	0 - 0
9	0 - 0	0 - 0	0 - 0	0 - 0
10	0 - 0	0 - 0	0 - 0	0 - 0
11	0 - 0	0 - 0	0 - 0	0 - 0
12	0 - 0	0 - 0	0 - 0	0 - 0
13	0 - 0	0 - 0	0 - 0	0 - 0
14	0 - 0	0 - 0	0 - 0	0 - 0
15	0 - 0	0 - 0	0 - 0	0 - 0
16	0 - 0	0 - 0	0 - 0	0 - 0
17	0 - 0	0 - 0	0 - 0	0 - 0
18	0 - 0	0 - 0	0 - 0	0 - 0
19	0 - 0	0 - 0	0 - 0	0 - 0
20	0 - 0	0 - 0	0 - 0	0 - 0
21	0 - 0	0 - 0	0 - 0	0 - 0
22	0 - 0	0 - 0	0 - 0	0 - 0
23	0 - 0	0 - 0	0 - 0	0 - 0
24	0 - 0	0 - 0	0 - 0	0 - 0
25	168 - 179	170 - 177	169 - 176	10 - 37
26	158 - 167	156 - 166	155 - 161	10 - 50
27	147 - 153	147 - 153	145 - 152	10 - 58
28	138 - 142	138 - 142	136 - 141	10 - 66
29	126 - 130	126 - 130	125 - 130	20 - 75
30	120 - 124	118 - 123	118 - 121	30 - 80
31	111 - 115	111 - 115	109 - 113	45 - 90

Table E.9: Ranges in TOF(ch) and Essd(ch) that define the PHA species boxes for N⁺.

PHA Box Limits for O ⁺⁺⁺				
DPPS Step	TOF(ch) Ranges			Essd(ch) Ranges
	Tel. 1	Tel. 2	Tel. 3	
0	0 - 0	0 - 0	0 - 0	0 - 0
1	0 - 0	0 - 0	0 - 0	0 - 0
2	0 - 0	0 - 0	0 - 0	0 - 0
3	0 - 0	0 - 0	0 - 0	0 - 0
4	0 - 0	0 - 0	0 - 0	0 - 0
5	0 - 0	0 - 0	0 - 0	0 - 0
6	0 - 0	0 - 0	0 - 0	0 - 0
7	0 - 0	0 - 0	0 - 0	0 - 0
8	0 - 0	0 - 0	0 - 0	0 - 0
9	0 - 0	0 - 0	0 - 0	0 - 0
10	0 - 0	0 - 0	0 - 0	0 - 0
11	0 - 0	0 - 0	0 - 0	0 - 0
12	0 - 0	0 - 0	0 - 0	0 - 0
13	0 - 0	0 - 0	0 - 0	0 - 0
14	0 - 0	0 - 0	0 - 0	0 - 0
15	0 - 0	0 - 0	0 - 0	0 - 0
16	0 - 0	0 - 0	0 - 0	0 - 0
17	0 - 0	0 - 0	0 - 0	0 - 0
18	167 - 181	167 - 181	167 - 181	15 - 45
19	158 - 170	158 - 170	158 - 170	22 - 50
20	142 - 159	142 - 159	142 - 159	30 - 55
21	130 - 150	130 - 150	130 - 150	39 - 60
22	122 - 138	122 - 138	122 - 138	45 - 70
23	115 - 130	115 - 130	115 - 130	53 - 83
24	105 - 122	105 - 122	105 - 122	65 - 95
25	100 - 115	100 - 115	100 - 115	80 - 110
26	90 - 108	90 - 108	90 - 108	90 - 125
27	85 - 100	85 - 100	85 - 100	114 - 140
28	80 - 97	80 - 97	80 - 97	130 - 170
29	75 - 91	75 - 91	75 - 91	155 - 190
30	76 - 85	76 - 85	76 - 85	180 - 230
31	67 - 77	67 - 77	67 - 77	220 - 260

Table E.10: Ranges in TOF(ch) and Essd(ch) that define the PHA species boxes for O⁺⁺⁺.

PHA Box Limits for O ₂ ⁺				
DPPS Step	TOF(ch) Ranges			Essd(ch) Ranges
	Tel. 1	Tel. 2	Tel. 3	
0	0 - 0	0 - 0	0 - 0	0 - 0
1	0 - 0	0 - 0	0 - 0	0 - 0
2	0 - 0	0 - 0	0 - 0	0 - 0
3	0 - 0	0 - 0	0 - 0	0 - 0
4	0 - 0	0 - 0	0 - 0	0 - 0
5	0 - 0	0 - 0	0 - 0	0 - 0
6	0 - 0	0 - 0	0 - 0	0 - 0
7	0 - 0	0 - 0	0 - 0	0 - 0
8	0 - 0	0 - 0	0 - 0	0 - 0
9	0 - 0	0 - 0	0 - 0	0 - 0
10	0 - 0	0 - 0	0 - 0	0 - 0
11	0 - 0	0 - 0	0 - 0	0 - 0
12	0 - 0	0 - 0	0 - 0	0 - 0
13	0 - 0	0 - 0	0 - 0	0 - 0
14	0 - 0	0 - 0	0 - 0	0 - 0
15	0 - 0	0 - 0	0 - 0	0 - 0
16	0 - 0	0 - 0	0 - 0	0 - 0
17	0 - 0	0 - 0	0 - 0	0 - 0
18	0 - 0	0 - 0	0 - 0	0 - 0
19	0 - 0	0 - 0	0 - 0	0 - 0
20	0 - 0	0 - 0	0 - 0	0 - 0
21	0 - 0	0 - 0	0 - 0	0 - 0
22	0 - 0	0 - 0	0 - 0	0 - 0
23	0 - 0	0 - 0	0 - 0	0 - 0
24	282 - 320	282 - 320	282 - 320	5 - 30
25	261 - 300	261 - 300	261 - 300	5 - 35
26	242 - 264	242 - 264	242 - 264	5 - 40
27	226 - 247	226 - 247	226 - 247	9 - 40
28	208 - 227	208 - 227	208 - 227	10 - 45
29	193 - 217	193 - 217	193 - 217	10 - 50
30	183 - 200	183 - 200	183 - 200	15 - 60
31	169 - 186	169 - 186	169 - 186	20 - 70

Table E.11: Ranges in TOF(ch) and Essd(ch) that define the PHA species boxes for O₂⁺.

Species	Telescope 1		Telescope 3	
	“no box”	“narrow box”	“no box”	“narrow box”
H ⁺	5,6,7	4	0,2,5,14	1,3,4,13
H ₂ ⁺	9,10,11	12	4,5,6,7,9,10	8, 11
He ⁺	15	14	8,9,11,12,14,15	
He ⁺⁺	9,10,11		4,6,7,8,9	5,8,11
O ⁺⁺			14	13

Table E.12: This is a copy of Table 4.12 showing the steps where bogus TOF counts interfere with the box counts for each ion species and telescope. For these steps, it is possible, during quiet times, to use more narrow box definitions as a way to limit the inclusion of bogus TOF counts. Since the TOF(ch) ranges in telescope 2 do not overlap any doubles channels, only telescopes 1 and 3 are shown. The column labeled “no box” means that the bogus TOF counts occur in the middle of the species peak and cannot be avoided, even with a narrow box. The column labeled “narrow box” means that the standard boxes contain bogus counts, but these bogus counts can be avoided using narrow TOF(ch) bounds. Tables E.13 to E.17 list narrow PHA species box definitions. Recall that the narrow boxes are only relevant for low rate periods.

The following tables of PHA box definitions give more narrow box ranges for a limited set of species and telescopes where more narrow box ranges are effective in removing bogus TOF counts. This technique only works during quiet (low count) intervals, because the species peaks are relatively narrow during such intervals. Tables E.13 to E.17 give complete box definitions, but only the rows mentioned in Table E.12 (which is a copy of Table 4.12 in the main text) have different box sizes – all other rows are just copies of the standard box widths given previously.

Narrow PHA Box Limits for H⁺

DPPS Step	TOF(ch) Ranges			Essd(ch) Ranges
	Tel. 1	Tel. 2	Tel. 3	
0	260 - 340	260 - 340	0 - 0	0 - 0
1	240 - 340	240 - 340	256 - 291	0 - 0
2	224 - 310	224 - 310	0 - 0	0 - 0
3	205 - 285	205 - 285	208 - 239	0 - 0
4	203 - 260	193 - 260	200 - 239	0 - 0
5	0 - 0	182 - 230	0 - 0	0 - 0
6	0 - 0	170 - 218	170 - 189	0 - 0
7	0 - 0	155 - 198	155 - 190	0 - 0
8	146 - 175	145 - 175	141 - 174	0 - 0
9	135 - 162	132 - 167	131 - 161	0 - 0
10	123 - 157	124 - 154	122 - 154	0 - 0
11	114 - 139	114 - 139	113 - 138	0 - 0
12	105 - 138	105 - 137	104 - 138	5 - 20
13	98 - 127	98 - 127	102 - 122	5 - 20
14	90 - 117	90 - 117	0 - 0	5 - 20
15	85 - 102	85 - 102	85 - 102	5 - 20
16	81 - 99	81 - 99	81 - 99	5 - 25
17	77 - 96	77 - 96	77 - 96	6 - 25
18	72 - 90	72 - 90	72 - 90	8 - 28
19	68 - 82	68 - 82	68 - 82	10 - 28
20	62 - 77	62 - 77	60 - 77	10 - 35
21	59 - 73	59 - 73	59 - 73	10 - 35
22	56 - 72	56 - 72	56 - 72	20 - 35
23	54 - 68	54 - 68	54 - 68	25 - 40
24	51 - 63	51 - 63	51 - 63	30 - 45
25	49 - 62	49 - 62	49 - 62	33 - 50
26	46 - 60	46 - 60	46 - 60	38 - 55
27	45 - 57	45 - 57	45 - 57	41 - 63
28	42 - 50	42 - 50	42 - 50	50 - 75
29	41 - 50	41 - 50	41 - 50	60 - 82
30	39 - 49	39 - 49	39 - 49	70 - 90
31	37 - 46	37 - 46	37 - 46	85 - 105

Table E.13: Ranges in TOF(ch) and Essd(ch) that define the PHA species boxes for H⁺. These box definitions are more narrow than the standard definitions and *should only be used in quiet times with relatively low count rates.*

Narrow PHA Box Limits for H ₂ ⁺				
DPPS Step	TOF(ch) Ranges			Essd(ch) Ranges
	Tel. 1	Tel. 2	Tel. 3	
0	380 - 490	380 - 490	380 - 490	0 - 0
1	368 - 460	361 - 460	364 - 460	0 - 0
2	340 - 420	340 - 420	340 - 420	0 - 0
3	307 - 390	307 - 390	307 - 390	0 - 0
4	287 - 360	287 - 360	0 - 0	0 - 0
5	260 - 325	260 - 325	0 - 0	0 - 0
6	240 - 300	240 - 300	0 - 0	0 - 0
7	225 - 270	225 - 270	0 - 0	0 - 0
8	209 - 245	209 - 245	209 - 238	0 - 0
9	0 - 0	195 - 242	0 - 0	0 - 0
10	0 - 0	176 - 221	0 - 0	0 - 0
11	0 - 0	167 - 205	169 - 191	0 - 0
12	154 - 180	154 - 191	154 - 191	0 - 0
13	144 - 174	144 - 175	144 - 175	0 - 0
14	135 - 157	132 - 157	134 - 156	0 - 0
15	124 - 149	125 - 149	122 - 144	0 - 0
16	116 - 137	115 - 136	115 - 134	5 - 17
17	108 - 127	109 - 124	107 - 124	5 - 19
18	102 - 118	99 - 118	100 - 115	6 - 21
19	91 - 110	90 - 110	89 - 110	8 - 25
20	81 - 102	81 - 102	81 - 102	5 - 28
21	83 - 97	83 - 97	79 - 98	5 - 30
22	79 - 89	79 - 89	75 - 90	5 - 35
23	70 - 88	70 - 88	70 - 88	5 - 37
24	70 - 83	70 - 83	70 - 83	10 - 42
25	63 - 80	63 - 80	63 - 80	11 - 47
26	62 - 73	62 - 73	62 - 73	17 - 54
27	58 - 69	58 - 69	58 - 69	10 - 60
28	56 - 65	56 - 65	56 - 65	50 - 70
29	51 - 63	51 - 63	51 - 63	60 - 78
30	50 - 60	50 - 60	50 - 60	70 - 90
31	47 - 56	47 - 56	47 - 56	85 - 100

Table E.14: Ranges in TOF(ch) and Essd(ch) that define the PHA species boxes for H₂⁺. These box definitions are more narrow than the standard definitions and *should only be used in quiet times with relatively low count rates.*

Narrow PHA Box Limits for He ⁺⁺				
DPPS Step	TOF(ch) Ranges			Essd(ch) Ranges
	Tel. 1	Tel. 2	Tel. 3	
0	380 - 450	380 - 450	380 - 440	0 - 0
1	349 - 401	349 - 401	345 - 401	0 - 0
2	320 - 380	320 - 380	320 - 380	0 - 0
3	302 - 360	300 - 360	305 - 360	0 - 0
4	280 - 339	280 - 339	0 - 0	0 - 0
5	260 - 310	259 - 310	258 - 289	0 - 0
6	236 - 290	236 - 290	0 - 0	0 - 0
7	217 - 266	226 - 266	0 - 0	0 - 0
8	210 - 250	205 - 250	200 - 235	0 - 0
9	0 - 0	192 - 239	0 - 0	0 - 0
10	0 - 0	176 - 220	0 - 0	0 - 0
11	0 - 0	167 - 205	169 - 191	0 - 0
12	154 - 180	154 - 182	154 - 182	5 - 20
13	144 - 169	144 - 169	144 - 169	7 - 22
14	132 - 153	132 - 156	134 - 156	15 - 25
15	124 - 140	125 - 145	122 - 144	17 - 26
16	116 - 137	115 - 136	115 - 134	18 - 30
17	108 - 127	109 - 124	107 - 124	20 - 35
18	102 - 118	99 - 118	100 - 115	22 - 38
19	91 - 110	90 - 110	89 - 110	26 - 42
20	81 - 102	81 - 102	81 - 102	30 - 47
21	83 - 97	83 - 97	79 - 98	35 - 55
22	79 - 89	79 - 89	75 - 90	40 - 60
23	70 - 88	70 - 88	70 - 88	48 - 67
24	70 - 83	70 - 83	70 - 83	55 - 76
25	60 - 80	60 - 80	60 - 80	66 - 87
26	62 - 73	62 - 73	62 - 73	75 - 98
27	55 - 69	55 - 69	55 - 69	90 - 115
28	56 - 65	56 - 65	56 - 65	109 - 130
29	50 - 63	50 - 63	50 - 63	125 - 145
30	49 - 60	49 - 60	49 - 60	147 - 165
31	44 - 56	44 - 56	44 - 56	168 - 190

Table E.15: Ranges in TOF(ch) and Essd(ch) that define the PHA species boxes for He⁺⁺. These box definitions are more narrow than the standard definitions and *should only be used in quiet times with relatively low count rates.*

Narrow PHA Box Limits for He ⁺				
DPPS Step	TOF(ch) Ranges			Essd(ch) Ranges
	Tel. 1	Tel. 2	Tel. 3	
0	550 - 674	568 - 674	550 - 674	0 - 0
1	505 - 611	505 - 611	505 - 603	0 - 0
2	473 - 579	473 - 570	473 - 572	0 - 0
3	439 - 543	439 - 543	428 - 531	0 - 0
4	399 - 481	399 - 481	399 - 481	0 - 0
5	372 - 440	377 - 440	372 - 438	0 - 0
6	344 - 400	340 - 400	341 - 400	0 - 0
7	320 - 376	321 - 361	323 - 361	0 - 0
8	300 - 350	300 - 350	0 - 0	0 - 0
9	281 - 318	277 - 319	0 - 0	0 - 0
10	260 - 296	250 - 292	258 - 290	0 - 0
11	235 - 296	235 - 270	0 - 0	0 - 0
12	222 - 255	220 - 254	0 - 0	0 - 0
13	211 - 232	205 - 233	204 - 233	0 - 0
14	201 - 215	187 - 217	0 - 0	5 - 15
15	0 - 0	175 - 200	0 - 0	5 - 16
16	166 - 185	166 - 185	166 - 185	7 - 18
17	156 - 175	156 - 175	156 - 175	7 - 23
18	143 - 162	143 - 162	143 - 162	7 - 23
19	132 - 154	132 - 154	132 - 154	7 - 26
20	120 - 144	120 - 144	120 - 144	10 - 28
21	113 - 130	113 - 130	113 - 130	10 - 30
22	108 - 126	108 - 126	108 - 126	15 - 35
23	99 - 116	99 - 116	100 - 116	20 - 38
24	92 - 108	92 - 108	92 - 108	25 - 41
25	82 - 101	82 - 101	82 - 101	30 - 48
26	79 - 93	79 - 93	81 - 91	35 - 55
27	78 - 89	77 - 89	79 - 89	40 - 60
28	72 - 83	72 - 83	72 - 83	45 - 70
29	70 - 77	70 - 78	69 - 77	59 - 79
30	64 - 73	64 - 73	64 - 73	68 - 86
31	64 - 69	64 - 69	64 - 69	79 - 100

Table E.16: Ranges in TOF(ch) and Essd(ch) that define the PHA species boxes for He⁺. These box definitions are more narrow than the standard definitions and *should only be used in quiet times with relatively low count rates.*

Narrow PHA Box Limits for O⁺⁺

DPPS Step	TOF(ch) Ranges			Essd(ch) Ranges
	Tel. 1	Tel. 2	Tel. 3	
0	0 - 0	0 - 0	0 - 0	0 - 0
1	0 - 0	0 - 0	0 - 0	0 - 0
2	0 - 0	0 - 0	0 - 0	0 - 0
3	0 - 0	0 - 0	0 - 0	0 - 0
4	0 - 0	0 - 0	0 - 0	0 - 0
5	0 - 0	0 - 0	0 - 0	0 - 0
6	0 - 0	0 - 0	0 - 0	0 - 0
7	0 - 0	0 - 0	0 - 0	0 - 0
8	404 - 521	404 - 521	404 - 521	0 - 0
9	403 - 514	403 - 514	403 - 514	0 - 0
10	360 - 450	360 - 450	360 - 450	0 - 0
11	343 - 413	343 - 413	343 - 413	0 - 0
12	325 - 380	325 - 380	325 - 380	0 - 0
13	303 - 334	303 - 334	311 - 343	0 - 0
14	284 - 318	284 - 317	0 - 0	0 - 0
15	260 - 286	259 - 288	261 - 280	9 - 20
16	240 - 270	240 - 270	240 - 270	5 - 23
17	220 - 250	220 - 250	220 - 250	5 - 25
18	209 - 230	209 - 230	208 - 230	10 - 30
19	190 - 215	190 - 215	190 - 215	10 - 35
20	180 - 200	180 - 200	178 - 199	13 - 37
21	165 - 182	165 - 182	165 - 182	16 - 44
22	155 - 170	155 - 170	155 - 170	20 - 48
23	140 - 160	140 - 160	140 - 158	28 - 57
24	130 - 150	130 - 150	130 - 150	35 - 65
25	122 - 139	122 - 139	122 - 139	40 - 75
26	110 - 127	110 - 127	110 - 127	53 - 85
27	105 - 120	105 - 120	105 - 120	60 - 98
28	100 - 110	100 - 110	100 - 110	80 - 110
29	90 - 105	90 - 105	90 - 105	90 - 126
30	87 - 98	87 - 98	87 - 98	101 - 145
31	79 - 92	79 - 92	79 - 92	125 - 172

Table E.17: Ranges in TOF(ch) and Essd(ch) that define the PHA species boxes for O⁺⁺. These box definitions are more narrow than the standard definitions and *should only be used in quiet times with relatively low count rates.*

Appendix F

CHEMS Efficiencies

The conversion of PHA counts to intensity, J , involves knowing the efficiency of a PHA species box. The efficiency for a species box indicates what fraction of incident ions of a particular species are actually captured by the region in $\text{Essd}(\text{ch})$ vs $\text{TOF}(\text{ch})$ space dedicated to that species. Section 4.5 describes how to compute intensities using equations 4.18 and 4.19, which refer to two kinds of efficiencies, ϵ_T for a triples-only efficiency, and ϵ_{tof} for a doubles plus triples efficiency. Each species has its own set of efficiencies, which vary by DPPS step, and each telescope may potentially have its own efficiency values. In practice, it was not possible to determine telescope specific efficiencies for a few species, and so these species have the same efficiencies in all telescopes, especially at higher E/Q values.

This section describes the derivation of efficiencies for the eleven ions for which CHEMS PHA species boxes have been defined. These species are listed in Table 4.8. The section concludes with Figures F.1 through F.10 that provide ϵ_{tof} and ϵ_T efficiency values for each species. Digital versions of the tables associated with each figure are available alongside this user guide and at the MIMI team web site [Kusterer and Vandegriff, 2011].

General Considerations

We use the pre-launch calibration data to determine the TOF efficiencies as a function of E/Q. Calibration data were obtained from two different models: the flight unit (FU) and the engineering model (EM). The flight unit is the instrument that is on Cassini. Most of the calibration data taken with the flight unit is from telescope 2. The engineering model functions the same way as the flight unit, with slight differences in energy steps and efficiency. Because the flight unit is the instrument on Cassini, we will weight the flight unit points more heavily when trying to determine the efficiencies, but data for some species at the highest portion of the CHEMS energy range are only available for the EM unit.

Calibration was performed at the NASA Goddard Space Flight Center. For the flight unit, ion beams of varying energy were focused on the aperture of CHEMS. A small electrostatic accelerator was used with a maximum energy of approximately 100 keV. The EM calibration data was done with a Van de Graff accelerator with energies up to 220 keV (the max of CHEMS).

To calculate the TOF efficiencies, we need to determine the start and stop efficiencies as a function of energy per charge. We calculate the start and stop efficiencies using the engineering rates:

$$\text{start efficiency} = \frac{\text{DCR}}{\text{STOP}} \quad (\text{F.1})$$

$$\text{stop efficiency} = \frac{\text{DCR}}{\text{START}} \quad (\text{F.2})$$

DCR, TCR, START, and STOP are counters in the CHEMS engineering rate data, where each telescope has its own set of these counters. Table 4.4 gives the exact names for these counters. DCR is the doubles counting rate, and TCR is the triples counting rate. DCR counts contains all the TCR counts, so that DCR is actually doubles plus triples. The TOF efficiency for doubles plus triples combined (ϵ_{tof}) is determined by multiplying the start and stop efficiency.

Because triples-only counts are used at higher E/Q to determine fluxes, we need to know the triples only efficiencies. To calculate the triples only efficiency (ϵ_{T}), we need to obtain TCR/DCR as a function of E/Q and multiply this ratio by ϵ_{tof} . TCR/DCR calibration data approaches one at high E/Q as the SSD efficiency approaches one and scattering in the foil becomes small. However, the ratio of the in-flight data approaches $\sim 0.85 - 0.90$. This difference results from the fact that narrow ion beams during calibration are aimed at the center of the telescope, so that scattering does not cause many ions to miss the SSD and fail to produce stop counts. Thus, we will use in flight PHA data to determine TCR/DCR as a function of E/Q.

Since the SSD on telescope 3 has a lower threshold, the triples only efficiency varies by telescope. Thus, we need to separate the data by telescope to measure the triples only efficiency. The lower threshold on telescope 3 causes the triples only efficiency of telescope 3 to be higher than telescopes 1 and 2. The difference between telescope 3 and the others is largest at energies where we first began to detect triples data efficiently. As E/Q increases, the triples efficiencies for the telescopes converge.

To get the TCR/DCR, we use the PHA box counts to determine the double and triple counts for each ion species. To get sufficient statistics, we combine time periods over several years of the Cassini mission. For O^{++} and He^+ , we use the Essd(ch) vs. TOF(ch) boxes discussed in Section 4.6 and tabulated in Appendix E. We determined the TCR/DCR for H^+ , W^+ , and H_2^+ before we switched to using Essd(ch) vs. TOF(ch) boxes. Thus, our current values for these three species are based on Mass versus M/Q boxes. The results from the Mass versus M/Q boxes do not differ very much from the Essd(ch) versus TOF(ch) boxes, so we don't need to update these values using the new boxes. The TCR/DCR is calculated by dividing the triple box counts by the total box counts (triple plus double counts).

Using the in flight data to get the TCR/DCR creates a few problems. Doubles background and bogus TOF counts can make it difficult to get an accurate measurement at certain DPPS steps. At DPPS steps where the species peak passes through a bogus TOF channel, we use interpolation to estimate the TCR/DCR. Another problem occurs when we need to use active periods to get the TCR/DCR. Because of limitations in telemetry, the DPU does not send down all PHA events. The DPU selects a random number of events and gives equal weighting to each range ID. Therefore, if the period is active, the ratio of the triple counts to total counts of the PHA data may not represent the actual TCR/DCR value.

Initially, we use the equatorial ring current data ($L=7-16, |Z| < 1.0R_S$) from 2004 – 2009 to get the TCR/DCR for H^+ , W^+ , and H_2^+ . However, this period was too active and resulted in us overestimating the TCR/DCR at certain points. Therefore, we switched to quieter time periods in the outer ring current ($L=16-21$) where the limited telemetry was not a problem. We still use the $L=7-16$ periods for O^{++} and O_2^+ , because we do not get sufficient statistics in the $L=16-21$ time periods.

We cannot use magnetospheric time periods to get the TCR/DCR for the helium data. The He^+ data contains a large amount of background in Saturn's magnetosphere and the H_2^+ data dominates the $M/Q = 2$ box. Thus, we use interplanetary data to get the TCR/DCR for the helium data. Since most of the interplanetary periods are quiet, our statistics are not as good as that from the magnetosphere. This creates a problem for telescope 1, since this telescope is rarely facing in the direction of the solar wind. Because of the lack of statistics for telescope 1 in interplanetary space, we assume that the TCR/DCR for He^+ and He^{++} for telescope 1 is the same as telescope 2. Since the threshold of the SSD for telescopes 1 and 2 are the same, this is not a bad approximation.

In this section, we only show the plots of the efficiency versus energy along with the values of the efficiency. These plots and numbers are shown in Figures 11-20 at the end of this section. We include only a brief description of how we determine the efficiencies for each ion species. A more detailed discussion of how we determined the efficiencies is beyond the scope of this user guide.

H^+ Efficiencies

The H^+ efficiencies are shown in Figure F.1. The TOF efficiency and triples only efficiency is easily obtained. We had H^+ calibration data for numerous E/Q values making the TOF efficiency easy to determine. H^+ is abundant in the $L=16-21$ equatorial time periods, so getting the TCR/DCR was not a problem. For $E/Q < 63$ keV/e, the TCR/DCR increases with energy. The TCR/DCR flattens at 0.90 for energies greater than 63 keV, so we set the TCR/DCR to 0.90 for DPPS steps 22-31.

O^+ Efficiencies (also used for W^+)

The O^+ efficiencies are shown in Figure F.7. Like H^+ , we have plenty of calibration points for O^+ . We have fewer calibration points for H_2O^+ , but the TOF efficiencies for O^+ and H_2O^+ do not differ significantly. We can assume that the O^+ TOF efficiency is the same as the H_2O^+ efficiency. We get plenty of PHA counts in the $L=16-21$ equatorial periods to get the TCR/DCR. The TCR/DCR increases significantly with energy for $E/Q < 83$ keV/e. Unlike the H^+ TCR/DCR, the W^+ TCR/DCR does not reach 0.90 at the highest E/Q step. For steps 24-31 ($E/Q = 83.4-220$ keV), the TCR/DCR slowly increases with energy and reaches 0.85 at the highest DPPS step.

H_2^+ Efficiencies

The H_2^+ efficiencies are shown in Figure F.2. We only have one flight unit calibration point and five engineering model points for H_2^+ . To get the TOF efficiently we perform a fit on the calibration data. The details of fitting these peaks have been omitted from this data user guide. The TCR/DCR

was obtained using the L=16-21 time periods. The H_2^+ TCR/DCR increases with energy until step 27 ($E/Q = 127$ keV/e). For $E/Q > 127$ keV/e, the TCR/DCR flattens out at 0.90, so we set the TCR/DCR to this value for steps 27-31 ($E/Q = 127-220$ keV/e).

When we determined the TCR/DCR for H_2^+ , we used the total box counts. Since we now only use the M=2 peak for steps 28-31, we need to adjust these values at the highest four DPPS steps. The M=2 counts contains 78% of the total H_2^+ counts for step 28 and 80% of the total H_2^+ counts for step 29-31. To correct for only using the Mass = 2 peak, we multiply the TCR/DCR at steps 28-31 (0.90) by these percentages.

He⁺ and He⁺⁺ Efficiencies

The efficiencies for He⁺ and He⁺⁺ are shown in Figures F.5 and F.3 respectively. We have He⁺ calibration data for several different E/Q values making it easy to obtain the TOF efficiency for He⁺. We base the TOF efficiency for He⁺⁺ on the He⁺ data. At the same E/Q, He⁺⁺ has twice the energy as He⁺. We assume that the He⁺⁺ efficiency at a specific E/Q is the same as the He⁺ efficiency at twice the E/Q. For example, the He⁺⁺ efficiency at 110 keV/e is approximately the same as the He⁺ efficiency at 220 keV/e.

We use active interplanetary periods to obtain the TCR/DCR for He⁺. Because of poor statistics and background problems in telescope 1, we assume the TCR/DCR for telescope 1 is the same as telescope 2. Since telescope 1 and telescope 2 have the same SSD threshold, this is not a bad approximation. Results from the other ion species indicate that the TCR/DCR for telescopes 1 and 2 do not differ significantly. The TCR/DCR of He⁺ increases with energy for $E/Q < 63.2$ keV/e and then flattens out at 0.90 for $E/Q > 63.2$ keV/e.

Because of poor statistics of the He⁺⁺ data, we determine the He⁺⁺ TCR/DCR the same way we determined the TOF efficiency. We assume that the He⁺⁺ TCR/DCR is the same as the He⁺ TCR/DCR at twice the E/Q. To avoid H_2^+ counts in the He⁺⁺ box for steps 14 and 15, we made our He⁺⁺ boxes at these steps very narrow. Because of the narrow box, we lose triples He⁺⁺ counts at these steps. Therefore, we need to reduce the TCR/DCR for steps 14 and 15 to compensate for the narrow He⁺⁺ boxes. We take the ratio of the counts in our narrow box to the total number of He⁺⁺ counts (see the previous section on PHA boxes to get these ratios). We then multiply this ratio by the TCR/DCR obtained by the He⁺ data to correct for the narrow boxes.

O⁺⁺ Efficiencies

The O⁺⁺ efficiencies are shown in Figure F.6. Our method for determining the TOF efficiency is similar to the method we used for the He⁺⁺ data. We assume the O⁺⁺ efficiency at a specific E/Q is the same as the O⁺ efficiency at twice the E/Q. Since there are not sufficient counts in the L=16-21 time periods to determine the TCR/DCR, we use time periods from L=7-16. The O⁺⁺ TCR/DCR increases with energy for $E/Q < 72.6$ keV/e. The O⁺⁺ TCR/DCR flattens out at 0.86 at higher energies (steps 22-31). Our transition to triples only at higher energies appears smooth, so using this active period does not seem to give us an inaccurate result.

O_2^+ Efficiencies

The O_2^+ efficiencies are shown in Figure F.10. The O_2^+ TOF efficiency was determined using the calibration data. We fit the 5 calibration points from the engineering model with a 2nd degree polynomial. Getting the TCR/DCR for O_2^+ from the in flight data is difficult. We used the L=7-16 data, because there were few O_2^+ counts in the L=16-21 range. The doubles data from W^+ distribution is very wide and some W^+ counts interfere with the O_2^+ . This creates some background problems with the O_2^+ doubles data, especially for steps 24 and 25. As a result, the efficiencies for step 24 and 25 may be underestimated. In addition to this problem, bogus TOF counts interfere with step 24 on telescope 3, so we had to extrapolate to get the TCR/DCR at step 24. Calculating the O_2^+ differential intensity at DPPS step 24 contains a large amount of uncertainty and we do not recommend using the O_2^+ data at this step.

H_3^+ Efficiencies

The H_3^+ efficiencies are shown in Figure F.4. We only have one flight unit calibration point and two engineering model points for H_3^+ , which makes it impossible to perform a fit based on calibration data. We assume the TOF efficiency for H_3^+ is the same as the TOF efficiency for H_2^+ . Since the TCR/DCR for H_3^+ differs significantly from H_2^+ , we cannot make this assumption for the triples only efficiency. Since the doubles data from the H_2^+ results in a wide distribution that will interfere with H_3^+ peak, we cannot use a long-term time period. We need to identify periods where H_3^+ is high compared with H_2^+ to get the TCR/DCR. We have identified two such periods that are listed in Table F.1. These time periods are short, but H_3^+ distinguishes itself from the H_2^+ peak. We use these time periods in addition to a calibration point from the engineering model to estimate the TCR to DCR. Because of poor statistics, we cannot separate H_3^+ TCR/DCR by telescope. In the future, if we could get more periods with a large amount of H_3^+ counts, we will be able to improve the statistics of our current values.

C^+ and N^+ Efficiencies

Both the C^+ and N^+ efficiencies are shown in Figure F.9. We have six flight unit calibration points and five engineering model calibration points for C^+ and N^+ . We can fit these calibration points and get a good estimate of the TOF efficiencies for C^+ and N^+ . We cannot use in flight data to determine the triples to doubles ratios, because C^+ and N^+ peaks are difficult to distinguish especially in the doubles data. To determine TCR/DCR for C^+ and N^+ , we used the calibration data for C^+ , N^+ , and O^+ , and the in flight results for the W^+ TCR/DCR. We fit the TCR/DCR calibration data of C^+ , N^+ , and O^+ . All the fits approach 1.0 at the highest DPPS steps, which disagrees with the in flight data. To determine the in flight TCR/DCR for C^+ , we take the ratio of the C^+ TCR/DCR calibration fit to the O^+ TCR/DCR calibration fit and then multiply this ratio by W^+ TCR/DCR from the flight data. When TCR/DCR reaches 0.85, we assume it remains at 0.85. We perform the same calculation for N^+ TCR/DCR.

O^{+++} Efficiencies

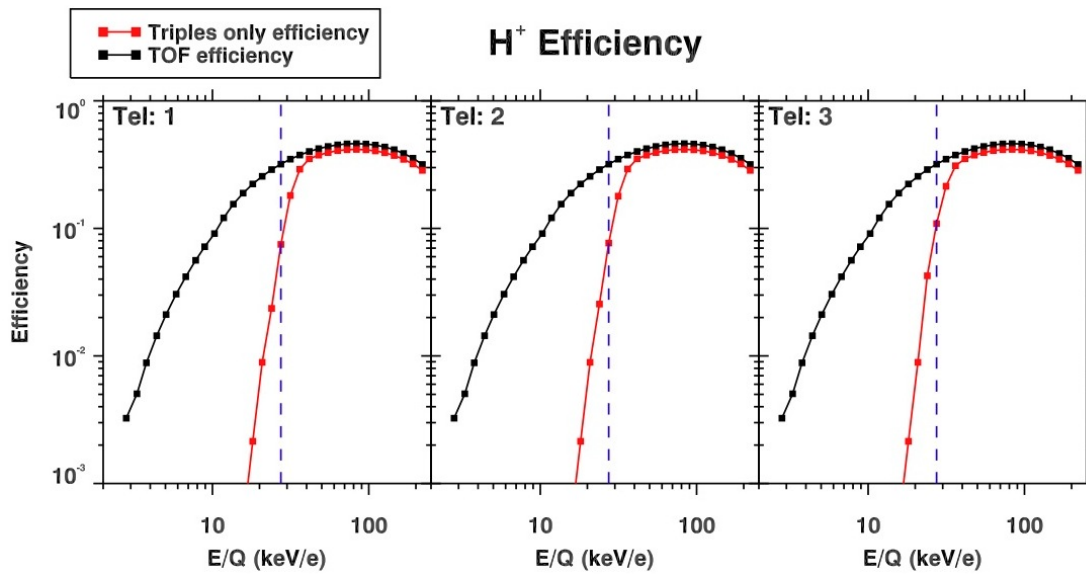
The O^{+++} efficiencies are shown in Figure F.8. We determine the O^{+++} efficiencies the same way we determine the O^{++} efficiencies. At the same DPPS step (i.e. the same E/Q), O^{+++} has three

Ion species	Time periods used to get TCR/DCR
He ⁺ and He ⁺⁺	2001 – 2004 active interplanetary periods
H ⁺ , W ⁺ , and H ₂ ⁺	2004 – 2009 $L = 16 - 21$ and $ Z < 1 R_S$
O ⁺⁺ and O ₂ ⁺	2004 – 2009 $L = 7 - 16$ and $ Z < 1 R_S$
H ₃ ⁺	2008 291 06:00 – 2008 291 18:00 2010 245 10:00 – 2010 245 15:00
O ⁺⁺⁺	based on O ⁺⁺
C ⁺ and N ⁺	based on O ⁺ TCR/DCR and calibration data

Table F.1: Since the calibration data does not provide an accurate estimate of the TCR/DCR ratio, in flight data was used to estimate the TCR/DCR ratios used in calculating efficiencies. Listed here are the time periods used to estimate the TCR/DCR ratio of each ion species for which there is a PHA species box.

times the energy as O⁺. We assume that the TOF efficiency of O⁺⁺⁺ at a specific E/Q is the same as the efficiency of O⁺ at three times the E/Q.

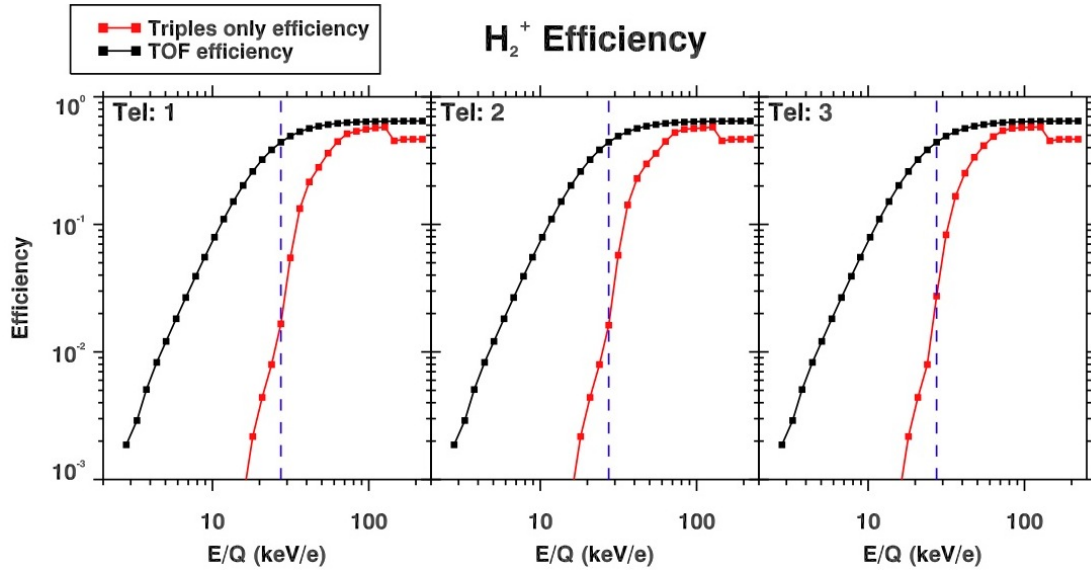
To get the triples only efficiency for O⁺⁺⁺, we use the TCR/DCR of the O⁺⁺ data. We assume the O⁺⁺⁺ triples only efficiency at a specific E/Q is the same as the O⁺⁺ triples only efficiency at 1.5 times the E/Q. Our O⁺⁺⁺ box begins at step 18 where the O⁺⁺ triples only efficiencies converge, so we do not need to worry about variations with telescope. Using the O⁺⁺ efficiencies gives us the data from steps 18-28 (E/Q = 36-145 keV/e). At higher energies, the O⁺⁺⁺ TCR/DCR approaches 0.89, so we set the O⁺⁺⁺ TCR/DCR at steps 29-31 (E/Q = 167-220 keV/e) to 0.89.



Efficiency Values for H⁺

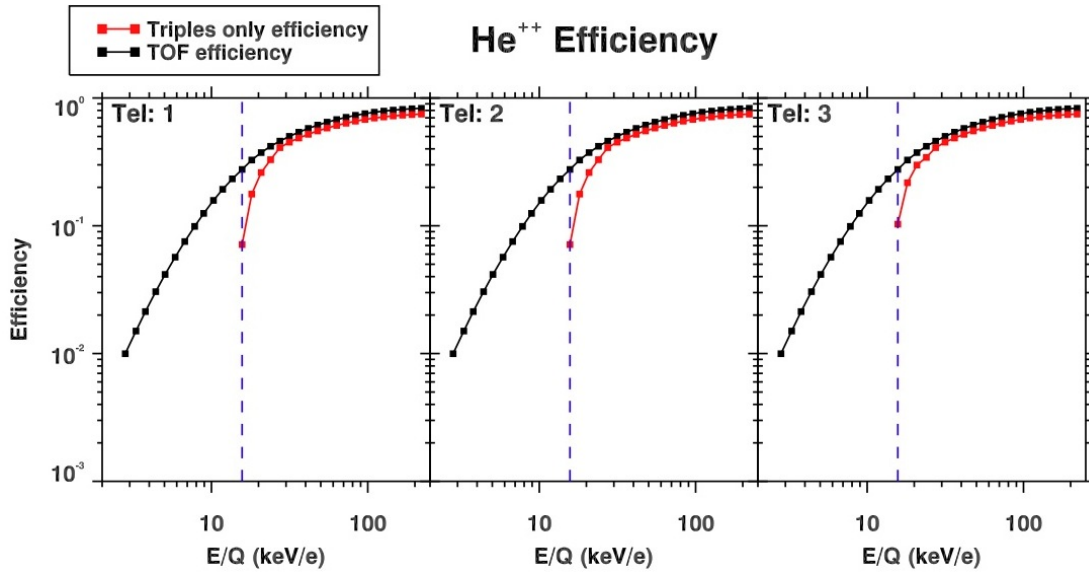
DPPS Step	Doubles+Triples		Triples Only		
	ϵ_{tof} all telescopes	Tel. 1	Tel. 2	Tel. 3	
0	3.25e-03	0	0	0	
1	5.05e-03	0	0	0	
2	8.83e-03	0	0	0	
3	1.44e-02	0	0	0	
4	2.11e-02	0	0	0	
5	3.05e-02	0	0	0	
6	4.18e-02	0	0	0	
7	5.62e-02	0	0	0	
8	7.18e-02	0	0	0	
9	9.10e-02	4.95e-06	4.95e-06	4.95e-06	
10	1.21e-01	4.15e-05	4.15e-05	4.15e-05	
11	1.55e-01	1.13e-04	1.13e-04	1.13e-04	
12	1.89e-01	4.74e-04	4.74e-04	4.74e-04	
13	2.23e-01	2.14e-03	2.14e-03	2.14e-03	
14	2.56e-01	8.91e-03	8.91e-03	8.91e-03	
15	2.89e-01	2.36e-02	2.55e-02	4.25e-02	
16	3.19e-01	7.49e-02	7.67e-02	1.09e-01	
17	3.49e-01	1.81e-01	1.79e-01	2.14e-01	
18	3.76e-01	2.91e-01	2.92e-01	3.10e-01	
19	4.01e-01	3.51e-01	3.51e-01	3.51e-01	
20	4.22e-01	3.75e-01	3.75e-01	3.75e-01	
21	4.39e-01	3.93e-01	3.93e-01	3.93e-01	
22	4.52e-01	4.07e-01	4.07e-01	4.07e-01	
23	4.60e-01	4.14e-01	4.14e-01	4.14e-01	
24	4.62e-01	4.16e-01	4.16e-01	4.16e-01	
25	4.59e-01	4.13e-01	4.13e-01	4.13e-01	
26	4.50e-01	4.05e-01	4.05e-01	4.05e-01	
27	4.35e-01	3.92e-01	3.92e-01	3.92e-01	
28	4.14e-01	3.73e-01	3.73e-01	3.73e-01	
29	3.87e-01	3.48e-01	3.48e-01	3.48e-01	
30	3.55e-01	3.20e-01	3.20e-01	3.20e-01	
31	3.17e-01	2.85e-01	2.85e-01	2.85e-01	

Figure F.1: A plot and a listing of CHEMS PHA species boxes efficiencies for detecting H⁺. The dashed blue line indicates that at step 16 (E/Q = 27.4 keV/e) and above, the triples only efficiency can be used. Below this step, the doubles plus triples must be used.



DPPS Step	Efficiency Values for H_2^+				
	Doubles+Triples		Triples Only		
	ϵ_{tof} all telescopes	Tel. 1	Tel. 2	Tel. 3	ϵ_T
0	1.87e-03	0	0	0	0
1	2.90e-03	0	0	0	0
2	5.07e-03	0	0	0	0
3	8.28e-03	0	0	0	0
4	1.21e-02	0	0	0	0
5	1.82e-02	0	0	0	0
6	2.67e-02	0	0	0	0
7	3.92e-02	0	0	0	0
8	5.53e-02	0	0	0	0
9	7.93e-02	0	0	0	0
10	1.10e-01	1.65e-05	1.65e-05	1.65e-05	1.65e-05
11	1.51e-01	2.02e-04	2.02e-04	2.02e-04	2.02e-04
12	2.02e-01	7.02e-04	7.02e-04	7.02e-04	7.02e-04
13	2.60e-01	2.17e-03	2.17e-03	2.17e-03	2.17e-03
14	3.22e-01	4.40e-03	4.40e-03	4.40e-03	4.40e-03
15	3.84e-01	7.96e-03	7.96e-03	7.96e-03	7.96e-03
16	4.41e-01	1.66e-02	1.62e-02	2.74e-02	1.66e-02
17	4.92e-01	5.47e-02	5.73e-02	8.28e-02	5.47e-02
18	5.33e-01	1.33e-01	1.42e-01	1.66e-01	1.33e-01
19	5.65e-01	2.15e-01	2.29e-01	2.52e-01	2.15e-01
20	5.89e-01	2.80e-01	2.98e-01	3.36e-01	2.80e-01
21	6.06e-01	3.62e-01	3.60e-01	4.14e-01	3.62e-01
22	6.19e-01	4.46e-01	4.47e-01	4.88e-01	4.46e-01
23	6.28e-01	5.13e-01	5.25e-01	5.43e-01	5.13e-01
24	6.34e-01	5.37e-01	5.56e-01	5.66e-01	5.37e-01
25	6.38e-01	5.57e-01	5.64e-01	5.74e-01	5.57e-01
26	6.41e-01	5.70e-01	5.70e-01	5.77e-01	5.70e-01
27	6.43e-01	5.79e-01	5.79e-01	5.79e-01	5.79e-01
28	6.44e-01	4.52e-01	4.52e-01	4.52e-01	4.52e-01
29	6.45e-01	4.64e-01	4.64e-01	4.64e-01	4.64e-01
30	6.46e-01	4.65e-01	4.65e-01	4.65e-01	4.65e-01
31	6.46e-01	4.65e-01	4.65e-01	4.65e-01	4.65e-01

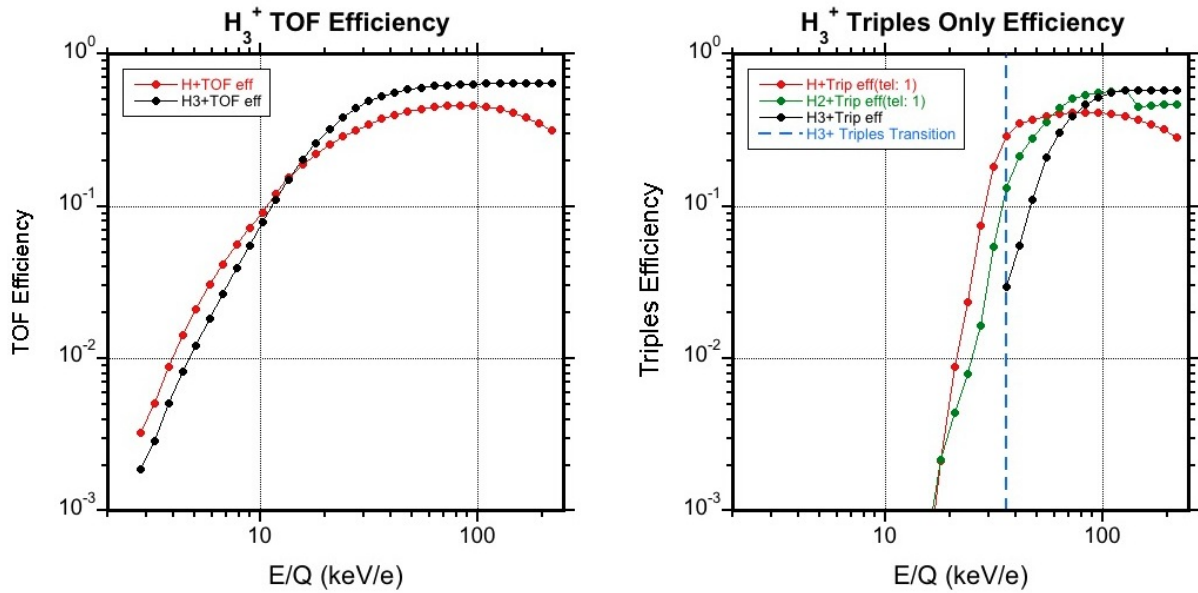
Figure F.2: A plot and a listing of CHEMS PHA species boxes efficiencies for detecting H_2^+ . Triples-only data can be used at and above DPPS step 16, $E/Q = 27.4$ keV/e (see the blue dashed line). At the highest four steps, 28-31, the efficiency values are lower because at these steps, only the Mass = 2 peak is used to collect H_2^+ PHA counts.



Efficiency Values for He⁺⁺

DPSS Step	Doubles+Triples		Triples Only		
	ϵ_{tof} all telescopes	Tel. 1	Tel. 2	Tel. 3	ϵ_{T}
0	9.97e-03	0	0	0	0
1	1.50e-02	0	0	0	0
2	2.13e-02	0	0	0	0
3	3.05e-02	0	0	0	0
4	4.16e-02	0	0	0	0
5	5.68e-02	0	0	0	0
6	7.53e-02	0	0	0	0
7	9.89e-02	0	0	0	0
8	1.25e-01	0	0	0	0
9	1.58e-01	0	0	0	0
10	1.93e-01	0	0	0	0
11	2.33e-01	0	0	0	0
12	2.76e-01	7.13e-02	7.13e-02	1.03e-01	
13	3.27e-01	1.77e-01	1.77e-01	2.17e-01	
14	3.74e-01	2.61e-01	2.61e-01	2.99e-01	
15	4.19e-01	3.29e-01	3.29e-01	3.43e-01	
16	4.60e-01	4.09e-01	4.09e-01	4.09e-01	
17	5.01e-01	4.51e-01	4.51e-01	4.51e-01	
18	5.40e-01	4.86e-01	4.86e-01	4.86e-01	
19	5.78e-01	5.20e-01	5.20e-01	5.20e-01	
20	6.14e-01	5.53e-01	5.53e-01	5.53e-01	
21	6.47e-01	5.82e-01	5.82e-01	5.82e-01	
22	6.78e-01	6.10e-01	6.10e-01	6.10e-01	
23	7.06e-01	6.35e-01	6.35e-01	6.35e-01	
24	7.32e-01	6.59e-01	6.59e-01	6.59e-01	
25	7.54e-01	6.79e-01	6.79e-01	6.79e-01	
26	7.74e-01	6.97e-01	6.97e-01	6.97e-01	
27	7.90e-01	7.11e-01	7.11e-01	7.11e-01	
28	8.04e-01	7.24e-01	7.24e-01	7.24e-01	
29	8.15e-01	7.34e-01	7.34e-01	7.34e-01	
30	8.24e-01	7.42e-01	7.42e-01	7.42e-01	
31	8.31e-01	7.48e-01	7.48e-01	7.48e-01	

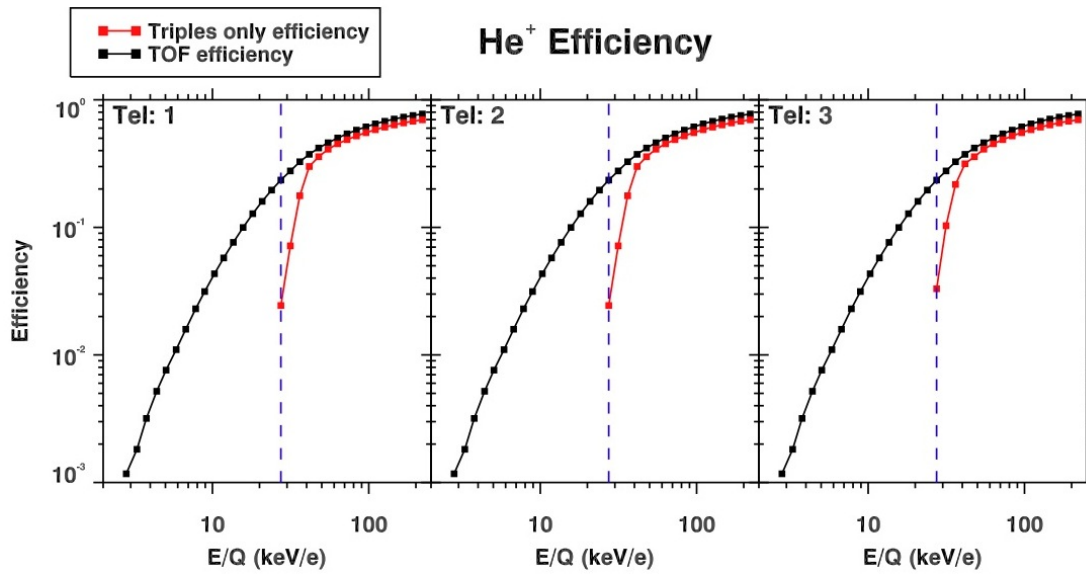
Figure F.3: A plot and a listing of CHEMS PHA species boxes efficiencies for detecting He⁺⁺. The dashed blue line indicates that at step 12 (E/Q = 15.7 keV/e) and above, the triples only efficiency can be used. Below this step, the doubles plus triples must be used.



Efficiency Values for H_3^+

DPPS Step	Doubles+Triples	Triples Only
	ϵ_{tof} all telescopes	ϵ_{T} all telescopes
18	5.33e-01	2.96e-02
19	5.65e-01	5.55e-02
20	5.89e-01	1.11e-01
21	6.06e-01	2.09e-01
22	6.19e-01	3.06e-01
23	6.28e-01	3.93e-01
24	6.34e-01	4.67e-01
25	6.38e-01	5.23e-01
26	6.41e-01	5.60e-01
27	6.43e-01	5.79e-01
28	6.44e-01	5.80e-01
29	6.45e-01	5.81e-01
30	6.46e-01	5.81e-01
31	6.46e-01	5.81e-01

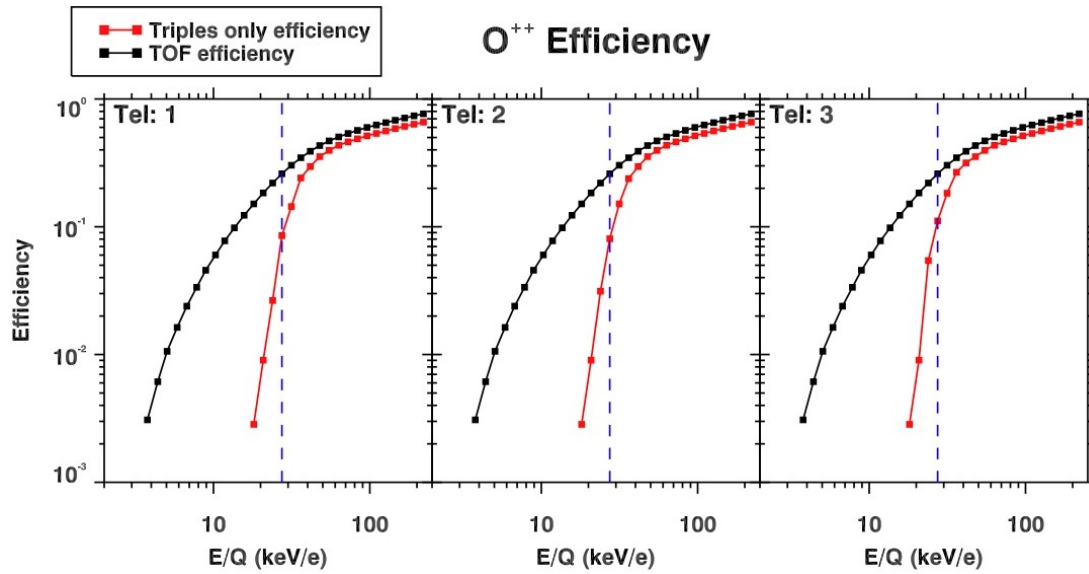
Figure F.4: A plot and a listing of CHEMS PHA species boxes efficiencies for detecting H_3^+ . Because of poor statistics, the H_3^+ triples only efficiency values cannot be separated by telescope. It was not possible to create a species box for $E/Q < 36.2$ keV/e (step 18), so the efficiencies below this energy are not shown.



Efficiency Values for He⁺

DPPS Step	Doubles+Triples		Triples Only		
	ϵ_{tof} all telescopes	Tel. 1	Tel. 2	Tel. 3	ϵ_T
0	1.17e-03	0	0	0	0
1	1.82e-03	0	0	0	0
2	3.18e-03	0	0	0	0
3	5.19e-03	0	0	0	0
4	7.60e-03	0	0	0	0
5	1.10e-02	0	0	0	0
6	1.59e-02	0	0	0	0
7	2.30e-02	0	0	0	0
8	3.14e-02	0	0	0	0
9	4.33e-02	0	0	0	0
10	5.76e-02	0	0	0	0
11	7.63e-02	0	0	0	0
12	9.98e-02	0	0	0	0
13	1.28e-01	0	0	0	0
14	1.60e-01	0	0	0	0
15	1.96e-01	0	0	0	0
16	2.35e-01	2.44e-02	2.44e-02	3.30e-02	
17	2.77e-01	7.16e-02	7.16e-02	1.03e-01	
18	3.27e-01	1.77e-01	1.77e-01	2.17e-01	
19	3.74e-01	3.00e-01	3.00e-01	3.15e-01	
20	4.19e-01	3.58e-01	3.58e-01	3.58e-01	
21	4.61e-01	4.10e-01	4.10e-01	4.10e-01	
22	5.02e-01	4.52e-01	4.52e-01	4.52e-01	
23	5.41e-01	4.87e-01	4.87e-01	4.87e-01	
24	5.79e-01	5.21e-01	5.21e-01	5.21e-01	
25	6.14e-01	5.53e-01	5.53e-01	5.53e-01	
26	6.48e-01	5.83e-01	5.83e-01	5.83e-01	
27	6.79e-01	6.11e-01	6.11e-01	6.11e-01	
28	7.07e-01	6.36e-01	6.36e-01	6.36e-01	
29	7.32e-01	6.59e-01	6.59e-01	6.59e-01	
30	7.54e-01	6.79e-01	6.79e-01	6.79e-01	
31	7.74e-01	6.97e-01	6.97e-01	6.97e-01	

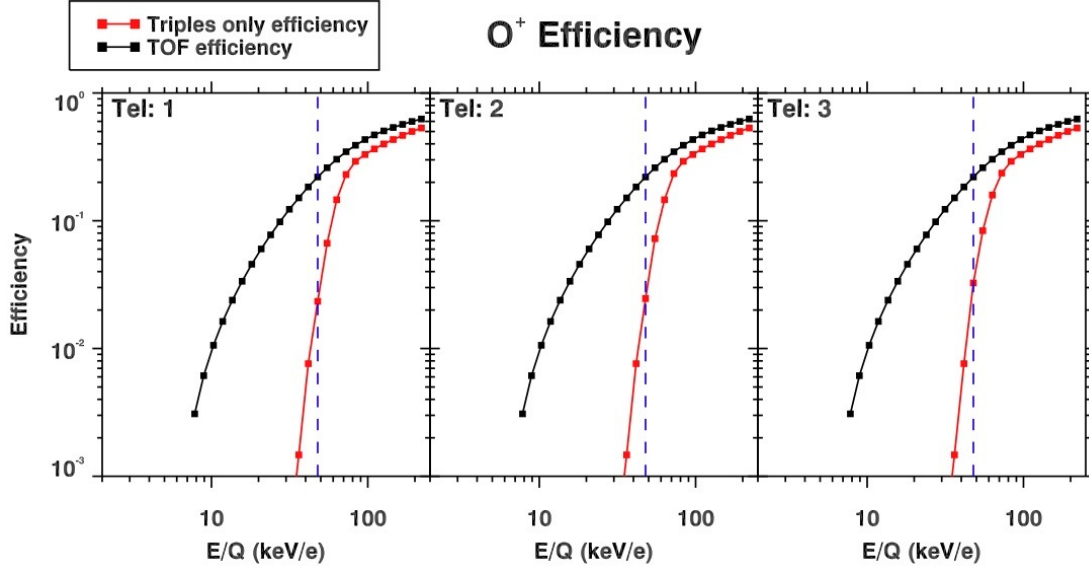
Figure F.5: A plot and a listing of CHEMS PHA species boxes efficiencies for detecting He⁺. The dashed blue line indicates that at step 16 (E/Q = 27.4 keV/e) and above, the triples only efficiency can be used. Below this step, the doubles plus triples must be used.



Efficiency Values for O⁺⁺

DPPS Step	Doubles+Triples		Triples Only		
	ϵ_{tof} all telescopes	Tel. 1	Tel. 2	Tel. 3	
0	0	0	0	0	
1	0	0	0	0	
2	3.08e-03	0	0	0	
3	6.13e-03	0	0	0	
4	1.06e-02	0	0	0	
5	1.63e-02	0	0	0	
6	2.39e-02	0	0	0	
7	3.36e-02	0	0	0	
8	4.57e-02	0	0	0	
9	6.02e-02	0	0	0	
10	7.76e-02	0	0	0	
11	9.81e-02	0	0	0	
12	1.23e-01	0	0	0	
13	1.51e-01	2.84e-03	2.84e-03	2.84e-03	
14	1.84e-01	9.03e-03	9.03e-03	9.03e-03	
15	2.20e-01	2.65e-02	3.13e-02	5.44e-02	
16	2.60e-01	8.53e-02	8.06e-02	1.11e-01	
17	3.03e-01	1.44e-01	1.51e-01	1.83e-01	
18	3.47e-01	2.41e-01	2.38e-01	2.67e-01	
19	3.90e-01	2.96e-01	2.96e-01	3.16e-01	
20	4.32e-01	3.54e-01	3.54e-01	3.54e-01	
21	4.70e-01	3.96e-01	3.96e-01	3.96e-01	
22	5.05e-01	4.34e-01	4.34e-01	4.34e-01	
23	5.37e-01	4.62e-01	4.62e-01	4.62e-01	
24	5.68e-01	4.88e-01	4.88e-01	4.88e-01	
25	5.99e-01	5.15e-01	5.15e-01	5.15e-01	
26	6.26e-01	5.38e-01	5.38e-01	5.38e-01	
27	6.53e-01	5.62e-01	5.62e-01	5.62e-01	
28	6.82e-01	5.87e-01	5.87e-01	5.87e-01	
29	7.10e-01	6.11e-01	6.11e-01	6.11e-01	
30	7.38e-01	6.35e-01	6.35e-01	6.35e-01	
31	7.66e-01	6.59e-01	6.59e-01	6.59e-01	

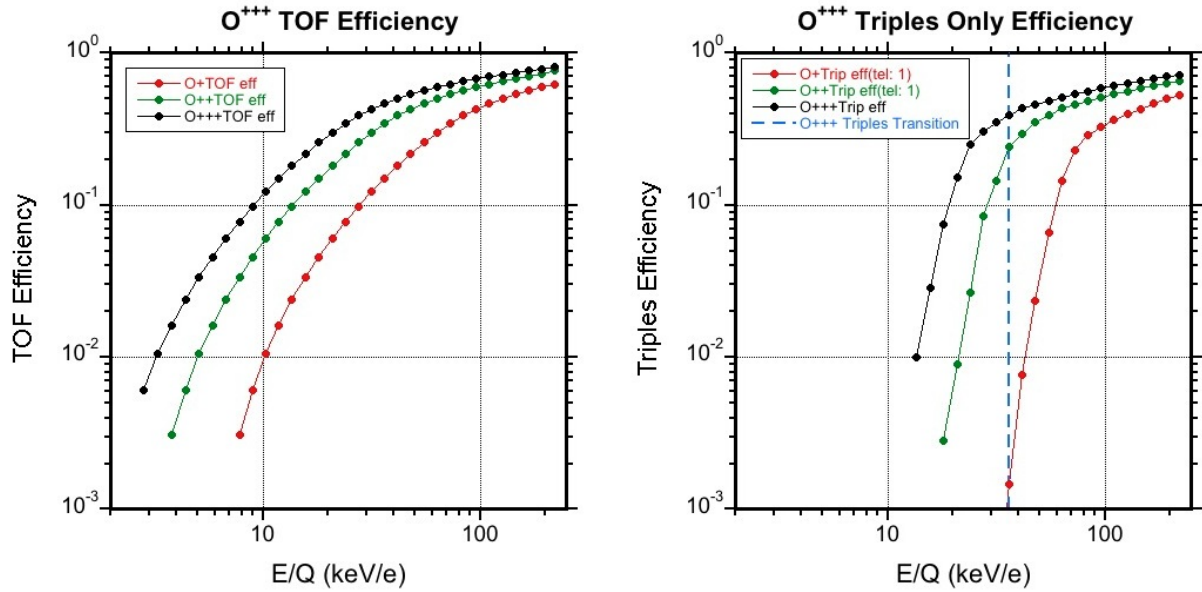
Figure F.6: A plot and a listing of CHEMS PHA species boxes efficiencies for detecting O⁺⁺. The dashed blue line indicates that at step 16 (E/Q = 27.4 keV/e) and above, the triples only efficiency can be used. Below this step, the doubles plus triples must be used.



Efficiency Values for W^+

DPPS Step	Doubles+Triples		Triples Only		
	ϵ_{tof} all telescopes	Tel. 1	Tel. 2	Tel. 3	ϵ_T
7	3.08e-03	0	0	0	0
8	6.13e-03	0	0	0	0
9	1.06e-02	0	0	0	0
10	1.63e-02	0	0	0	0
11	2.39e-02	0	0	0	0
12	3.36e-02	0	0	0	0
13	4.57e-02	0	0	0	0
14	6.02e-02	0	0	0	0
15	7.76e-02	0	0	0	0
16	9.81e-02	4.18e-05	4.18e-05	4.18e-05	4.18e-05
17	1.23e-01	3.31e-04	3.31e-04	3.31e-04	3.31e-04
18	1.51e-01	1.47e-03	1.47e-03	1.47e-03	1.47e-03
19	1.84e-01	7.61e-03	7.61e-03	7.61e-03	7.61e-03
20	2.20e-01	2.34e-02	2.46e-02	3.26e-02	2.34e-02
21	2.60e-01	6.67e-02	7.24e-02	8.36e-02	6.67e-02
22	3.03e-01	1.46e-01	1.46e-01	1.59e-01	1.46e-01
23	3.47e-01	2.30e-01	2.34e-01	2.36e-01	2.30e-01
24	3.90e-01	2.92e-01	2.92e-01	2.92e-01	2.92e-01
25	4.32e-01	3.30e-01	3.30e-01	3.30e-01	3.30e-01
26	4.70e-01	3.65e-01	3.65e-01	3.65e-01	3.65e-01
27	5.05e-01	3.99e-01	3.99e-01	3.99e-01	3.99e-01
28	5.37e-01	4.32e-01	4.32e-01	4.32e-01	4.32e-01
29	5.68e-01	4.66e-01	4.66e-01	4.66e-01	4.66e-01
30	5.99e-01	5.00e-01	5.00e-01	5.00e-01	5.00e-01
31	6.26e-01	5.32e-01	5.32e-01	5.32e-01	5.32e-01

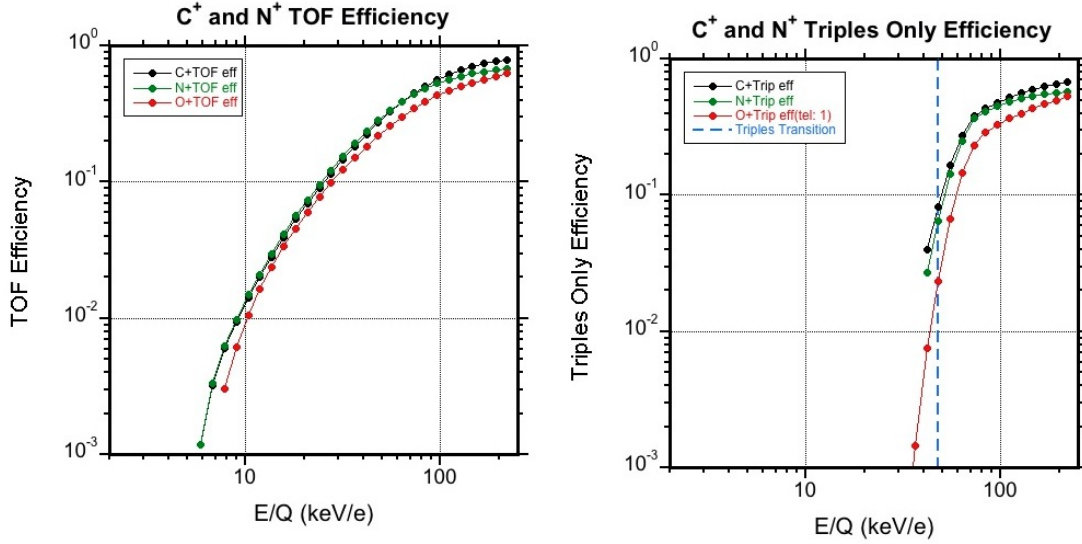
Figure F.7: A plot and a listing of CHEMS PHA species boxes efficiencies for detecting W^+ . The calibration data shows that O^+ and H_2O^+ have roughly the same TOF (doubles plus triples) efficiencies. Therefore, we use O^+ efficiencies for the W^+ group. We can begin to use triples only data at step 20 ($E/Q = 47.8$ keV/e), as indicated by the blue vertical dashed line.



Efficiency Values for O⁺⁺⁺

DPPS Step	Doubles+Triples	Triples Only
	ϵ_{tof} all telescopes	ϵ_{T} all telescopes
11	1.84e-01	9.94e-03
12	2.20e-01	2.86e-02
13	2.60e-01	7.54e-02
14	3.03e-01	1.52e-01
15	3.47e-01	2.50e-01
16	3.90e-01	3.04e-01
17	4.32e-01	3.50e-01
18	4.70e-01	3.96e-01
19	5.05e-01	4.34e-01
20	5.37e-01	4.62e-01
21	5.68e-01	4.88e-01
22	5.99e-01	5.15e-01
23	6.26e-01	5.38e-01
24	6.53e-01	5.62e-01
25	6.77e-01	5.87e-01
26	7.00e-01	6.11e-01
27	7.23e-01	6.35e-01
28	7.45e-01	6.59e-01
29	7.66e-01	6.82e-01
30	7.88e-01	7.01e-01
31	8.09e-01	7.20e-01

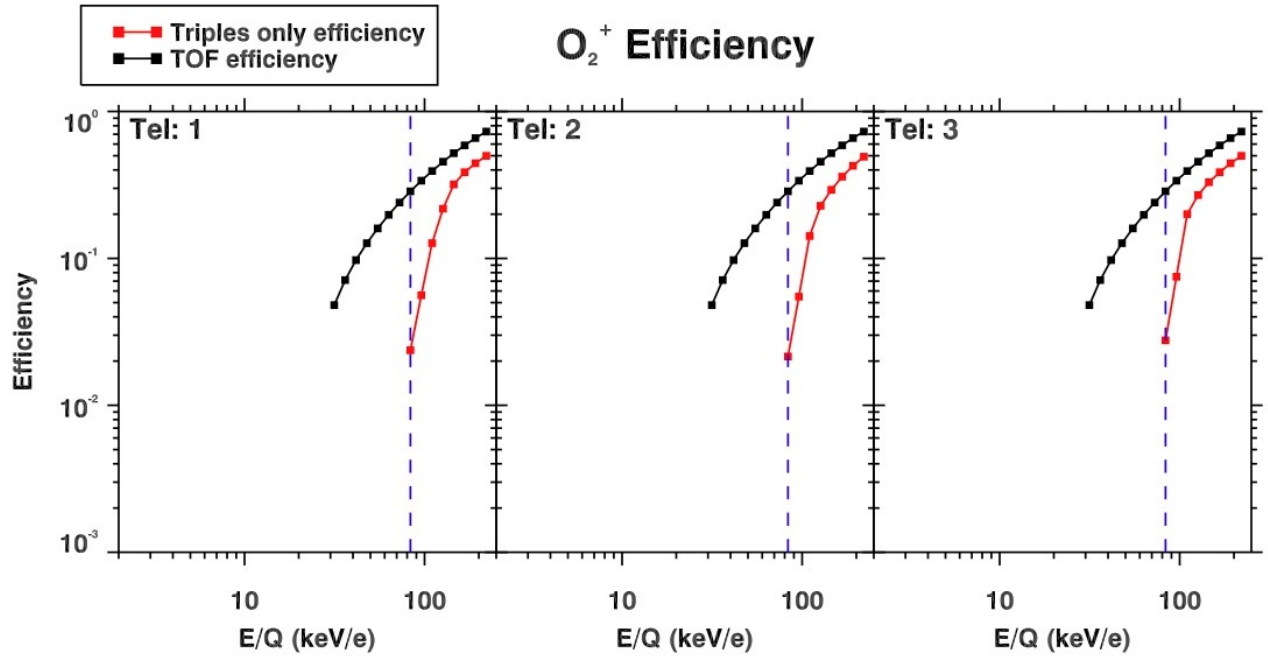
Figure F.8: A plot and a listing of CHEMS PHA species boxes efficiencies for detecting O⁺⁺⁺. Only triples data should be used when calculating the differential intensity for O⁺⁺⁺ because the doubles box for O⁺⁺⁺ contains too much background. The triples-only efficiency for O⁺⁺⁺ starts becoming useful at step 18 (the vertical dashed line), and also there are no valid box definitions for O⁺⁺⁺ below step 18.



Efficiency Values for C^+ and N^+

DPPS Step	for C^+		for N^+	
	Doubles+Triples	Triples Only	Doubles+Triples	Triples Only
	ϵ_{tof}	ϵ_T	ϵ_{tof}	ϵ_T
	all telescopes	all telescopes	all telescopes	all telescopes
8	9.42e-03	0	9.85e-03	0
9	1.42e-02	0	1.49e-02	0
10	2.02e-02	0	2.11e-02	0
11	2.83e-02	0	2.97e-02	0
12	3.93e-02	0	4.13e-02	0
13	5.38e-02	0	5.64e-02	0
14	6.97e-02	0	7.36e-02	0
15	8.97e-02	0	9.53e-02	0
16	1.14e-01	0	1.22e-01	0
17	1.45e-01	0	1.54e-01	0
18	1.82e-01	0	1.92e-01	0
19	2.25e-01	3.99e-02	2.36e-01	2.69e-02
20	2.74e-01	8.27e-02	2.84e-01	6.44e-02
21	3.29e-01	1.66e-01	3.36e-01	1.44e-01
22	3.89e-01	2.73e-01	3.88e-01	2.50e-01
23	4.49e-01	3.82e-01	4.39e-01	3.70e-01
24	5.09e-01	4.33e-01	4.87e-01	4.14e-01
25	5.67e-01	4.82e-01	5.31e-01	4.51e-01
26	6.19e-01	5.26e-01	5.68e-01	4.83e-01
27	6.67e-01	5.67e-01	6.00e-01	5.10e-01
28	7.07e-01	6.01e-01	6.26e-01	5.32e-01
29	7.42e-01	6.31e-01	6.47e-01	5.50e-01
30	7.70e-01	6.55e-01	6.63e-01	5.64e-01
31	7.93e-01	6.74e-01	6.76e-01	5.75e-01

Figure F.9: A plot and a listing of CHEMS PHA species boxes efficiencies for detecting C^+ . Triples only efficiencies for C^+ and N^+ cannot be obtained for each telescope, because data from all three telescopes had to be combined to get enough statistics. It is impossible to get an accurate measurement for C^+ and N^+ in the doubles data, so only the triples data should be used when calculating the differential intensity for C^+ and N^+ . As can be seen in this plot, the efficiencies are valid at step 20 and above (vertical dashed line), but note that box definitions for C^+ and N^+ are available only above steps 24 and 25 respectively.



Efficiency Values for O_2^+

DPPS Step	Doubles+Triples		Triples Only		
	ϵ_{tof} all telescopes		ϵ_T Tel. 1	Tel. 2	Tel. 3
17	4.81e-02		0	0	0
18	7.12e-02		0	0	0
19	9.74e-02		0	0	0
20	1.27e-01		0	0	0
21	1.60e-01		0	0	0
22	1.98e-01		0	0	0
23	2.40e-01		0	0	0
24	2.86e-01		2.37e-02	2.15e-02	2.77e-02
25	3.38e-01		5.61e-02	5.49e-02	7.50e-02
26	3.93e-01		1.27e-01	1.42e-01	2.00e-01
27	4.55e-01		2.18e-01	2.28e-01	2.70e-01
28	5.20e-01		3.19e-01	2.93e-01	3.30e-01
29	5.88e-01		3.86e-01	3.60e-01	3.86e-01
30	6.59e-01		4.44e-01	4.27e-01	4.44e-01
31	7.30e-01		4.99e-01	4.92e-01	4.99e-01

Figure F.10: A plot and a listing of CHEMS PHA species boxes efficiencies for detecting O_2^+ . Triples only values can be used at and above DPPS step 24 ($E/Q = 83.4$ keV/e). However, the triples only efficiencies at steps 24 and 25 contain a lot of uncertainty due to doubles background in the in flight data. Some caution should be used when calculating the flux at these energies.

Appendix G

INCA MCP Efficiencies

Full PDF versin of Kostas Dialynas 2013 paper follows

Compensation for INCA MCP efficiencies decrease in years 2010 and 2012
by, *Dialynas K., D. G. Mitchell & S. M. Krimigis*

Emmeritus PI: S. M. Krimigis (*inception to 2015*)

Current PI: D. G. Mitchell (*2016-to date*)

Deputy PI: C. P. Paranicas (*2016-to date*)

Summary

INCA is a large ($\epsilon G \sim 2.4 \text{ cm}^2 \text{ sr}$; where G is the geometric geometry factor, and ϵ is the efficiency) detector, part of the Magnetospheric Imaging Instrument (MIMI) on board the Cassini spacecraft, that analyzes separately the composition and direction of motion of the incident energetic neutral atom (ENA). The detector utilizes a broad field of view (FOV) of $90^\circ \times 120^\circ$ to image large parts of Saturn's magnetosphere (nominal angular resolution of $\sim 5^\circ$ for H). Owing to an on-demand voltage operator in its magnesium deflection plates (serrated to inhibit forward scattering of incident particles), INCA is capable of alternating between two detection modes, namely "ion" and "neutral". When in neutral mode, the $< 500 \text{ keV/e}$ energetic ion particles are adequately swept out of the detector. The detection of the ENAs is then based on the time-of-flight (TOF) technique, and several discrete energy passbands are defined within the energy range of 5.2 to 200 keV.

The measurement technique that INCA incorporates, involves a set of MicroChannel Plates (MCP). When the particles pass through the thin aperture foils, secondary electrons are produced which are first accelerated perpendicular to the foil and are then directed electrostatically onto a "start" MCP, providing the start time for determining the TOF of the neutral particle through the instrument. The incident particle continues through the detector and strike on a foil which is mounted in front of the "stop" MCP assembly, thus creating secondary electrons. These electrons are accelerated towards the stop MCP and the second foil and its secondary electrons provide a stop time for the TOF measurement. In addition, the electrons are projected into a two dimensional position sensitive anode which maps the incident particles. The number of secondary electrons produced in each foil is dependent on the atomic number of the neutral atom and the MCP pulse-height is sufficient to discriminate hydrogen from oxygen, i.e. the two species that INCA measures.

As MCPs age with time, and/or are frequently found in high intensity environments for a long time (thus, getting triggered very often) they start to decay. This decay translates to an efficiencies decrease over time, meaning that the FWHM of the pulse height (PH) distributions slowly decrease over time, that results in underestimating the measured particle rates. This effect can be restored with a MCP voltage raise, but each MCP voltage raise addresses the problem for a limited amount of time before the MCPs start to degrade again. The MIMI team performed two MCP voltage raises, in DOY 15/2011 and DOY 32/2013, to compensate for the sensitivity loss over the years 2010 and 2012 respectively. On-site ion measurements from both the Low-Energy Magnetospheric Measurement System (LEMMS) and the Charge-Energy Measurement System (CHEMS) that complement the MIMI suite, were employed during those periods to determine the level of the gain increase. Recently, in order to compensate for the time periods before the HV gain increases, a new analysis was performed that resulted in time-depended flux factors that were applied to the INCA intensities over the years 2010 and 2012 respectively. Here we will describe the analysis that involves the compensation of INCA MCP efficiencies decrease, and we note that other tasks performed in INCA instrument, e.g. flat field effect etc. are not discussed in this report.

Data used in the analysis

The data used in the present analysis are H^+ from both CHEMS and INCA from Saturn's magnetosphere and correspond to the time period: DOY 206/2009 - DOY 033/2016.

During all cases examined, INCA was on ion mode and the spacecraft was spinning (to obtain a good coverage). CHEMS H^+ measurements are a sum of all three telescopes ($BR0_{sum}$ and $BR3_{sum}$), whereas the INCA measurements are *Avg HiEnergyRes* (Both acquired from MIDL; for details contact Jon Vandegriff). The INCA Pulse Height-PH (back and front) distributions were also used in the analysis, and were obtained from the MIMI code (for details contact Martha Kusterer).

All data used, i.e. both CHEMS (spectra) and INCA (spectra, PH back, PH front & TOF channel line plots) can be found inside the "INCA-MCP-ANALYSIS/DATA" directory that accompany this manuscript (in the following link: [PENDING: The link where all data used here can be found; I have to coordinate with Martha](#))

Effects of INCA efficiencies decrease in TOF channel measurements

During the summer of 2010 we have started taking a close look at the INCA PHA data over the Saturn Tour, and found that the sensitivity at that time was down by $\sim 20\%$ relative to 2004. Furthermore, the single electron peak on the Stop MCP was approaching the electronic threshold, which indicated that the decline was likely to get steeper in the future (which, indeed, turned out to be the case). Due to that, on DOY15/2011 a new set of MCP instructions was uploaded to INCA. Specifically, the MCP voltages increased by $\sim 50V$ (start) and $\sim 100V$ (stop). By continuously monitoring the INCA PHA data after the aforementioned voltage raise, over the first days of 2013 we identified that INCA gain had declined (again) and the MCP voltages were raised accordingly. The final step of increasing the voltages occurred on DOY32/2013 and kept the sensitivity high for the rest of the mission.

This section will explain the effects of the INCA efficiencies decrease in the measurements during years 2010 and 2012. First, we will focus on the Pulse Height distributions (PH) and subsequently on the INCA energy spectra.

INCA Pulse Height Distributions

Figure 1 shows an example of the INCA PH matrix data (PH back), collected in DOY206/2009 (00:00 to 07:00), before the MCP efficiencies decrease. By summing all counts that are found between e.g. 24 to 35 keV energy range (shaded area in Figure 1), one can obtain the TOF5 PH-Back distribution as shown in the right panel of Figure 1.

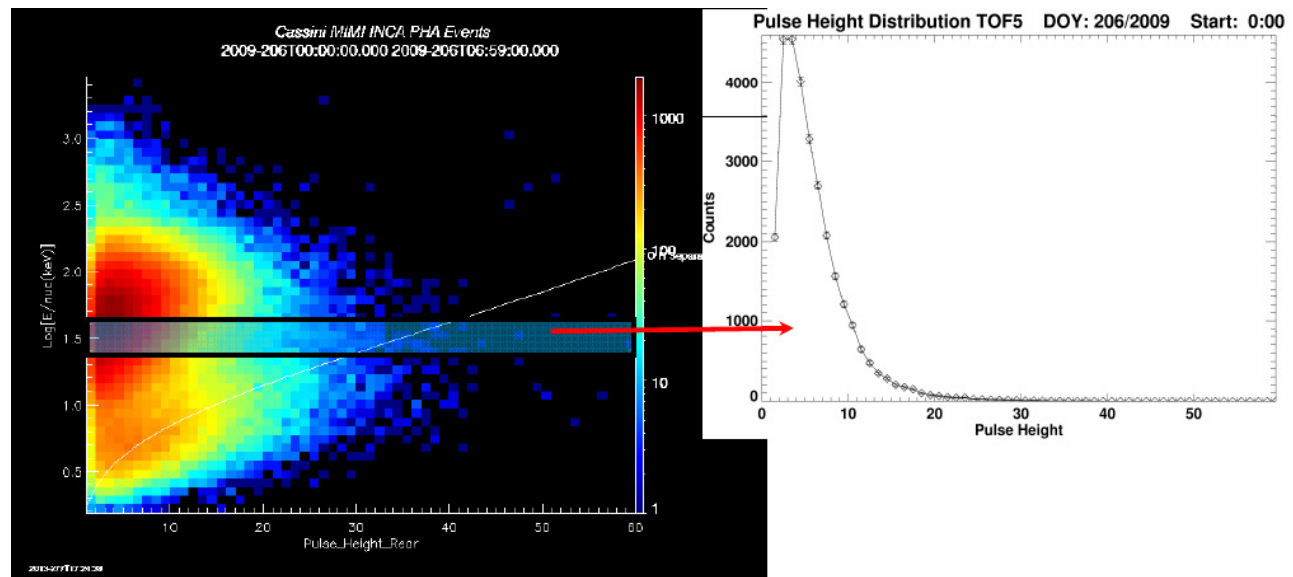


Figure 1: Example of INCA PH-Back matrix (left panel) and the formed TOF5 distribution (right panel) from DOY206/2009.

Ideally, we want to compare all Pulse height distributions through the years and observe the changes that these distributions undergo due to the INCA sensitivity decrease. However, the peak of each distribution can significantly vary in each different case. Therefore, to be able to compare them, we have "self scaled" the distributions according to the following equation (note that the original data as shown in the plots above are in "counts" (C), so the errors related to these data are \sqrt{C}):

$$C_{Scaled} = \frac{C - C_{min}}{C_{max} - C_{min}} \quad (1)$$

This self-scaling of the PH data, transforms the original measurements from the $C_{min} \leq C \leq C_{max}$ space to $0 \leq C_{Scaled} \leq 1$ (since as $C = C_{min}$ or $C = C_{max}$, then $C_{Scaled} = 0$ or $C_{Scaled} = 1$, respectively). As expected, this procedure introduces an error to the self-scaled PH data, imposed by the uncertainties related to the C , C_{min} and C_{max} quantities. The uncertainties per each pixel can be calculated by using the error propagation function:

$$\delta C_{scaled} = \sqrt{\left(\frac{\partial C_{scaled}}{\partial C_{min}} \cdot \delta C_{min}\right)^2 + \left(\frac{\partial C_{scaled}}{\partial C_{max}} \cdot \delta C_{max}\right)^2 + \left(\frac{\partial C_{scaled}}{\partial C} \cdot \delta C\right)^2} \Rightarrow$$

$$\delta C_{scaled} = \sqrt{\left(\frac{\delta C}{C_{max} - C_{min}}\right)^2 + \left(\frac{\delta C_{max}}{C_{max} - C_{min}}\right)^2 \cdot \left(\frac{C - C_{min}}{C_{max} - C_{min}}\right)^2 + \left(\frac{\delta C_{min}}{C_{max} - C_{min}}\right)^2 \cdot \left(\frac{C_{max} - C}{C_{max} - C_{min}}\right)^2} \quad (2)$$

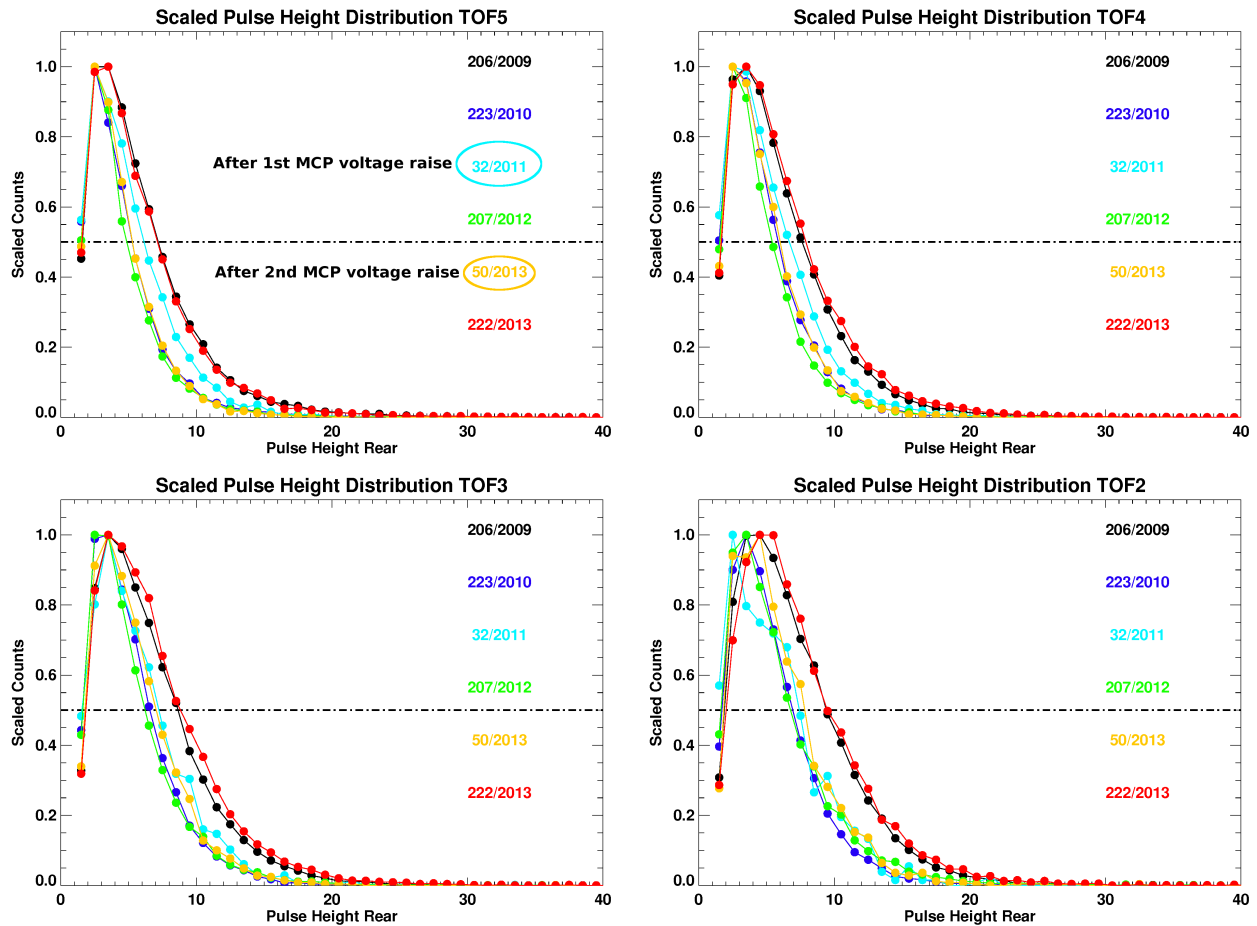


Figure 2: Examples of scaled INCA PH-Back matrix distributions (TOF5-TOF2) for various time periods before and after the 1st and 2nd MCP voltage increases.

It is clear from Eq.1 that since the self-scaling involves a stretching operator between minimum and maximum values, as explained above, the resulting errors in the data will be stretched also (Eq.2), due to the quadrature terms related to the δC_{min} and δC_{max} values. However, for this particular task, we do not calculate the errors in the scaled counts because: 1) we do not expect that those errors will play significant role in the task we are performing (we care for the possible movement of the PH distributions peaks towards lower PHs); and 2) the original data have very small relative errors, $\frac{\delta C}{C}$.

Figures 2 & 3 show some examples of the TOF5-TOF2 Back and Front PH distributions, respectively, before and after the first (DOY15/2011) and second (DOY32/2013) MCP voltage increases. The FWHM of the distributions in Figure 2, for all TOF channels, slowly decreases over time (probably due to the MCP aging) and is restored after each MCP voltage raise. For example, the FWHM of the TOF5 distribution decreases within 2010, it then increases

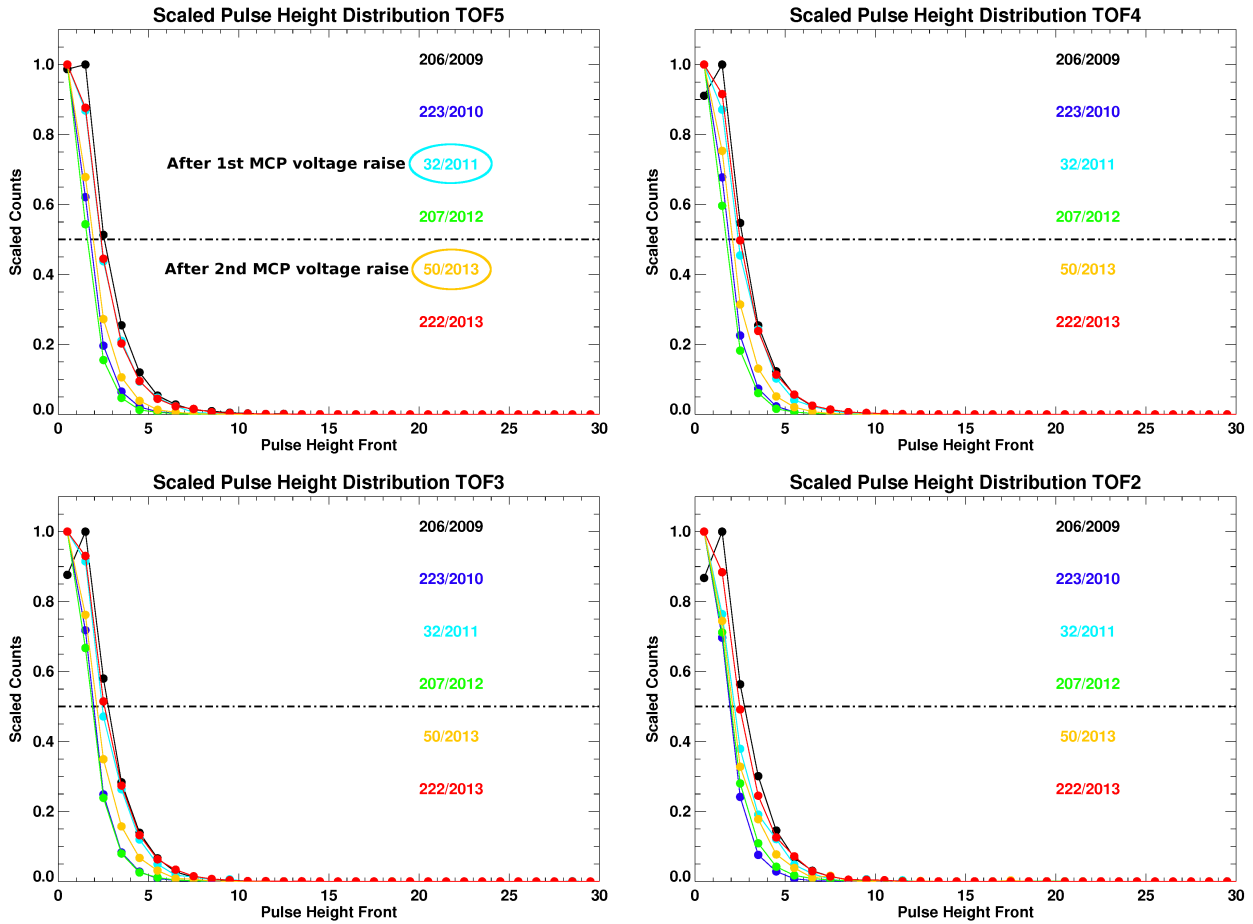


Figure 3: Examples of scaled INCA PH-Front matrix distributions (TOF5-TOF2) for various time periods before and after the 1st and 2nd MCP voltage increases.

after the first MCP voltage raise takes place (DOY 15/2011) and then it is fully restored to the 2009 standards after the second MCP voltage raise that took place in DOY 32/2013. This behavior seems to be systematic among all TOF channels.

The situation concerning the Front PH distributions in Figure 3 is the same as described above. The Front PH distributions showed that the single electron peak on the Start MCP was very close to the electronic threshold, as was the case for the Back PH distributions. However, the Front PH distributions revealed an additional complication:

The front PH distributions are quite narrow (narrower than the “back PH” distributions, as expected) and their peaks are very close to that threshold (or better say “crushed” towards that threshold), which is not something that was done strictly after the INCA sensitivity went out of calibration. By contrast, this appears to be the case, even in the 2005 front PH distributions and it got worst after INCA started losing sensitivity. Each voltage raise gets the FWHM of the PH distributions to the 2009 levels (which are in good agreement with the 2005 levels), but

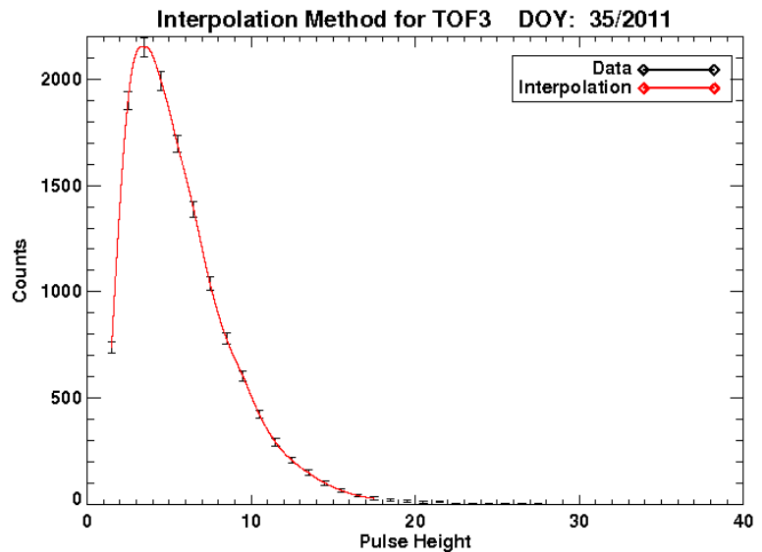


Figure 4: Example of a spline interpolation on the TOF3 PH distribution from DOY35/2011.

the peak still remains very close to the threshold. The reason that the Start PH has never been far above the electronic threshold is unclear, but it is clear that increasing the HV even higher on the MCP generally does not result in a significantly higher PH.

Returning back to the “problem at hand”, the question is: *what happens to the peak of each PH distribution over the years and after each MCP voltage raise?* One method to examine this is by fitting the TOF distributions with Gaussian functions in order to extract information for both the FWHM and the positions of the peaks. However, we have used this method and we have evaluated that it does not work (and if it does work sometimes, it is more or less accidental), simply because these TOF distributions are not necessarily Gaussians (among other reasons).

But, since we are not aiming to obtain a precise model for these data, we can use a simple interpolation method that gives exactly the position of the peak of each TOF distribution. It is much simpler, and much more correlated to the actual TOF data that we analyze than the Gaussian fits (or any other fit). Figure 4 gives an example of the “interpolation method” on the TOF3 distribution from DOY35/2011.

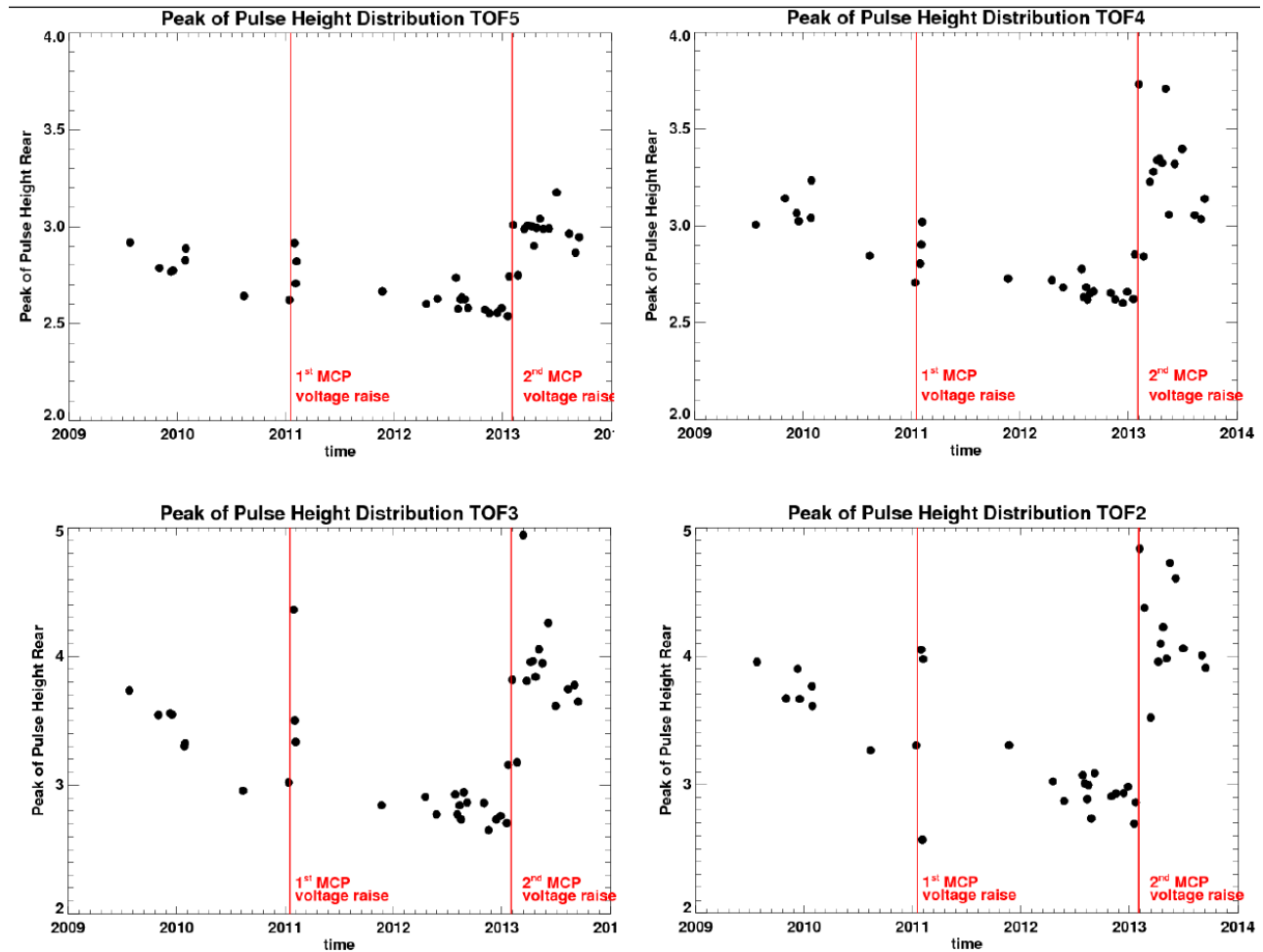


Figure 5: Decay of the peaks of the INCA PH distributions (TOF5-TOF2) as a function of time and restoration after each MCP voltage raise.

This technique showed that the peak of each TOF distribution occurs at lower pulse heights over time following the efficiencies decrease (see Figure 5). Notably, the peaks of the TOF distributions continuously drop before the year 2011, are restored to the 2009 levels after the first MCP voltage raise in DOY 15/2011, they drop again during 2012 and are restored again after the 2nd MCP voltage raise in DOY 32/2013. Clearly, the pulse height distributions undergo significant changes through the last years (>2010) as the MCP age with time. The PH distributions, not only they become narrower with time but their peak also moves to lower pulse heights. This effect is fixed for a limited amount of time, after each MCP HV raise occurs. Here we should note that whether this decay becomes more and more important as time goes by, *i.e.* if, for example, INCA goes out of calibration faster after the second MCP voltage raise compared to the first one, was not examined thoroughly and we cannot draw safe conclusions on this front.

CHEMS and INCA H⁺ Energy Spectra

Figures 6 to 10 show that the INCA spectra are in good agreement with CHEMS during the year 2009, while after that time period (during 2010) the INCA data fall “below” the corresponding CHEMS data. This is fixed after the 1st MCP voltage raise (DOY 15/2011). The INCA data fall again- below CHEMS during 2012 and come back into agreement with CHEMS after the 2nd MCP voltage raise (DOY 32/2013).

To obtain a more “precise” measure of the INCA vs. CHEMS disagreement over the years and (most importantly) what happens after each MCP voltage raise, we have compared the INCA TOF channels directly to the corresponding CHEMS. Of course, the INCA energy passbands do not exactly match the defined CHEMS passbands, so we have used the closest neighbors. For example, the INCA TOF5 channel (24 to 35 keV energy range, i.e. $\sqrt{24 \cdot 35} = 28.98$ keV) is compared to CHEMS 28.13 keV channel, the INCA TOF4 channel (43.87 keV) is compared to CHEMS 42.71 keV channel etc. Table 1 bellow provides all relevant information between the CHEMS-INCA channel comparison.

Table 1. Channel Comparison	
CHEMS Channel (keV)	INCA Channel (keV)
27.3969	28.9828 (TOF5)
41.5953	43.8748 (TOF4)
72.5918	70.3562 (TOF3)
110.088	115.802 (TOF2)

Notably, the comparison was performed/restricted to the TOF5-TOF2 channels and we have not included the other INCA channels to the analysis. The reason is that those channels are the “safest” to use, since, for example, TOF7 is subject to O⁺ contamination and the high energy INCA channels are known to have e⁻ contributions. These contributions, either Oxygen and/or electrons can skew the results and, consequently those “suspect” channels were excluded from the analysis. (Ideally, to be precise, one needs to search over the mission data for time periods inside the magnetosphere where H⁺ measurements are statistically significant so that a comparison between the CHEMS and INCA measured parameters can be performed, but at the same time no O⁺ and/or e⁻ to be present at all, which is definitely not the case.)

The plots shown in Figure 11 are the result of this comparison for each different TOF channel. If we symbolize the CHEMS channels as “C” (this only symbolizes the instrument channels; it is not “counts”!) and INCA TOF channels as “I” (again, this is not the symbol for “intensities”), then the ratio (R) between the corresponding channels is given as:

$$R = \frac{C}{I}, \delta R = \sqrt{\left(\frac{\partial R}{\partial C} \cdot \delta C\right)^2 + \left(\frac{\partial R}{\partial I} \cdot \delta I\right)^2} \quad (3)$$

The comparison between the CHEMS and INCA intensities per each channel in Figure 11 finds INCA struggling to keep up with CHEMS, while each voltage raise seems to get INCA back into agreement with CHEMS for a certain time period. So, the question here is *how much time is this “time period”?*

If we set an arbitrary measure of an “acceptable disagreement” between CHEMS and INCA (i.e. this gray transparent area shown in each plot), we can see that the CHEMS/INCA ratio falls back into this area after each voltage raise, while being outside it every other time. We should note however that the comparison of INCA with CHEMS remained pretty stable after the second MCP voltage raise (which was more “aggressive” than the first one), and, thus, no actions on this front were taken beyond the DOY 32/2013. Although not shown in Figure 11, the CHEMS/INCA ratio remained close to the “acceptable limits” up to the year 2017.

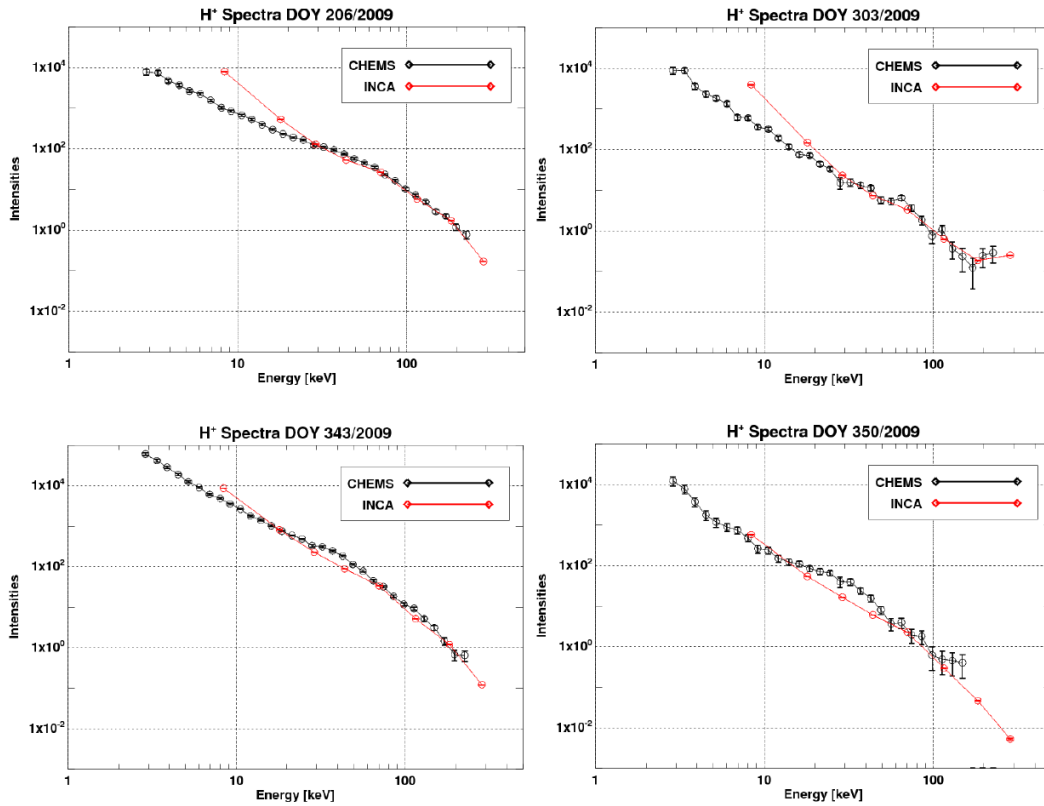


Figure 6: INCA and CHEMS energy spectra over the year 2009, before the INCA efficiencies decrease.

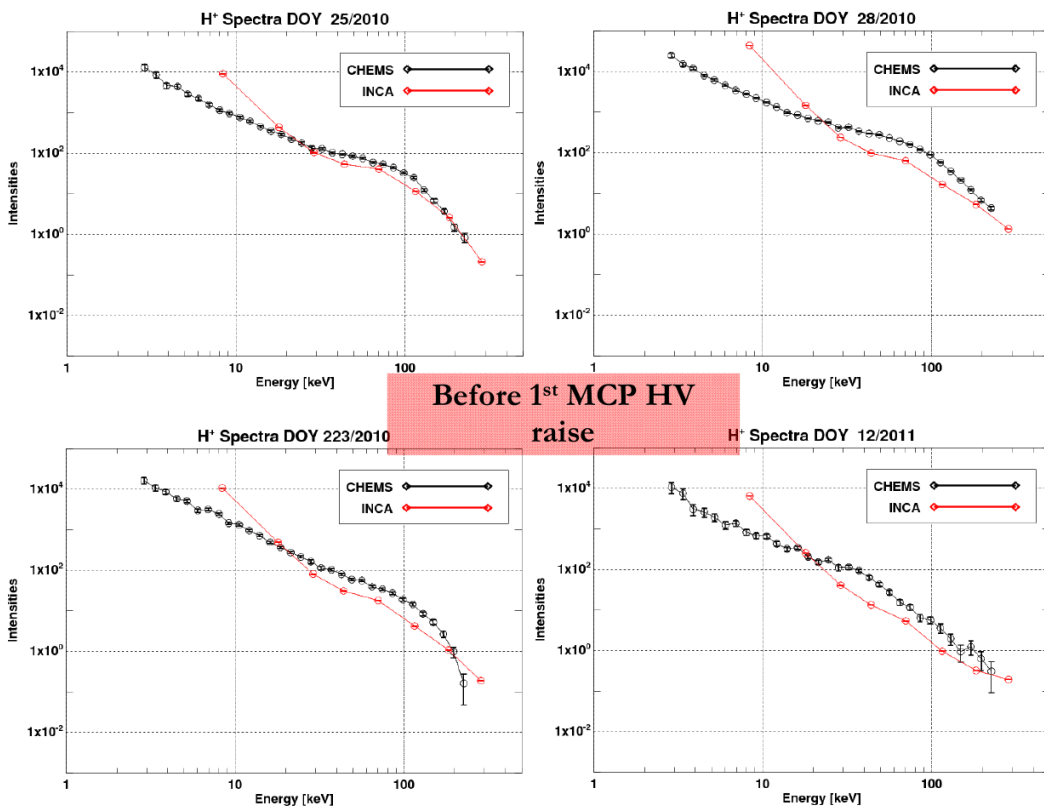


Figure 7: INCA and CHEMS energy spectra over the year 2010, where the INCA efficiencies began to gradually decrease.

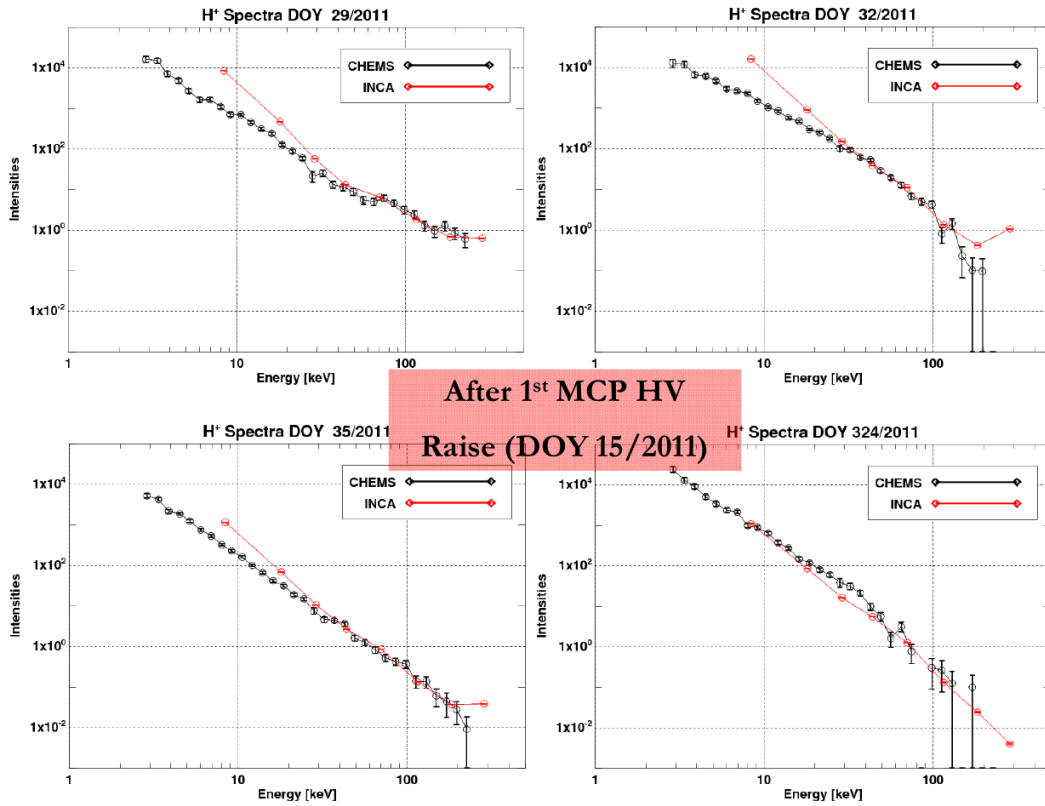


Figure 8: INCA and CHEMS energy spectra over the year 2011, after the 1st MCP voltage raise that was performed in DOY15/2011 to compensate for the INCA efficiencies decrease during 2010.

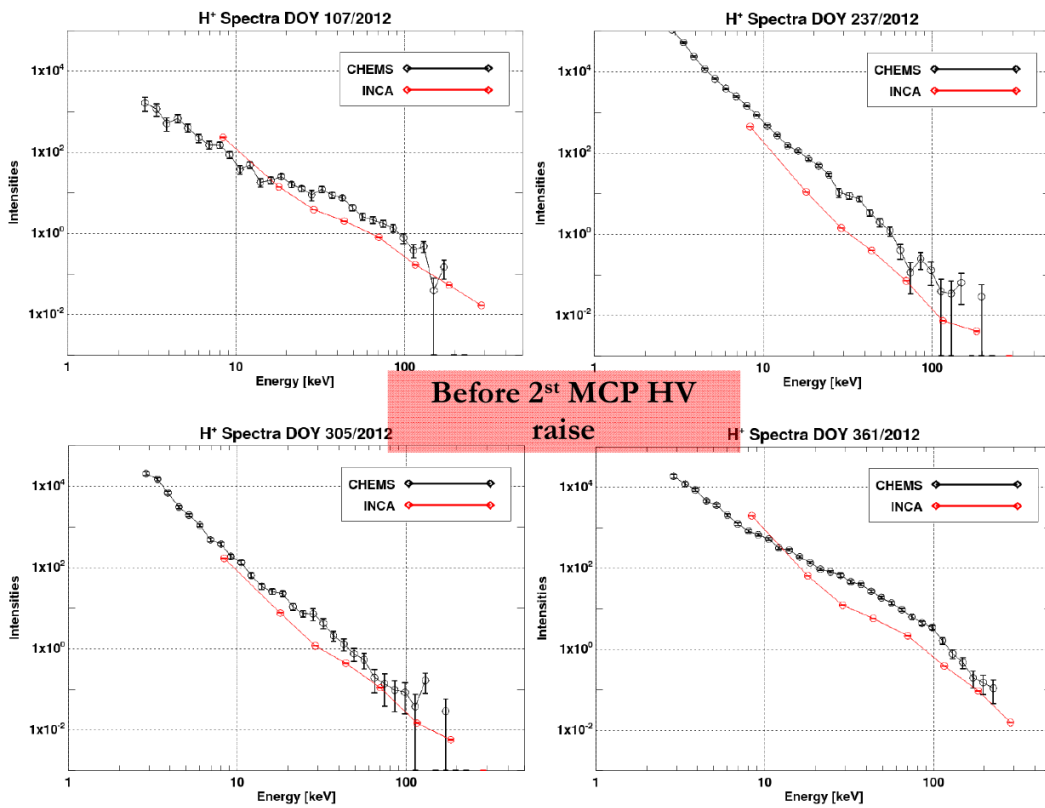


Figure 9: INCA and CHEMS energy spectra over the year 2012, where the INCA efficiencies began to gradually decrease for the second time.

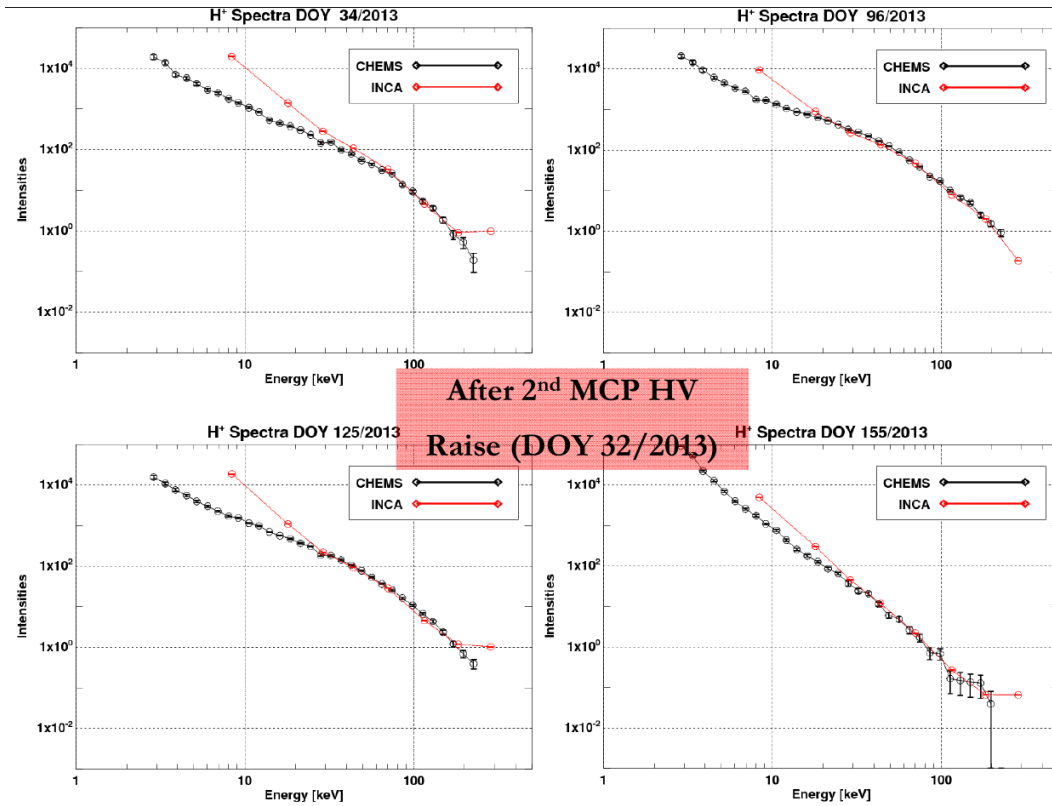


Figure 10: INCA and CHEMS energy spectra over the year 2013, after the 2nd MCP voltage raise that was performed in DOY32/2013 to compensate for the INCA efficiencies decrease during 2012.

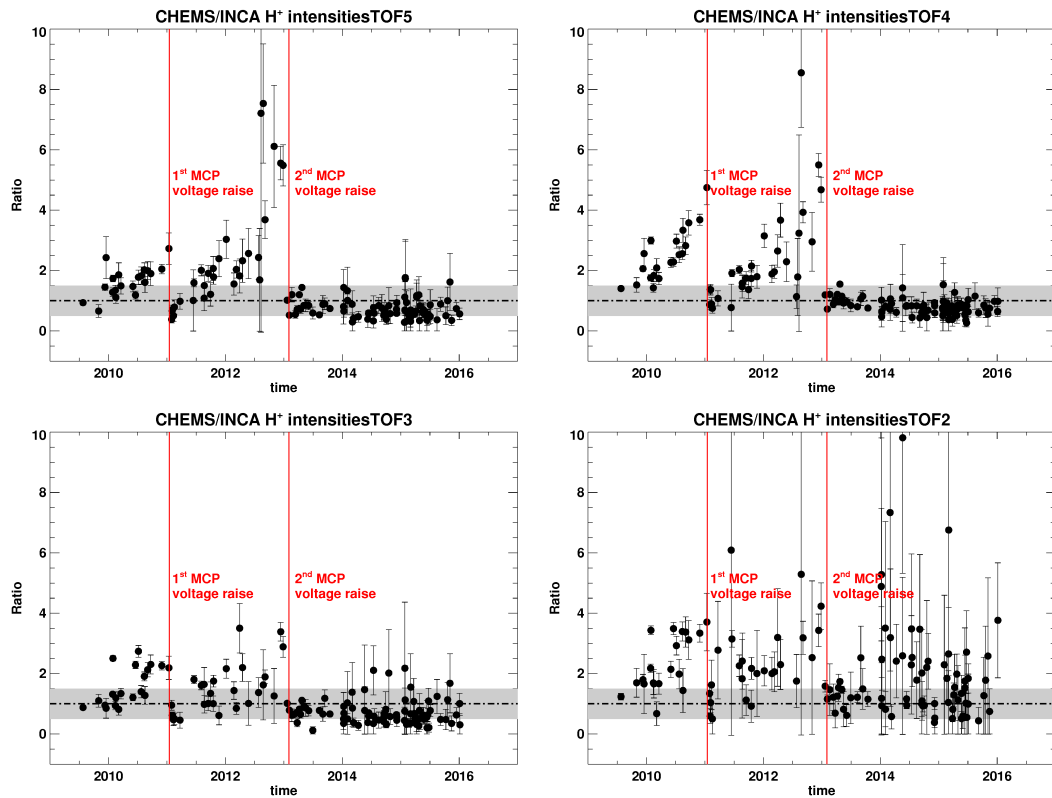


Figure 11: CHEMS/INCA ratio (per each channel; TOF5-TOF2) as a function of time, using Equation 3, as detailed in the text. The positions in time of each MCP voltage raise is shown with red lines.

Compensation for INCA efficiencies decrease

As noted above, each MCP voltage raise fixed the problem for a limited amount of time and we determined that the INCA data over the time periods from the mission beginning up to 2010, 2011 (day 15) to 2012 and 2013 (Day 32) to the end of mission could be trusted and used as acquired from the team's processing software. However, this meant that the INCA data over the years 2010 and 2012 needed to be re-examined and multiplied by some (unknown) factor in order to become useful. This posed two questions: a) what is this factor (and is it the same for 2010 and 2012)? and b) is this factor constant through time (e.g. over the whole 2010 and 2012)?

Figure 11 provides a quick answer to both questions: a) Due to the comparison with CHEMS measurements, the "unknown factor" can be calculated, but it is definitely not the same for 2010 and 2012 and b) whatever this "factor" is, it is definitely not constant throughout 2010 and 2012 (but time dependent). In retrospective, we realized that the unknown factor is not even the same for each TOF channel. Therefore, our goal is to obtain a realistic set of functions (for each TOF channel) that we can use in order to compensate for the low INCA intensities due to the instrument's efficiencies decrease over the years 2010 and 2012, before the 1st and 2nd MCP voltage increases.

We assume that the INCA efficiencies decrease is manifested in the CHEMS per INCA ratios, as explained earlier (Equation 3). Given all the aforementioned techniques, assumptions and interpretations, after producing the ratios as a function of time per each TOF channel, we seek for a function that provides the best fit to these ratios. This analysis treats each TOF channel separately, meaning that each TOF channel Ratio is fitted separately and we obtain a different intensity function.

Since the INCA and CHEMS channels do not match exactly (as noted before and shown in Table 1), we have interpolated the CHEMS intensity measurements in the INCA energy channels and produced the ratios between the interpolated CHEMS data and the native INCA ones. Due to CHEMS' high energy resolution, such an interpolation results in a very accurate reconstruction of the energy spectra (see Figures 13 & 15) giving confidence for the performed analysis. Note that we also performed the same analysis by comparing the INCA measurements to the closest neighbors of CHEMS channels (the native CHEMS channels, as shown in Table 1), but the results were no different from the interpolation method (with the interpolation method producing slightly better results, in terms of χ^2 fit values).

Here we should note that this method is custom and specific to INCA for the time periods mentioned above. Thus, unfortunately there are no published papers in the literature (we have not found any) that deals with such issues in a more robust and technical manner.

This means that we don't really know what a "realistic" function (or set of functions) would be for this task, but since we are looking for "intensity functions", i.e. functions that provide the correct multiplying factors for the INCA intensities for different times, one reasonable interpretation of a realistic function is the following:

1. It has to be a monotonically (one on one) increasing function: The efficiencies can only decrease with time and not change between "decrease" to "increase" and vice versa;
2. It has to be a continuous function (at all times);
3. It has to be a "smooth" function (does not include discontinuities in specific time periods), i.e. its first derivative has to be continuous.

Since we were completely unaware of what kind of function could produce good results, we have used several different "function families", i.e. linear, exponential, polynomial etc as well as different fitting methods e.g. Levenberg-Marquardt, Singular Value Decomposition etc.

The analysis on the 2010 measurements revealed that a 2nd degree "polynomial function" [$f(t) = A + Bt + Ct^2$] provides the best fits (Figures 12, 13), whereas for 2012 a combination of "polynomial" and "linear" [$f(t) = A + Bt$] functions was used (Figures 14, 15).

Results: 2010

1. TOF5: The contribution of parameter C is very small, which makes the function behave almost linearly. The function reduces to ~ 1 towards 2009, a fact that gives confidence to the fit, due to the fact that INCA and CHEMS measurements were comparable over 2009.
2. TOF4: The C parameter is larger here, revealing a more "curved" function. Again, the function reduces to ~ 1 towards 2009.
3. TOF3: Similar results here also.

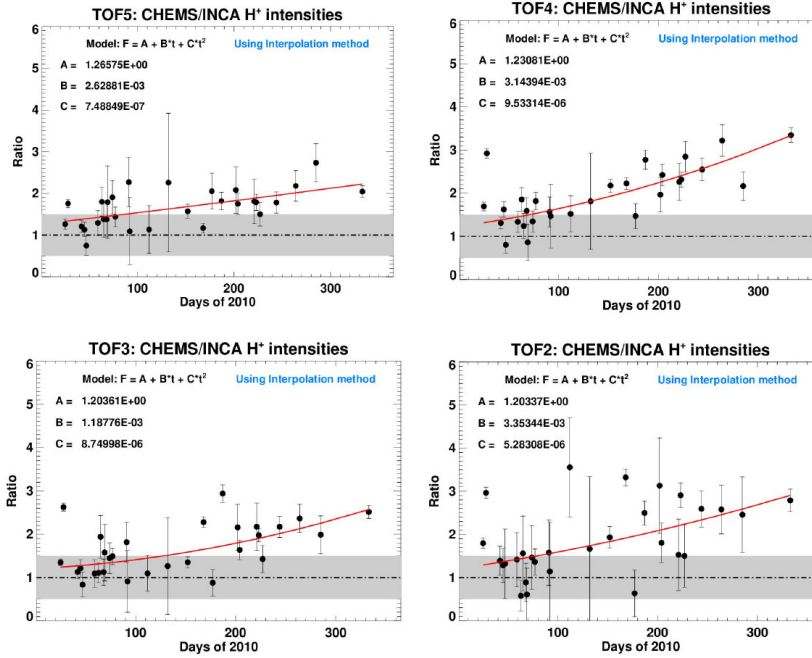


Figure 12: CHEMS/INCA ratio (per each channel; TOF5-TOF2) as a function of time (days within 2010), using Equation 3, as detailed in the text. The red lines represent fits the measurements using a Polynomial function.

4. **TOF2**: Unfortunately, the spread of the data is large, but the function captures the “increasing trend” of the data relatively well (within error bars).

We remind here that we have calculated the ratios for the TOF5-TOF2 channels, as those are the “safest” channels to use for this particular task (see previous section for details). We also make the reasonable assumption that TOF7 & TOF6 will have the same function as TOF5, whereas TOF1 & TOF0 will have the same function as TOF2.

In result, the functions below, apply for the INCA intensities ($cnts/(cm^2srskV)$) over the following time period: **DOY 1/2010 (January 1, 2010) up to DOY 14/2011 (January 14, 2011)**. See Figure 12.

$$\begin{aligned}
 \text{TOF7: } F &= 1.265750 + 2.628812 \times 10^{-3}t + 7.488492 \times 10^{-7}t^2 \\
 \text{TOF6: } F &= 1.265750 + 2.628812 \times 10^{-3}t + 7.488492 \times 10^{-7}t^2 \\
 \text{TOF5: } F &= 1.265750 + 2.628812 \times 10^{-3}t + 7.488492 \times 10^{-7}t^2 \\
 \text{TOF4: } F &= 1.230812 + 3.143936 \times 10^{-3}t + 9.533141 \times 10^{-6}t^2 \\
 \text{TOF3: } F &= 1.203614 + 1.187760 \times 10^{-3}t + 8.749975 \times 10^{-6}t^2 \\
 \text{TOF2: } F &= 1.203367 + 3.353442 \times 10^{-3}t + 5.283079 \times 10^{-6}t^2 \\
 \text{TOF1: } F &= 1.203367 + 3.353442 \times 10^{-3}t + 5.283079 \times 10^{-6}t^2 \\
 \text{TOF0: } F &= 1.203367 + 3.353442 \times 10^{-3}t + 5.283079 \times 10^{-6}t^2
 \end{aligned}$$

The “time” (t) in these equations is in decimal days.

Now we must calculate the uncertainties for the new intensities after applying the flux factors: If our initial INCA intensities are $(J \pm \delta J)$, then the new intensities become $J' = a \cdot J$, where $a = \text{appropriate flux factor extracted from the different } F(t) \text{ functions for each TOF channel at a given time}$. The uncertainty due to this transformation is calculated as $J' = a \cdot \delta J$, meaning that we do not apply any uncertainty due to the flux factor functions that are applied to the initial measurements.

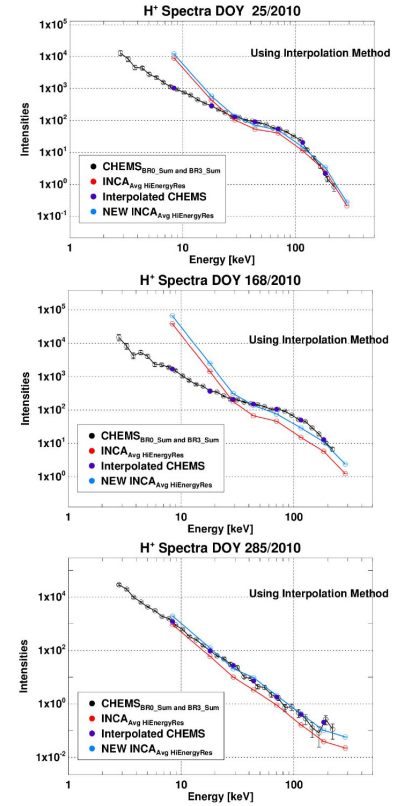


Figure 13: Example CHEMS and INCA energy spectra from early, mid and late 2010 (see label for details).

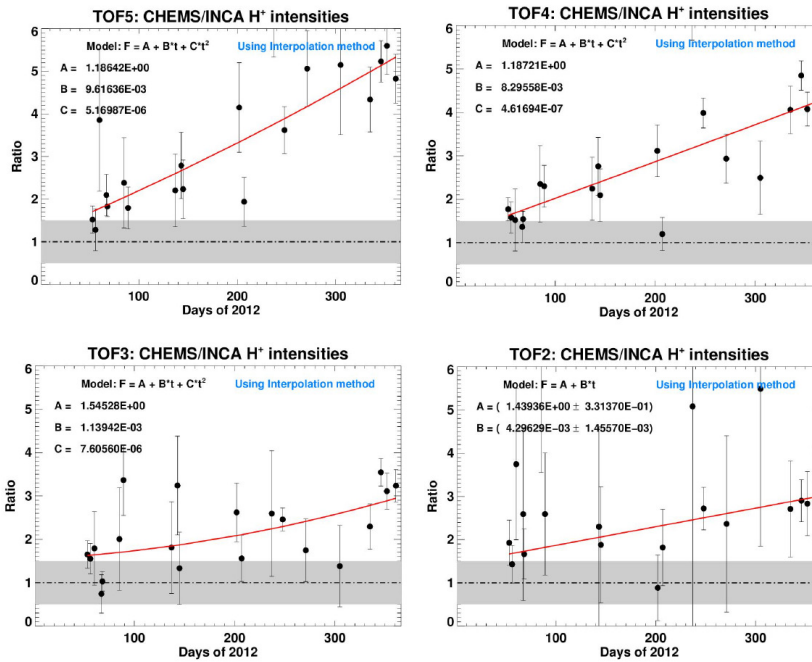


Figure 14: CHEMS/INCA ratio (per each channel; TOF5-TOF2) as a function of time (days within 2012), using Equation 3, as detailed in the text. The red lines represent fits the measurements using a Polynomial (TOF5-TOF3) and a Linear (TOF2) function.

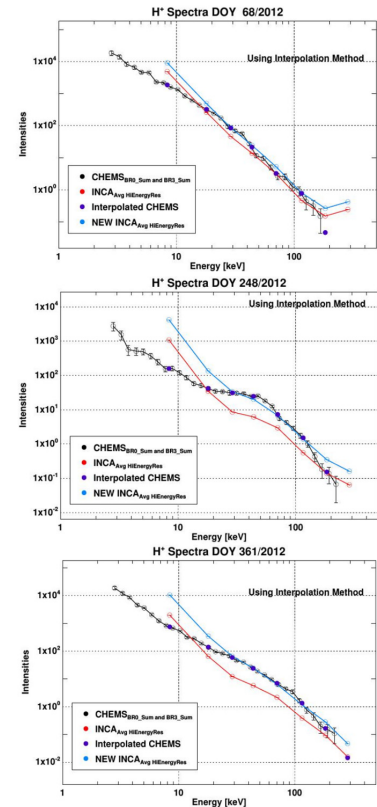


Figure 15: Example CHEMS and INCA energy spectra from early, mid and late 2012 (see label for details).

Figure 13 shows the initial INCA spectra (red line) and the resulting INCA spectra (light blue line) after applying the appropriate flux factors over selected time periods during 2010. The CHEMS spectra (black line) are also plotted for comparison, together with the interpolated CHEMS data (purple points) at energies that are directly comparable to the INCA ones.

Results: 2012

We have applied the same methods as explained in the previous section and we have concluded that:

1. TOF5: The contribution of parameter C in this Polynomial function is very small, which makes the function behave almost linearly. The Linear function (not shown here) gives very similar results with the Polynomial function, while both functions reduce to ~ 1 towards 2011, a fact that gives confidence to the fit, due to the fact that INCA and CHEMS measurements were comparable over 2011.
2. TOF4: Same results here as well.
3. TOF3: The TOF3 ratios are fitted better with the Polynomial function, rather than the Linear (not shown here), but the C parameter is still very small.
4. TOF2: Again, as shown in the 2010 case in the previous section, unfortunately, the spread of the data is large. However, the Polynomial fit (not shown here) was not monotonically increasing and overestimated the ratios towards the start of 2012. By contrast, the Linear function gave significantly better results and captures the “increasing trend” of the data relatively well (within error bars).

The functions below, apply for the INCA intensities ($cnts/(cm^2 sr sk eV)$) over the following time period: **DOY 1/2012 (January 1, 2012) up to DOY 9/2013 (January 9, 2013)**. See Figure 14.

TOF7: $F = 1.186416 + 9.616357 \times 10^{-3}t + 5.169868 \times 10^{-6}t^2$
TOF6: $F = 1.186416 + 9.616357 \times 10^{-3}t + 5.169868 \times 10^{-6}t^2$
TOF5: $F = 1.186416 + 9.616357 \times 10^{-3}t + 5.169868 \times 10^{-6}t^2$
TOF4: $F = 1.187214 + 8.295584 \times 10^{-3}t + 4.616939 \times 10^{-7}t^2$
TOF3: $F = 1.545283 + 1.139424 \times 10^{-3}t + 7.605603 \times 10^{-6}t^2$
TOF2: $F = 1.439359 + 4.296288 \times 10^{-3}t$
TOF1: $F = 1.439359 + 4.296288 \times 10^{-3}t$
TOF0: $F = 1.439359 + 4.296288 \times 10^{-3}t$

Again, the “time” (t) in these equations is in decimal days.

Figure 15 shows the initial INCA spectra (red line) and the resulting INCA spectra (light blue line) after applying the appropriate flux factors over selected time periods during 2012. The CHEMS spectra (black line) are also plotted for comparison, together with the interpolated CHEMS data (purple points) at energies that are directly comparable to the INCA ones.

Example on using the Flux Factors

At this point, let us give an example of how these functions work, by using a test case scenario:

The red line in Figure 16 shows the “old” INCA energy spectra on DOY221/2010, 10:00 am, before we apply the flux factors, together with the CHEMS energy spectra over the same time period (black line) and the reconstructed CHEMS energy spectra using a simple interpolation method (purple line).

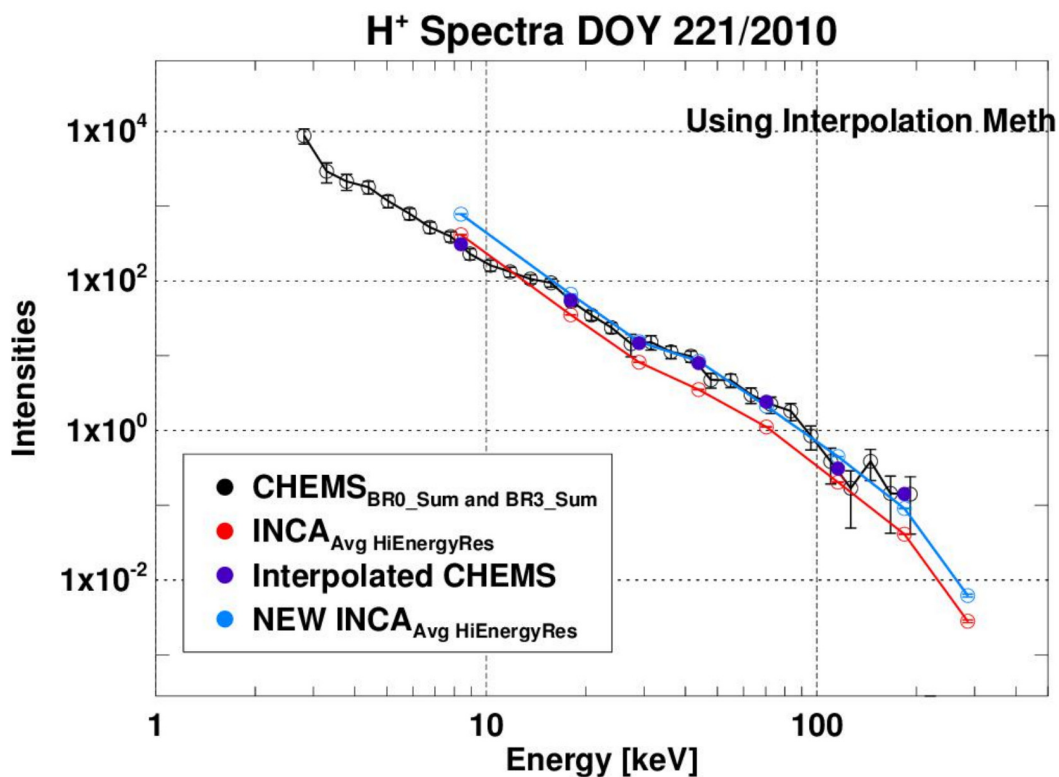


Figure 16: Red Line: Measured INCA spectra. Light blue line: Resulting INCA spectra after applying the flux factors, using $t = 221.417$. Black Line: CHEMS spectra (combined $BR0_{sum}$ and $BR3_{sum}$). Dark blue points: Interpolated CHEMS intensities in the positions of INCA energy passbands (geometrical mean, $E = \text{SQRT}(E1 * E2)$).

The actual data related to the red lines are:

E (keV)	Intensity ($cnts/(cm^2srskV)$)	uncertainty ($cnts/(cm^2srskV)$)
8.37854	414.117	2.41982
18.0000	35.2477	0.127222
28.9828	8.16354	0.0285907
43.8748	3.52391	0.0102265
70.3562	1.11566	0.00358110
115.802	0.203423	0.000791474
183.910	0.0411093	0.000311935
285.867	0.00281371	0.000122192

As we noted, the spectra are sampled on DOY221/2010, 10:00 am which means that -for this particular case- $t = (221 + 10./24.) = 221.417$. This number should be used in the “2010 flux equations” in order to obtain the flux factors for TOF7-TOF0. If we do that, then we find that:

TOF7, TOF6 and TOF5 intensities should be multiplied by a factor of 1.88453; TOF4 by a factor of 2.39430; TOF3 by a factor of 1.89558 and TOF2, TOF1 and TOF0 by a factor of 2.20488. The uncertainties should be treated similarly.

Consequently, the correct INCA spectra for this particular time period would be:

E (keV)	Intensity ($cnts/(cm^2srskV)$)	uncertainty ($cnts/(cm^2srskV)$)
8.37854	780.416	4.56022
18.0000	66.4253	0.239754
28.9828	15.3844	0.0538800
43.8748	8.43730	0.0244853
70.3562	2.11482	0.00678826
115.802	0.448523	0.00174511
183.910	0.0906411	0.000687779
285.867	0.00620389	0.000269419

These corrections are implemented in the MIMI code and no actions from the user are needed on this front.